WRDC-TR-89-3079   **AD-A216 714**

INFLUENCE OF FOREBODY GEOMETRY ON AERODYNAMIC CHARACTERISTICS AND A DESIGN GUIDE FOR DEFINING DEPARTURE/ SPIN RESISTANT FOREBODY CONFIGURATIONS

W. BIHRLE, JR.
B. BARNHART
E. DICKES

Bihrle Applied Research, Incorporated
400 Jericho Turnpike
Jericho, New York 11753

DTIC
ELECTE
JAN 0 9 1990
S E D

FLIGHT DYNAMICS LABORATORY
WRIGHT RESEARCH AND DEVELOPMENT CENTER
AIR FORCE SYSTEMS COMMAND
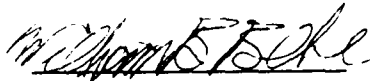WRIGHT PATTERSON AIR FORCE BASE, OHIO 45433-6553
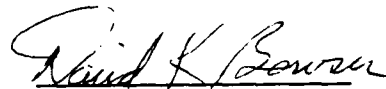
90 01 09 147

NOTICE

WHEN GOVERNMENT DRAWINGS, SPECIFICATIONS, OR OTHER DATA ARE USED FOR ANY PURPOSE OTHER THAN IN CONNECTION WITH A DEFINITELY GOVERNMENT-RELATED PROCUREMENT, THE UNITED STATES GOVERNMENT INCURS NO RESPONSIBILITY OR ANY OBLIGATION WHATSOEVER. THE FACT THAT THE GOVERNMENT MAY HAVE FORMULATED OR IN ANY WAY SUPPLIED THE SAID DRAWINGS, SPECIFICATIONS, OR OTHER DATA, IS NOT TO BE REGARDED BY IMPLICATION, OR OTHERWISE IN ANY MANNER CONSTRUED, AS LICENSING THE HOLDER, OR ANY OTHER PERSON OR CORPORATION; OR AS CONVEYING ANY RIGHTS OR PERMISSION TO MANUFACTURE, USE, OR SELL ANY PATENTED INVENTION THAT MAY IN ANY WAY BE RELATED THERETO.

THIS REPORT HAS BEEN REVIEWED BY THE OFFICE OF PUBLIC AFFAIRS (ASD/PA) AND IS RELEASABLE TO THE NATIONAL TECHNICAL INFORMATION SERVICE (NTIS). AT NTIS IT WILL BE AVAILABLE TO THE GENERAL PUBLIC INCLUDING FOREIGN NATIONS.

THIS TECHNICAL REPORT HAS BEEN REVIEWED AND IS APPROVED FOR PUBLICATION.

WILLIAM B. BLAKE
Project Engineer
Control Dynamics Branch
Flight Control Division

DAVID K. BOWSER, Chief
Control Dynamics Branch
Flight Control Division

FOR THE COMMANDER

H. MAX DAVIS, Assistant for
Research and Technology
Flight Control Division
Flight Dynamics Laboratory

IF YOUR ADDRESS HAS CHANGED, IF YOU WISH TO BE REMOVED FROM OUR MAILING LIST, OR IF THE ADDRESSEE IS NO LONGER EMPLOYED BY YOUR ORGANIZATION PLEASE NOTIFY ___WRDC/FIGC___ , WRIGHT-PATTERSON AFB, OH 45433-_6553_ TO HELP MAINTAIN A CURRENT MAILING LIST.

COPIES OF THIS REPORT SHOULD NOT BE RETURNED UNLESS RETURN IS REQUIRED BY SECURITY CONSIDERATIONS, CONTRACTUAL OBLIGATIONS, OR NOTICE ON A SPECIFIC DOCUMENT.

REPORT DOCUMENTATION PAGE

1a. REPORT SECURITY CLASSIFICATION		1b. RESTRICTIVE MARKINGS	
UNCLASSIFIED			

2a. SECURITY CLASSIFICATION AUTHORITY	3. DISTRIBUTION/AVAILABILITY OF REPORT
2b. DECLASSIFICATION/DOWNGRADING SCHEDULE	Approved for public release; distribution is unlimited.

4. PERFORMING ORGANIZATION REPORT NUMBER(S)	5. MONITORING ORGANIZATION REPORT NUMBER(S)
BAR 89-3	WRDC-TR-89-3079

6a. NAME OF PERFORMING ORGANIZATION	6b. OFFICE SYMBOL (If applicable)	7a. NAME OF MONITORING ORGANIZATION
Bihrle Applied Research, Inc.		Flight Dynamics Laboratory (WRDC/FI) Wright Research and Development Center

6c. ADDRESS (City, State, and ZIP Code)	7b. ADDRESS (City, State, and ZIP Code)
400 Jericho Turnpike Jericho, NY 11753	WRDC/FIGC Wright-Patterson AFB, OH 45433-6553

8a. NAME OF FUNDING/SPONSORING ORGANIZATION	8b. OFFICE SYMBOL (If applicable)	9. PROCUREMENT INSTRUMENT IDENTIFICATION NUMBER
		F33615-86-C-3624

8c. ADDRESS (City, State, and ZIP Code)	10. SOURCE OF FUNDING NUMBERS			
	PROGRAM ELEMENT NO	PROJECT NO	TASK NO	WORK UNIT ACCESSION NO
	65502F	3005	30	77

11. TITLE (Include Security Classification)

Influence of Forebody Geometry on Aerodynamic Characteristics and a Design Guide for Defining Departure/Spin Resistant Forebody Configurations

12. PERSONAL AUTHOR(S)

W. Bihrle, Jr., B. Barnhart, E. Dickes

13a. TYPE OF REPORT	13b. TIME COVERED	14. DATE OF REPORT (Year, Month, Day)	15. PAGE COUNT
Final	FROM 9/86 TO 2/89	89 September	290

16. SUPPLEMENTARY NOTATION

17. COSATI CODES			18. SUBJECT TERMS (Continue on reverse if necessary and identify by block number)	
FIELD	GROUP	SUB-GROUP	Aerodynamics	Departure
01	01		Rotary Balance	Spin
20	04			

19. ABSTRACT (Continue on reverse if necessary and identify by block number)

This report discusses the influence of forebody geometry on aerodynamic characteristics and a design guide for defining departure/spin resistant forebody configurations.

20. DISTRIBUTION/AVAILABILITY OF ABSTRACT			21. ABSTRACT SECURITY CLASSIFICATION
☒ UNCLASSIFIED/UNLIMITED	☐ SAME AS RPT	☐ DTIC USERS	UNCLASSIFIED

22a. NAME OF RESPONSIBLE INDIVIDUAL	22b. TELEPHONE (Include Area Code)	22c. OFFICE SYMBOL
William B. Blake	(513) 255-6764	WRDC/FIGC

DD Form 1473, JUN 86   *Previous editions are obsolete.*

FOREWORD

This report was prepared for the United States Air Force by Bihrle Applied Research, Inc., Jericho, New York, in fulfillment of Contract F33615-86-C-3624, a Phase II SBIR effort, entitled "Development of a Design Guide and Criterion for Defining Departure/Spin Resistant Forebody Configurations." The work reported herein was performed during the period from August 1987 through September 1988, under the sponsorship of the USAF Aeronautical Systems Division, Wright-Patterson Air Force Base, Ohio 45433-6503. Mr. Dieter Multhopp and Mr. William Blake, WRDC/FIGC, monitored the study as the Air Force Project Engineers.

Accession For	
NTIS GRA&I	⊠
DTIC TAB	☐
Unannounced	☐
Justification	
By	
Distribution/	
Availability Codes	
Dist	Avail and/or Special
A-1	

DTIC COPY INSPECTED

iii

TABLE OF CONTENTS

v

LIST OF ILLUSTRATIONS

LIST OF ILLUSTRATIONS (Cont'd)

LIST OF ILLUSTRATIONS (Cont'd)

LIST OF ILLUSTRATIONS (Cont'd)

LIST OF ILLUSTRATIONS (Concluded)

LIST OF TABLES

NOMENCLATURE

b	wing span
$\bar{c}$	mean aerodynamic chord
$\bar{q}$	dynamic pressure
S	wing area
V	free-stream velocity
α	angle of attack, deg.
β	sideslip angle, deg.
Ω	angular velocity about spin axis
$\Omega b/2V$	spin coefficient, positive for clockwise spin
C_L	lift coefficient, Lift force/$\bar{q}S$
$C_{L_{MAX}}$	maximum lift coefficient, Maximum lift force/$\bar{q}S$
C_l	body-axis rolling-moment coefficient, Rolling moment/$\bar{q}Sb$
C_{l_o}	static body-axis rolling-moment coefficient at zero sideslip angle
C_{l_β}	body-axis lateral stability derivative, deg^{-1}
C_m	pitching-moment coefficient, Pitching moment/$\bar{q}S\bar{c}$
C_n	body-axis yawing-moment coefficient, Yawing moment/$\bar{q}Sb$
C_{n_o}	static body-axis yawing-moment coefficient at zero sideslip angle
C_{n_β}	body-axis directional stability derivative, deg^{-1}
FGP	forebody geometry parameter
FR	forebody fineness ratio, forebody length divided by the height of its base
H/W	ratio of forebody base height to width
PYMP	propelling yawing-moment parameter

SECTION 1

INTRODUCTION

The loss of airplanes and occupants attributable to departures from controlled flight and ensuing spins has been a problem since the earliest days of aviation. These losses have plagued both the military and general aviation communities. The phenomena responsible for such losses take on added significance because, in the past ten years, high angle-of-attack capability in the post-stall region has been shown to significantly enhance the air combat maneuvering effectiveness of fighter airplanes and, therefore, this is not a region to be avoided, but rather exploited, if possible. Fortunately, the aerodynamic characteristics that produce departures and spins have been identified within the past few years through rotary balance tests, which identify an airplane's aerodynamic characteristics in a steady rotational flow environment.

It was demonstrated in the Phase I study (Reference 1) that the high angle-of-attack aerodynamic characteristics are very configuration dependent and that forebody geometry can have a significant influence on these characteristics. In the extreme case, an aircraft's undesirable aerodynamics can be completely attributable to the forebody. In this instance, autorotative yawing and rolling moments, as well as increasing nose-up pitching moments with increasing rotation rate, are realized. In addition, large yawing and rolling moments may exist for symmetrical flight conditions. All of these characteristics can be exhibited over a large angle-of-attack range and are most conducive to departure from controlled flight and spins. During the Phase I study, an extensive high angle-of-attack body-alone data base for military configurations was utilized to correlate static and rotational aerodynamic characteristics with forebody design parameters. The results of this study were formulated into a preliminary design guide, which related high angle-of-attack characteristics with forebody geometry.

The good correlation which led to the preliminary design guide indicated that a systematic experimental program and analysis could successfully predict the aircraft behavior associated with forebody geometry. With such information, aircraft designers can perform forebody geometry trade-offs with a high level of confidence that the final forebody geometry selected will not induce departures from controlled

flight or spins, with all the attendant benefits to be realized with vehicles having no angle-of-attack limitations. Of course, the wing and empennage must also be selected on the bases of desirable high angle-of-attack aerodynamics to exploit this maneuvering capability.

The principal technical objective of this Phase II study, therefore, was to develop an appropriate design guide that could be used to predict the aerodynamic characteristics and resulting aircraft responses as a function of forebody geometry. Another objective was to determine the forebody's contribution to static directional stability. (Other researchers have also investigated the forebody's influence on static stability, e.g. References 2 and 3.) To achieve these objectives, the following tasks had to be accomplished:

1) Experimentally determine the static and rotational aerodynamic characteristics for a series of forebodies, selected on the bases of the Phase I study, having different geometric characteristics in the presence of an afterbody. During this task, the fineness ratio, and cross-sectional area were systematically varied.

2) Experimentally determine the aerodynamic contribution for selected forebodies in the presence of a wing and vertical tail representative of a fighter configuration.

3) Develop a forebody design guide employing the experimental results.

4) Experimentally determine the effect of forebody modifications, such as blunting or inclining the forebody or the addition of strakes and chines.

SECTION 2

SUMMARY OF PHASE I EFFORT

All of the airplane models tested on the rotary balance in the past were fabricated such that the wing, horizontal, and vertical tails were independently removable from the body in order to study the aerodynamic contribution of the individual components. As a result of these component build-up tests, body-alone data for all tested military configurations were available for the data base utilized for the Phase I development. The availability of these body-alone data permitted a preliminary analysis of the influence of forebody design characteristics on the static and rotational aerodynamics.

Although it was demonstrated in the Phase I report that the forebody influenced all three body axes moments, these data also indicated that the forebody's most pervasive and critical influence was on the static and rotational yawing-moment characteristics. Therefore, yawing-moment characteristics alone were considered for determining a forebody design guide. However, it was also found from these results that when the forebody produced highly adverse yaw characteristics, the airplane also exhibited adverse roll and pitch characteristics.

The standard practice when computing airplane coefficient data is to non-dimensionalize them with respect to wing area, wing span, chord, and free-stream dynamic pressure. However, in order to compare body-alone data of various airplane configurations, an area and length common to all the bodies was required for the non-dimensionalization. Since the forebody was of concern in the study, the available body yawing-moment data were non-dimensionalized with respect to forebody geometry.[1] The body-alone yawing-moment coefficients based on this non-dimensionalization were designated as C_n* to differentiate them from the standard airplane yawing-moment coefficients.

The study indicated that forebody fineness ratio and cross-sectional shape were important geometric design parameters in determining the aerodynamic

---

[1] The reference area was the cross-sectional area at the forebody planform centroid, and the reference length was the distance from the airplane's moment center to the tip of the forebody.

3

characteristics of forebodies. To include both geometric design parameters within one design guide, a forebody geometry parameter (FGP) was considered which was the product of nose fineness and cross-sectional area ratios (see Figure 1a).

Forebodies were found to produce propelling yaw characteristics in two ways. First, they can generate yawing moments in symmetric flight (C_{n_o}) due to asymmetric vortex shedding. Such static moments can produce nose-slice departures, i.e., the airplane begins to rotate in the direction determined by the sign of the yawing moment. Secondly, they can produce propelling rotational moments such that, when the airplane begins to rotate, the rotation generates moments to increase the rate of rotation. Consequently, a propelling yawing-moment coefficient parameter (PYMP) was developed which consisted of the average area[2] under the C_n^* vs $\Omega b/2V$ curve measured up to 0.4 $\Omega b/2V$ between 40° and 70° angle of attack every 10°. This area was chosen because it is a direct measure of the yawing-moment characteristics discussed above. The angle-of-attack range was chosen because it is generally the region where forebodies have their greatest aerodynamic effect.

It should be appreciated that greatly differing afterbody types were represented within this data set, ranging from essentially slender tubes to flying bodies having widely separated side-mounted engine nacelles. Also, a highly blended configuration was included with strakes that extended from the forebody to the wing leading-edge. Such widely varying afterbody designs might be expected to have some influence on the body-alone yawing moment data and, therefore, produce scatter in the resulting correlation. However, despite this concern, a distinct relationship between PYMP and the FGP was demonstrated (see Figure 1c).

Consequently, the ability to develop this preliminary design guide indicated that a systematic experimental program, with appropriate analysis, could successfully define the forebody geometry that would not induce departures from controlled flight or spins.

---

[2] The area measured was in the propelling quadrant and having C_n^*'s of the same sign as C_{n_o} if present (see Figure 1b).

SECTION 3

EXPERIMENTAL INVESTIGATION

3.1 Technical Approach

Because of the correlation between forebody geometry and aerodynamic characteristics, as demonstrated by the Forebody Geometry Parameter vs PYMP chart in Phase I, the experimental program was designed with the goal of providing a systematic investigation of forebody characteristics as a function of forebody geometry, without varying aft fuselage geometries. In addition, the influence of other parameters, such as forebody bluntness, inclination, chines, and strakes were to be investigated.

After obtaining the forebody data, the tests were repeated for a selected set of forebodies with a wing and vertical tail added to the afterbodies. This was done to illustrate the aerodynamics resulting from the possible interaction of the forebody vortices with other aircraft components.

3.1.1 Models

3.1.1.1 Basic Forebodies

The forebody dimensions chosen are tabulated in Table I (which also includes total body dimensions). These dimensions resulted in a systematic variation of the fineness ratio and cross-sectional shape, as shown in Figure 2. The basis for selecting the 24 forebody models is illustrated by Figure 3, which compares the Phase II model forebodies with the Phase I PYMP vs forebody geometry parameter chart. As shown, the models selected resulted in a large variation in the forebody geometry parameter that extends considerably beyond the range experienced by existing fighter aircraft.

Six forebody fineness ratios were selected, namely 1, 2, 3, 4, 4.5 and 5. The fineness ratio (FR) is defined as the length between the tip and base of the forebody, divided by the height of the forebody at its base. Three cross-sectional shapes (H/W ratios of 0.6, 0.8, and 1.0), having the same base cross-sectional area were constructed. In each case, the forebodies were mounted on afterbodies having constant cross-sections equal to those of the base of the forebodies. Photographs of the FR=4

5

models are presented in Figure 4. The H/W=0.8 forebodies were also rolled 90 degrees and tested on a vertical ellipse afterbody, thus permitting H/W=1.25 forebodies to be tested (see Figure 4d). These forebodies when mounted on the vertical ellipse afterbody, because of the definition of fineness ratio, yielded slightly diminished FR values. However, the resulting fineness ratios (from 0.8 to 4) still provided adequate coverage of probable aircraft values.

3.1.1.2 Airplane

Experience has shown that forebody geometries that have an appreciable aerodynamic influence due to a strong asymmetric vortex in symmetric flight will, in the presence of other components, have additional aerodynamic influences not detected with the isolated forebody. For example, in the presence of the wing, static rolling-moment coefficient off-set values may be realized as well as a different rotational rolling-moment vs angle of attack relationship (see Reference 1). The yawing-moment contribution of the vertical tail may, in the extreme case, also be affected. These effects arise due to interaction of the forebody vortices on the affected surfaces. The aerodynamic characteristics attributable to these forebodies may also be altered (adversely or favorably) when an instrument boom is installed, or by the presence of a canard (possibly with the undeflected and deflected surface producing different effects).

To illustrate the possible influence of forebody characteristics on other airplane components, a vertical tail and wing were added to H/W=0.6 and 1.0 bodies having FR 2 and 5 forebodies. A photograph of the airplane model with the H/W=1.0, FR=5, body is presented in Figure 5. The model dimensions are presented in Figure 6 and are representative of a typical 1/10-scale fighter aircraft model.

3.1.1.3 Blunted Forebodies

To determine the influence of nose bluntness, additional forebody models were constructed for the elliptical cross-sections. These forebodies were constructed with the same shape as the original forebodies up to a point 3" from the tip. From this point to the tip, a polynomial curve fit of the form $r(x)=a_1x^{1/2}+a_2x+a_3x^2$ was used. For example, forebodies with a fineness ratio 5 had their tips rounded to produce equivalent 4.5 and 4 FR forebodies. A sketch of these forebodies is presented in Figure

6

7, and a photograph of the H/W=0.6, FR=5, blunted to 4.5 model is shown in Figure 8. Using the same procedure, the 4 FR forebody shapes were modified to generate equivalent 3 FR blunt forebodies. Table II presents the dimensional characteristics for the blunted forebodies and total body configurations.

3.1.1.4 Inclined Forebodies

By modifying the forebody's upper surface to meet pilot visibility requirements, designers produce an effective droop in the forebody that typically lies between 6° and 10°. To simulate this effect, a wedge was placed between the body and forebody, producing a 7.5° inclined forebody. Investigation of the influence of inclination was conducted with the circular (H/W=1.0) and the elliptical (H/W=0.6) cross-sectional shapes at fineness ratios of 3 and 5. A photograph of the inclined H/W=1.0, FR=5 forebody model is presented in Figure 9. It can be seen that although this technique truly simulated the effect of inclining the forebody, it exaggerates the geometric effect as it would apply to most fighter configurations, since the lower surface of the forebody and aft body would not display the discontinuity shown here.

3.1.1.5 Forebody Chines

Two chine forebodies, which introduced a sharp-edged discontinuity or cusp extending laterally along the length of the forebody, were investigated. The chines of these forebodies, however, were not extended onto the afterbody. Cross-sections of the selected 45° and 135° chine configurations are depicted in Figure 10. Figure 11 presents a photograph of the 135° chine configuration. It should be noted that the projected planform area of the 45° chine forebody was considerably larger than those of the other forebodies tested. The influence of chines was investigated only for a fineness ratio 4, H/W=1.0 forebody.

3.1.1.6 Forebody Strakes

Other considerations may dictate the use of a forebody whose geometry has undesirable aerodynamic characteristics at high angles of attack. Therefore, it would be extremely useful if some device were available to alter the aerodynamics of such a forebody. Various strakes have been used on forebodies, primarily to alter their static directional contribution at and beyond wing stall. Consequently, a strake configuration

(see Figure 12) was tested on a forebody model to illustrate its influence in altering the aerodynamics, both statically and rotationally.

3.1.2 Test Equipment

A rotary balance measures the forces and moments acting on a model while it is subjected to rotational flow conditions. Historical background for this testing technique is discussed in Reference 4. A sketch of the rotary balance apparatus installed in the NASA Langley Spin Tunnel is shown in Figure 13. The system's rotary arm, which rotates about a vertical axis at the tunnel center, is supported by a horizontal boom and is driven by a motor external to the test section.

A NASA six-component strain gauge balance, affixed to the bottom of the rotary balance apparatus and mounted inside the model, is used to measure the six forces and moments acting along and about the model body axis. Controls located outside of the tunnel test section are used to activate motors on the rig, which position the model to the desired attitude. The angle-of-attack range of the rig is $0°$ to $90°$, and the sideslip-angle range is $±30°$. Spin radius and lateral displacement motors are used to position the moment center of the balance on, or at a specific distance from, the spin axis. (This is done for each combination of angle of attack and sideslip angle.) Electrical currents from the balance and to the motors on the rig are conducted through slip rings. Figure 13 identifies various components of the rig and shows how the rig is positioned in angle of attack and sideslip.

The system is capable of rotating up to 90 rpm in either direction. A range of $\Omega b/2V$ values can be obtained by adjusting rotational speed and/or tunnel air flow velocity. (Static aerodynamic forces and moments are obtained when $\Omega=0$.)

The data acquistion, reduction, and presentation system is composed of a 12-channel scanner/voltmeter, a computer with internal printer, a plotter, and a CRT display. This equipment permits data to be presented via on-line digital print-outs and/or graphical plots.

3.1.3 Test Procedures

Rotary aerodynamic data are obtained in two steps. First, the inertial forces and moments (tares) acting on the model at different attitudes and rotational speeds must be determined. Ideally, these inertial terms would be obtained by rotating the model in a vacuum, thus eliminating all aerodynamic forces and moments. As a practical approach, this is approximated closely by enclosing the model in a sealed spherical structure, which rotates with the model without touching it, such that the air immediately surrounding the model is rotated with it. As the rig is rotated at the desired attitude and rate, the inertial forces and moments generated by the model are measured and stored on magnetic disc for later use.

The enclosure is then removed and the force and moment data recorded with the wind tunnel operating. The tares, measured earlier, are then subtracted from these data, leaving only the aerodynamic forces and moments, which are converted to coefficient form.

3.1.4 Test Conditions

The experimental investigation was conducted at a velocity of 25 ft/sec, which corresponds to a Reynolds number of 5.3×10^4 and 2.09×10^5 based on the referenced body diameter and wing chord, respectively. All of the models were tested through an angle-of-attack range of $0°$ to $90°$, in $5°$ increments. Measurements were obtained for each configuration at $\Omega b/2V$ values of 0, 0.05, 0.1, 0.2, 0.3 and 0.4, in both clockwise (pilot's right) and counter-clockwise directions. Additional static data, for a limited angle-of-attack range of $0°$ to $50°$, were also obtained with an aft-mounted sting arrangement to investigate the possibility of sting interference, as well as to evaluate levels of static stability at sideslip angles of $-2.5°$, $-5°$ and $\pm 10°$. The electrical center of the balance was located in the afterbody where the 1/4-chord of a wing would be located, such that the absolute magnitude of the forebody moments measured are representative of an airplane configuration.

3.1.5 Data Presentation

Comparison plots of selected data are presented in this report to illustrate the analysis. In addition, all of the data measured during this investigation are presented in tabulated form in Reference 5. All of these data, both herein and in Reference 5, are non-dimensionalized with respect to the following wing geometric parameters: span=2.8 ft, chord=1.317 ft, and area=3.09 ft^2. This was done so that the relative magnitudes of the coefficient data would be meaningful to aircraft designers. All of the data are presented relative to the body axis[3] for a cg location, as mentioned above, at the 1/4-chord of the wing.

3.2 Forebody Aerodynamic Characteristics

3.2.1 Static

Body-alone static longitudinal and directional aerodynamic characteristics are presented in Figures 14 through 22 as functions of angle of attack. The data are plotted both at constant fineness ratio, to demonstrate the effect of forebody cross-sectional shape, and at constant H/W to demonstrate the influence of fineness ratio. Since an aircraft's body produces essentially no lateral moments, no lateral data are presented.

3.2.1.1 Longitudinal

The influence of cross-sectional shape and fineness ratio on the lift and normal-force coefficient characteristics is presented in Figures 14 and 15, respectively. It is shown that cross-sectional shape rather than fineness ratio is the dominant geometric characteristic influencing these coefficients. The influence of cross-sectional shape is significant throughout most of the angle-of-attack range irrespective of the value of fineness ratio, whereas the main influence of fineness ratio is restricted to approximately the 40°-60° angle-of-attack range for fineness ratios greater than 3.

As one would expect, both maximum lift and normal-force coefficients increase with decreasing H/W at all FR's. On average, the maximum body-alone C_L is attained at

---

[3] except, of course, for the lift coefficient plots included herein

10

approximately 50° angle of attack and for an H/W=0.6 body is approximately 60 percent larger than for an H/W=1.0 body.

The influence of fineness ratio and cross-sectional shape on the pitching-moment coefficient characteristics is presented in Figures 16 and 17, respectively. As shown, fineness ratio affects the pitch characteristics considerably more than cross-sectional shape. The body-alone pitching-moment becomes consistently more nose-up with increasing fineness ratios at all H/W's (Figure 16) as would be expected since increasing FR increases both the moment arm and the area forward of the moment center. The small influence of cross-sectional shape manifests itself as a generally more nose-up moment (see Figure 17), reflecting increased lift and normal force as H/W decreases.

3.2.1.2 Directional

Forebodies can produce yawing moments in symmetric flight (i.e. with no sideslip or rotation) because of asymmetric shedding of the forebody vortices. The symmetric flight yawing-moment coefficients, C_{n_0}'s, are plotted for constant values of H/W in Figure 18. It is seen that, for all H/W's, increasing the fineness ratio increases the peak C_{n_0} experienced and increases the angle-of-attack range over which these C_{n_0}'s exist. In general, the peak C_{n_0}'s also increase with increasing H/W's (see Figure 19) and for fineness ratios greater than 4, all H/W's produced large C_{n_0} values.

The variation of body-alone directional stability with cross-sectional shape is shown in Figure 20 to have generally similar characteristics at each tested fineness ratio. These results were derived by sloping the data between ±10° of sideslip. The vertical ellipse (H/W=1.25) is directionally unstable at all tested angles of attack, while the horizontal ellipse forebodies are stable between approximately 20° and 70°. The circular forebody is generally slightly unstable at all angles of attack. At forebody fineness ratios greater than 4, however, the circular body becomes stable at the higher tested angles of attack, and exhibits a peak level of stability at FR=5 that is comparable to that of the horizontal ellipses.

When the directional stability characteristics are plotted at constant H/W, as in Figure 21, it is seen that the increase in stability for the H/W=0.6 horizontal elliptical bodies occurs at lower angles of attack and increase more rapidly with increasing fineness ratio. At an H/W=0.8, this influence is not as dramatic, and the peak stability levels tend to occur at a higher angle of attack. The circular body is not strongly influenced by fineness ratio,

11

except at FR=5 where the body becomes strongly stable. The vertical ellipse forebody generally becomes more unstable with increasing fineness ratio (except at the largest fineness ratios and angles of attack tested).

The directional stability data from Figure 21 were cross-plotted against H/W at selected angles of attack of 30°, 40°, and 50°, in Figure 22. This figure further illustrates the two trends shown in Figure 20 and 21:

1. Regardless of the fineness ratio, for H/W values of approximately 1.0 and higher, the bodies are unstable, whereas they are stable for H/W values less than 0.9.

2. The stability or instability associated with a given cross-sectional shape generally becomes increasingly magnified with increasing fineness ratio.

3.2.2 Rotational

3.2.2.1 Longitudinal

The influence of fineness ratio on the body-alone rotational pitching-moment characteristics was similar at each tested H/W. Figure 23 presents these characteristics for the H/W=1.0 bodies. For fineness ratios less than 4, any incremental pitching moment produced by rotation is slightly nose-down, while rotation produces slightly nose-up increments for fineness ratios of 4 or greater in the 30° through 50° angle-of-attack range. Above 50°, the rotational effect is nose-down at all tested fineness ratios.

3.2.2.2 Directional

The influence of forebody fineness ratio on the rotational yawing-moment characteristics of the tested bodies is presented in Figures 24 through 27 for all the cross-sectional shapes.

For the two horizontally elliptical forebodies, H/W=0.6 and 0.8, forebody fineness ratio had no significant effect on the yaw characteristics below approximately 20° angle of attack. However, for all angles of attack above 20°, the rotational yaw characteristics did vary as a function of fineness ratio (Figures 24 and 25). These forebodies are generally

12

autorotative in yaw between 20° and approximately 60°, with the autorotative moments generally increasing with increasing fineness ratio. Between 60° and 70° angle of attack, the bodies transition from being propelling to being damped. Above 70°, all configurations were damped in yaw, with a small increase in damping being produced by increasing fineness ratio.

The effect of fineness ratio on the body-alone rotational yawing-moment characteristics for the circular (H/W=1.0) cross-section forebodies is presented in Figure 26. For these forebodies, fineness ratio had no influence through 10° angle of attack. Above 10° and continuing through approximately 25° angle of attack, the yaw damping increases with increasing fineness ratio. Above 25°, the damping still generally increases with increasing fineness ratio for the lower fineness ratios (≤3). In general, the forebodies with circular cross-sections retain damped yawing-moment slopes at all angles of attack for all tested fineness ratios ≤4.5. The fineness ratio 5 forebody, however, becomes propelling in the 40° through 55° angle-of-attack region. It was previously observed that this forebody also exhibited positive directional stability in this same angle-of-attack region. Both of these characteristics are similar to those observed for the horizontal ellipse cross-section forebodies. Evidently, with a sufficiently large fineness ratio, the nose vortex behavior of the circular forebody produces similar results to those produced by an elliptical cross-section at lower FR's.

The vertical ellipse cross-section forebodies (H/W=1.25) are damped in yaw and exhibit similar influences of fineness ratio on rotational yawing moment as those observed for the circular forebody (Figure 27). However, no fineness ratios greater than four were tested for these forebodies, so it is not known if propelling yaw characteristics could be attained for a vertical ellipse by a sufficiently long forebody.

The body-alone rotational yawing-moment coefficient data were replotted at constant fineness ratio to demonstrate the influences of H/W in Figures 28 through 33 for fineness ratios of 1 to 5, respectively. In most cases, the circular cross-sectional bodies (H/W=1.0) are significantly more damped than the H/W=0.6 elliptical bodies, especially between 25° and 60° angles of attack where the H/W=0.6 bodies are very propelling and the H/W=1.0 bodies are generally modestly to well damped. The rotational yawing-moment characteristics of the H/W=0.8 elliptical bodies generally lie between those of the H/W=0.6 and 1.0 bodies, but in most cases they more nearly mirror the results of the H/W=0.6 bodies.

At the largest fineness ratios (FR=5), as shown previously, the H/W=1.0 body becomes propelling, nearly to the same extent as the two horizontal ellipse cross-sections between 30° and 50° angles of attack. However, it becomes damped again by 60°, whereas the H/W=0.6 body remains propelling to nearly 70°.

3.3 Forebody Interaction with Airplane Components

Experience has shown that the forebody geometries that have an appreciable influence on rotational yaw characteristics will, in the presence of other components, produce additional aerodynamic influences not detected with the isolated forebody. This evidently occurs because of interaction of the forebody vortices on the other aircraft components.

An investigation was conducted to measure the force and moment characteristics for bodies of circular and elliptic cross sections (H/W=0.6) attached to a thin wing and vertical tail. Details of the wing and vertical tail are shown in Figure 6. The wing has a 50 degree leading-edge sweep and an aspect ratio of 5.08. The vertical tail was mounted on the tested fuselages as shown in Figure 6.

3.3.1 Static

Component build-up plots of the symmetric flight static yawing and rolling-moment coefficients are presented in Figure 34 for all the tested body cross-section and forebody fineness ratio combinations. It is seen that large total airplane C_{n_O} characteristics are basically determined by the forebody characteristics; i.e. at low FR's, where the forebody does not produce significant C_{n_O}'s, the presence of the wing and vertical tail does not introduce any sizable C_{n_O} either. At large FR's, however, where the body produces large levels of C_{n_O}, the other configurations also exhibit large C_{n_O}'s (although they may be modified or lessened by the presence of the other components).

The wing, in the presence of a low FR forebody, does not produce large rolling moments in symmetric flight. The presence of a high fineness ratio forebody, however, produces significant levels of C_{l_O}. Apparently, the asymmetric forebody vortices that produce the C_{n_O}'s also influence the wing by causing a difference in local angle of attack and/or dynamic pressure between significant portions of the right and left wings. This

14

results in a greater normal force being generated on one wing than on the other and, hence, a rolling moment in symmetric flight.

Vertical tails, typically, produce virtually all of an aircraft's directional stability in the normal flight regime, but they generally become ineffective, or counter productive, near stall and above. Some designers, therefore, have tailored their forebody shapes to provide directional stability significantly beyond stall.

The directional stability characteristics of total airplane configurations (body+wing+vertical tail) having elliptical (H/W=0.6) and circular (H/W=1.0) cross-sectional shapes and forebody fineness ratios of 2 and 5 are presented in Figure 35. Having a directionally stable body-alone configuration may not necessarily result in a directionally stable total airplane, once the vertical tail ceases to provide stability, as demonstrated in Figure 35 by the elliptical FR=2 and circular FR=5 results. Although each of these bodies was directionally stable above 25° an$r$'. $\ldots$ attack, their total configurations became unstable above approximately 25°. The directionally stable elliptical FR=5 forebody, however, did produce an airplane that remained statically stable through the tested angle-of-attack region. Not surprisingly, the directionally unstable circular FR=2 body also resulted in an unstable airplane configuration beyond stall. Obviously, the phenomenon involved in determining a total configuration's yaw characteristics at high angles of attack can be complicated by interference effects.

3.3.2 Rotational

For the H/W=0.6 body with a FR=2 forebody, the addition of the vertical tail and wing resulted in a damped configuration at virtually all angles of attack (Figure 36), primarily because the vertical tail contributed yaw damping at all angles of attack and the wing also contributed damping through approximately 60°. These contributions were sufficient to overcome the propelling yawing moments produced by the body alone. However, when the forebody fineness ratio is increased to 5, the vertical tail and wing contributions are no longer able to overcome the propelling body contribution by 40° angle of attack (Figure 37). In fact, at 50° angle of attack, the total airplane's yawing-moment characteristics are completely dominated by the body's contribution. Evidently, the forebody's vortices produce significant interference effects on the vertical tail and wing, such that they are completely ineffective at these angles of attack. Above 65° angle of attack, the vertical tail is again able to produce a damped configuration.

For the circular (H/W=1.0) body with a FR=2 forebody, the body's yaw contribution is damped at all angles of attack (Figure 36), and, consequently, adding the wing and vertical tail produced damped yaw characteristics that equalled or exceeded those of the body alone. For the circular body with a FR=5 forebody (Figure 37), adding the wing and vertical tail produced a configuration that was damped in yaw at all angles of attack, largely because of the modifying influence of the wing at the angles of attack where the body alone was very propelling.

All of these results are probably dependent on the relative forebody/wing/vertical tail arrangement chosen for this study. In general, the ability of the wing or vertical tail to overcome a propelling forebody characteristic should not be relied upon.

Most airplanes exhibit some propelling rolling moments near stall as a result of differences in lift between the downgoing and upgoing wings. Figures 38 and 39 present the rotational rolling moment build-ups for airplane configurations with H/W's of 0.6 and 1.0 and fineness ratios of 2 and 5, respectively, at selected angles of attack. As would be expected, the bodies alone produce essentially no rolling moment; however, the forebodies do influence the rolling moment produced by the wing.

At FR=2, the wing exhibits propelling rolling moments only between approximately 30° and 40° angles of attack that are not significantly influenced by the body cross-sectional shape, as shown in Figure 38. For an airplane configuration having a forebody fineness ratio of 5, however, body cross-sectional shape significantly influences the roll damping characteristics, as shown in Figure 39. For the elliptical cross-section, the airplane wing is highly autorotative over a large angle-of-attack range, whereas for the circular cross-section body the wing is damped in this region.

A comparison of the forebody data presented in Figures 38 and 39b illustrate that forebody fineness ratio also can greatly alter a wing's rolling characteristics. These results demonstrate that the influence of forebody geometry on wing characteristics must also be considered during the design phase.

The rotational pitch characteristics of the bodies alone are reflected in those of the total airplane, i.e. at the low fineness ratios rotation produces additional nose-down increments, but at the larger fineness ratios, the incremental pitch due to rotation is nose-up

over a significant angle-of-attack range. Plots of the component build-up pitching moments are not included here, but the data are all available in Reference 5.

These test results, as well as those of many fighter aircraft configuration studies (e.g., Reference 6), have clearly indicated that forebody configurations that produce highly propelling yawing moments (e.g. horizontally elliptical cross-sections of high fineness ratio) tend to produce airplane configurations that are also highly propelling in roll and can produce nose-up rotational pitch increments. These characteristics are all undesirable for flight at large angles of attack and could lead to violent departures and spins.

3.4 Effect of Modifying Forebodies

3.4.1 Blunted

As shown in Figure 7 and discussed earlier, a series of forebodies were constructed that had their tips blunted to a lower fineness ratio. The H/W=0.6, 0.8, and 1.25 bodies were selected for this study.

The static lift and normal-force coefficient data are plotted in Figures 40 through 42 for the three H/W's tested. In general, fineness ratio has little influence on these data, except near $C_{L_{MAX}}$. As would be expected, blunting also has little influence except in this same region. Depending on the cross-sectional shape and original fineness ratio, blunting appears to have either no significant effect, or to produce a lower $C_{L_{MAX}}$ than the unblunted forebody. The influence of forebody blunting on body-alone static pitch characteristics (Figures 43 through 45) is to generally produce peak moments lying between those of the original pointed forebody and a pointed forebody having the same fineness ratio as the blunted one.

The influence of forebody blunting on static yawing moment in symmetric flight is demonstrated by Figures 46 through 48. In general, forebody blunting will either have no significant influence or will reduce appreciably the angle-of-attack range where C_{n_0}'s are realized, and/or greatly reduce the C_{n_0} magnitude. Only for the H/W=0.6 forebody, blunted from 4 to 3 fineness ratio, was the resulting C_{n_0} increased over that of the pointed forebodies, and none of these levels was large compared to the C_{n_0}'s produced by the pointed FR=4.5 to 5 forebodies. Figures 49 and 50 demonstrate that forebody blunting had no significant influence on the body-alone static directional stability.

17

Blunting the forebodies, generally, produced rotational pitch characteristics similar to those of a pointed forebody of the same fineness ratio (Figure 51).

This limited evaluation of the influence of forebody blunting for bodies alone indicates that, below 50° angle of attack, blunting the nose may have either a beneficial effect or a negligible effect on yaw damping, but based on these results at least, it does not appear to have any adverse effects. Above 50° angle of attack, forebody blunting apparently can introduce propelling yawing moments in some cases. The degree of influence due to nose blunting appears to be dependent on the forebody cross-sectional shape, as discussed below.

Figure 52 presents the rotational yawing-moment characteristics of the H/W=0.6 forebody with a 5 fineness ratio shape blunted to a 4.5 fineness ratio. The sharp-tipped 5 and 4.5 fineness ratio data are shown, too, for comparison. Figure 53 presents similar results for the same forebody shape blunted from 5 to 4 fineness ratio. All of these forebodies, whether blunted or pointed, are propelling, with the 4.5 and 5.0 pointed forebodies having nearly identical yaw characteristics. Comparison of Figures 52 and 53 shows that for the H/W=0.6 forebody cross-section, blunting the 5 fineness ratio forebody to either 4.5 or 4 produces rotational yaw characteristics that are nearly identical to the pointed 4 fineness ratio results, which are generally slightly less propelling than the longer fineness ratio sharp forebodies.

For the H/W=0.6 pointed forebodies, there, also, is little difference between the fineness ratio 4 and 3 rotational yawing-moment characteristics. The yaw characteristics obtained for a forebody blunted from a 4 to a 3 fineness ratio are, likewise, essentially the same except that they are shifted slightly relative to the zero rotation rate (Figure 54). This shift is responsible for the larger C_{n_o}'s observed for this blunted forebody compared to either of those for the 3 or 4 pointed forebodies (Figure 46c).

Blunting the H/W=0.8 elliptical cross-sectional forebodies from 5 to either 4.5 or 4 generally produces less propelling yawing moments below approximately 50°, but more propelling moments by 60° angle of attack (Figure 55). When the forebody is blunted to 4, the improvement in damping at the lower angles of attack is much greater than when it is blunted to 4.5, but it becomes more propelling at 60°.

18

The rotational yawing-moment characteristics of the H/W=0.8 pointed forebodies show a much greater difference between the fineness ratio 4 and 3 data than was observed for the H/W=0.6 forebodies. Consequently, for this cross-sectional shape, blunting the 4 forebody shows a larger influence as well (Figure 56). At angles of attack through approximately 50°, the blunted forebody data, in general, behaves more like the pointed FR=3 forebody data; while at 60° angle of attack it behaves more like the 4 fineness ratio pointed forebody data.

For the H/W=1.25 bodies, which were damped in yaw at all angles of attack, blunting the forebody did not appreciably alter the damped characteristics of this series of forebodies. It did shift the rotational yawing-moment curves somewhat at a given angle of attack (e.g. Figure 58).

3.4.2 Inclined

A limited test was performed to investigate the effect of inclining the forebody , for pilot visibility requirements, on the aerodynamic characteristics. A wedge was placed between the forebody and afterbody, producing a 7.5 degree inclined forebody. Although additional tests are needed to fully quantify these effects, some observations have been made.

Inclining the forebody had effectively no influence on the lift or normal-force coefficients and resulted in a small shift of the pitching moment versus angle of attack. While this shift is not equal to the incline angle, the correspondence is generally close enough to indicate that the cause is roughly geometric. The static pitching-moment coefficient versus angle of attack for the basic and inclined nose fineness ratio 3 and 5 forebody configurations is presented in Figures 59 and 60 for H/W=0.6 and 1.0, respectively.

The maximum values of yawing moment in symmetric flight were also affected by the inclined forebodies (see Figures 61 and 62), as well as the angle-of-attack range over which they are experienced. These inclined effects appear to be a function of forebody cross-section and fineness ratio.

The rotational yawing-moment coefficients are presented in Figures 63 through 65 for the tested inclined forebodies (H/W=0.6 and 1.0 for fineness ratios of 3 and 5).

Generally, inclining the forebodies did not greatly influence the overall yawing-moment characteristics of the propelling H/W=0.6 bodies, nor the damped characteristics of the circular fineness ratio 3 body. For the circular cross-section fineness ratio 5 forebody, however, a significant beneficial effect of the inclined forebody is clearly evident, as shown in Figure 65.

Directional stability results for the basic and inclined forebody configurations are presented in Figures 66 and 67 for the H/W=0.6 and 1 forebodies, respectively. In general, inclining the forebody had only small, generally destabilizing influences on the body-alone directional stability, except for the circular (H/W=1.0) fineness ratio 5 forebody where it completely eliminated the directional stability generated by this uninclined forebody above 25° angle of attack.

3.4.3 Chines

As shown in Figure 10, two chined forebodies were also tested. These represented two different chine angles (45° and 135°) attached to a circular cross-sectioned forebody of fineness ratio 4. The 45° chine, as shown, produced a significant increase in forebody planform area compared to the unchined circular forebody. The 135° chine, on the other hand, represented only a very small increase in forebody planform area. As a result of their relative planform areas, the 45° chined forebody exhibited larger lift and normal force (Figure 68) and pitching moments (Figure 69) than the basic unchined body, while the differences due to the 135° chine were not significant.

The basic unchined body, due to the long forebody fineness ratio, exhibits significant C_{n_o}'s in the 30 to 70 degree angle-of-attack region. These static zero-sideslip yawing moments are essentially eliminated with the addition of either chine, as shown in Figure 69. Figure 70 shows directional stability results for the basic and chined-nose configurations. Above 20 degrees angle of attack both sets of chines provide similar stabilizing effects.

The rotational yawing-moment characteristics of the chined forebodies are dramatically different than those of the basic circular forebody (Figure 71). The basic circular body exhibits very damped yawing-moments with rotation throughout the tested angle-of-attack range, albeit with significant static yawing-moment off-sets in the 35° to

20

65° angle-of attack region. While either chine essentially eliminates these static off-set values, they also produce significant propelling yawing moments.

For the case considered here, the addition of either chine to a damped basic forebody produced a propelling forebody. Evidently, the presence of the chines caused the forebody to behave, both statically and rotationally, more like a horizontally elliptical cross-sectioned forebody. Adding chines to a different shaped forebody, such as one that was already elliptical for example, may produce different results.

3.4.4 Strakes

As shown in Figure 12, small strakes were tested at the forebody tip of the H/W=0.8, FR=4.5 forebody. These strakes were mounted in a "V" position, as shown, being raised 40° from the horizontal on both sides. This configuration was chosen because of its demonstrated efficacy on previously tested airplane configurations.

The influence of the V-strakes on static symmetric flight yawing moment is shown in Figure 72. These strakes did not greatly improve the significant C_{n_0}'s observed with this forebody. The V-strakes also caused a reduction in body-alone directional stability above 30° angle of attack (Figure 73).

The V-strakes, however, dramatically influenced the rotational yaw characteristics of this body, as shown in Figure 74, by changing the propelling yawing moments observed through 50° angle of attack without the strakes to highly damped moments with them.

Therefore, such strakes provide a means to significantly modify a highly propelling forebody, but possibly at the expense of directional stability at very high angles of attack. These effects should be systematically investigated in the presence of other airplane components, as well, to determine if body-alone static characteristics are reflected in the total airplane characteristics and if they have any influence on the airplane's lateral characteristics.

SECTION 4

DEVELOPMENT OF DEPARTURE/SPIN RESISTANT DESIGN GUIDE

As mentioned previously, the Phase I report demonstrated that a distinct relationship (see Figure 1c) existed between the body propelling yawing-moment characteristics and airplane forebody geometry[4]. Because of the successful Phase I correlation, a similar exercise was performed with the basic forebody yawing-moment data obtained during Phase II.

The propelling yawing-moment parameter (PYMP) values were determined by measuring the area under the rotational yawing-moment curve, between 0 and $0.4 \, \Omega b/2V$, when the curve was in a propelling quadrant. This was done at each tested angle of attack between 30° and 65°, and the results were averaged to determine the PYMP value. This differs slightly from the procedure used during Phase I because the Phase II tests measured data at every 5° angle of attack, whereas body-alone data used for the Phase I analysis was only available at 10° increments. As a result, more data points are averaged to determine the Phase II PYMP values.

Although many geometric parameters were considered for the independent variable when presenting PYMP values, the most practical and logical was found to be fineness ratio. Figure 75 presents such a plot for all the basic forebodies tested.

When fineness ratio has an influence on the measured PYMP values, these values increase linearly at essentially the same rate for all cross-sectional shapes, and the resulting slope is displaced to increasingly higher values of PYMP for decreasing values of H/W. Increasing the fineness ratio beyond 4 produces no further increase in PYMP for the H/W=0.6, 0.8, and 1.0 cross-sectional forebodies. For the vertical ellipse (H/W=1.25), this is also the case for fineness ratios above 3. For the circular and vertical ellipse forebody cross-sections, there is essentially no PYMP produced at fineness ratios of 2 or less. Trend lines have been drawn through the data on Figure 75 that reflect these

---

[4] See Section 2, Review of Phase I Results, for a synopsis of these results and Reference 1 for a complete discussion.

observations. Consequently, these trend lines constitute the PYMP criterion that, as presented in Figure 76 without data points, attempts to predict PYMP values as a function of forebody geometry. It appears that the criterion can serve this function based on the correlation obtained between actual airplane body PYMP values and the criterion shown in Figure 77.

Since forebody modifications, such as blunting or adding chines, can either improve or degrade the body's yawing-moment characteristics, the criterion based on unmodified forebodies, therefore, should not be expected to predict PYMP values for modified forebodies. A significantly larger data base would be required before a criterion could be developed for blunted or chined forebody configurations.

Many internal requirements, as well as aerodynamic considerations, dictate a forebody's dimensions. To aid the designer in his trade-offs, cross-plots of constant PYMP levels were prepared as functions of fineness ratio and H/W, as shown in Figure 78. Also shown in this figure are symbols which define whether the data at a particular FR and H/W combination were generally characterized as damped or propelling, and whether there were significant C_{n_0}'s generated.

These results show that for any combination of fineness ratio and H/W that results in a PYMP level below approximately 0.20, the yawing moment is essentially damped. For forebody geometries producing PYMP values greater than 0.2, the degree of propelling yawing moment experienced increases with increasing PYMP. Figure 78 also shows that there is a value of fineness ratio at each H/W below which little or no C_{n_0}'s are produced. This fineness ratio is approximately 4 at 0.6 H/W and decreases with increasing H/W to a value between 1 and 1.5 at H/W=1.25. Above these values, the levels of C_{n_0} increase with increasing fineness ratios.

Therefore, it can be seen that as H/W decreases below 1.0, the forebody length that will not produce propelling yawing moments decreases rapidly, while, however, a greater tolerance to yawing-moment offsets at longer forebody lengths is observed. A forebody that exhibits significant C_{n_0}'s but a low PYMP value will be characterized by a tendency for the nose to wander during high-α maneuvers, but, assuming no other adverse characteristics such as a propelling empennage design, will not tend to depart and spin because of its damped yaw characteristics. A body with large PYMP levels and little or no C_{n_0}, while it would not exhibit nose wandering in a straight symmetric maneuver, would

23

be highly susceptible to departures and spins once it started to rotate because of its highly propelling yaw characteristics. Also, as was demonstrated when other airplane components were present, the forebodies at these high PYMP levels can also cause large Cl_o's, increase the wing's propelling rolling moments, and produce nose-up rotational pitching-moment increments. These characteristics will cause departures from controlled flight and can lead to spin modes. Therefore, the more deeply the forebody geometry lies within the low H/W-high fineness ratio corner, the more adverse will be the forebody's contribution to the airplane's high angle-of-attack aerodynamics.

These conclusions are illustrated by the design guide presented in Figure 79. The heavy boundary is approximately the PYMP=0.2 line, and the increasingly darker shading to the left of the boundary represents the increasingly adverse aerodynamic characteristics that will be experienced in those regions. The other boundary represents the onset of Cn_o's.

SECTION 5
·CONCLUDING REMARKS

The results of this study clearly indicate that there is a definite relationship between forebody geometry and the aerodynamic characteristics to be expected, both from the body-alone and from the total airplane. A design chart that summarized these findings was generated to provide a tool to assess the impact of forebody geometry on expected airplane high angle-of-attack flight characteristics. An analysis of the data used to develop this design chart provided the following observations:

- The rotational yawing moment becomes more propelling as the forebody cross-sectional shape becomes more elliptical, when the major axis is in the horizontal plane.

- Generally, increasing fineness ratio amplifies the influence of cross-sectional shape. Therefore, ·· ⌐ ·.ost propelling forebodies are ones that are highly elliptical with large fir ⌐ ⌐ ratios.

- Forebody configurations that produce highly propelling yawing-moment characteristics tend to produce nose-up rotational pitch increments and, through interaction with the wing, to also produce roll offsets and adverse rotational roll characteristics.

- Yawing moments in symmetric flight that are caused by asymmetric vortex shedding from the forebody generally increase with increasing forebody fineness ratio, and decrease with decreasing forebody height/width ratio.

- The body-alone static directional stability levels, in the 30° to 50° angle-of-attack region tend, generally, to be stable for forebody height/width ratios below approximately 0.95 and unstable for values above. Increasing fineness ratio tends to increase either the directional stability or instability determined by the cross-sectional shape.

- All of the physical forebody characteristics that had a favorable influence on **body-alone** rotational yaw characteristics during this study adversely influenced body-alone directional stability, and vice-versa.

25

A limited study of the influences of forebody modifications, such as blunting or inclining the forebody, or the addition of strakes and chines, has indicated the following:

- Blunting the forebody tip may introduce some changes in the aerodynamic characteristics compared to the unmodified pointed body. However, the results are generally within the bounds to be expected at the reduced fineness ratio of the blunted forebody. This also means that, for the tested forebodies, the results were similar at a given fineness ratio, regardless of whether the tip was pointed or blunt.

- Inclining the forebody produced aerodynamic characteristics consistent with the local angle of attack of the forebody.

- A very limited investigation of forebody strakes has shown that they can radically improve an adverse forebody's rotational characteristics, but can degrade the configuration's static directional stability.

- The limited chine investigation, also undertaken during this study, indicated that the two chine configurations tested each improved the static directional stability, but degraded the rotational aerodynamics significantly. These results may differ for other forebody geometries.

REFERENCES

1. Bihrle, W. Jr., Barnhart, B., and Dickes, E.: "A Preliminary Design Guide for Departure/Spin Resistant Forebody Configurations," BAR 85-10, January 1986.

2. Brandon, J.M. and Nguyen, L.T.: "Experimental Study of the Effects of Forebody Geometry on High Angle-of-Attack Static and Dynamic Stability," AIAA Paper 86-0331 presented at the 24th Aerospace Sciences Meeting, Reno, Nevada, January 6-9, 1986.

3. Carr, Peter C. and Gilbert, William P.: "Effects of Fuselage Forebody Geometry on Low Speed Lateral-Directional Characteristics of Twin-Tail Fighter Model at High Angles of Attack," NASA Technical Paper 1592, 1979.

4. Bihrle, W. Jr. and Barnhart, B.: "Spin Prediction Techniques," *Journal of Aircraft*, Vol. 20, No. 2, February 1983, pp. 97-101.

5. Bihrle, W. Jr., Barnhart B., and Dickes E.: "Static and Rotational Aerodynamic Data from 0° to 90° Angle of Attack for a Series of Basic and Altered Forebody Shapes," WRDC-TR-89-3090, September 1989.

6. Ralston, John N.: "Rotary Balance Data and Analysis for the X-29A Airplane for an Angle-of-Attack Range of 0° to 90°," NASA CR 3747, August 1984.

TABLE I.- BODY DIMENSIONAL CHARACTERISTICS

H/W	H	W	FOREBODY FR	FOREBODY LENGTH Inches	FOREBODY PLANFORM AREA Inches^2	FOREBODY SIDE AREA Inches^2	TOTAL BODY FR	TOTAL BODY LENGTH Inches	TOTAL BODY PLANFORM AREA Inches^2	TOTAL BODY SIDE AREA Inches^2
0.6	3.10	5.16	1.0	3.10	11.18	6.71	16.82	52.10	264.22	158.51
			2.0	6.20	21.60	12.96	17.82	55.20	274.64	164.76
			3.0	9.30	32.18	19.31	18.82	58.30	285.22	171.11
			4.0	12.39	42.80	25.68	19.82	61.39	295.84	177.48
			4.5	13.94	48.12	28.87	20.32	62.94	301.16	180.67
			5.0	15.49	53.44	32.06	21.82	64.49	306.48	183.86
0.8	3.58	4.47	1.0	3.58	11.18	8.95	14.69	52.58	230.31	184.27
			2.0	7.16	21.60	17.28	15.69	56.16	240.73	192.60
			3.0	10.73	32.18	25.74	16.69	59.73	251.31	201.06
			4.0	14.31	42.80	34.24	17.69	63.31	261.93	209.56
			4.5	16.10	48.12	38.49	18.19	65.10	267.25	213.81
			5.0	17.90	53.49	42.75	18.69	66.90	272.57	218.07
1.0	4.00	4.00	1.0	4.00	11.37	11.37	13.27	53.07	207.37	207.37
			2.0	8.00	21.95	21.95	14.28	57.14	217.95	217.95
			3.0	12.00	32.59	32.59	15.29	61.16	228.59	228.59
			4.0	16.00	43.04	43.04	16.27	65.09	239.04	239.04
			4.5	18.00	48.32	48.32	16.77	67.08	244.32	244.32
			5.0	20.00	54.31	54.31	17.33	69.33	250.31	250.31
1.25	4.47	3.58	0.8	3.58	8.95	11.18	11.76	52.58	184.27	230.31
			1.6	7.16	17.28	21.60	12.56	56.16	192.60	240.73
			2.4	10.73	25.74	32.18	13.36	59.73	201.06	251.31
			3.2	14.31	34.24	42.80	14.16	63.31	209.56	261.93
			3.6	16.10	38.49	48.12	14.56	65.10	213.81	267.25
			4.0	17.90	42.75	53.44	14.97	66.90	218.07	272.57

TABLE II.- BLUNTED BODY DIMENSIONAL CHARACTERISTICS

H/W	H	W	FR ORIG→BLUNT	FOREBODY LENGTH Inches	FOREBODY PLANFORM AREA Inches^2	FOREBODY SIDE AREA Inches^2	FR	TOTAL BODY LENGTH Inches	TOTAL BODY PLANFORM AREA Inches^2	TOTAL BODY SIDE AREA Inches^2
0.6	3.10	5.16	4→3	9.30	38.33	23.00	18.82	58.30	291.37	174.82
	→	→	5→4.5	13.94	52.33	31.40	20.32	62.94	305.37	183.22
			5→4	12.39	49.81	29.89	19.82	61.39	302.84	181.70
0.8	3.58	4.47	4→3	10.73	38.44	30.75	16.69	59.73	257.57	206.06
	→	→	5→4.5	16.10	52.38	41.90	18.19	65.10	271.51	217.21
			5→4	14.31	49.89	39.91	17.69	63.31	269.03	215.22
1.25	4.47	3.58	3.2→2.4	10.73	30.75	38.44	13.36	59.73	206.06	257.57
	→	→	4.0→3.6	16.10	41.90	52.38	14.56	65.10	217.21	271.51
			4.0→3.3	14.31	39.91	49.89	14.16	63.31	215.22	269.03

30

Shaded areas represent those used for PYMP calculations

$\dot{c}_{n_o}$

$\dfrac{\Omega b}{2V}$

$\dot{c}_n$

b) Demonstration of areas used for PYMP calculations

depth(d) of body at centroid

Forebody planform

length

centroid location

Fineness Ratio = length/depth

$$\text{Cross-sectional area parameter} = \dfrac{\text{centroid cross-sectional area}}{\pi\,(\,d^2/4\,)}$$

Forebody Geometery Parameter(FGP) = Fineness Ratio x Cross-sectional area parameter

a) - Forebody geometry parameter definition

PYMP

1.6

1.2

0.8

0.4

0.0

0   1   2   3   4   5   6

FOREBODY GEOMETRY PARAMETER
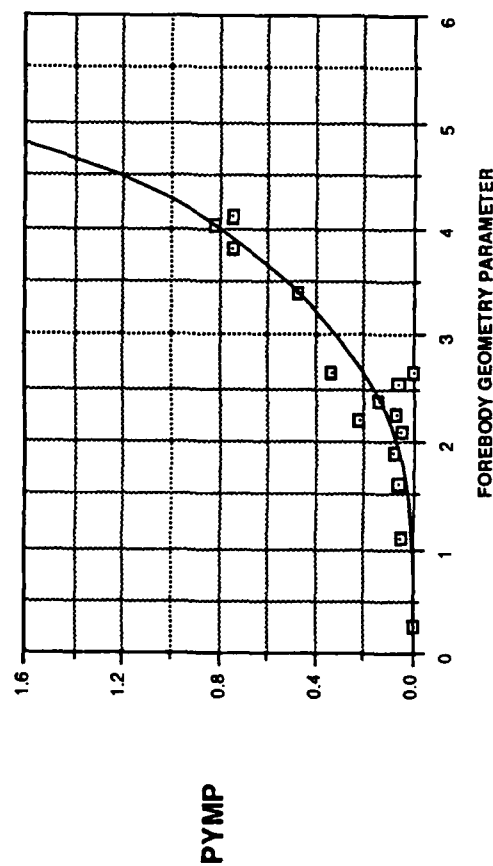
c) - Correlation of propelling yawing-moment characteristics with forebody geometry

Figure 1. - Phase I Criterion Development Parameters

31
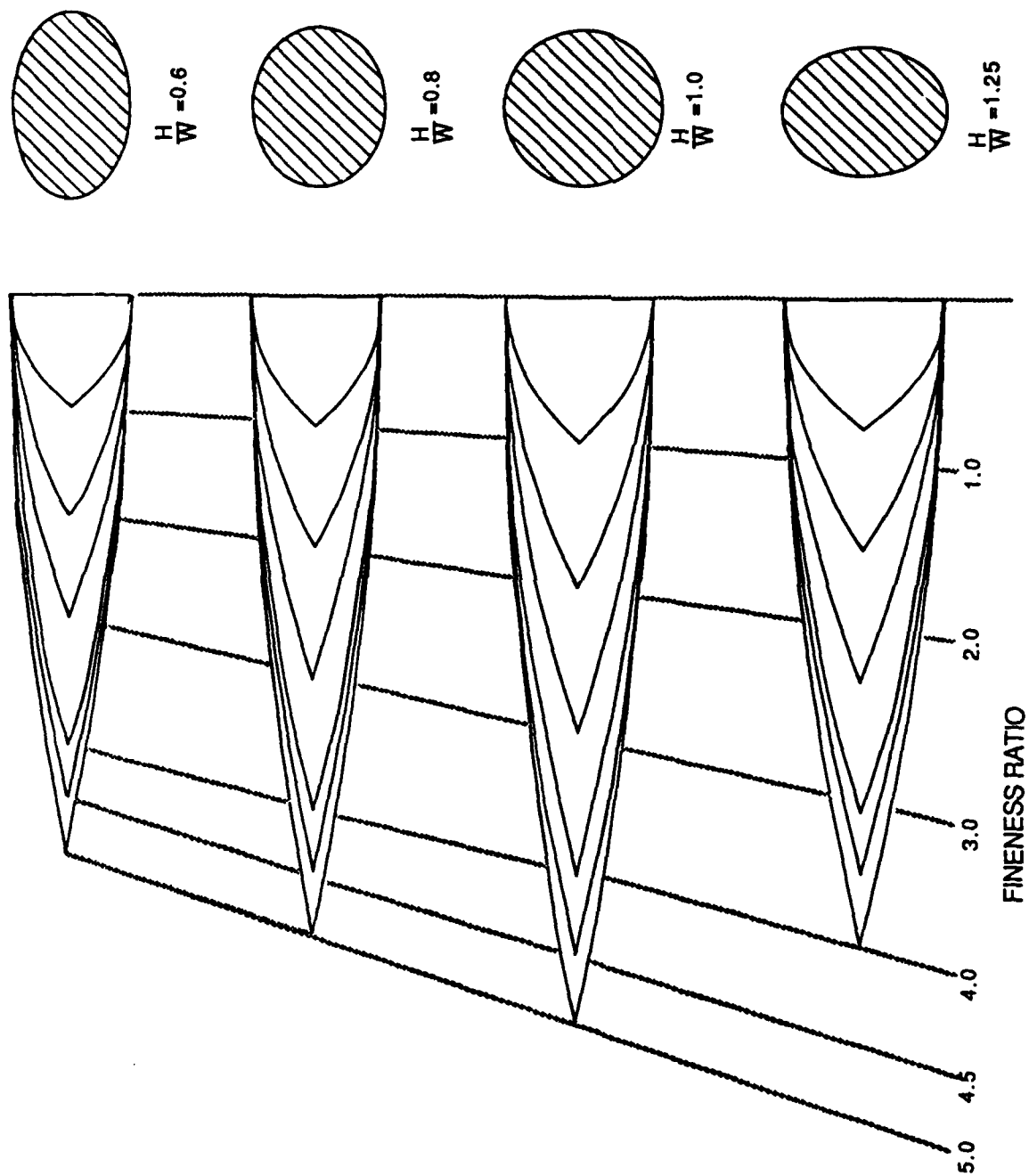
Figure 2. - Forebodies tested during the Phase II study
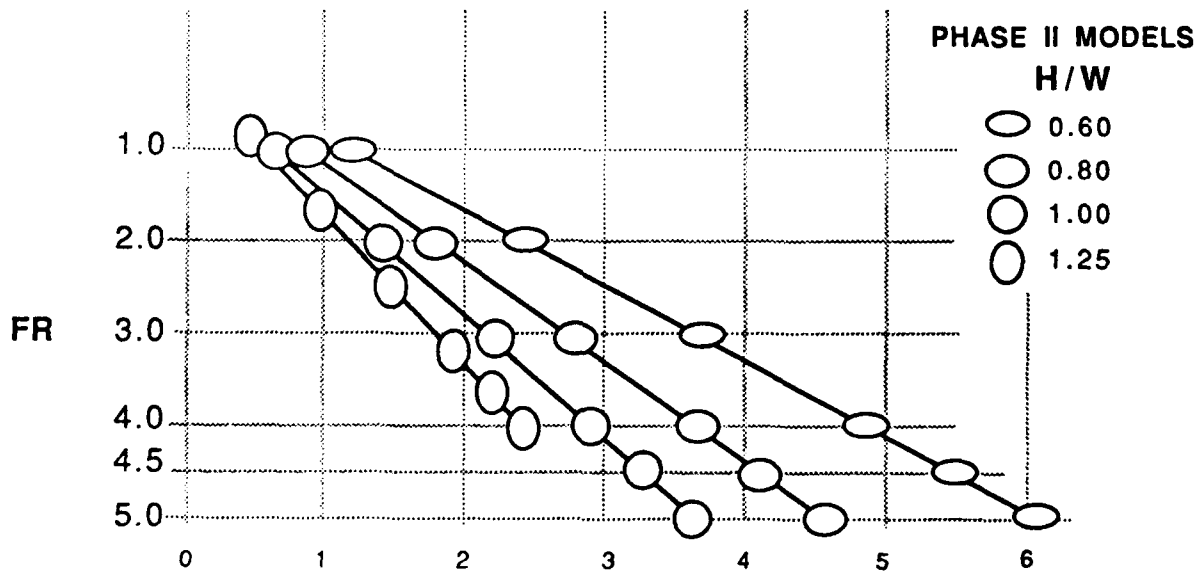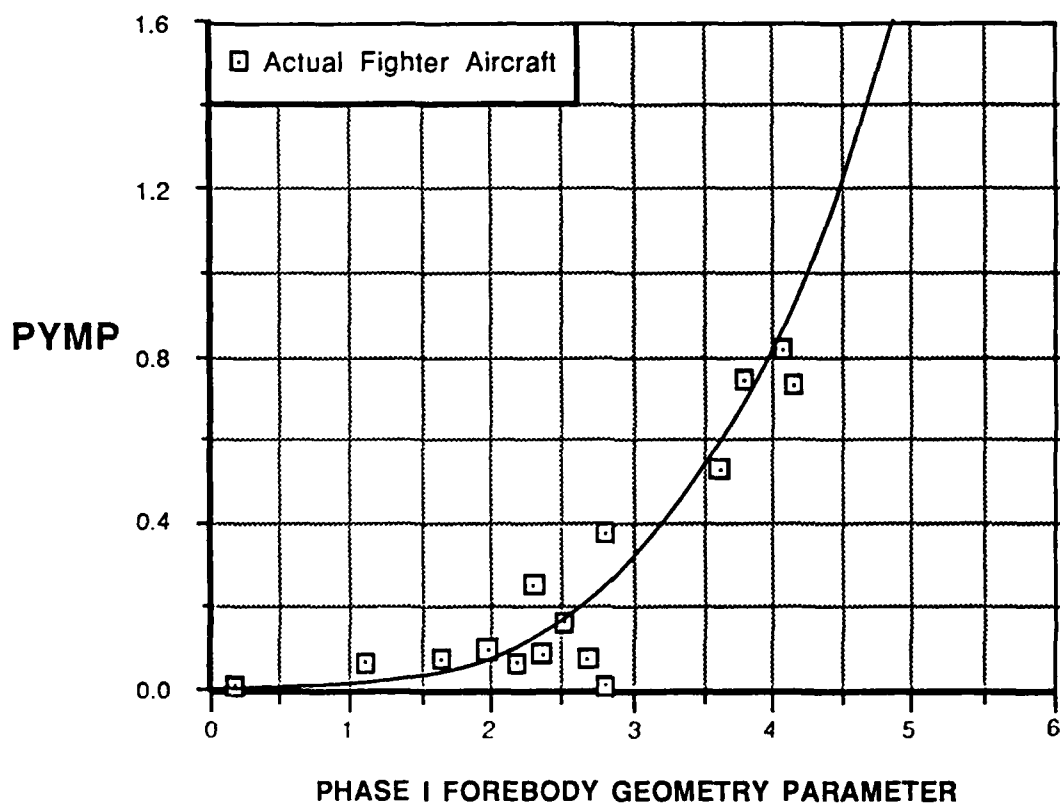
Figure 3.- Comparison of Phase I design chart with tested Phase II models

33
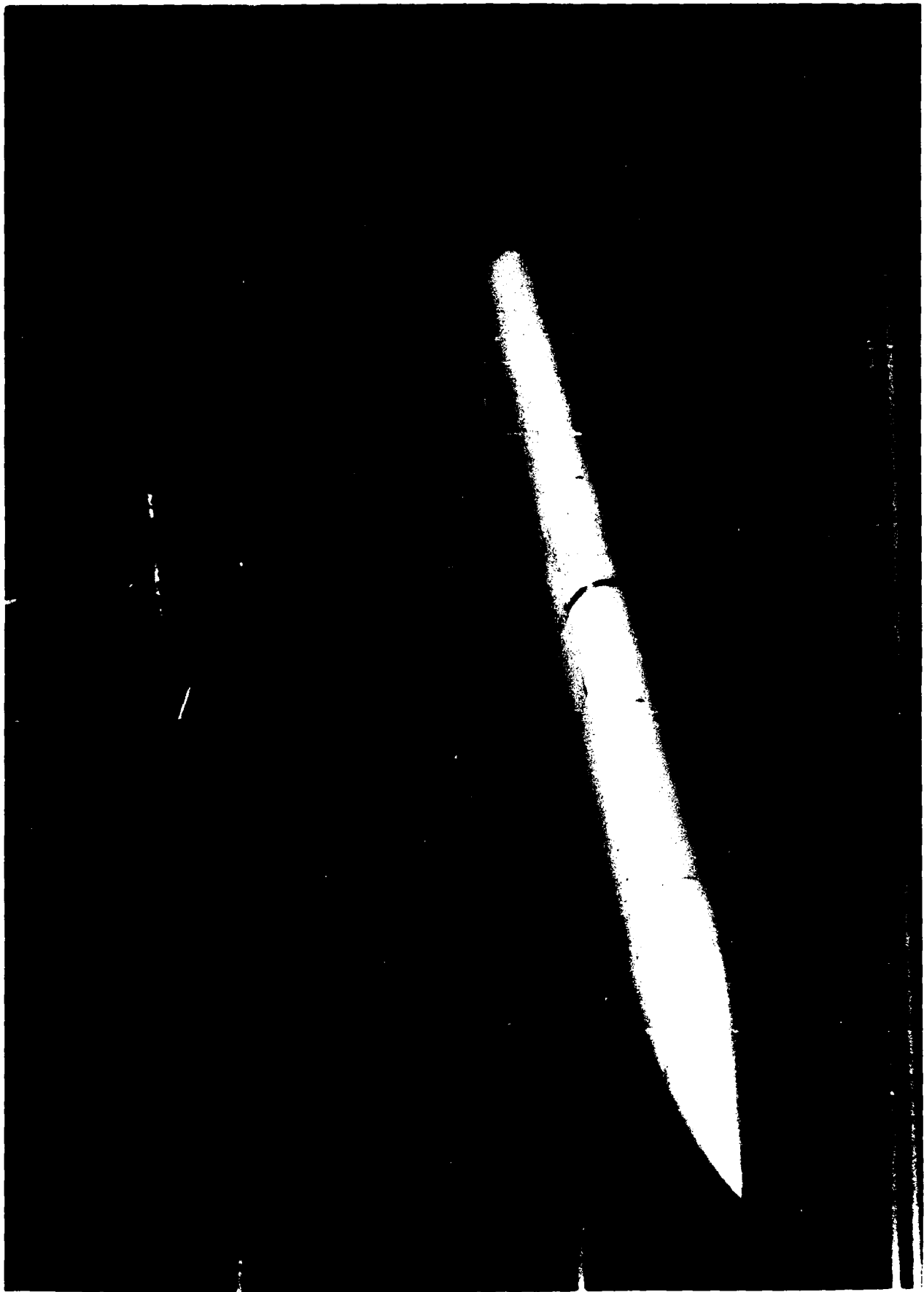
a) H/W=0.6 FR=4

Figure 4.- Photographs of model bodies mounted on rotary balance
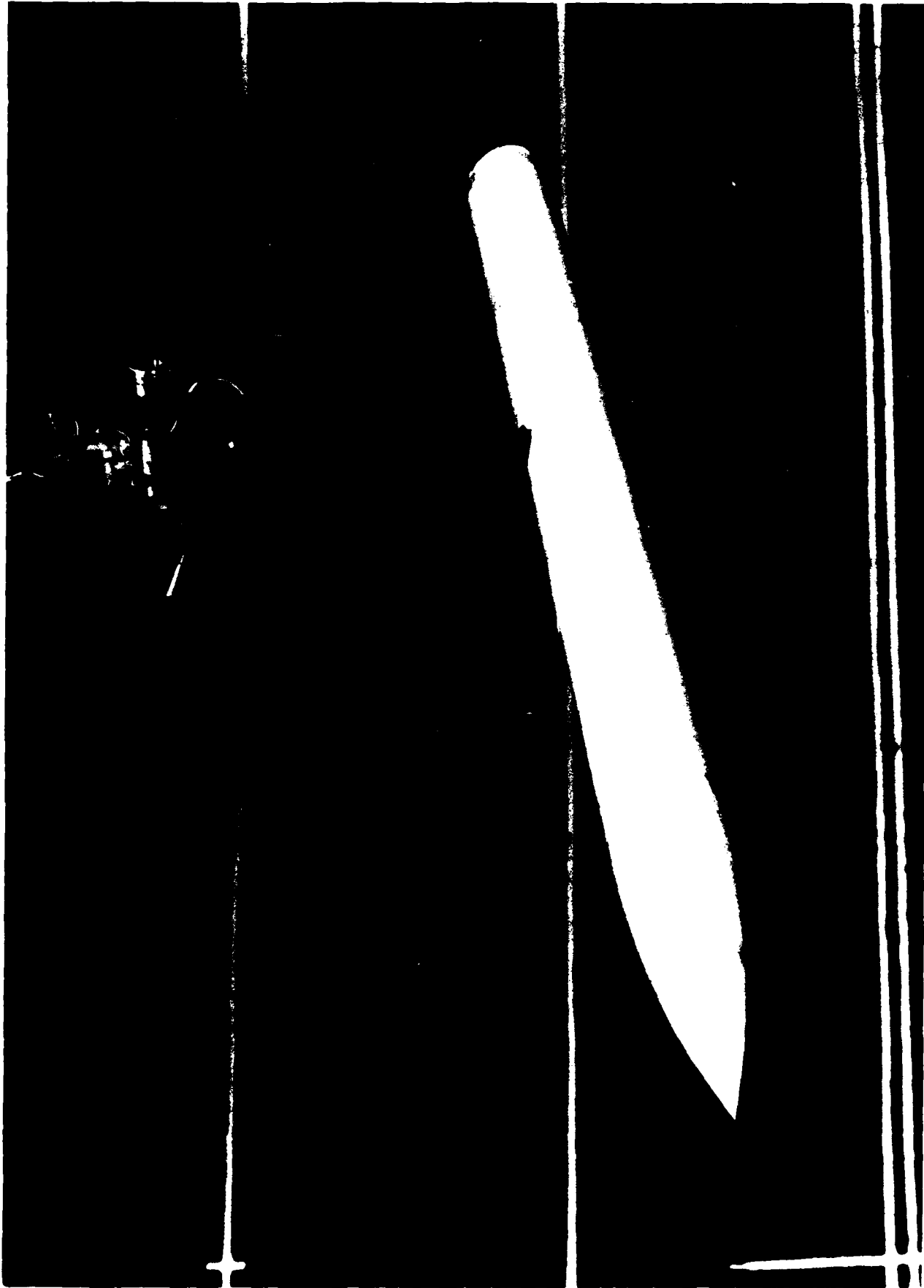
b) H/W=0.8 FR=4

Figure 4 .- Continued

35
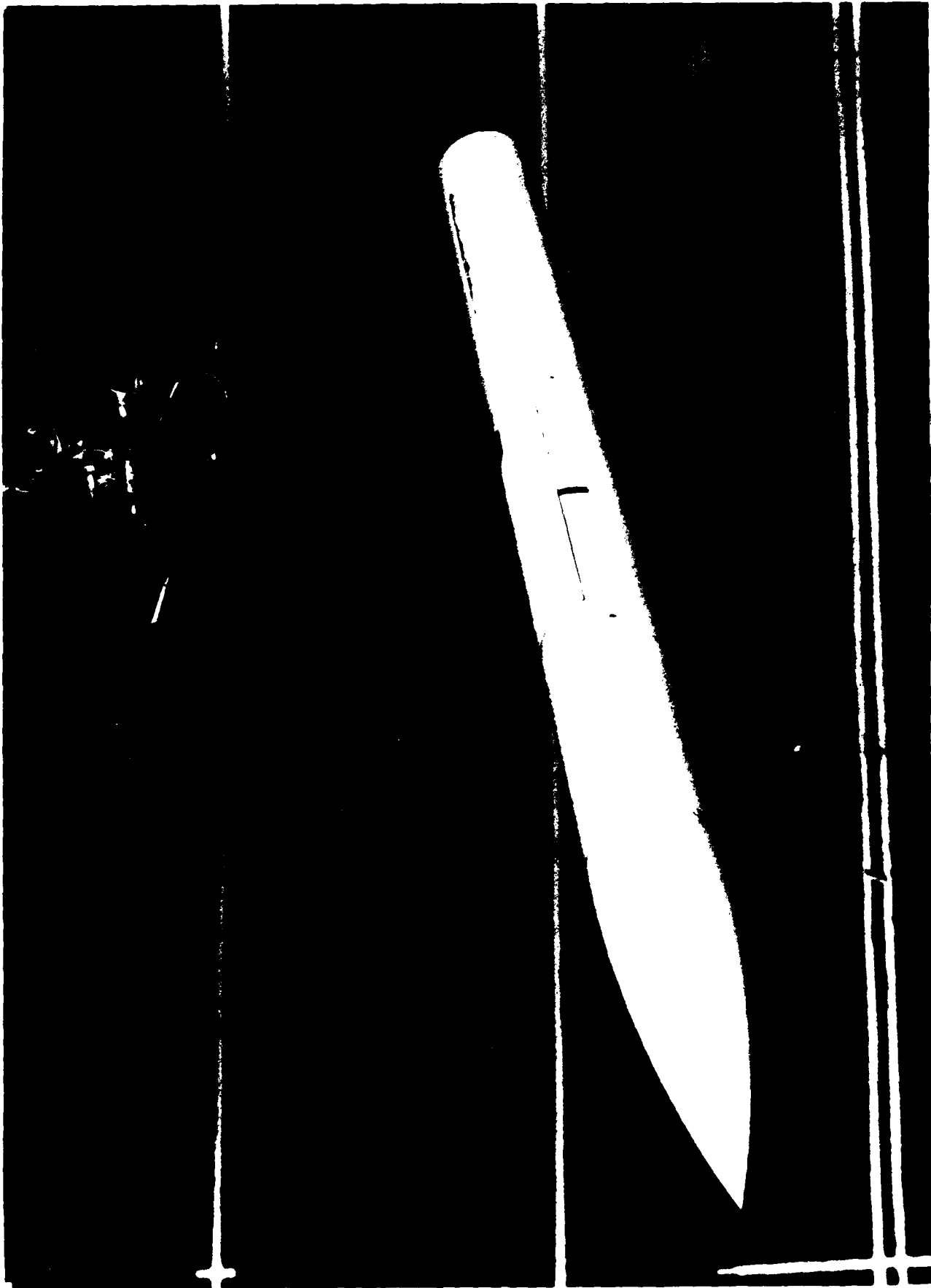
c) H/W=1.0 FR=4

Figure 4.- Continued

36
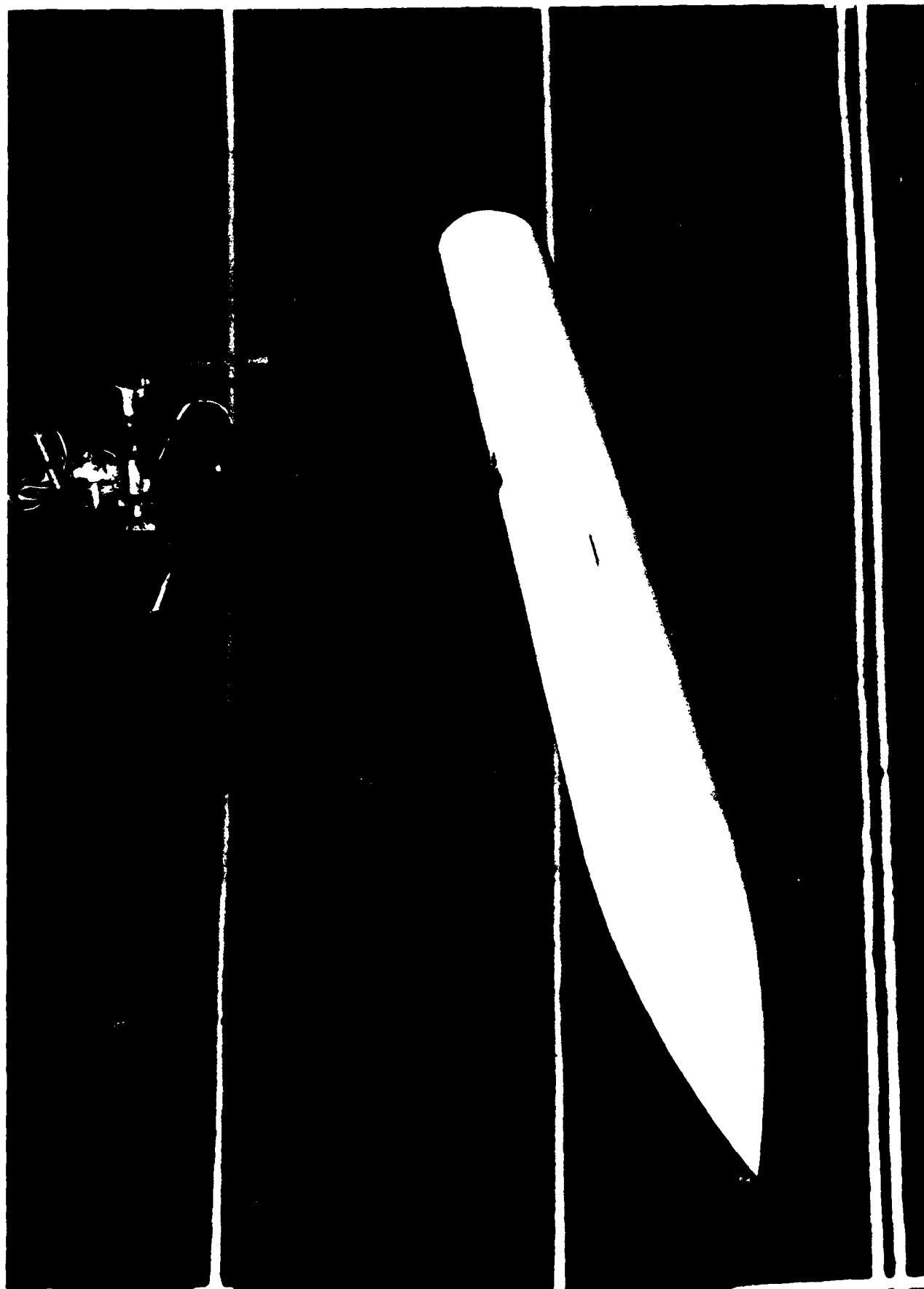
d) H/W=1.25 FR=4

Figure 4.- Concluded

37
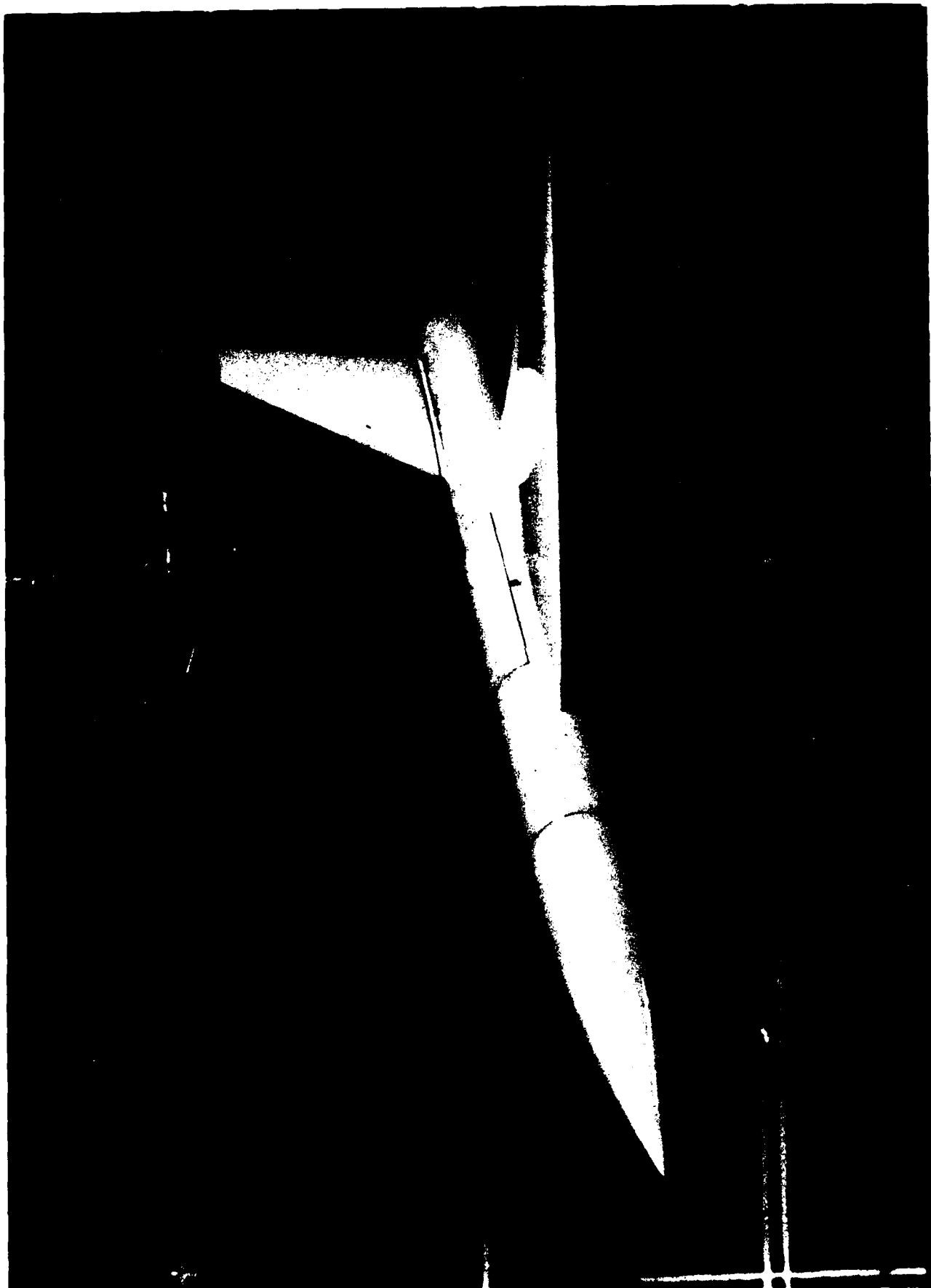
Figure 5.- Photograph of an airplane model with H/W=1, FR=5 forebody

Wing Airfoil: Bi-convex $t/c = 0.043$

Vert. Tail Airfoil: Bi-convex $t/c = 0.038$

9.56"

4.5"

VERTICAL
TAIL
SIDE-VIEW

14"

33.7"

49"

$\Lambda_{LE} = 50^\circ$

19"
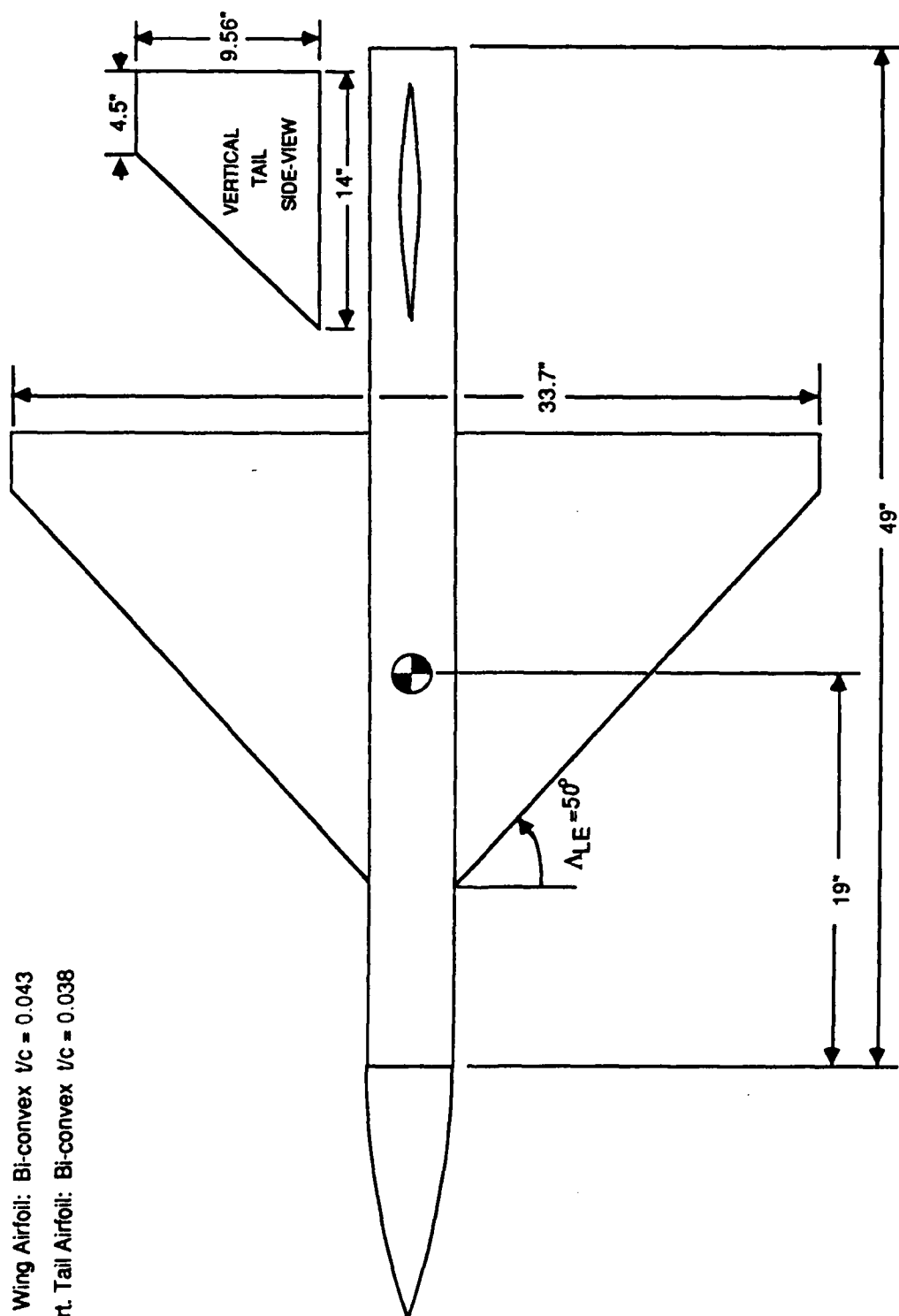
Figure 6.- Sketch of airplane model

39

FR 5 → 4.5

FR 5 → 4

FR 4 → 3
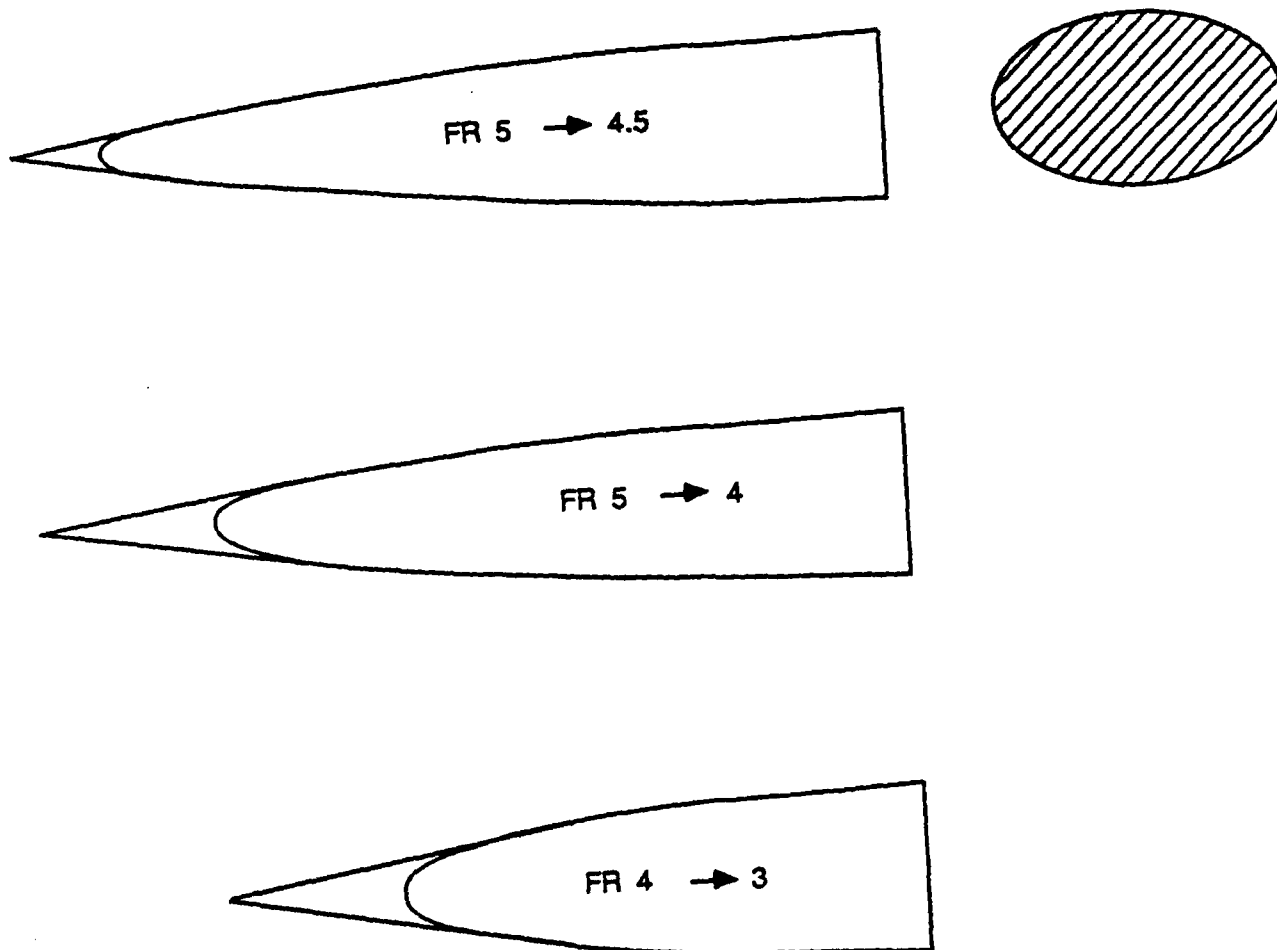
a) H/W = 0.6

Figure 7.- Blunted forebodies tested during Phase II study

FR 5 → 4.5

FR 5 → 4

FR 4 → 3
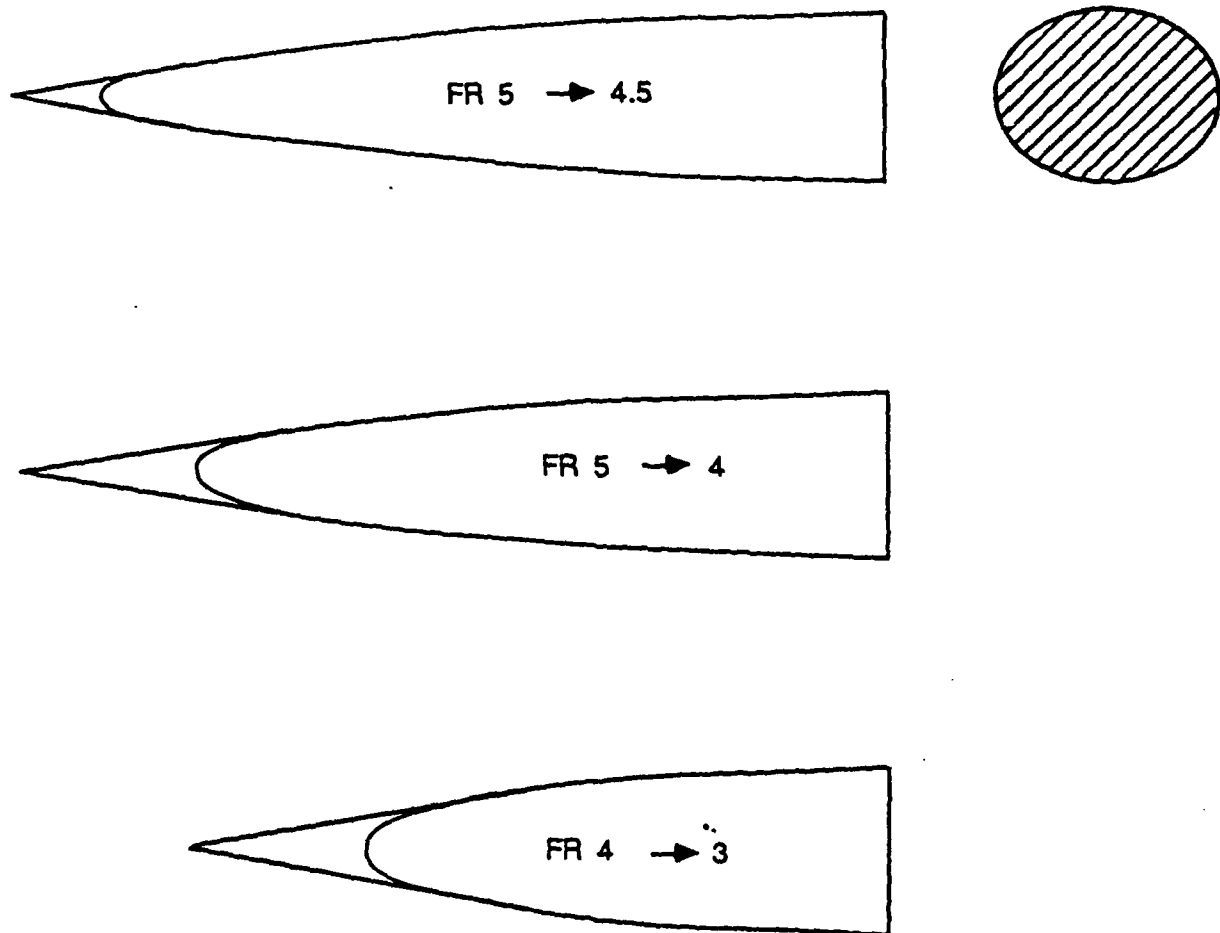
b) H/W = 0.8

Figure 7.- Concluded
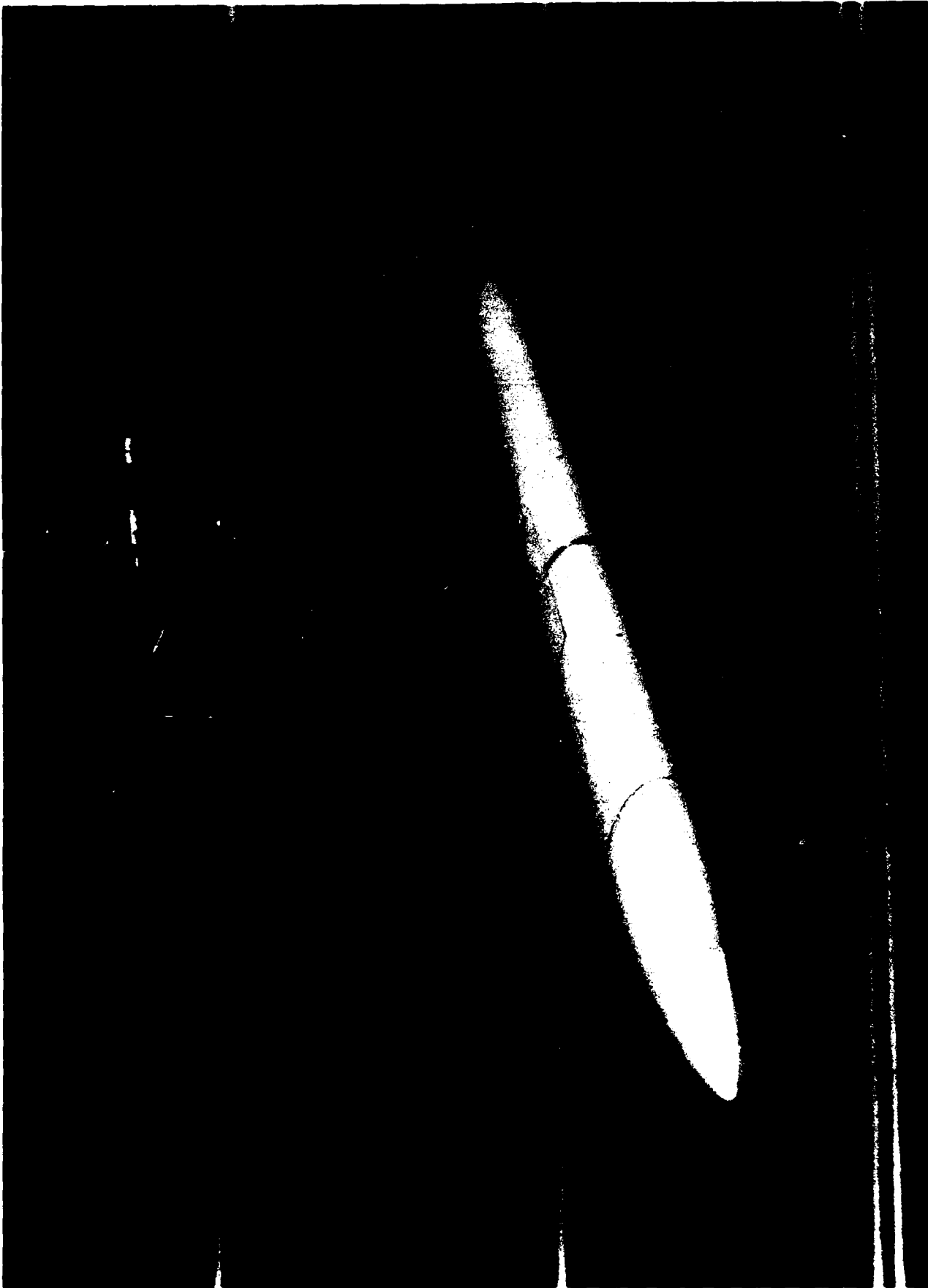
Figure 8.- Photograph of H/W=0.6 body with a FR=5.0 forebody blunted to 4.5 mounted or rotary balance
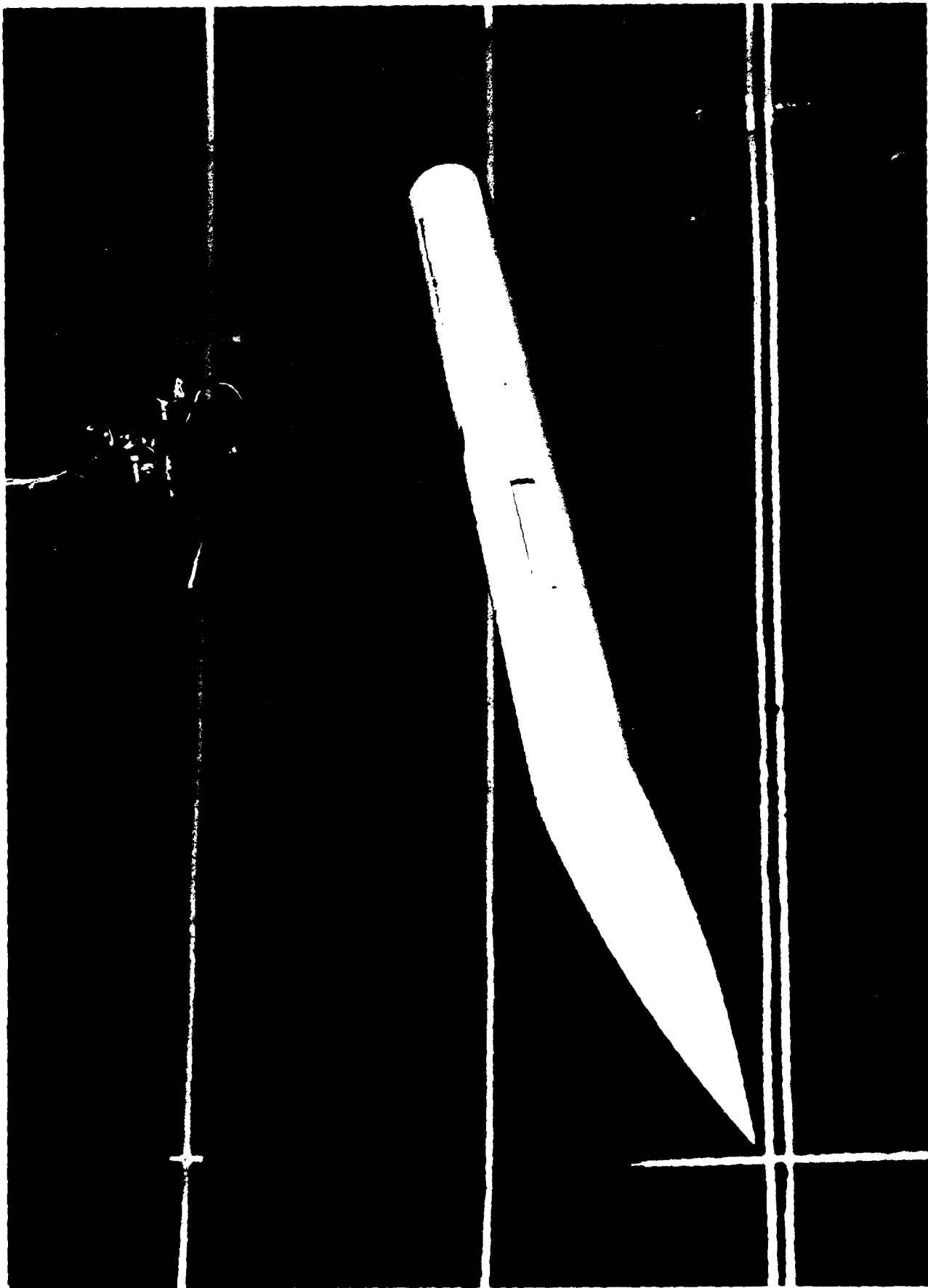
Figure 9.- Photograph of body with H/W=1.0, FR=5.0 forebody inclined 7.5° mounted on rotary balance

43

F.S. 6.0

F.S. 14.0

F.S. 4.0

F.S. 12.0

F.S. 2.0
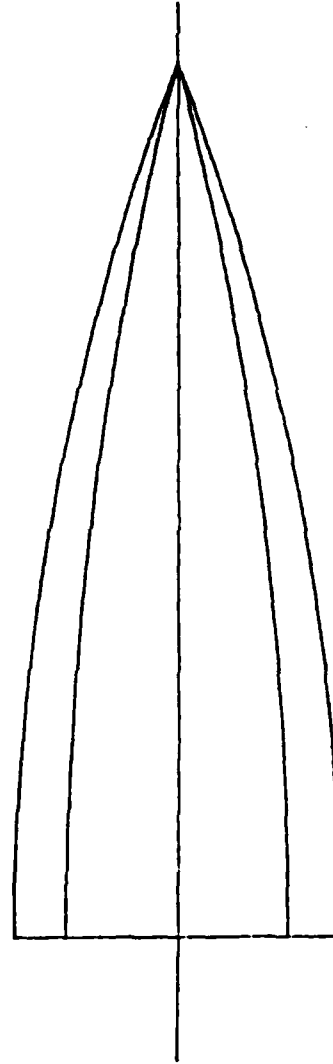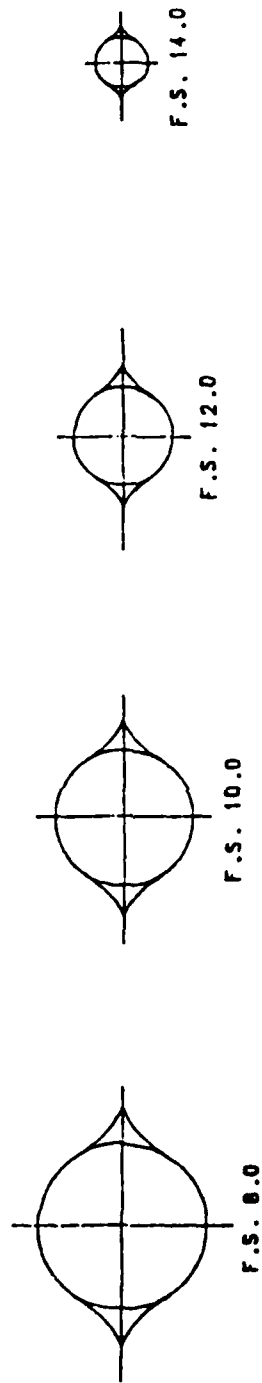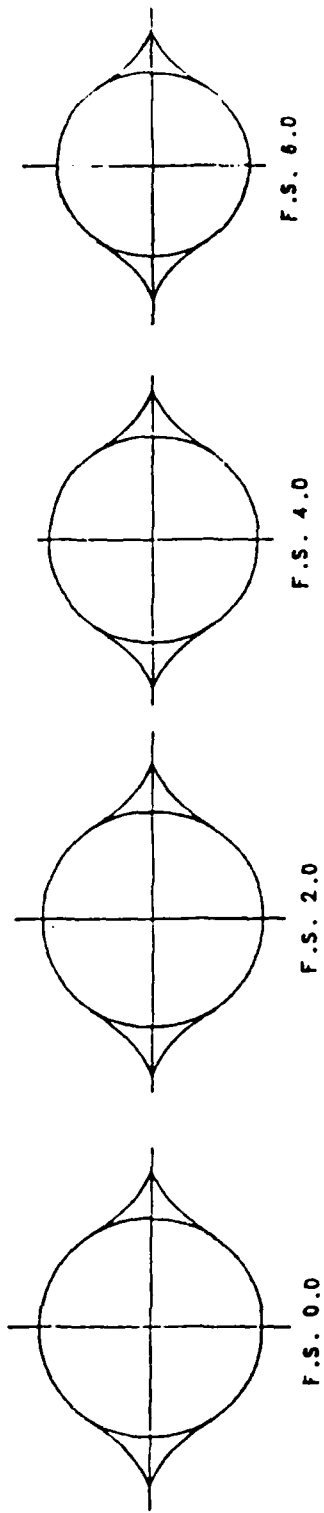
F.S. 10.0

F.S. 0.0

F.S. 8.0

a) 45° chine

Figure 10.- Plan view and cross-sectional cuts of chined forebodies

44
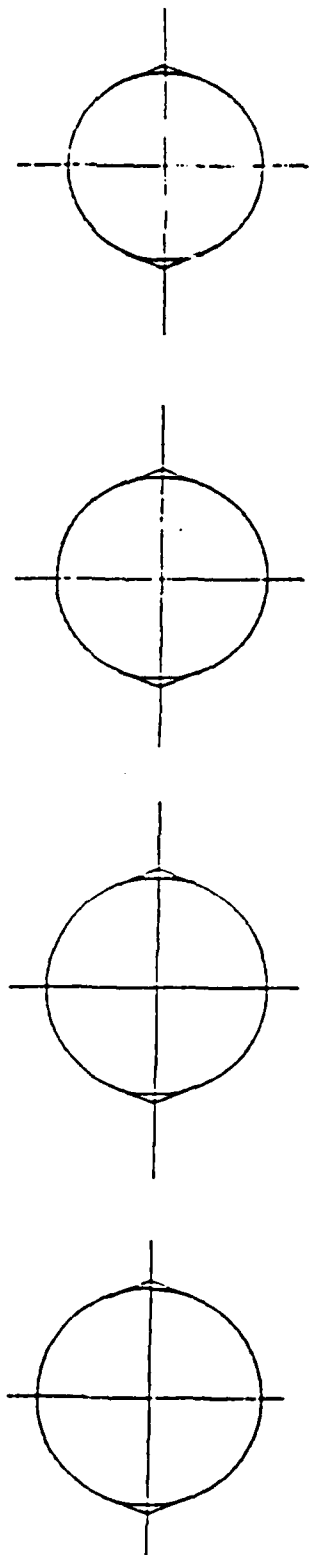
F.S. 6.0

F.S. 14.0

F.S. 4.0

F.S. 12.0

F.S. 2.0

F.S. 10.0

F.S. 0.0
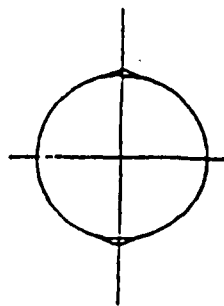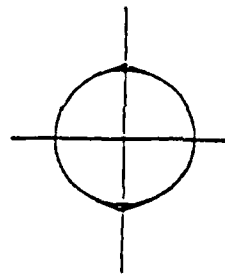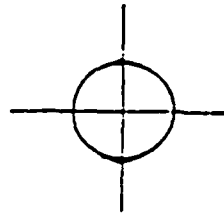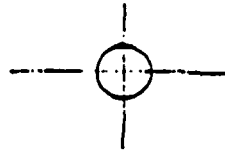
F.S. 8.0
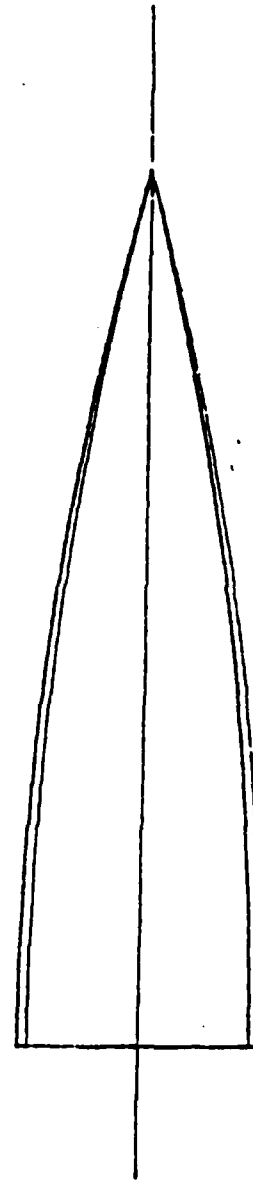
b) 135° chine

Figure 10.- Concluded

45
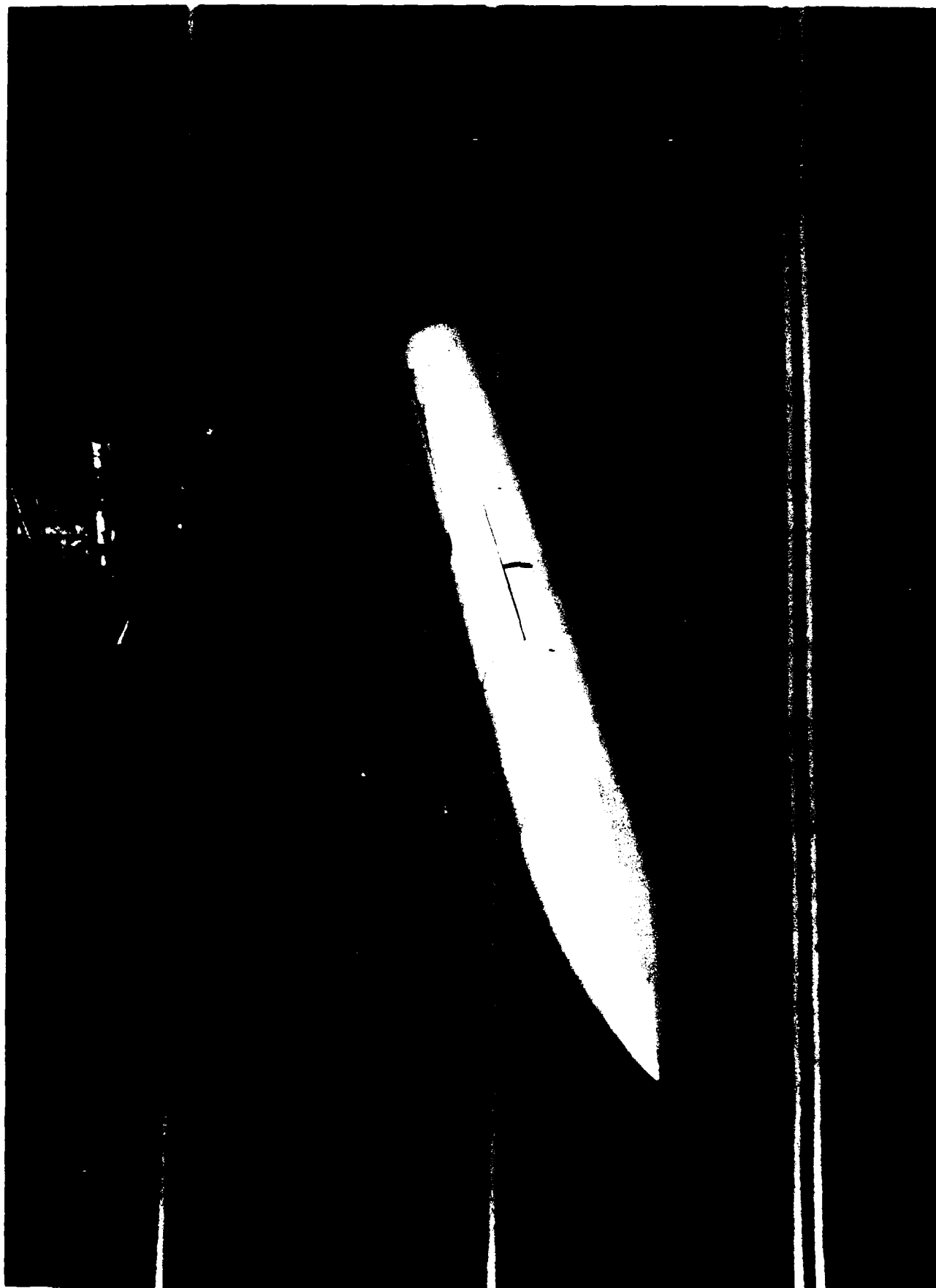
Figure 11.- Photograph of chined H/w=1.0, FR=4.0 forebody configuration mounted on rotary balance

NOTE: Tip of strake aligned with tip of forebody

5/16"

2"

40°
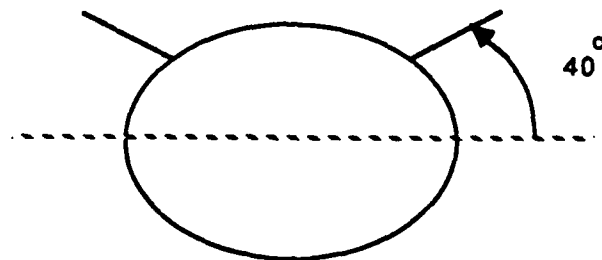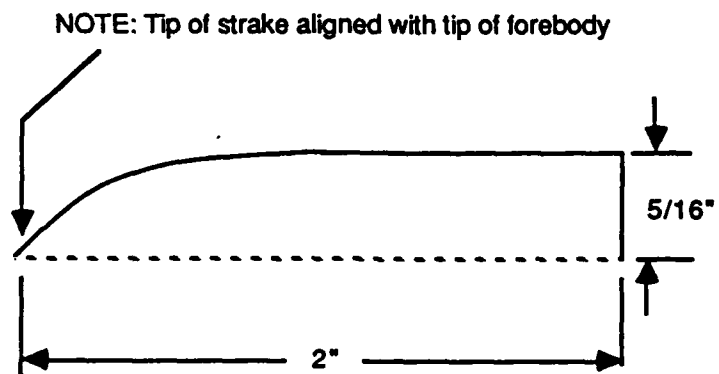
Figure 12.- V-Strake tested on H/W = 0.8, FR = 4.5 forebody

A   Slip ring housing
B   Drive shaft
C   Support boom
D   Spin radius offset potentiometer
E   Counterweight
F   Strut
G   Angle of attack positioning motor

Spin axis

Velocity vector
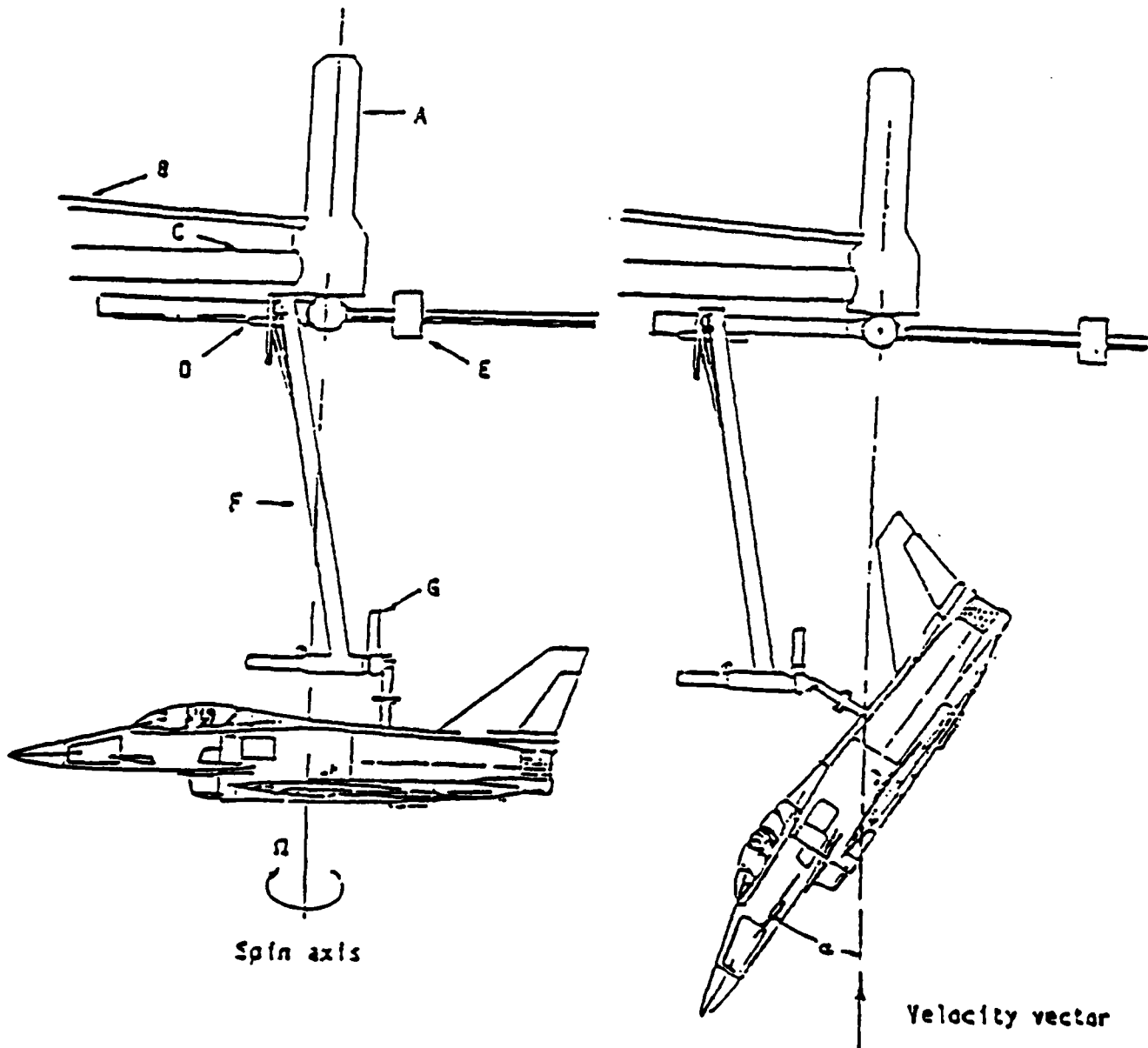
a)   Side view of model

Figure 13.- Sketch of rotary balance apparatus

48

A Slip ring housing
B Spin radius offset potentiometer
C Lateral offset drive gears
D Lateral offset potentiometer
E Strut
F Sideslip angle potentiometer
G Sideslip angle positioning motor
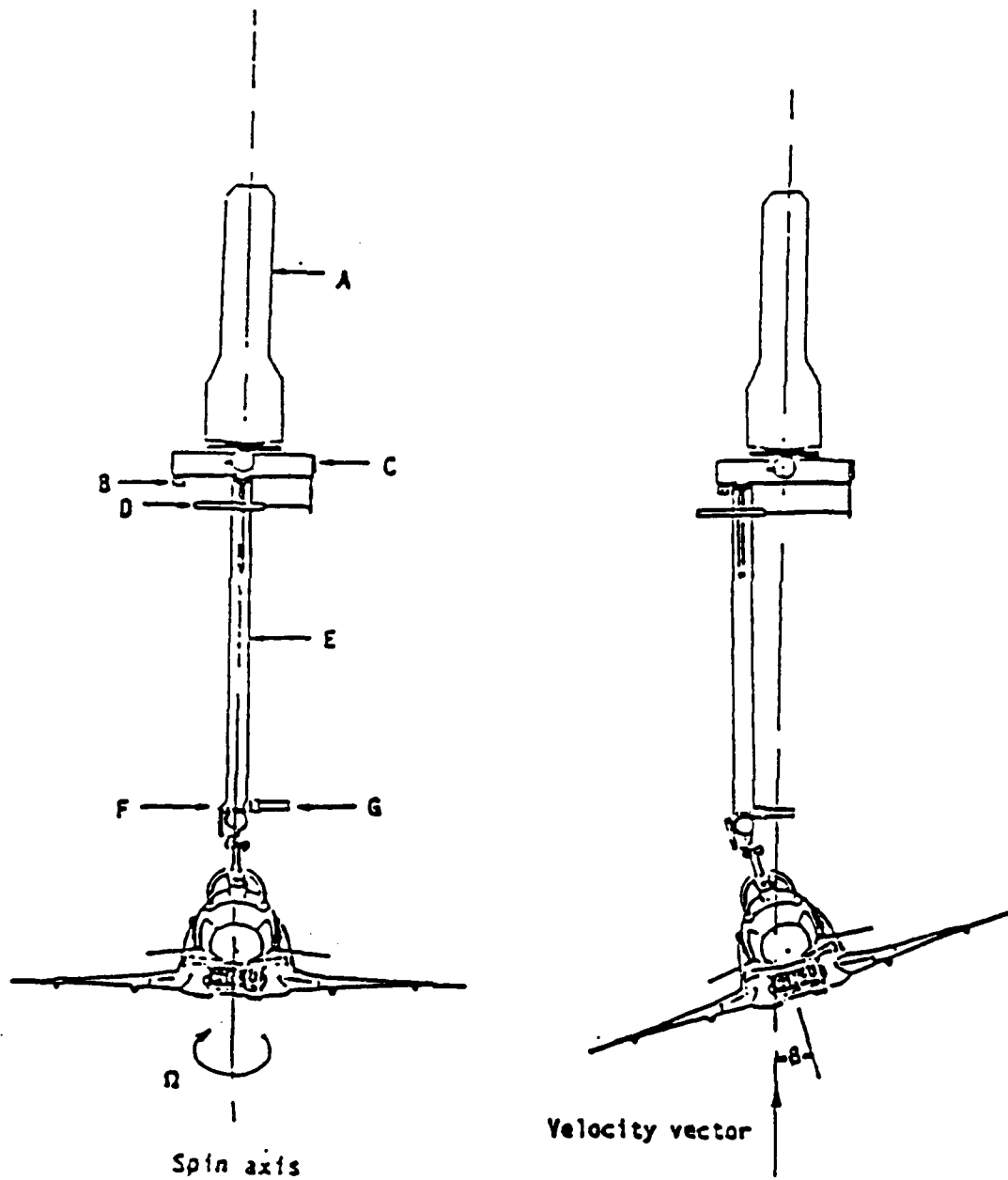
b)   Front view of model

Figure 13.- Concluded
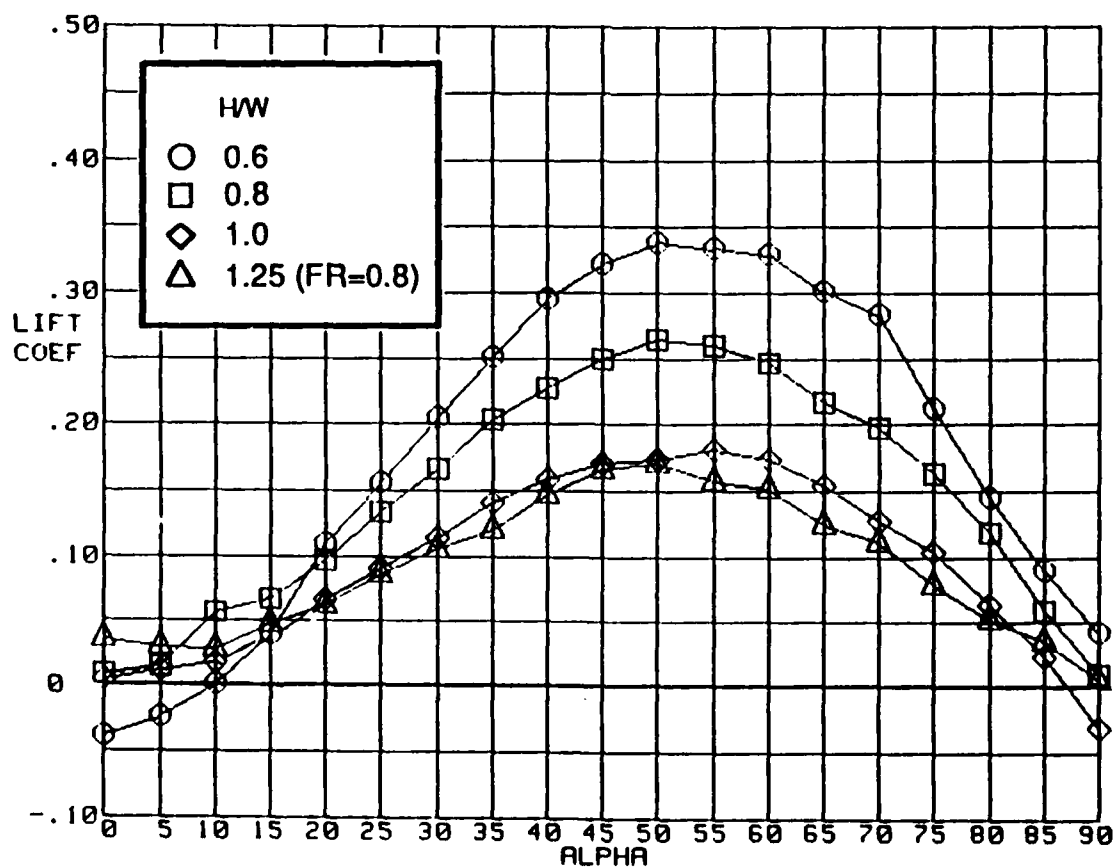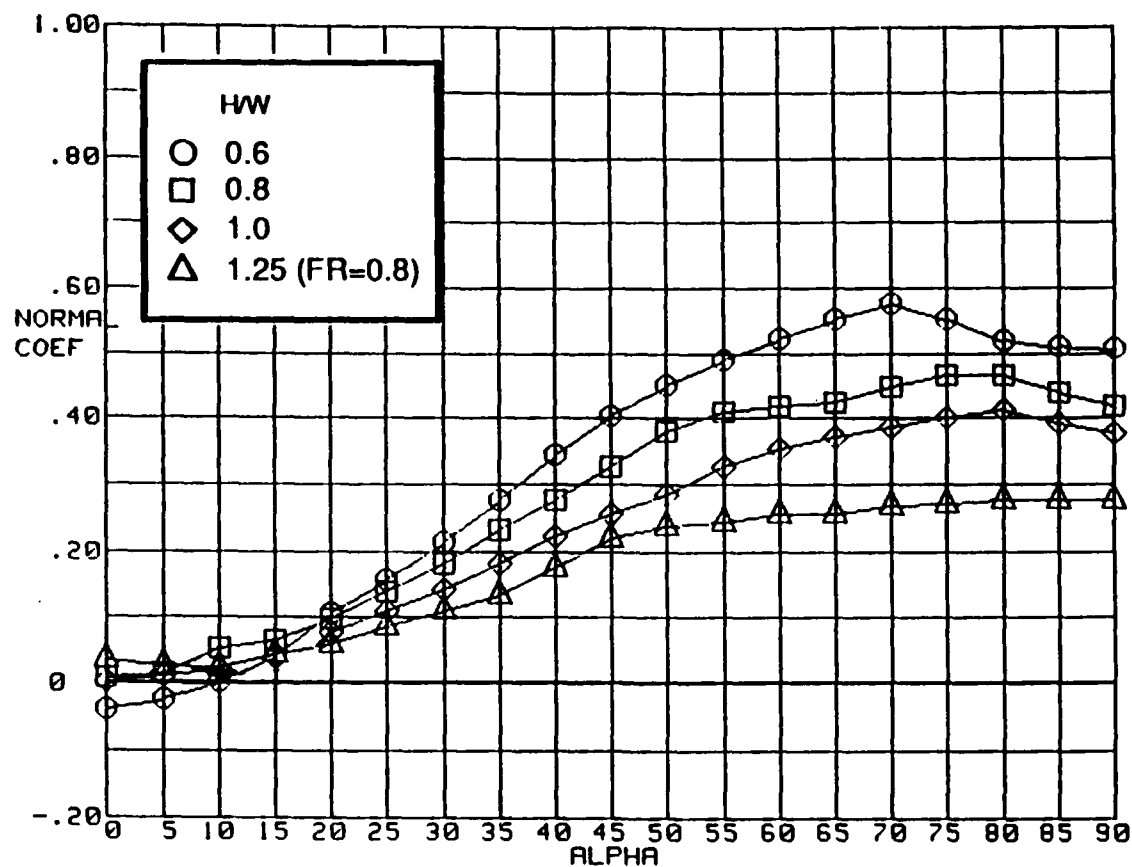
a)   FR=1

Figure 14.- Influence of forebody cross-sectional shape on lift and
normal-force coefficient variation with angle of attack at
specified values of fineness ratio

50
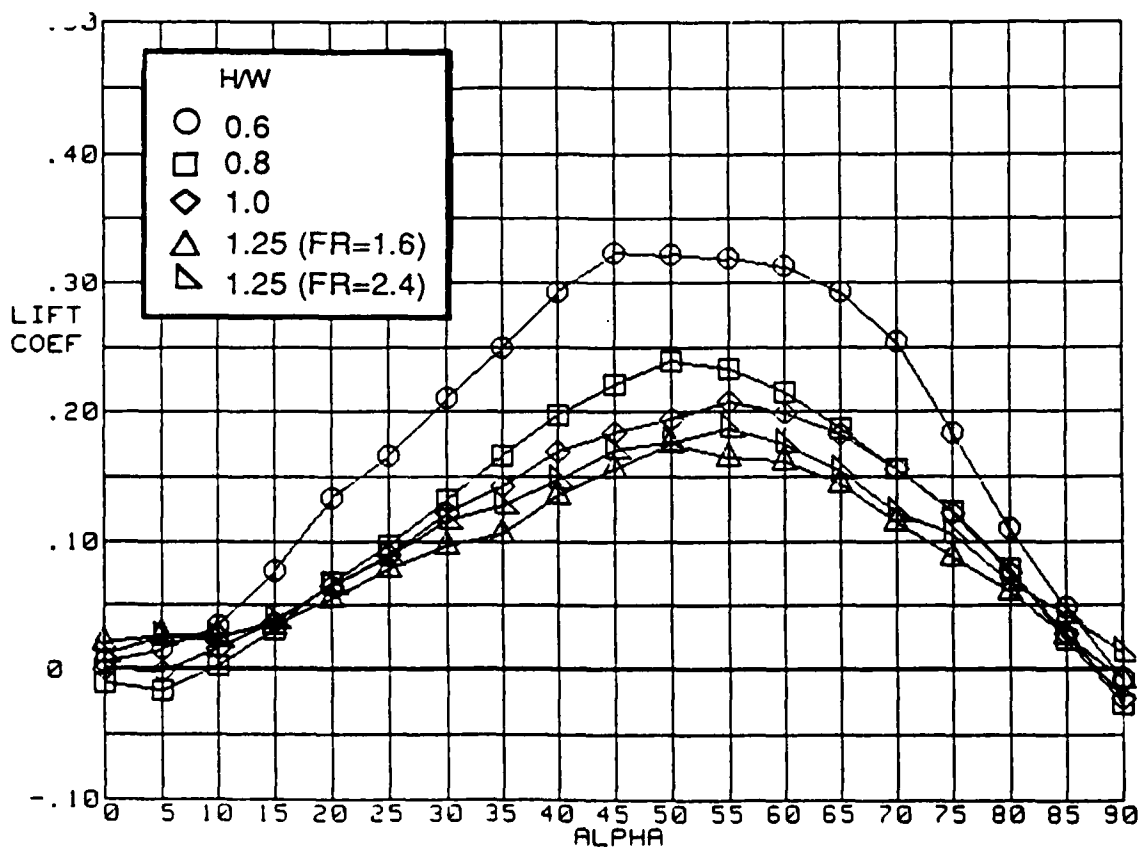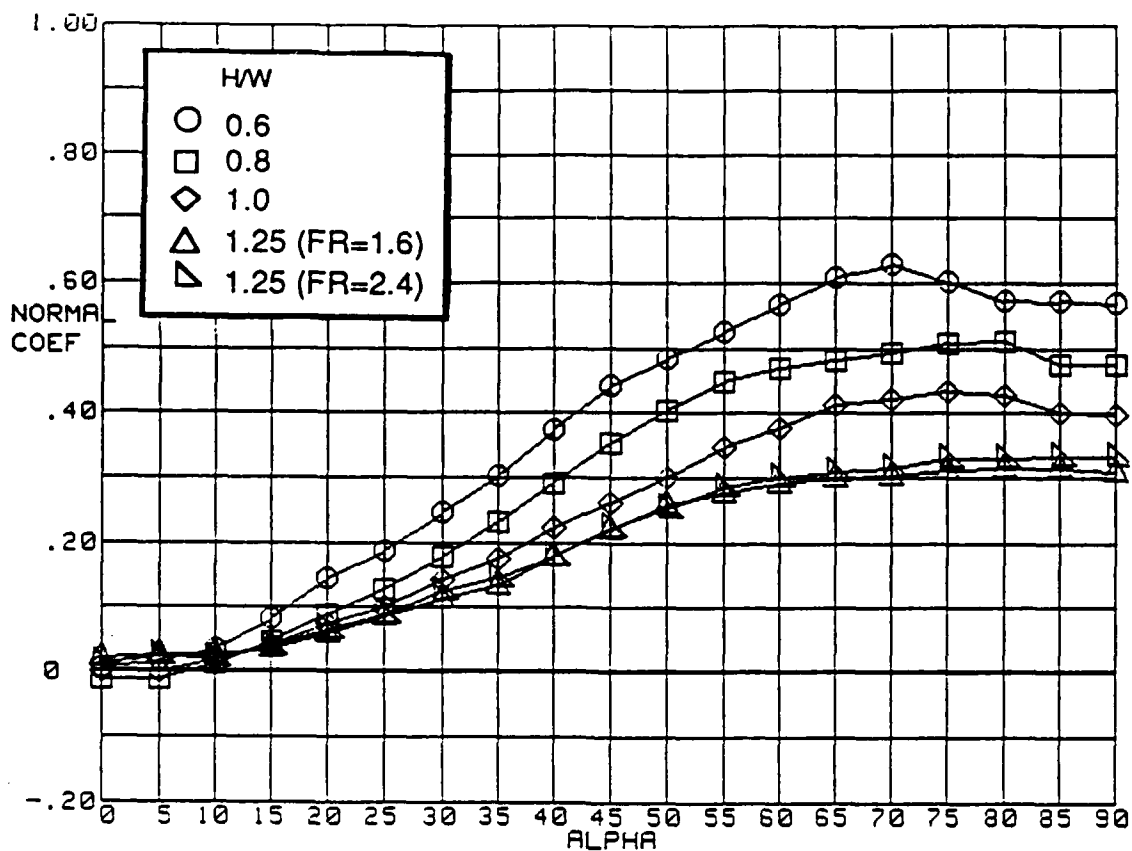
b) FR=2

Figure 14.- Continued
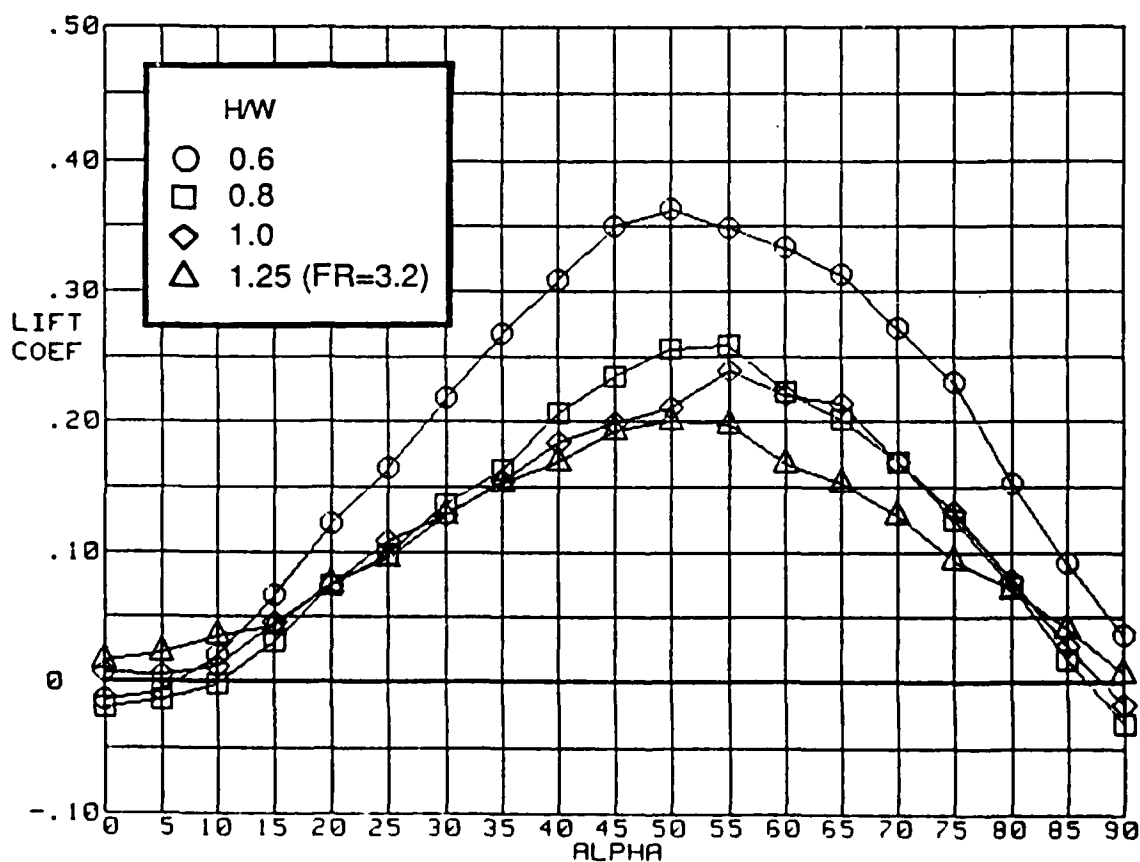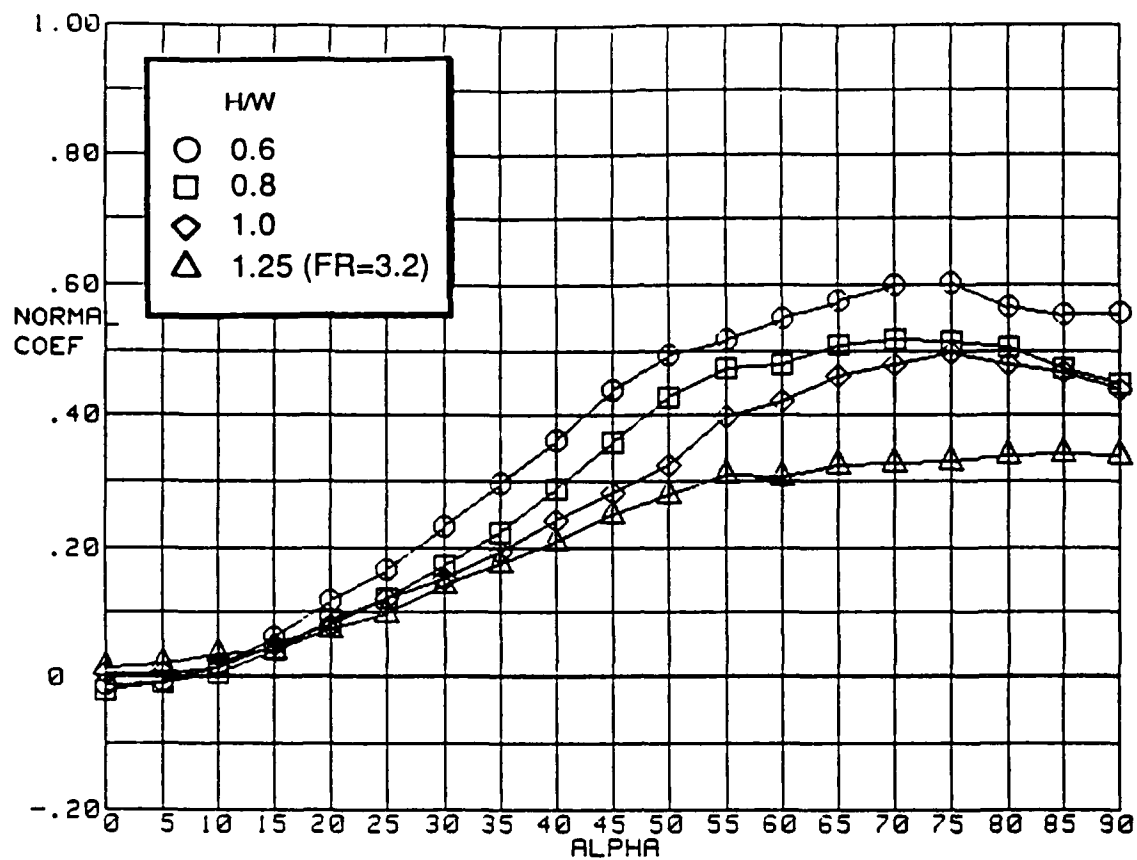
c) FR=3

Figure 14.- Continued
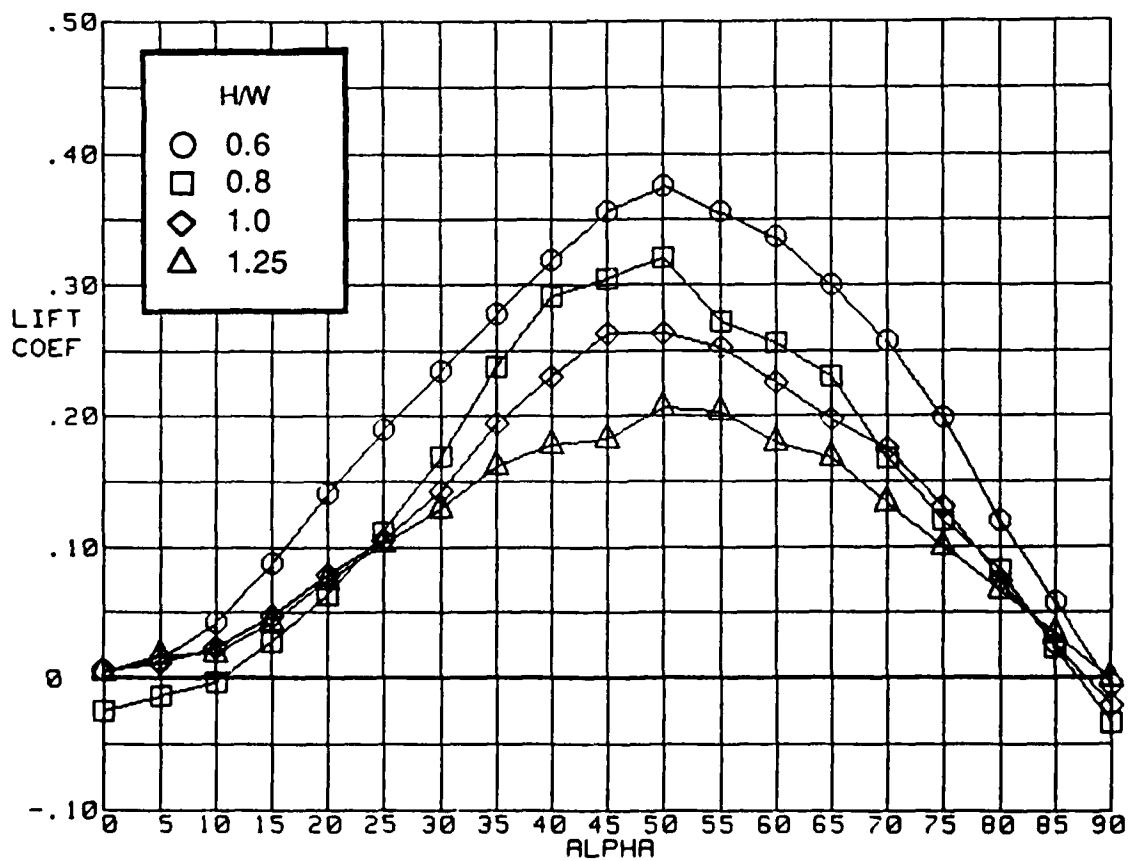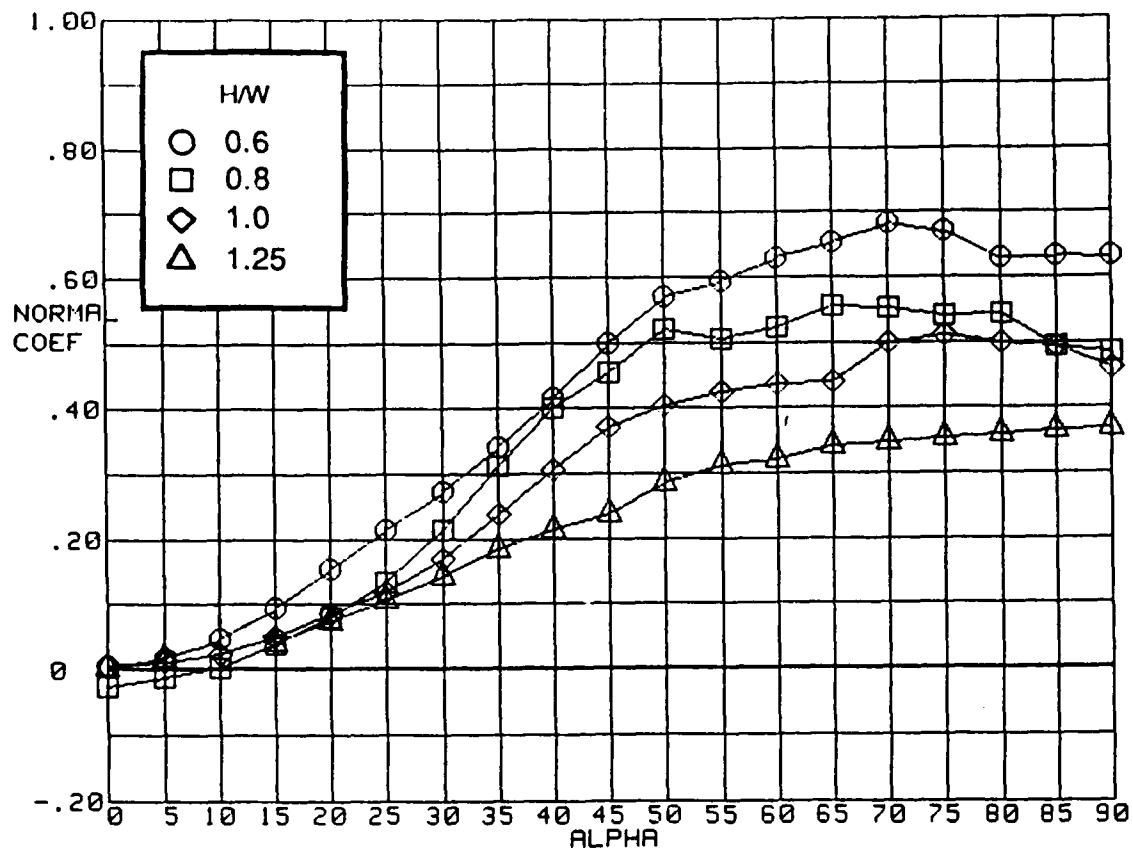
d) FR = 4

Figure 14.- Continued

53
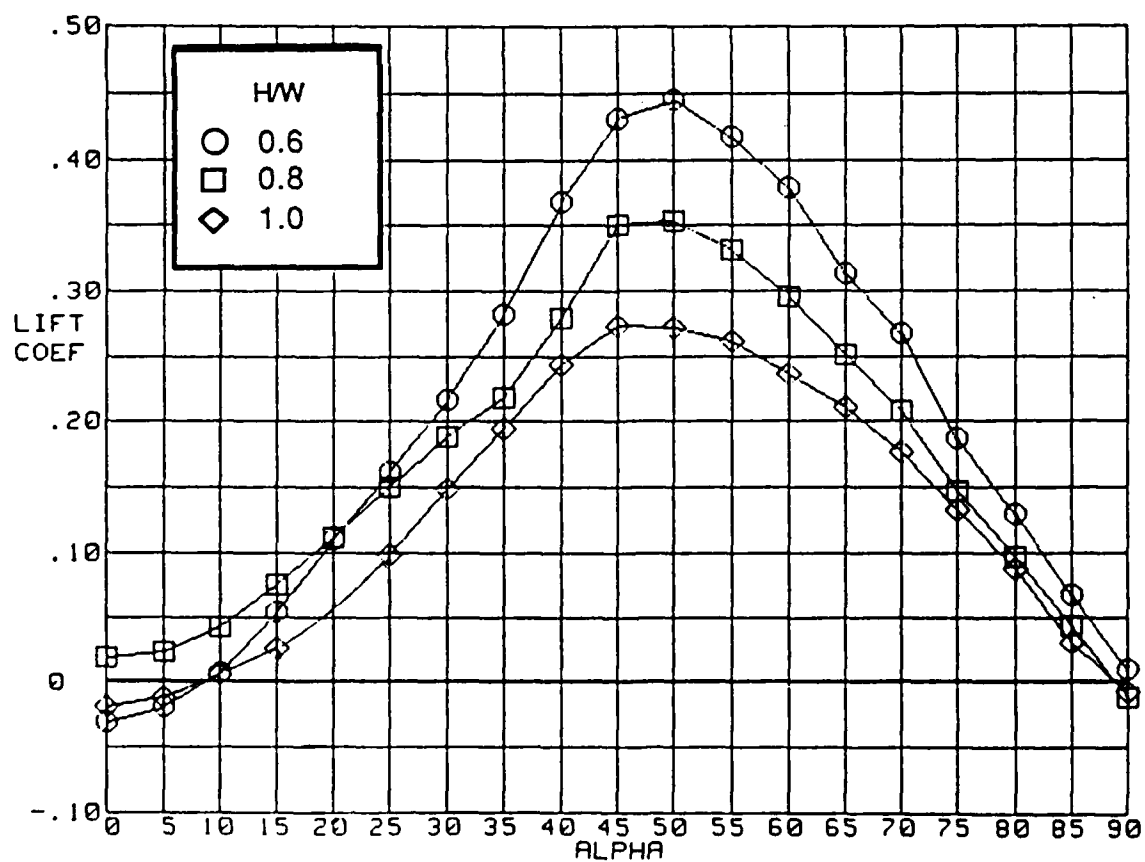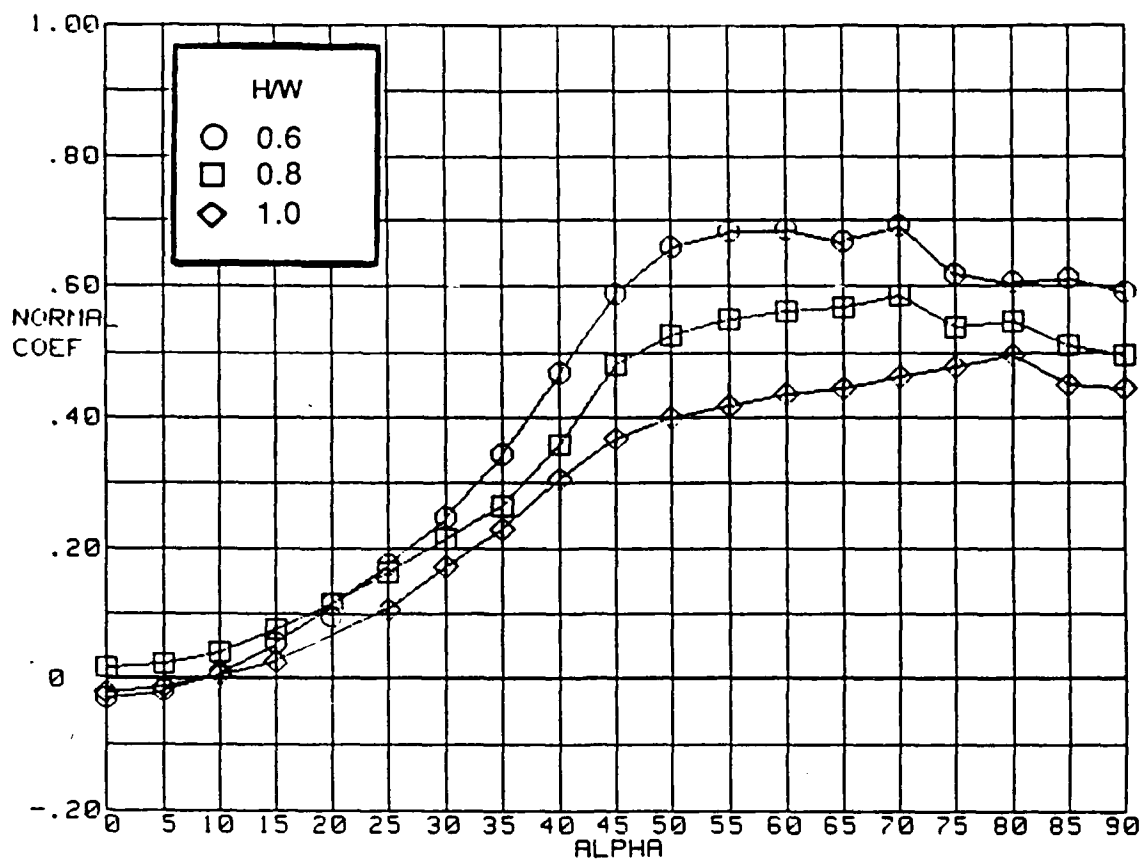
e) FR=4.5

Figure 14.- Continued

54
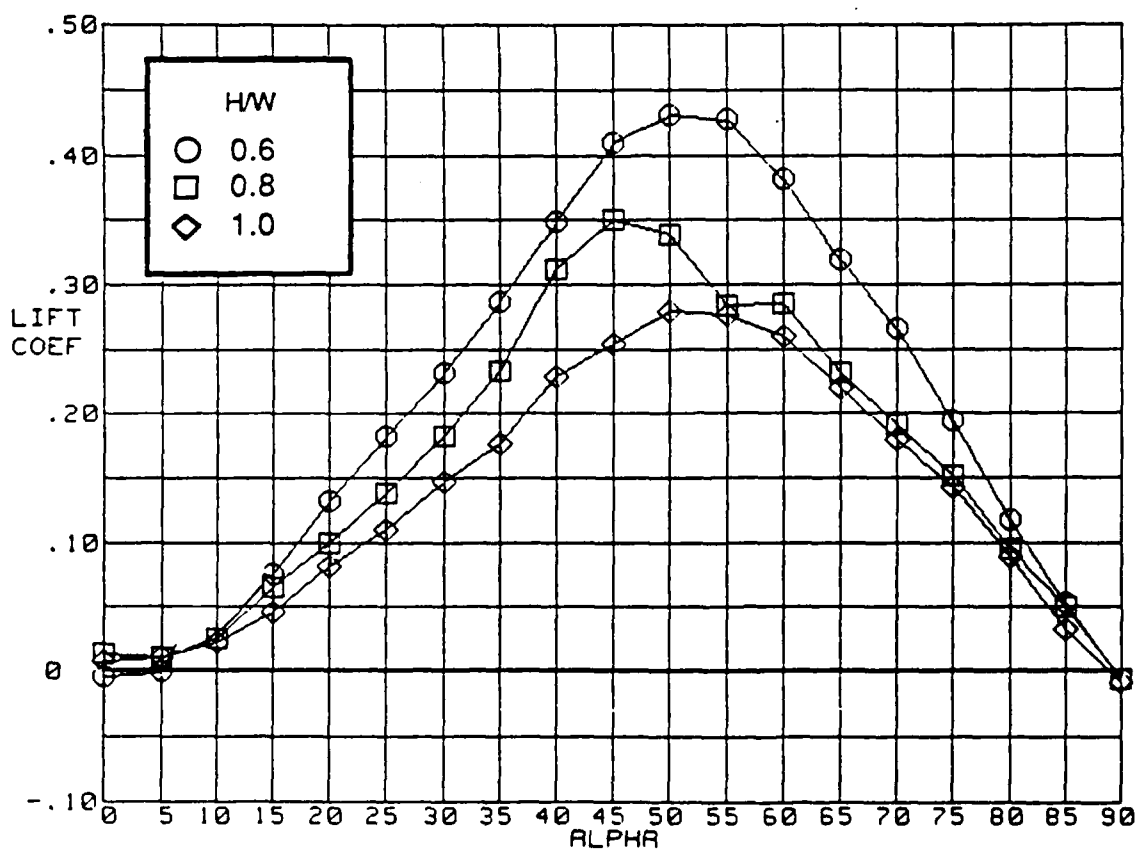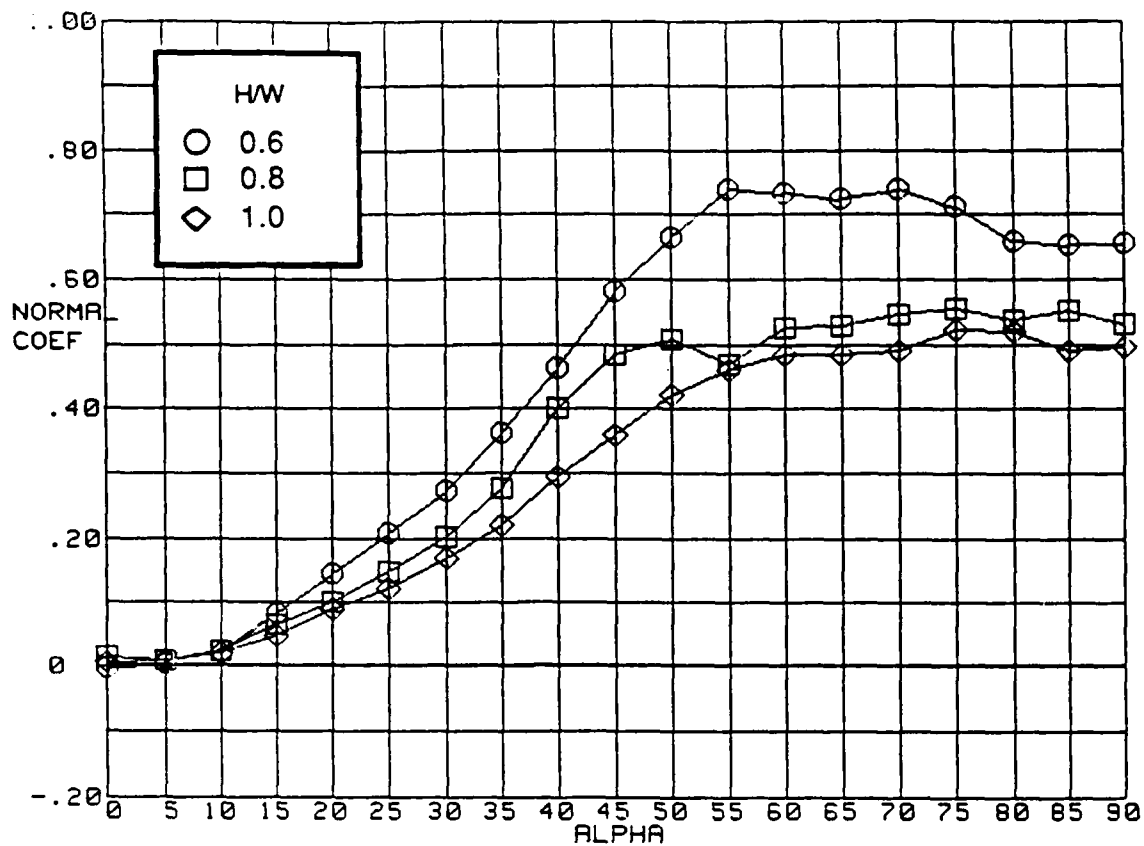
f)   FR=5

Figure 14.- Concluded

55
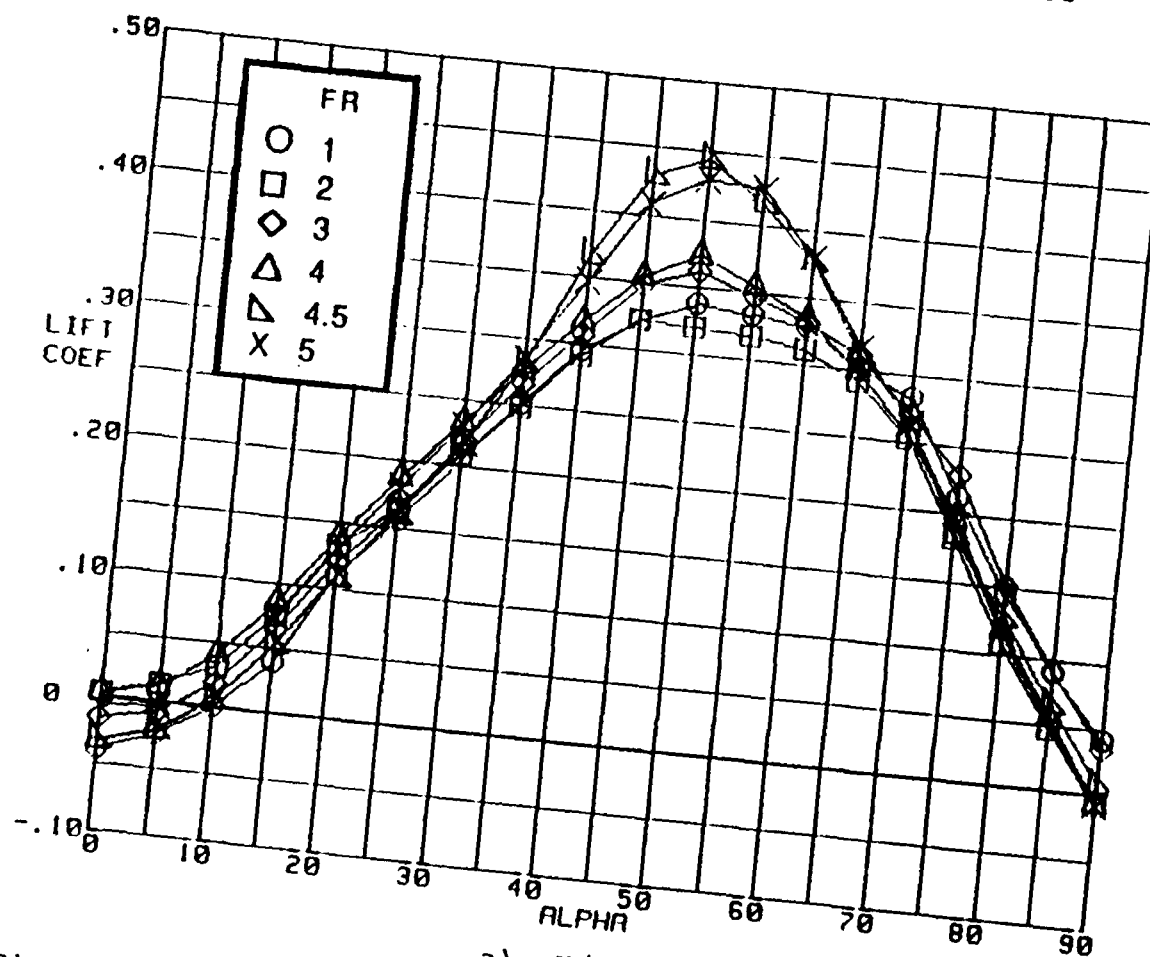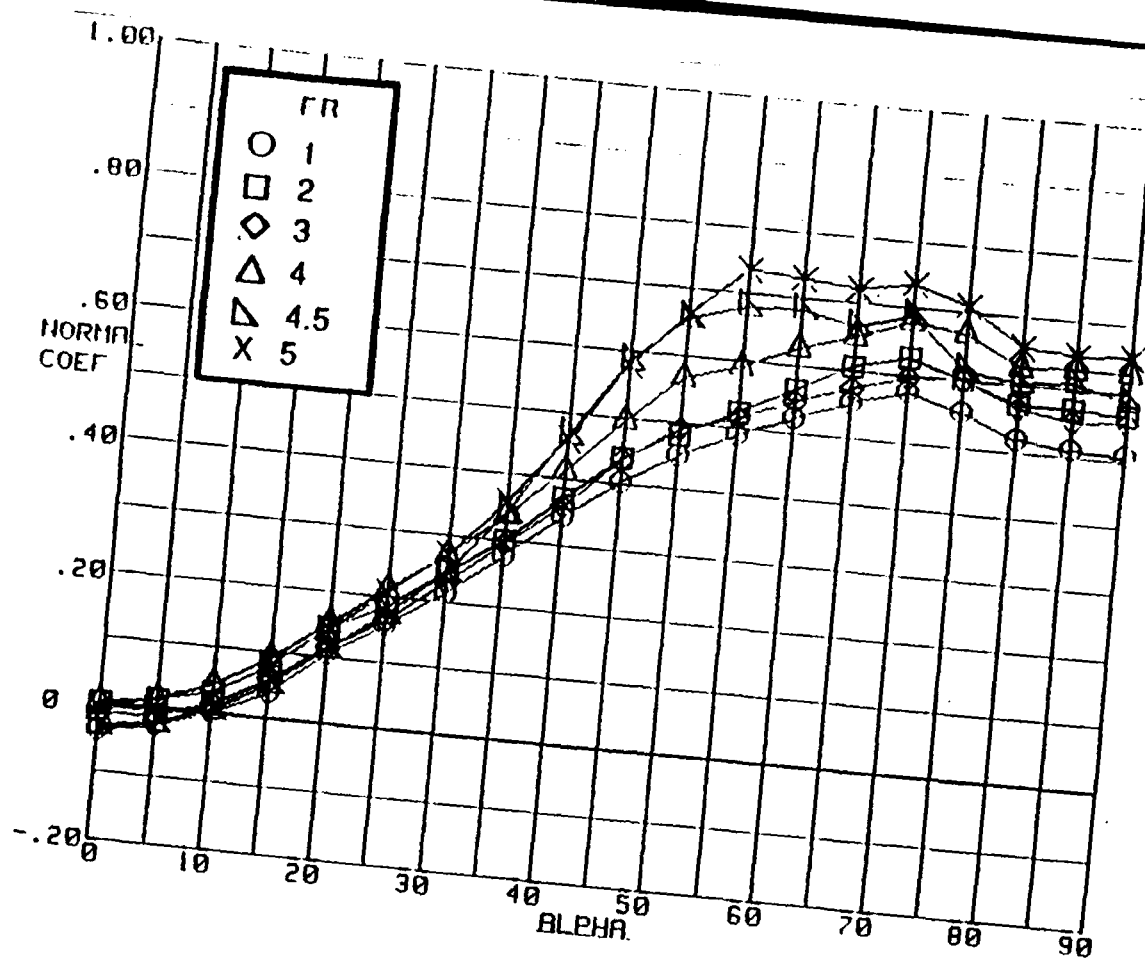
Figure 15.- Influence of forebody fineness ratio on lift and normal-
force coefficient variation with angle of attack for
specified cross-sectional shapes

a)   H/W=0.6

56
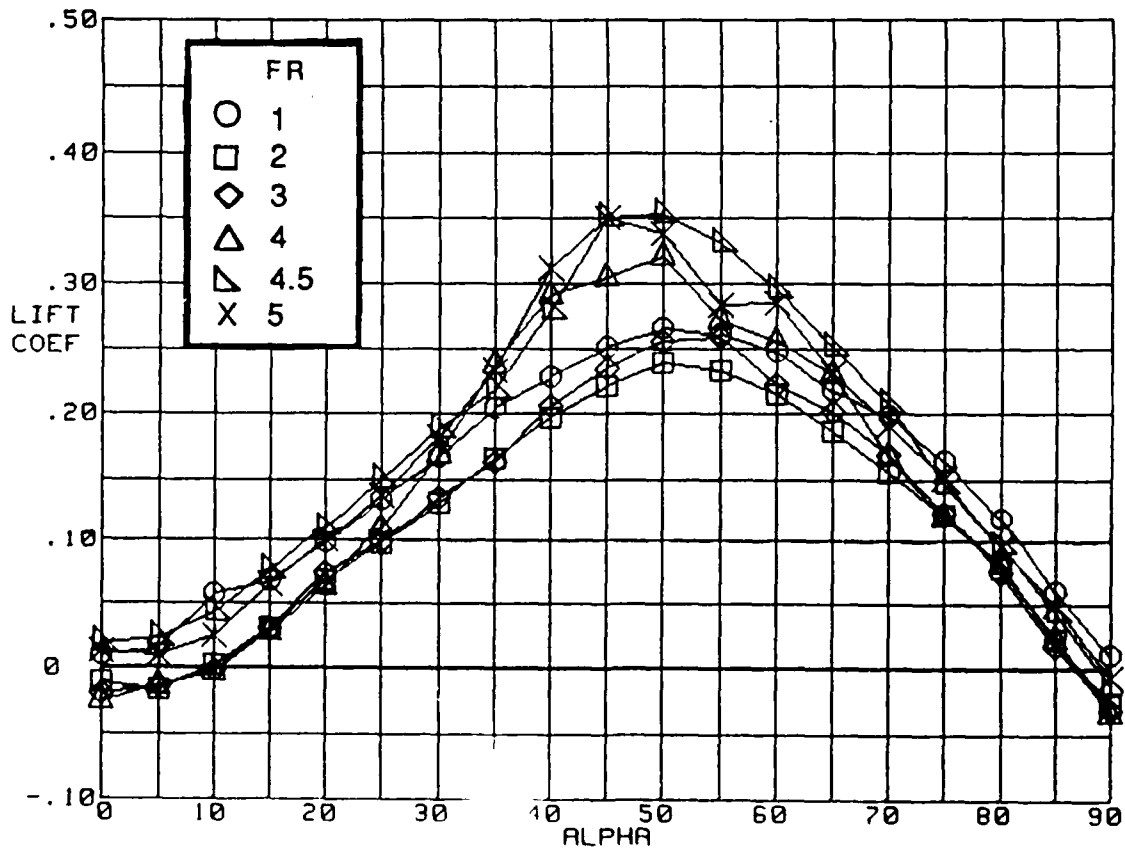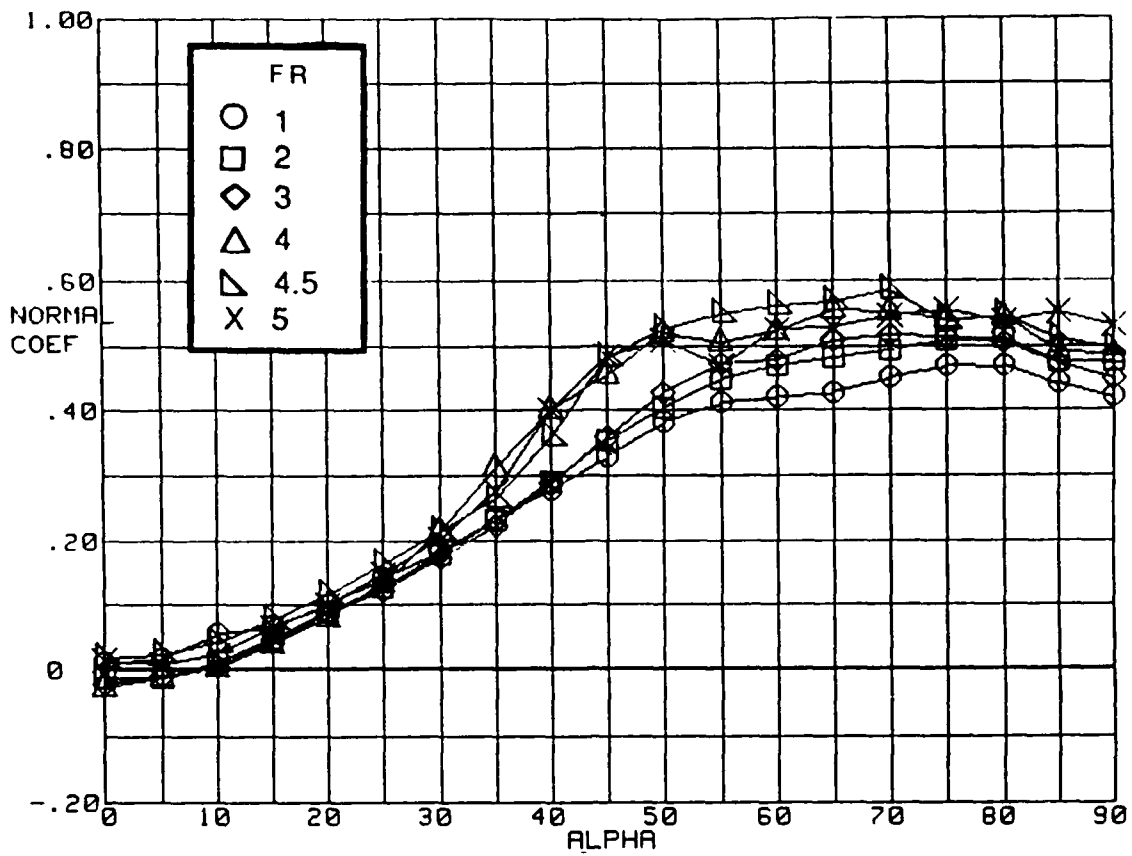
b) H/W=0.8

Figure 15.- Continued

57
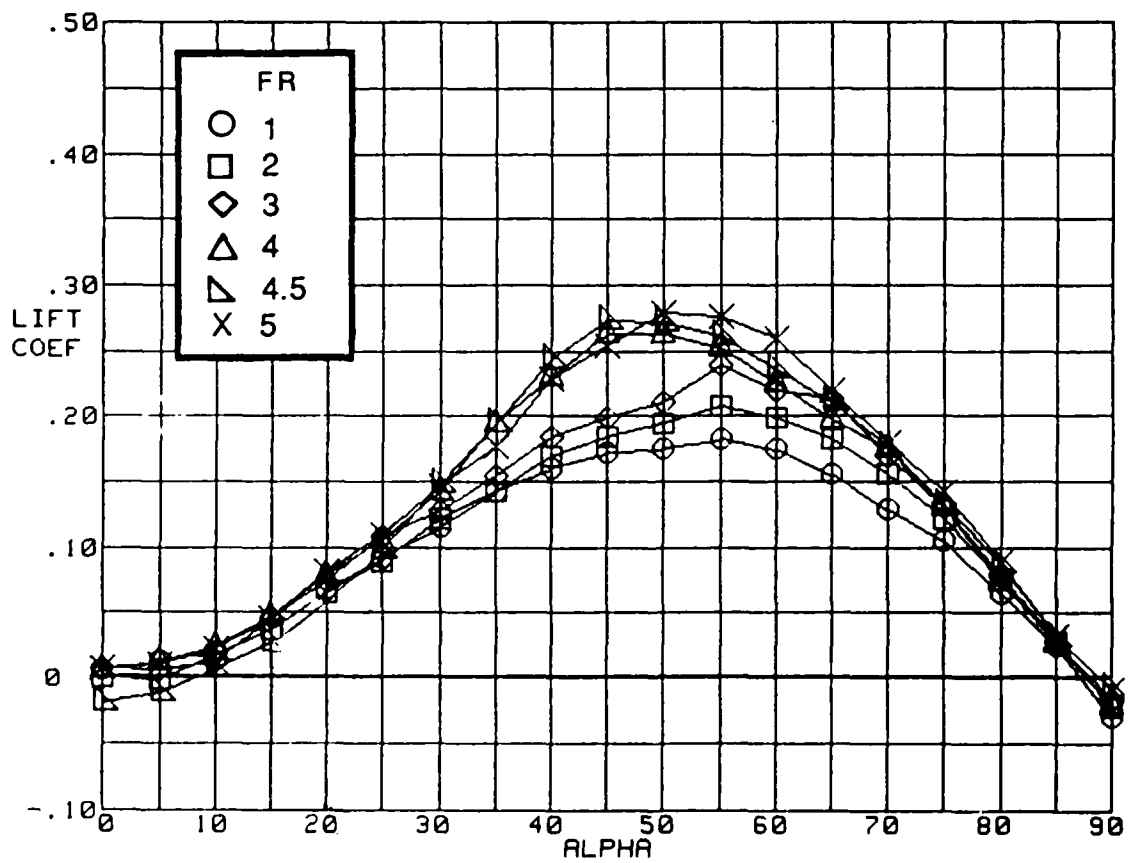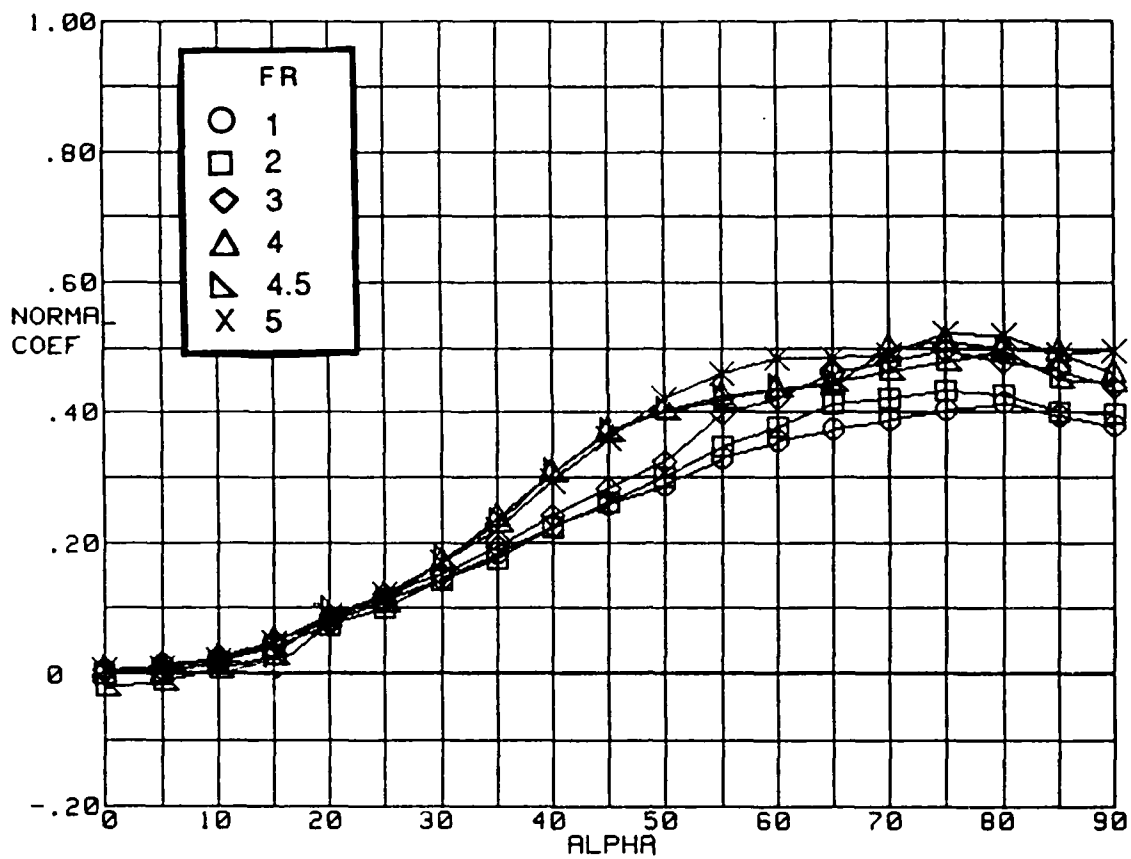
c) H/W=1.0

Figure 15.- Continued
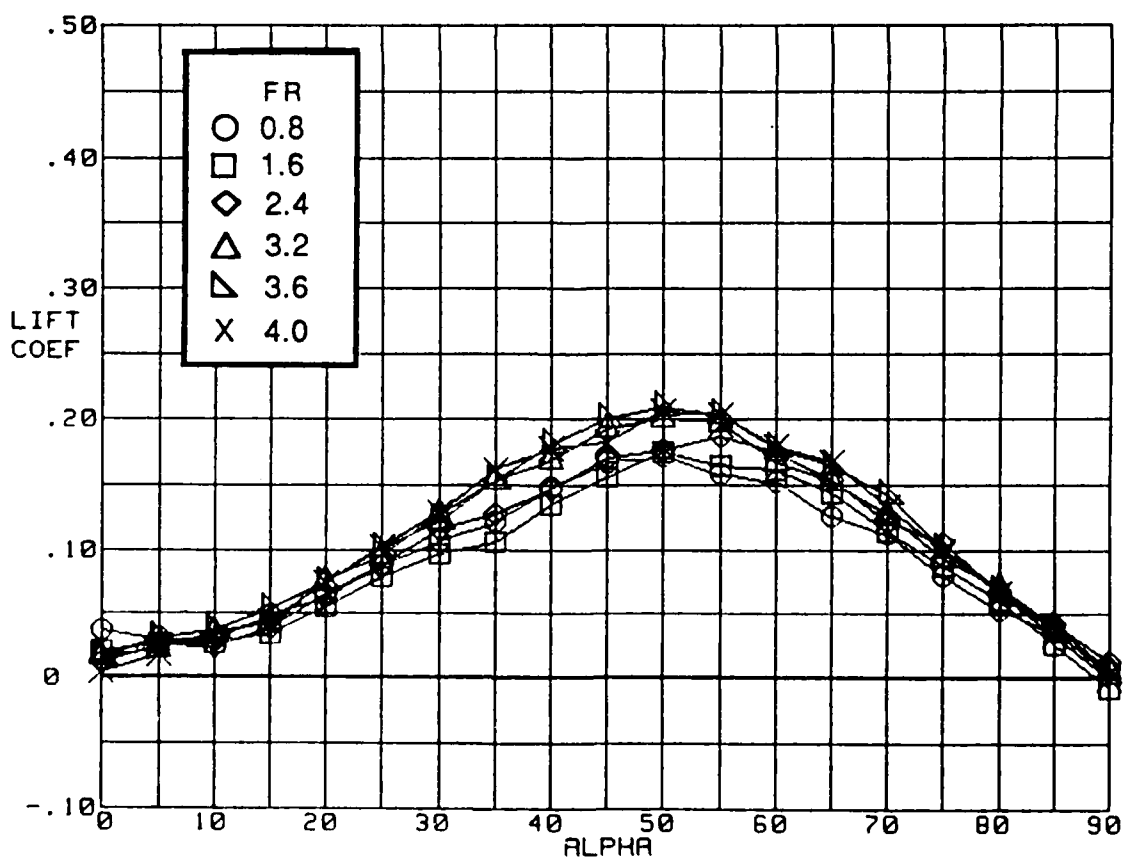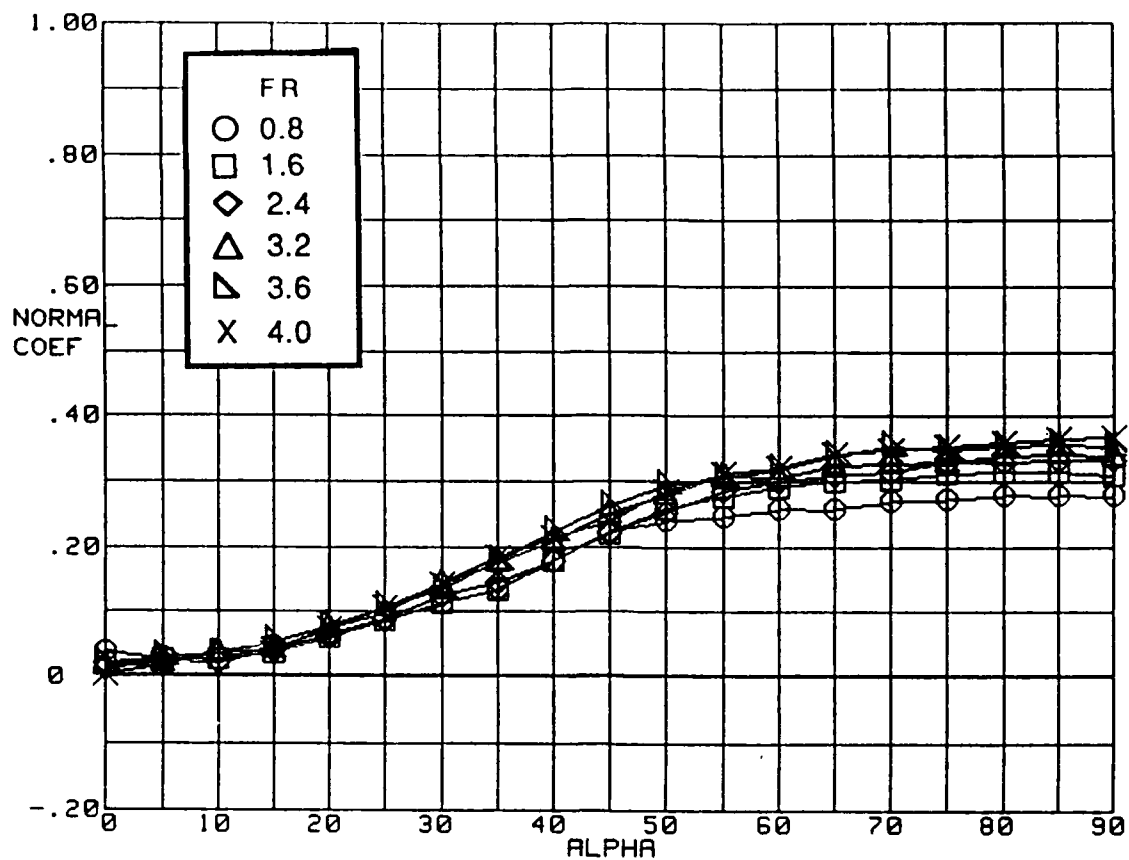
d) H/W=1.25

Figure 15.- Concluded

59
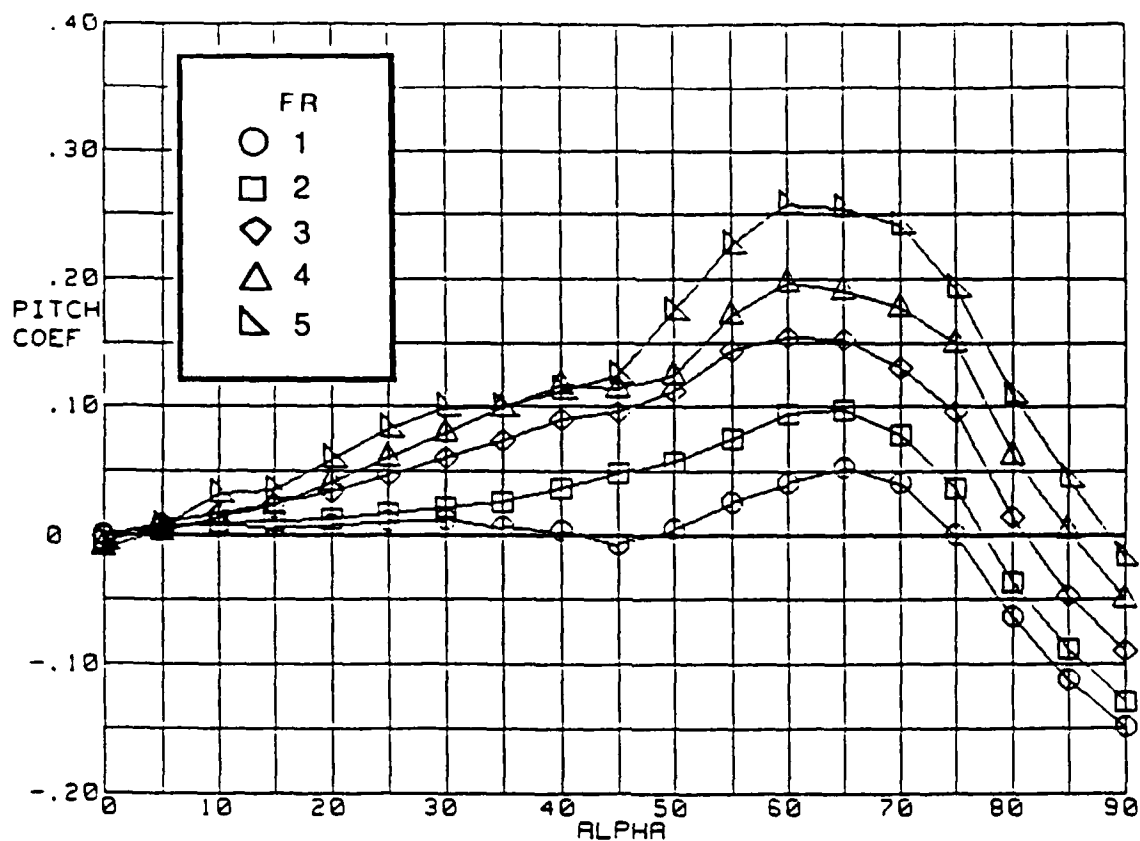
a)   H/W=0.6
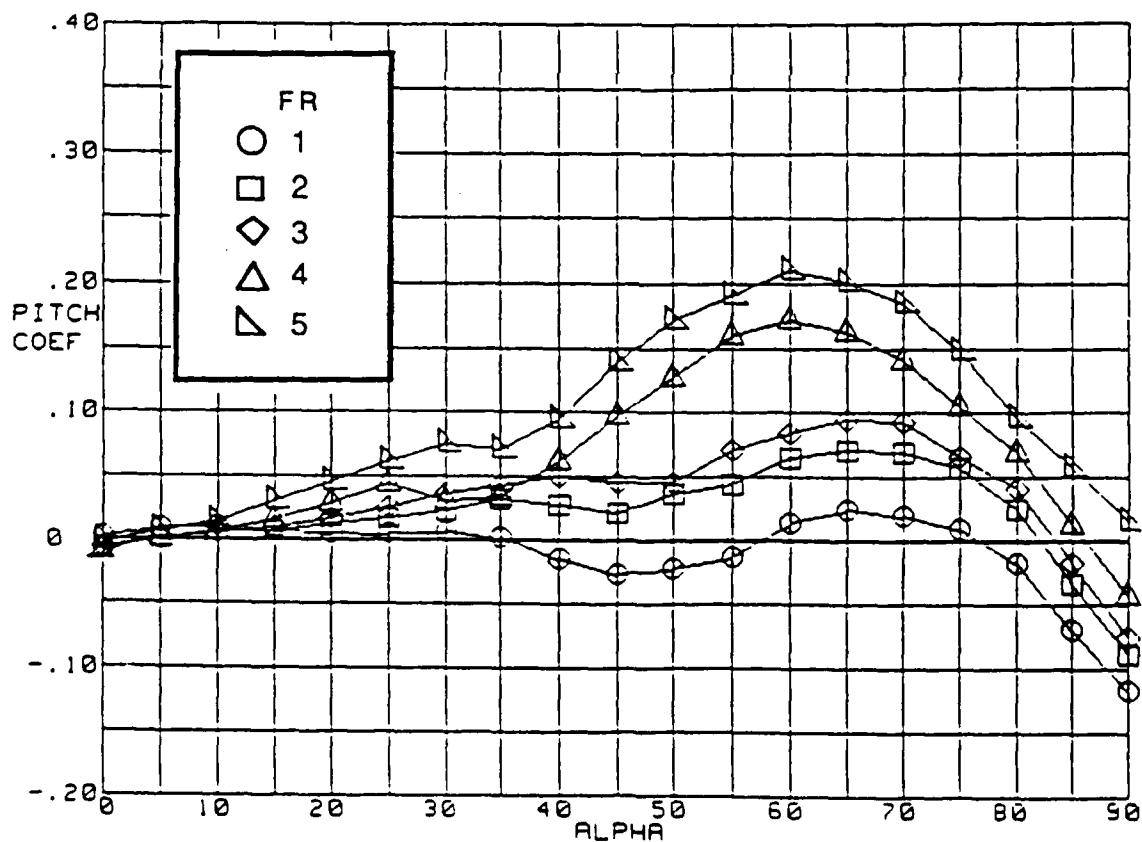
b)   H/W=0.8

Figure 16.- Influence of forebody fineness ratio on pitching-moment
coefficient variation with angle of attack for specified
cross-sectional shapes

60
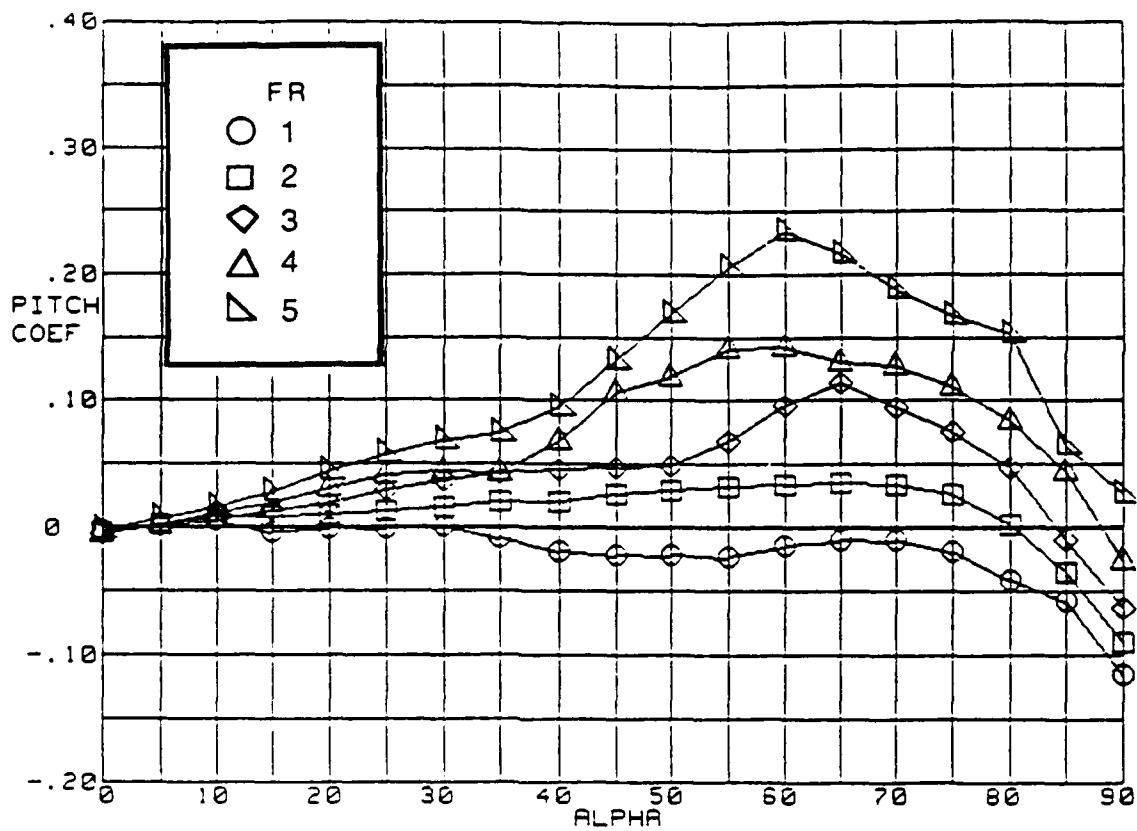
c) H/W=1.0
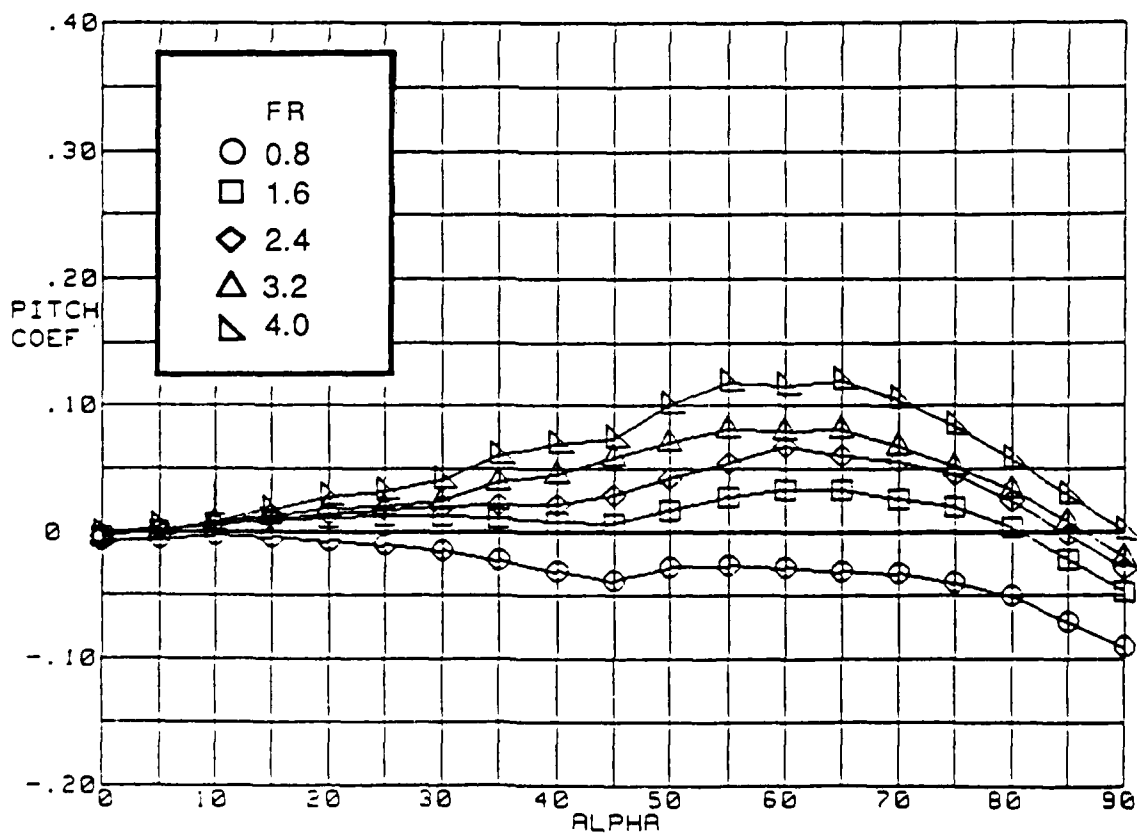
d) H/W=1.25

Figure 16.- Concluded

a) FR=1

b) FR=2
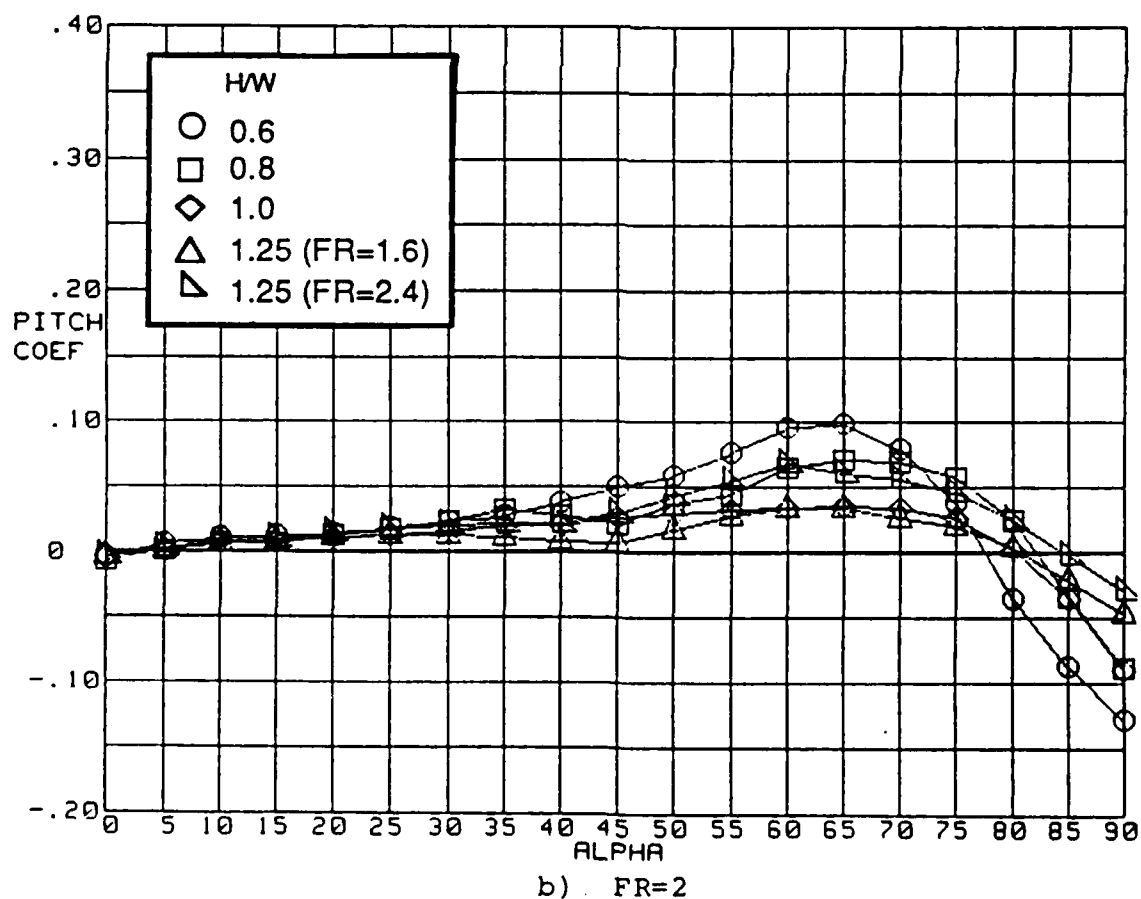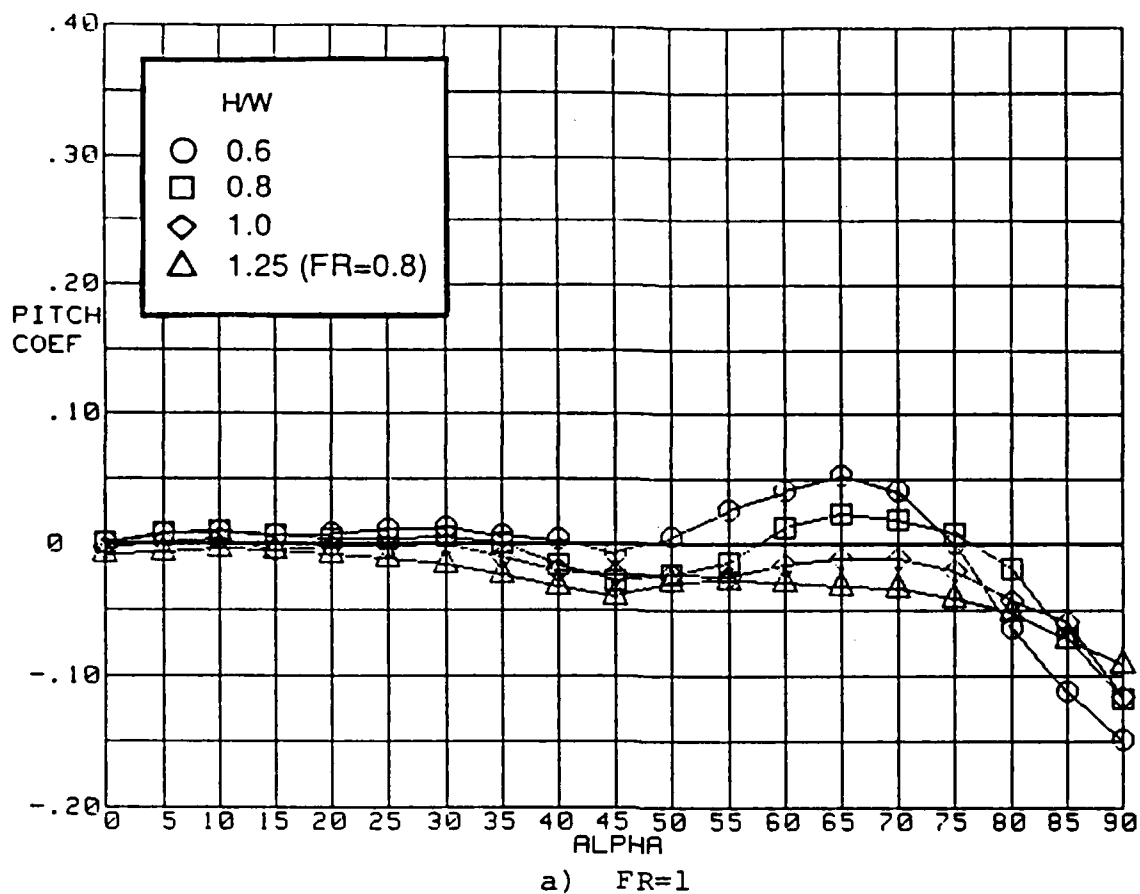
Figure 17.- Influence of forebody cross-sectional shape on pitching-
moment coefficient variation with angle of attack at
specified values of fineness ratio

62
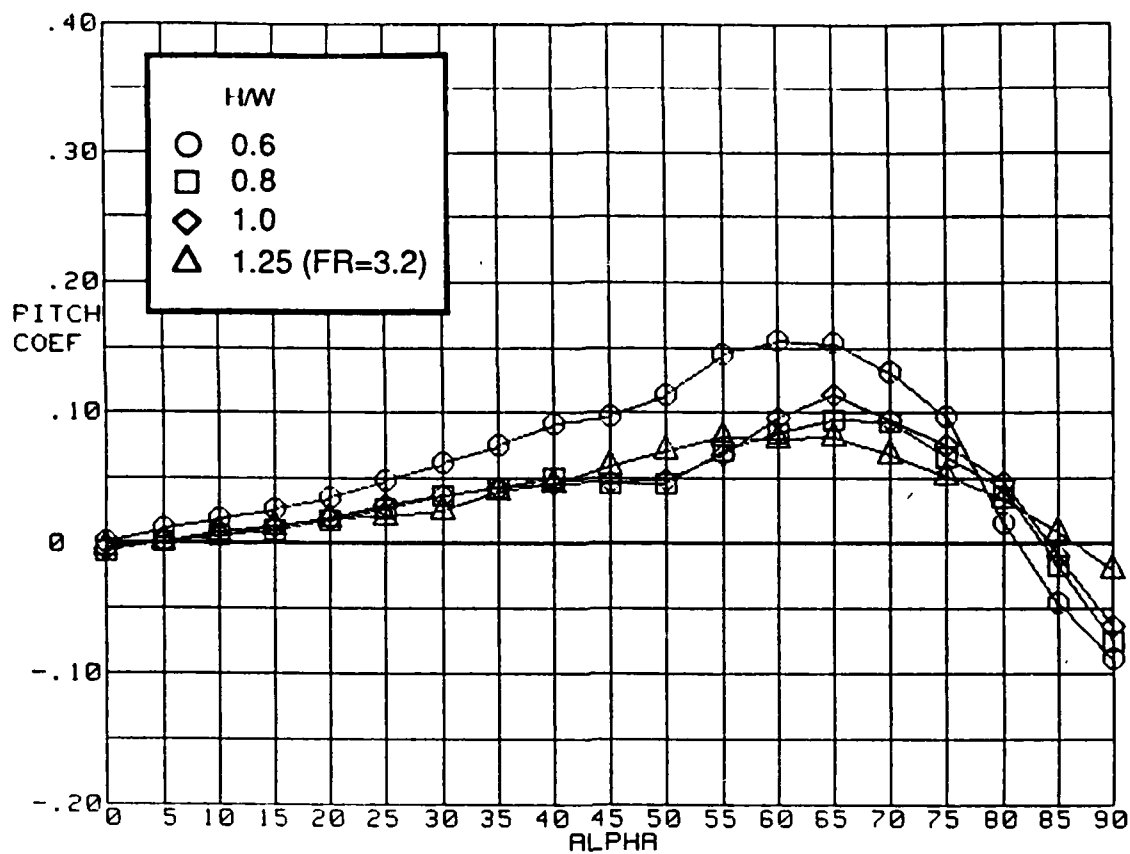
c)   FR=3
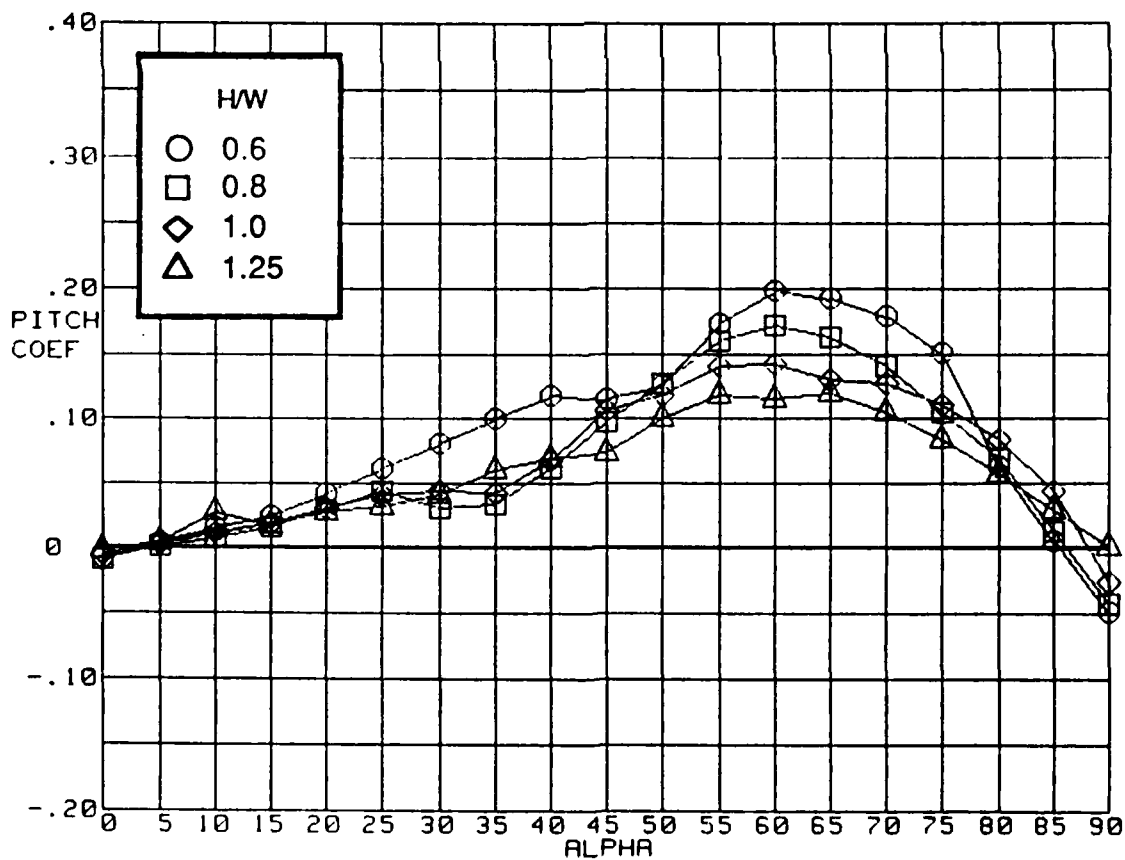
d)   FR=4

Figure 17.- Continued

63
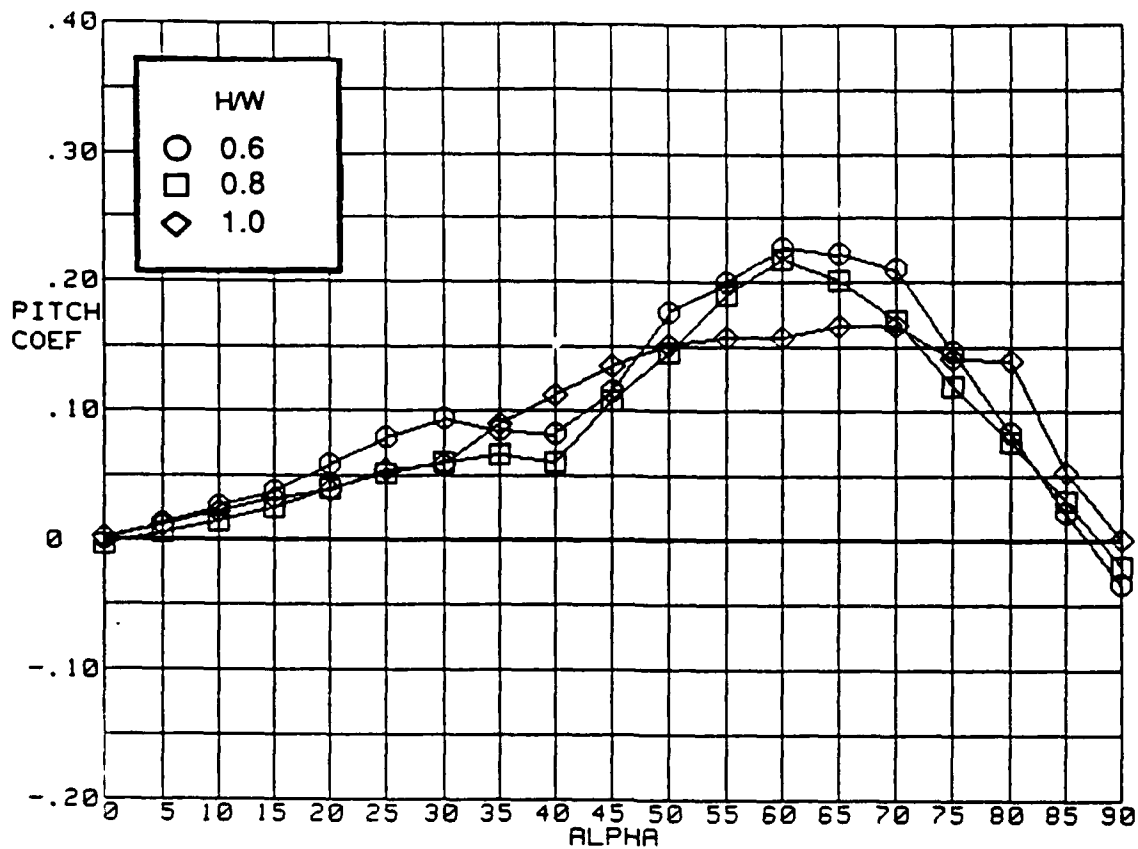
e)   FR=4.5
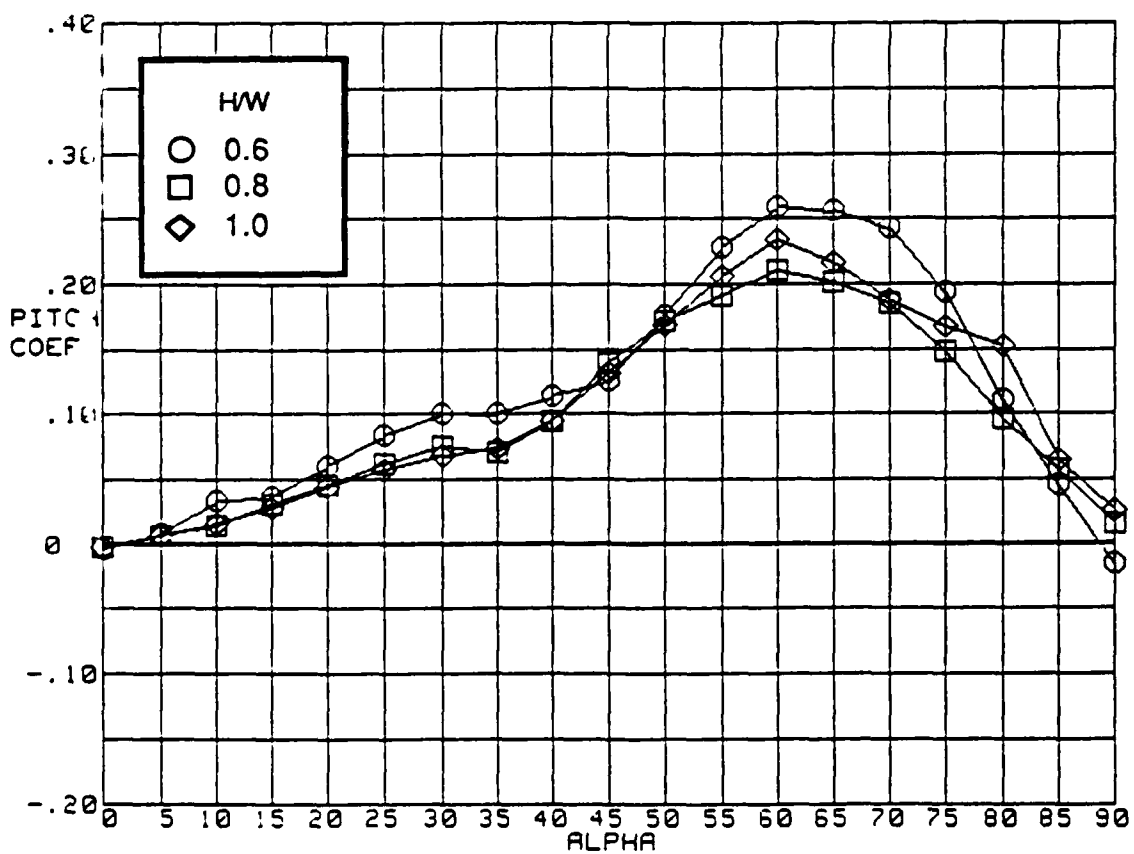
f)   FR=5

Figure 17.- Concluded

64
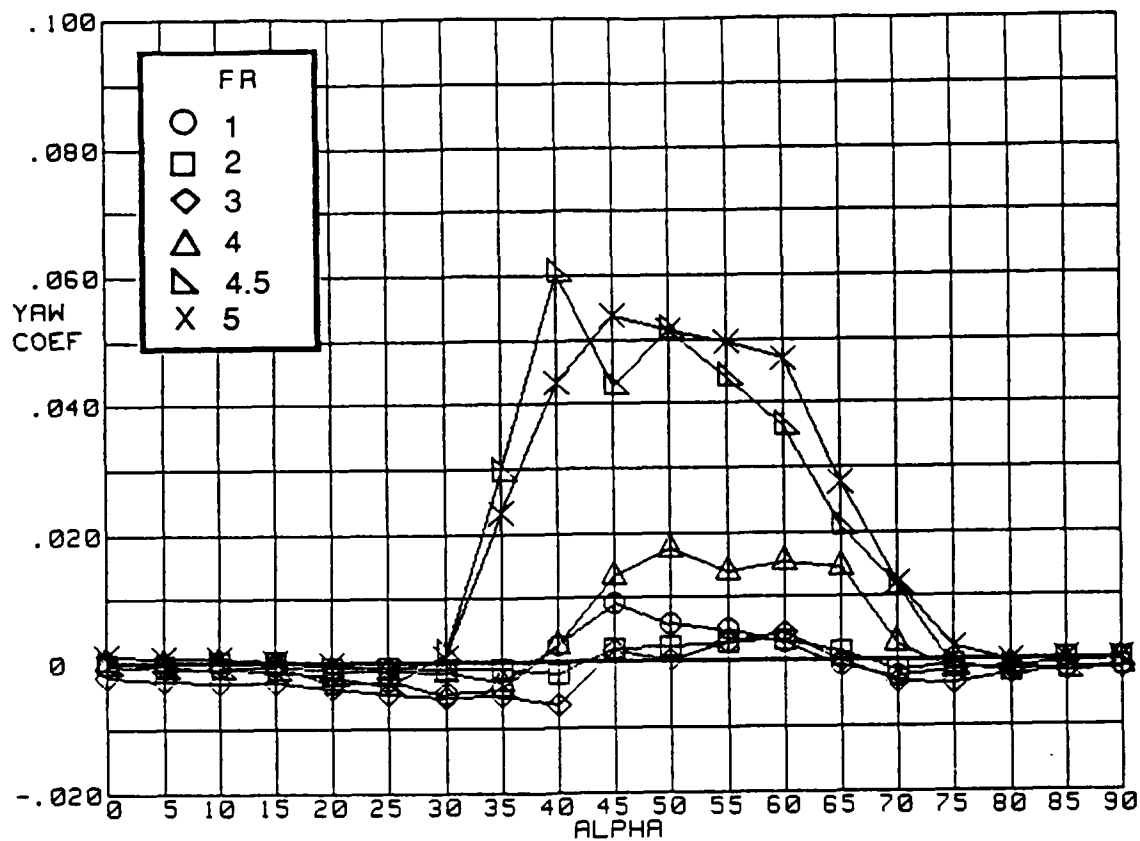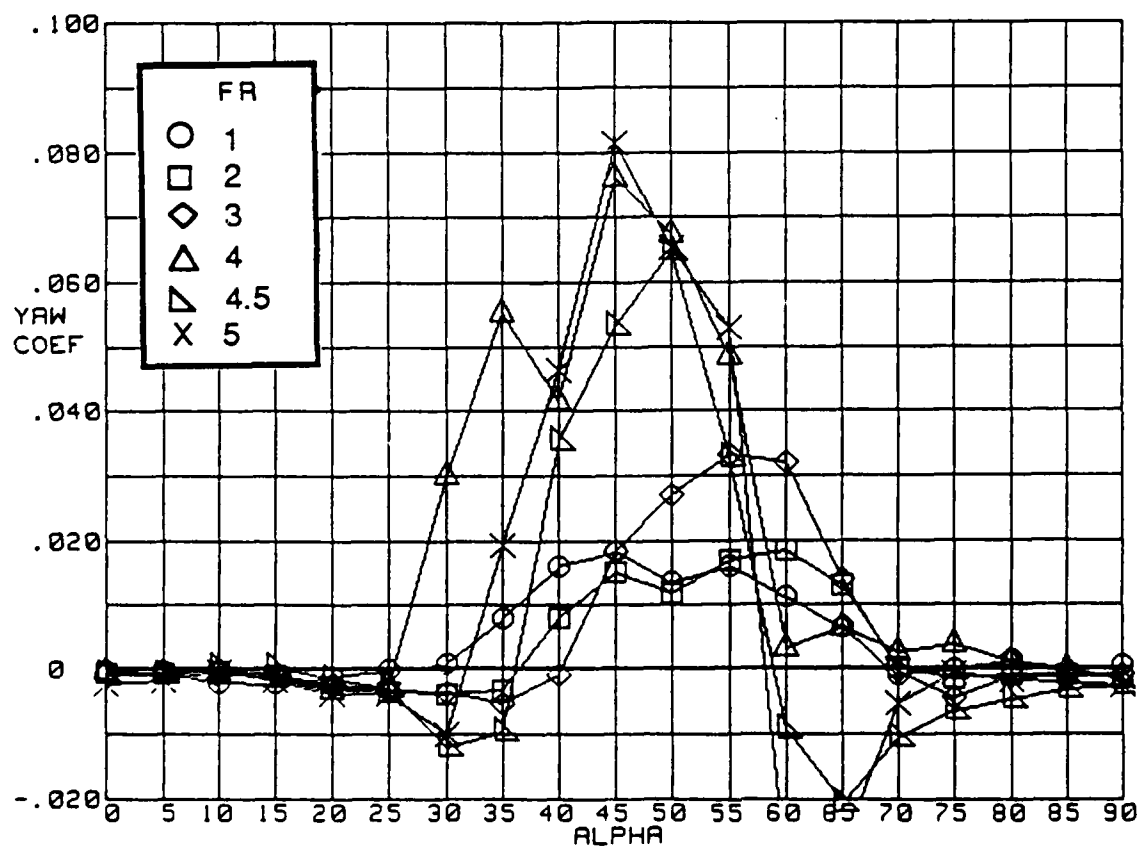
Figure 18.- Influence of forebody fineness ratio on symmetrical
flight yawing-moment coefficient variation with angle of attack
for specified cross-sectional shapes

65
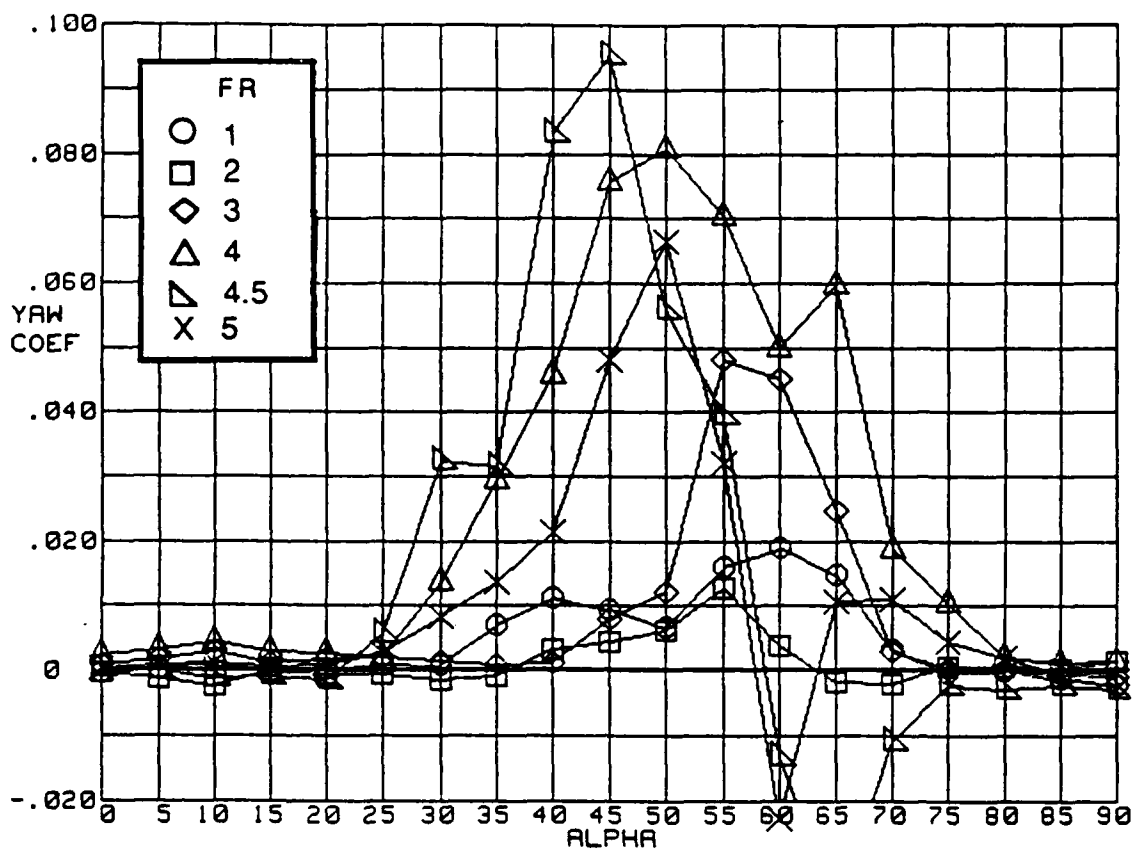
c) H/W=1.0
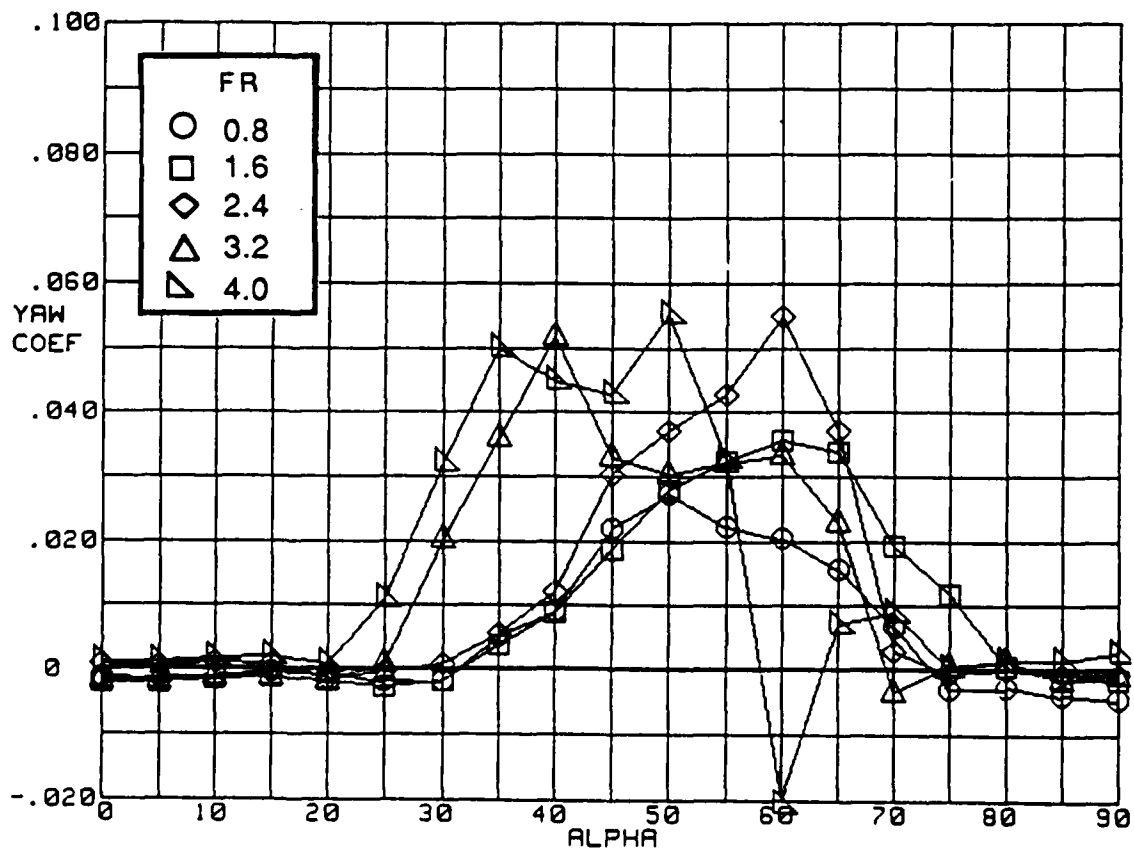
d) H/W=1.25

Figure 18.- Concluded

66
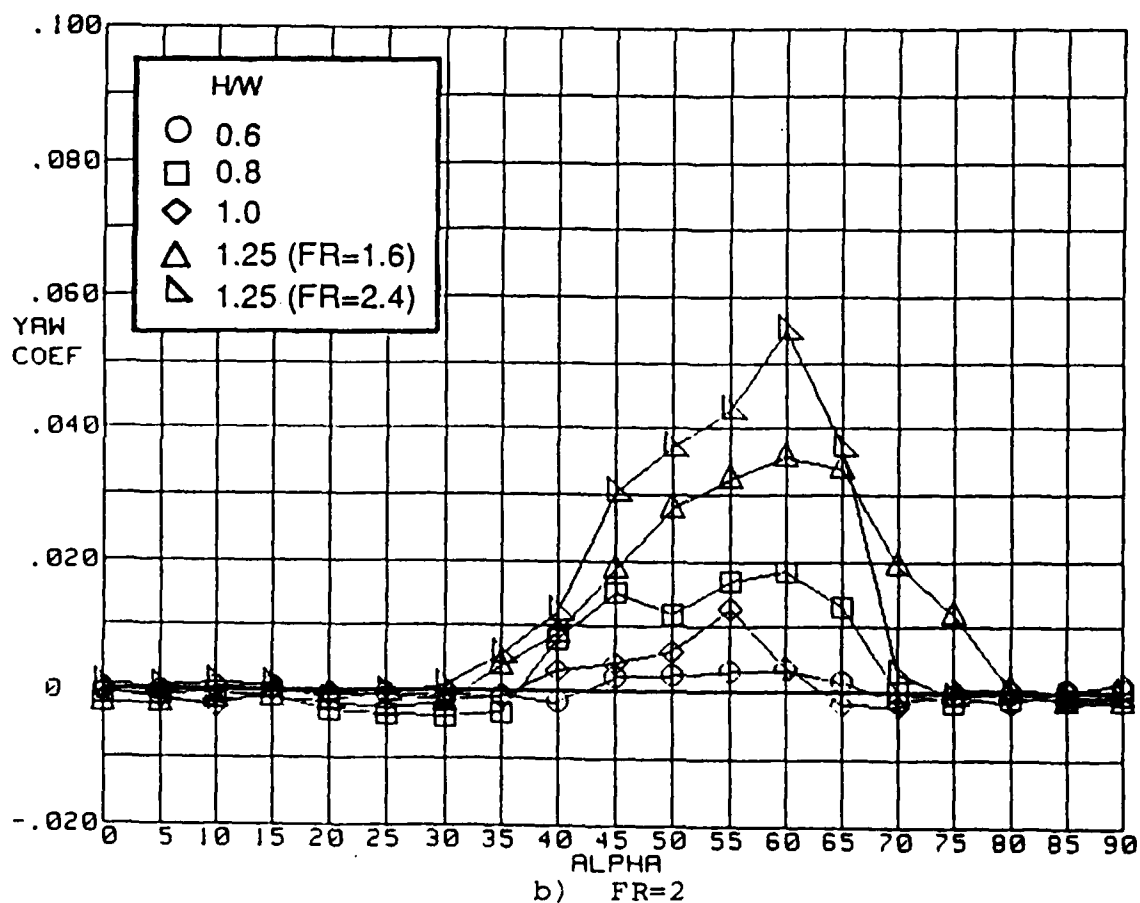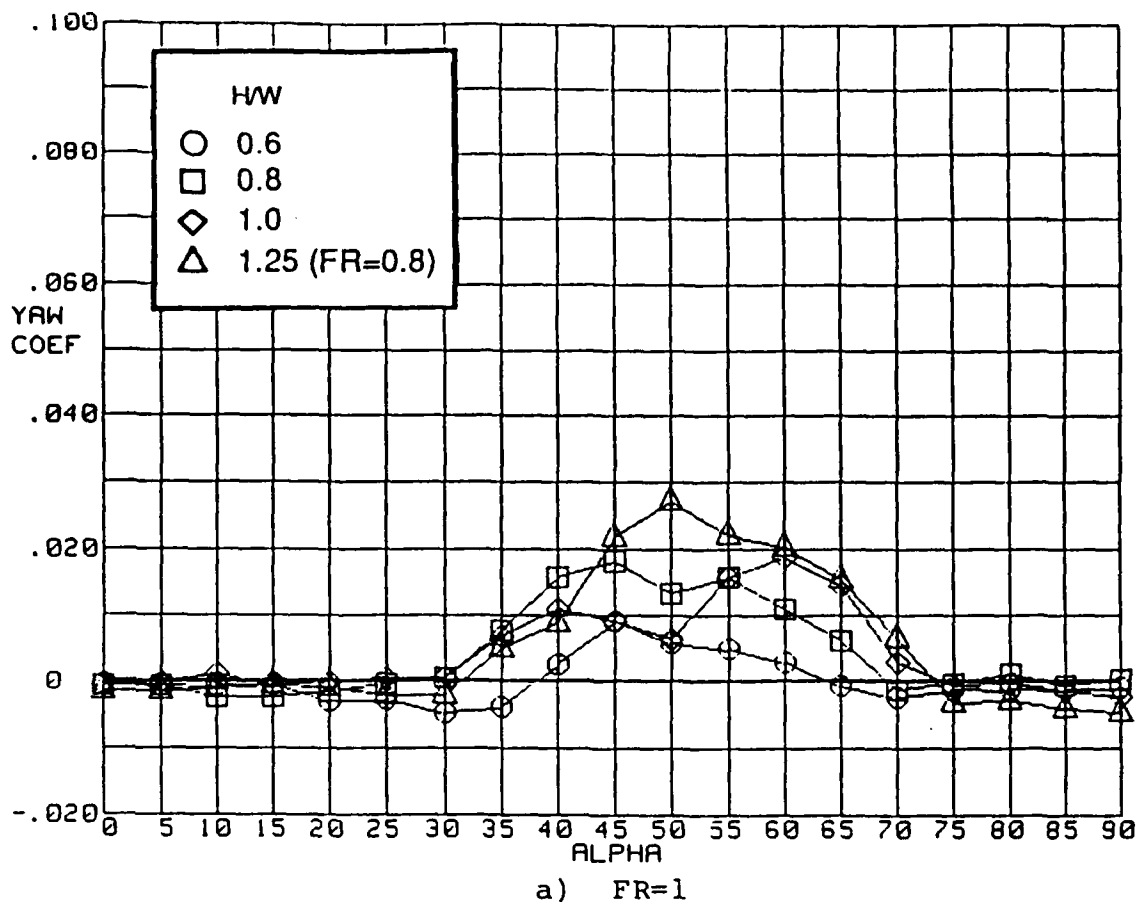
Figure 19.- Influence of forebody cross-sectional shape on symmetrical
flight yawing-moment coefficient variation with angle of attack at
specified values of fineness ratio

67

c) FR=3
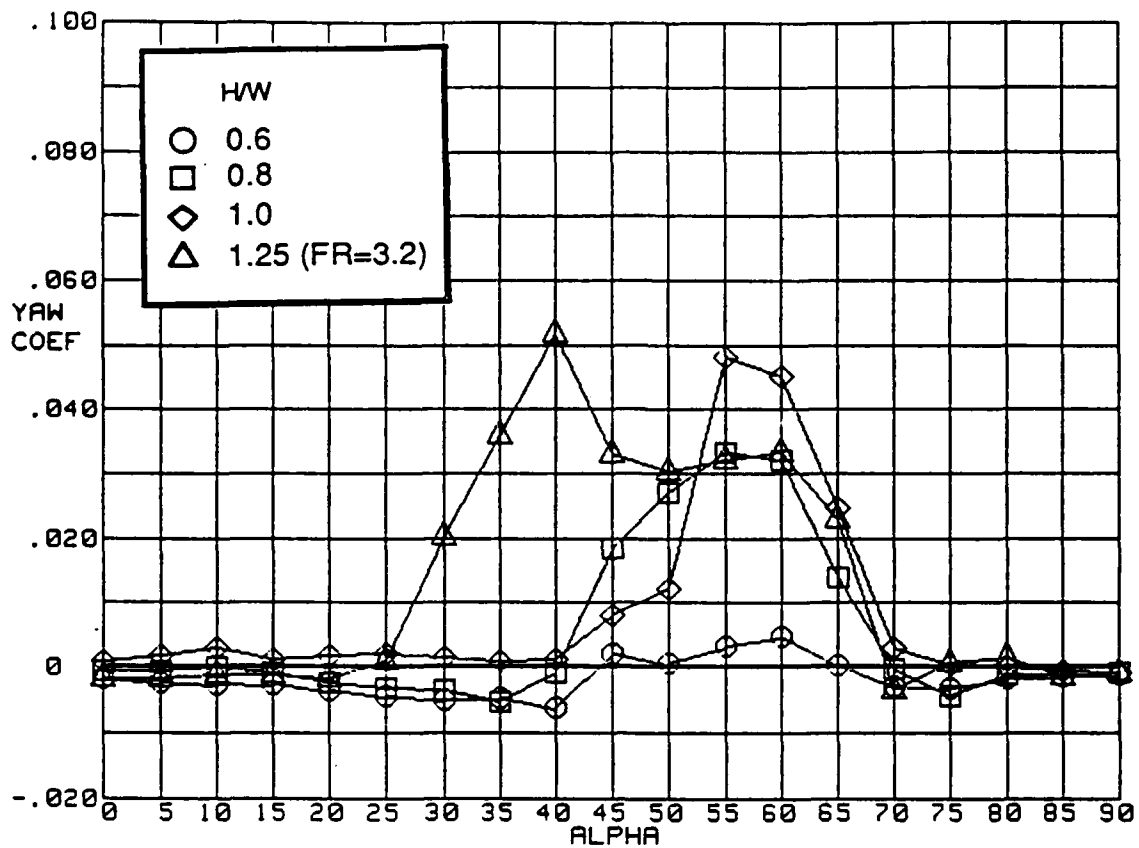
d) FR=4
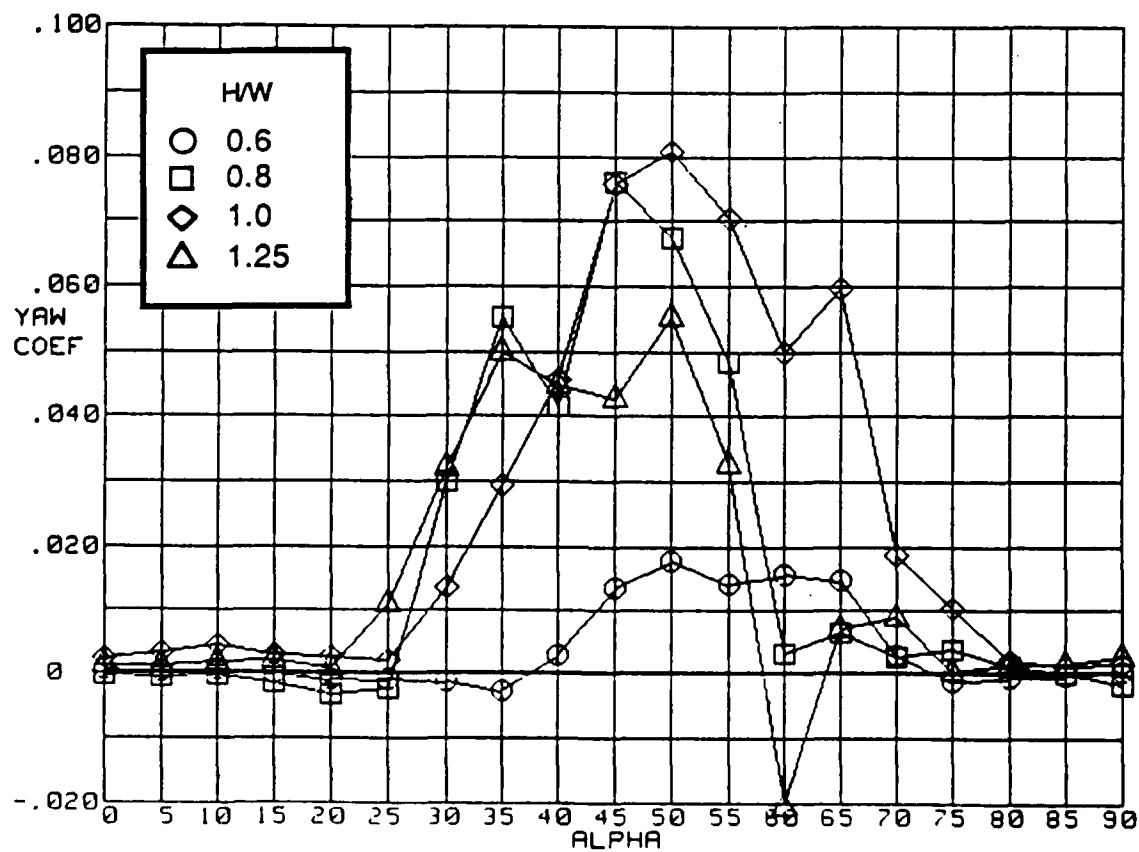
Figure 19.- Continued
68
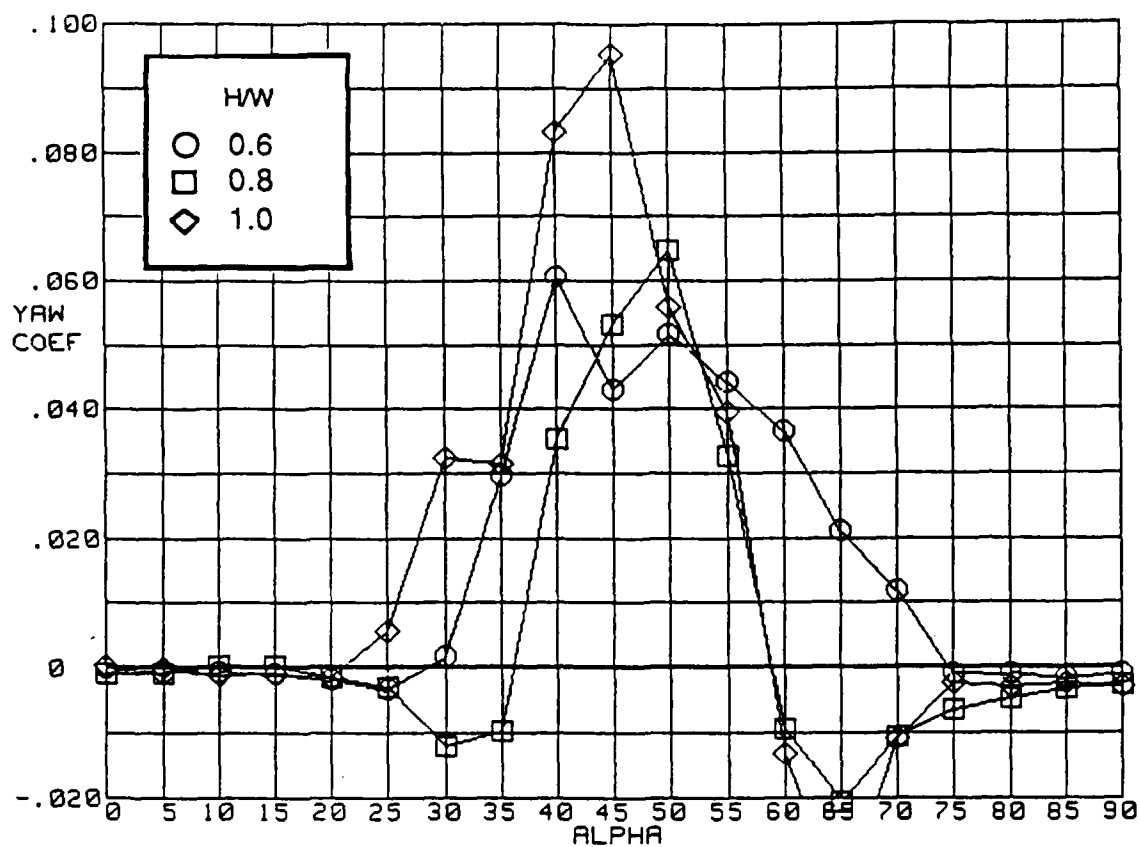
e) FR=4.5
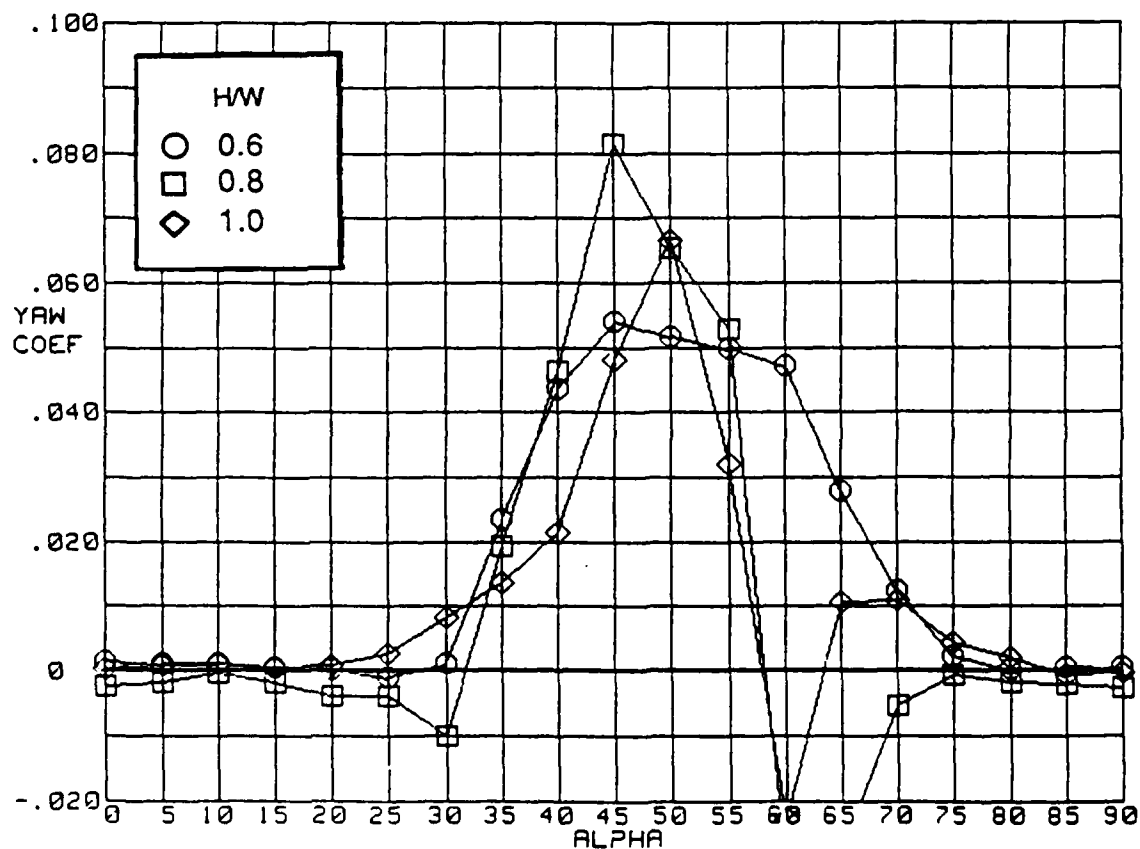
f) FR=5

Figure 19.- Concluded

69
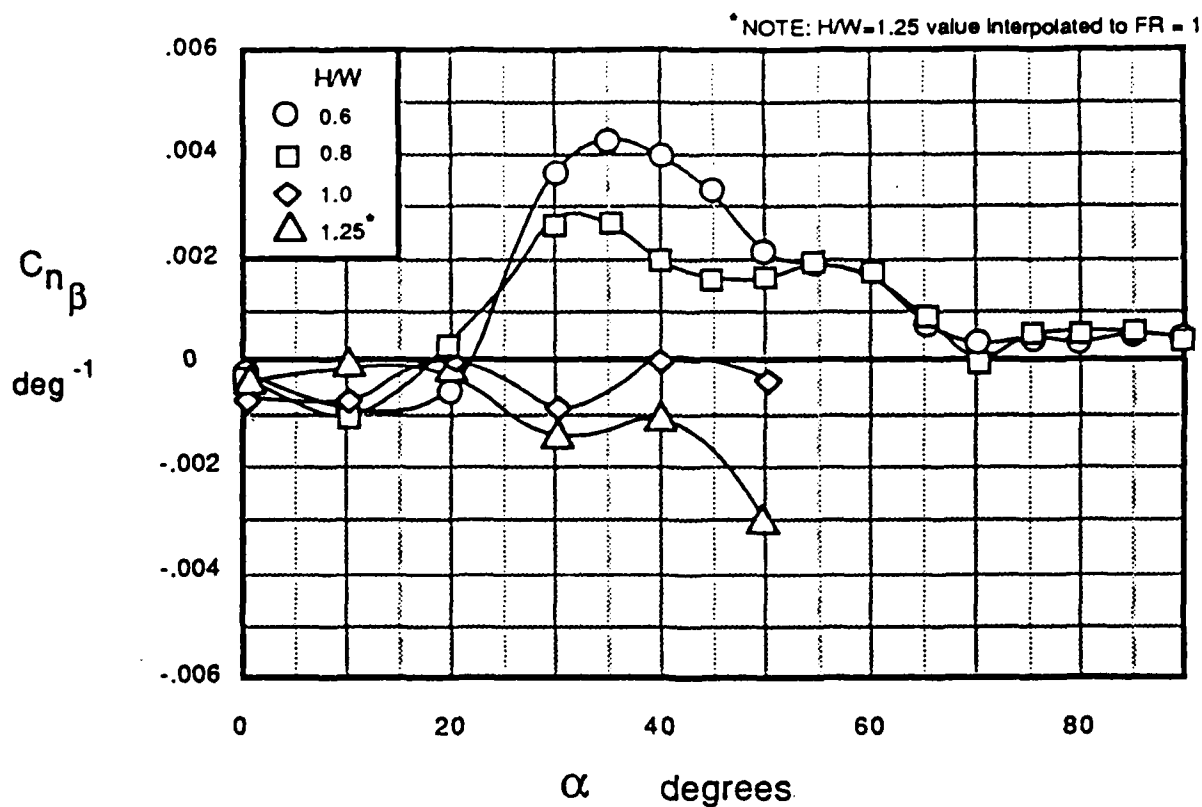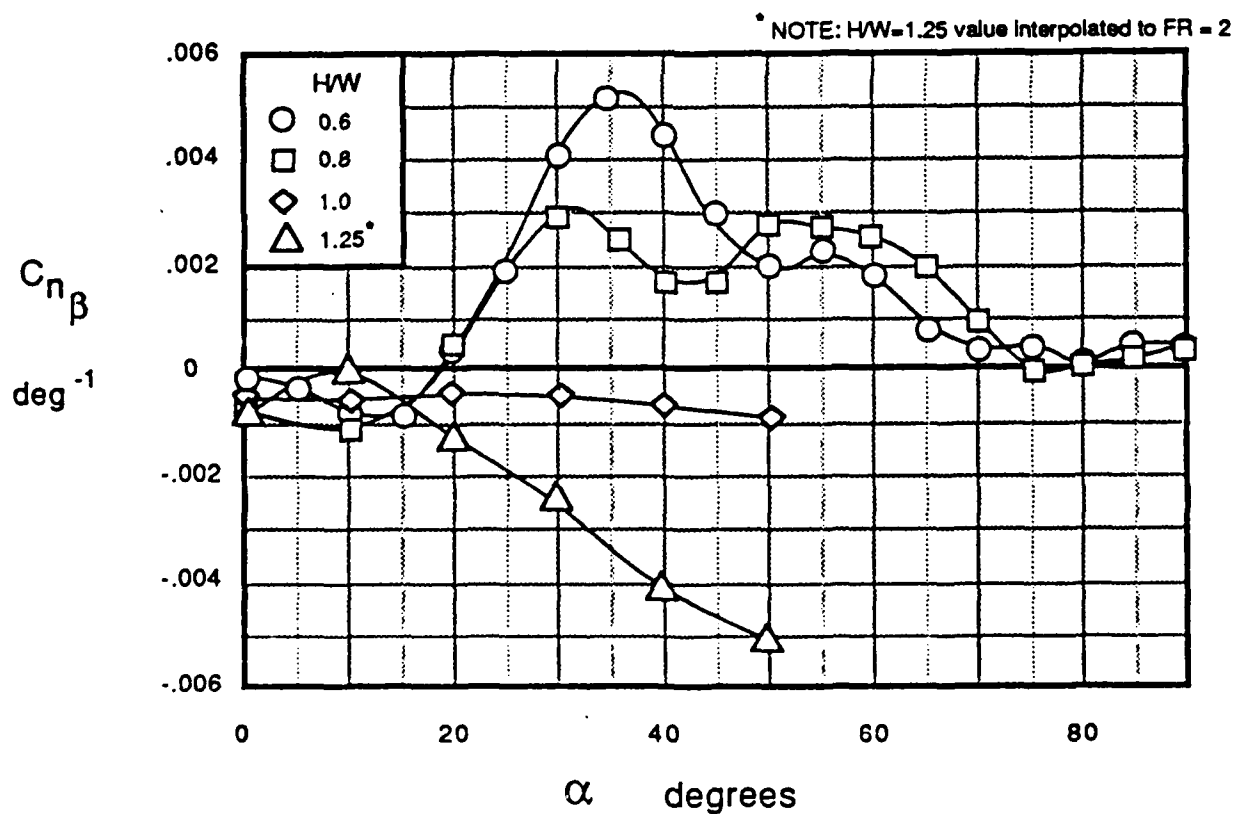
a) Fineness ratio = 1

b) Fineness ratio = 2

Figure 20. - Effect of cross-sectional shape on body-alone directional stability

70
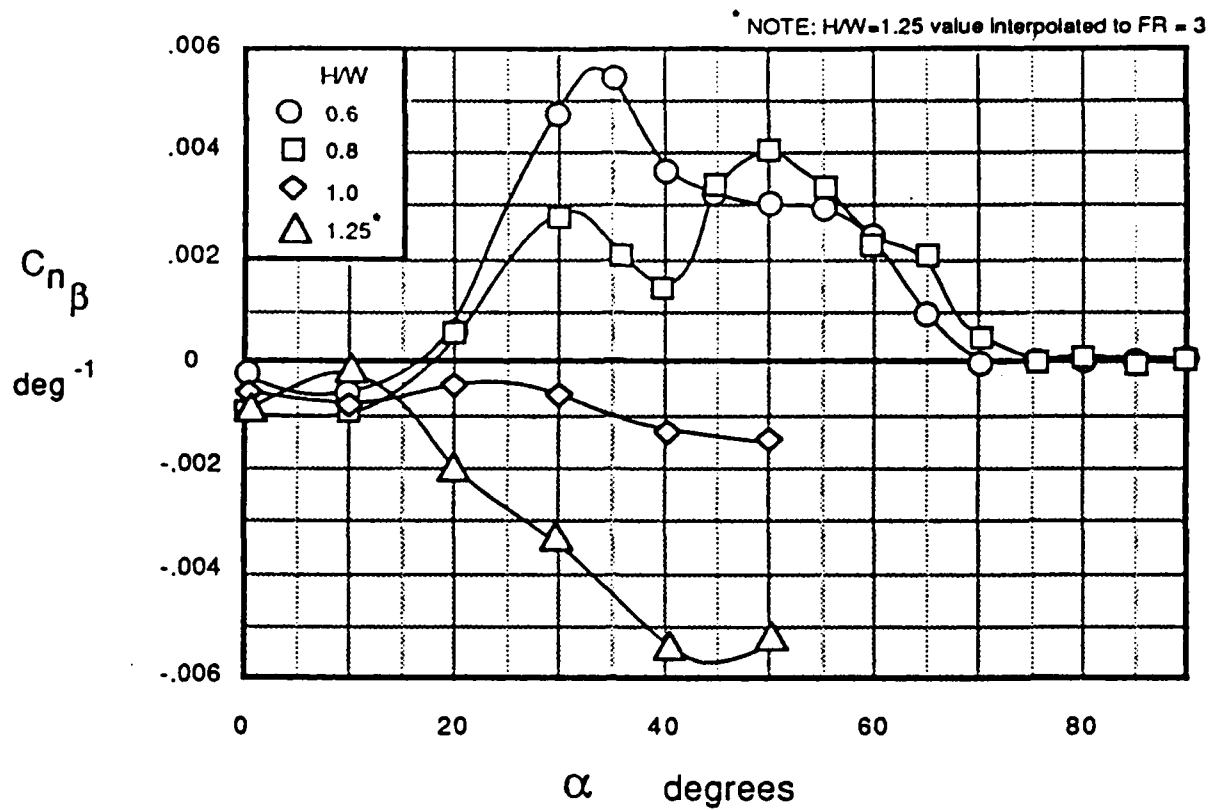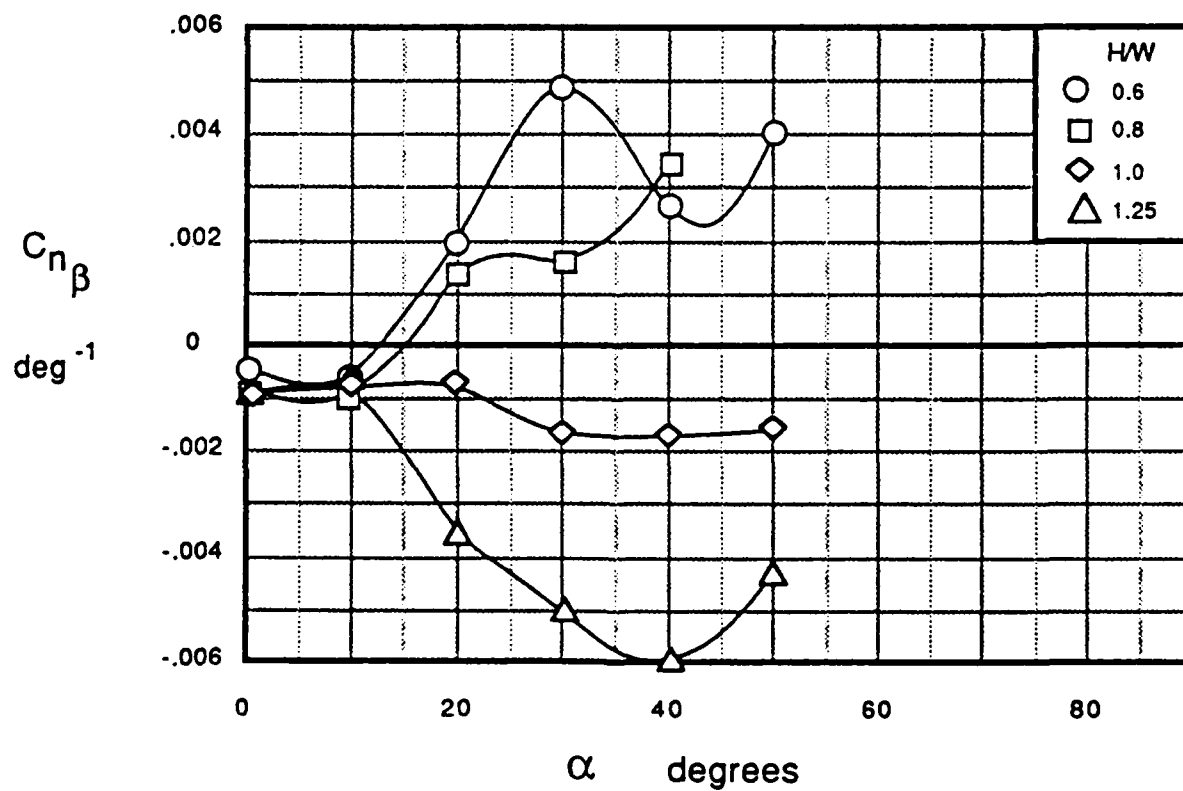
c) Fineness ratio = 3

d) Fineness ratio = 4

Figure 20. - Continued
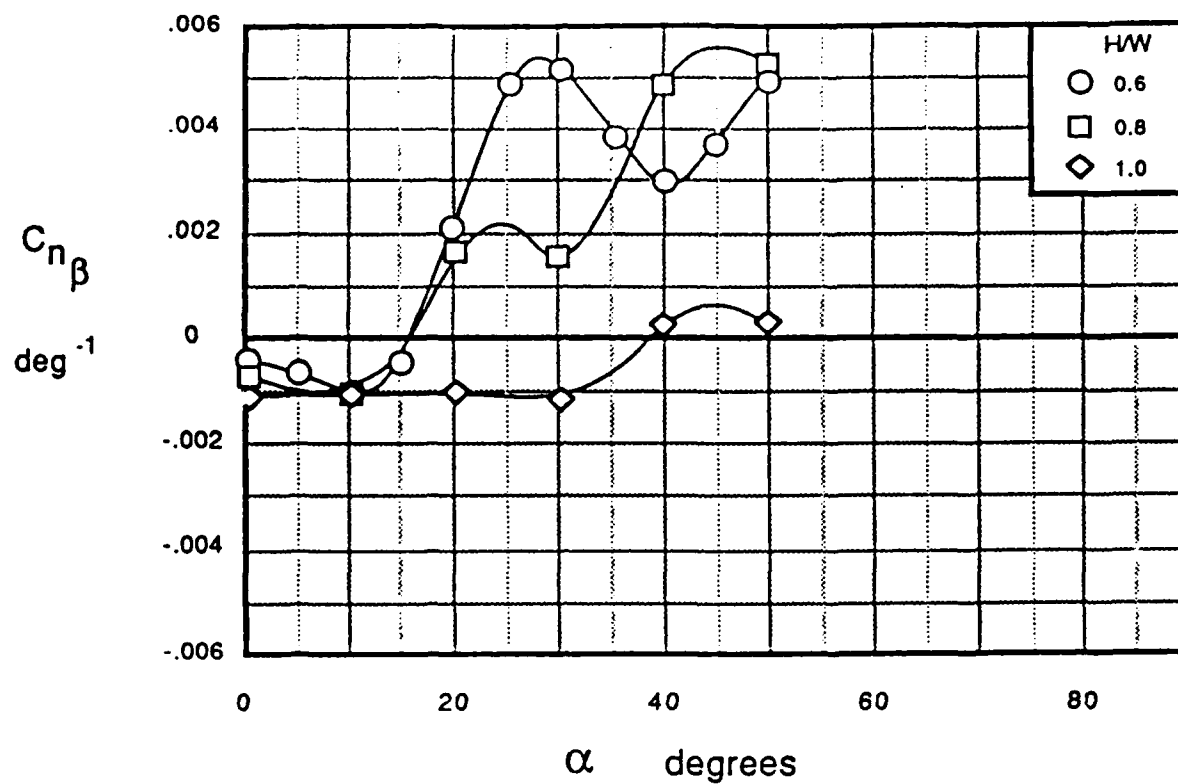
e) Fineness ratio = 4.5
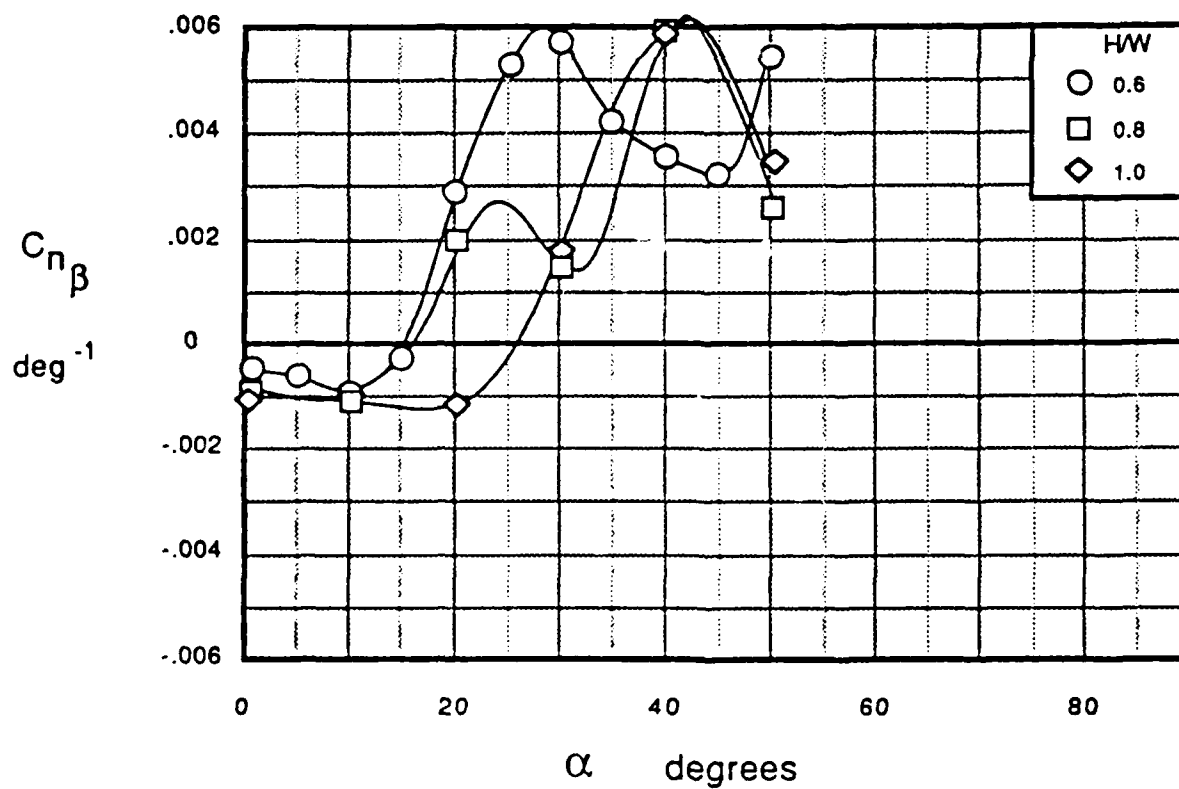
f) Fineness ratio = 5

Figure 20. - Concluded
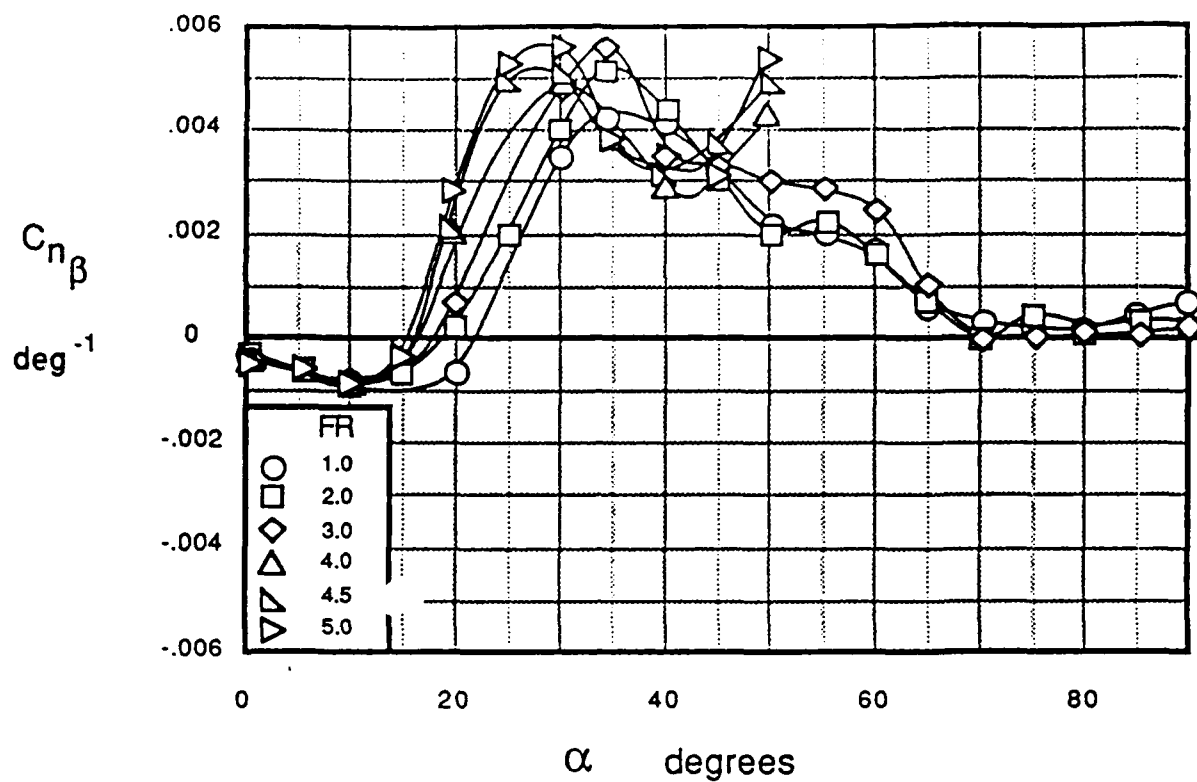
a) H/W = 0.6
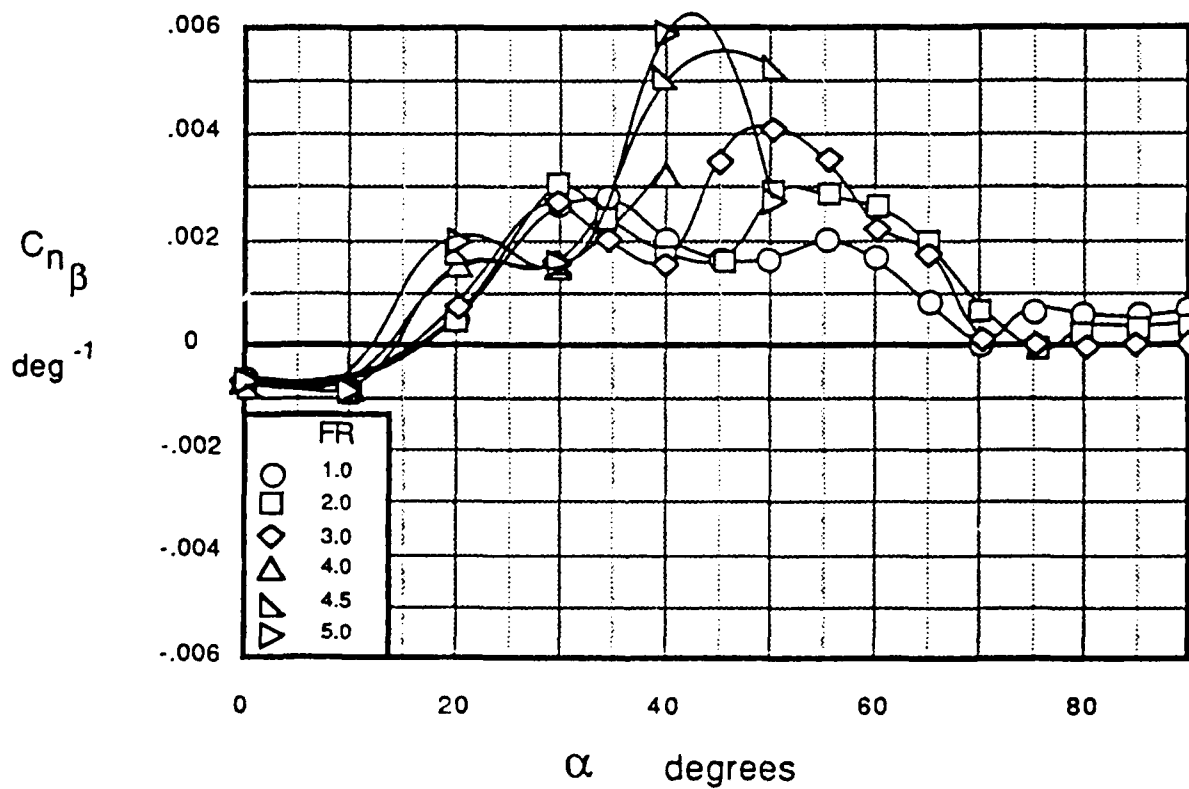
b) H/W = 0.8

Figure 21. - Effect of forebody fineness ratio on body-alone directional stability

c) H/W = 1.0

d) H/W = 1.25
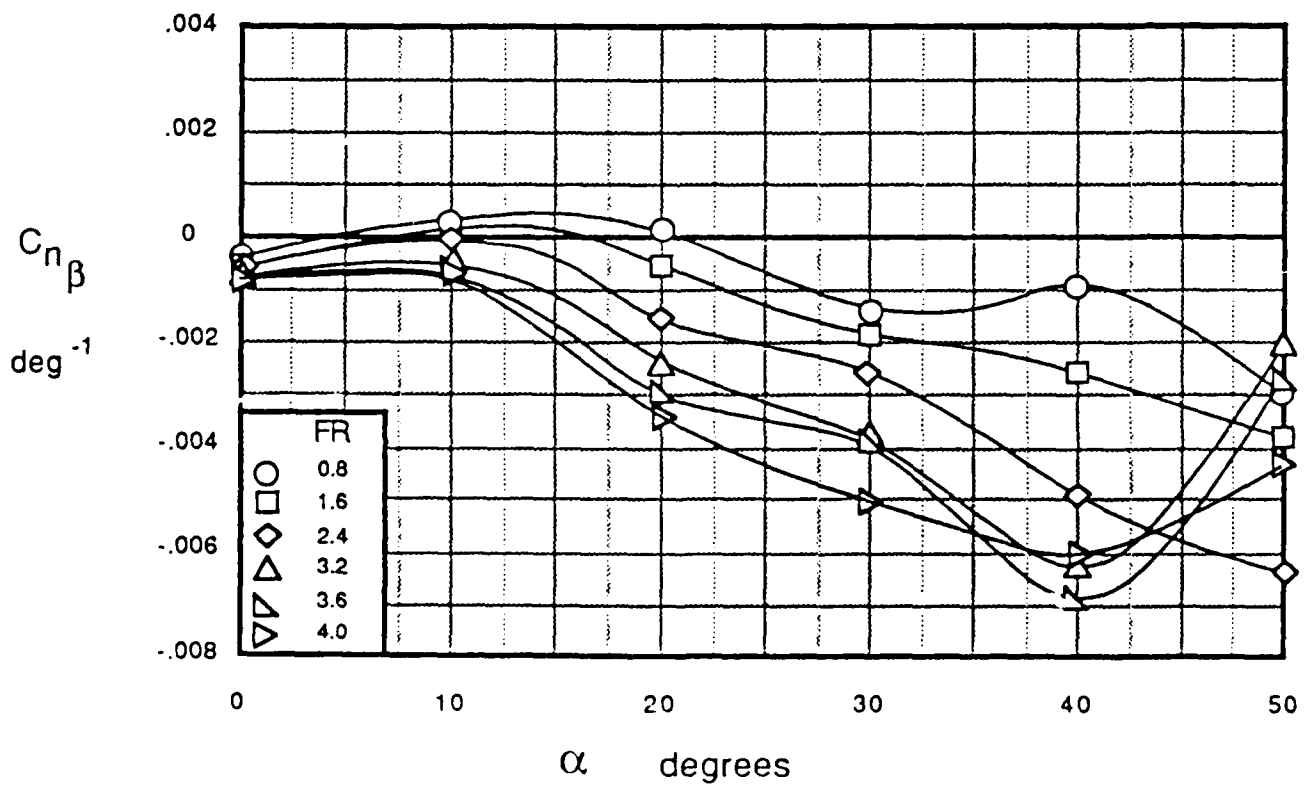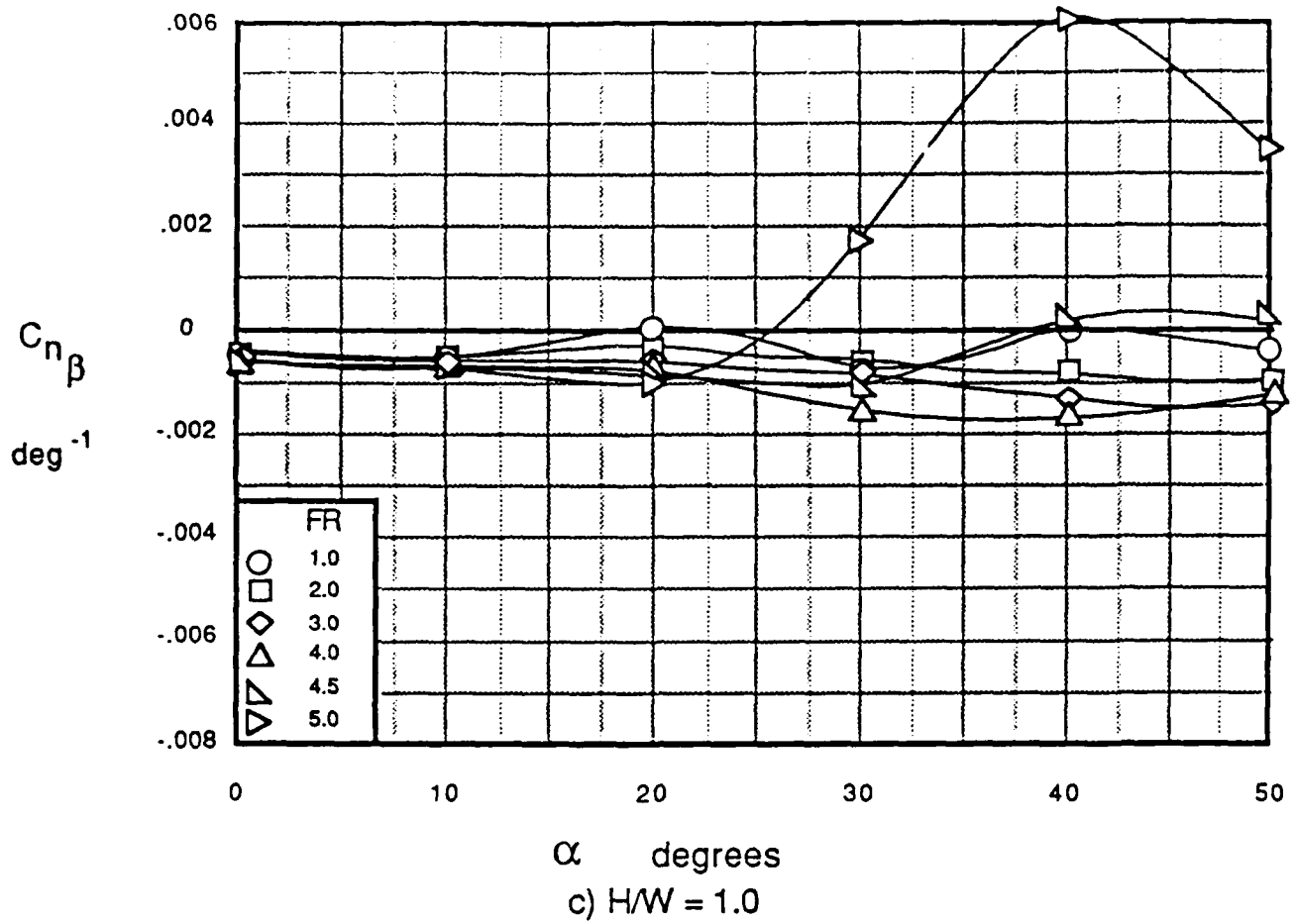
Figure 21. - Concluded

74
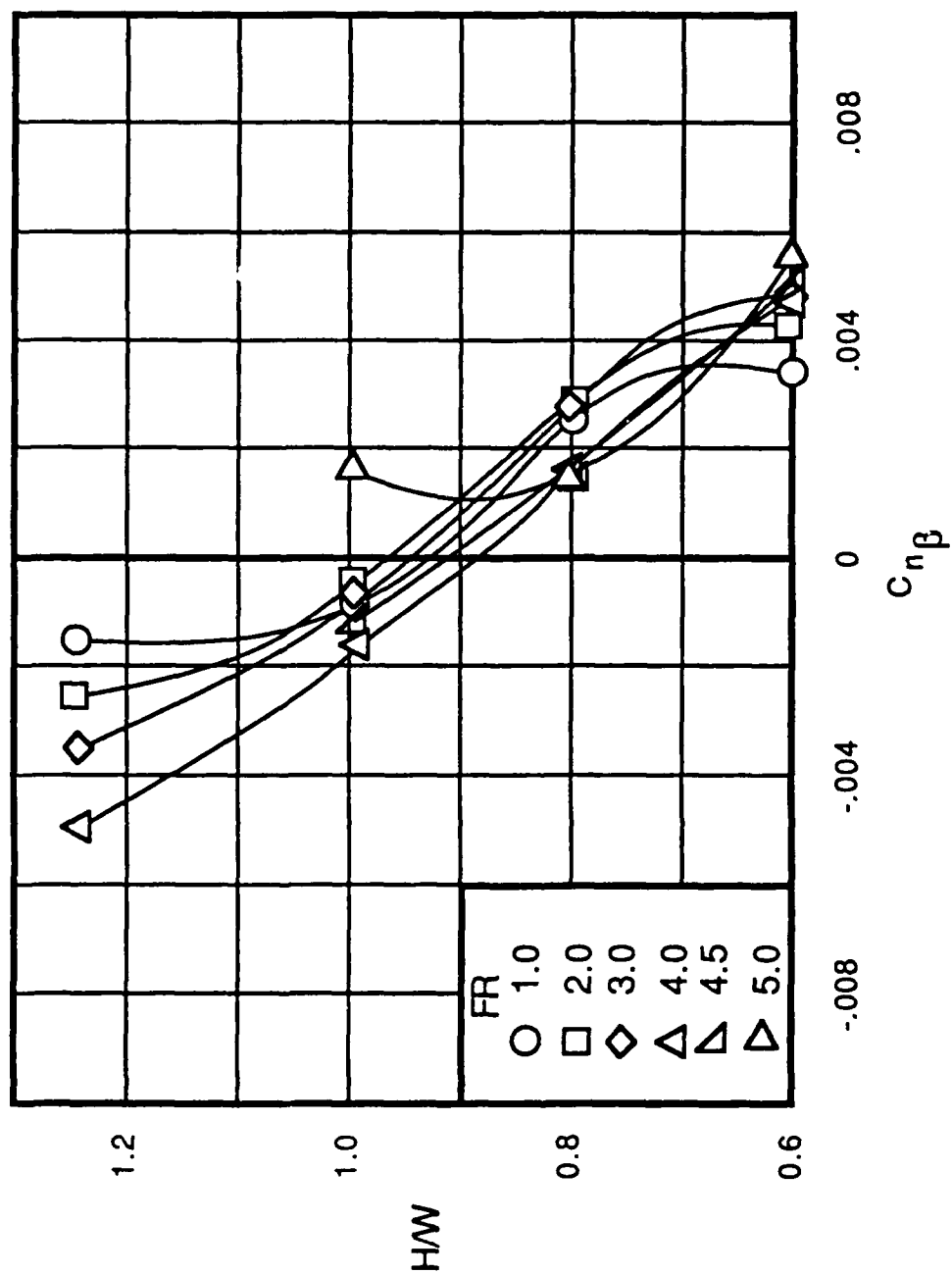
Figure 22. - Effect of cross-sectional shape and fineness ratio on directional stability at selected angles of attack

(a) $\alpha = 30^{o}$
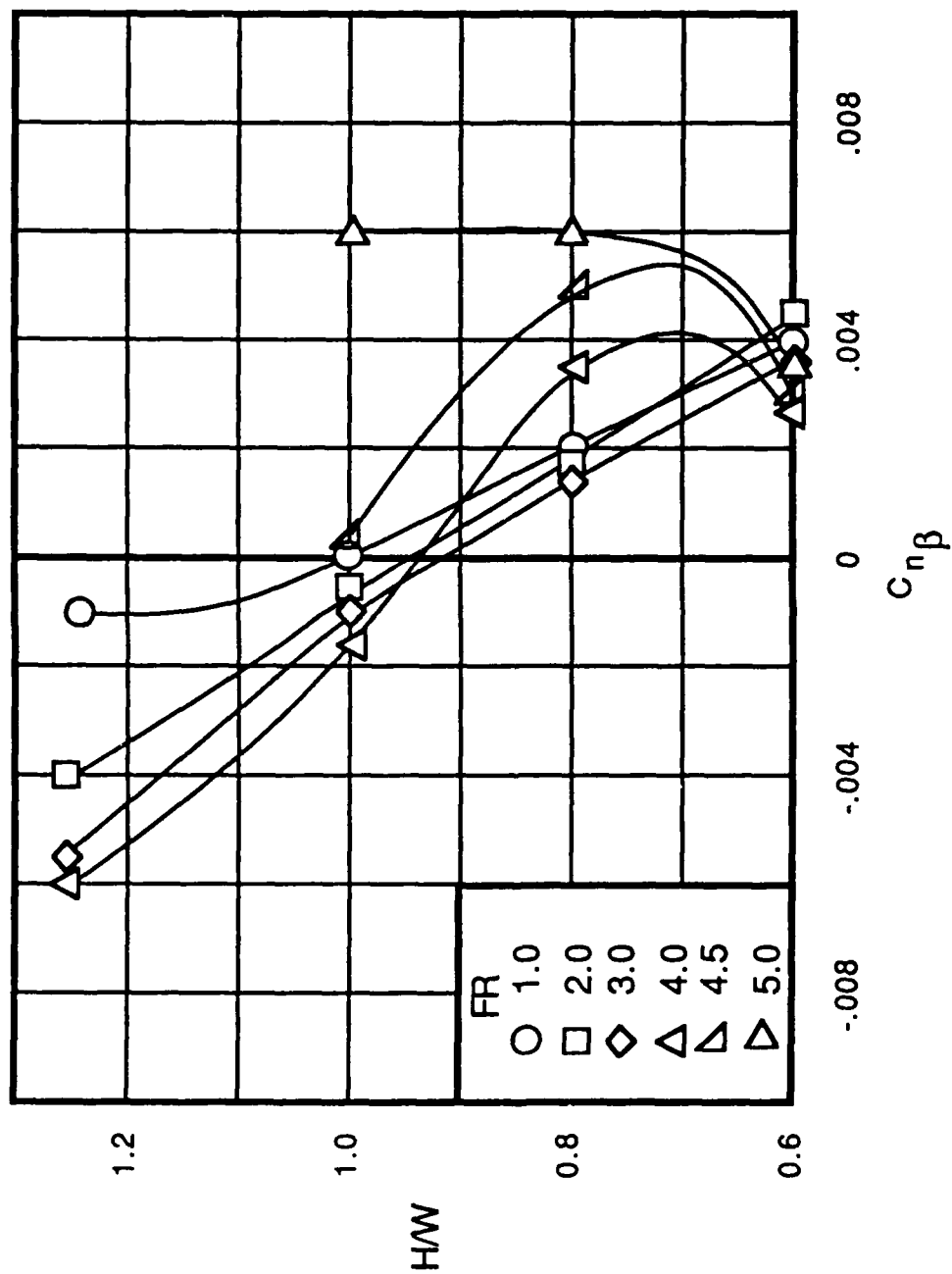
(b) $\alpha = 40°$

Figure 22. - Continued
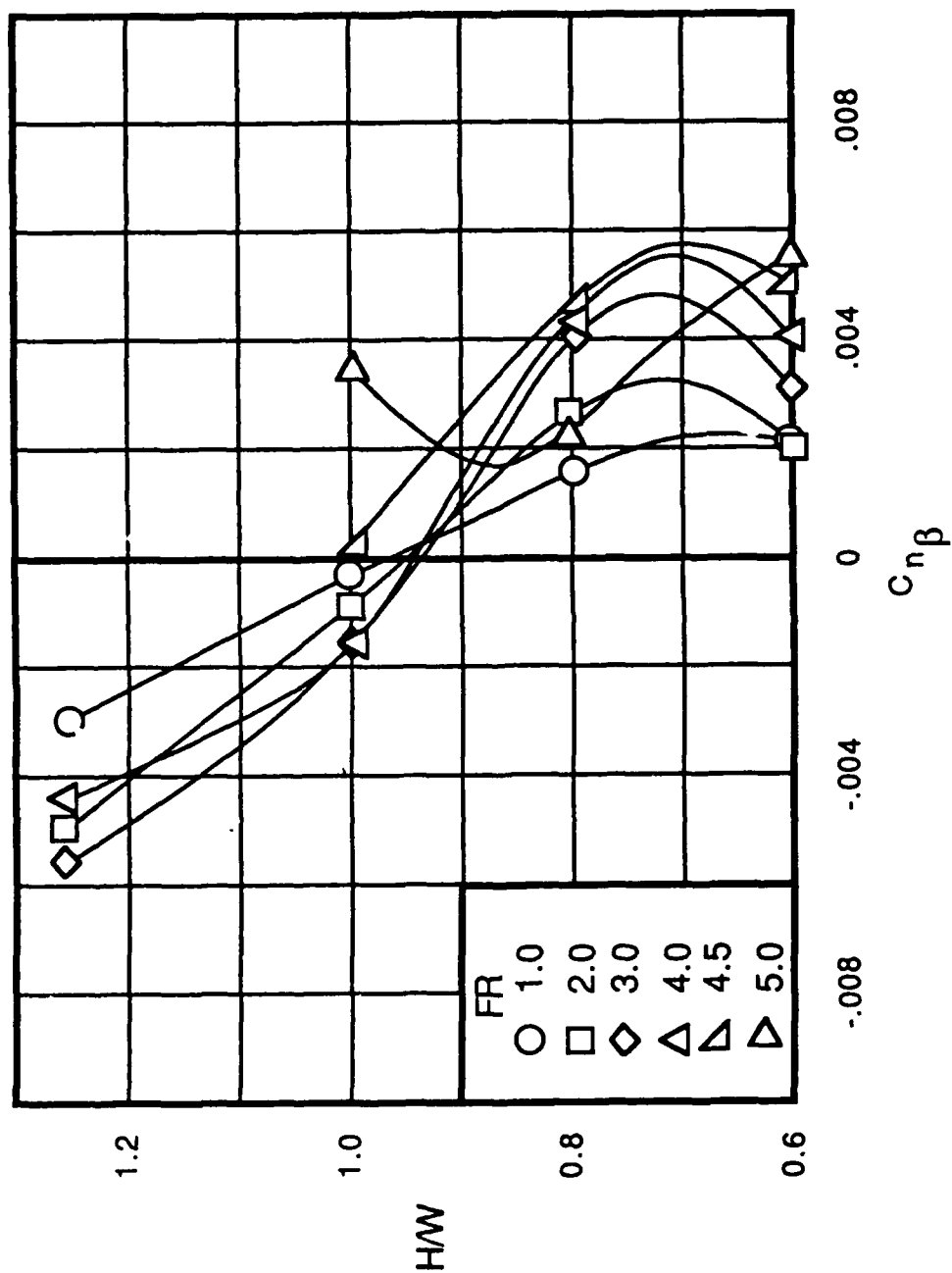
(c) $\alpha = 50°$
Figure 22. - Concluded

77
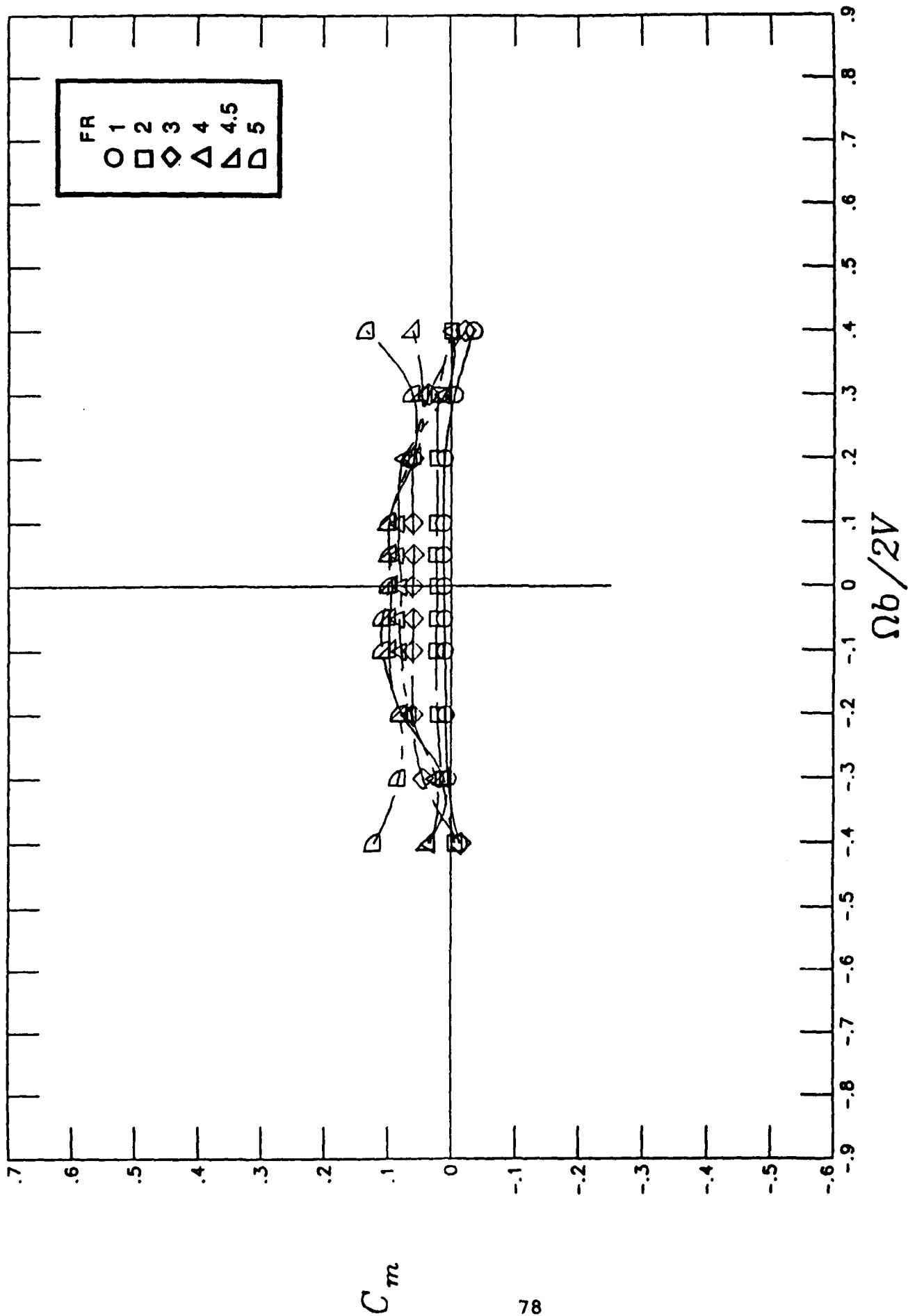
Figure 23.- Influence of forebody fineness ratio on rotational pitching-moment coefficient characteristics for a H/W=1.0 cross-sectional shape

a) α=30°

$\Omega b/2V$

b) $\alpha = 35°$

Figure 23.- Continued

79

$\Omega b/2V$
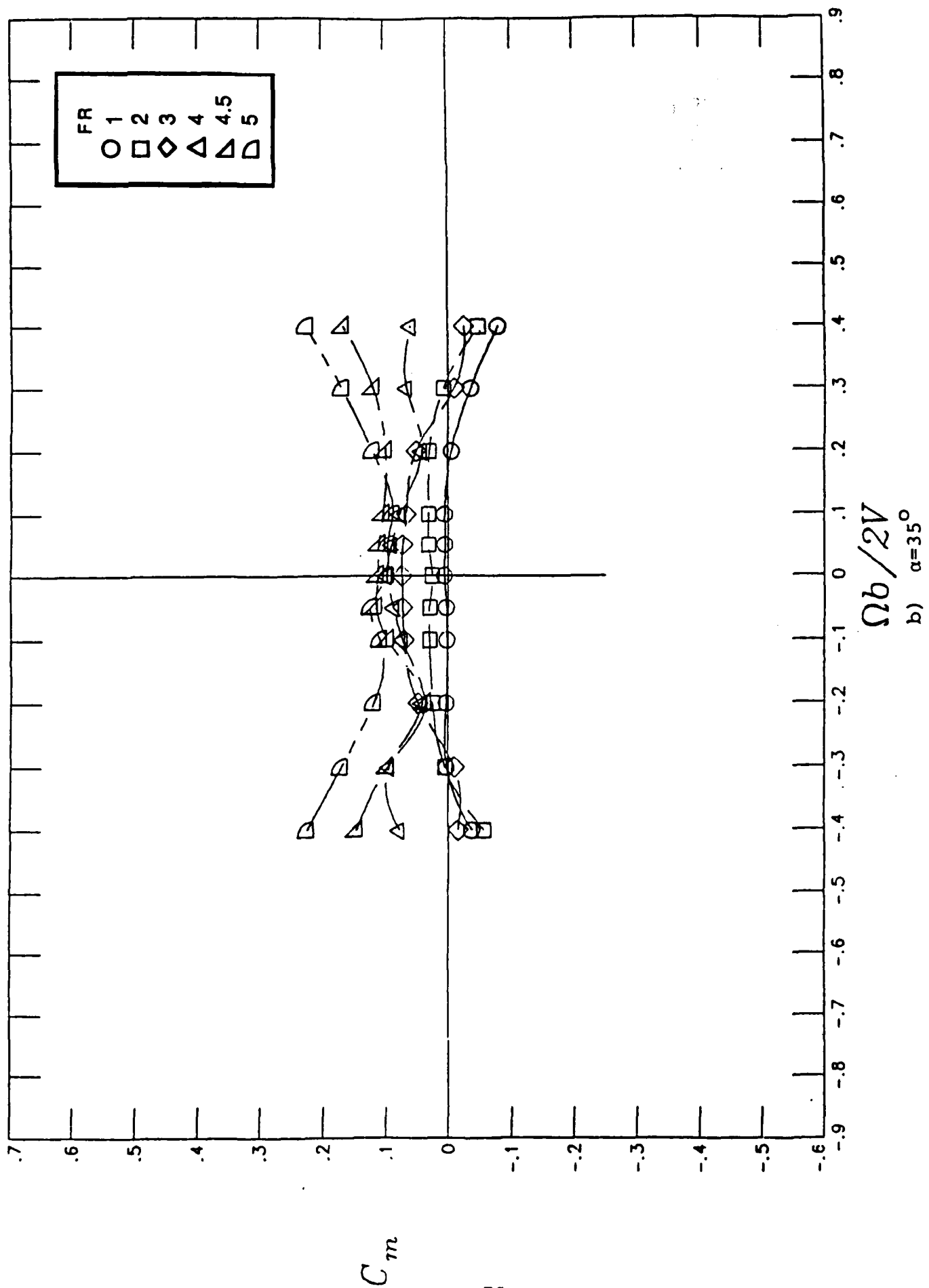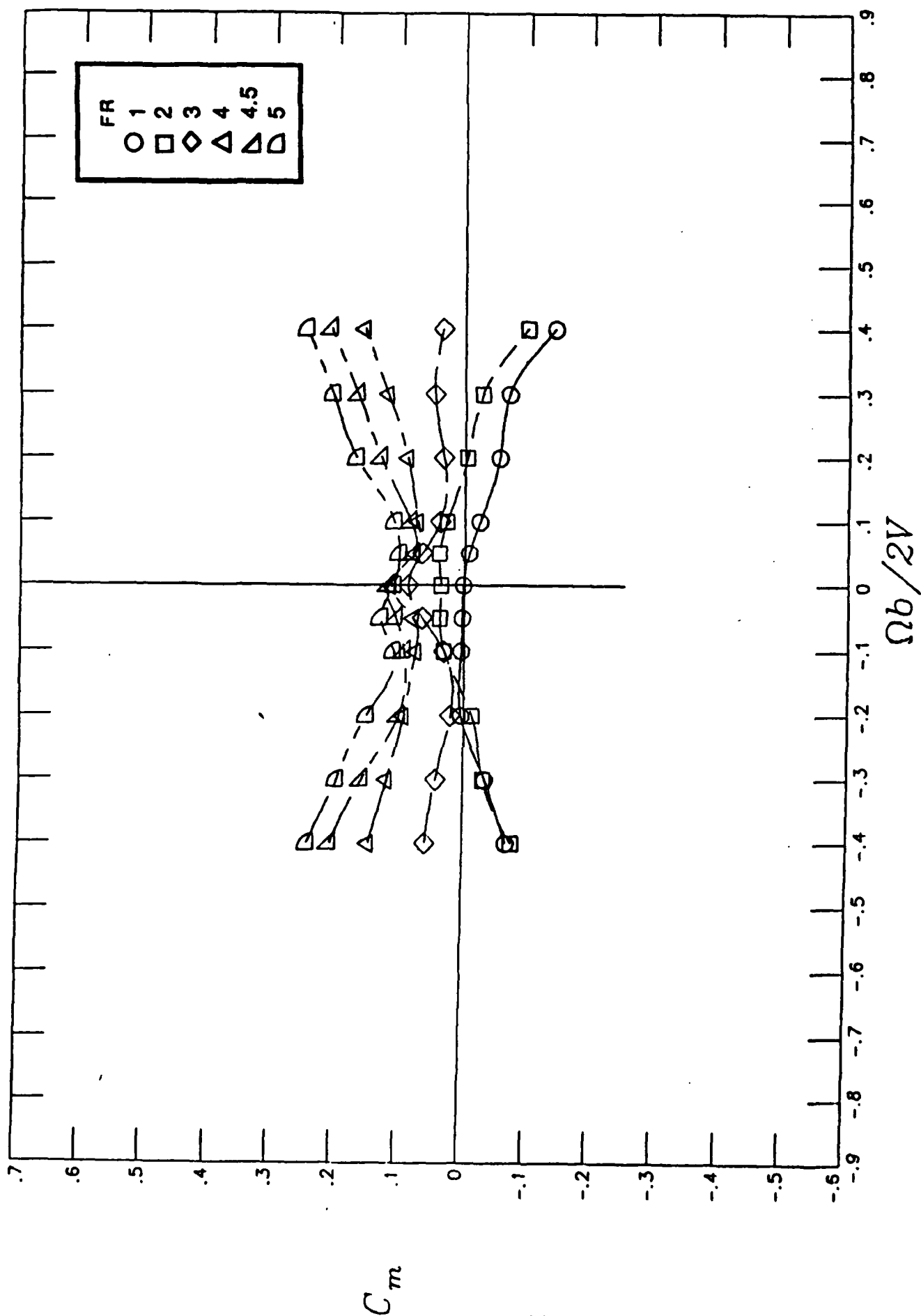
c) $\alpha = 40°$

Figure 23.- Continued

80

$\Omega b/2V$
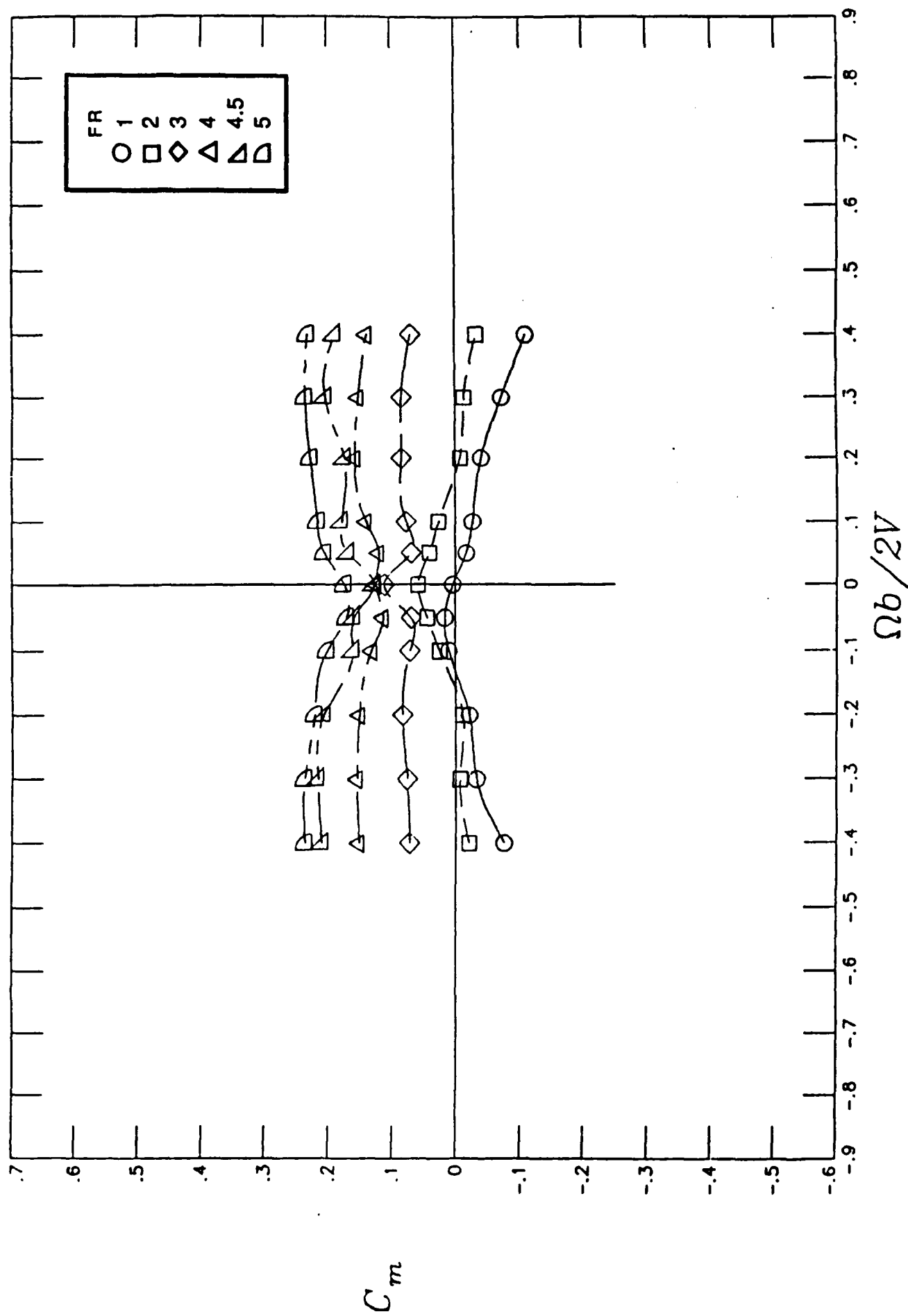
d) $\alpha=50^\circ$

Figure 23.- Continued

81

e) $\alpha = 70°$

Figure 23.- Continued

82

$\Omega b/2V$
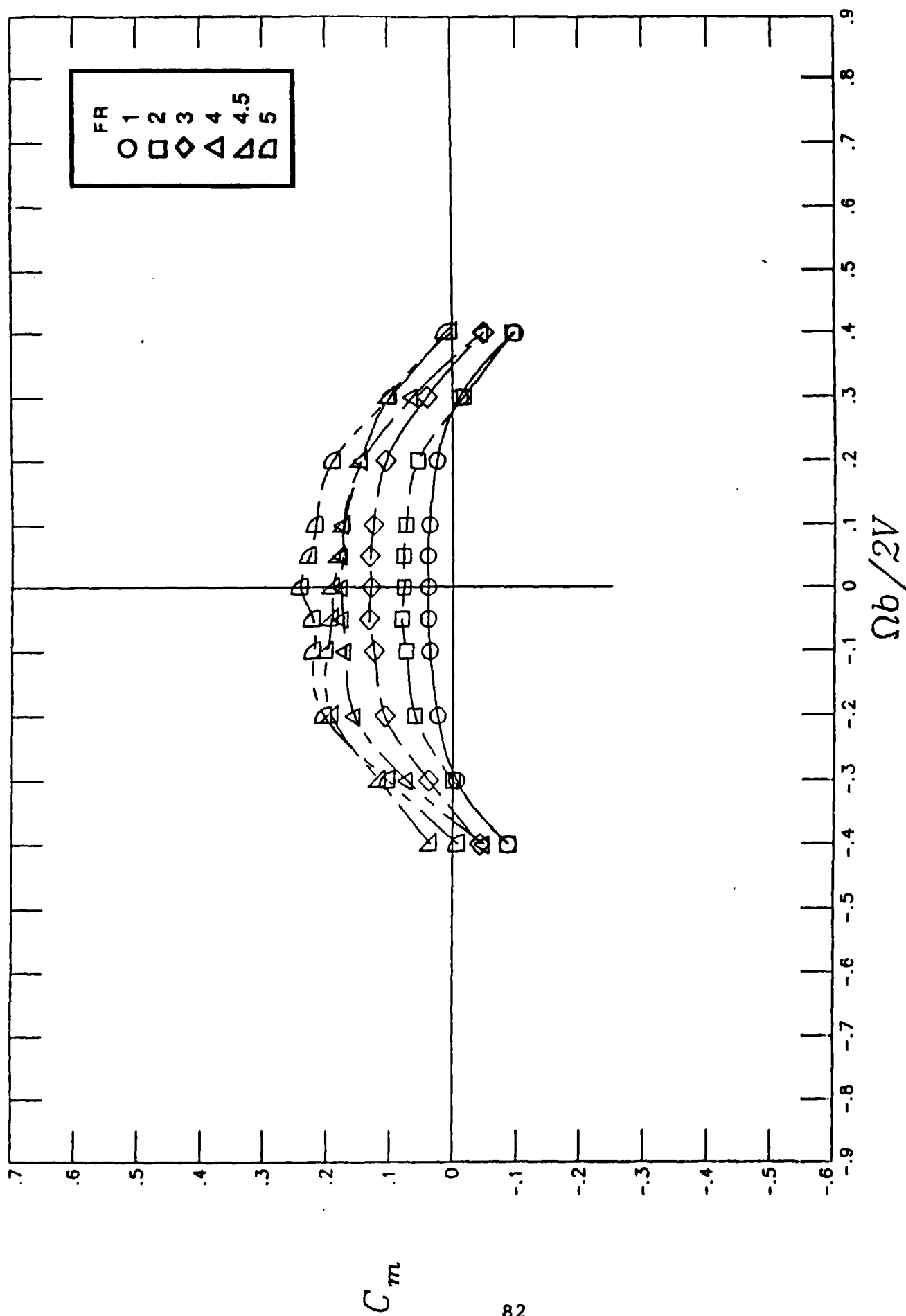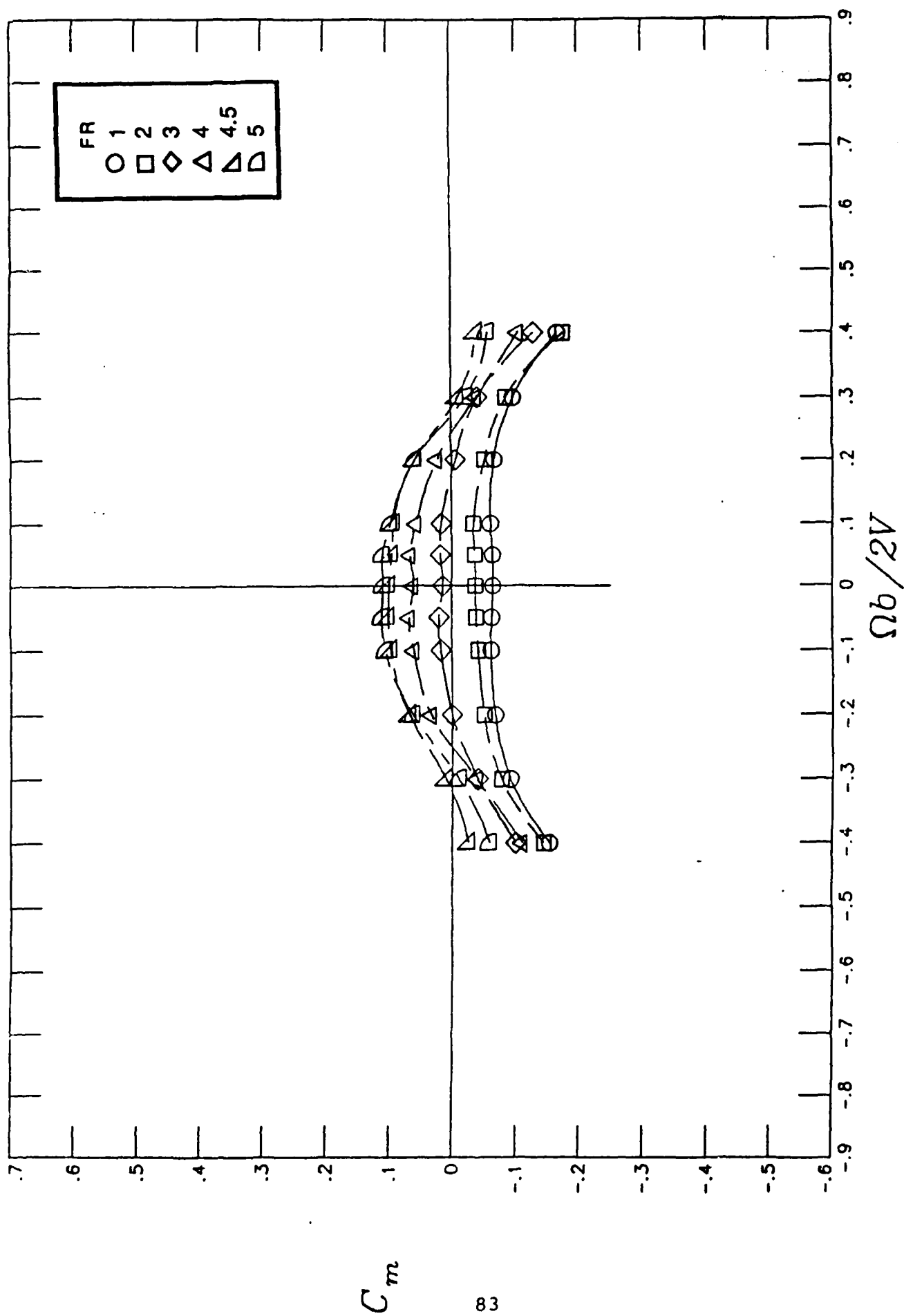
f) $\alpha=80°$

Figure 23.- Continued

C_m

83
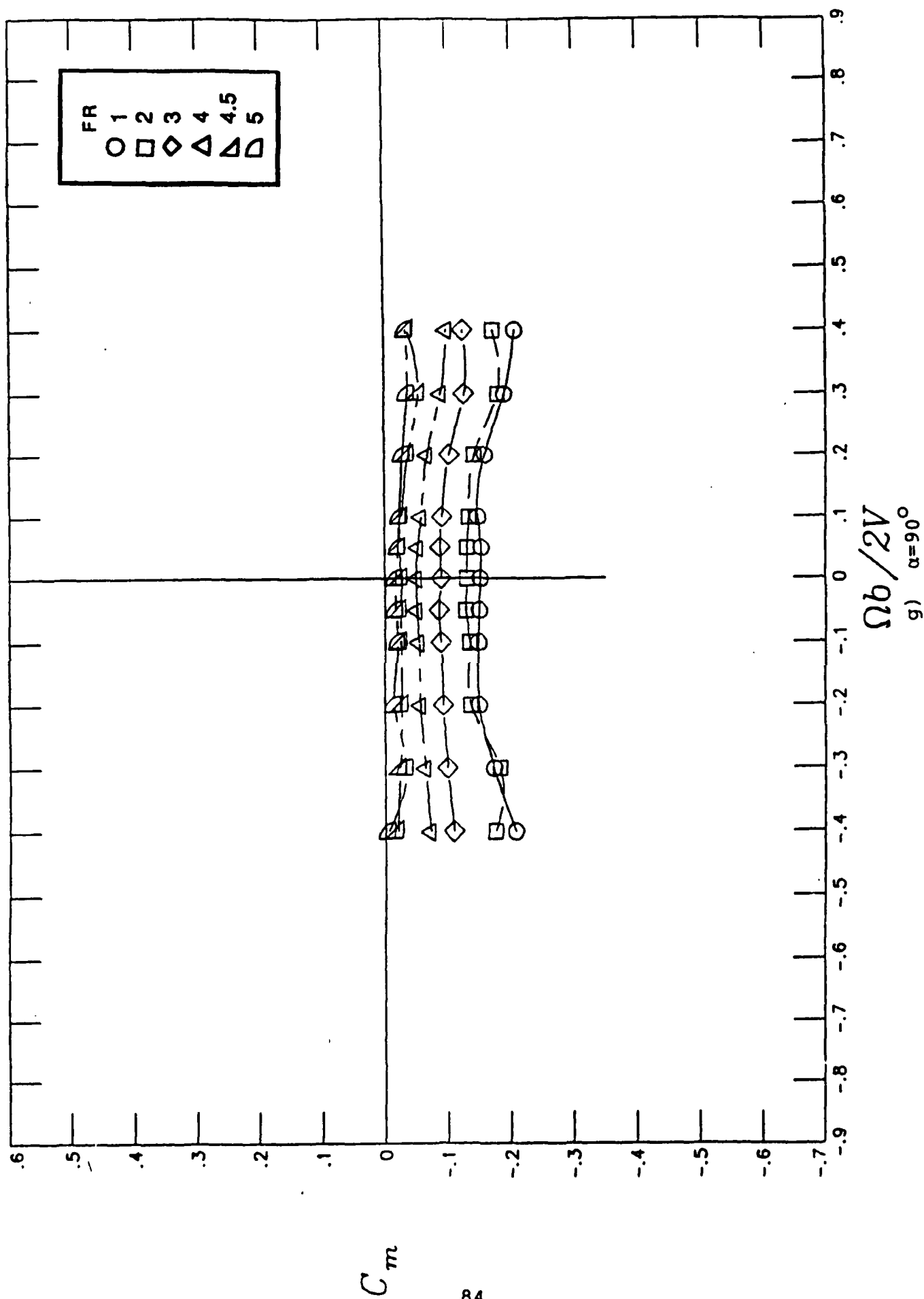
$\Omega b/2V$

g) $\alpha = 90°$

Figure 23.- Concluded

84
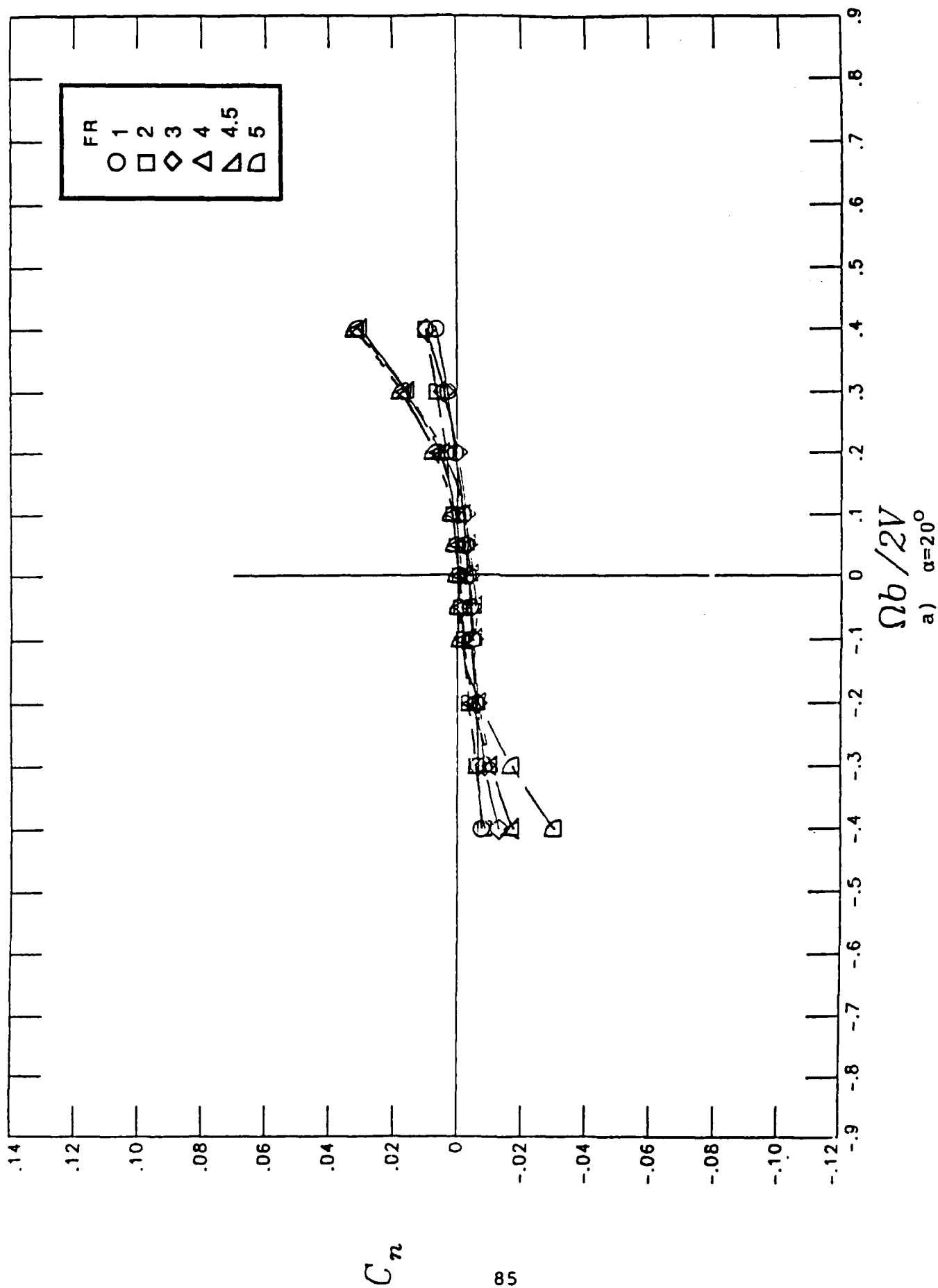
Figure 24.- Influence of forebody fineness ratio on rotational yawing-moment coefficient characteristics for a H/W=0.6 cross-sectional shape
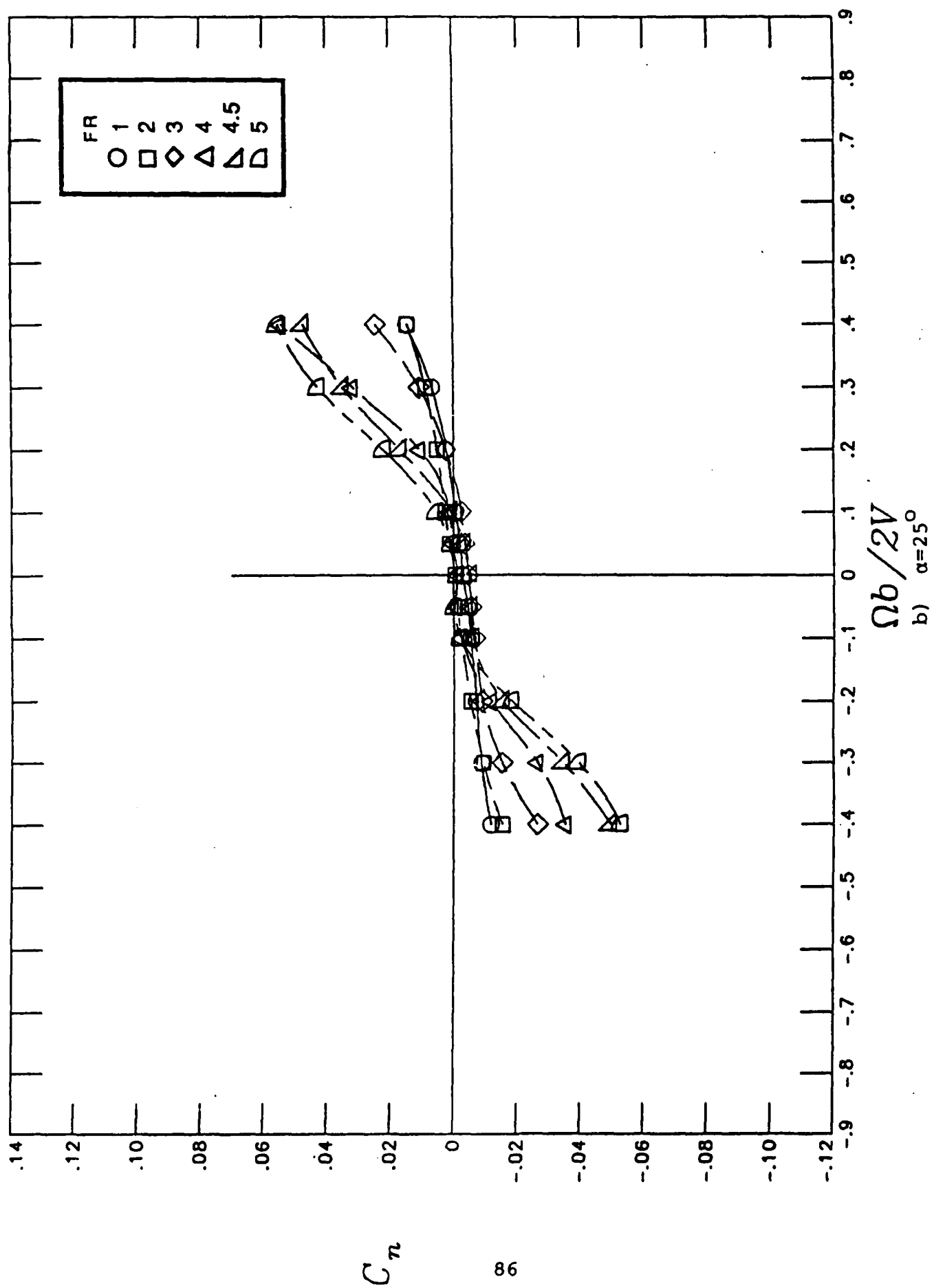
a) α=20°

85

$\Omega b / 2V$

b) $\alpha = 25^\circ$

Figure 24.- Continued

86

$\Omega b/2V$

c) $\alpha=30^{o}$

Figure 24.- Continued

C_n

87
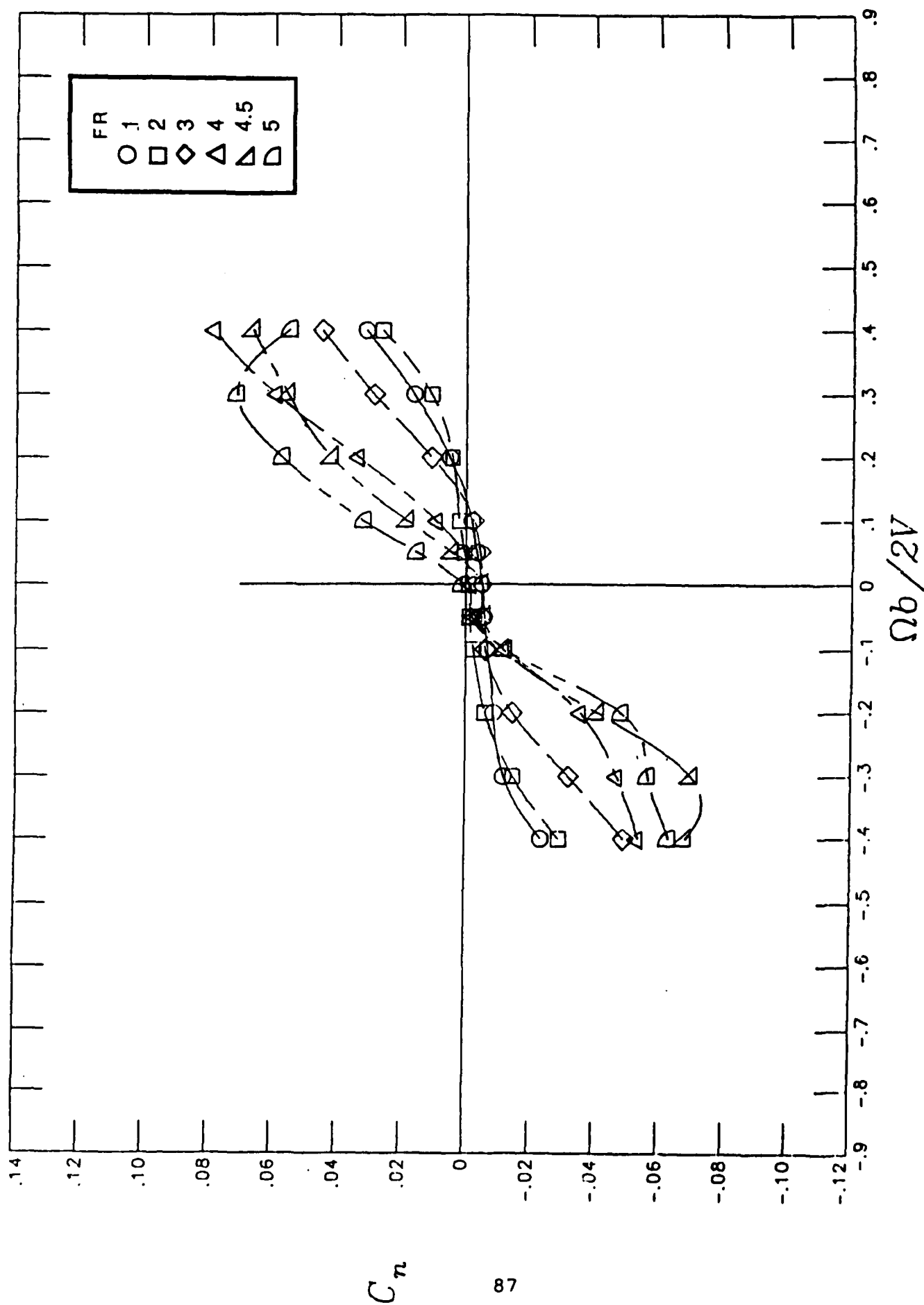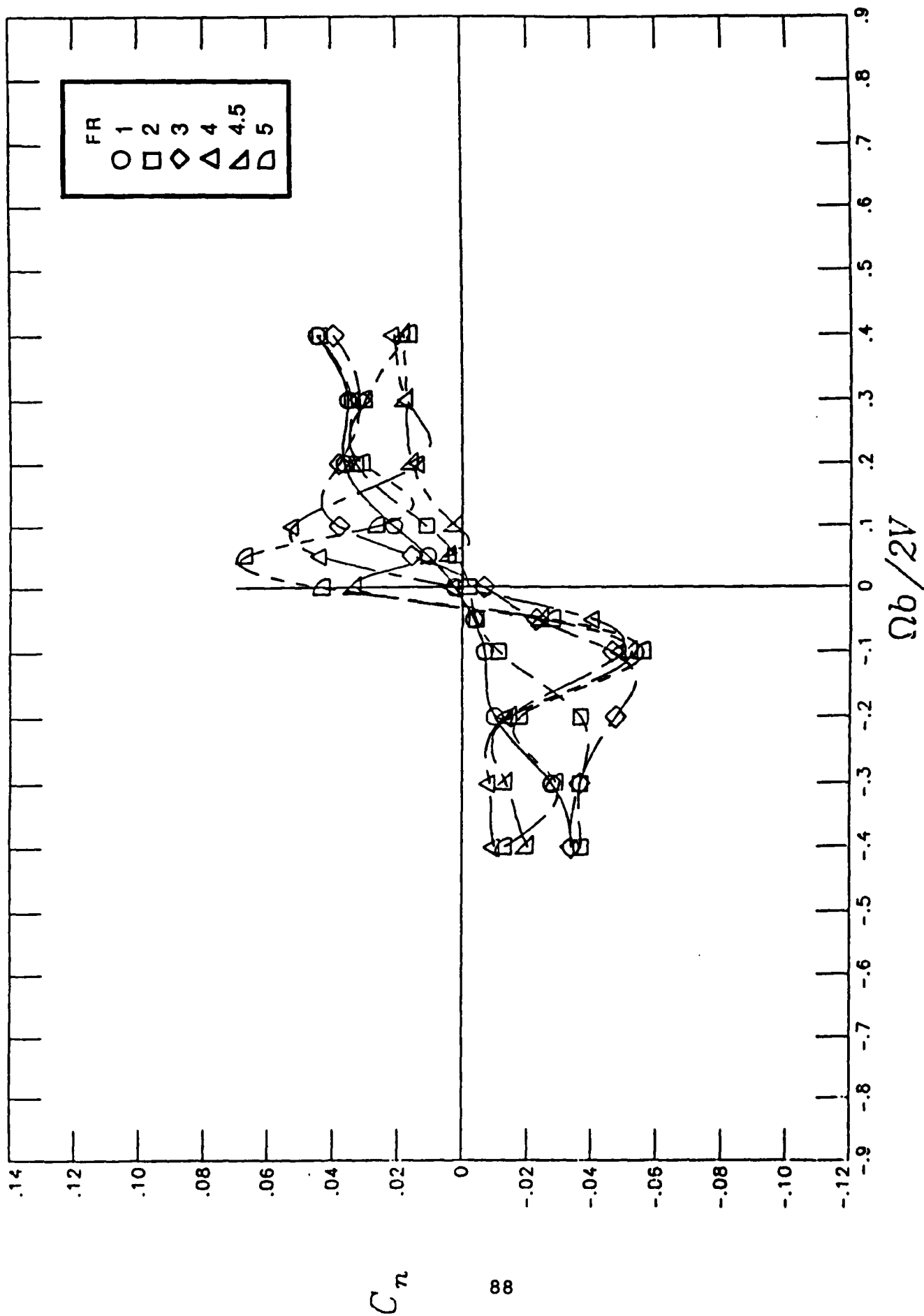
d) $\alpha=40^{\circ}$

Figure 24.- Continued

88

$\Omega b/2V$

e) $\alpha=50^\circ$

Figure 24.- Continued

C_n

89
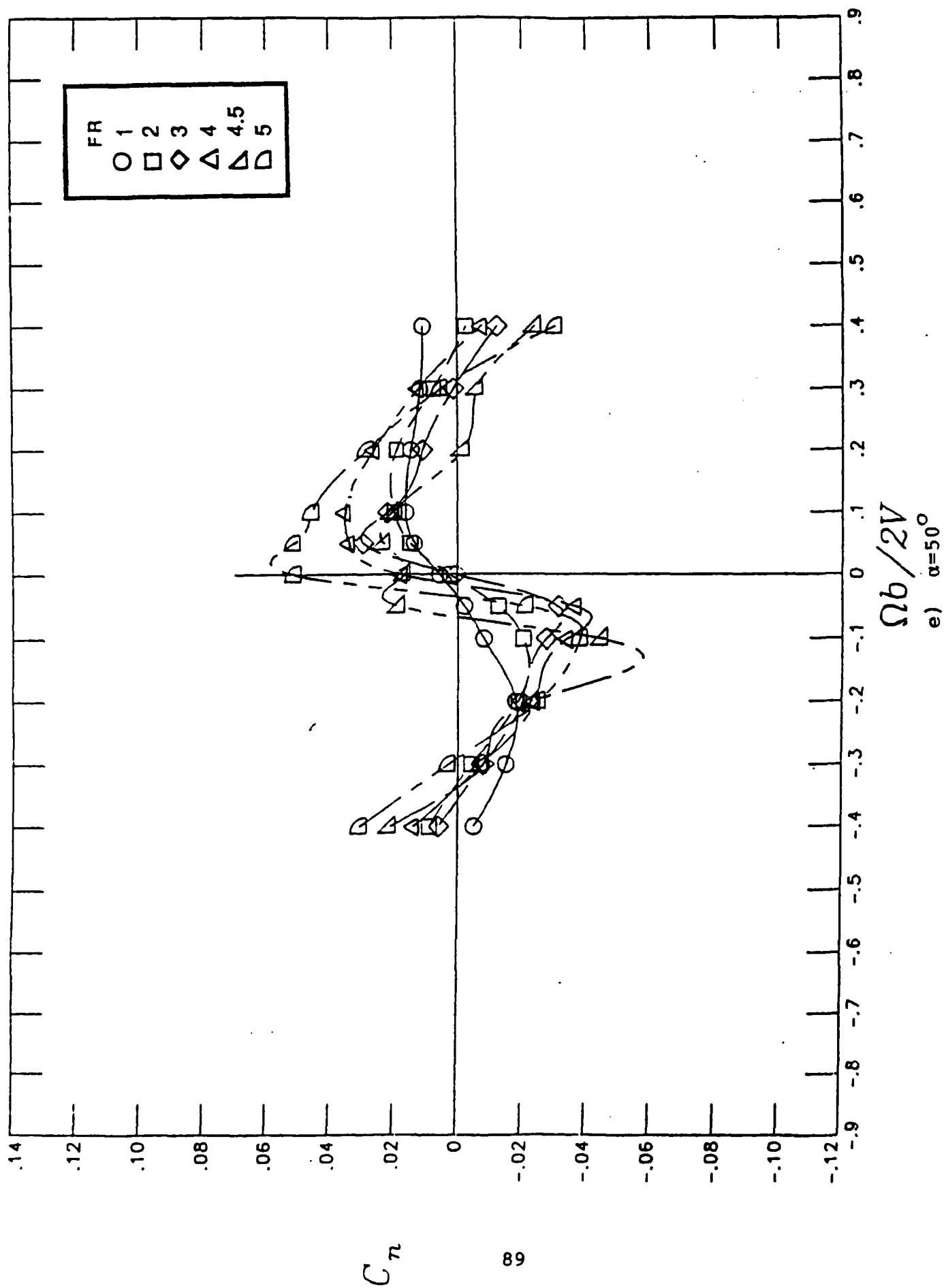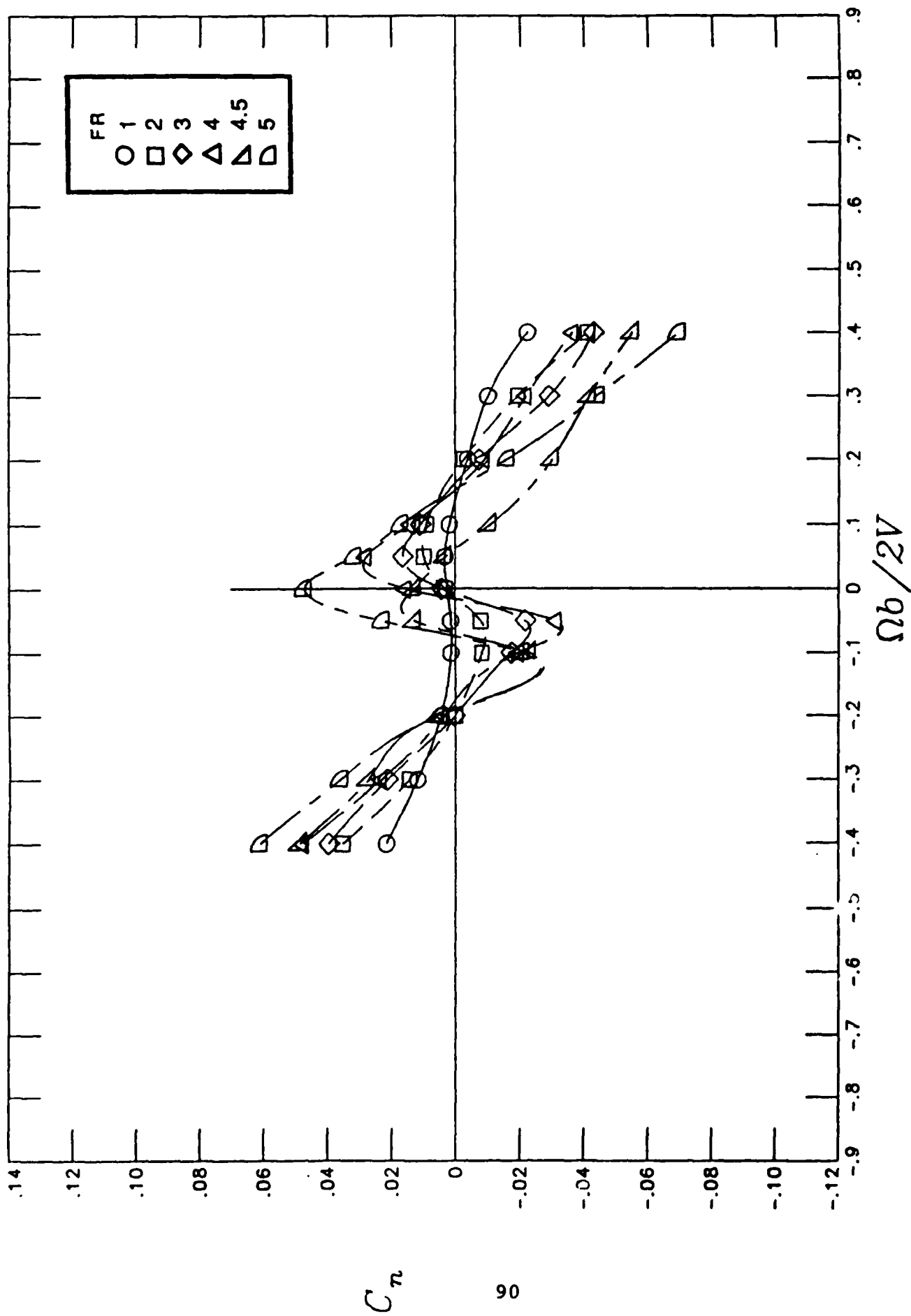
f) $\alpha=60°$

Figure 24.- Continued

90

$\Omega b/2V$

g) $\alpha = 65^\circ$

Figure 24.- Continued

91

$\Omega b/2V$

h) $\alpha=70^{\circ}$

Figure 24.- Continued

C_n

92

Figure 24.- Continued

i) $\alpha=80^\circ$

$\dfrac{\Omega b}{2V}$

C_n

93

$\dfrac{\Omega b}{2V}$

j) $\alpha = 90°$
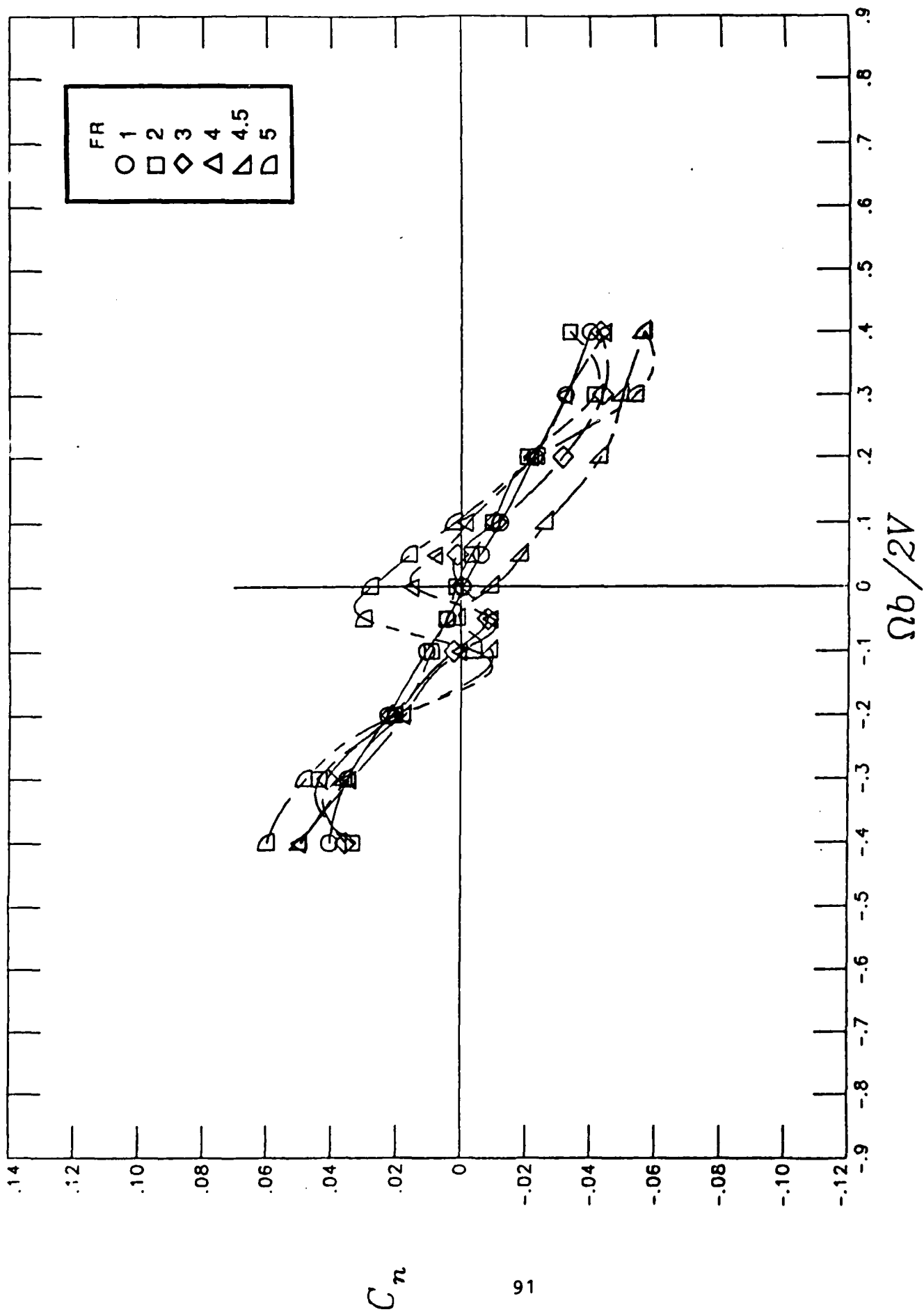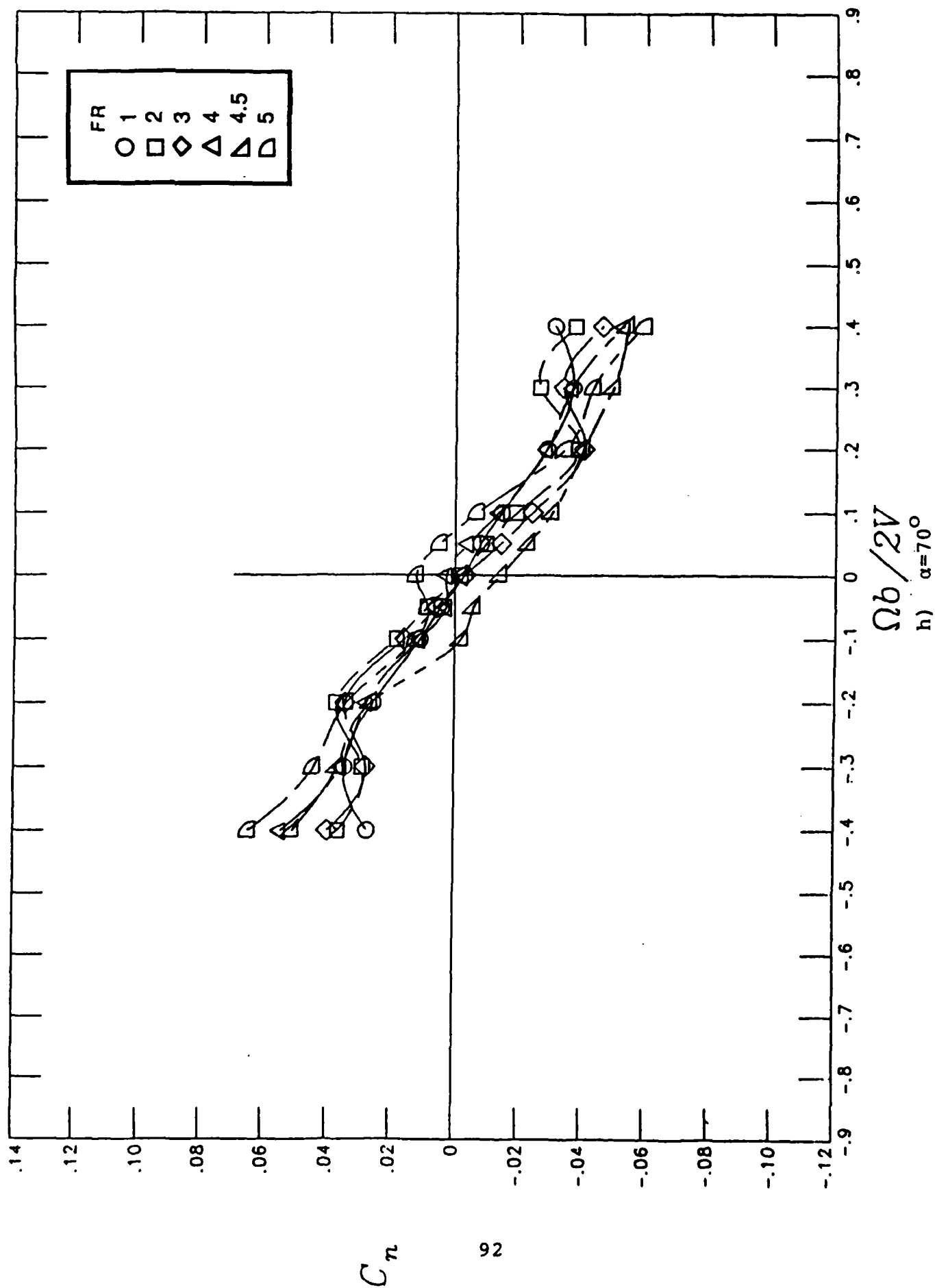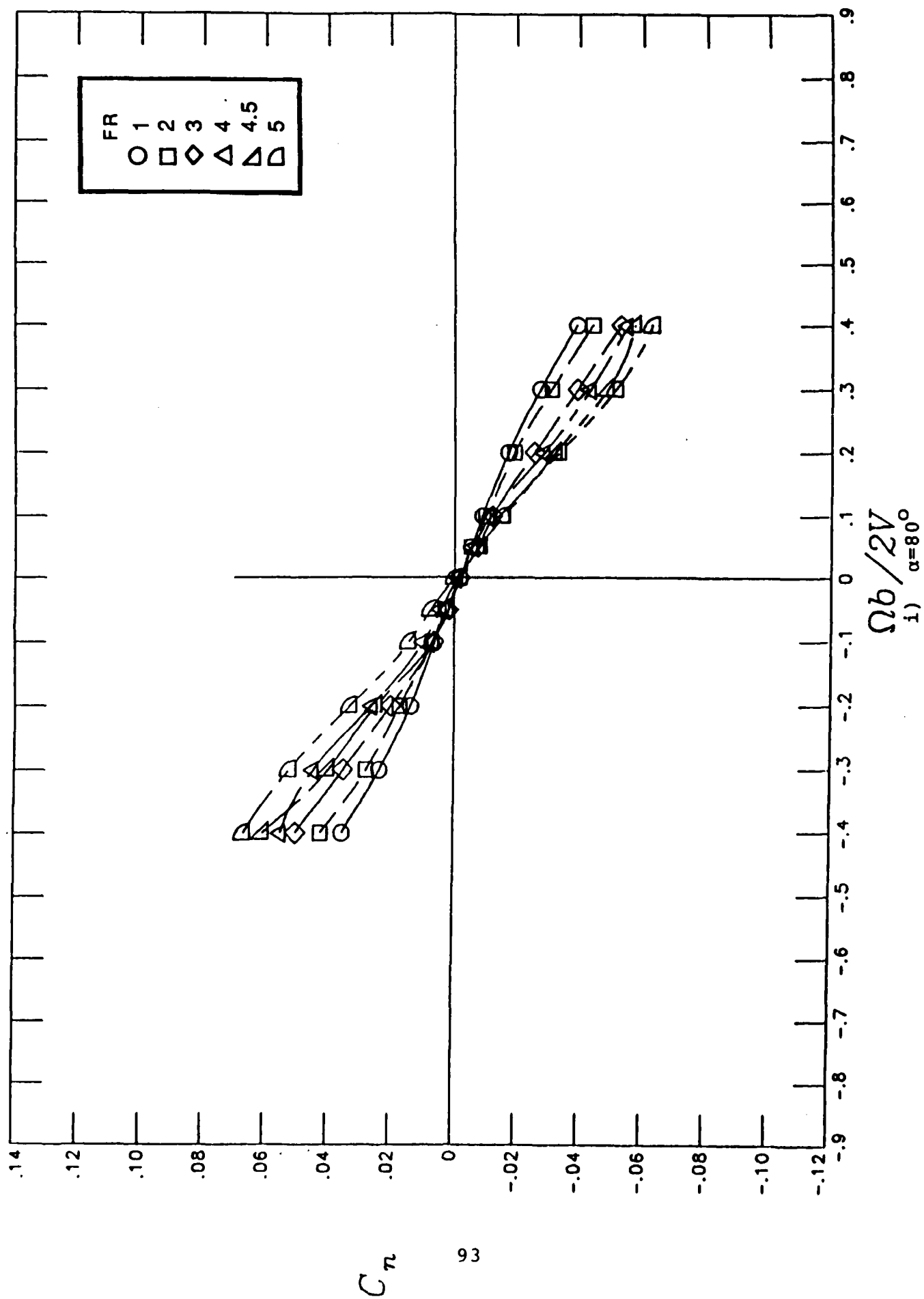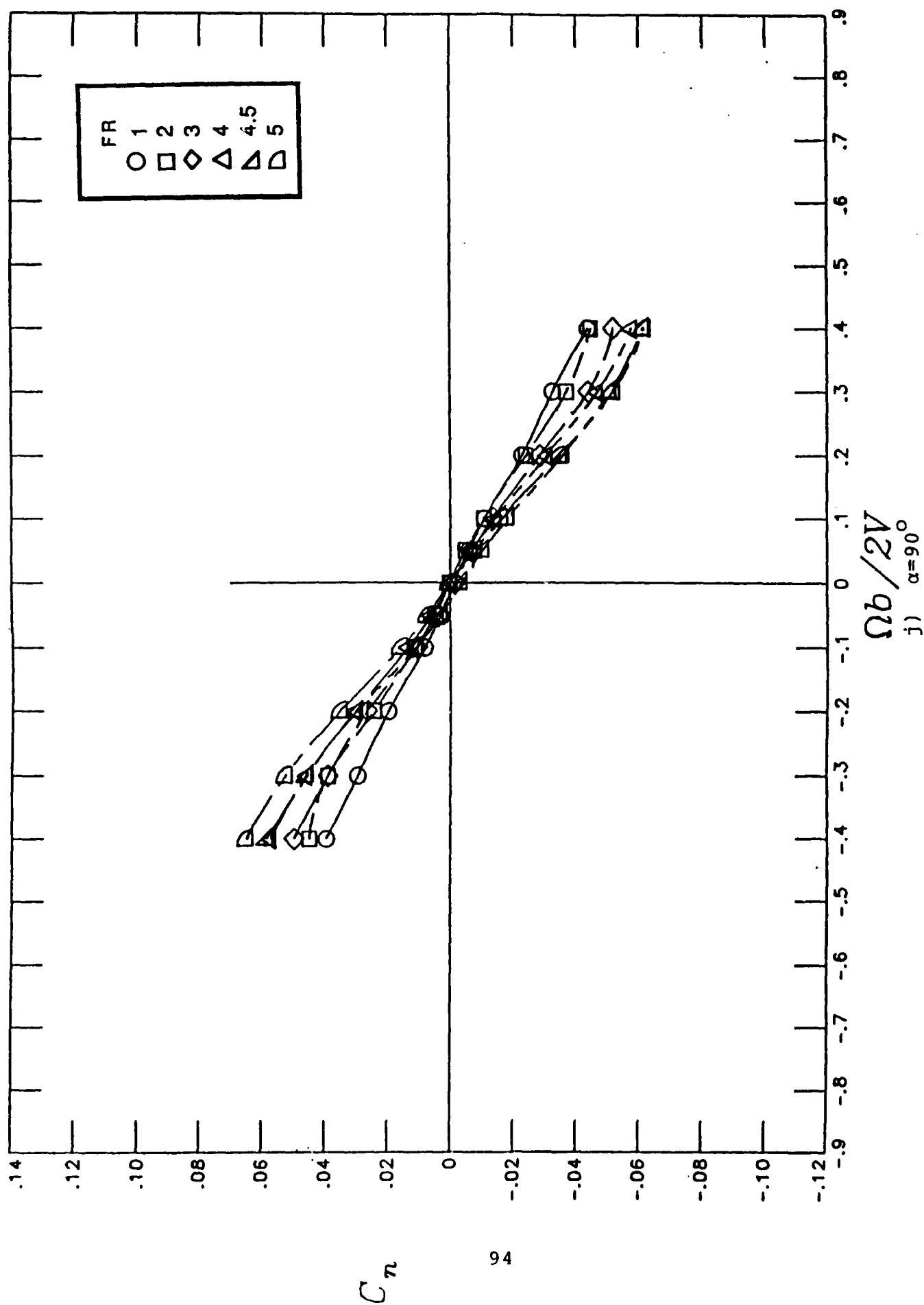
Figure 24.- Concluded

94
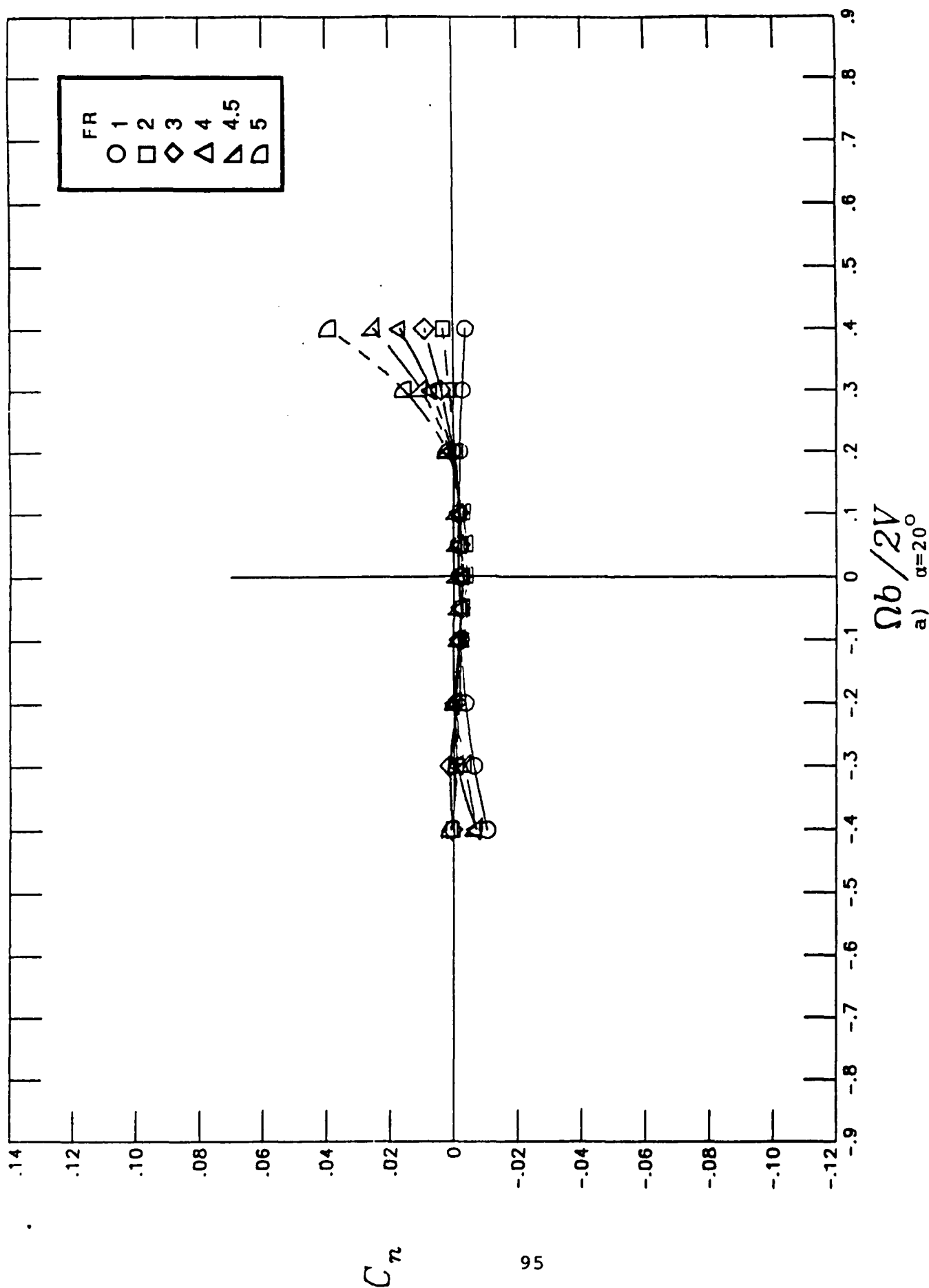
Figure 25.– Influence of forebody fineness ratio on rotational yawing-moment coefficient characteristics for a H/W=0.8 cross-sectional shape

95

b) $\alpha = 25^\circ$

Figure 25.- Continued

96

c) $\alpha=30^{o}$

Figure 25.- Continued

97

d) $\alpha=40^\circ$
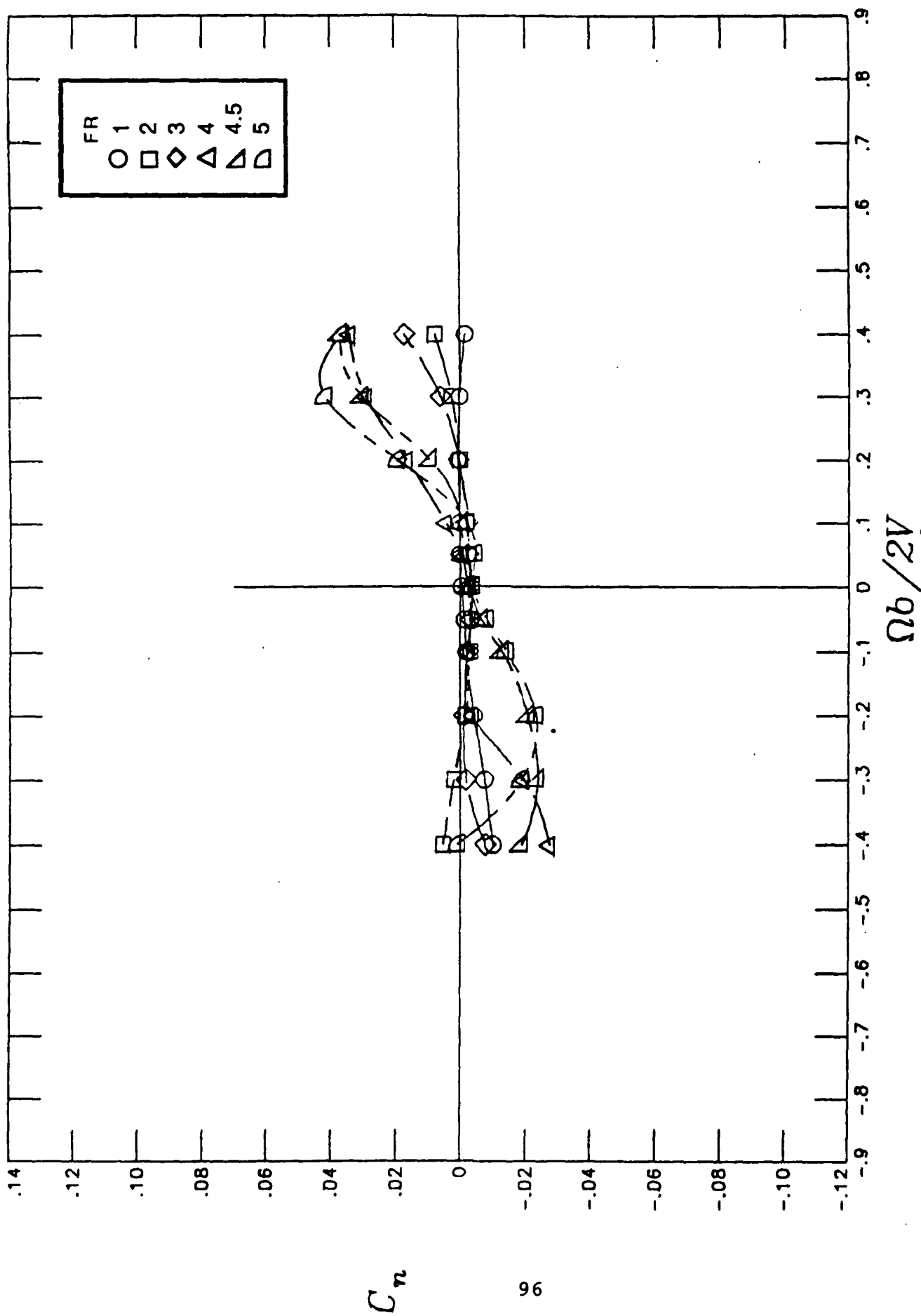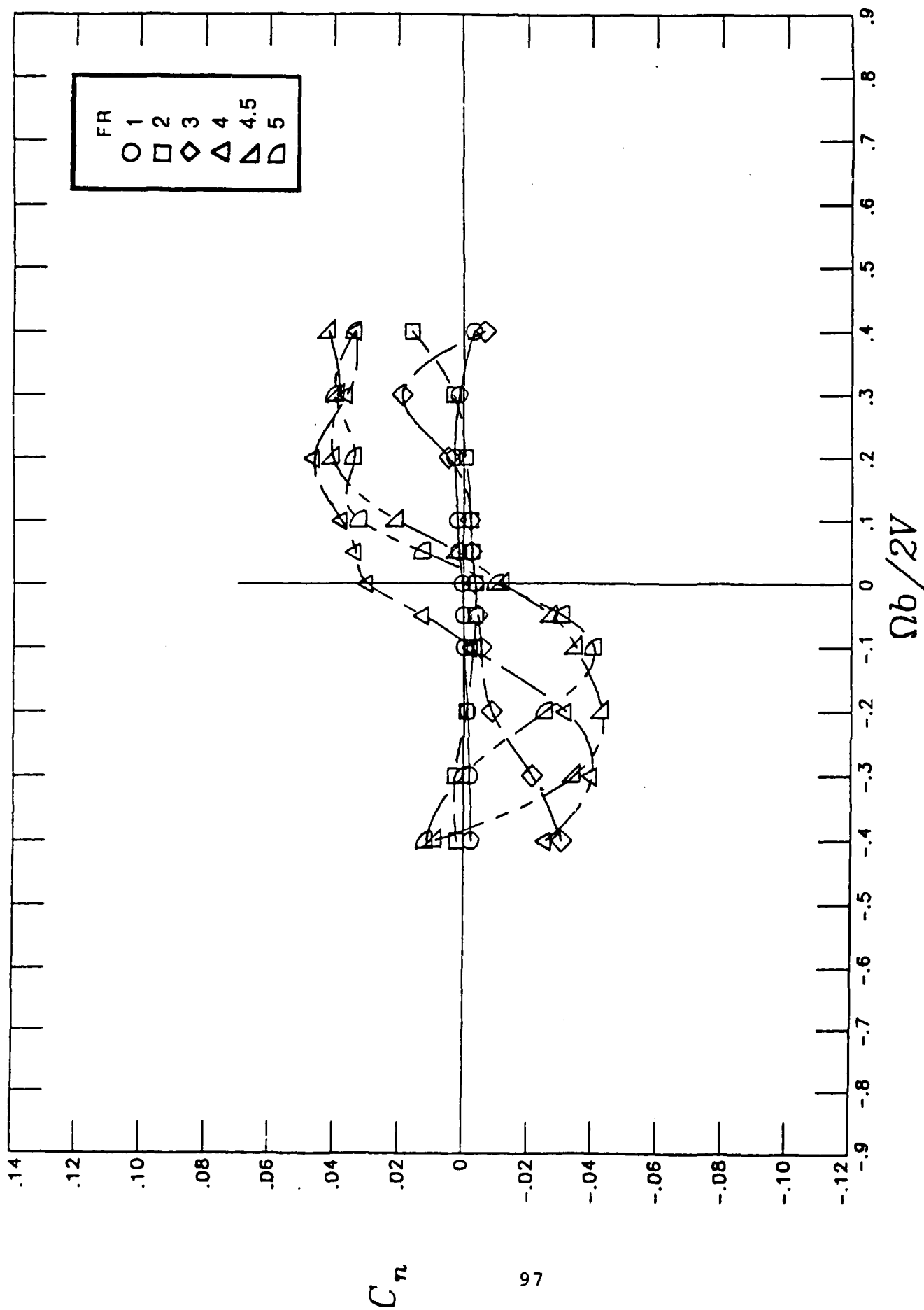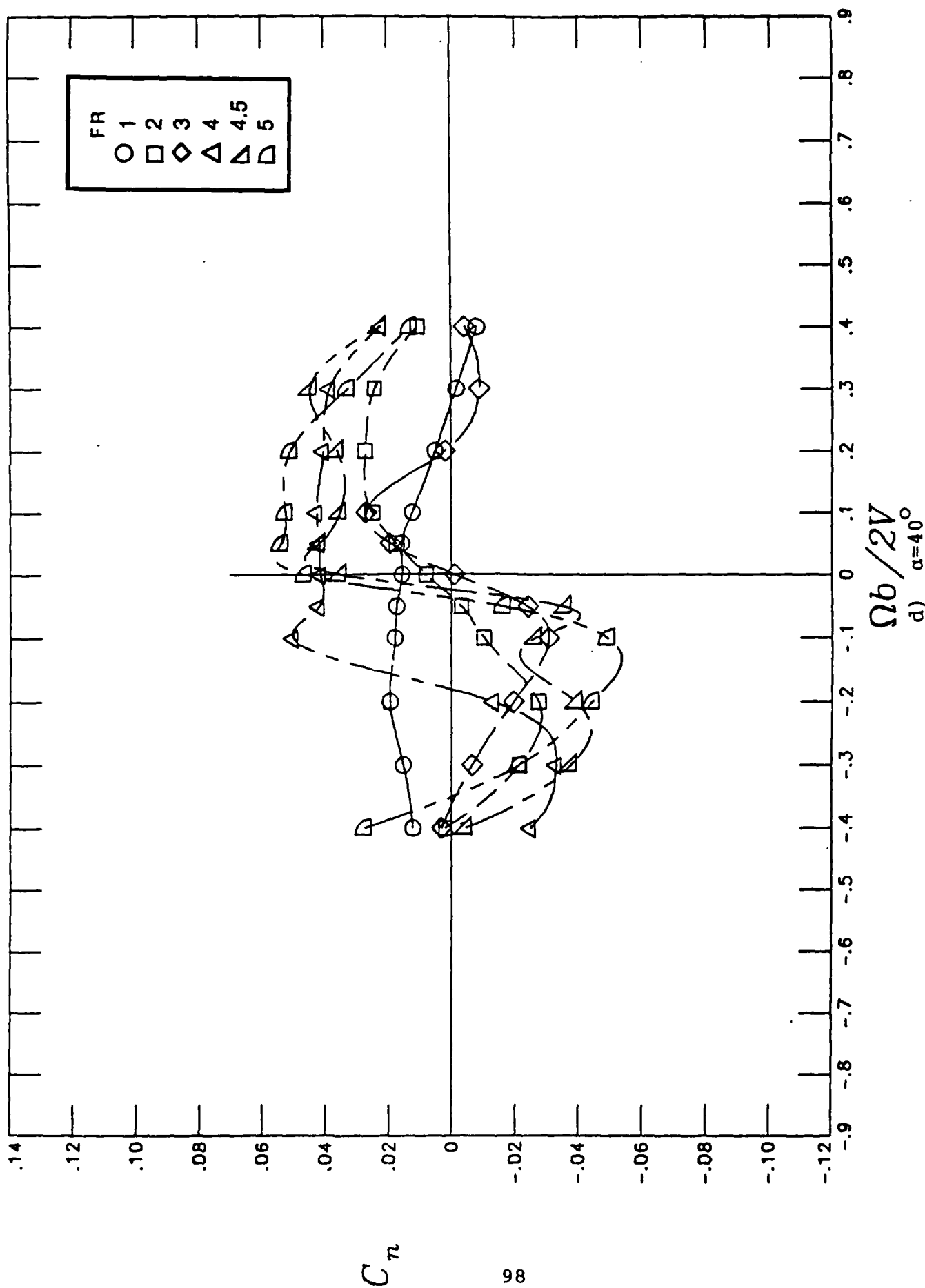
Figure 25.- Continued
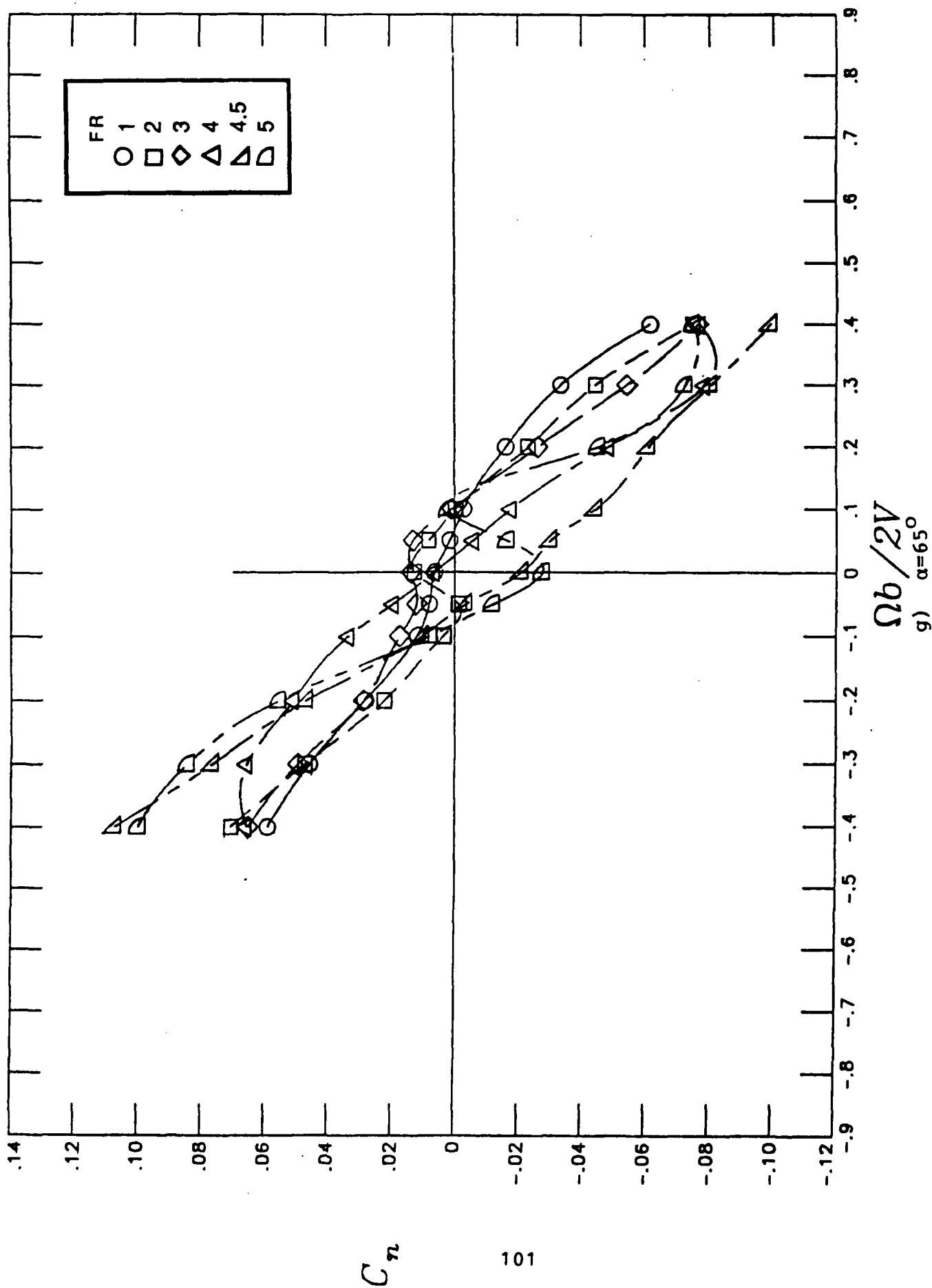
Figure 25. – Continued

e) $\alpha = 50°$

C_n

$\Omega b / 2V$

99

f) $\alpha = 60^o$

Figure 25.- Continued

100

Figure 25.– Continued

g) $\alpha=65^{\circ}$

C_n

$\Omega b/2V$

101

C_n

$\dfrac{\Omega b/2V}{\text{h) } \alpha=70^\circ}$

Figure 25. - Continued

102

Figure 25.- Continued

i) $\alpha = 80°$

C_n

$\Omega b / 2V$

FR
1 ○
2 □
3 ◇
4 △
4.5 △
5 ◻

103
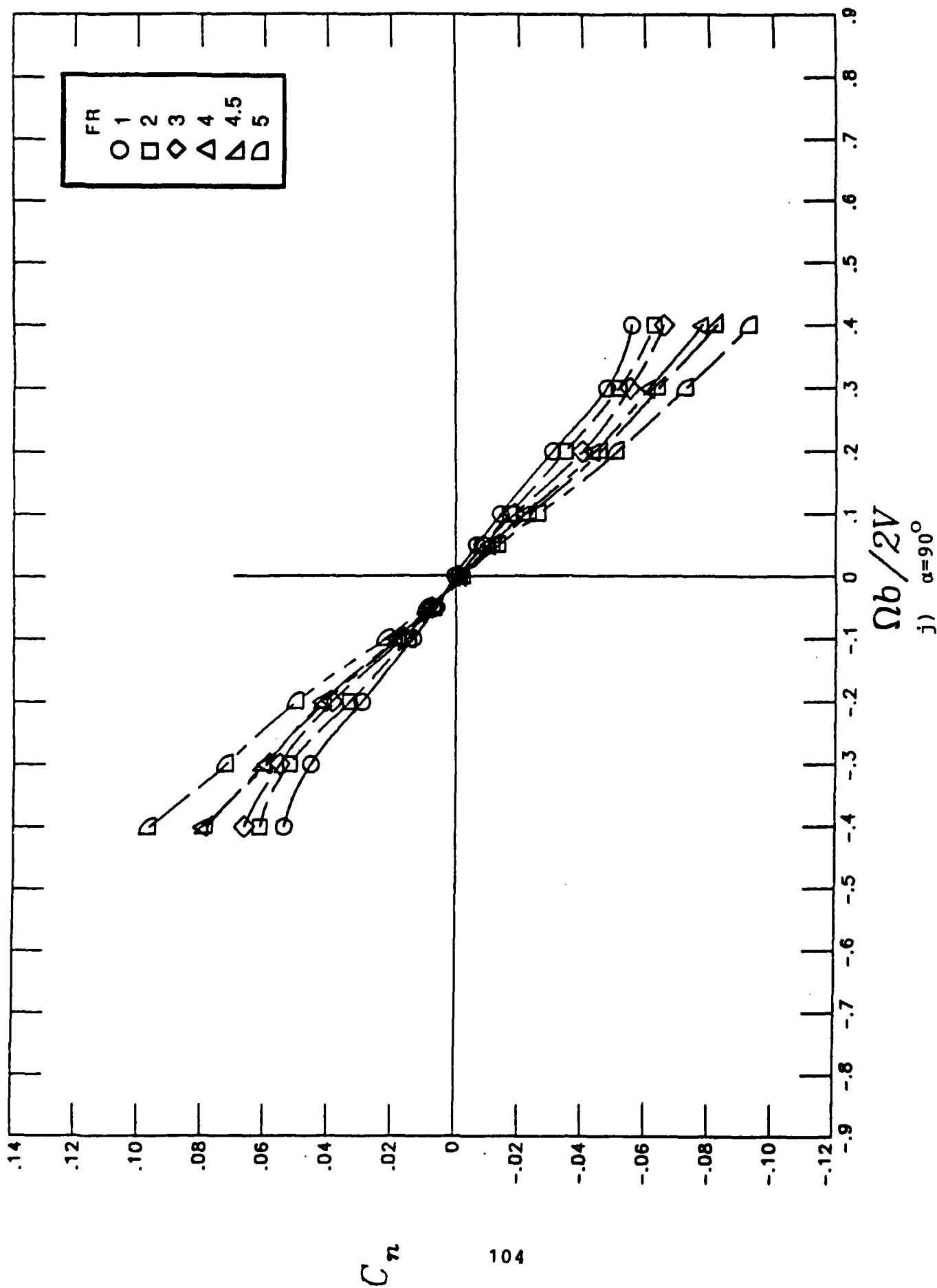
Figure 25.- Concluded

j) $\alpha=90^{\circ}$

$\Omega b/2V$

C_n

104
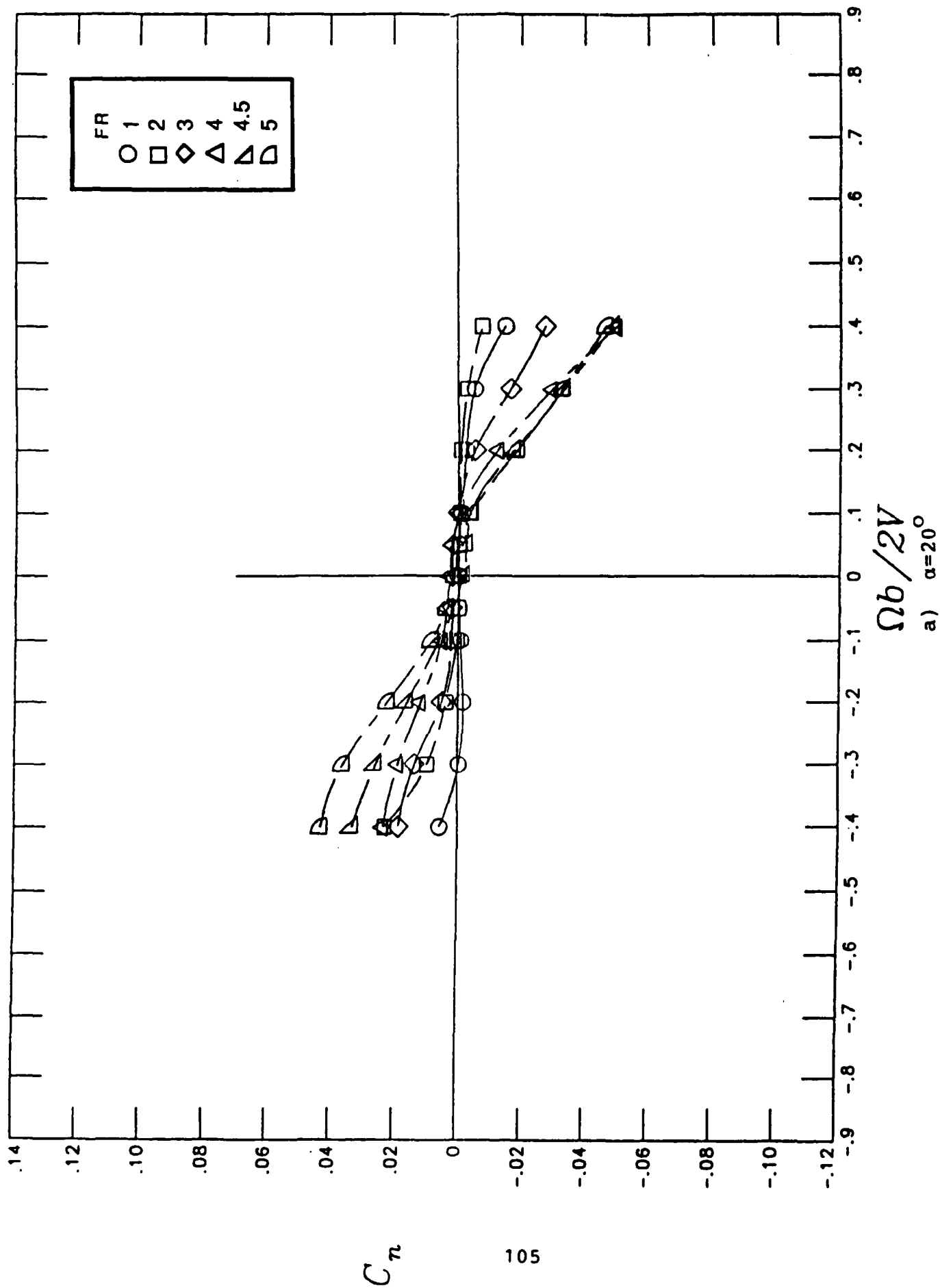
Figure 26.- Influence of forebody fineness ratio on rotational yawing-moment coefficient characteristics for a H/W=1.0 cross-sectional shape

a) $\alpha=20°$

105

C_n
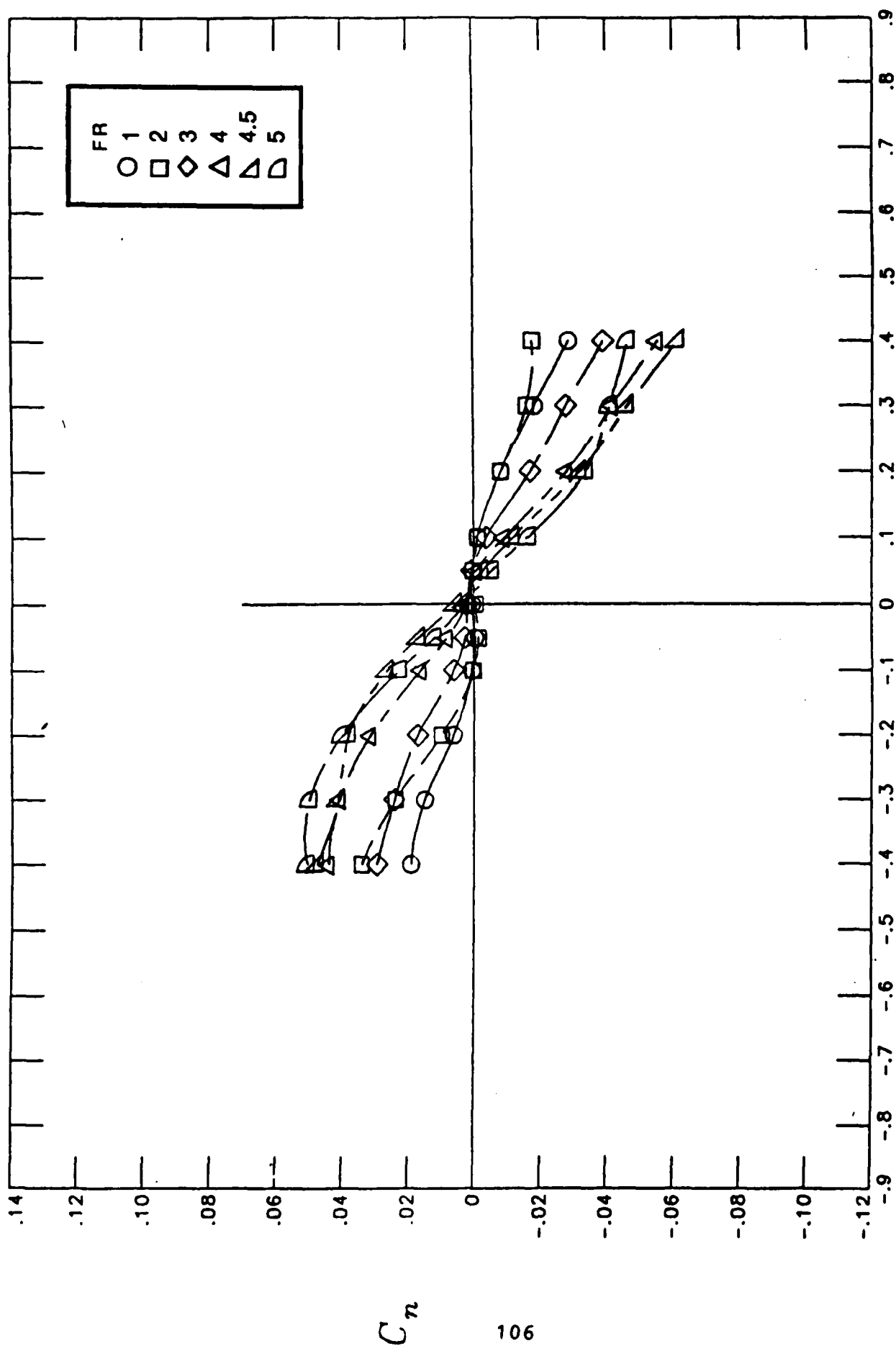
$\Omega b/2V$

b) $\alpha = 25°$

Figure 26.- Continued
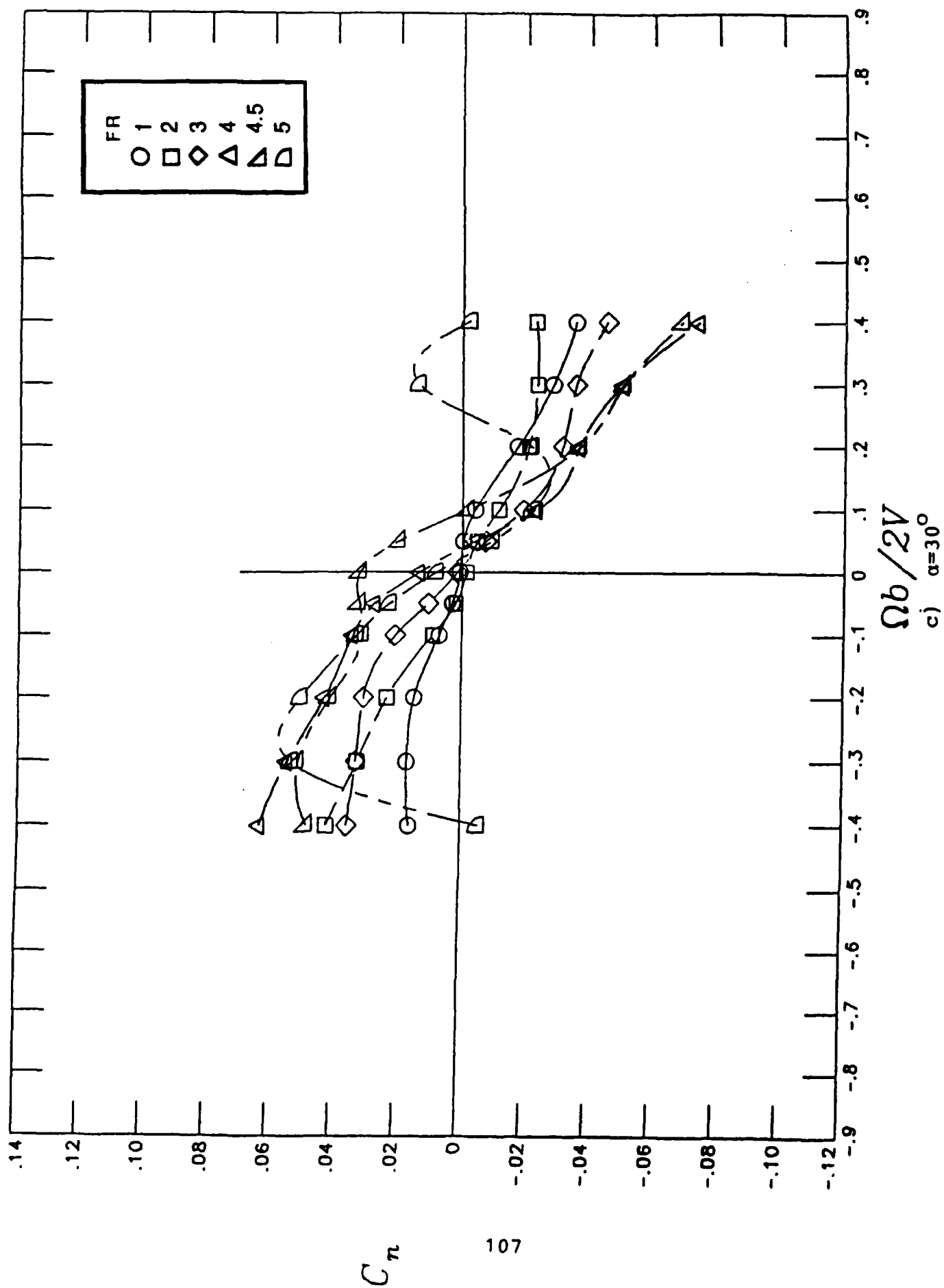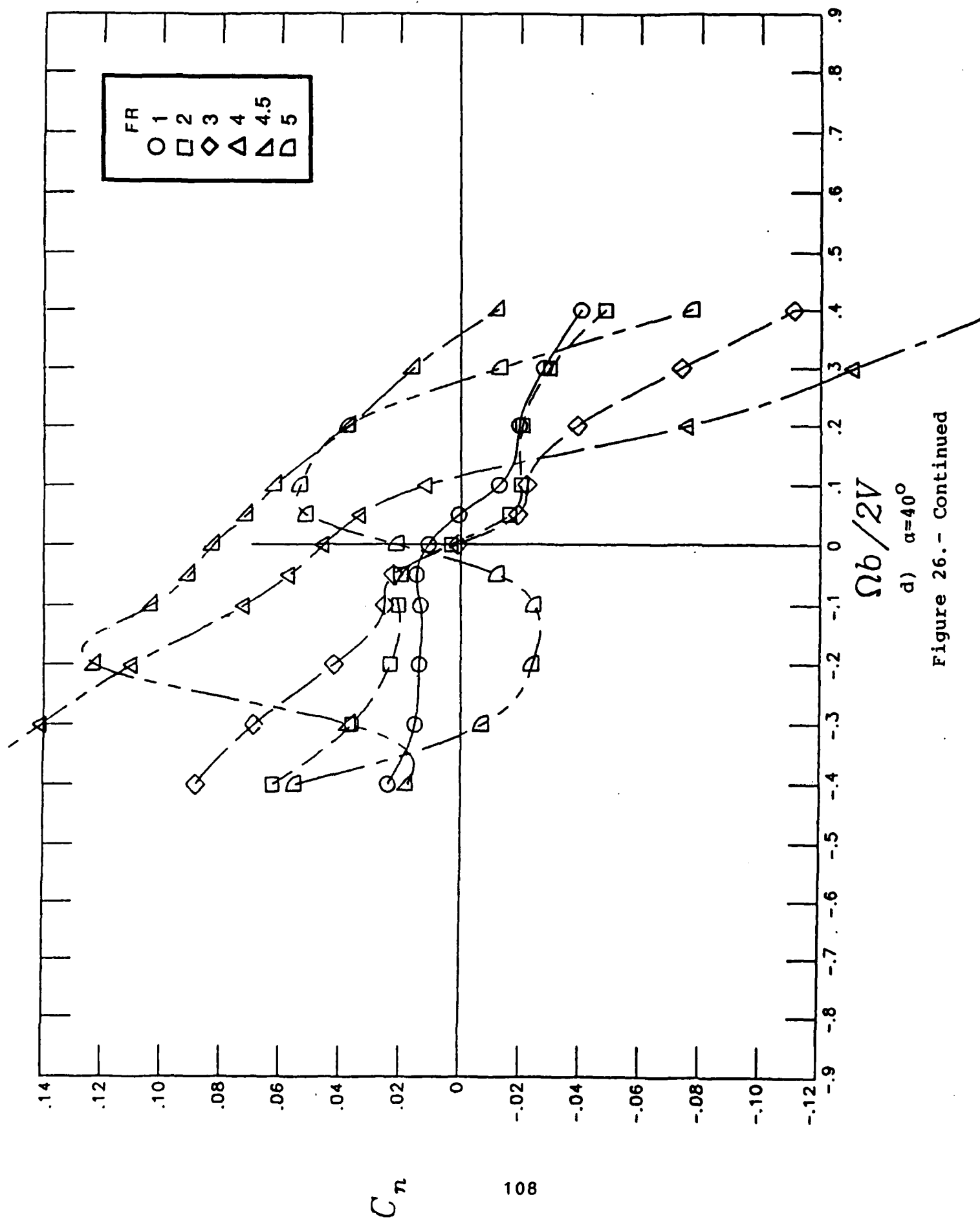
106

Figure 26.- Continued

c) α=30°

$\Omega b/2V$

C_n

107

$\Omega b/2V$

d) $\alpha=40^{\circ}$

Figure 26.- Continued
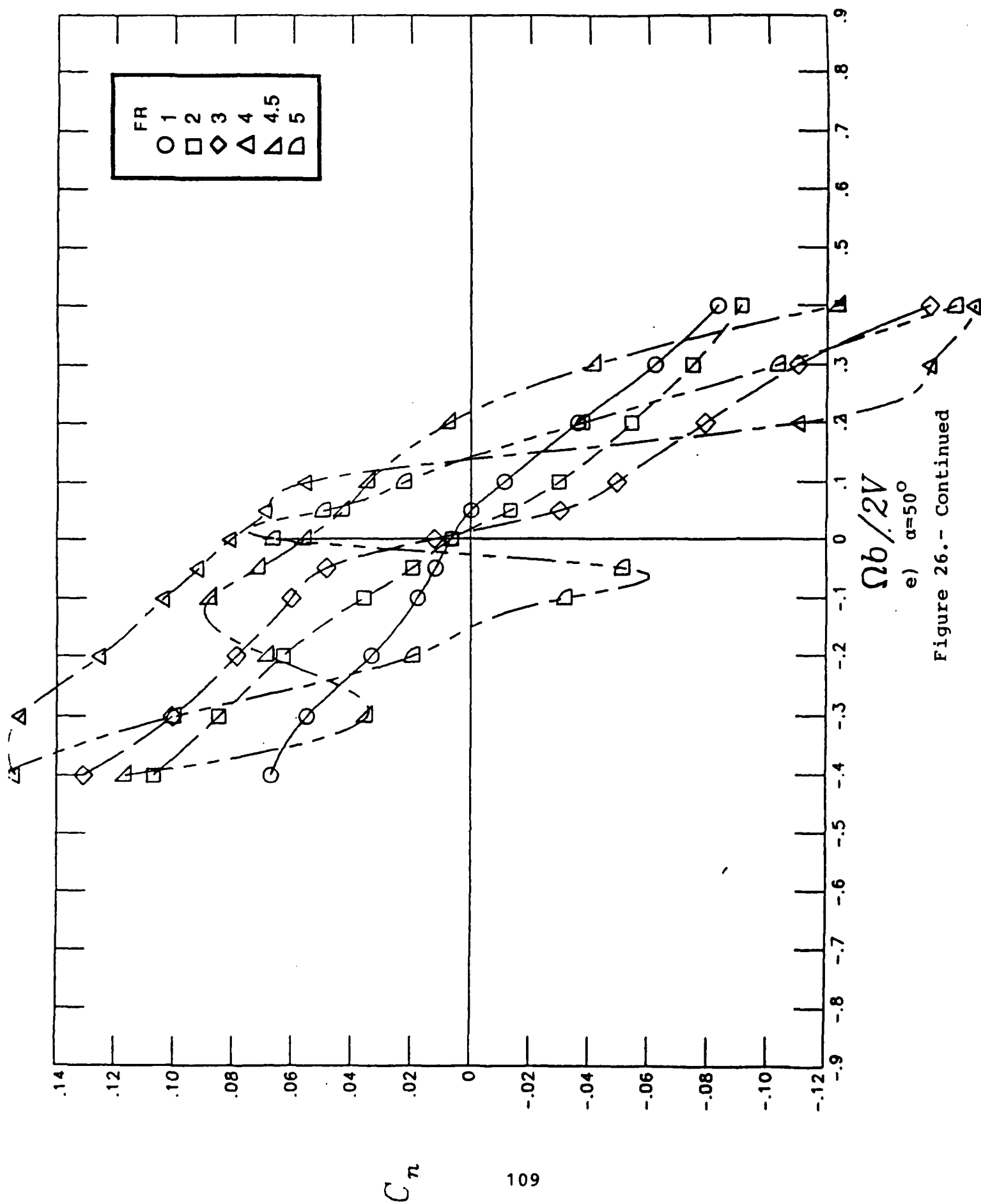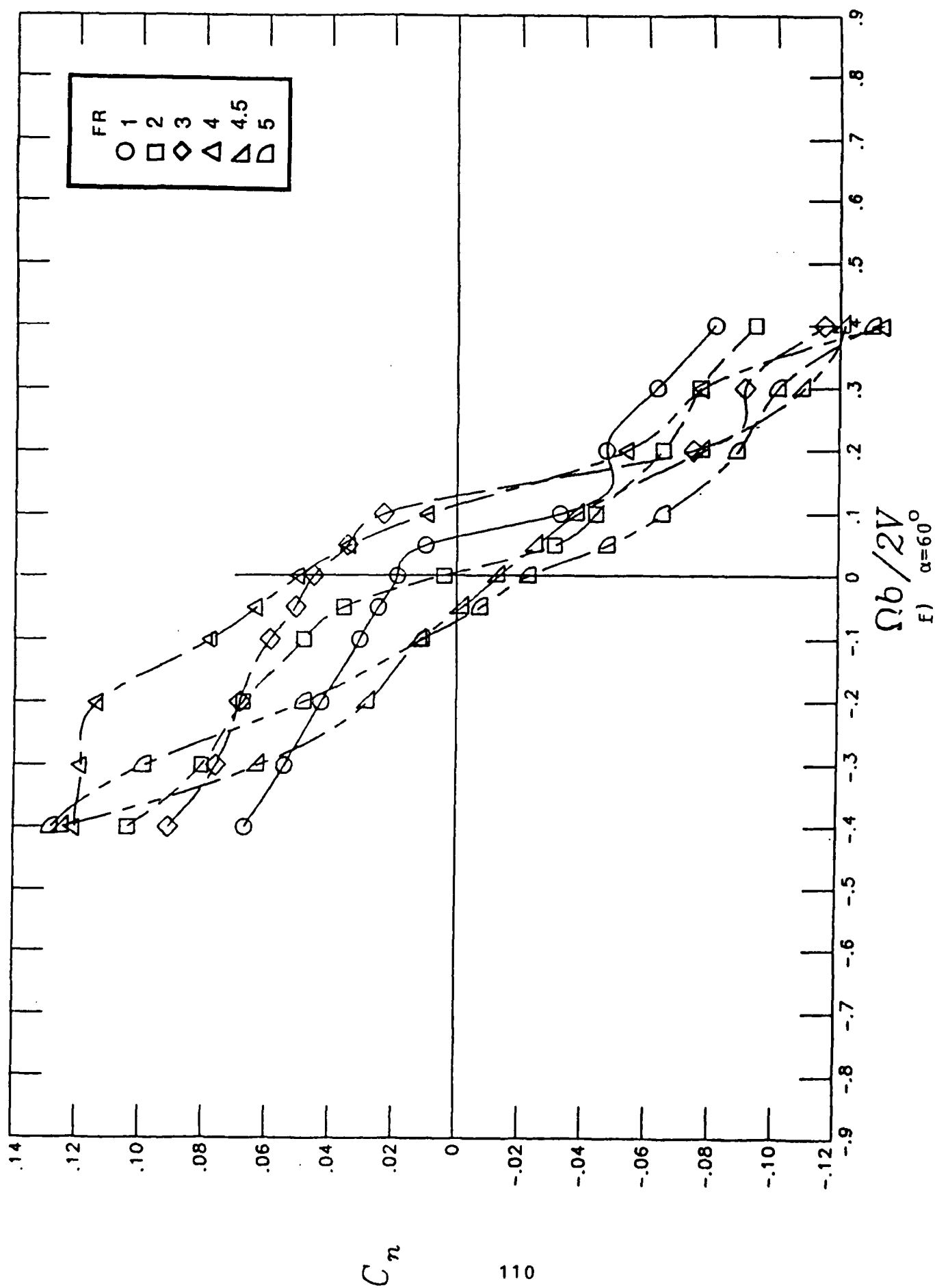
C_n

108

Figure 26.- Continued

e) $\alpha = 50°$

$\Omega b/2V$

C_n

109

$\Omega b/2V$

f) $\alpha = 60°$

Figure 26.- Continued

C_n

Figure 26.- Continued

g) $\alpha = 65^\circ$

$\dfrac{\Omega b}{2V}$

C_n

h) $\alpha = 70°$

Figure 26.– Continued

112

$\dfrac{\Omega b/2V}{\text{1) } \alpha=80^\circ}$

Figure 26.- Continued

C_n

113

$\Omega b/2V$
j) $\alpha = 90°$
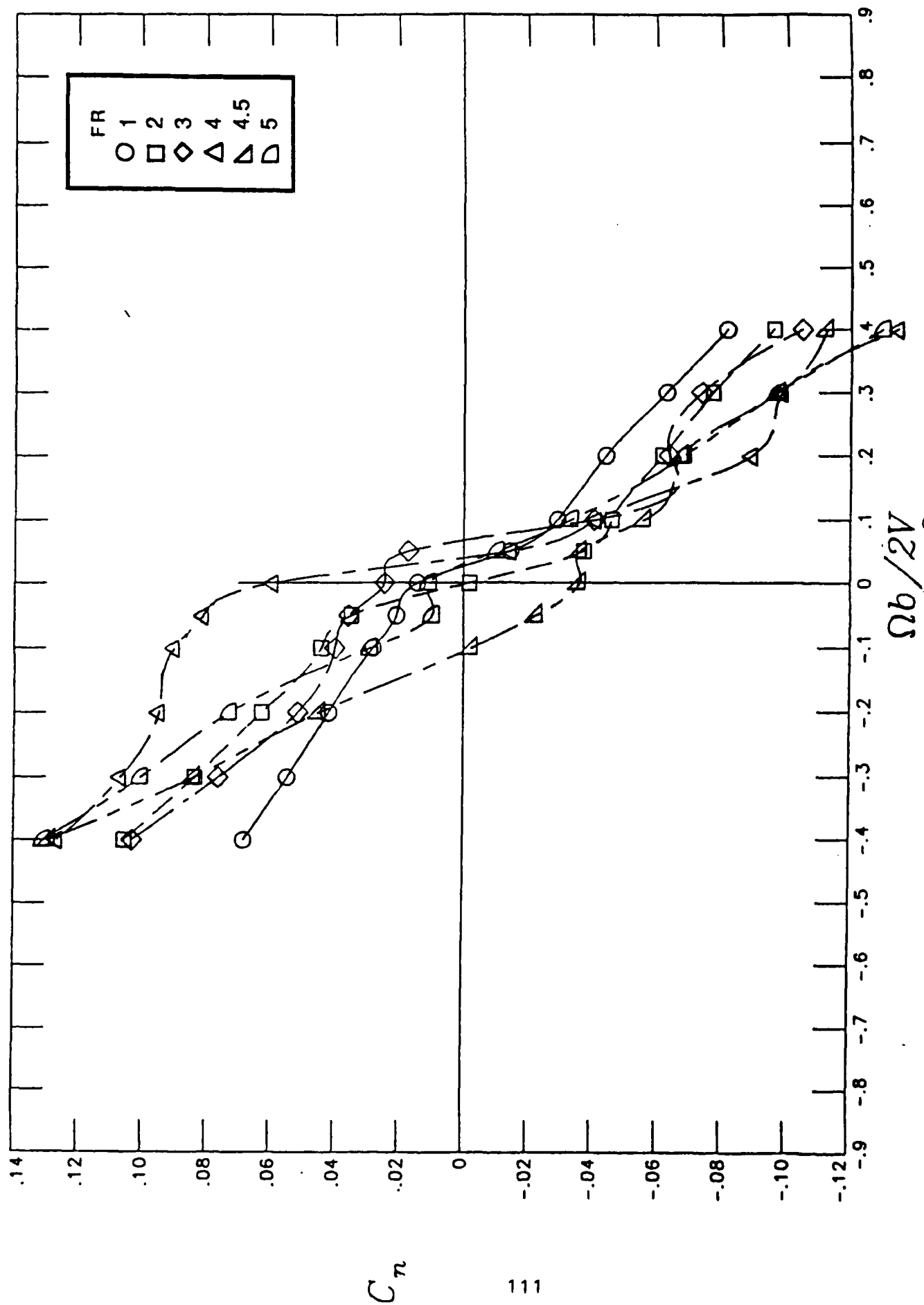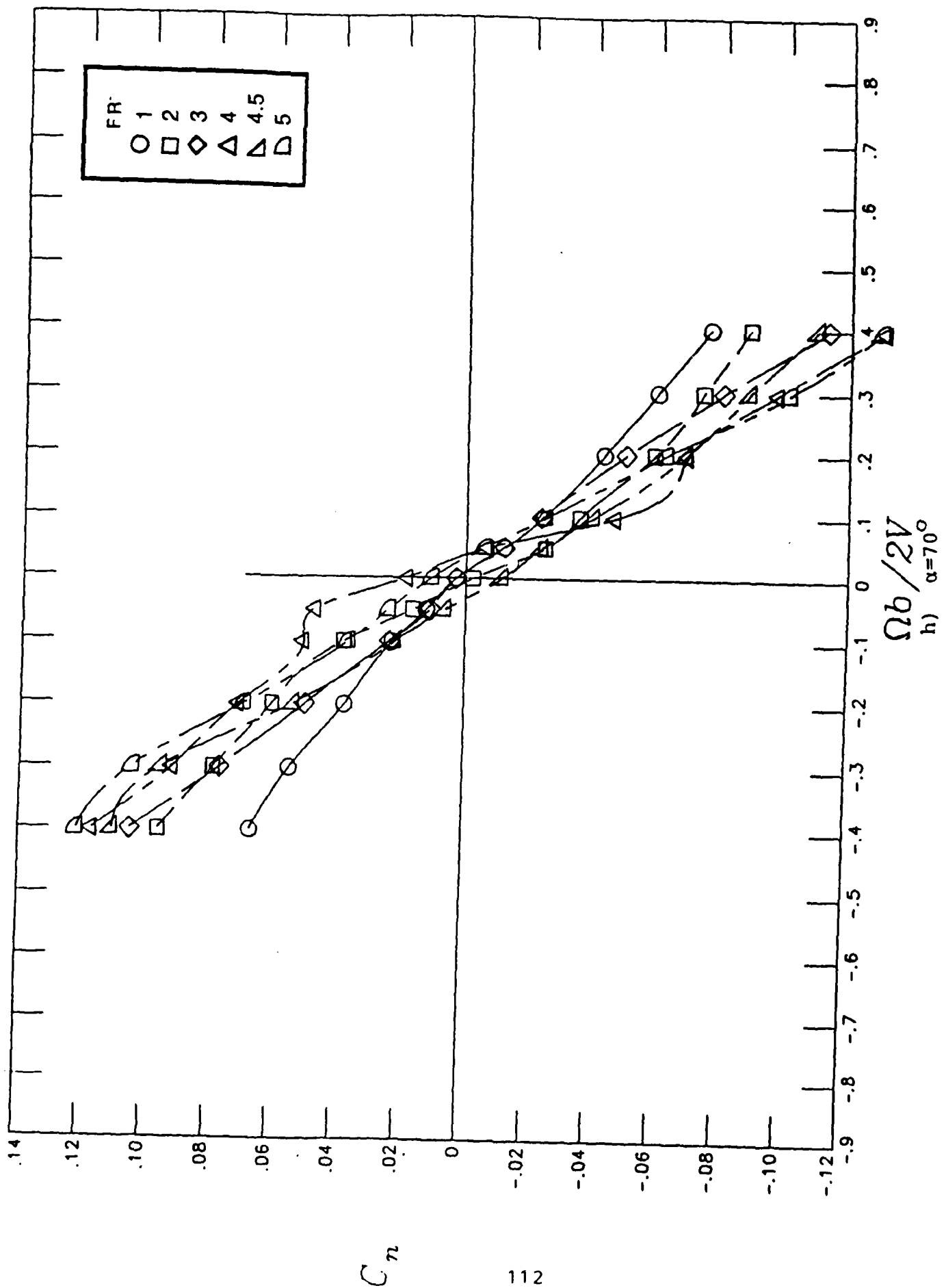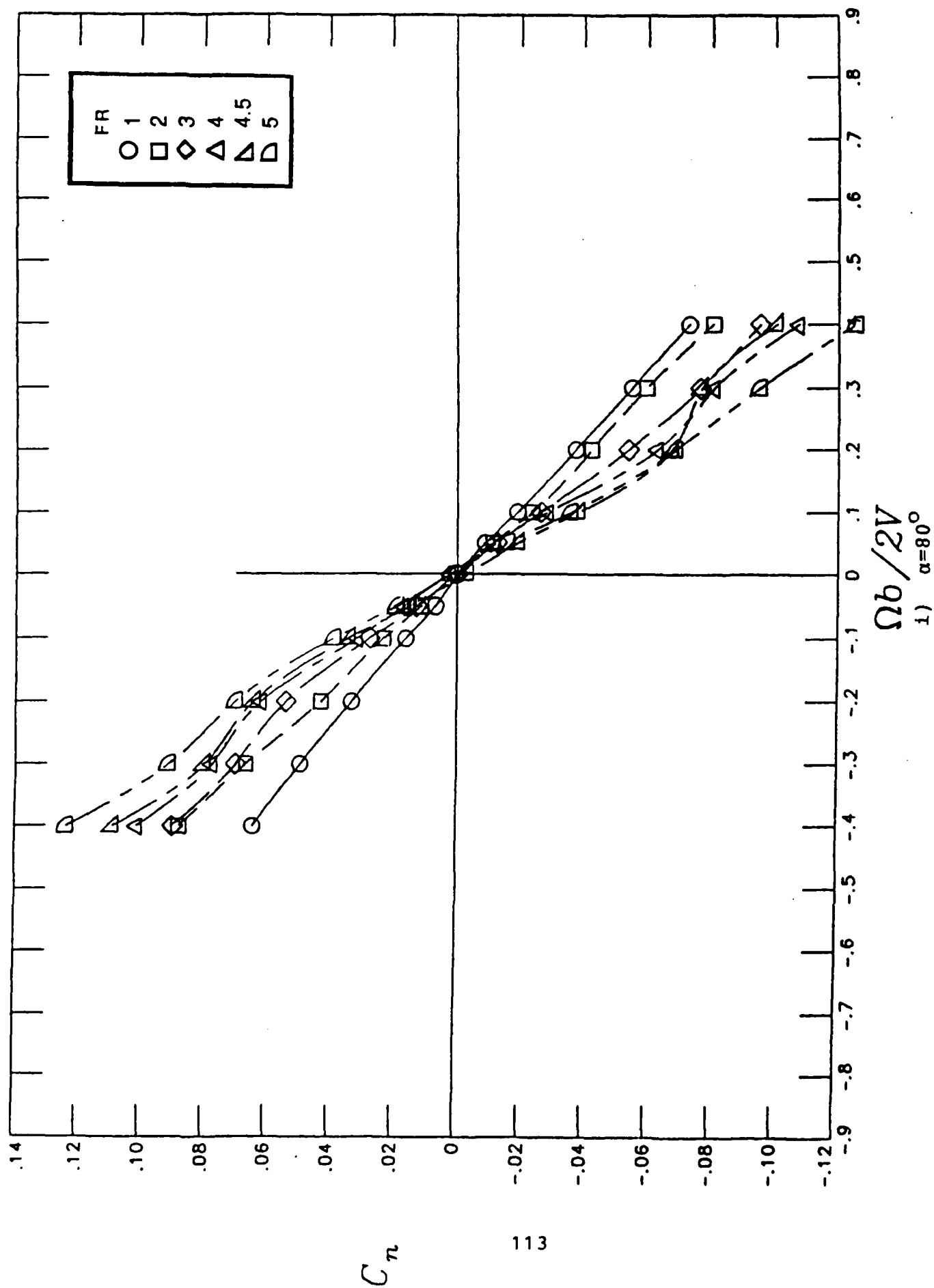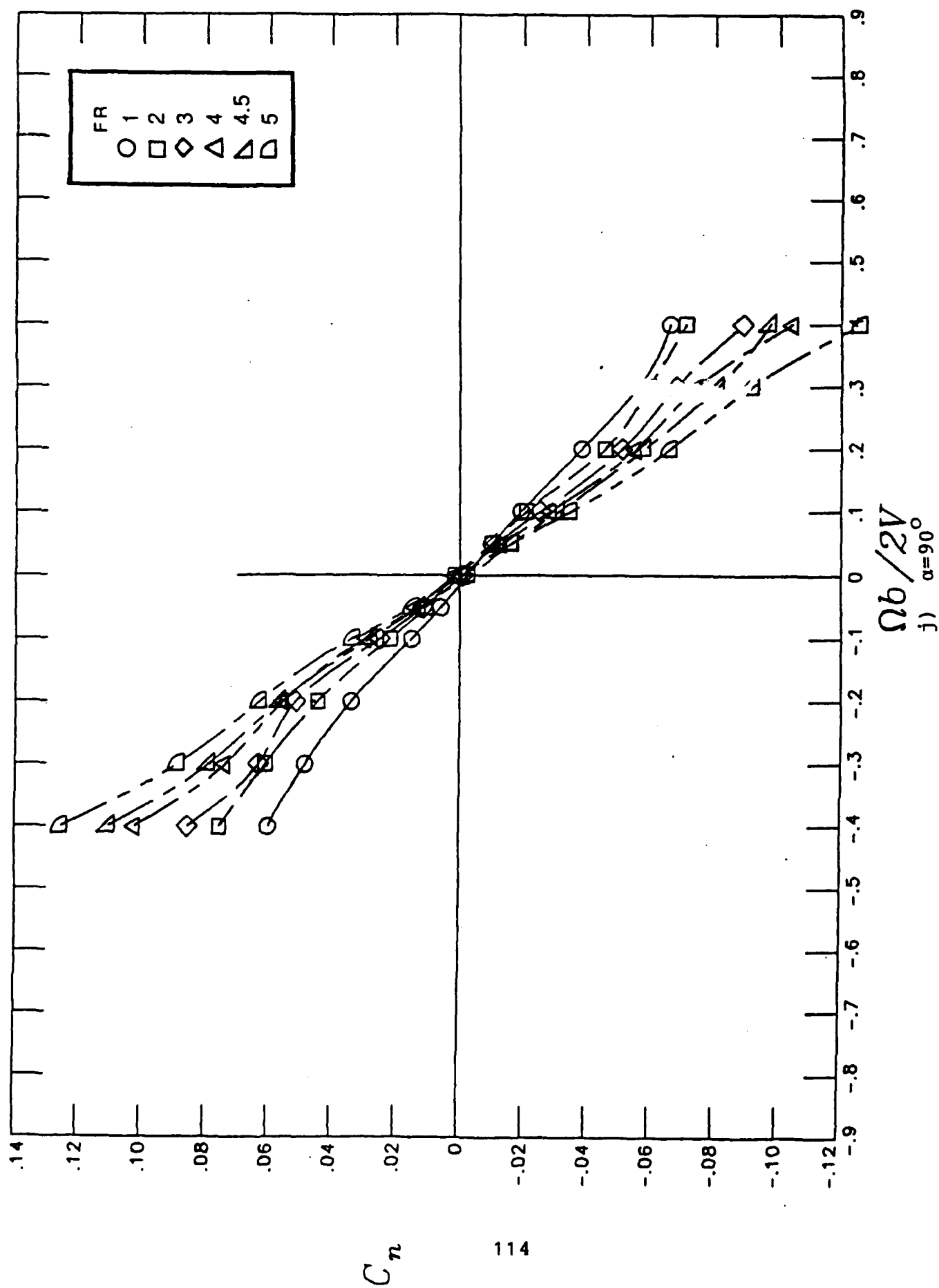
Figure 26.- Concluded

114
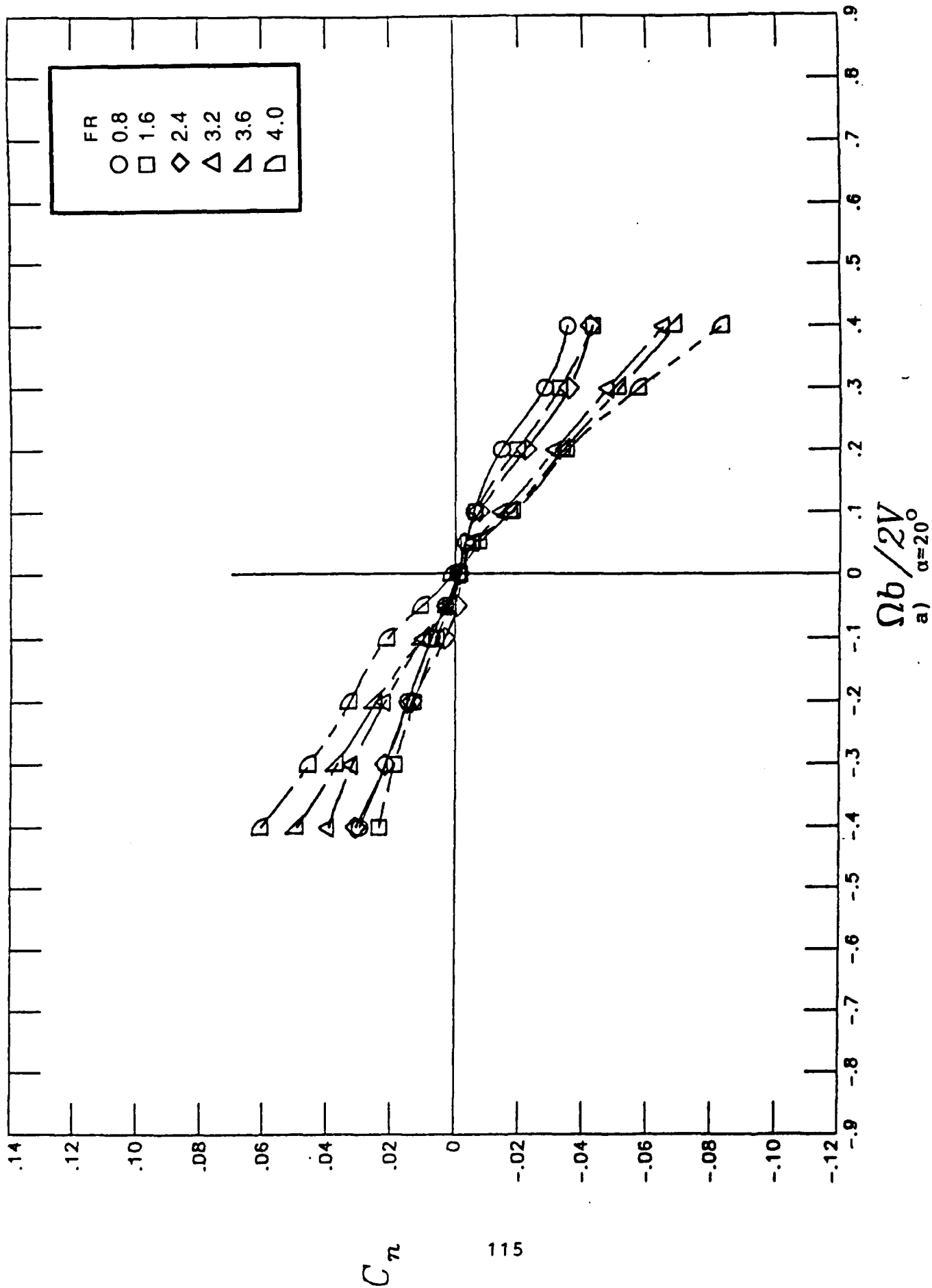
Figure 27.- Influence of forebody fineness ratio on rotational yawing-moment coefficient characteristics for a ll/w=1.25 cross-sectional shape

115

$\dfrac{\Omega b/2V}{\text{b)} \quad \alpha = 25^\circ}$

Figure 27.- Continued

116

$\Omega b/2V$

c) $\alpha=30^{\circ}$

Figure 27.- Continued

C_n

117

d) $\alpha = 40°$

Figure 27.- Continued

C_n

118

$\Omega b/2V$

e) $\alpha=50^\circ$

Figure 27.- Continued

C_n

119
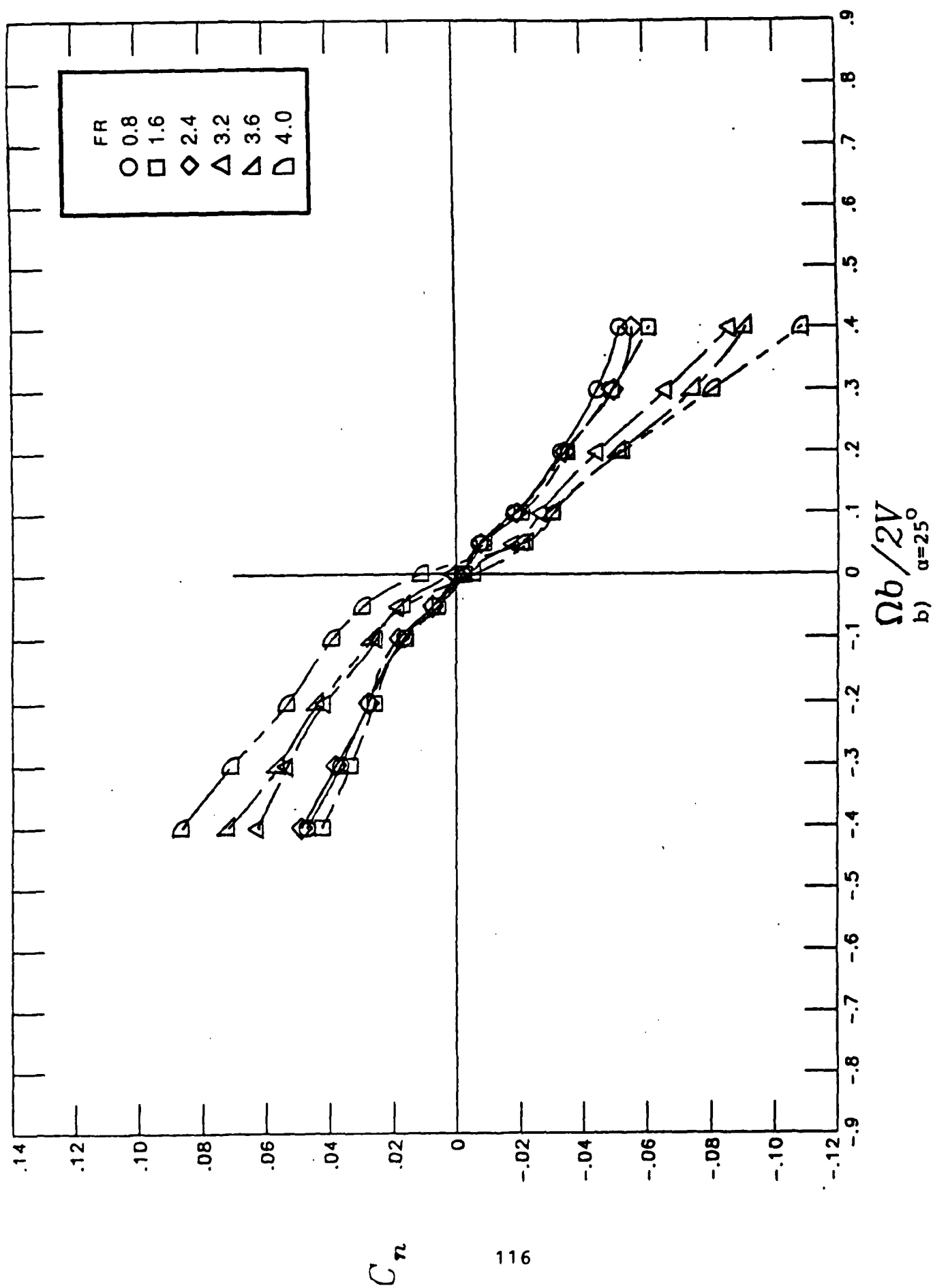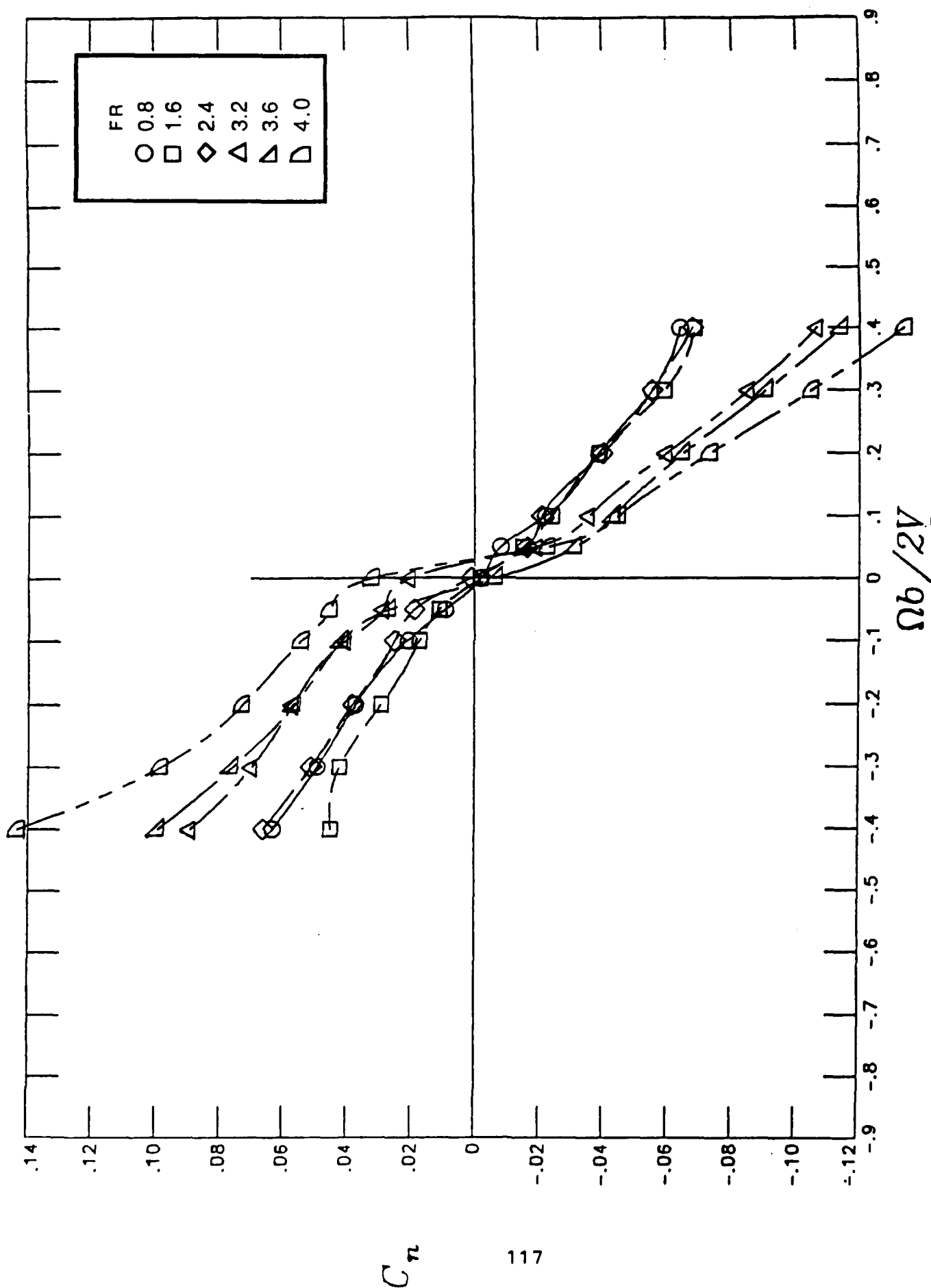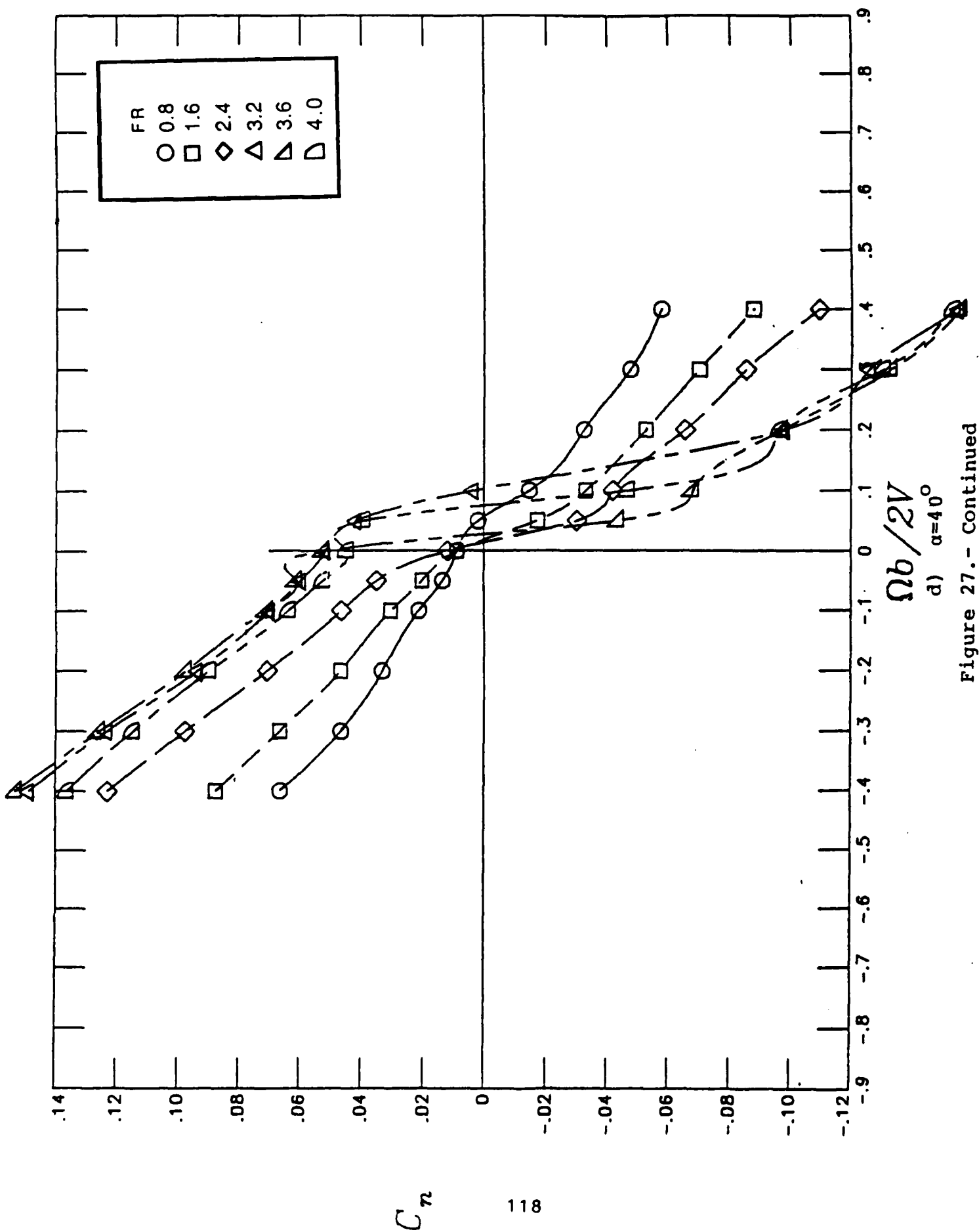
Figure 27.- Continued

f) $\alpha = 60°$

$\dfrac{\Omega b}{2V}$

C_n

120

$\Omega b/2V$

g) $\alpha=65^\circ$

Figure 27.- Continued

121

C_n

$\Omega b/2V$

h) $\alpha = 70°$

Figure 27.- Continued

122

Figure 27.- Continued

i) $\alpha = 80°$

$\Omega b/2V$

C_n

123
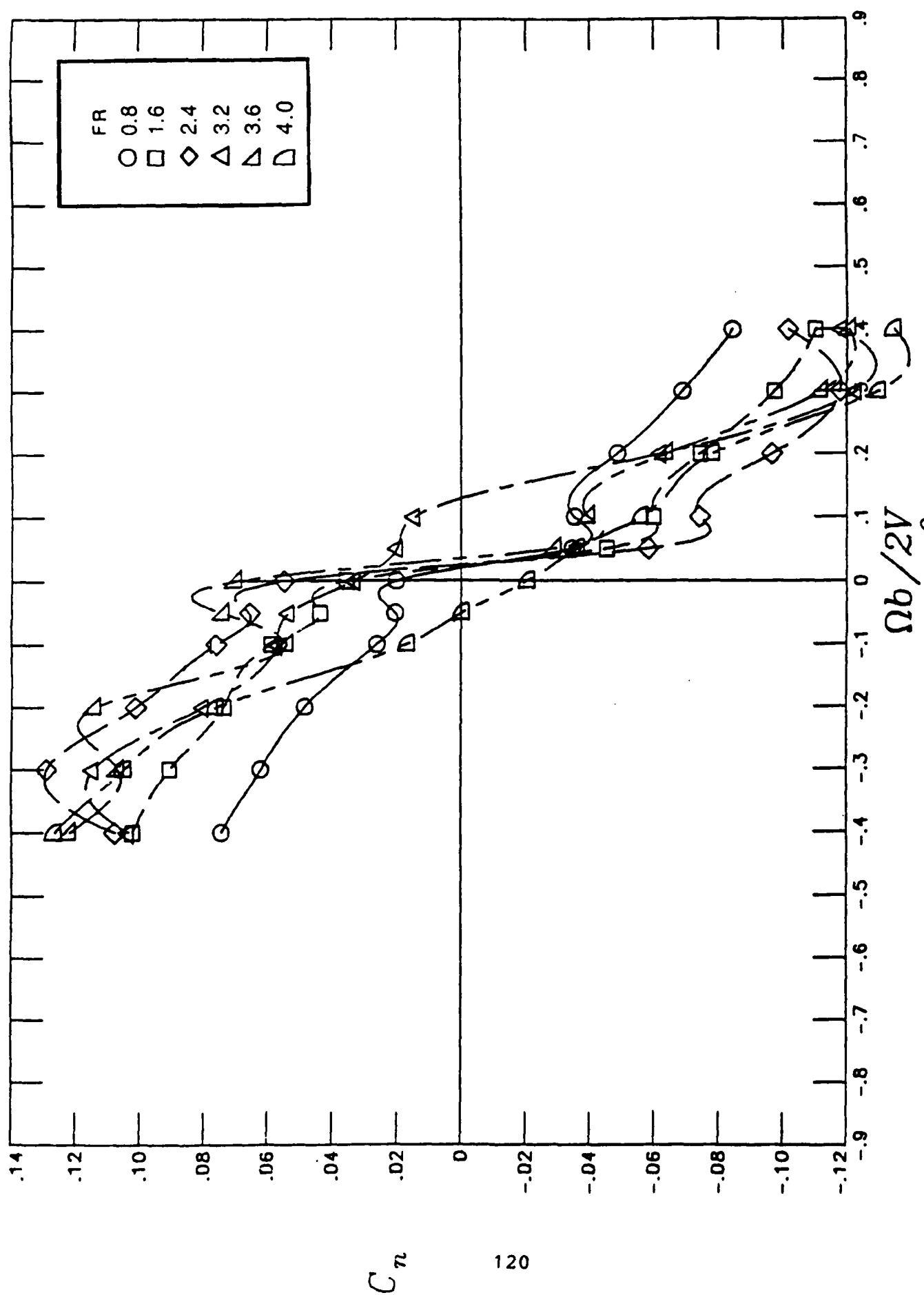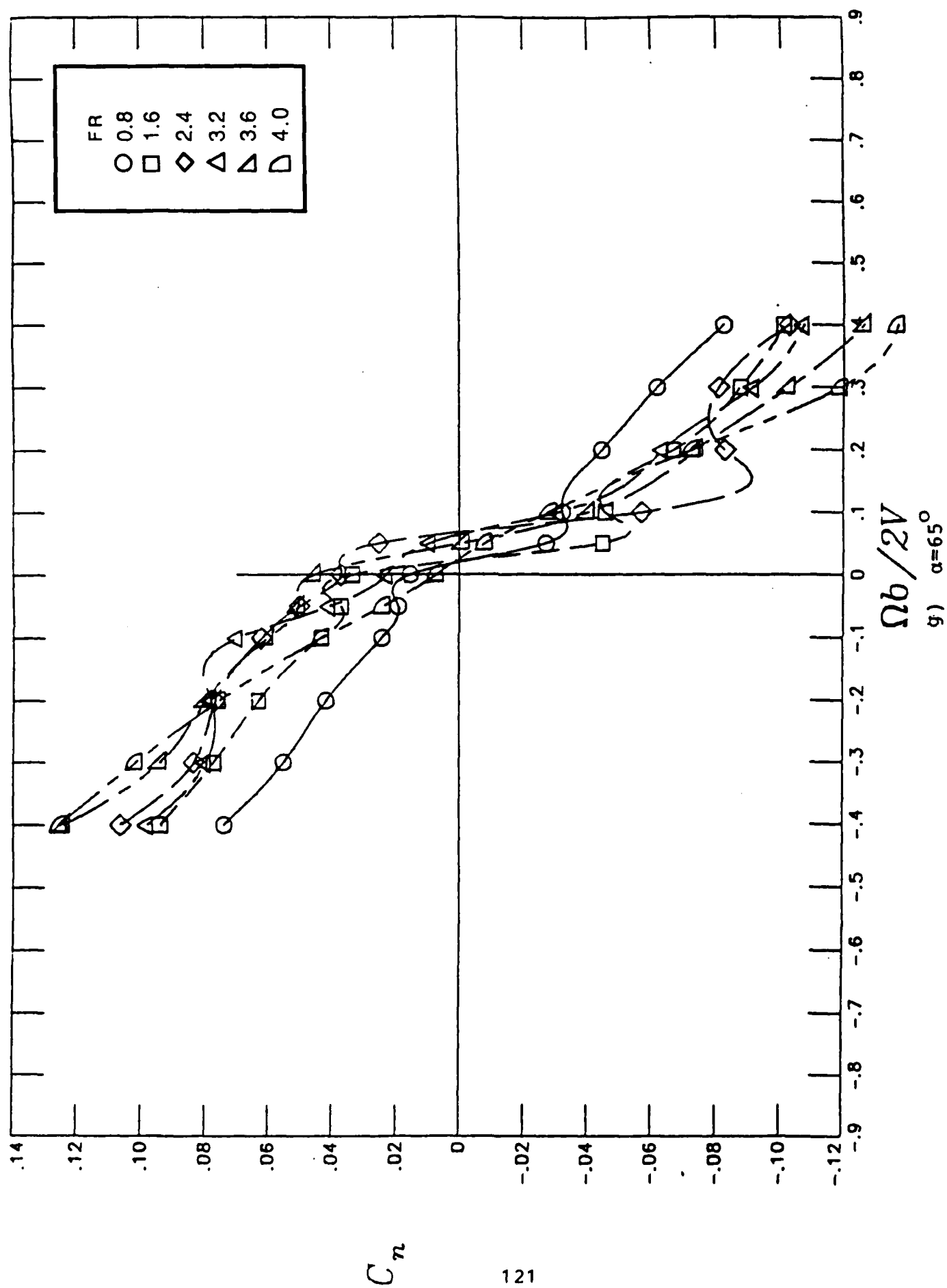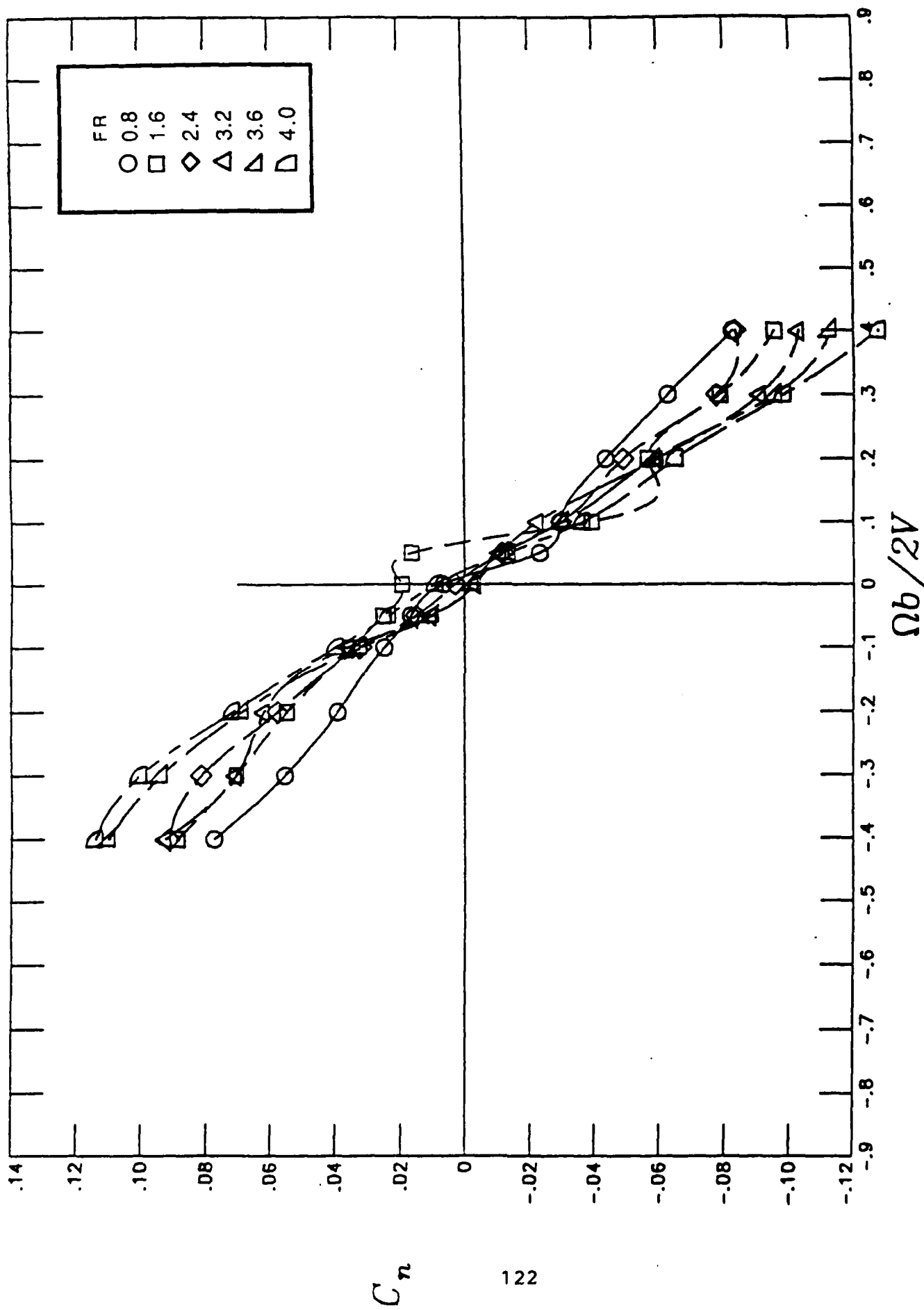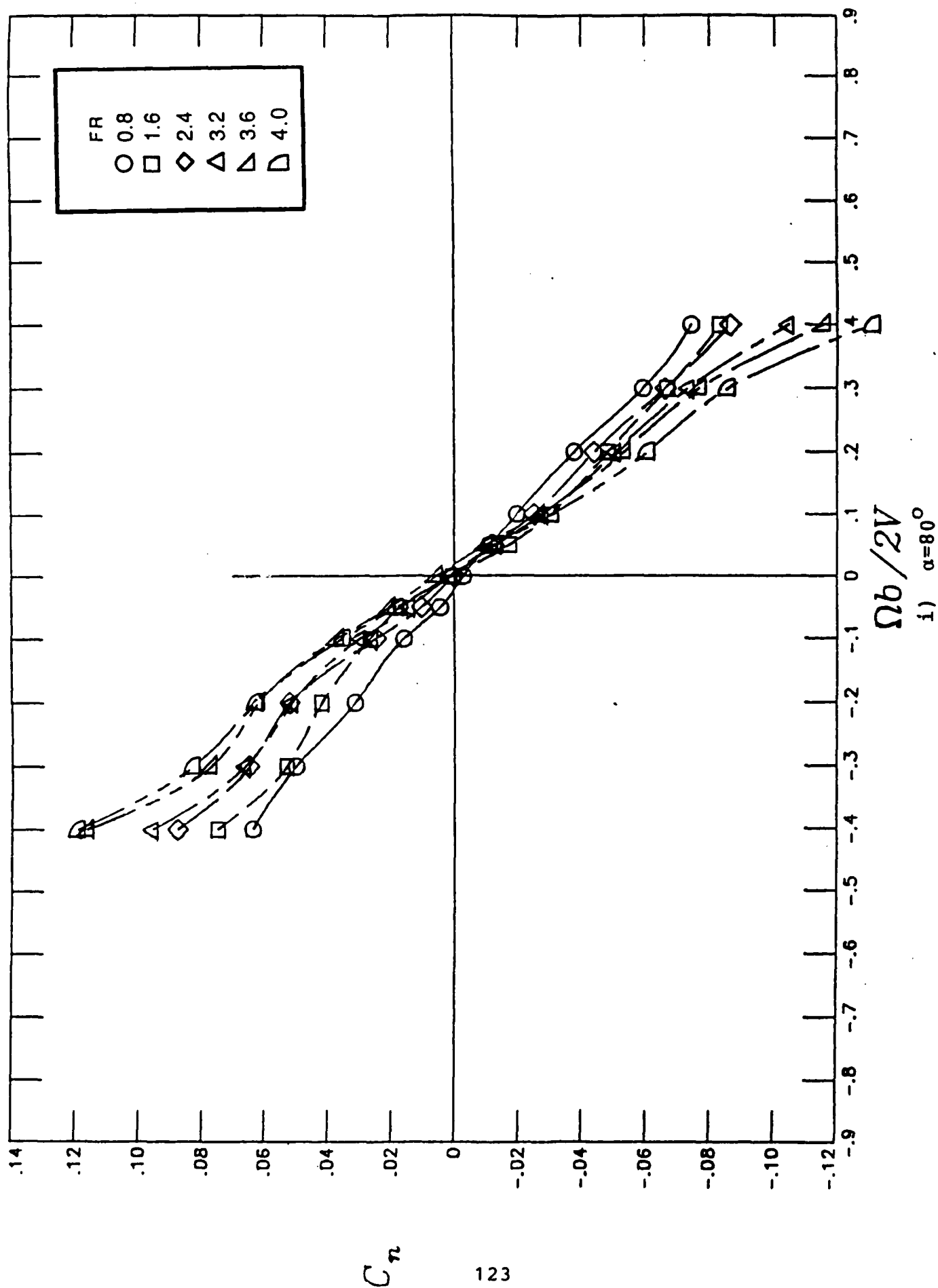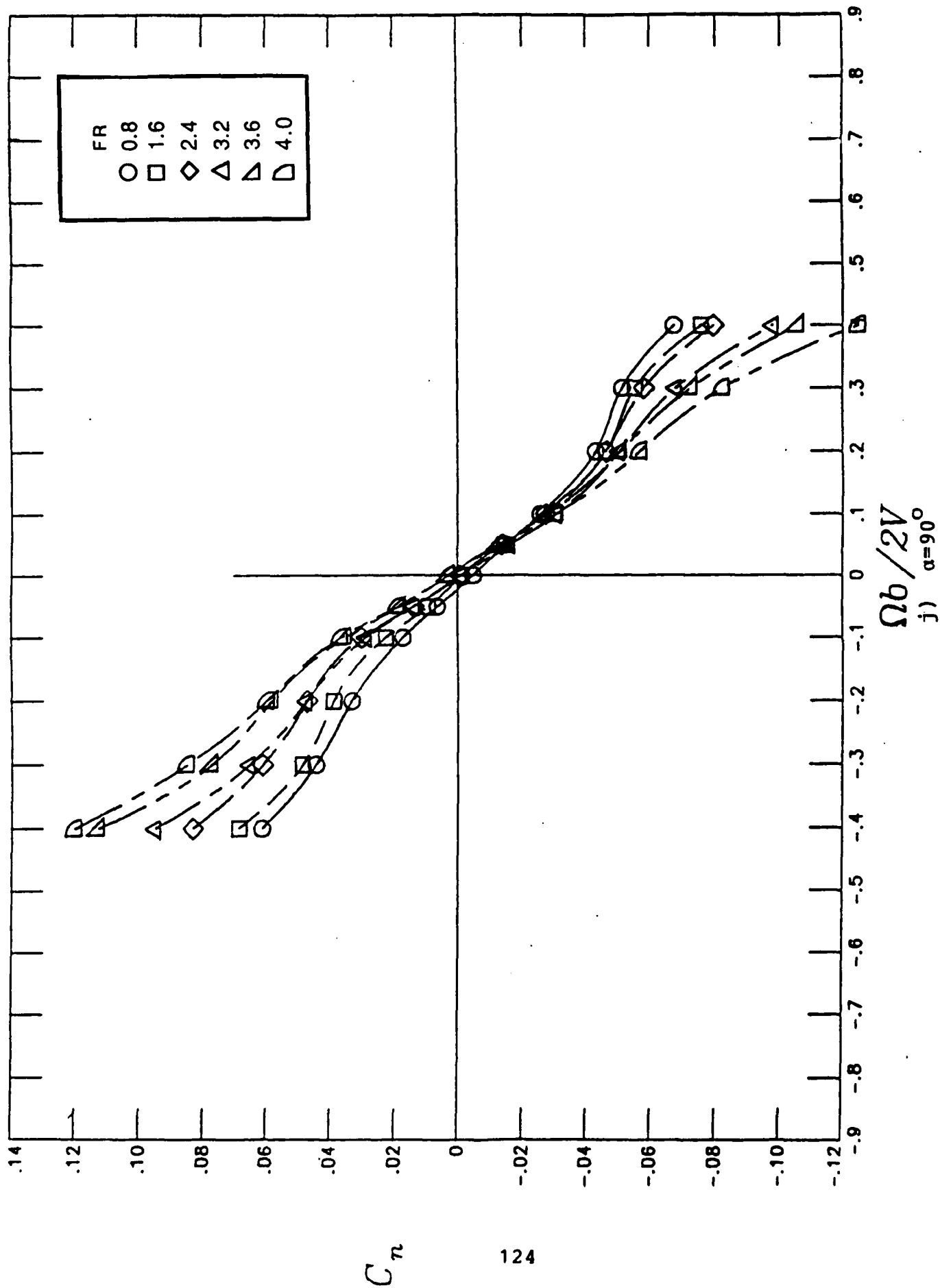
Figure 27.- Concluded

j) $\alpha = 90°$

$\Omega b / 2V$

C_n
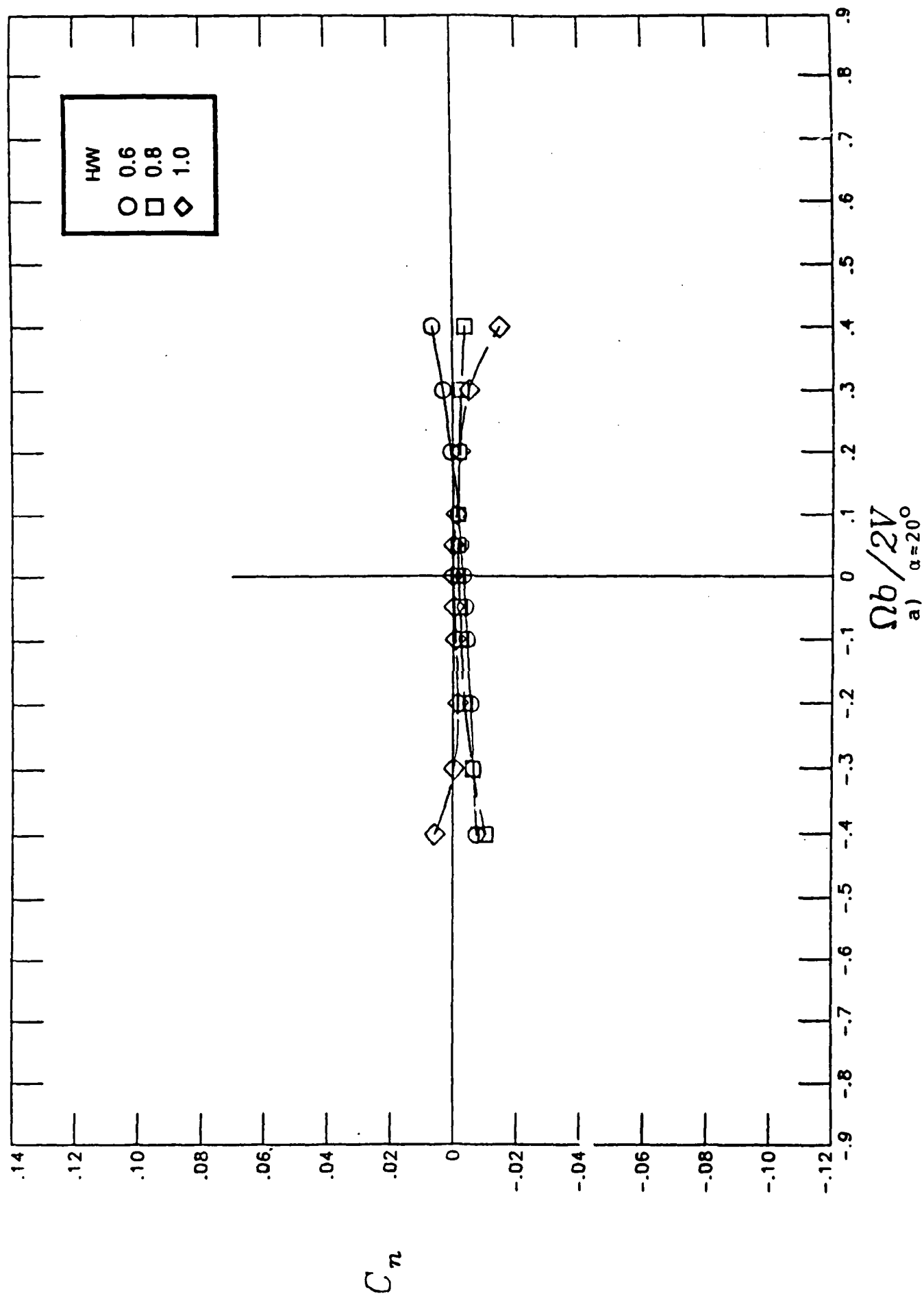
Figure 28.- Influence of forebody cross-sectional shape on rotational yawing-moment coefficient characteristics at a fineness ratio value of 1
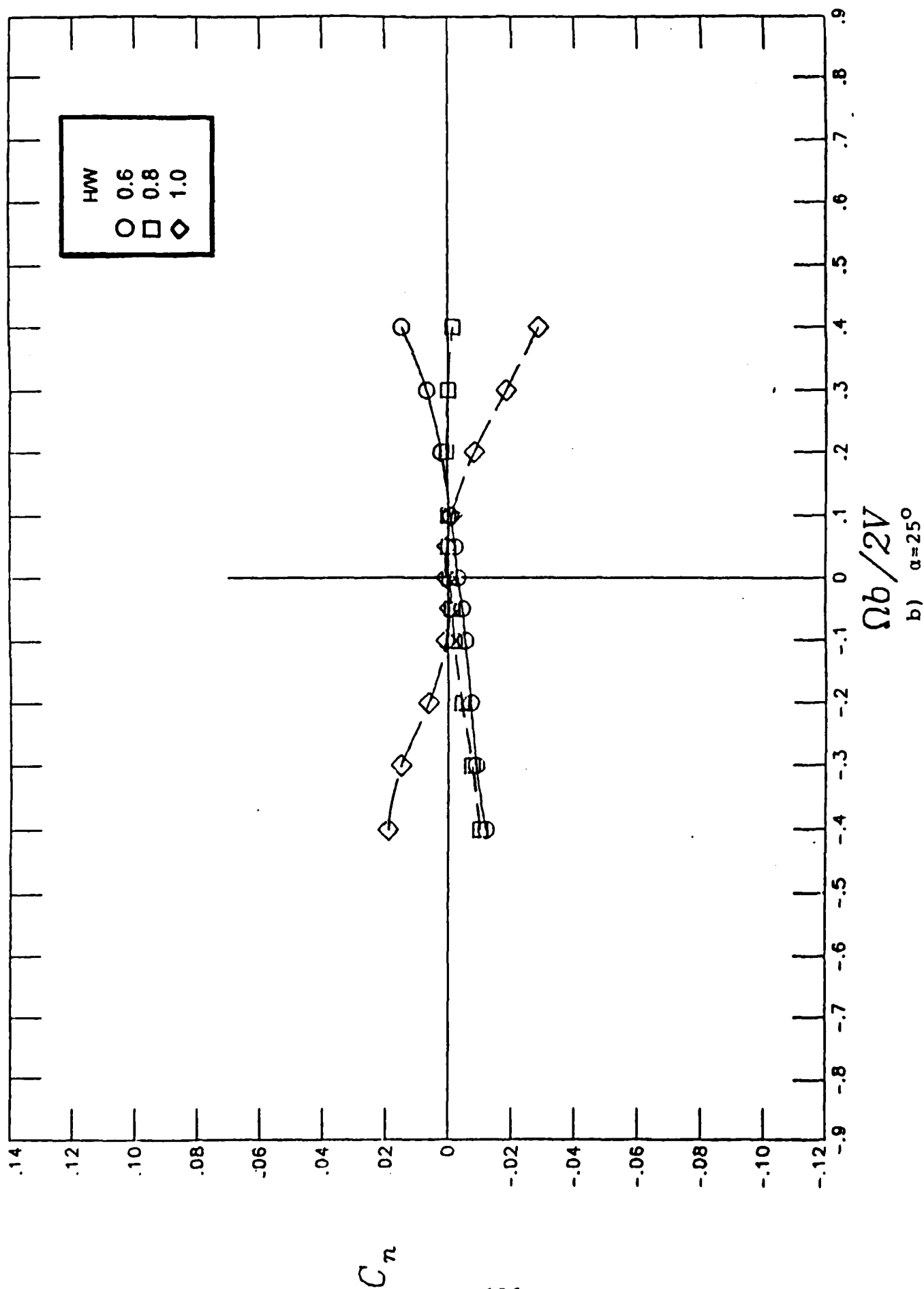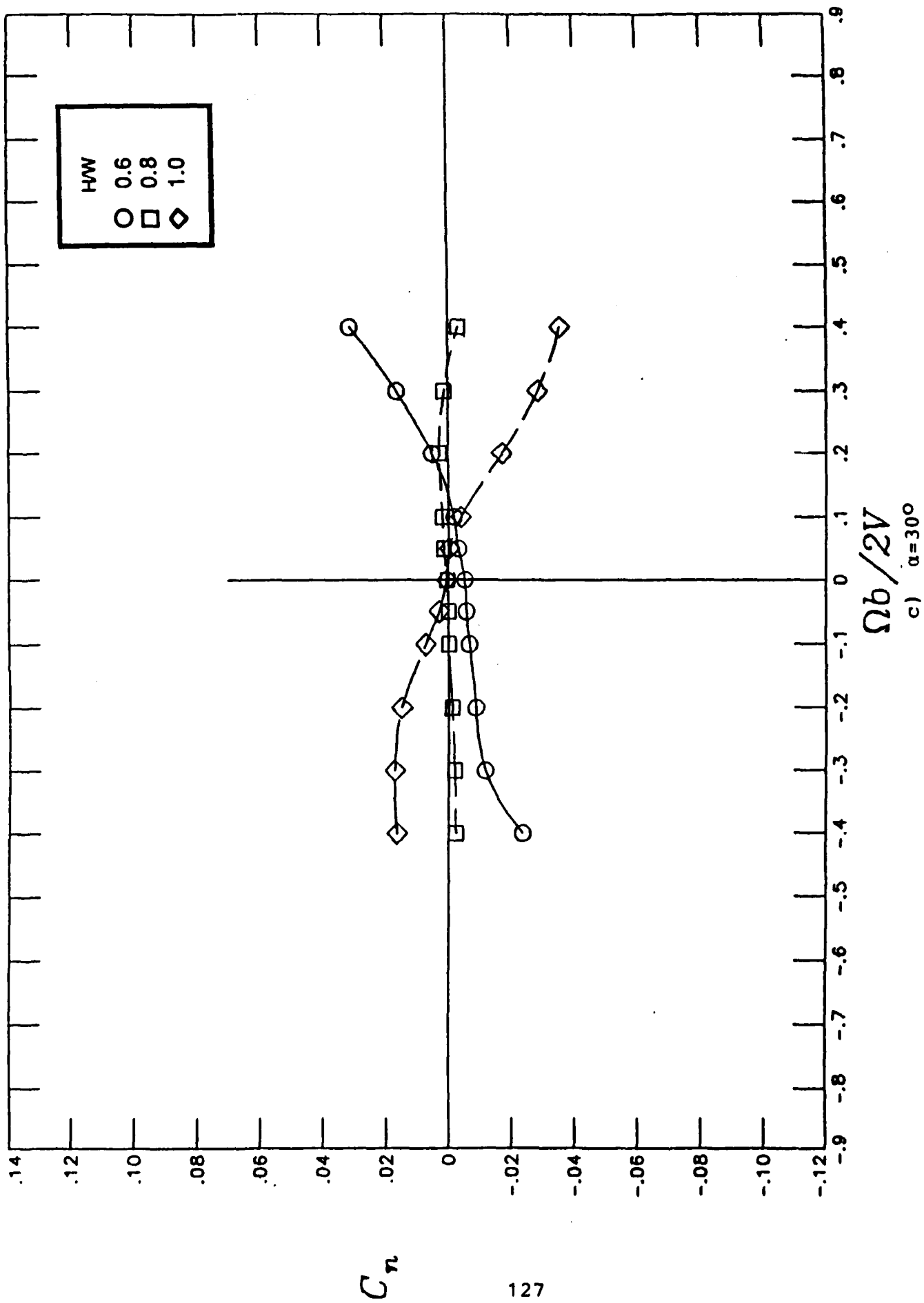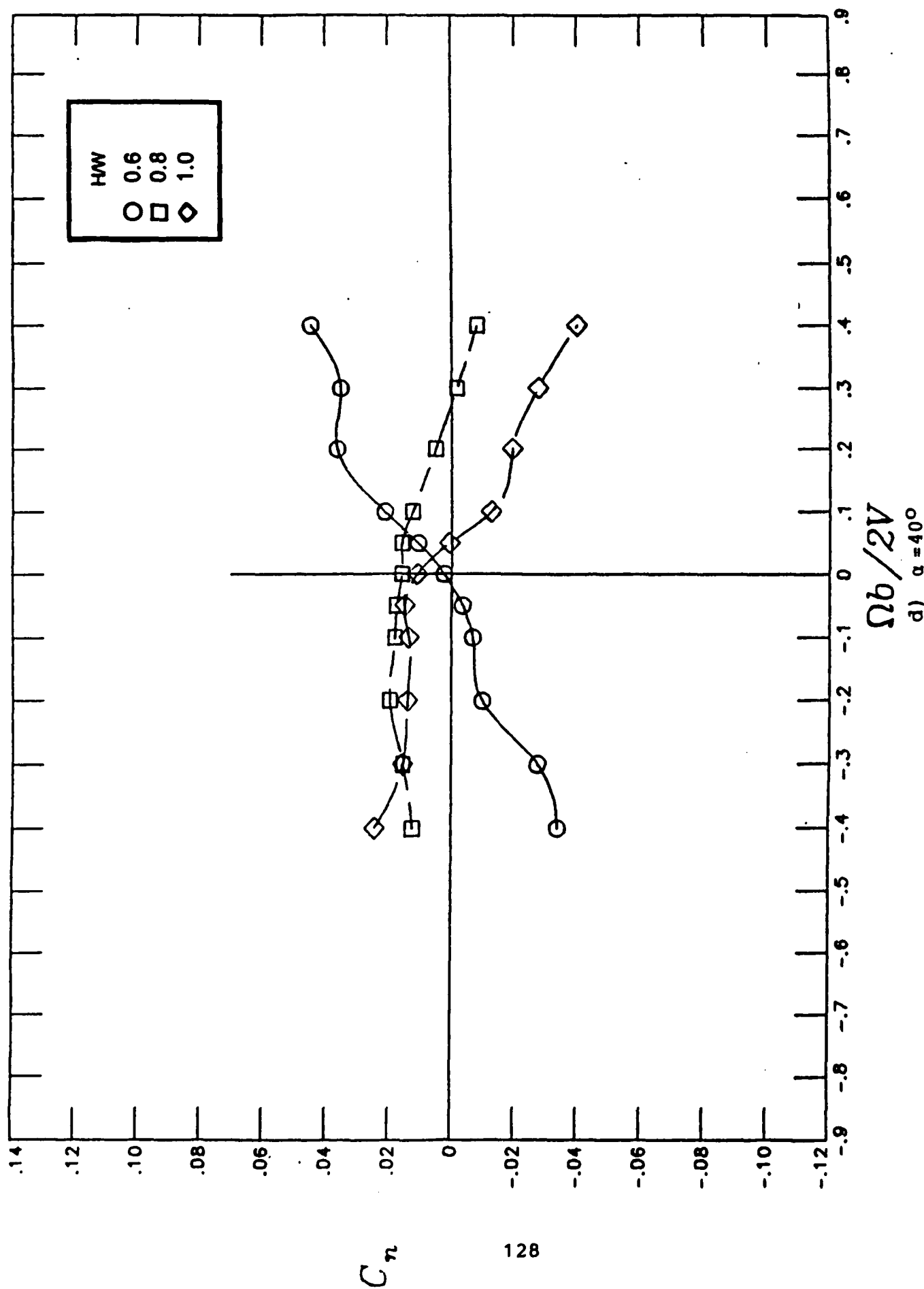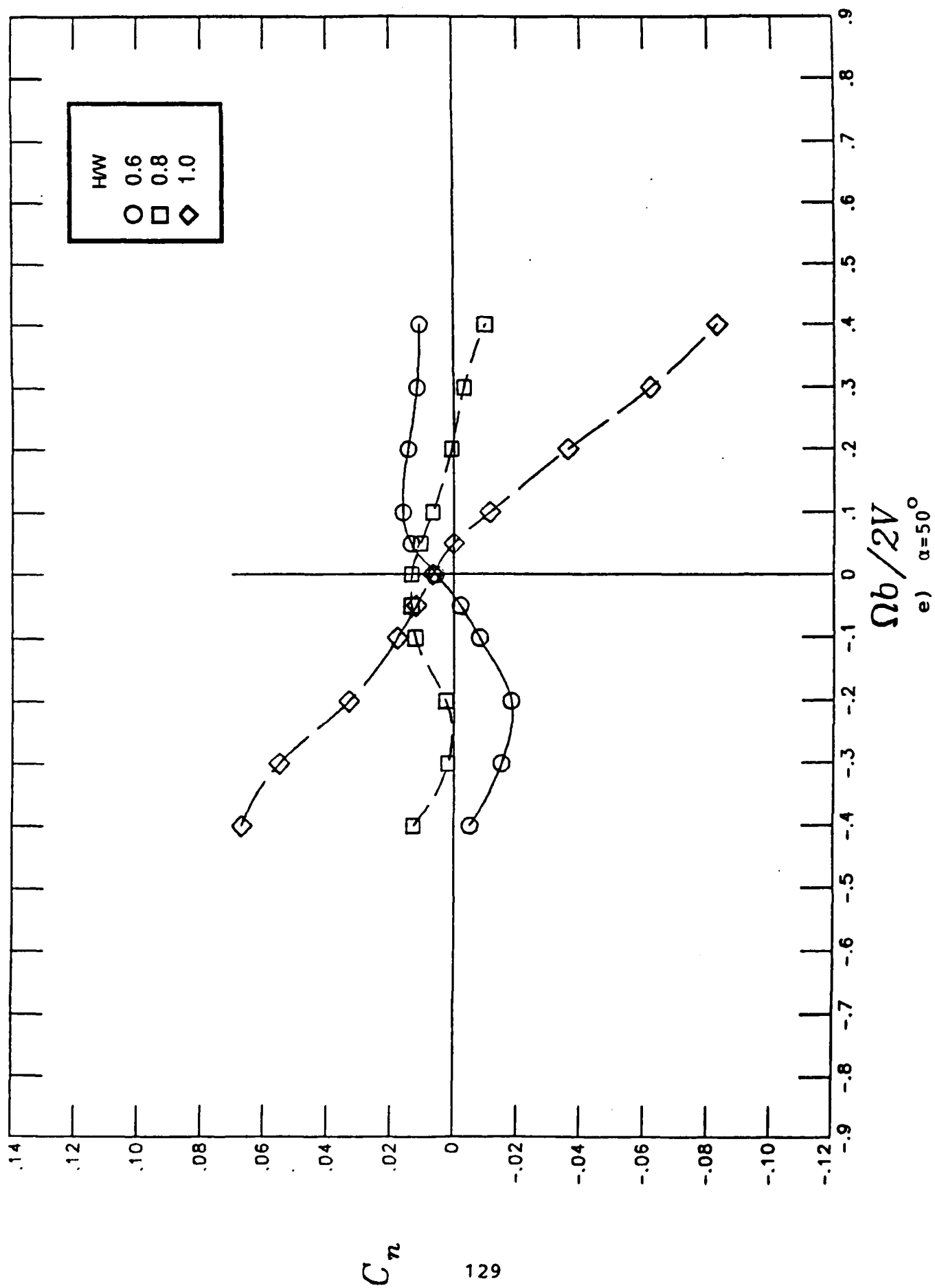
b) $\alpha = 25^\circ$

Figure 28.- Continued

126

Figure 28.- Continued

c) $\alpha = 30°$

$\Omega b/2V$

C_n

127

$\dfrac{\Omega b}{2V}$

d) $\alpha = 40°$

Figure 28.- Continued

128

e) $\alpha = 50^\circ$

Figure 28.- Continued

129

$\Omega b/2V$

f) $\alpha = 60°$

Figure 28.- Continued

C_n

130

$\frac{\Omega b}{2V}$

g) $\alpha=65°$

Figure 28.- Continued

131

$\dfrac{\Omega b}{2V}$

h) $\alpha = 70^\circ$

Figure 28.- Continued

132

Figure 28.- Continued

i) α=80°

$\Omega b/2V$

C_n

133

$\Omega b/2V$

j) $\alpha=90°$
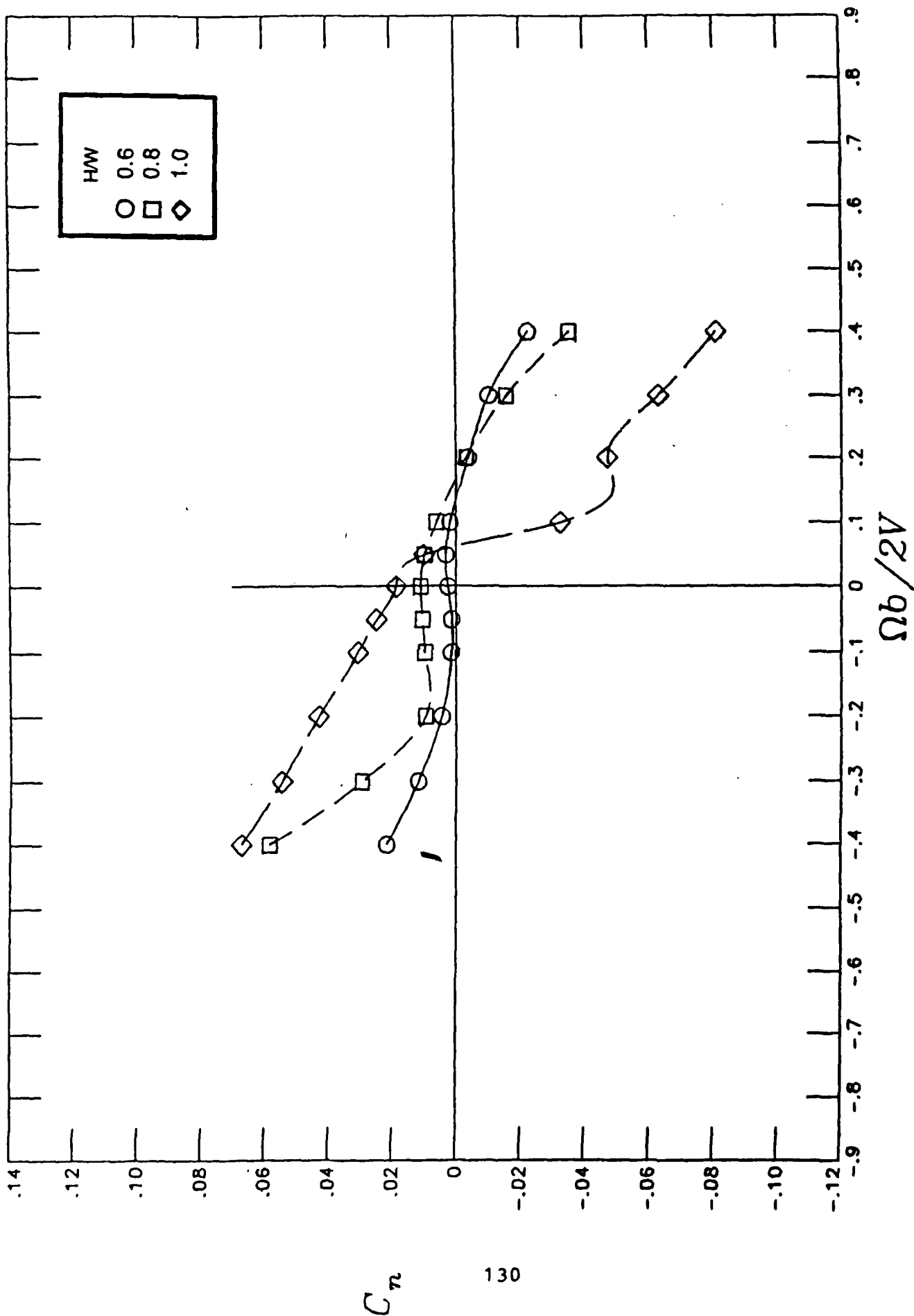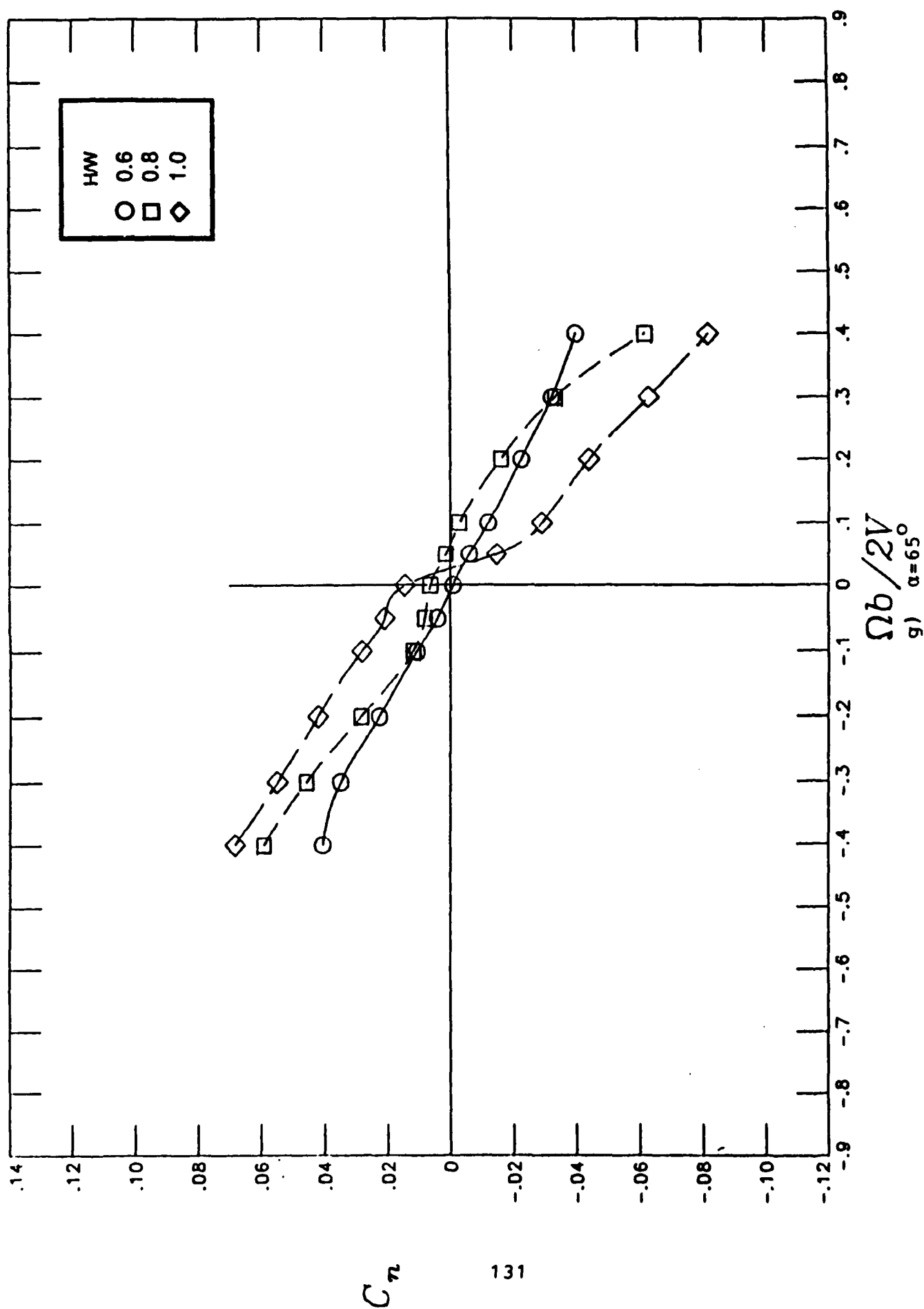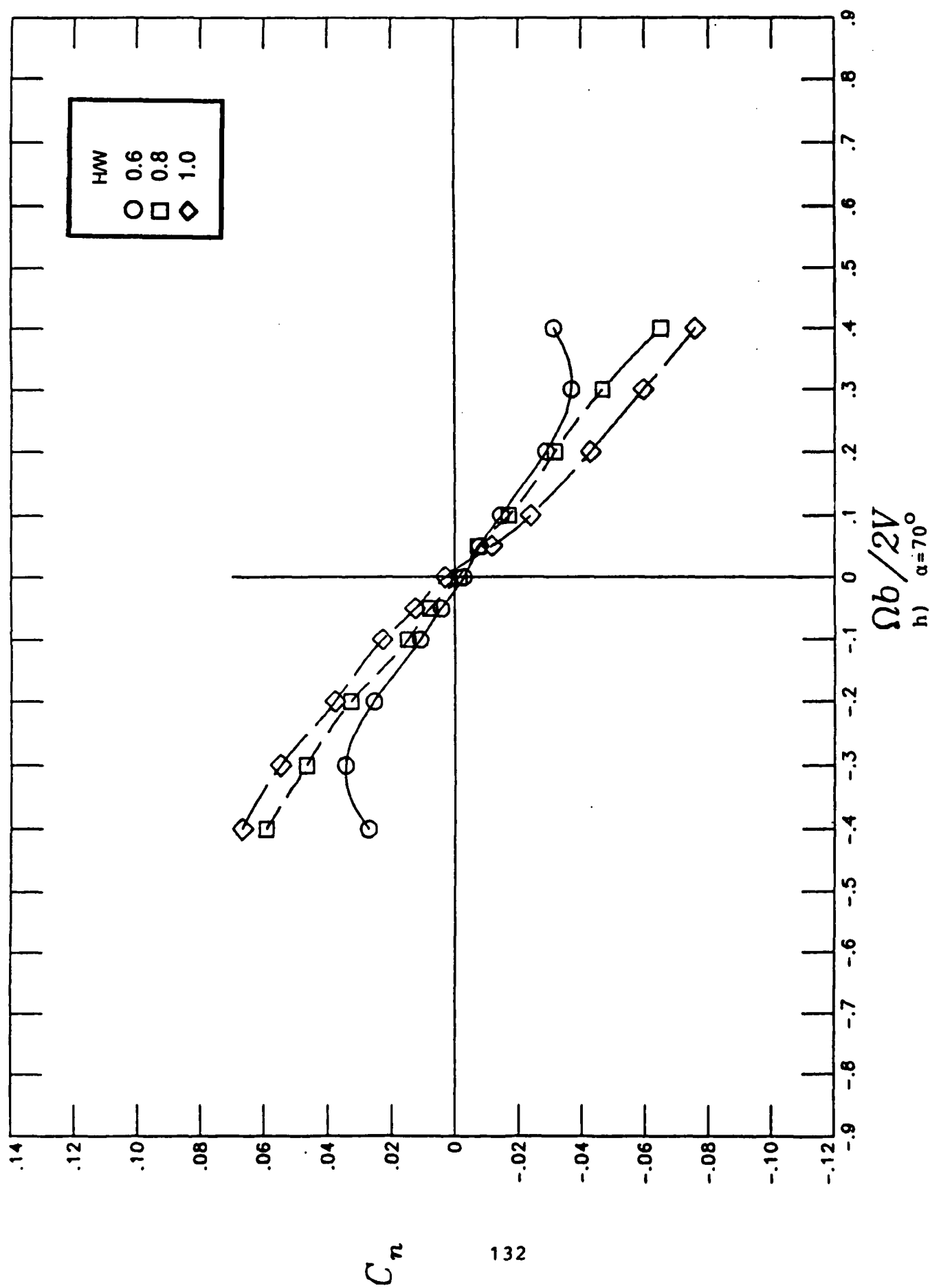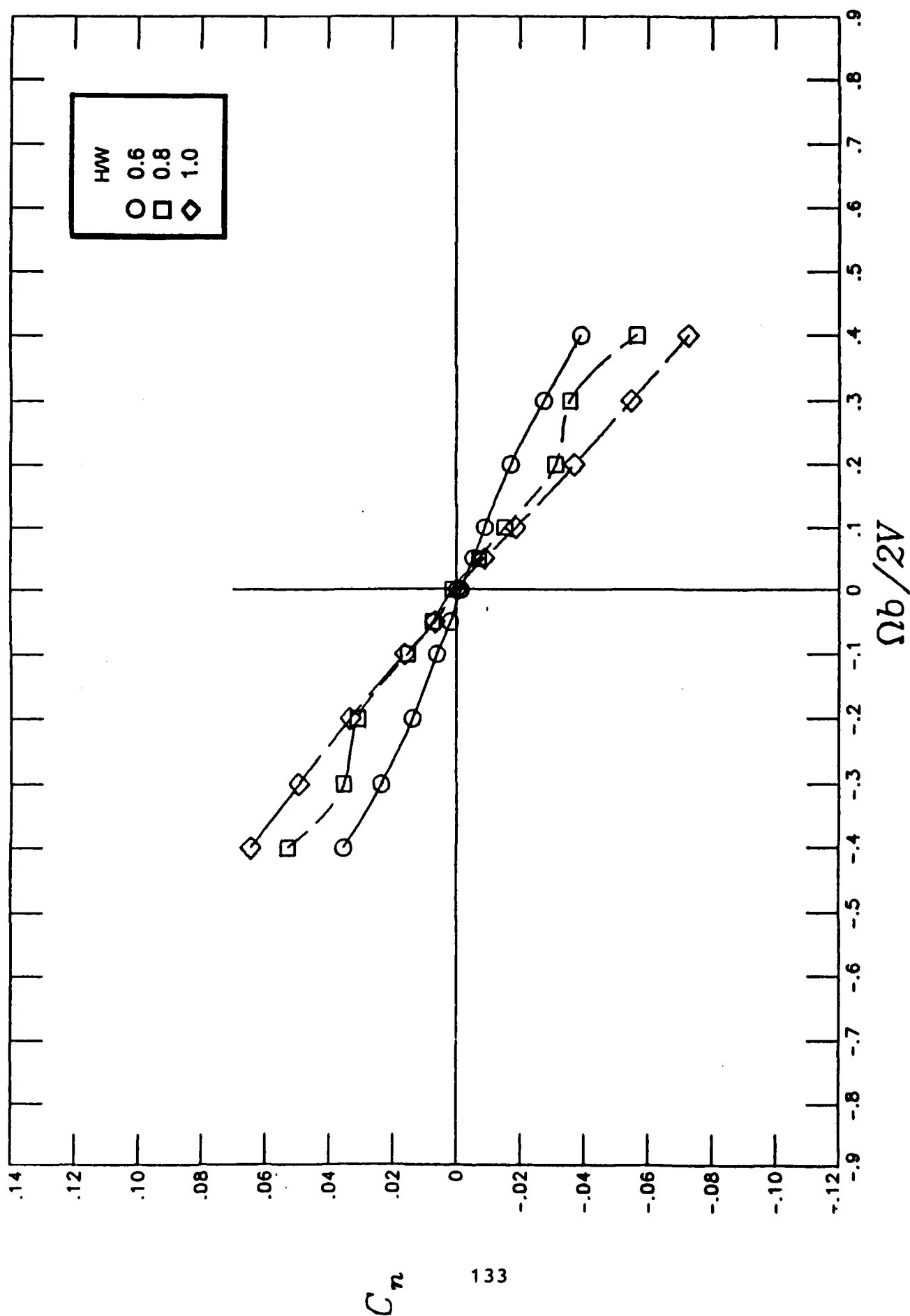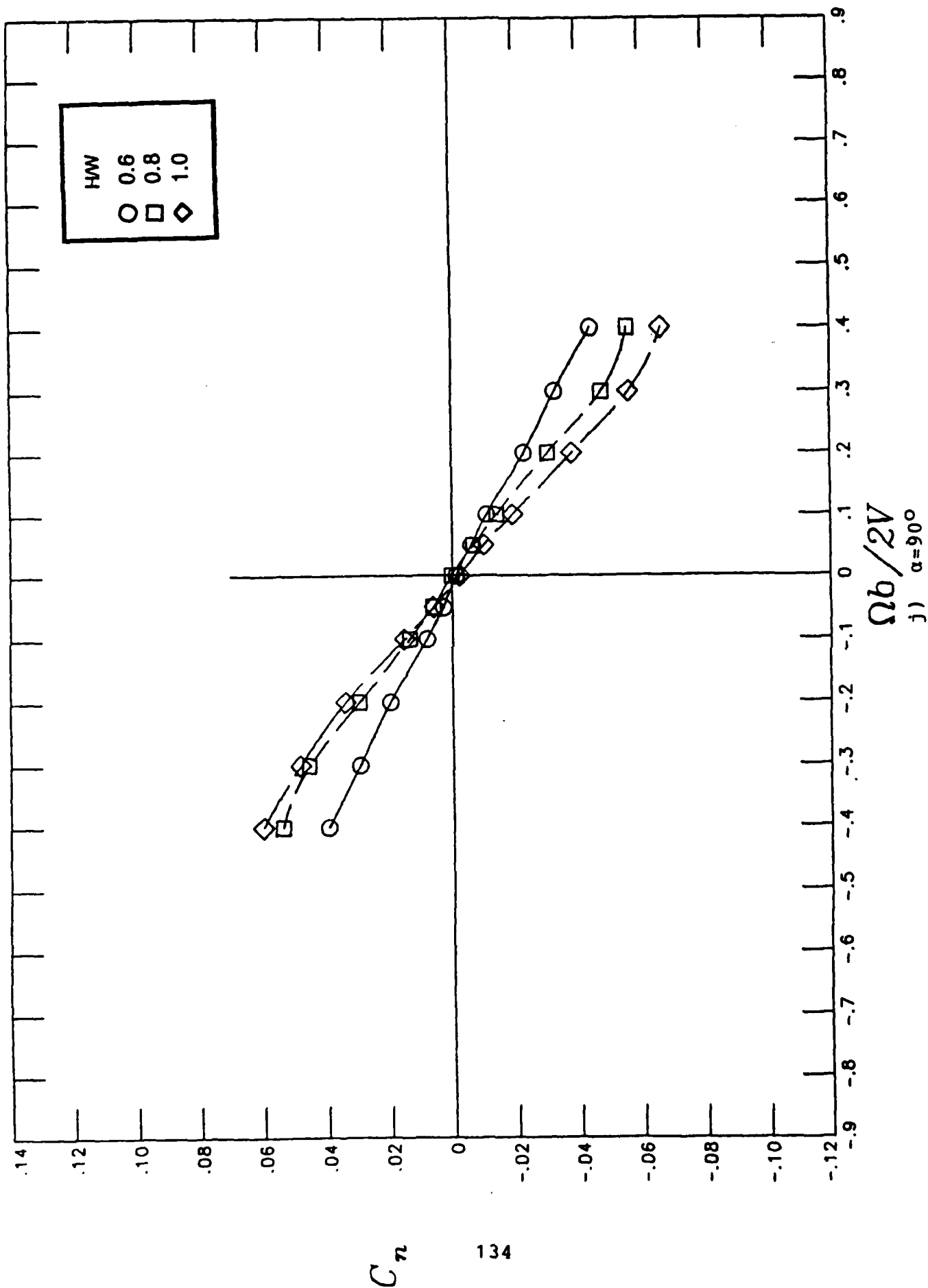
Figure 28.- Concluded

C_n

134
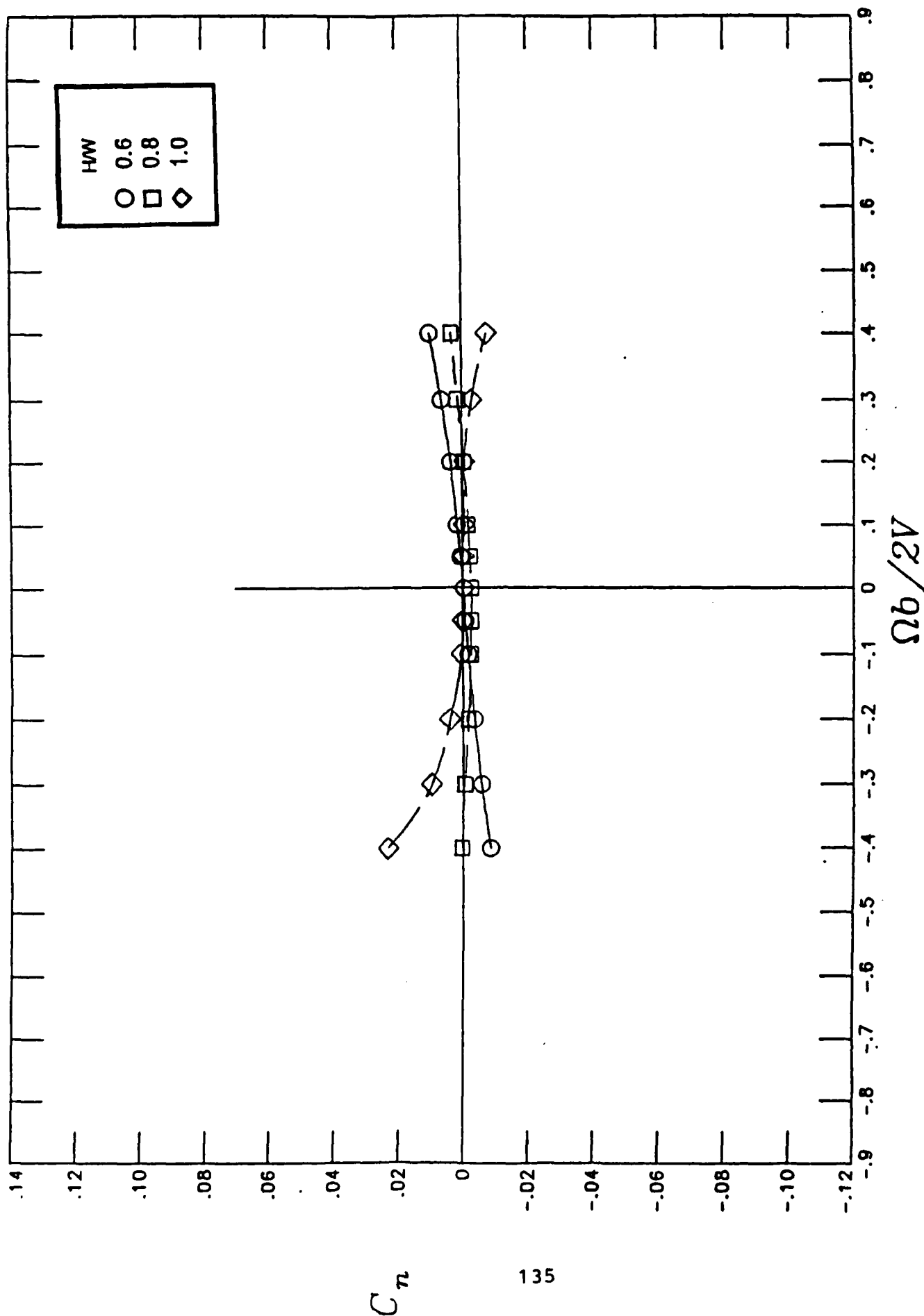
Figure 29.- Influence of forebody cross-sectional shape on rotational yawing-moment coefficient characteristics at a fineness ratio value of 2

a) $\alpha = 20^{\circ}$
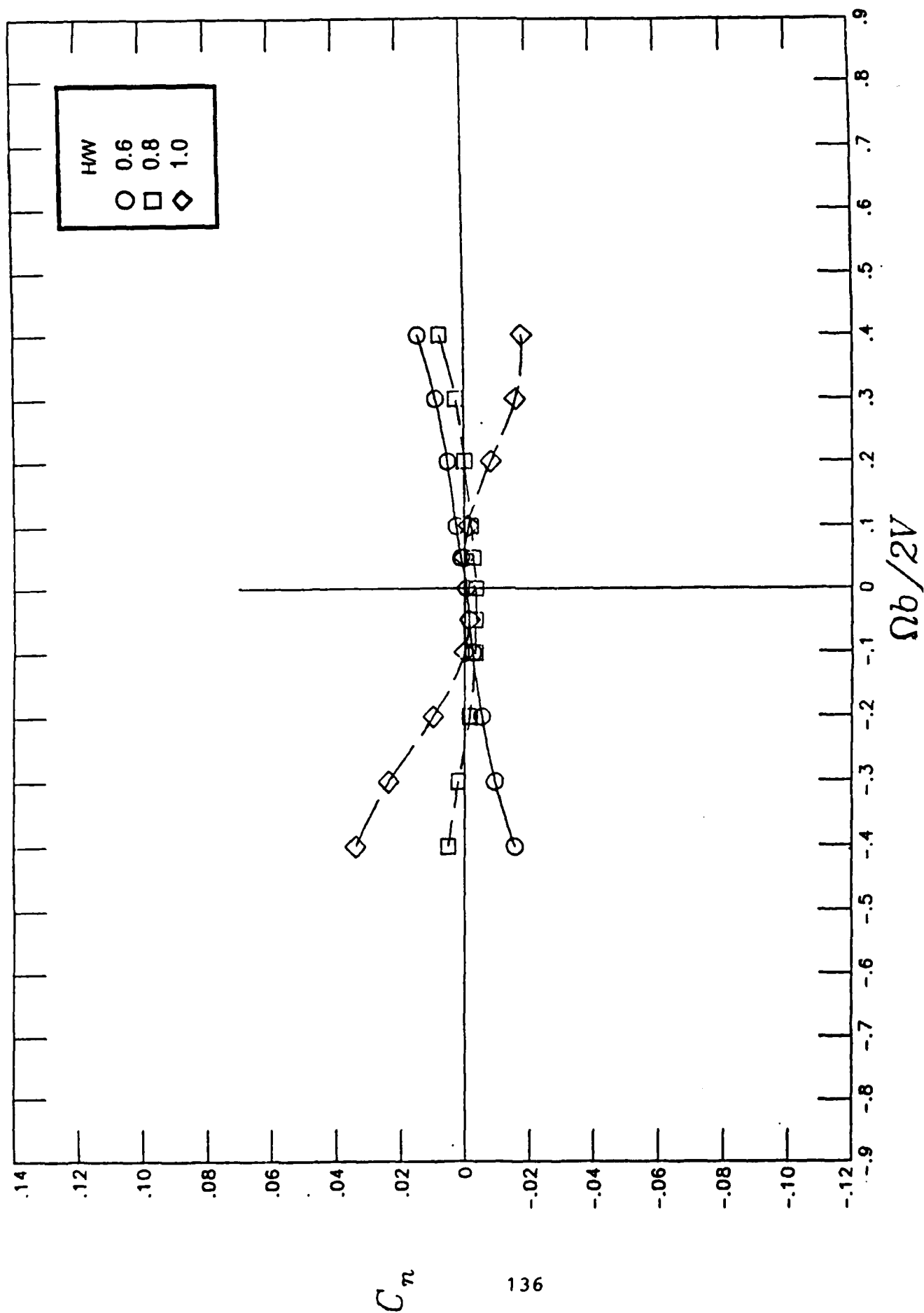
135

C_n

$\Omega b/2V$

b) $\alpha = 25^\circ$

Figure 29.- Continued
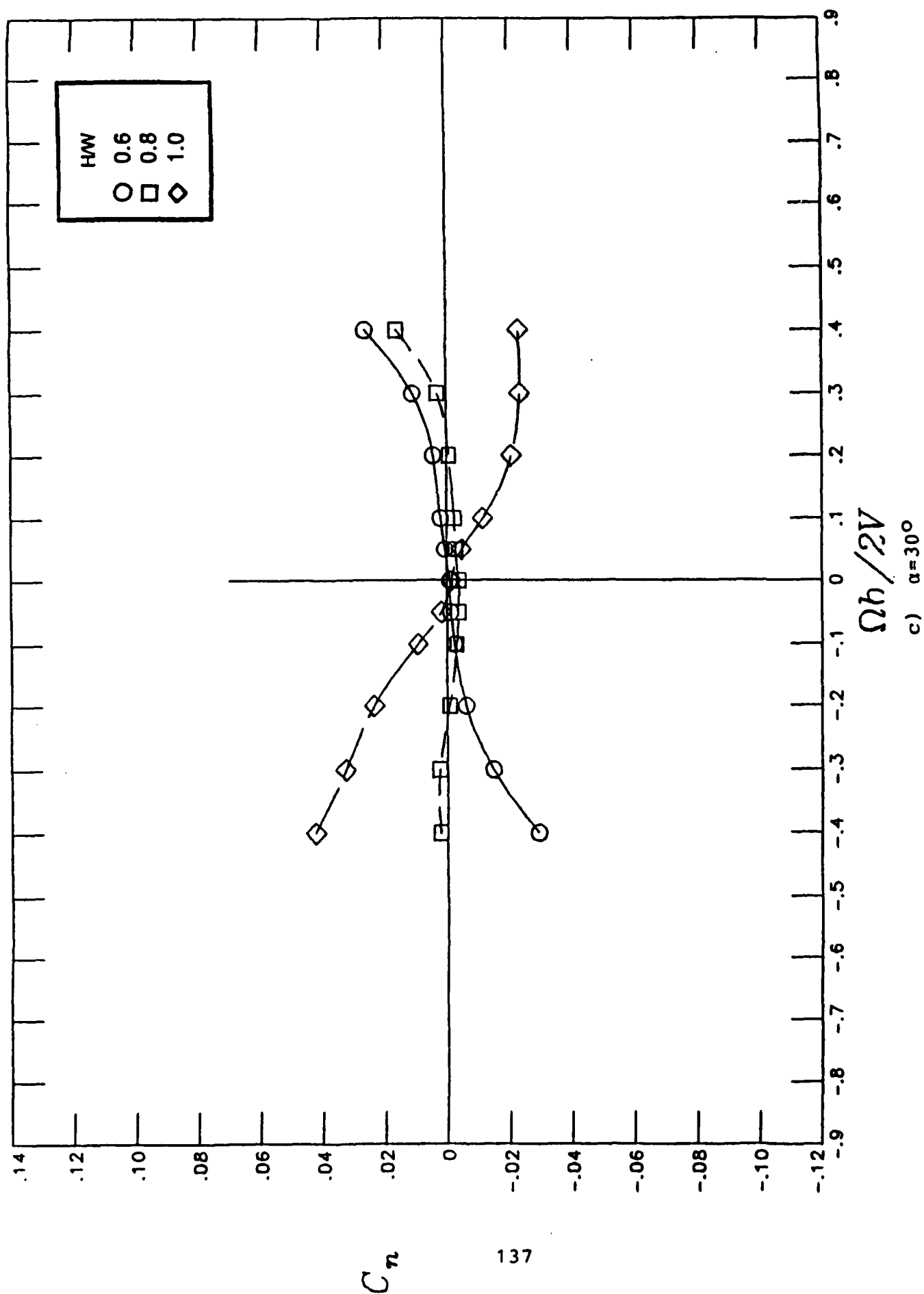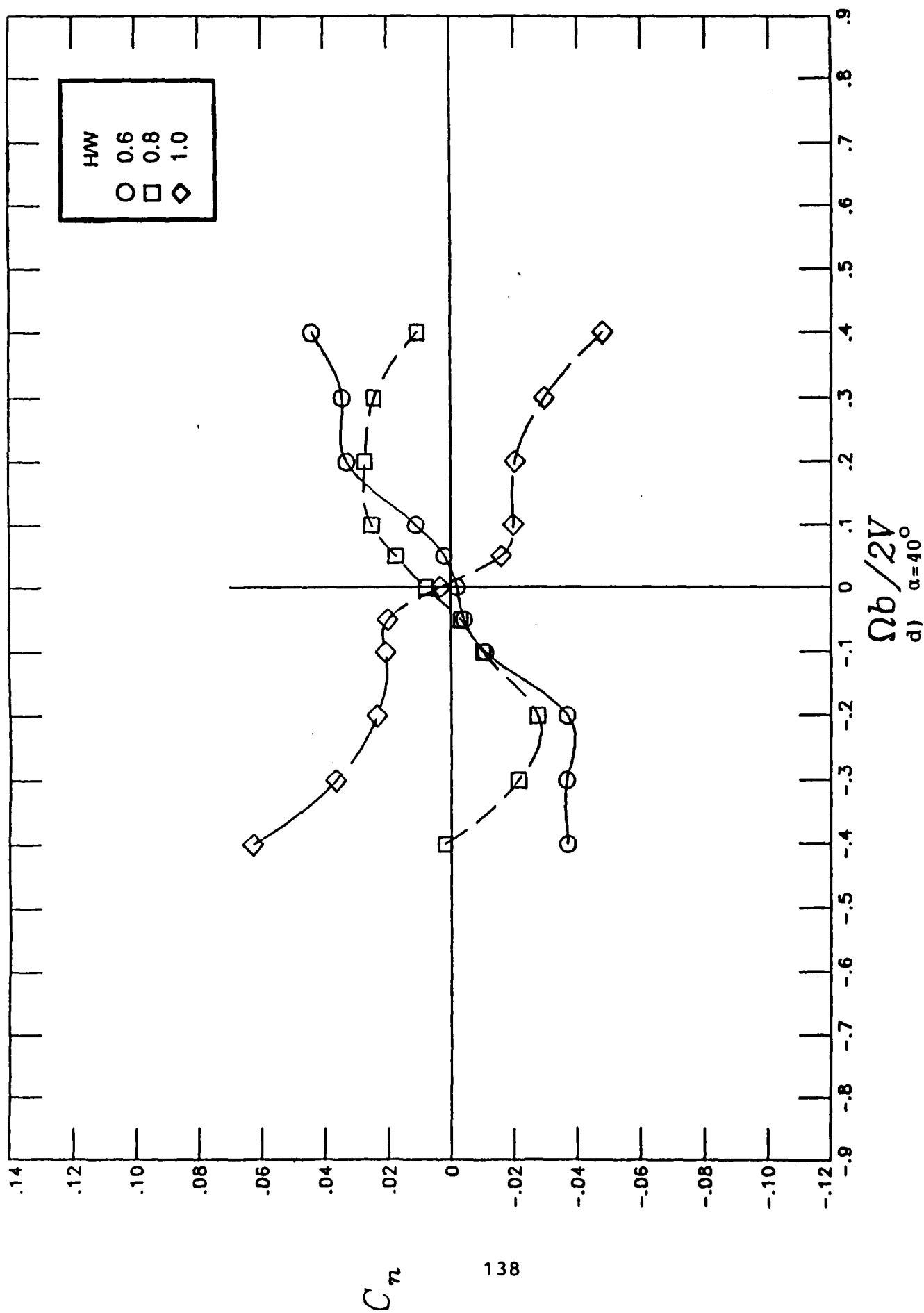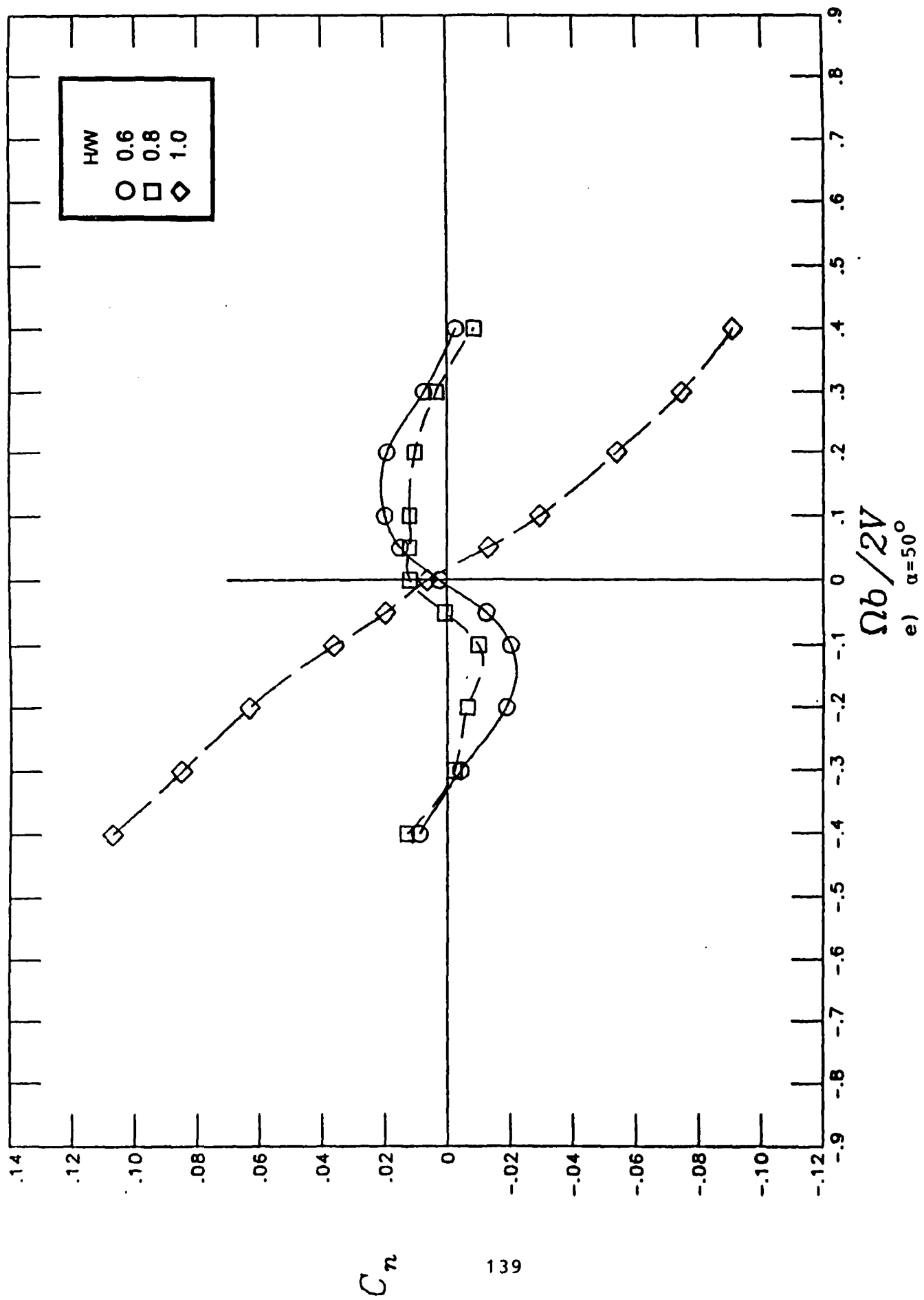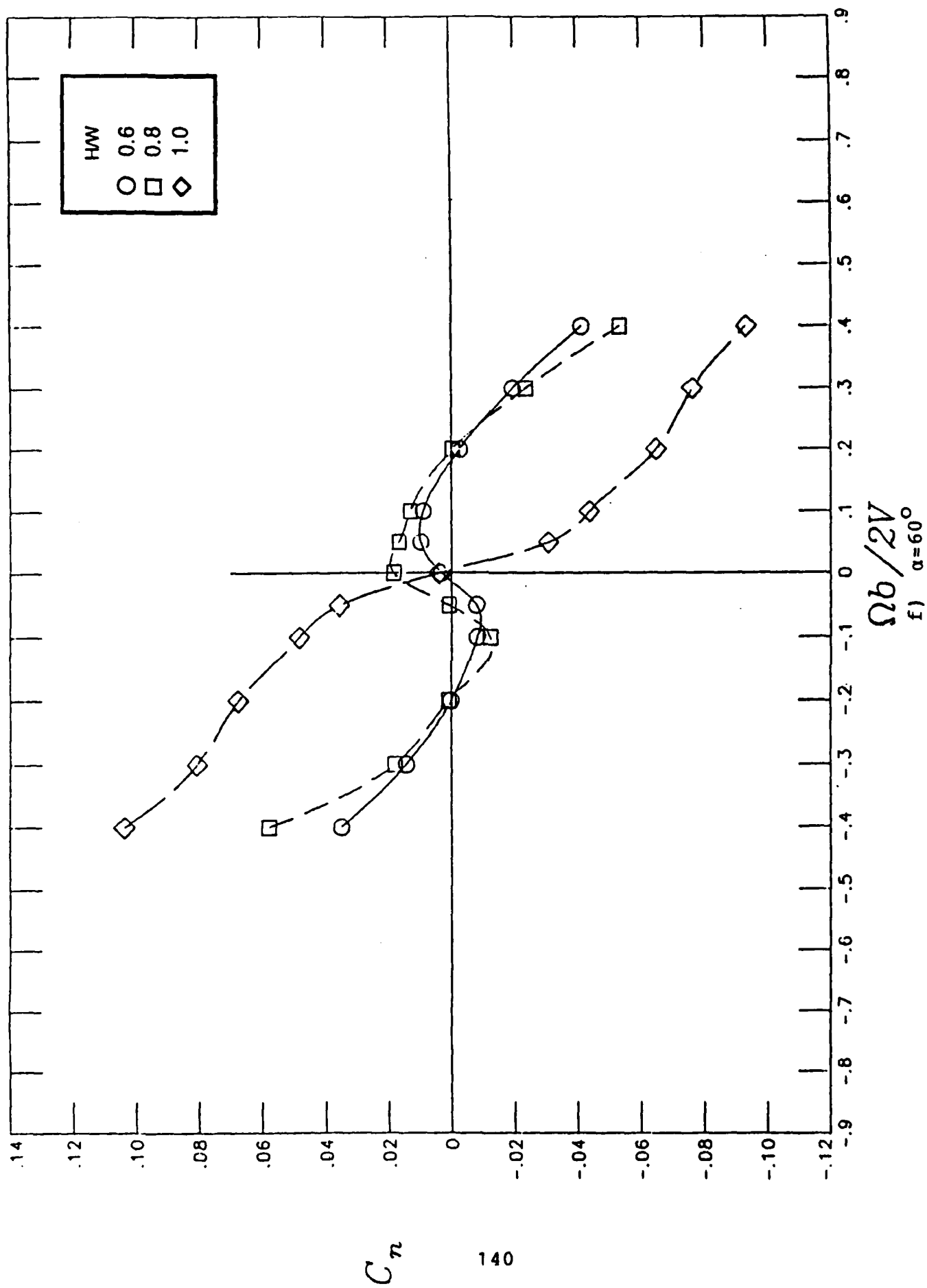
136

$\Omega h / 2V$

c) $\alpha=30°$

Figure 29.- Continued

137

Figure 29.- Continued

d) $\alpha = 40°$

$\Omega b / 2V$

C_n

138

$\Omega b/2V$

e) $\alpha = 50°$

Figure 29.- Continued

C_n

139

$\Omega b/2V$

f) $\alpha = 60^\circ$

Figure 29.- Continued

C_n

140

g) α=65°

Figure 29.- Continued

141

C_n

$\Omega b/2V$

h) $\alpha=70°$

Figure 29.- Continued

142

$\Omega b/2V$

i) $\alpha=80^\circ$

Figure 29.- Continued

C_n

143

$\Omega b / 2V$

j) $\alpha = 90°$
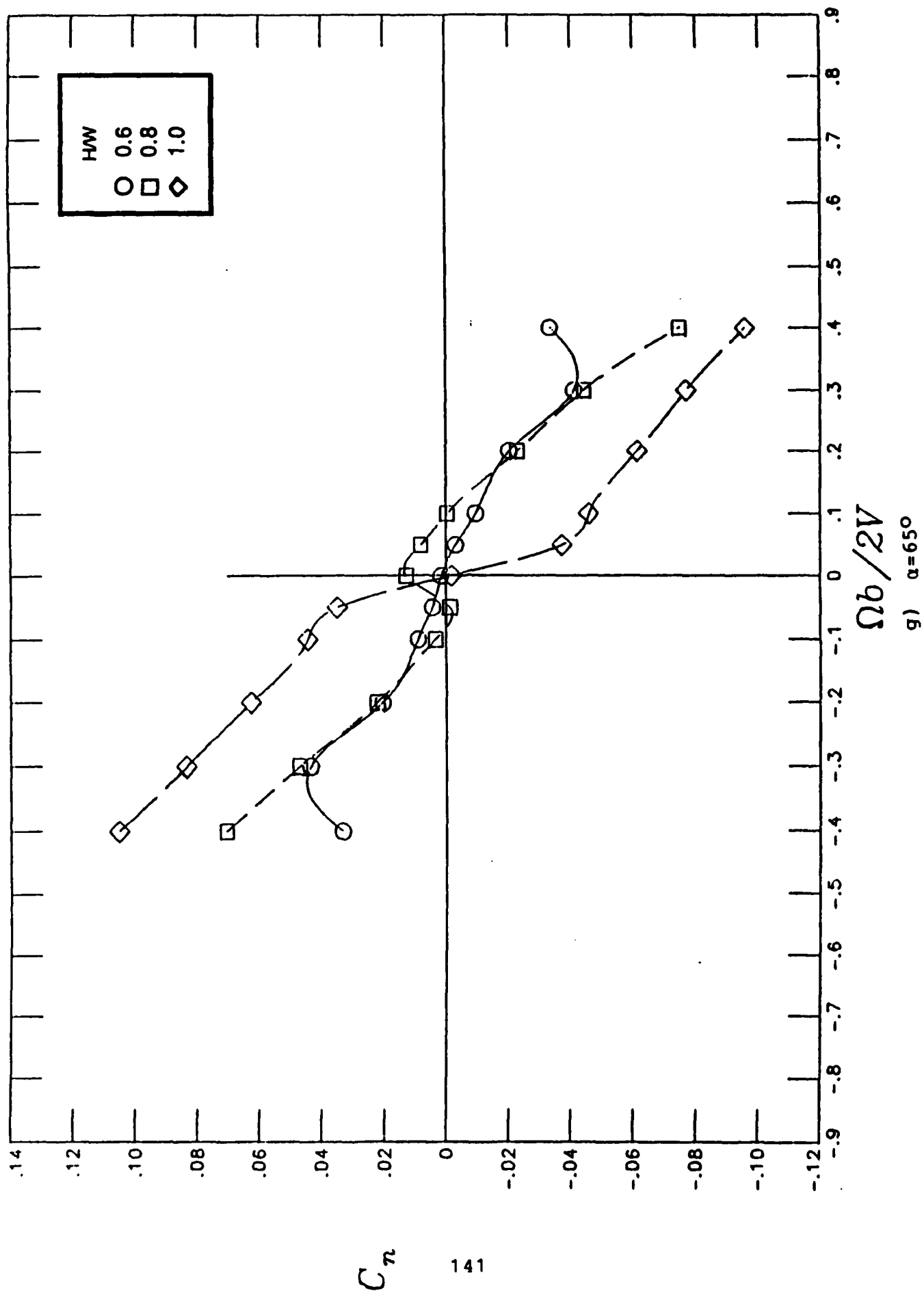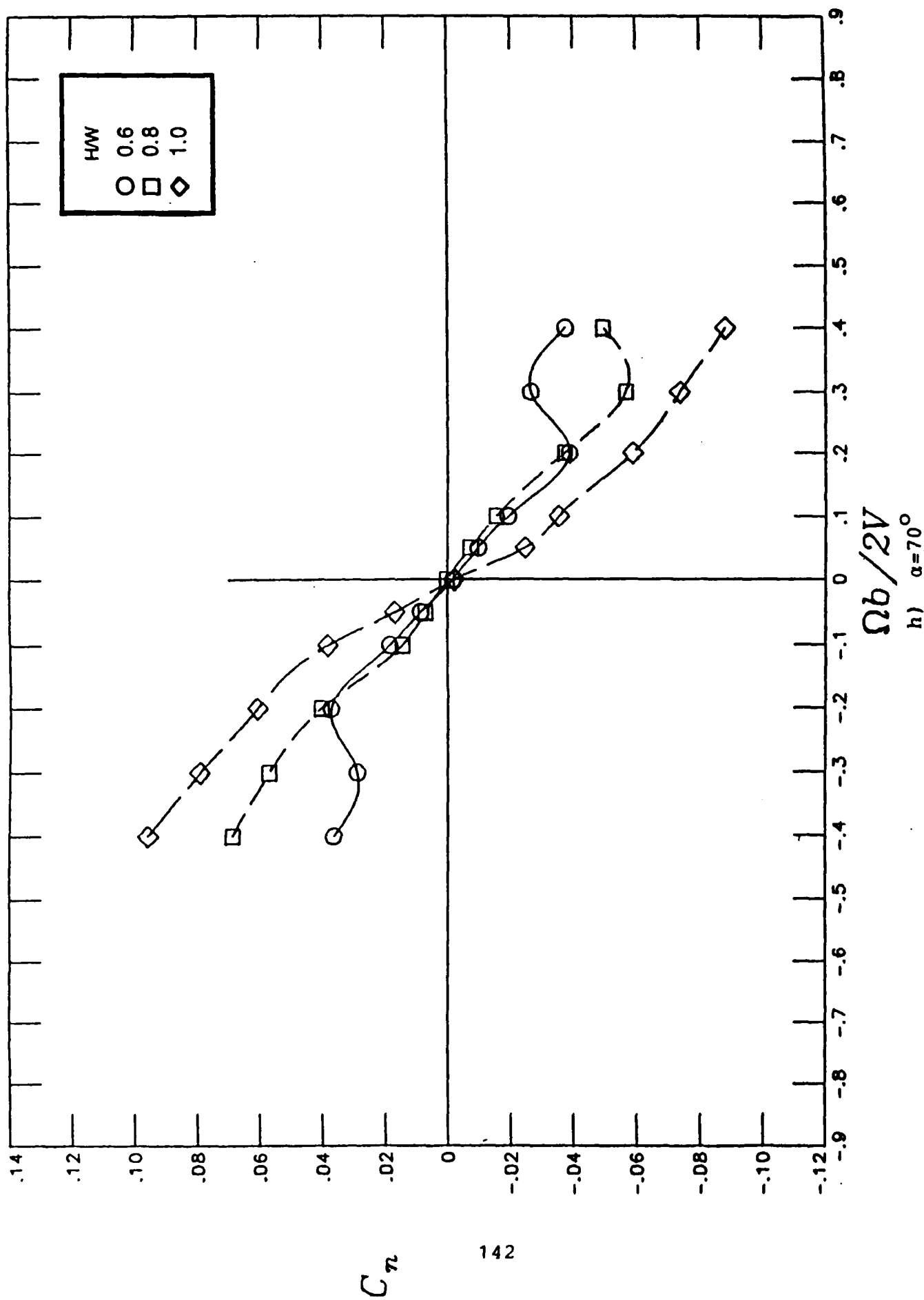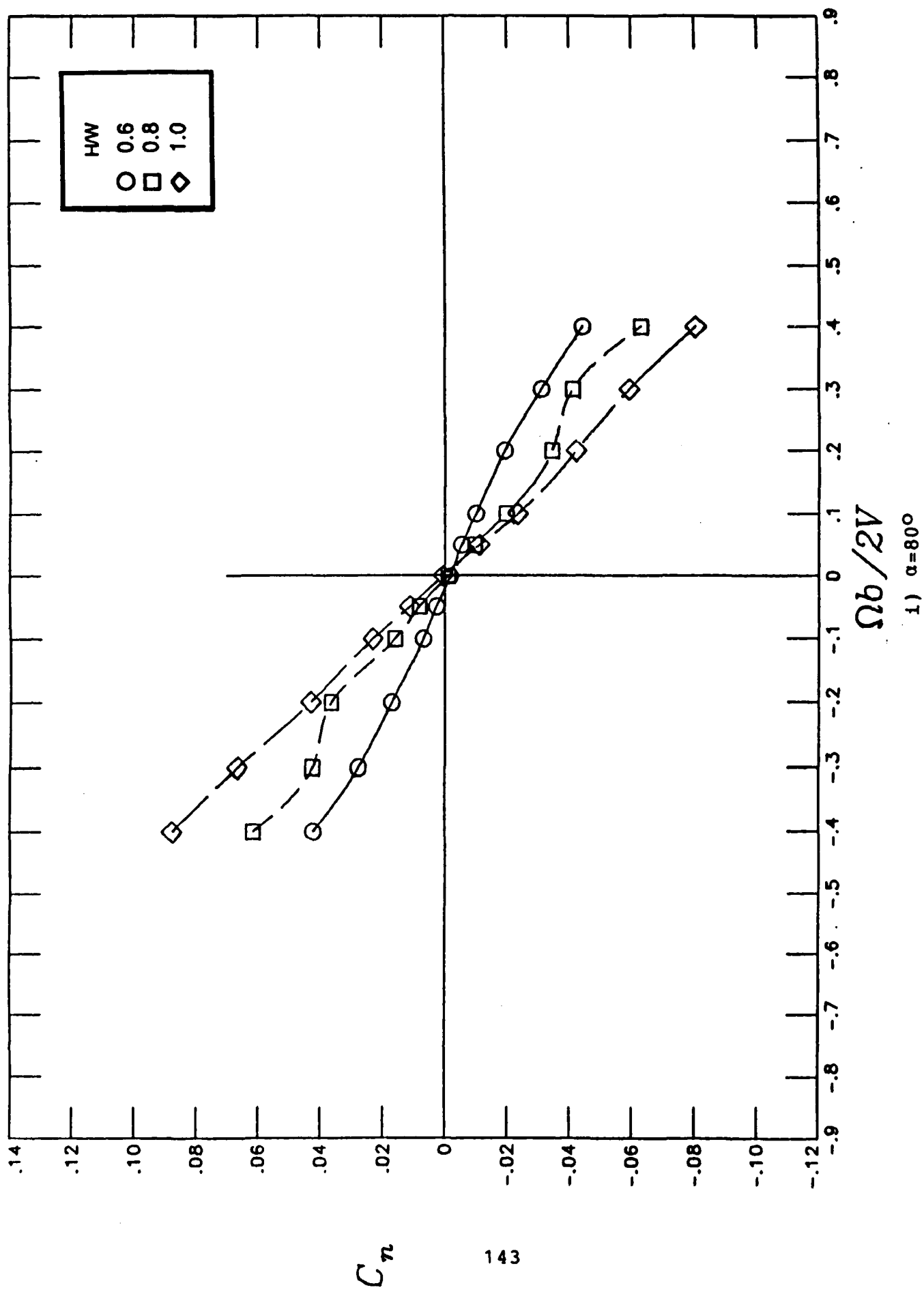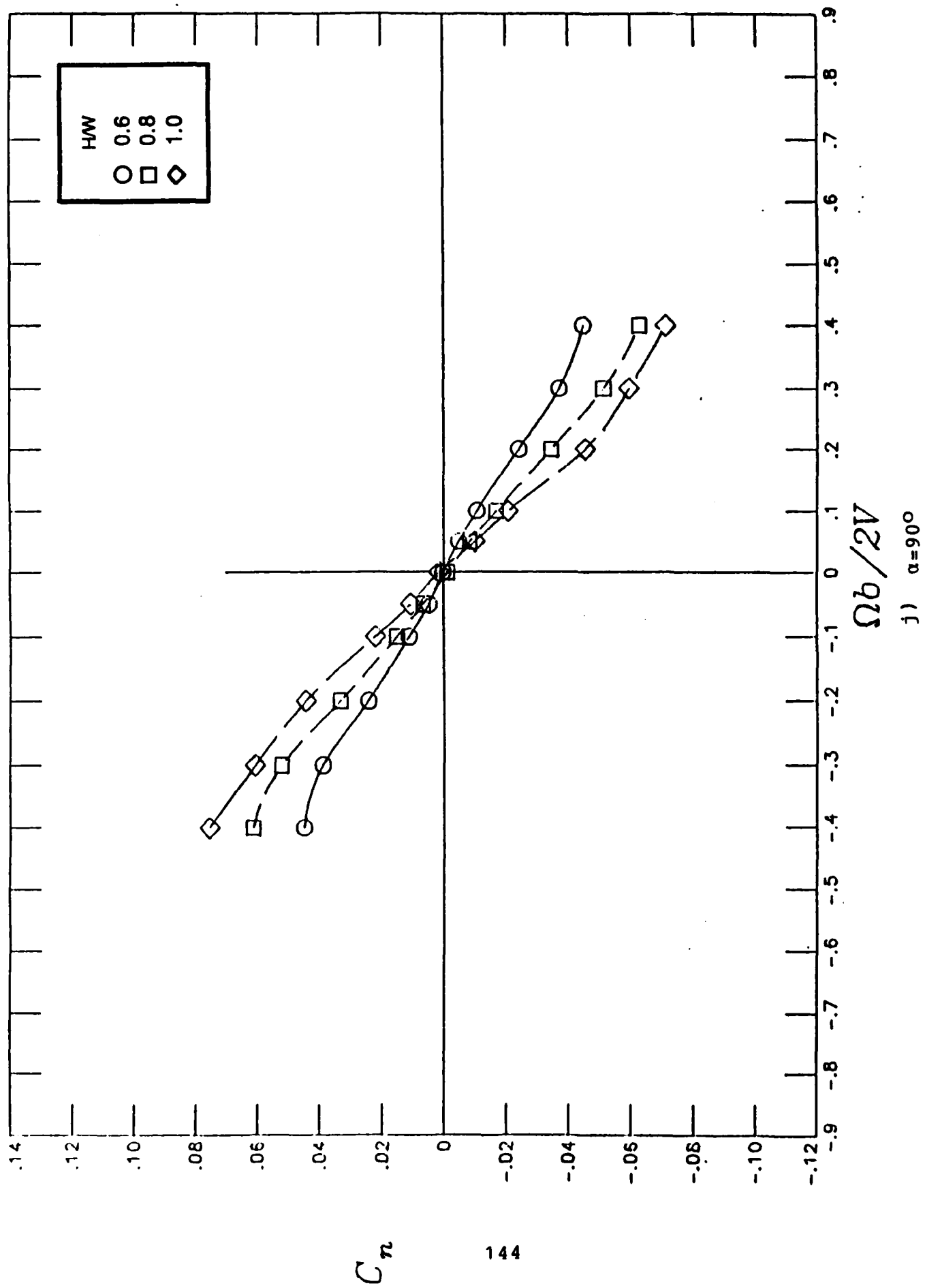
Figure 29.- Concluded

C_n

144
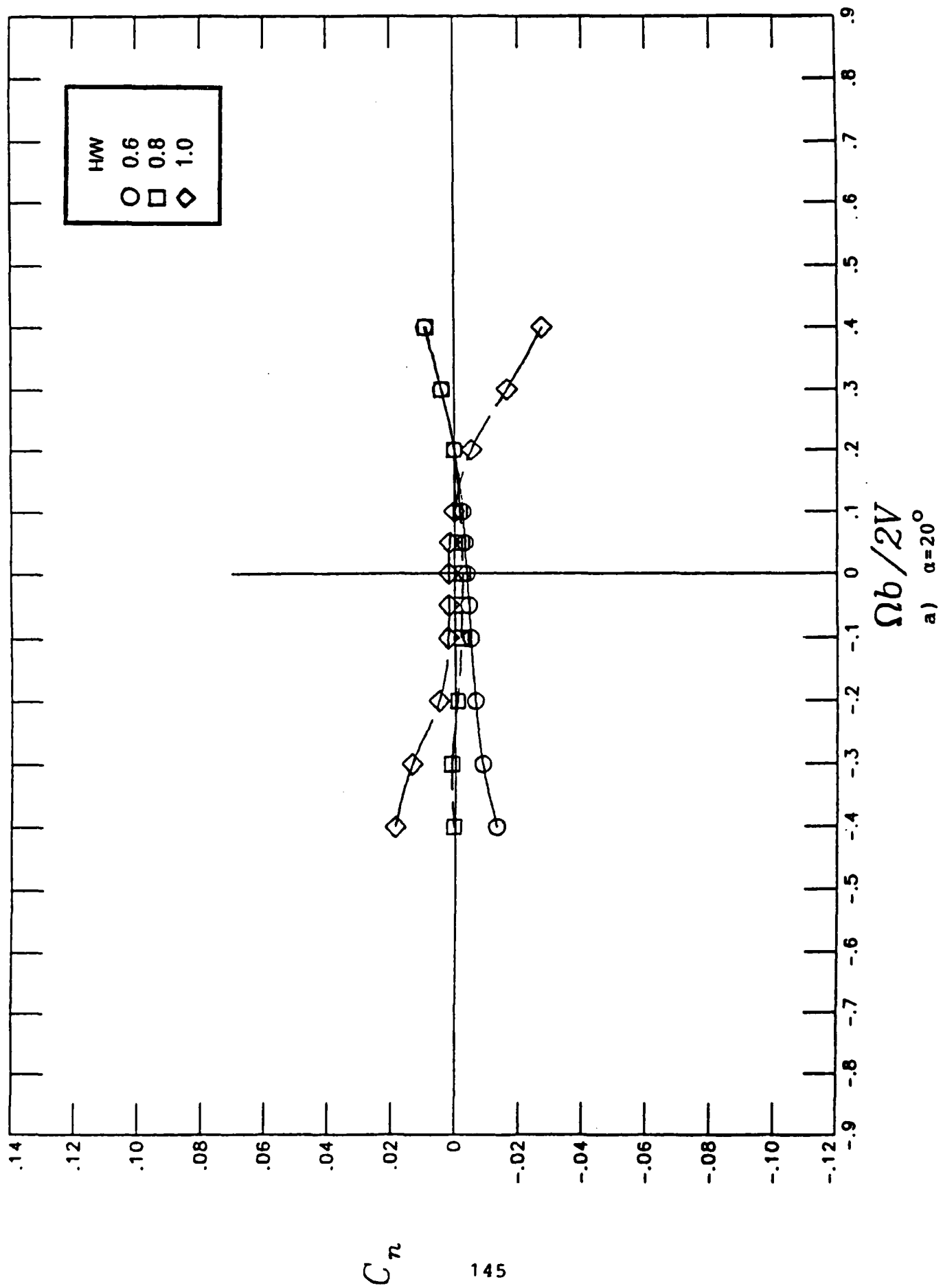
Figure 30.- Influence of forebody cross-sectional shape on rotational yawing-moment coefficient characteristics at a fineness ratio value of 3

a) $\alpha = 20°$
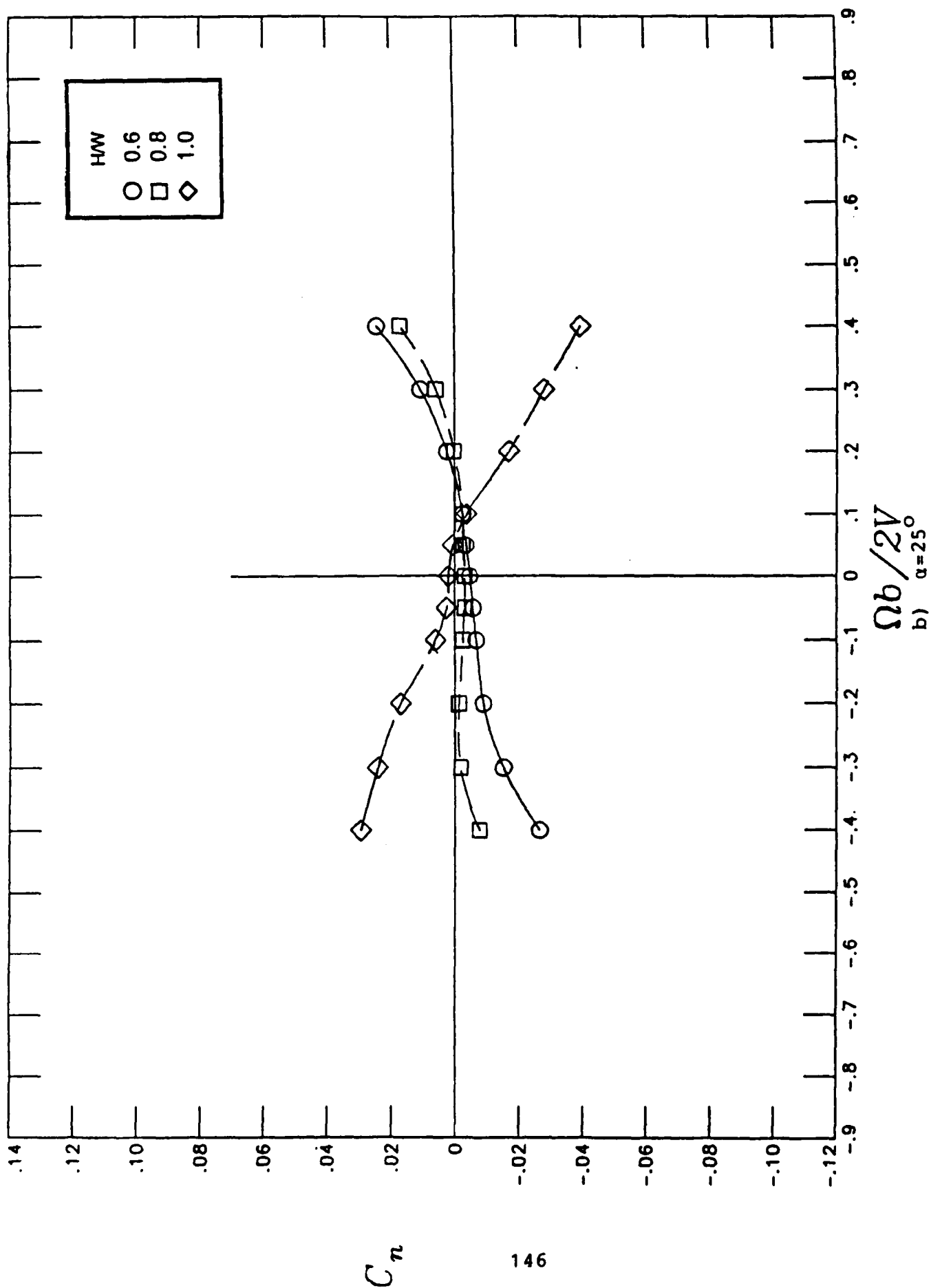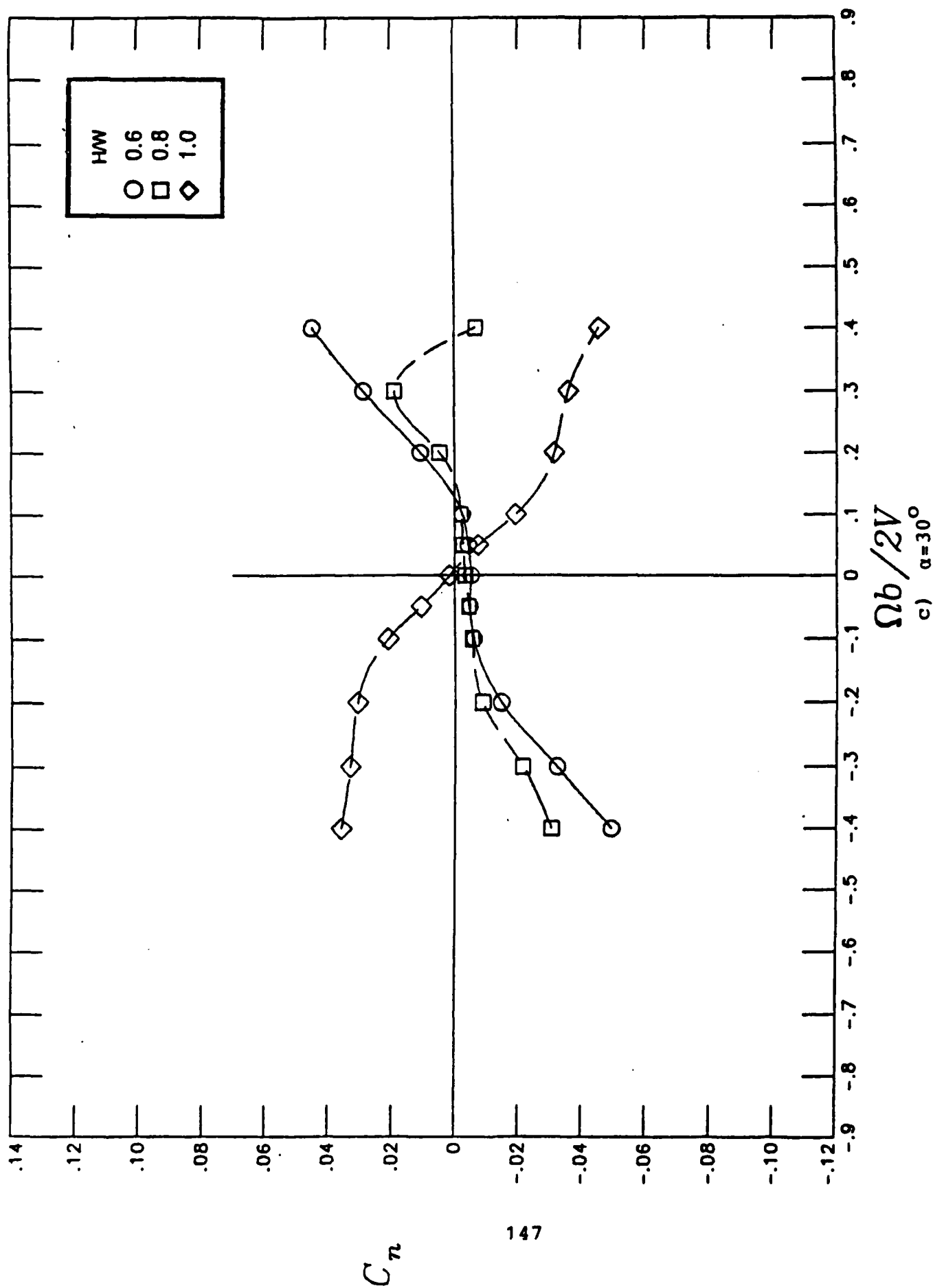
145

b) $\alpha = 25°$

Figure 30.- Continued

146

$\Omega b/2V$

c) $\alpha=30^\circ$

Figure 30.- Continued

147

Figure 30.- Continued

d) $\alpha = 40°$

$\dfrac{\Omega b}{2V}$

C_n

148

Figure 30.- Continued

e). $\alpha = 50°$

149

$\Omega b / 2V$

f) $\alpha = 60°$

Figure 30.- Continued

C_n

150

g) Figure 30.- Continued

151
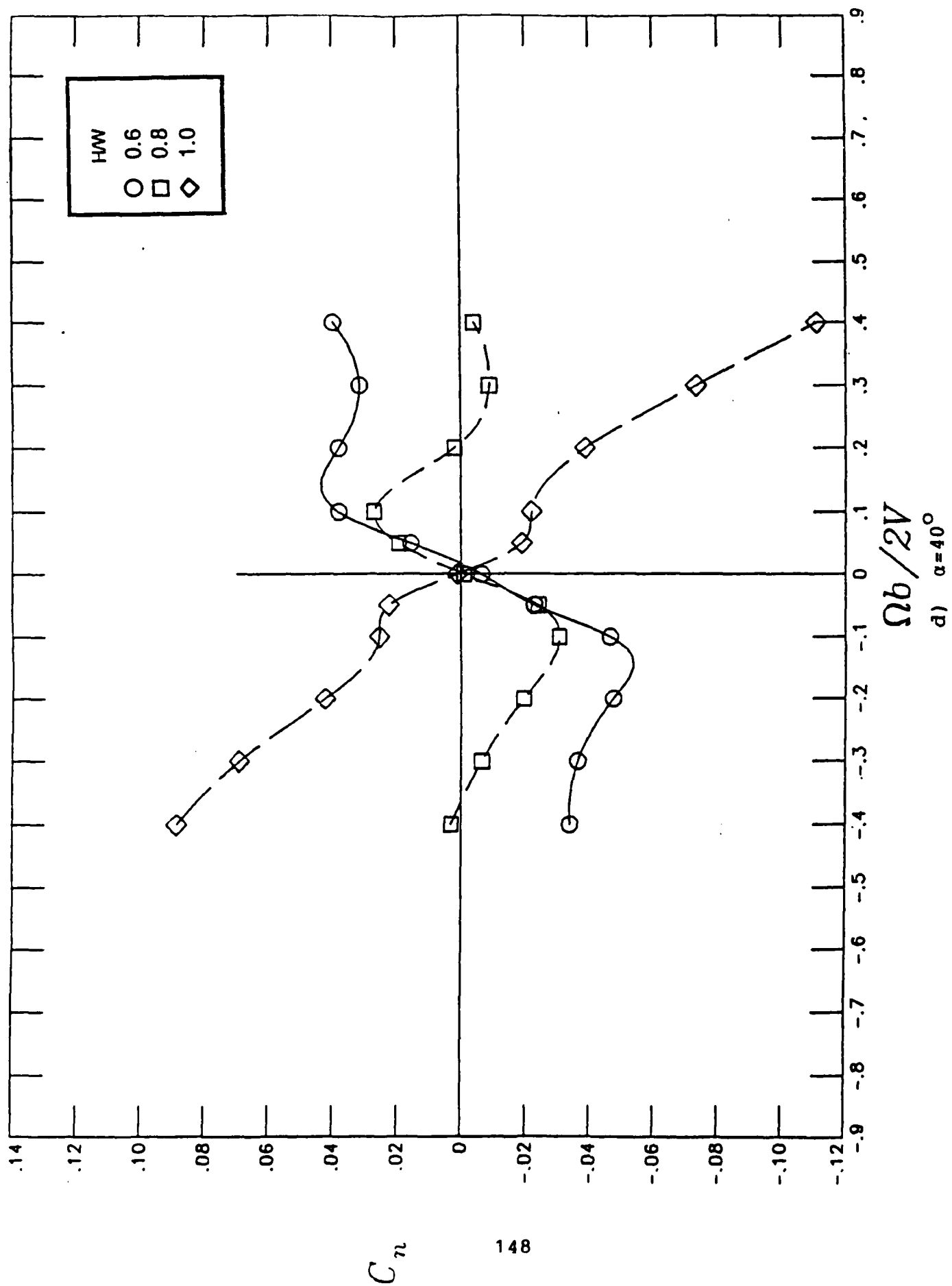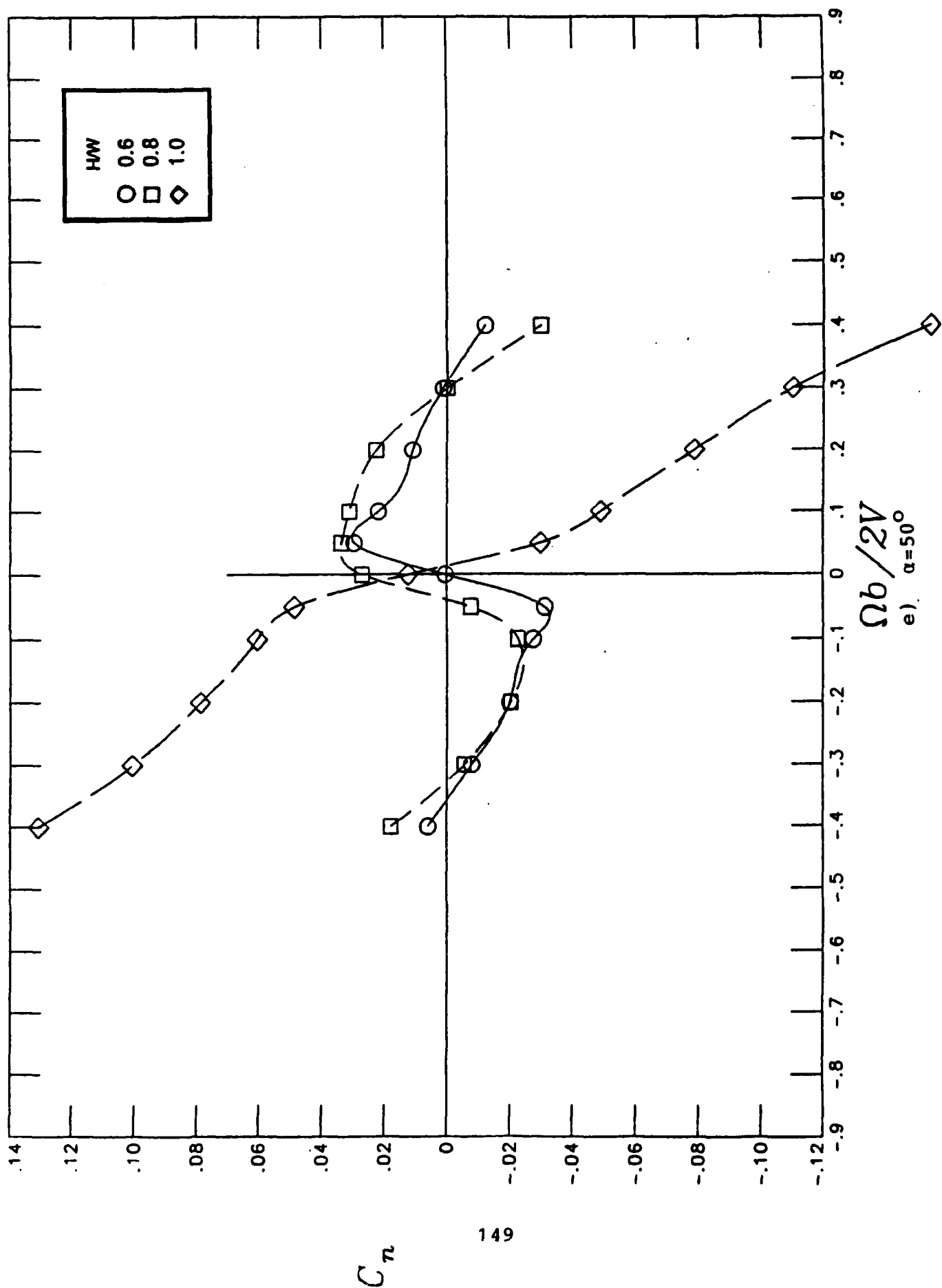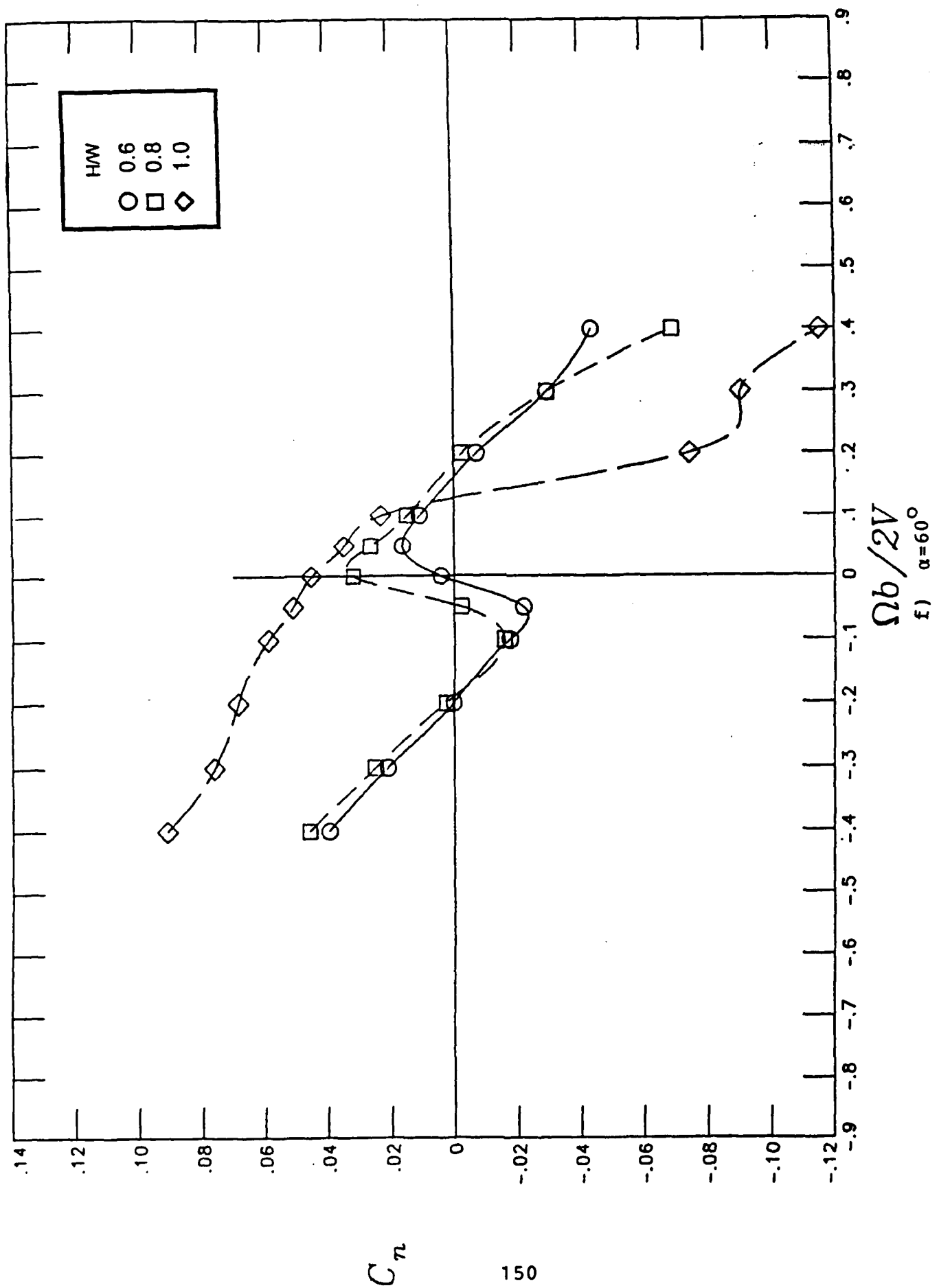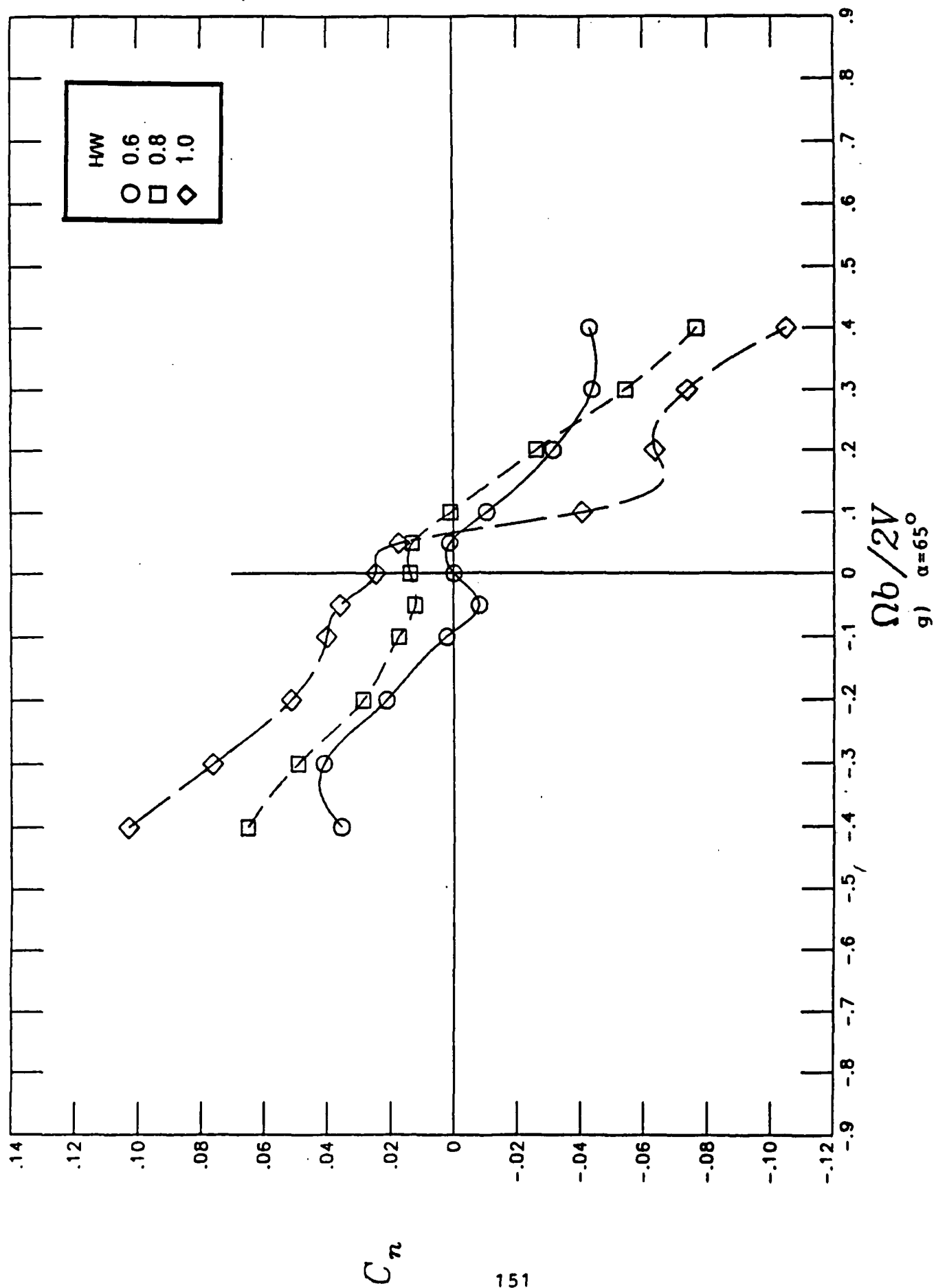
Figure 30.- Continued

h) $\alpha = 70^\circ$

C_n

$\Omega b / 2V$

152

Figure 30.- Continued

1) $\alpha = 80^\circ$

$\Omega b / 2V$

C_n

153
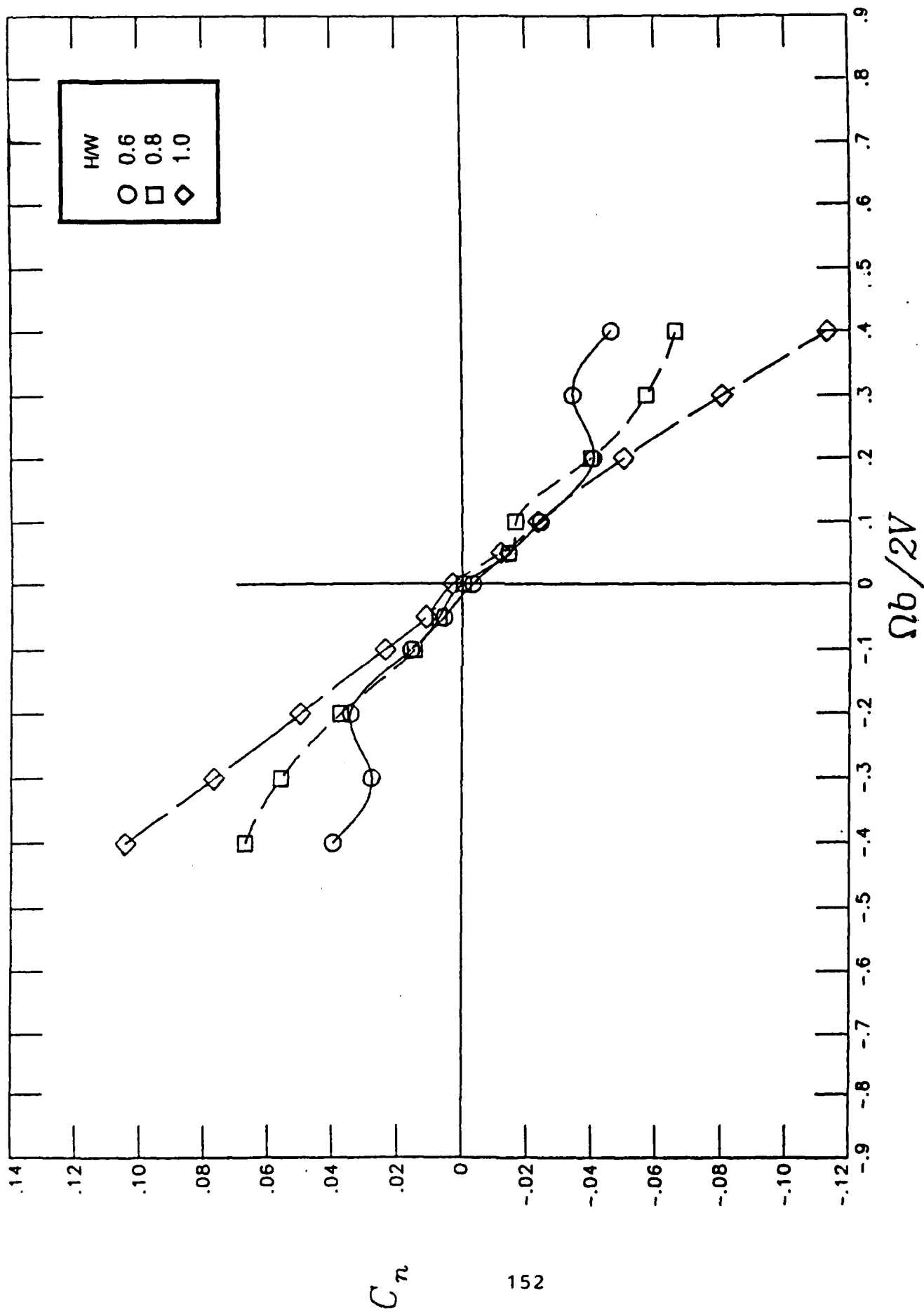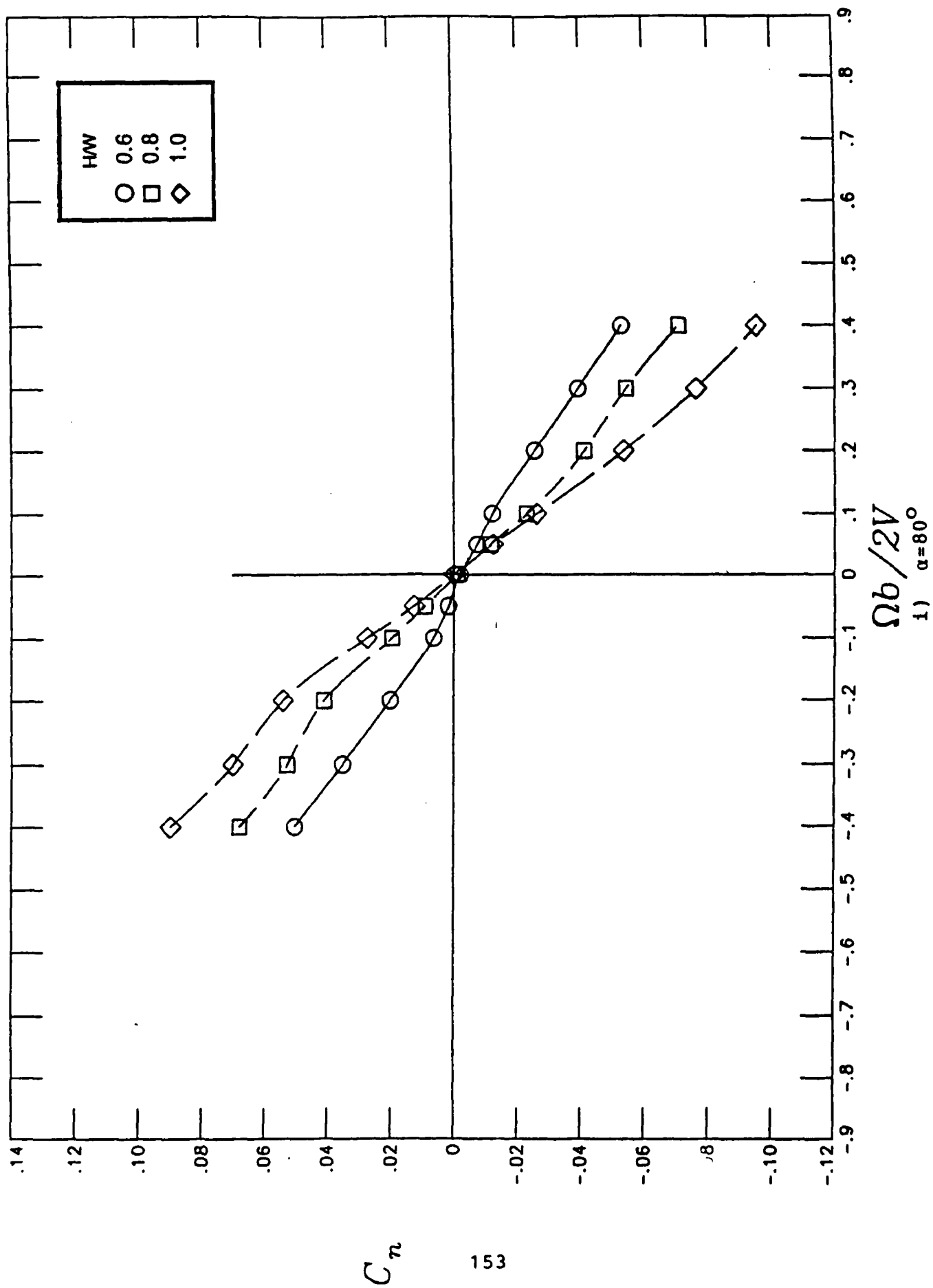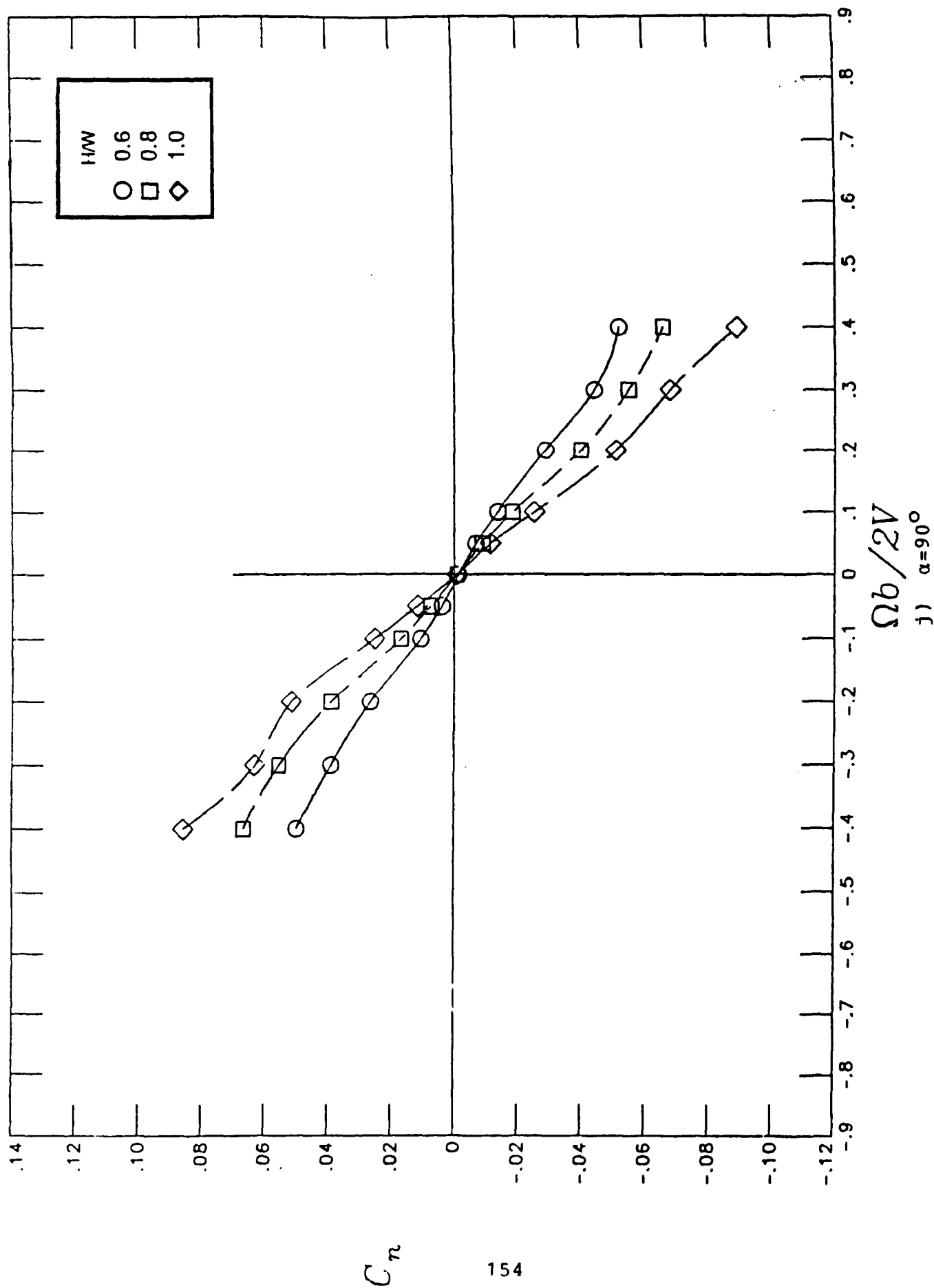
Figure 30.- Concluded

j) α=90°
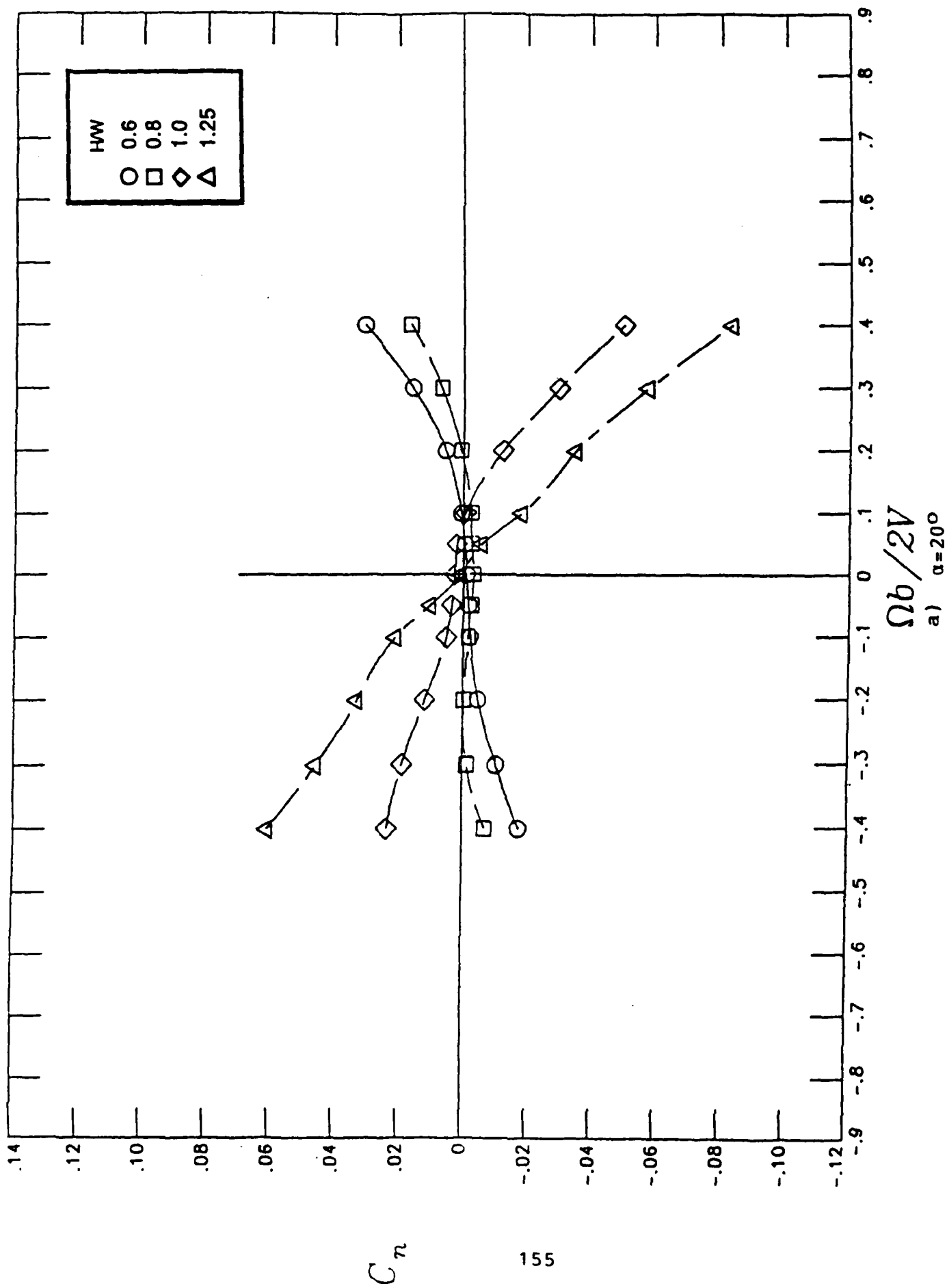
Figure 31.- Influence of forebody cross-sectional shape on rotational yawing-moment coefficient characteristics at a fineness ratio value of 4

$\Omega b / 2V$

b) $\alpha = 25^{\circ}$

Figure 31.- Continued
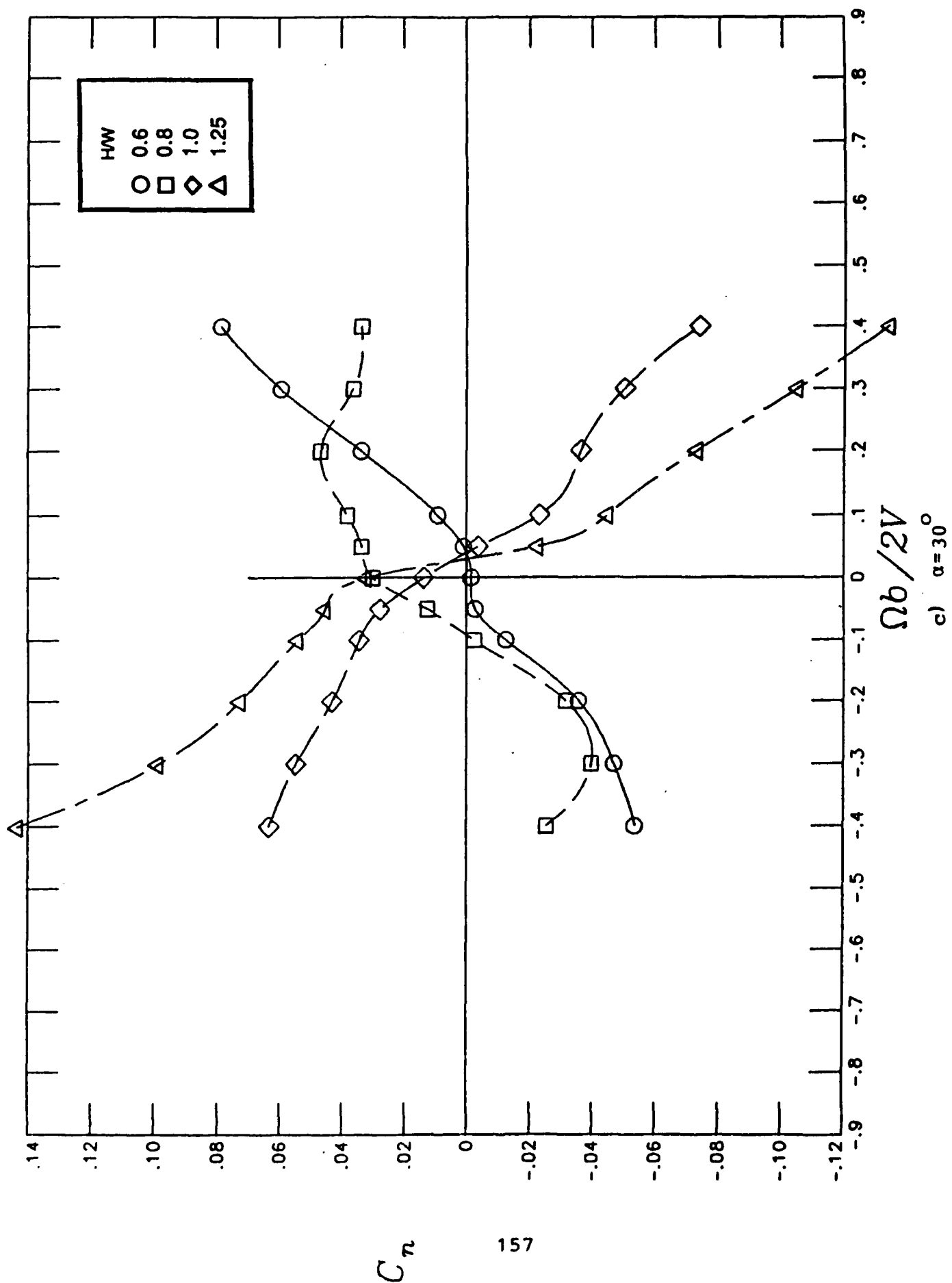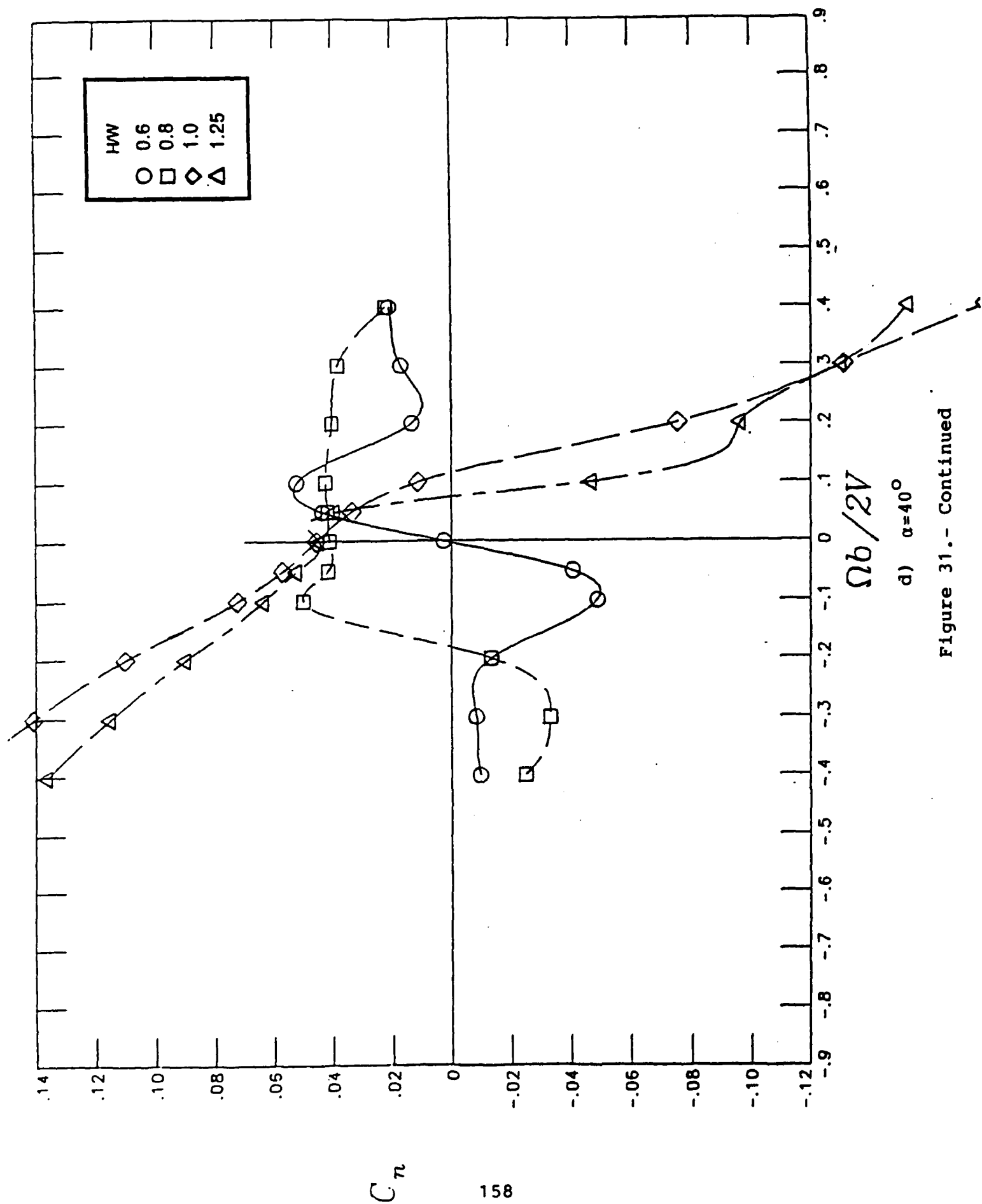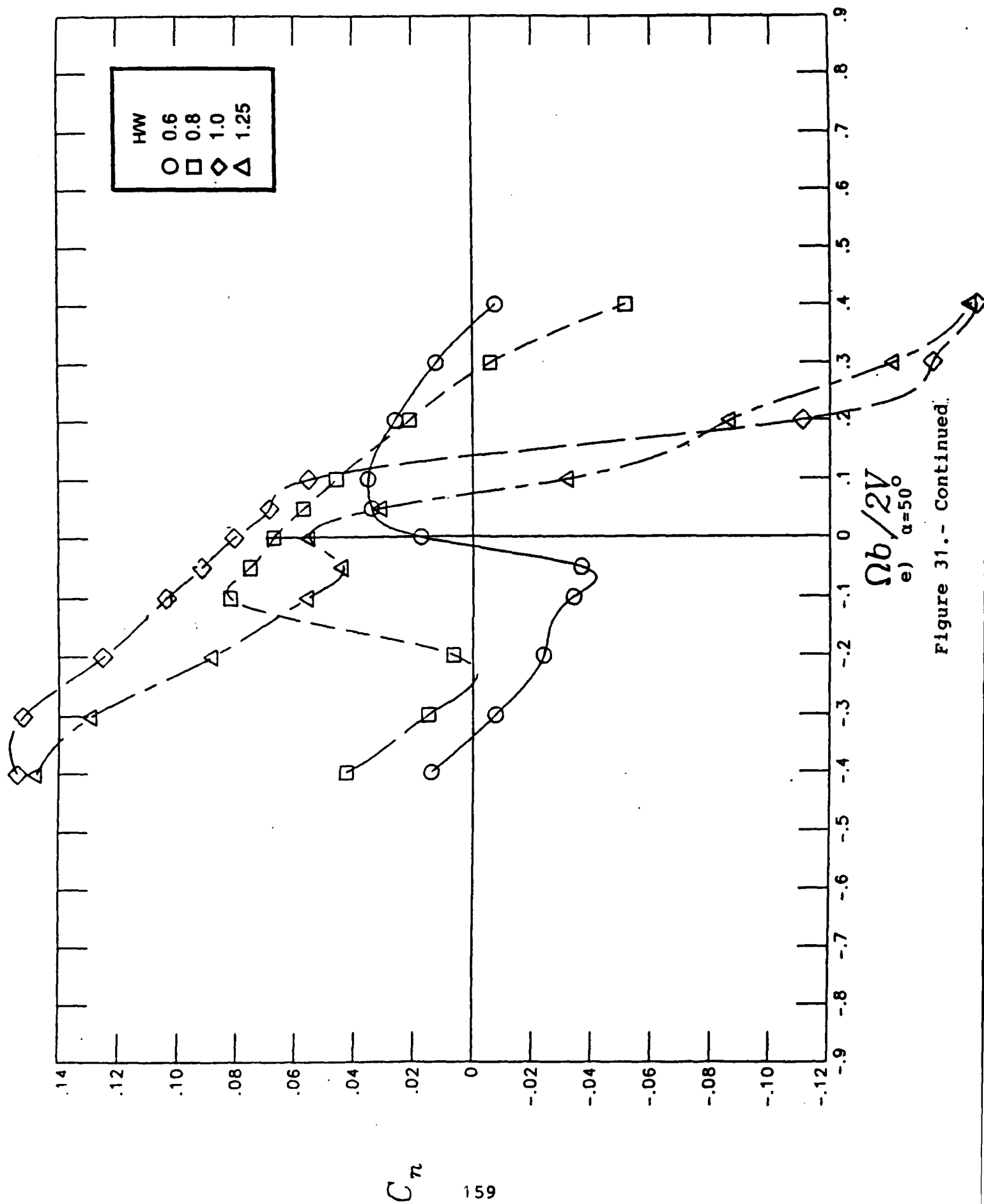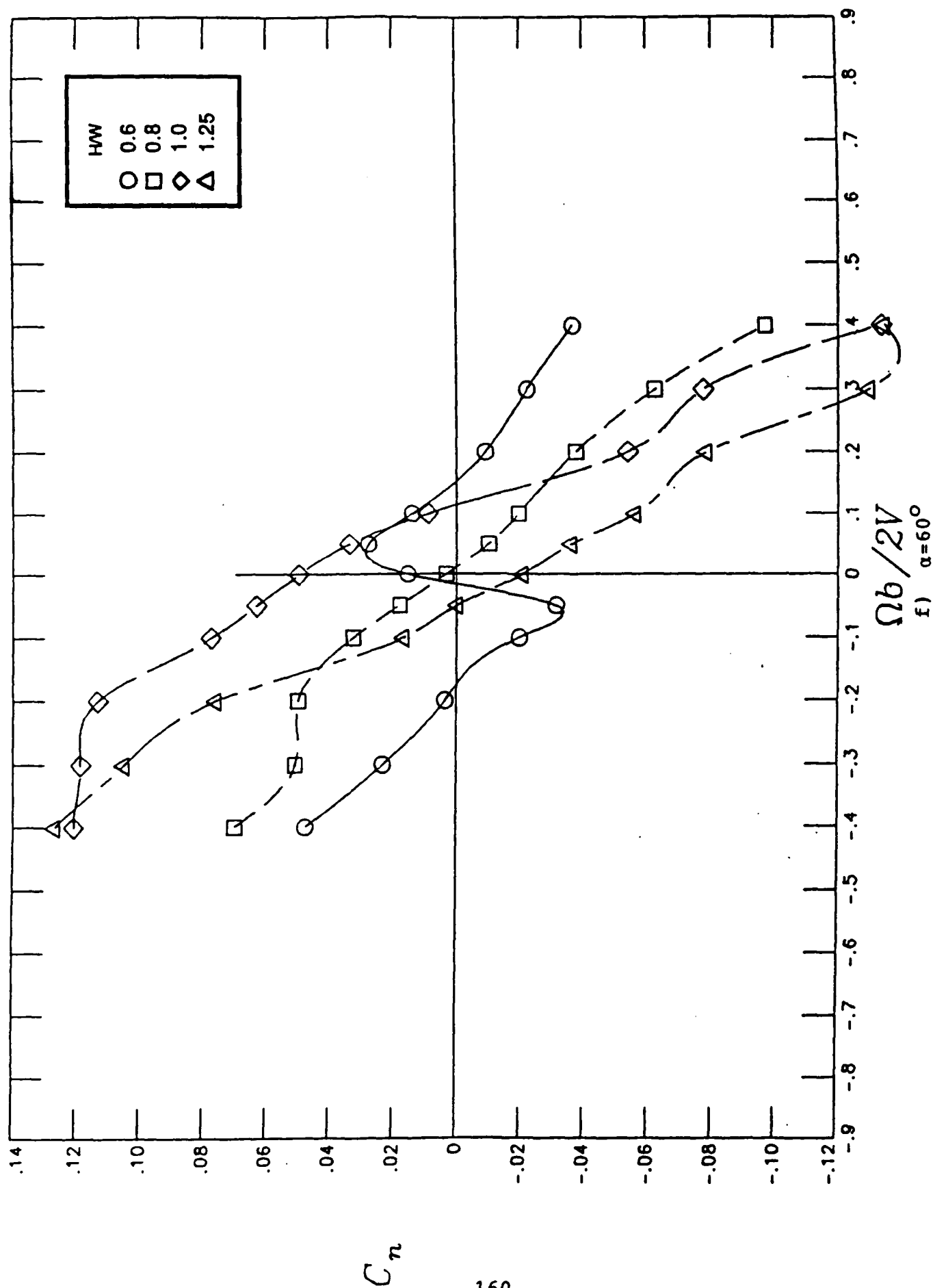
156

c) $\alpha = 30°$

Figure 31.- Continued

157

d) $\alpha = 40^\circ$

Figure 31.- Continued

158

$\dfrac{\Omega b/2V}{\text{e) } \alpha = 50^\circ}$

Figure 31.- Continued.

C_n

159

Figure 31.- Continued

$\Omega b/2V$

f) $\alpha = 60°$

C_n

160

$\Omega b / 2V$

g) $\alpha = 65°$

Figure 31.- Continued

161

$\dfrac{\Omega b}{2V}$

h) $\alpha = 70°$

Figure 31.- Continued

162

C_n

$\dfrac{\Omega b}{2V}$

i) $\alpha = 80^\circ$

Figure 31.- Continued

163

$\Omega b/2V$
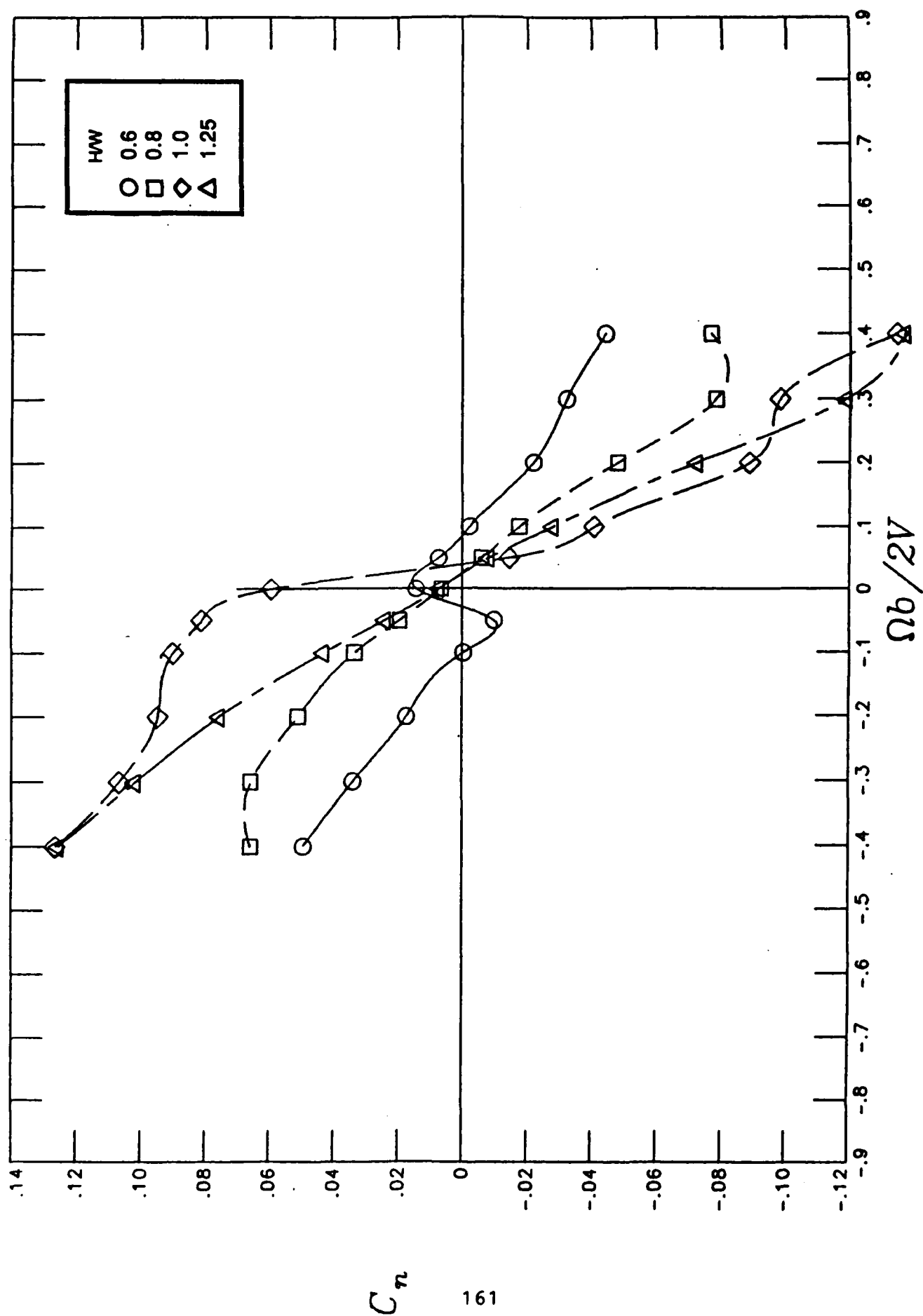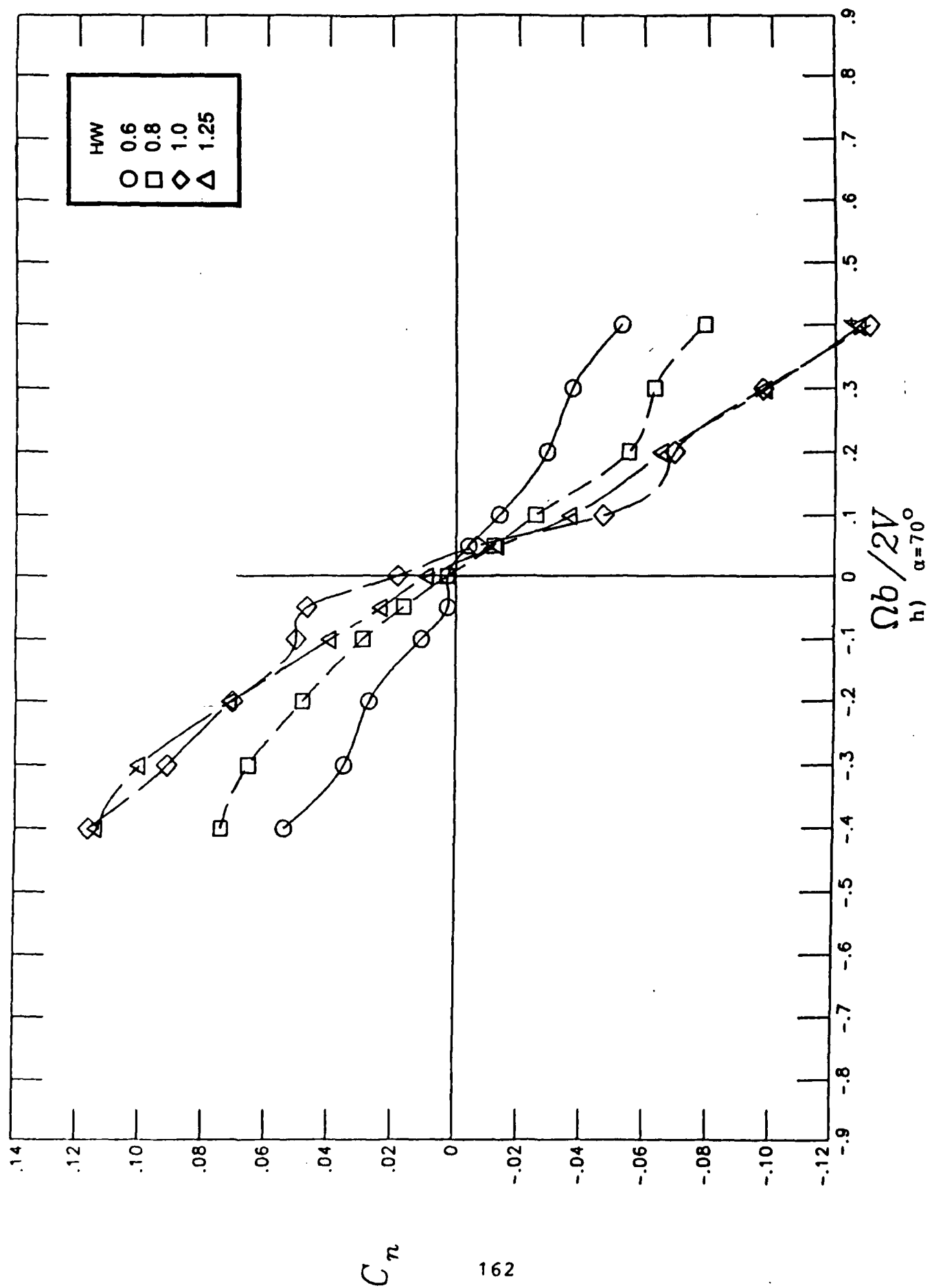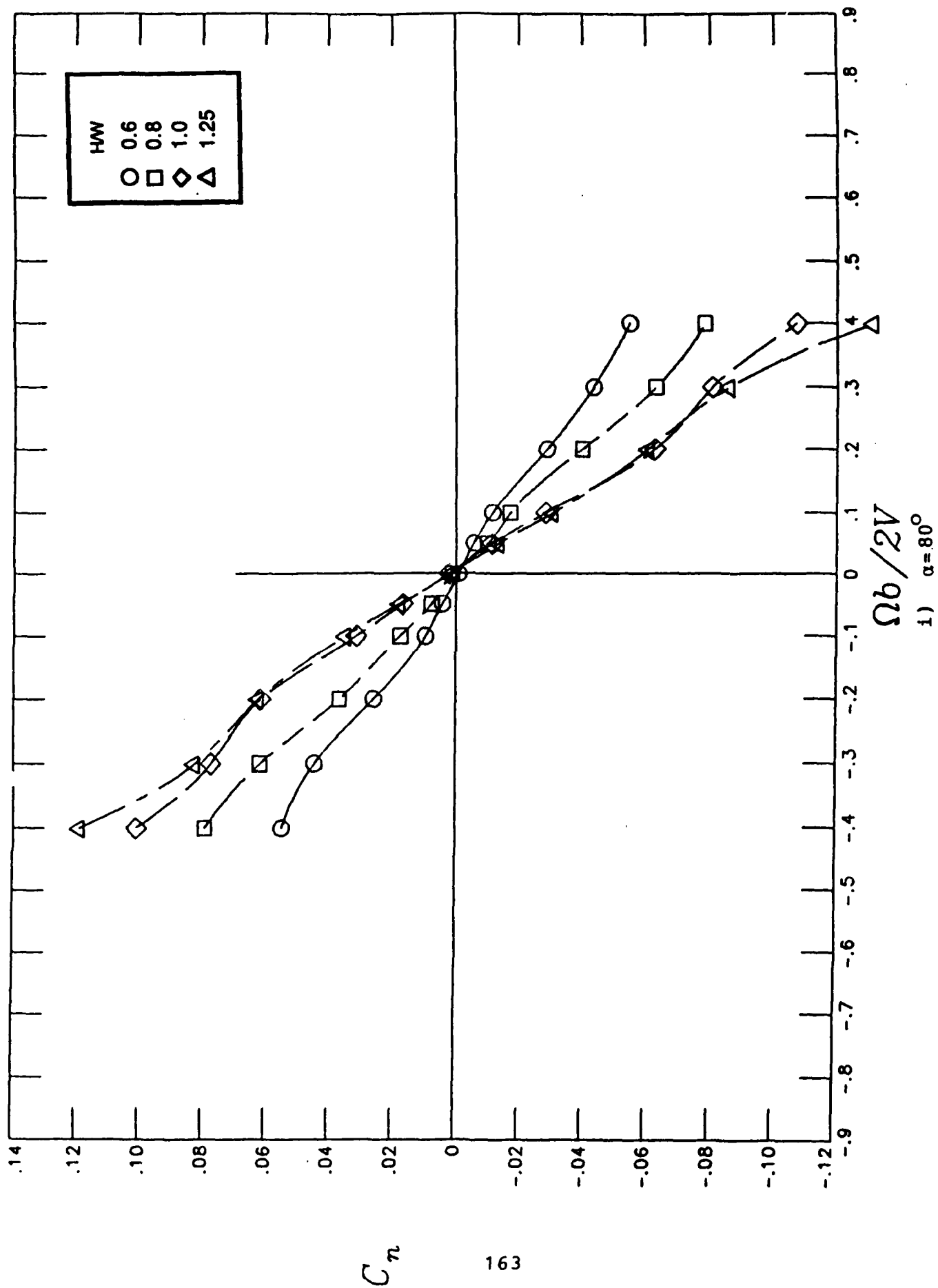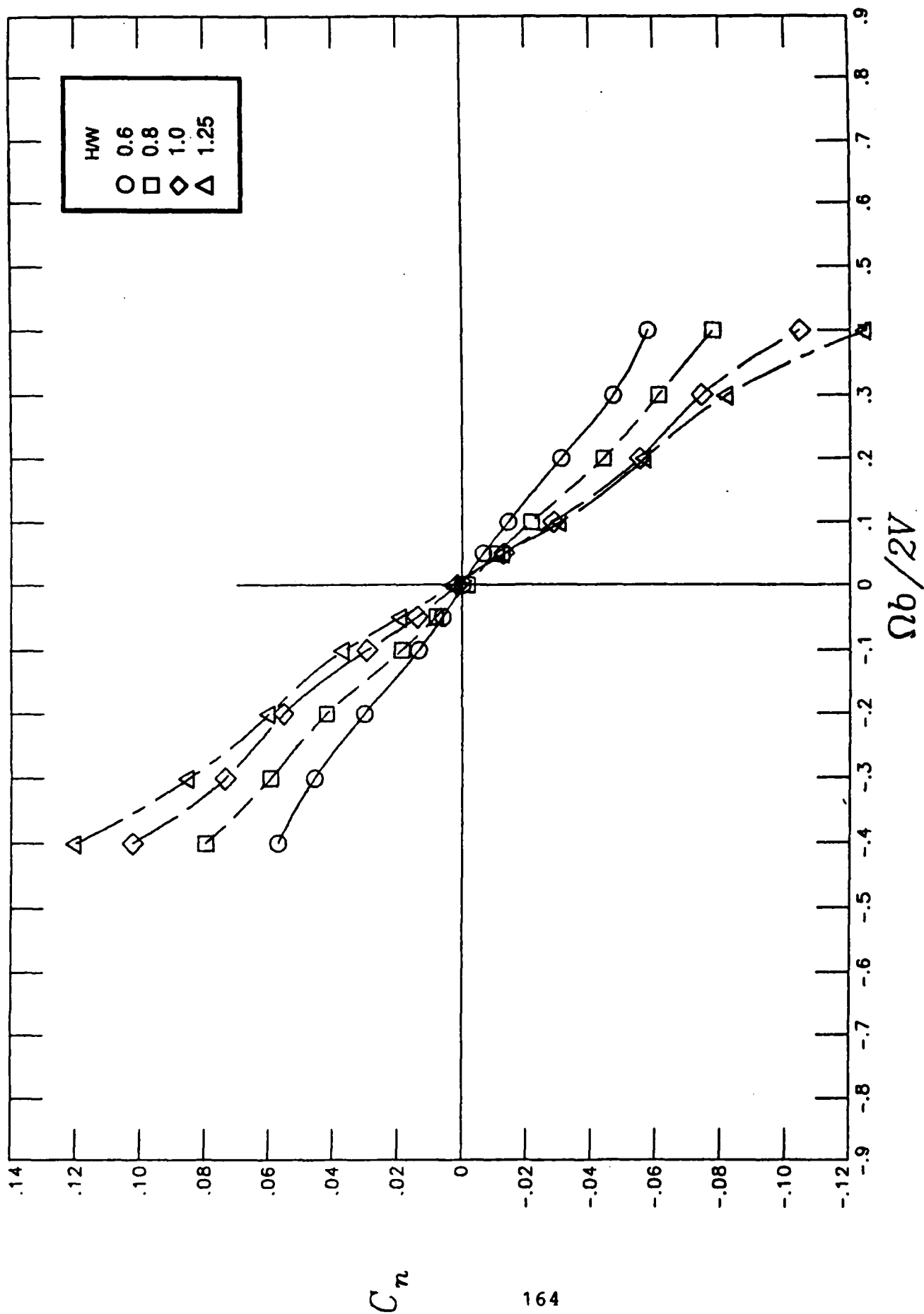
j) $\alpha = 90°$

Figure 31.- Concluded

C_n
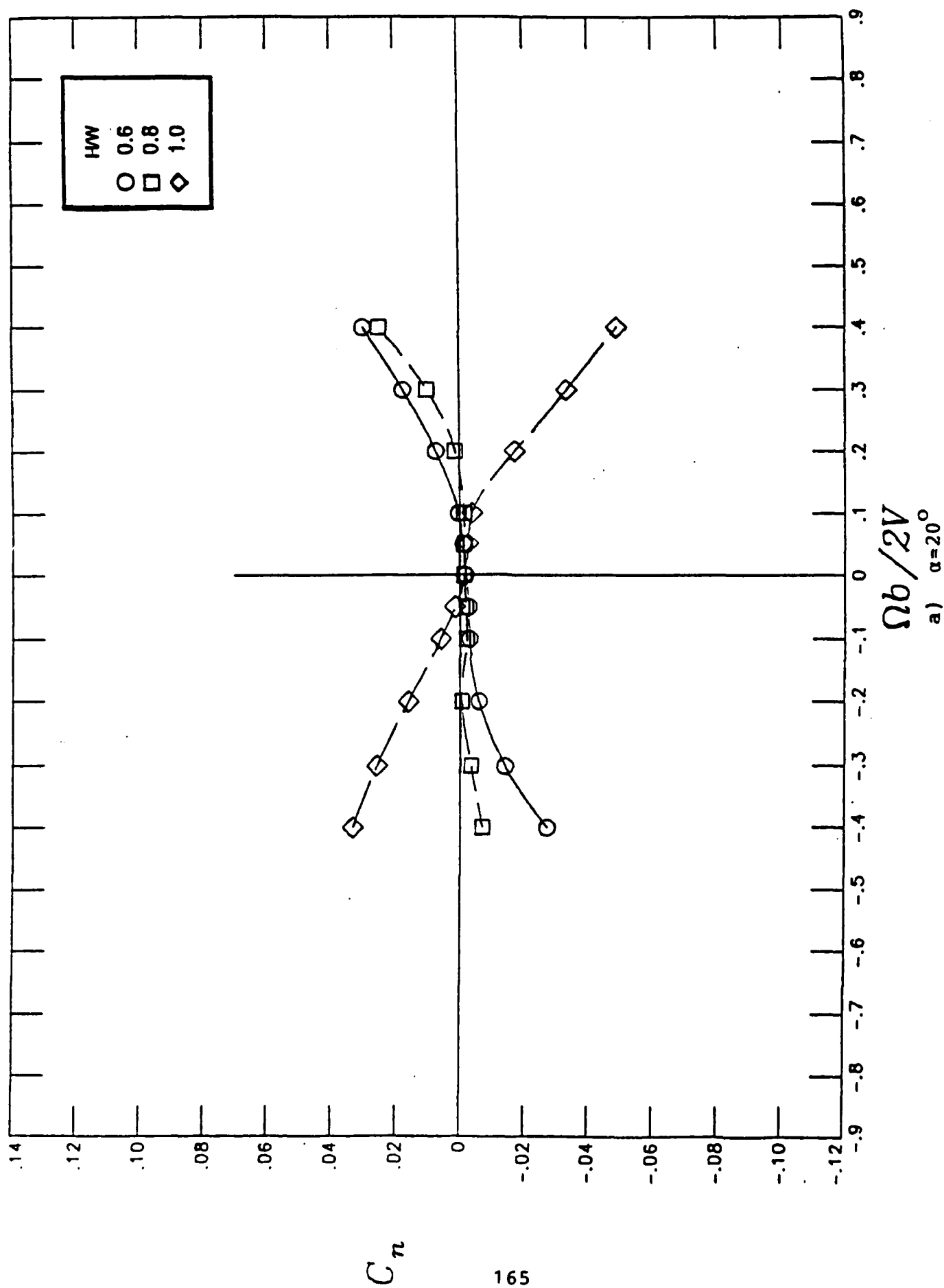
Figure 32.- Influence of forebody cross-sectional shape on rotational yawing-moment coefficient characteristics at a fineness ratio value of 4.5
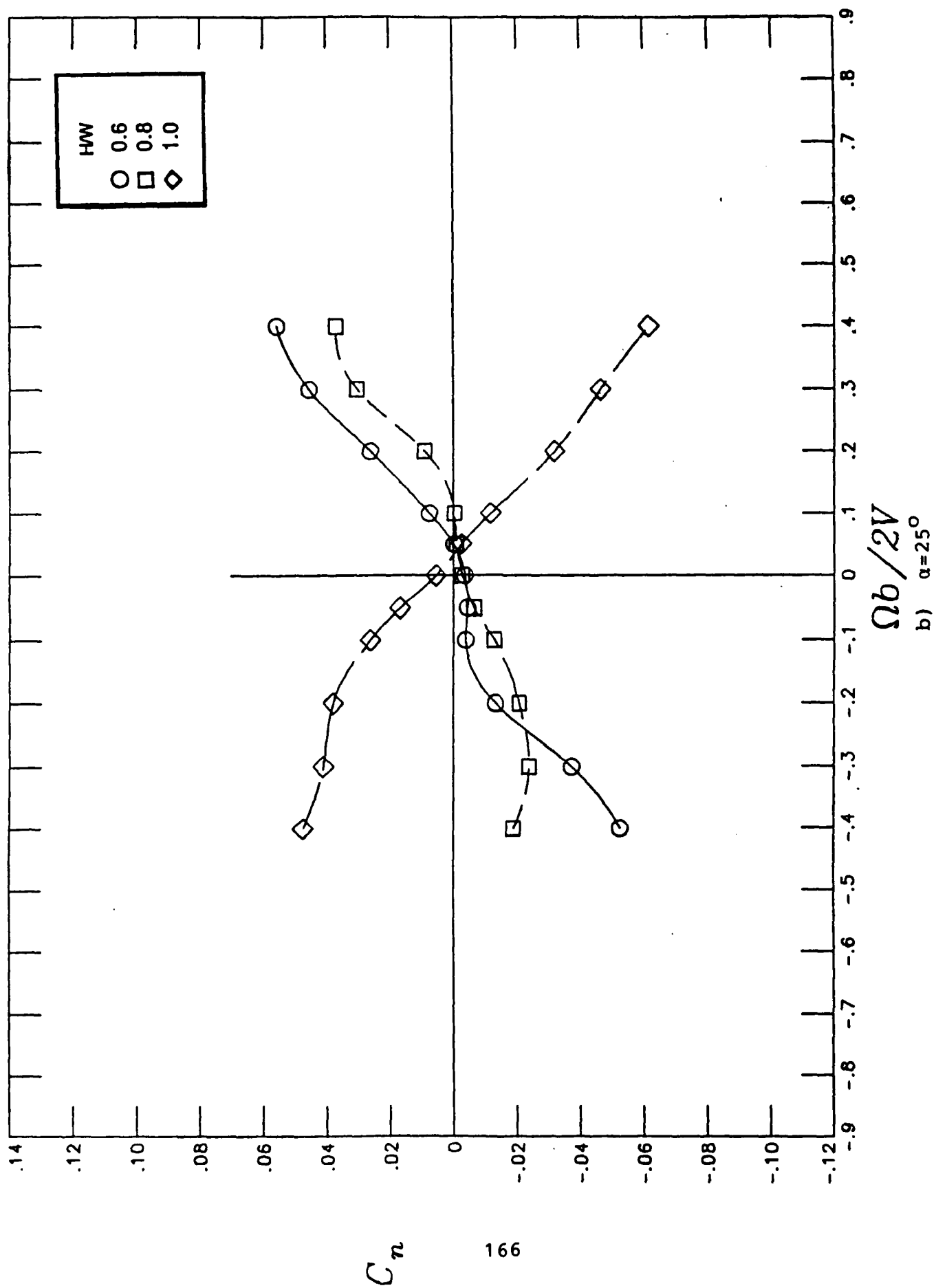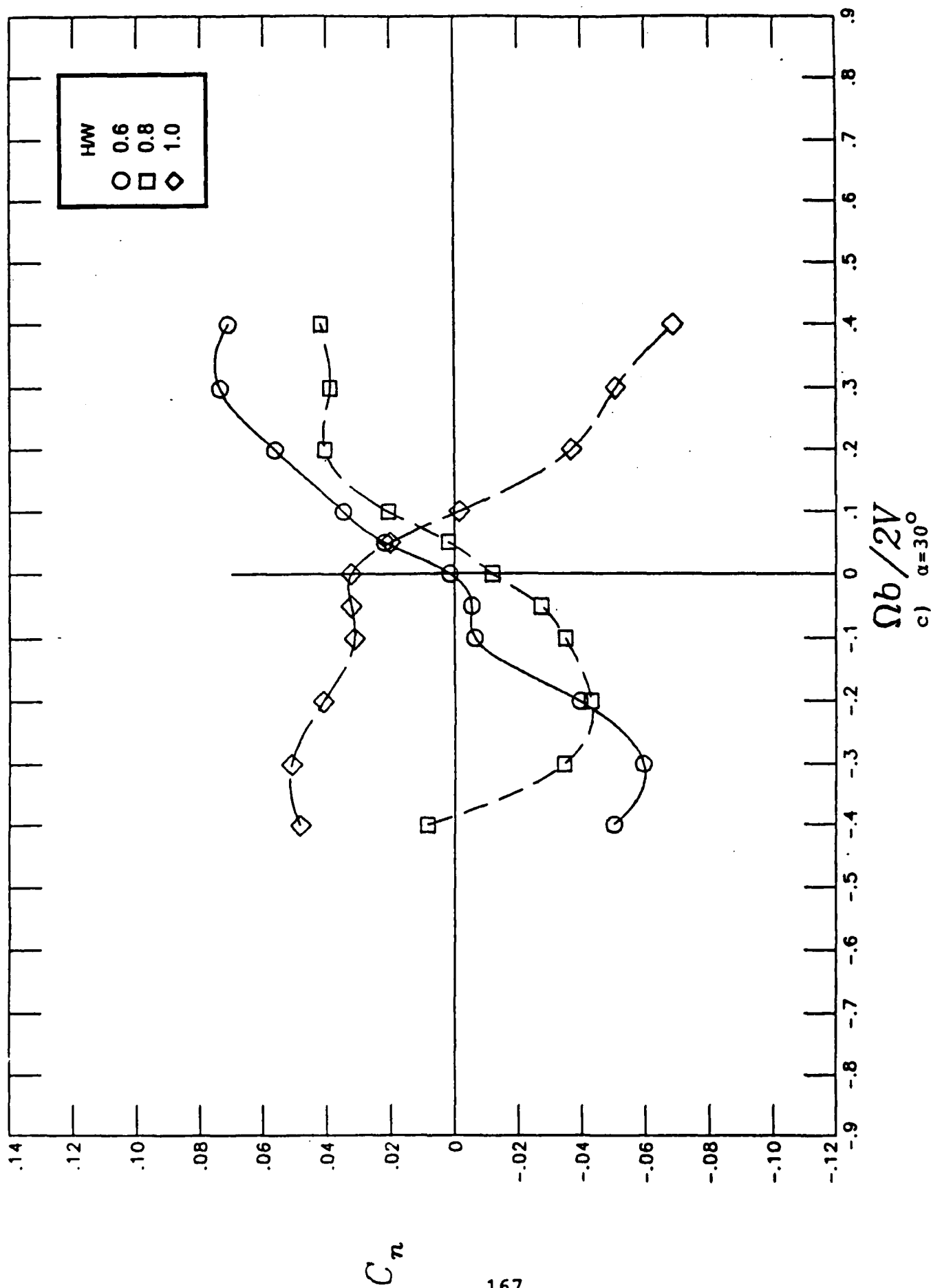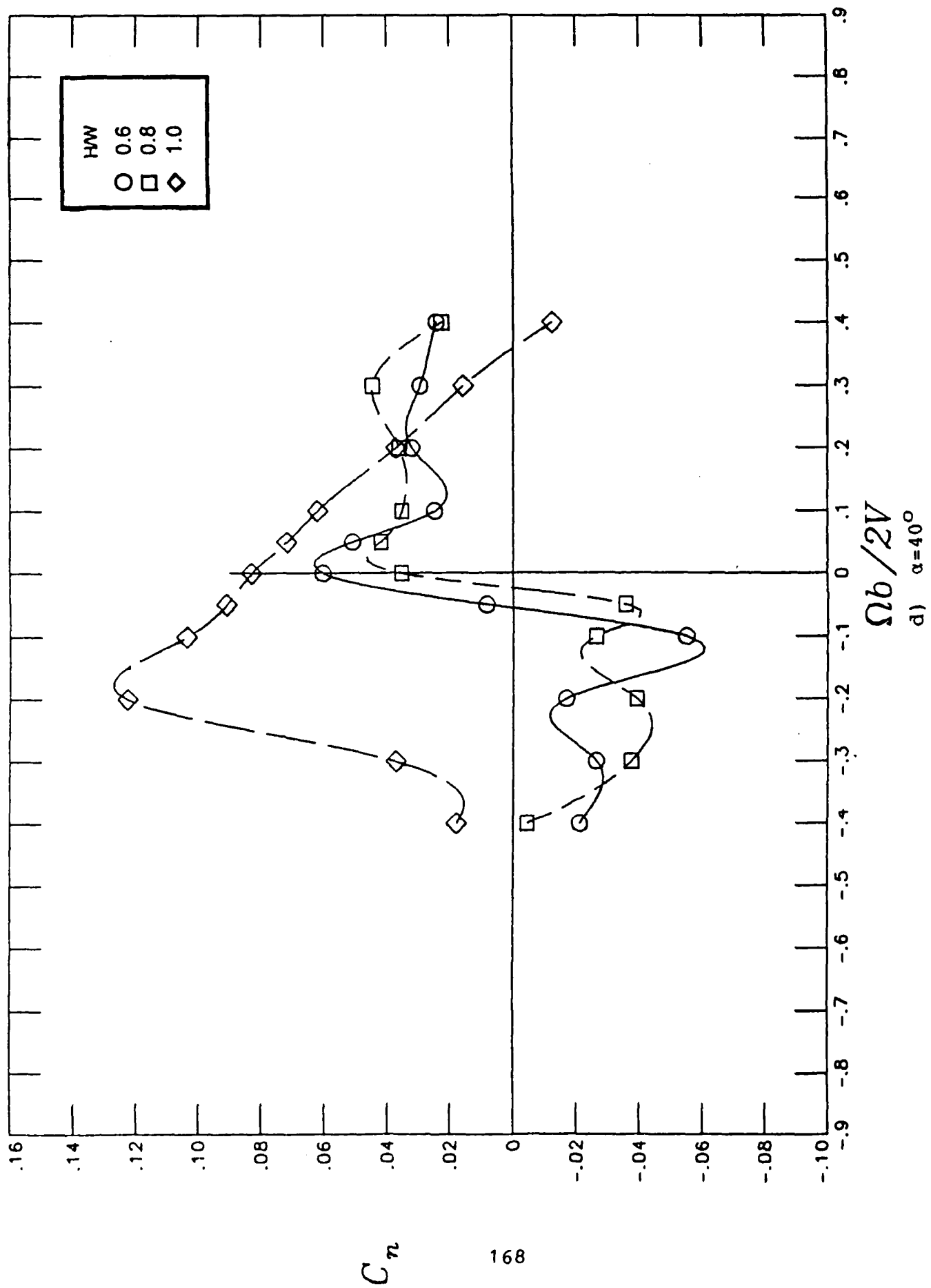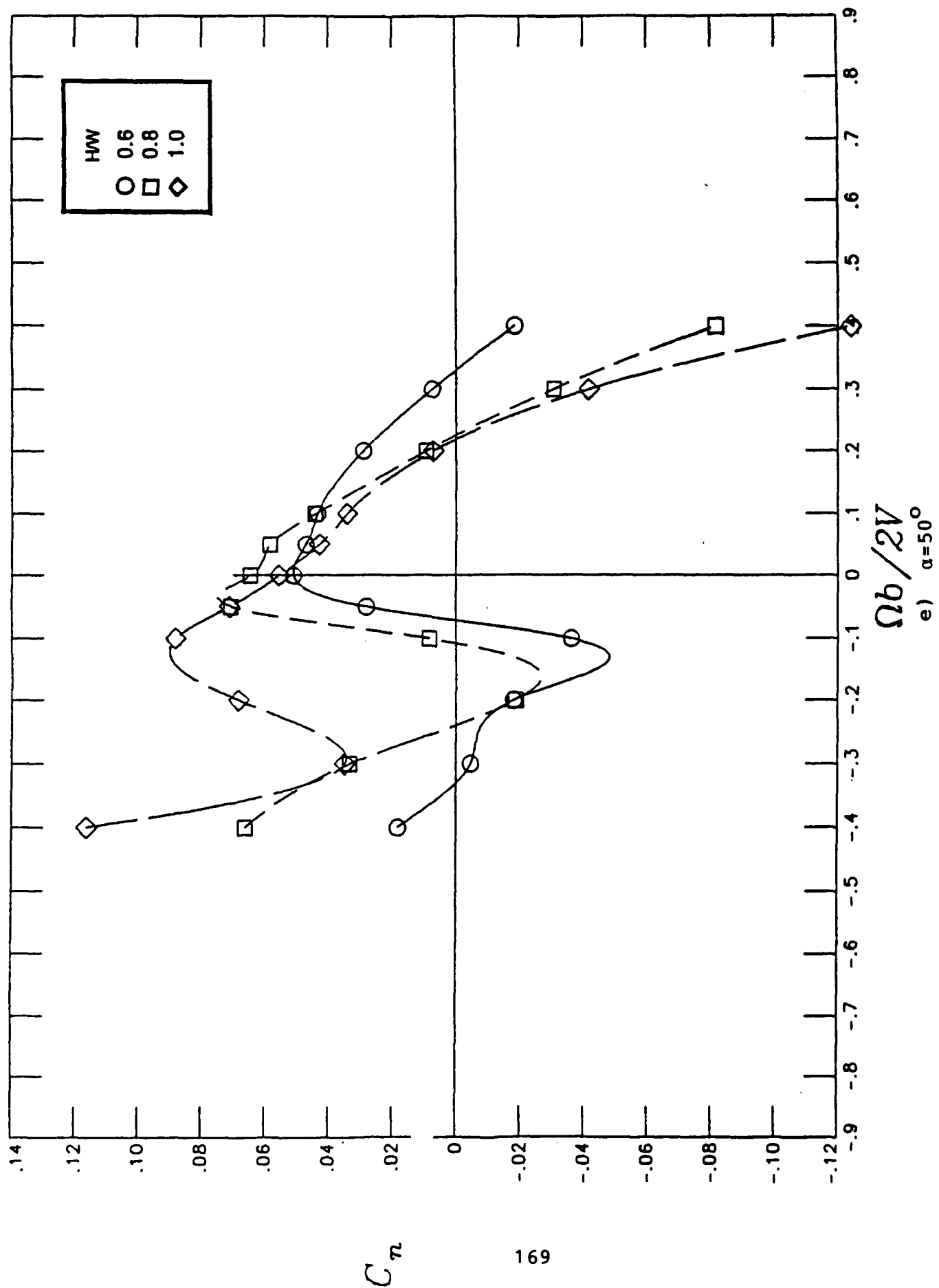
165

b) $\alpha=25^\circ$

Figure 32.- Continued

$\Omega b/2V$

c) $\alpha = 30°$

Figure 32.- Continued

167

$\Omega b/2V$

d) $\alpha=40^{o}$

Figure 32.- Continued

168

Figure 32.- Continued

e) $\alpha = 50°$

$\Omega b / 2V$

C_n

169

f) $\alpha=60^\circ$

Figure 32.- Continued

170

Figure 32.- Continued

g) $\alpha = 65°$

$\dfrac{\Omega b}{2V}$

C_n

171

h) $\alpha = 70°$

Figure 32.- Continued

172

Figure 32.- Continued

1) $\alpha = 80^{o}$

$\Omega b / 2V$

C_n

173

$\Omega b/2V$

j). $\alpha=90^\circ$
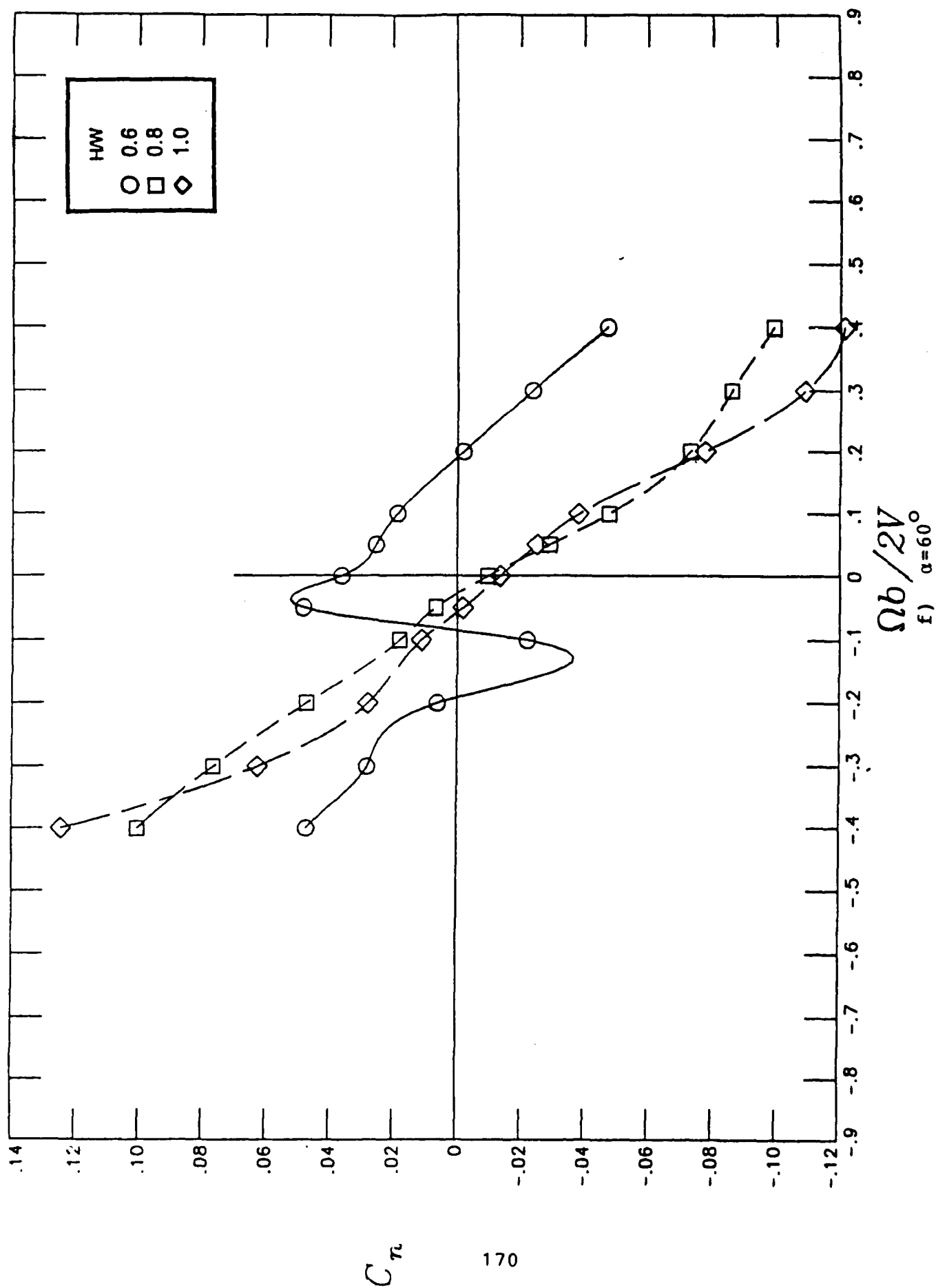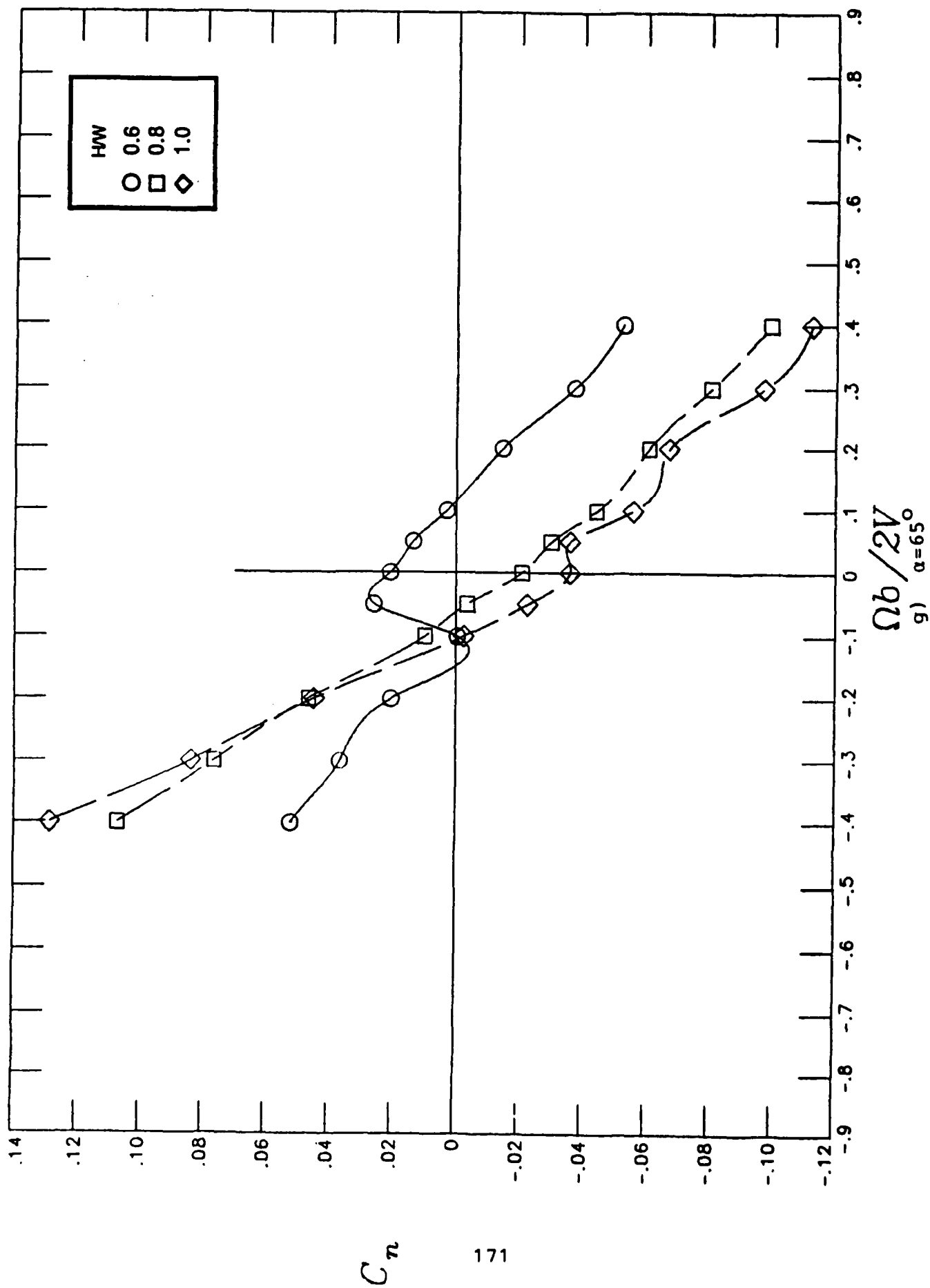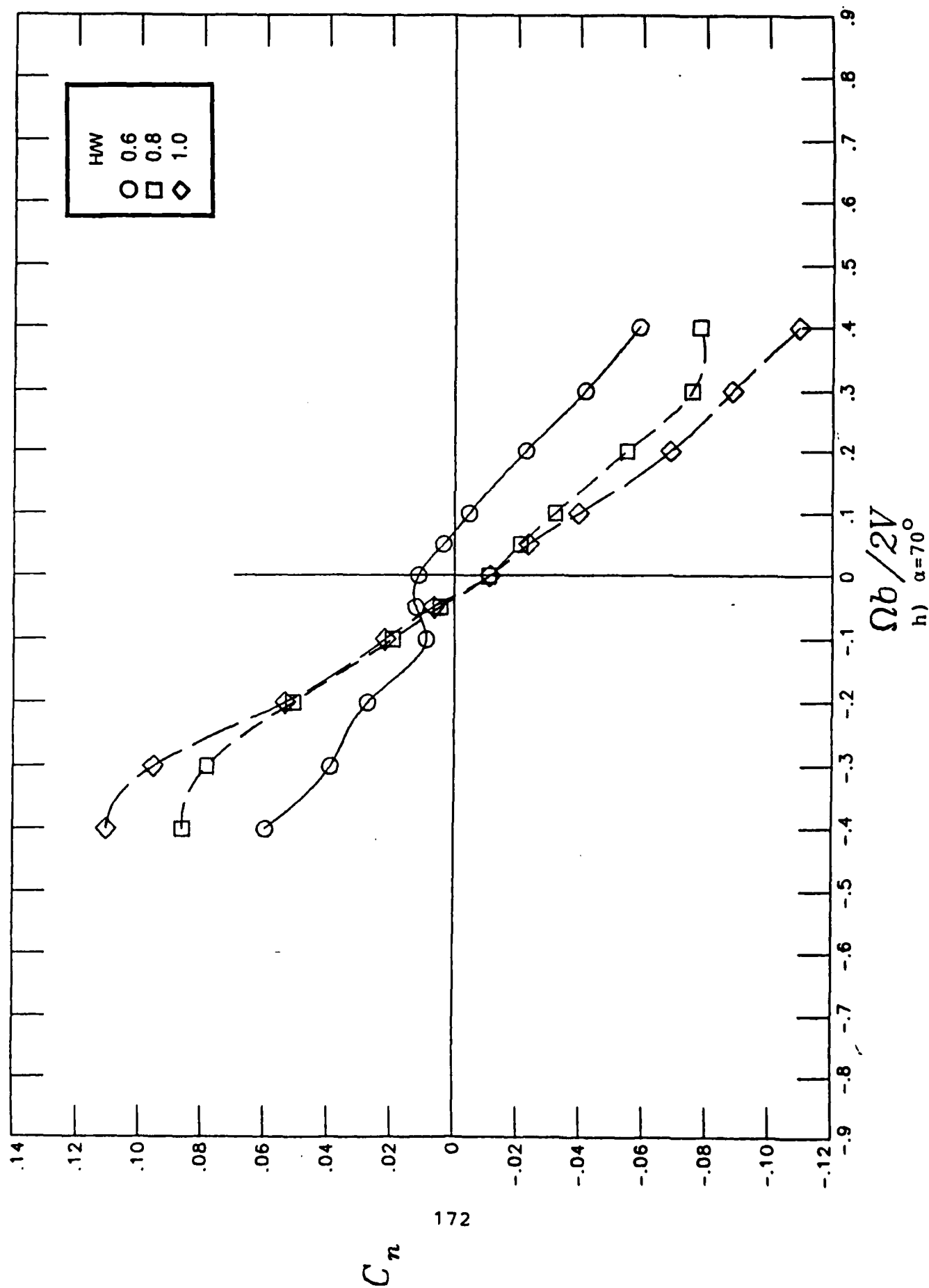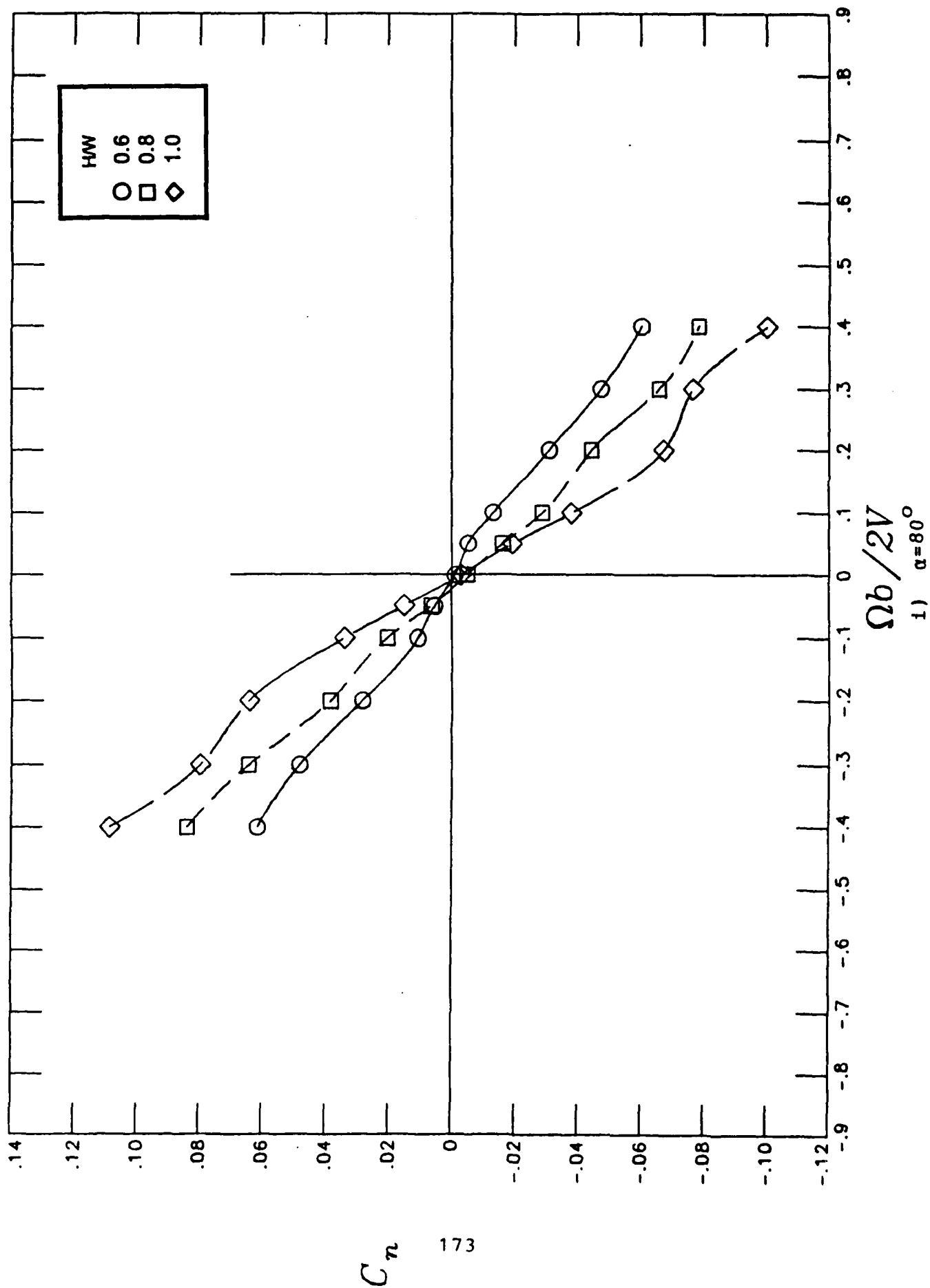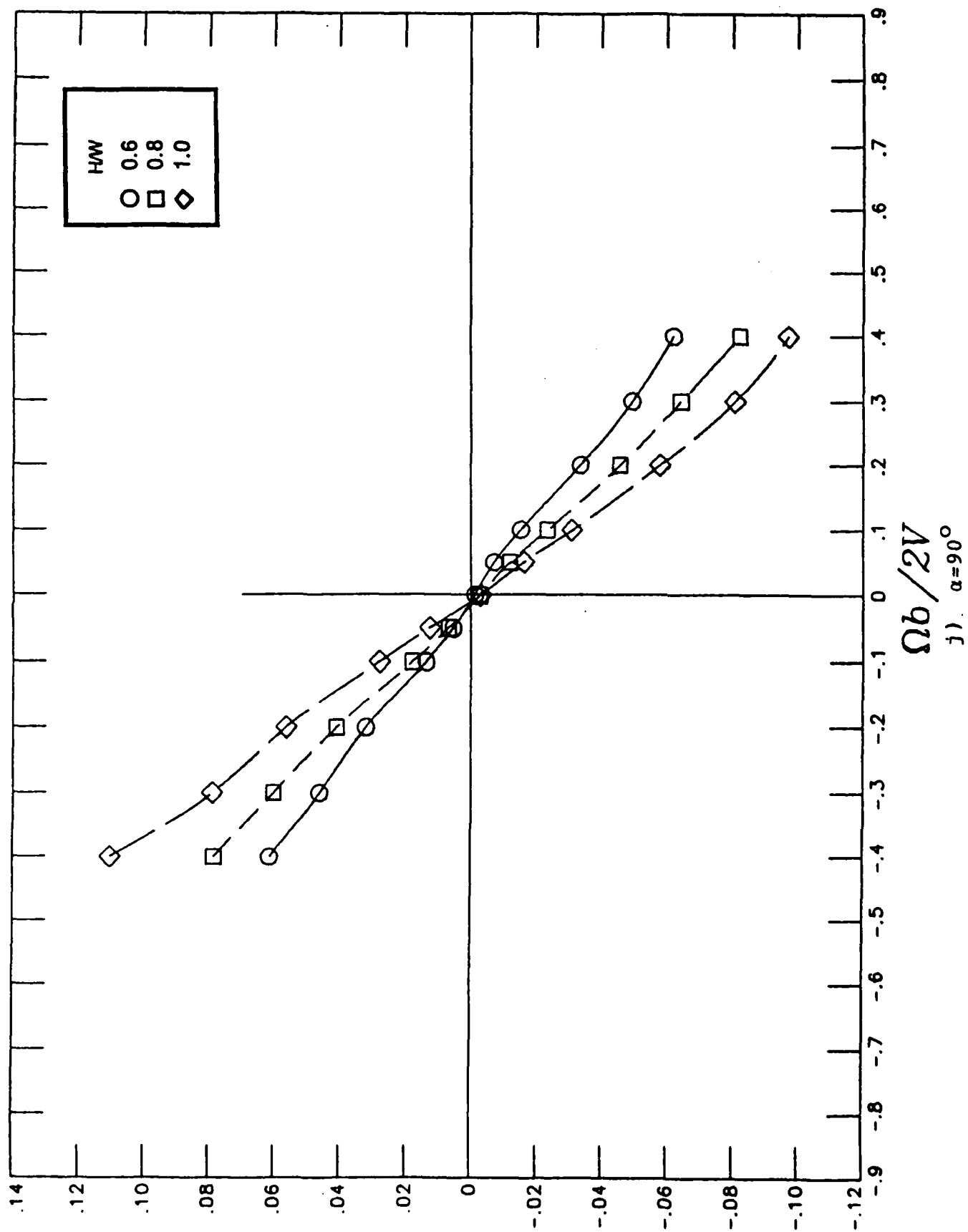
Figure 32.- Concluded

C_n

174
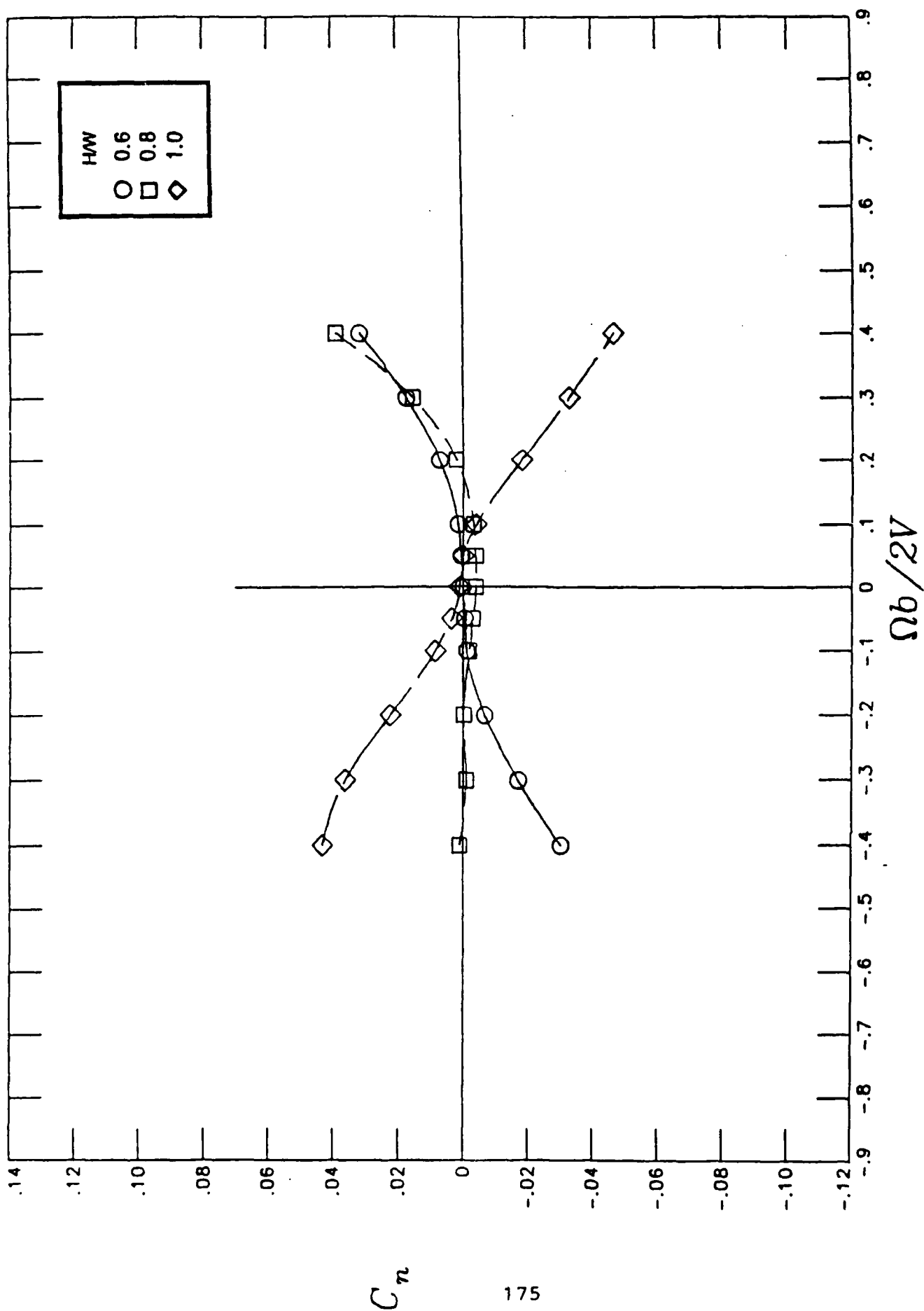
Figure 33.- Influence of forebody cross-sectional shape on rotational yawing-moment
coefficient characteristics at a fineness ratio value of 5

Figure 33.- Continued

b) $\alpha = 25°$

$\Omega b / 2V$

C_n

176

c) $\alpha = 30°$

Figure 33.- Continued

C_n

177

d) $\alpha = 40°$

Figure 33.- Continued

178

e) $\alpha = 50°$

Figure 33.- Continued

179
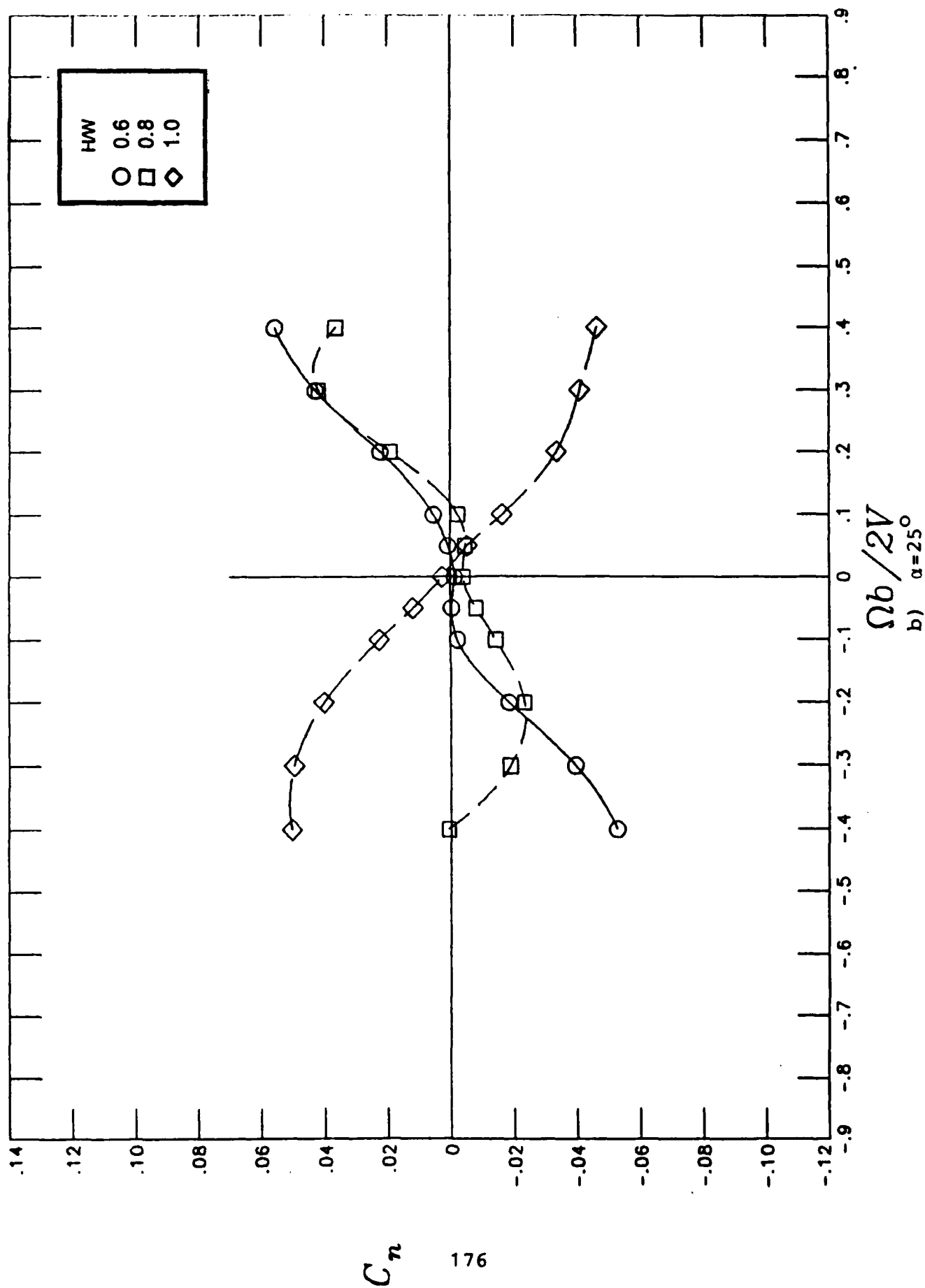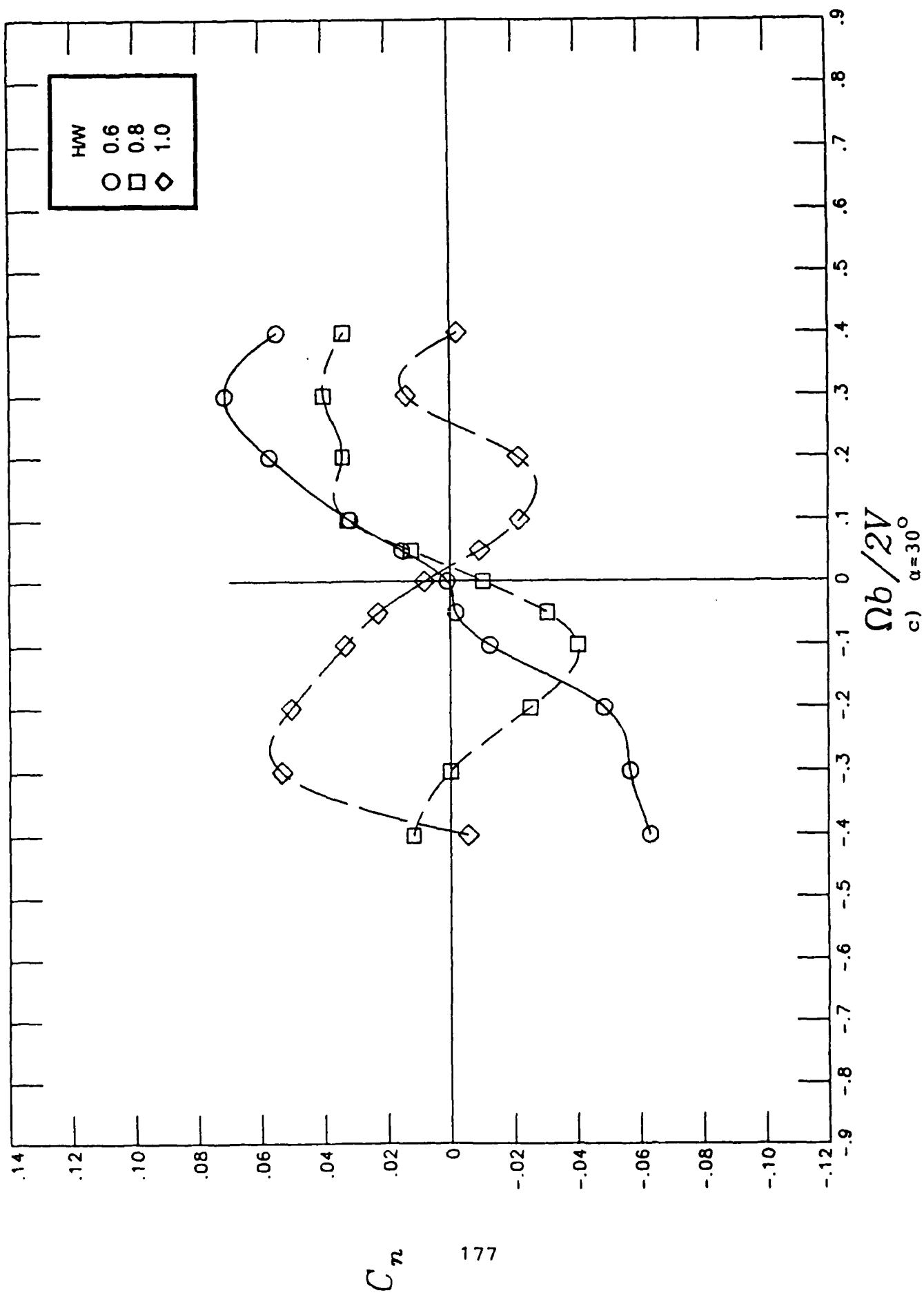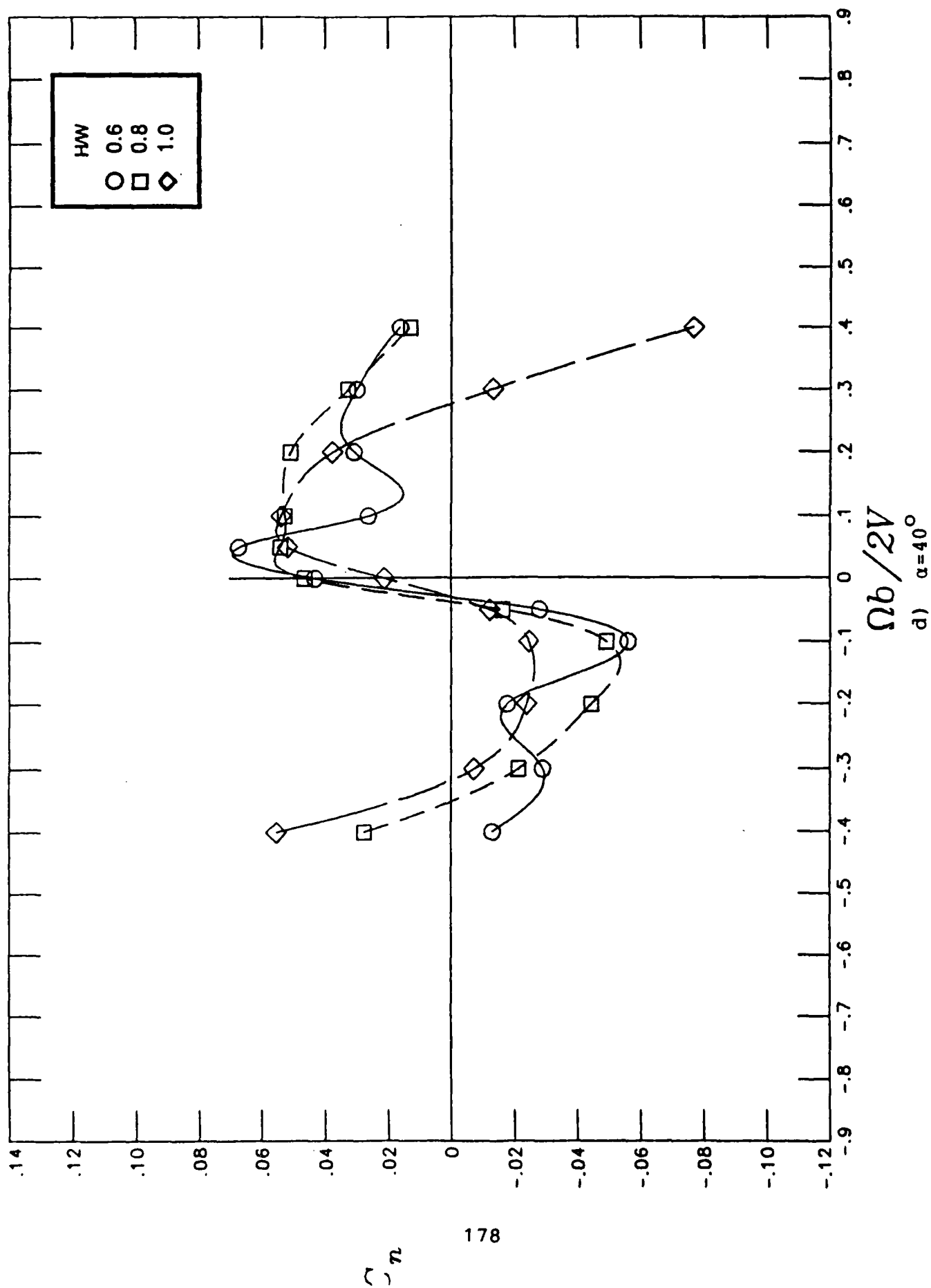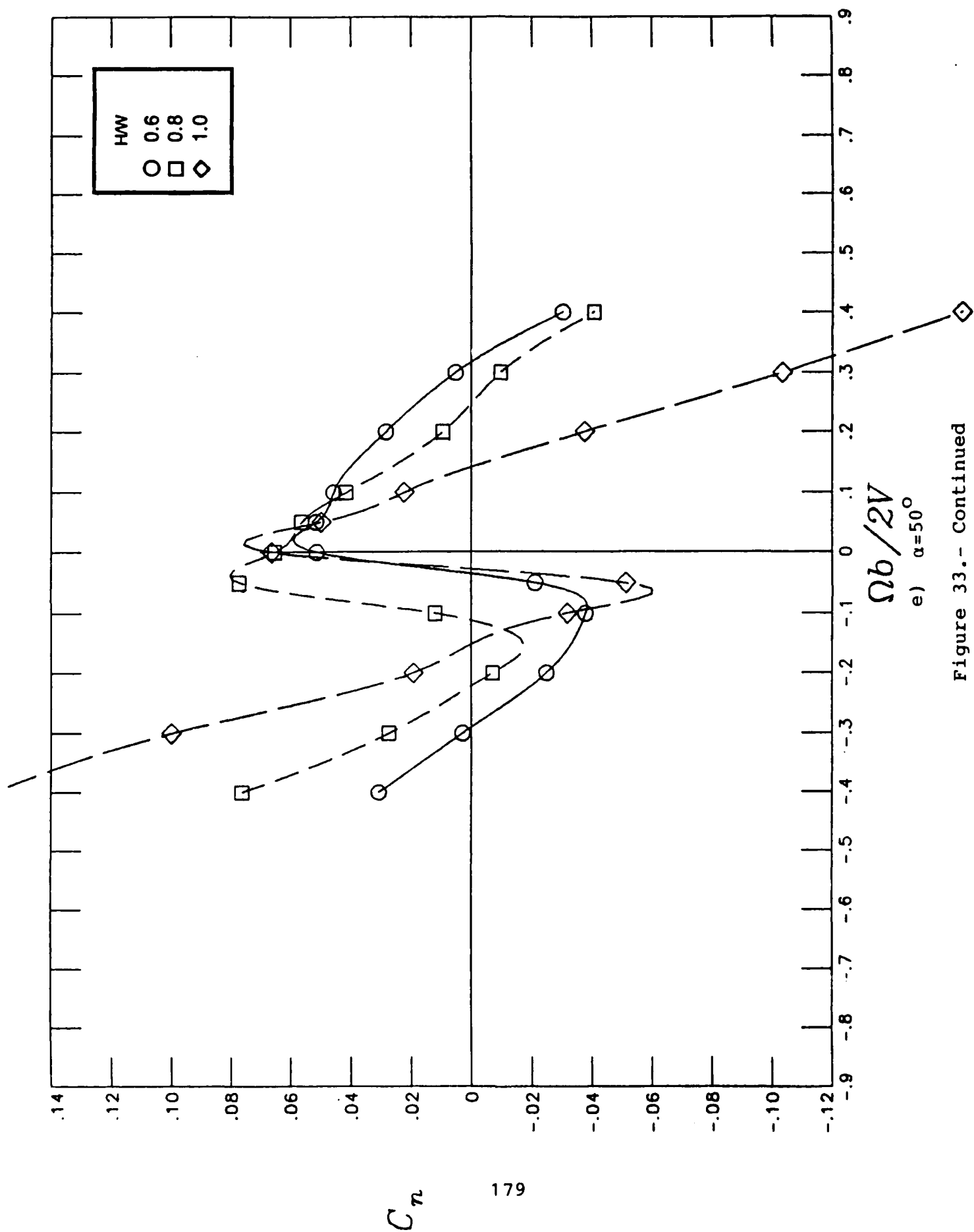
Figure 33.- Continued

f) $\alpha = 60°$

180

Figure 33.- Continued

g) $\alpha=65°$

$\Omega b/2V$

C_n

181

$\Omega b/2V$

h) $\alpha=70°$

Figure 33.- Continued

182

Figure 33.- Continued

i) α=80°

C_n

183

C_n

$\Omega b/2V$
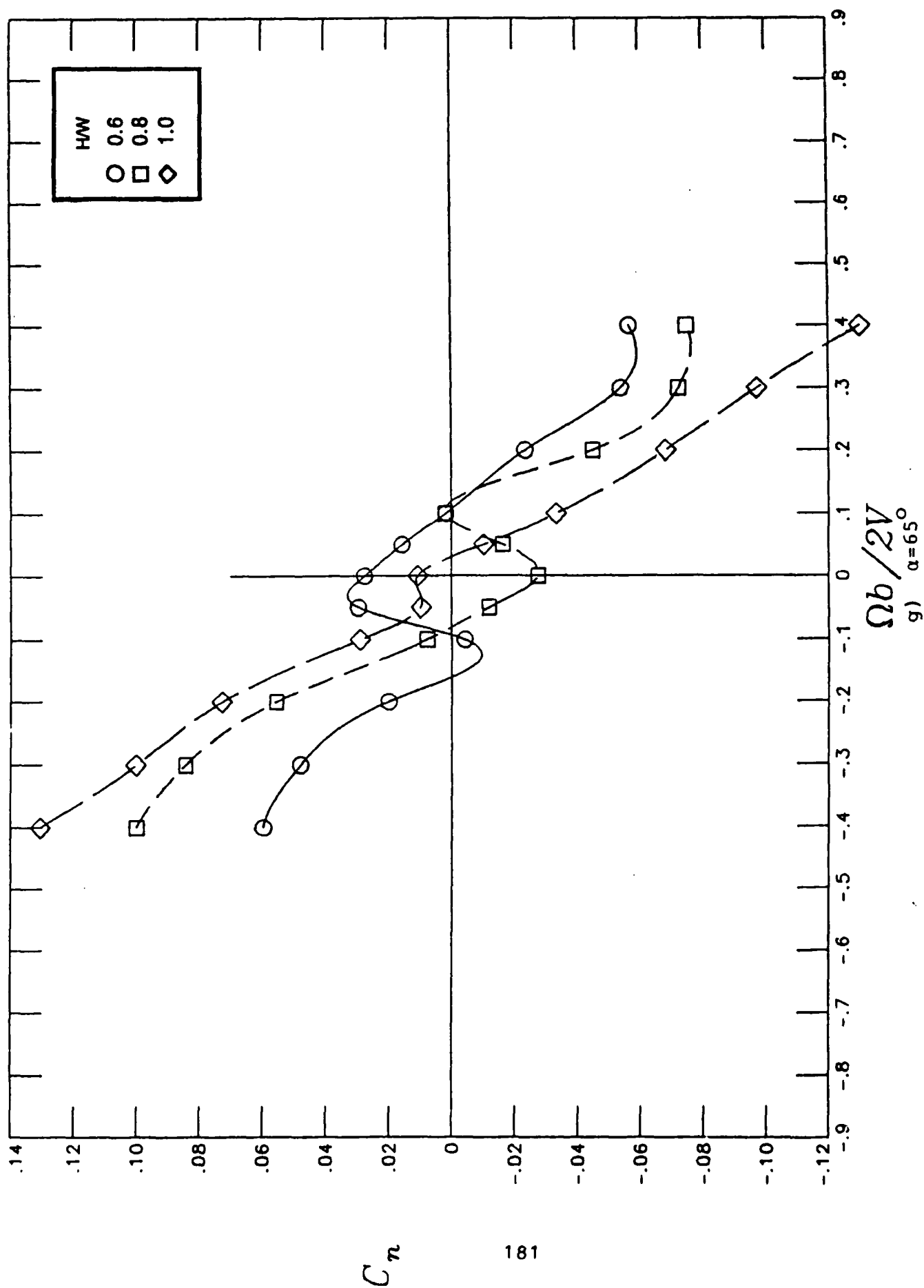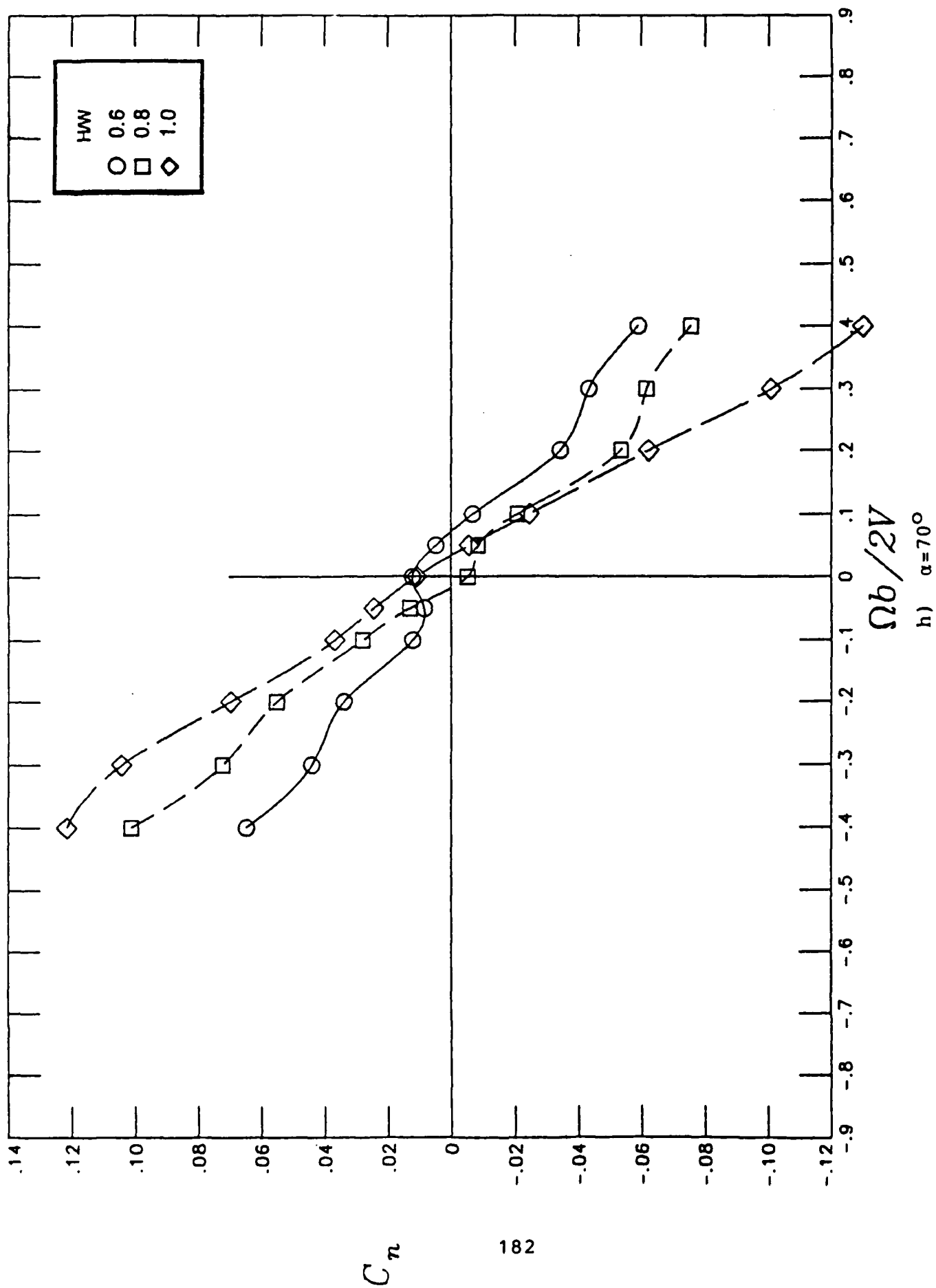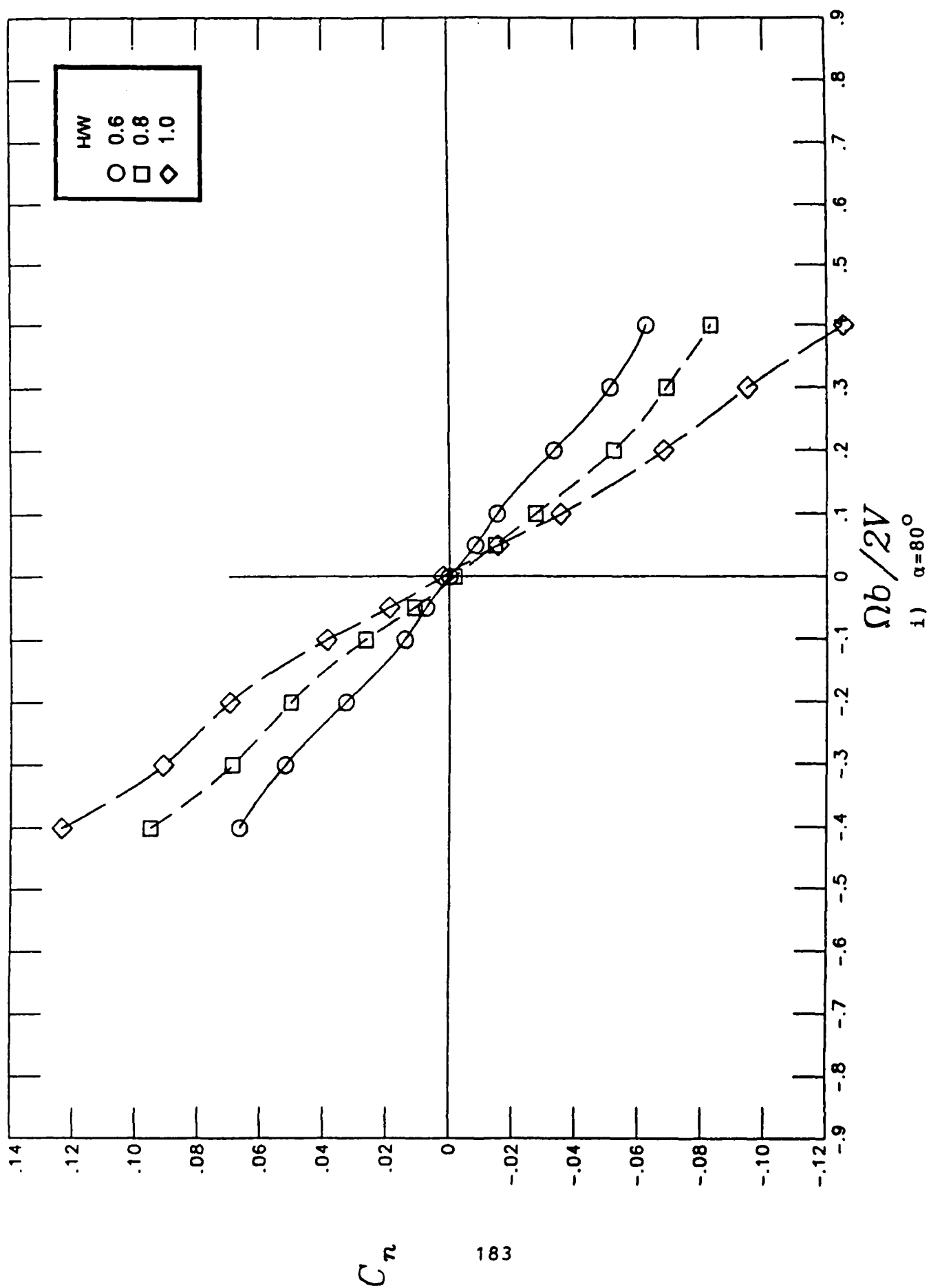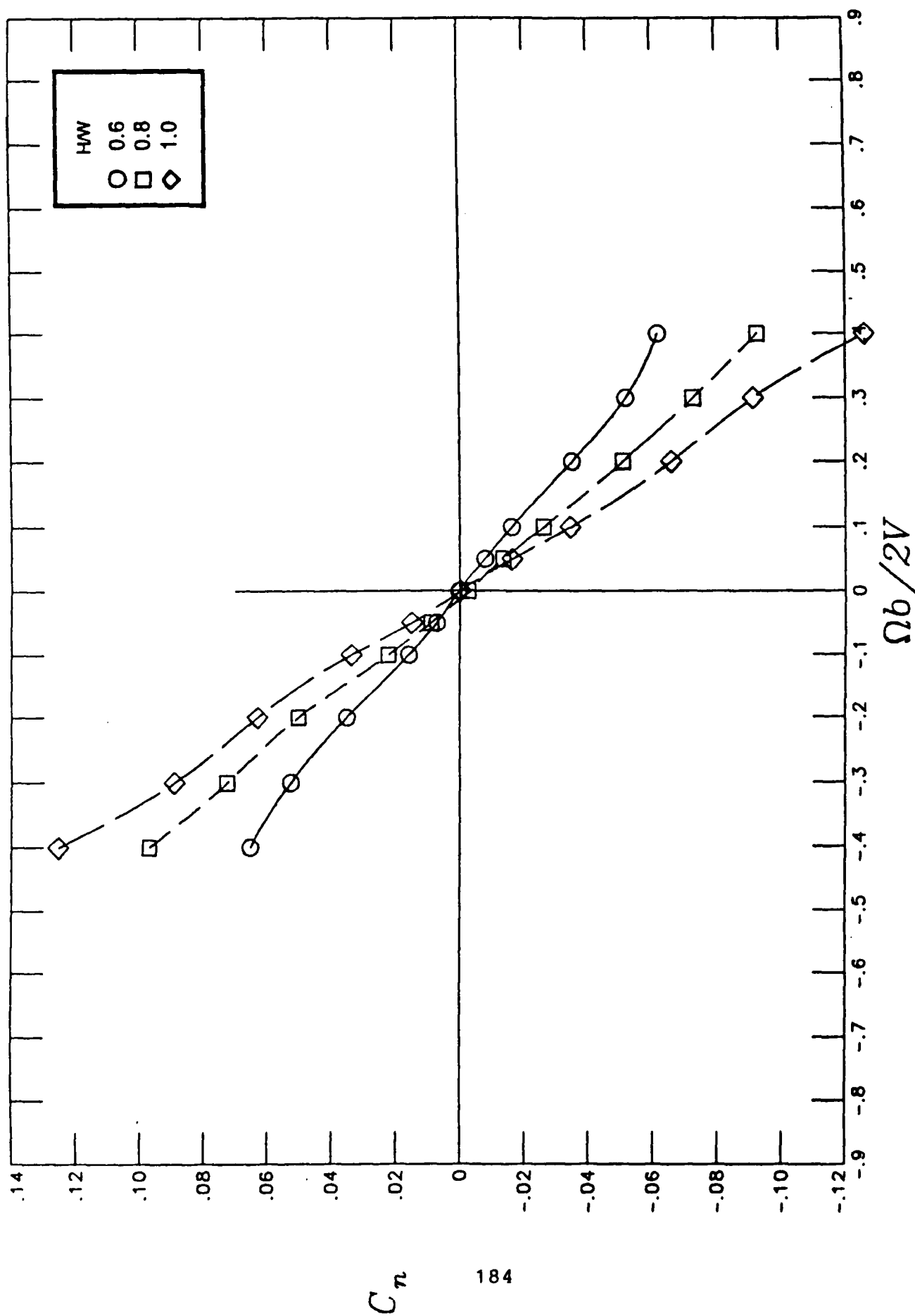
j) $\alpha=90^\circ$

Figure 33.- Concluded

184
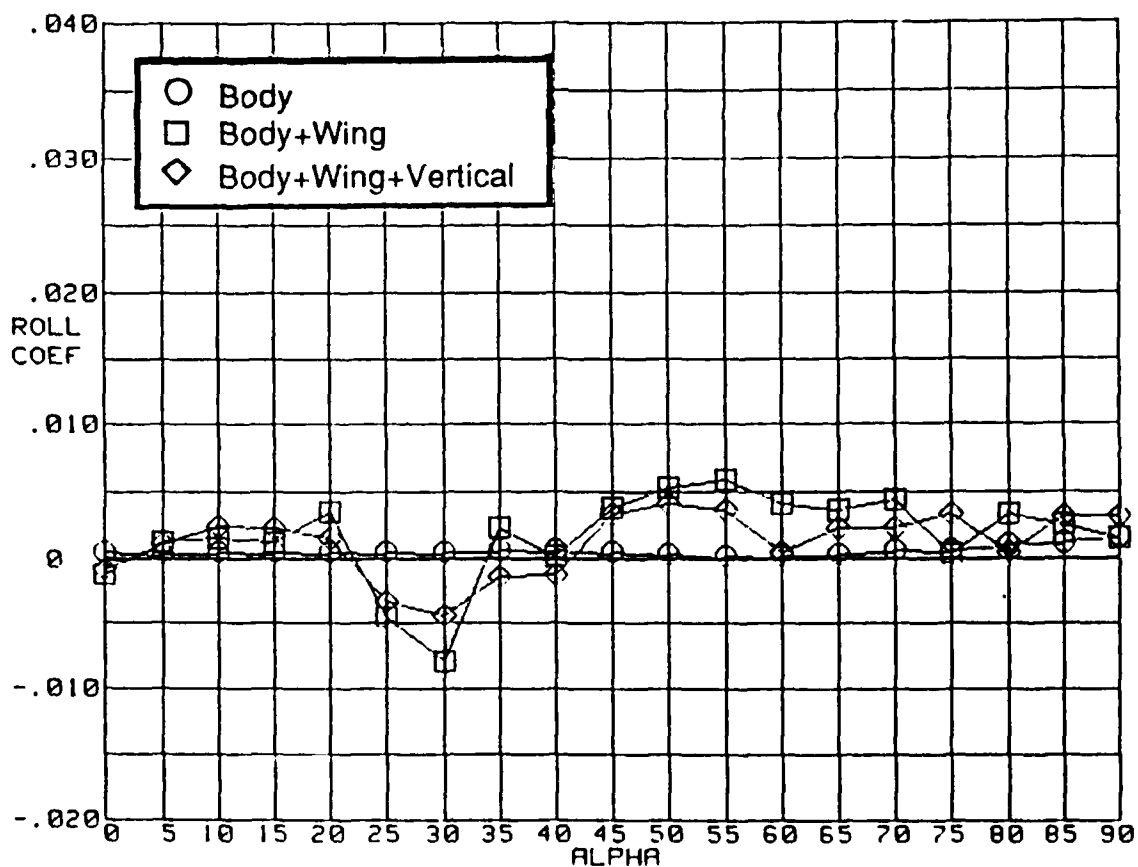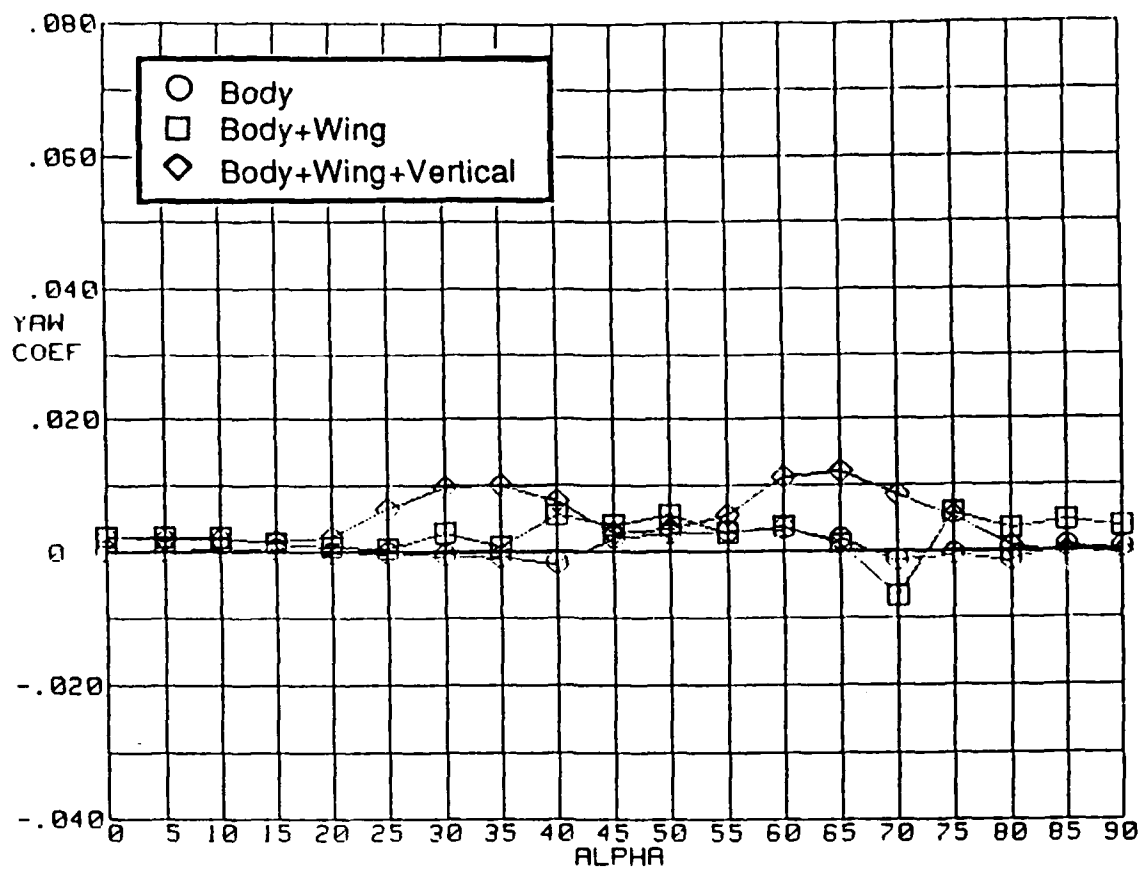
a)   H/W=0.6   FR=2

Figure 34.- Influence of forebody geometry in the presence of
other airplane components on symmetrical flight rolling-
and yawing-moment coefficients

185
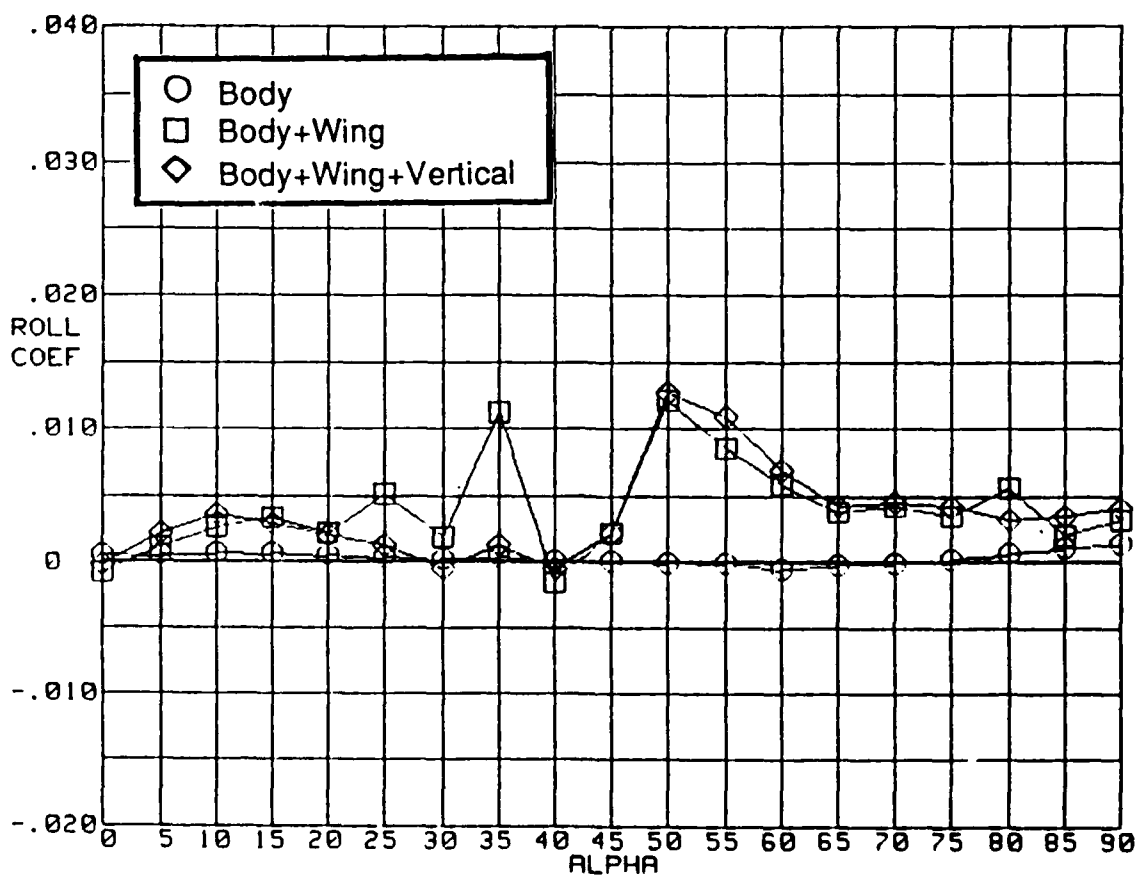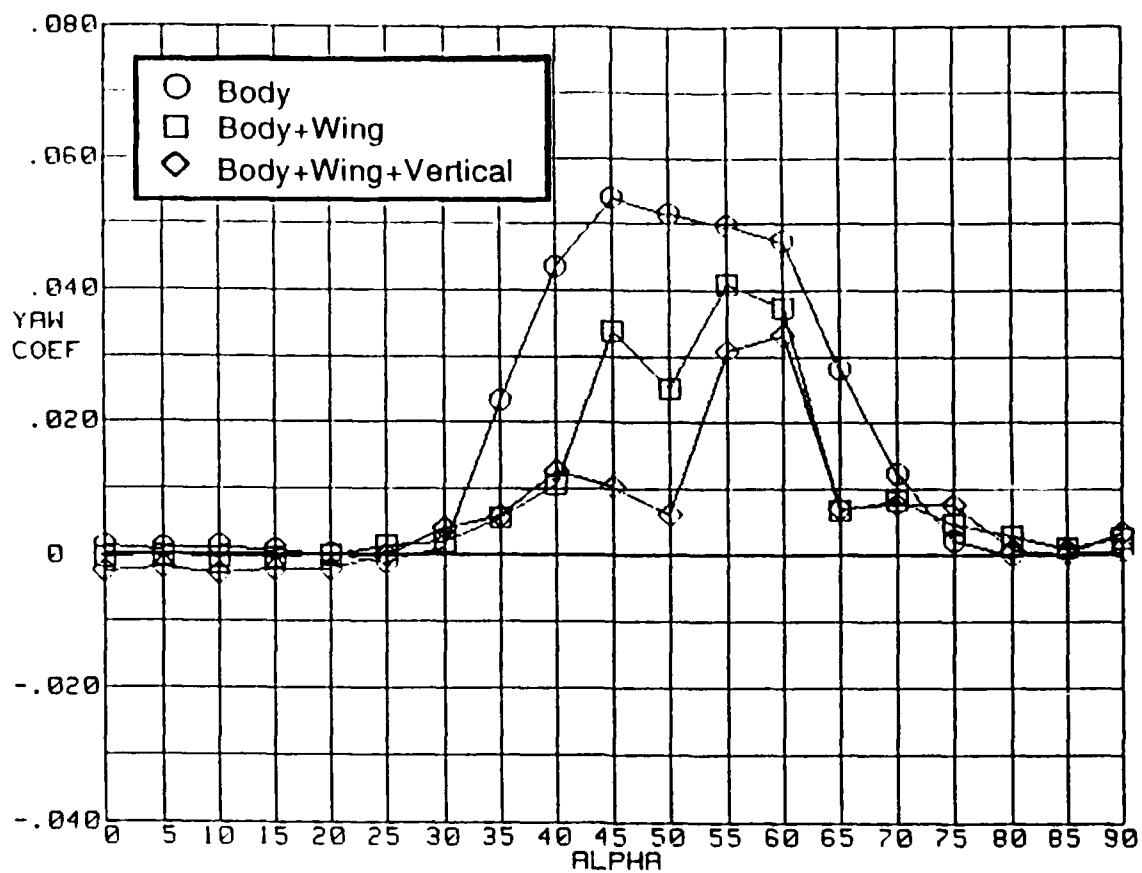
b) H/W=0.6 FR=5

Figure 34.- Continued
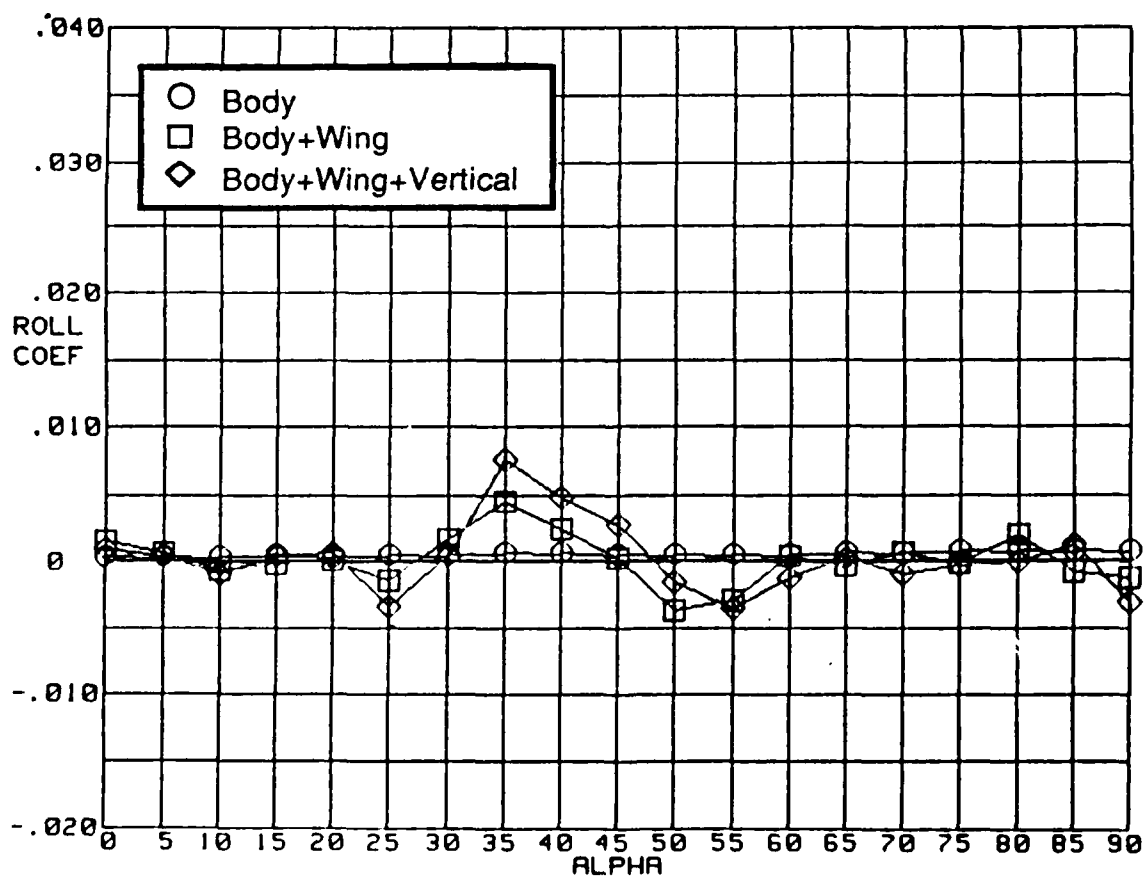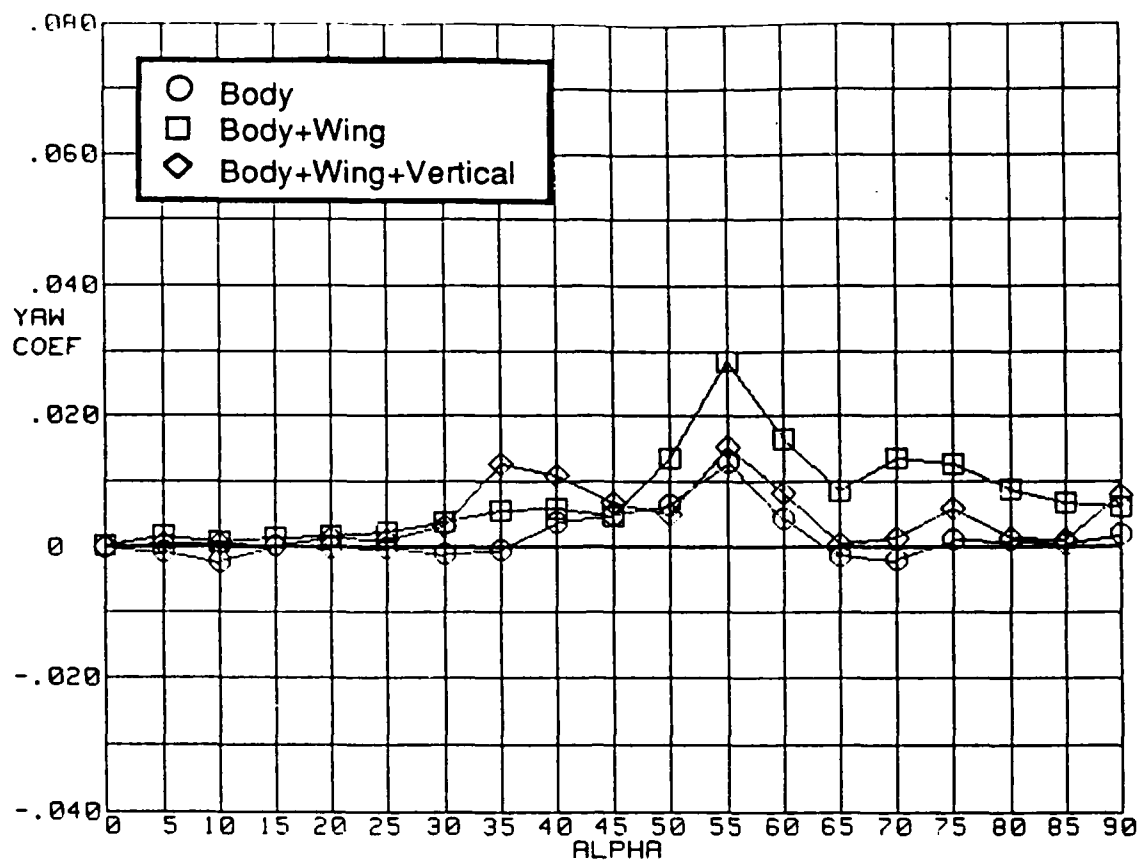
c) H/W=1.0 FR=2

Figure 34.- Continued

187
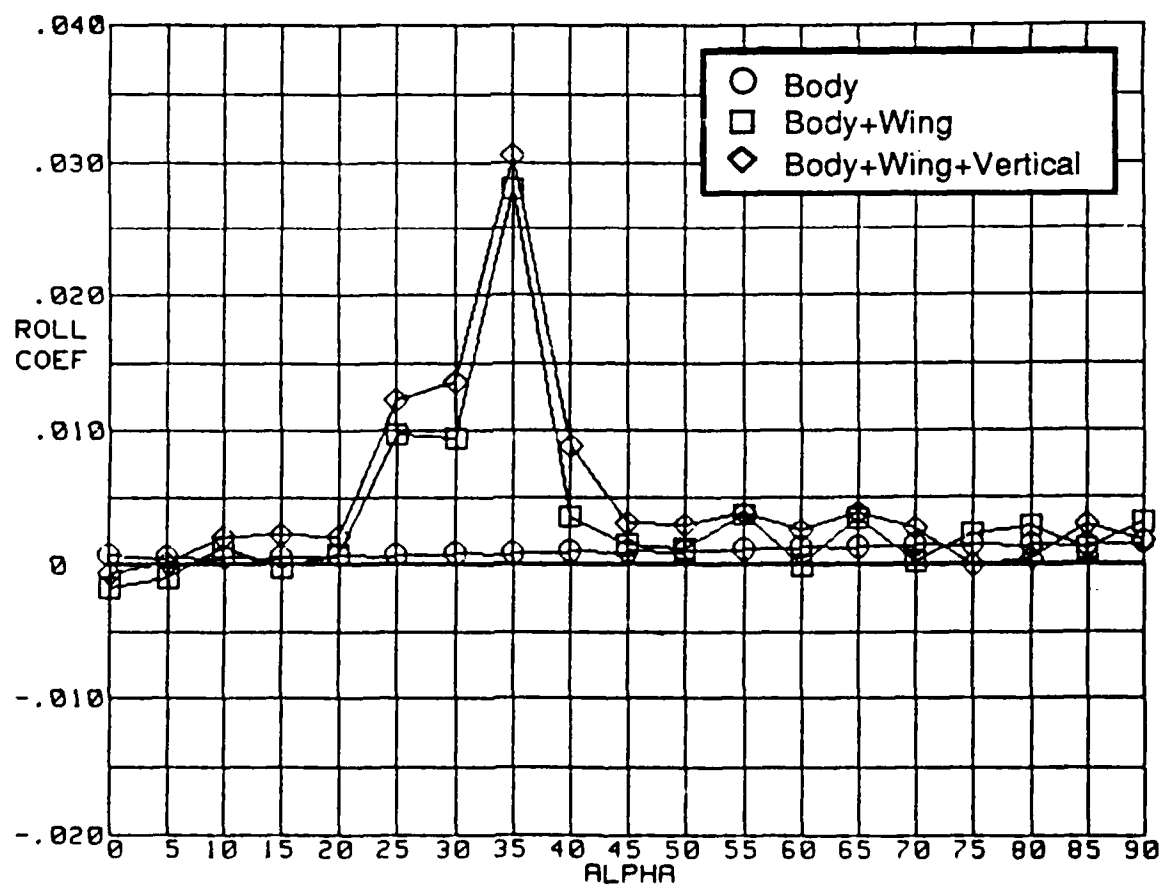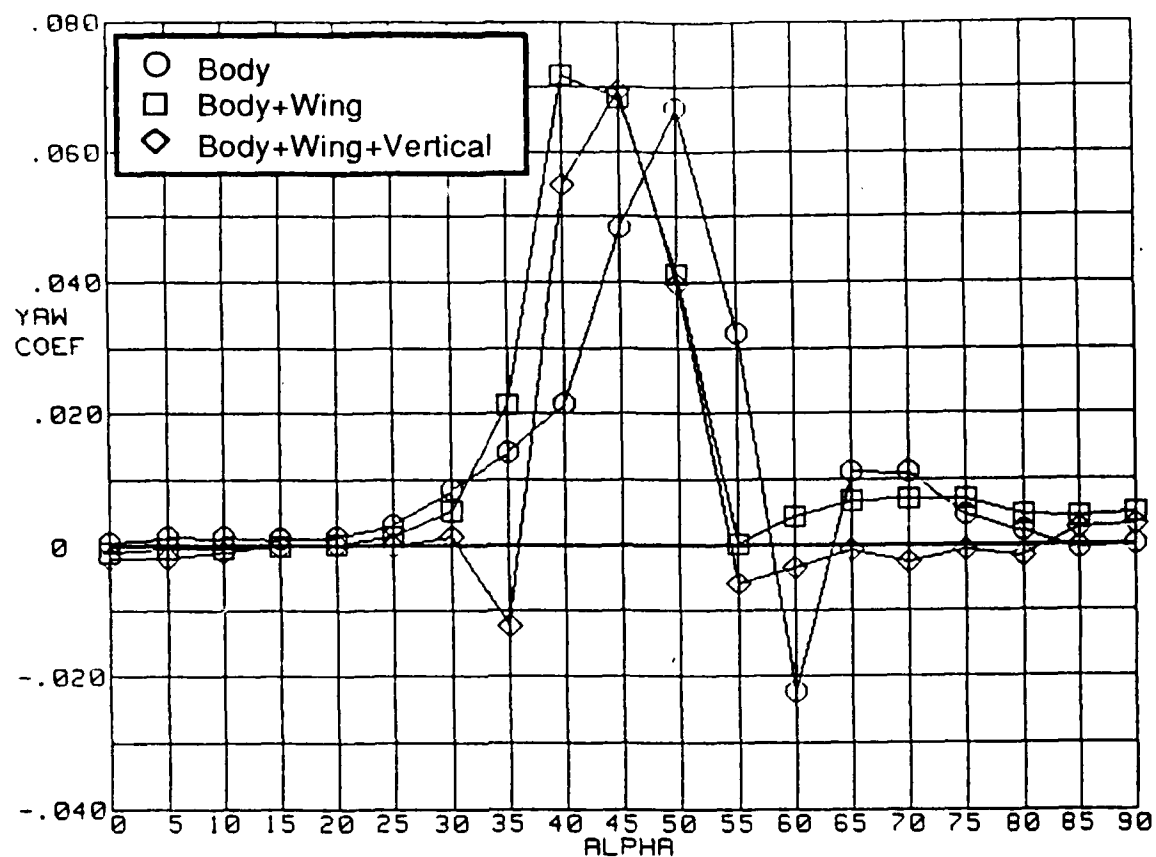
d) H/W=1.0 FR=5

Figure 34.- Concluded
188
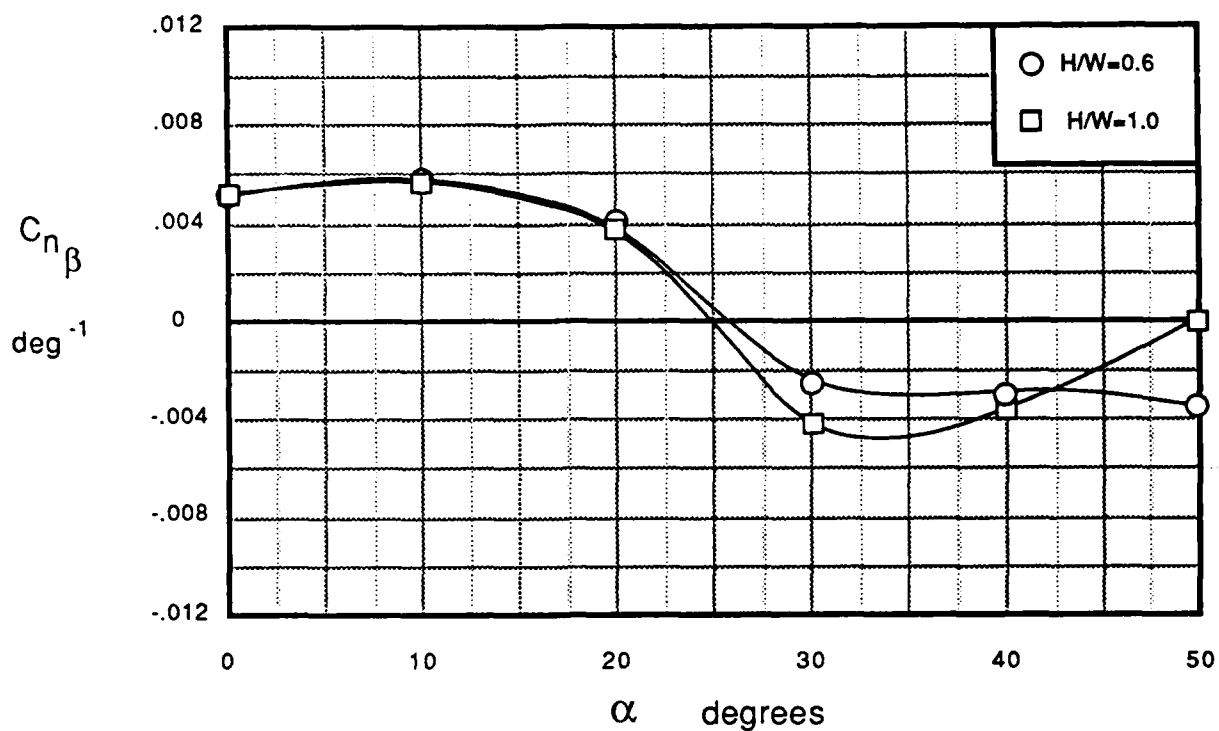
a) Fineness ratio = 2
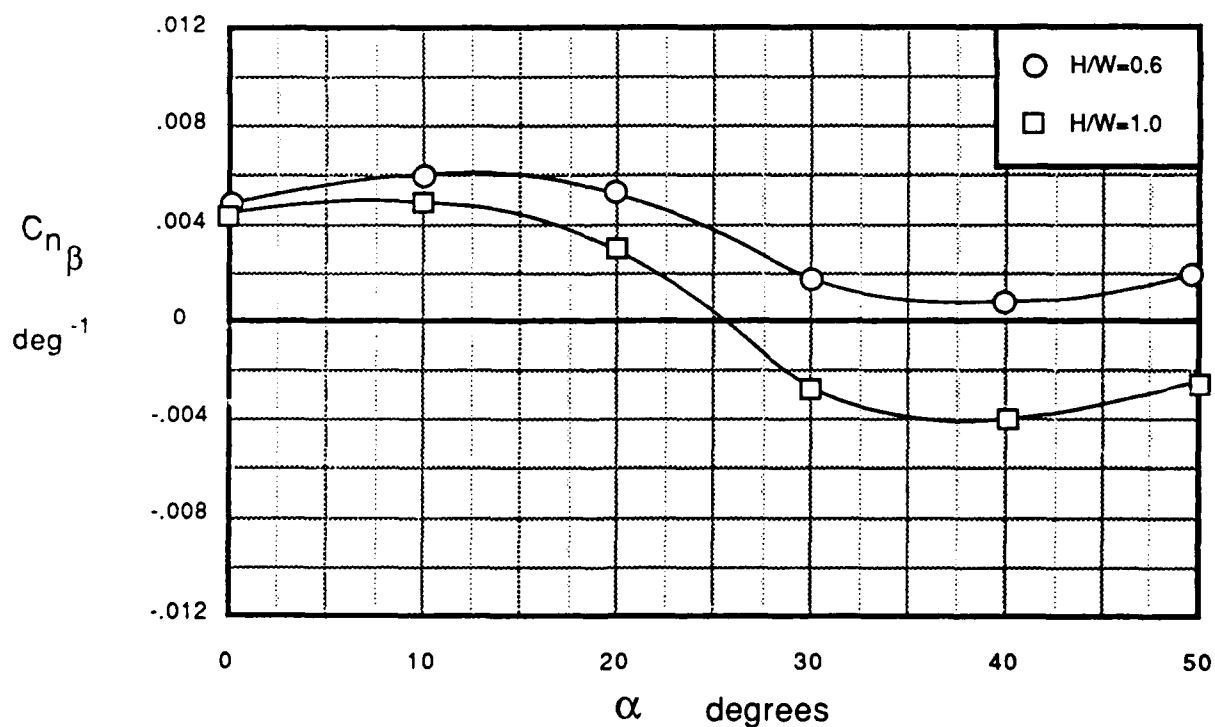
b) Fineness ratio = 5

Figure 35. - Influence of forebody cross-sectional shape in the presence of other airplane components on directional stability for specified fineness ratios

189
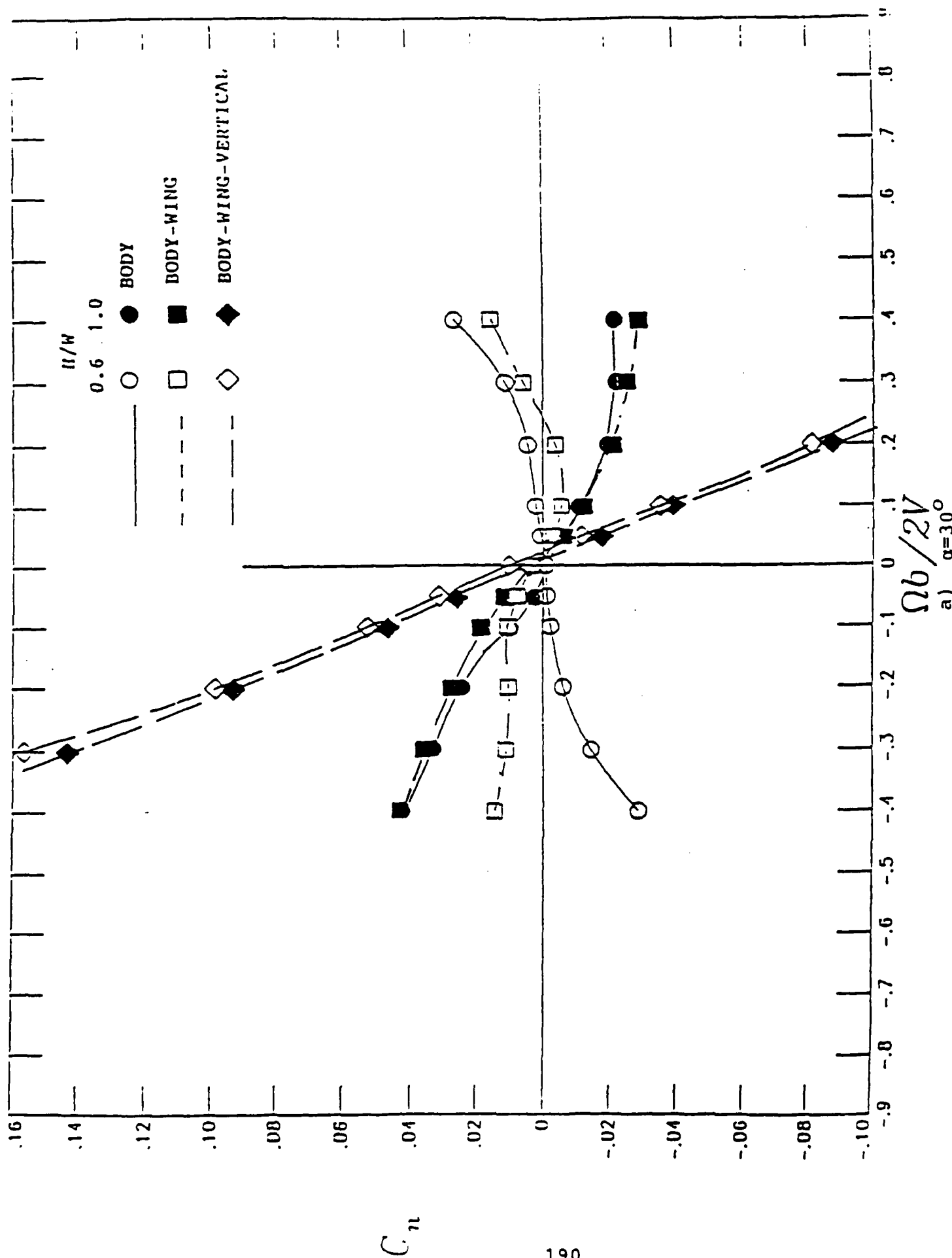
Figure 36.- Influence of forebody cross-sectional shape in the presence of other airplane components on the rotational yawing-moment coefficient characteristics for a FR=2 forebody

190

b) $\alpha = 50°$
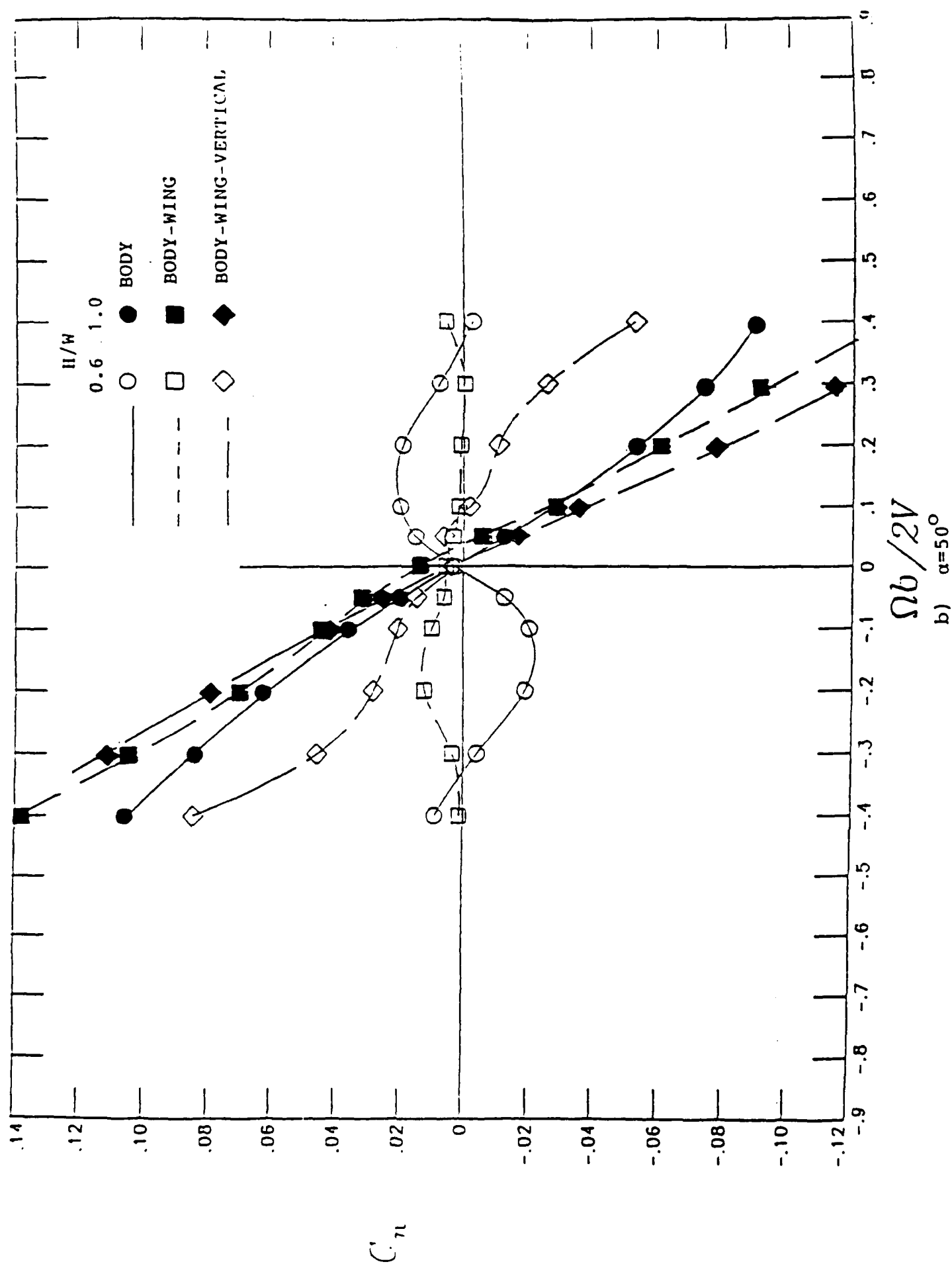
Figure 36.-- Continued

191
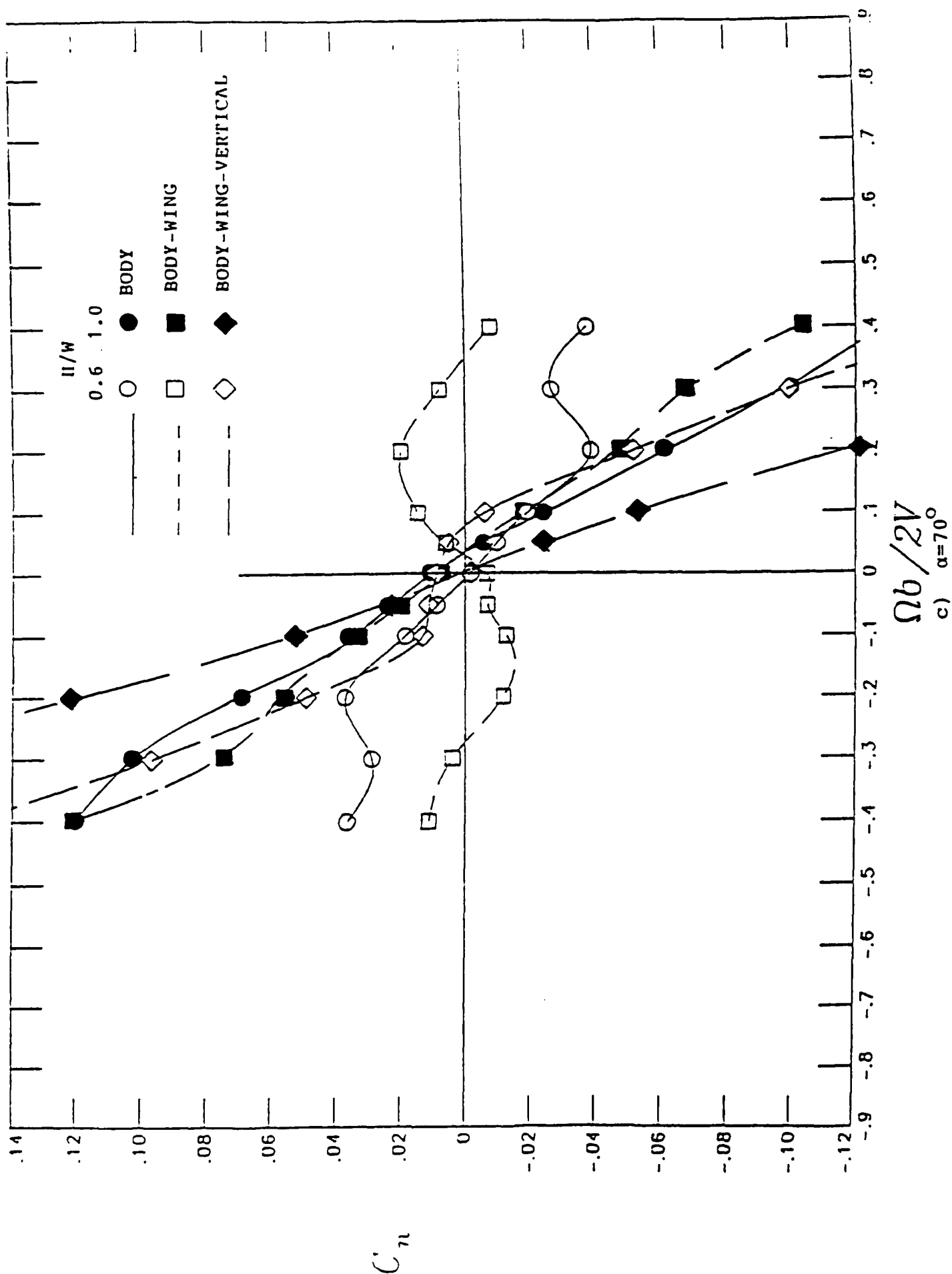
Figure 36.- Concluded

c) $\alpha = 70°$

$\dfrac{\Omega b}{2V}$

C_n
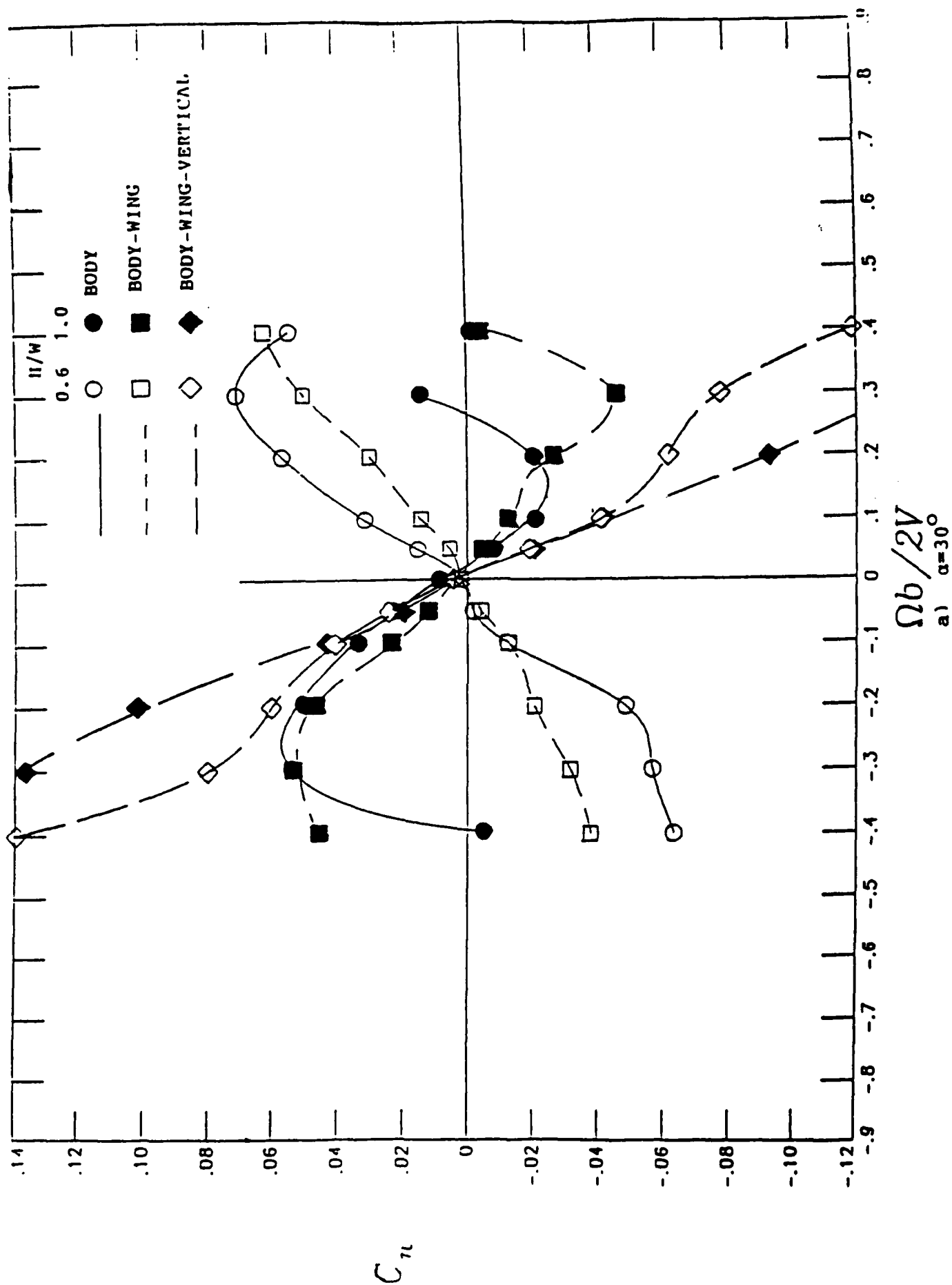
Figure 37.- Influence of forebody cross-sectional shape in the presence of other airplane components on the rotational yawing-moment coefficient characteristics for a FR=5 forebody

a) $\alpha=30°$

193
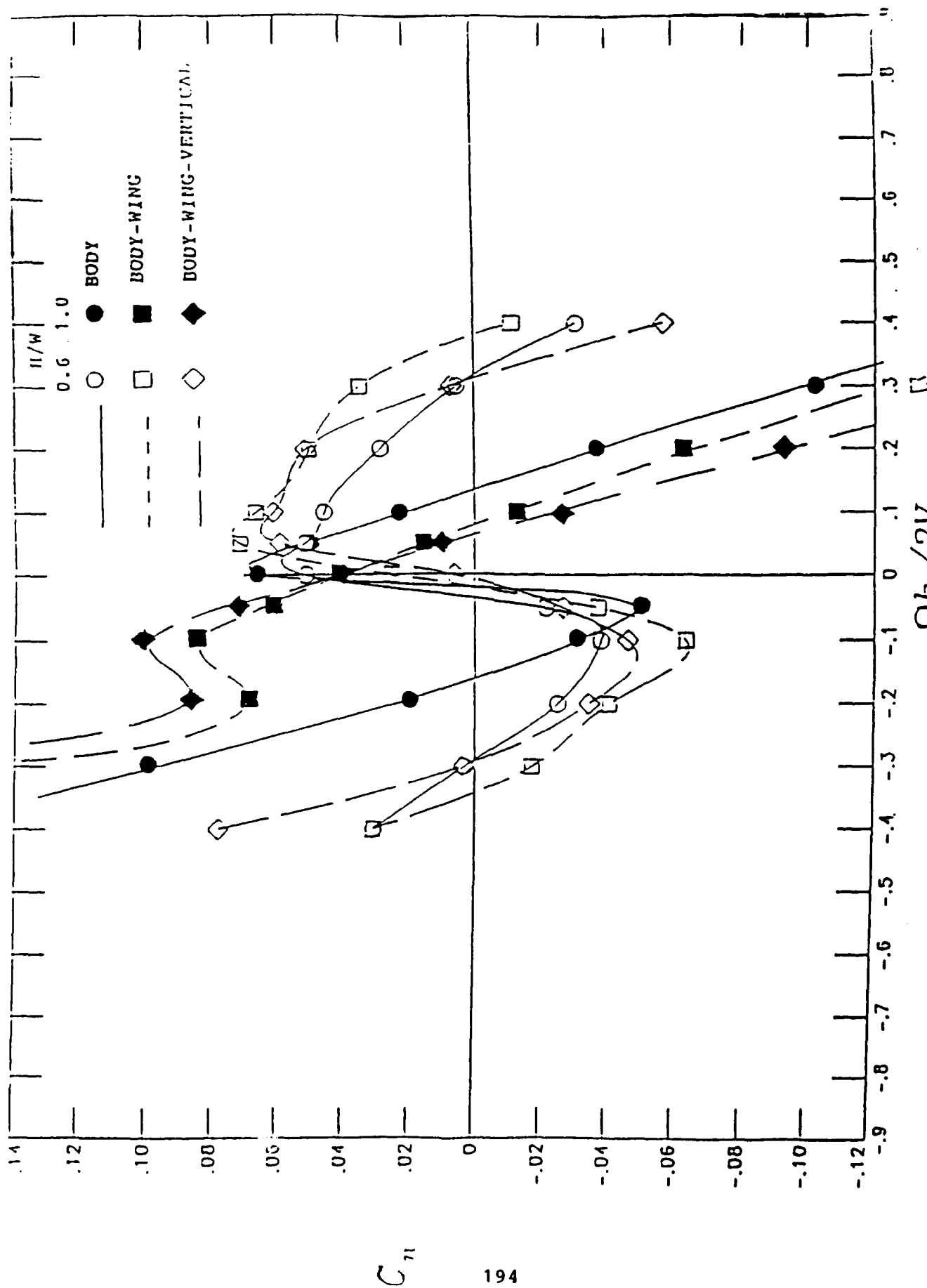
b) $\alpha = 50°$

Figure 37.- Continued

194
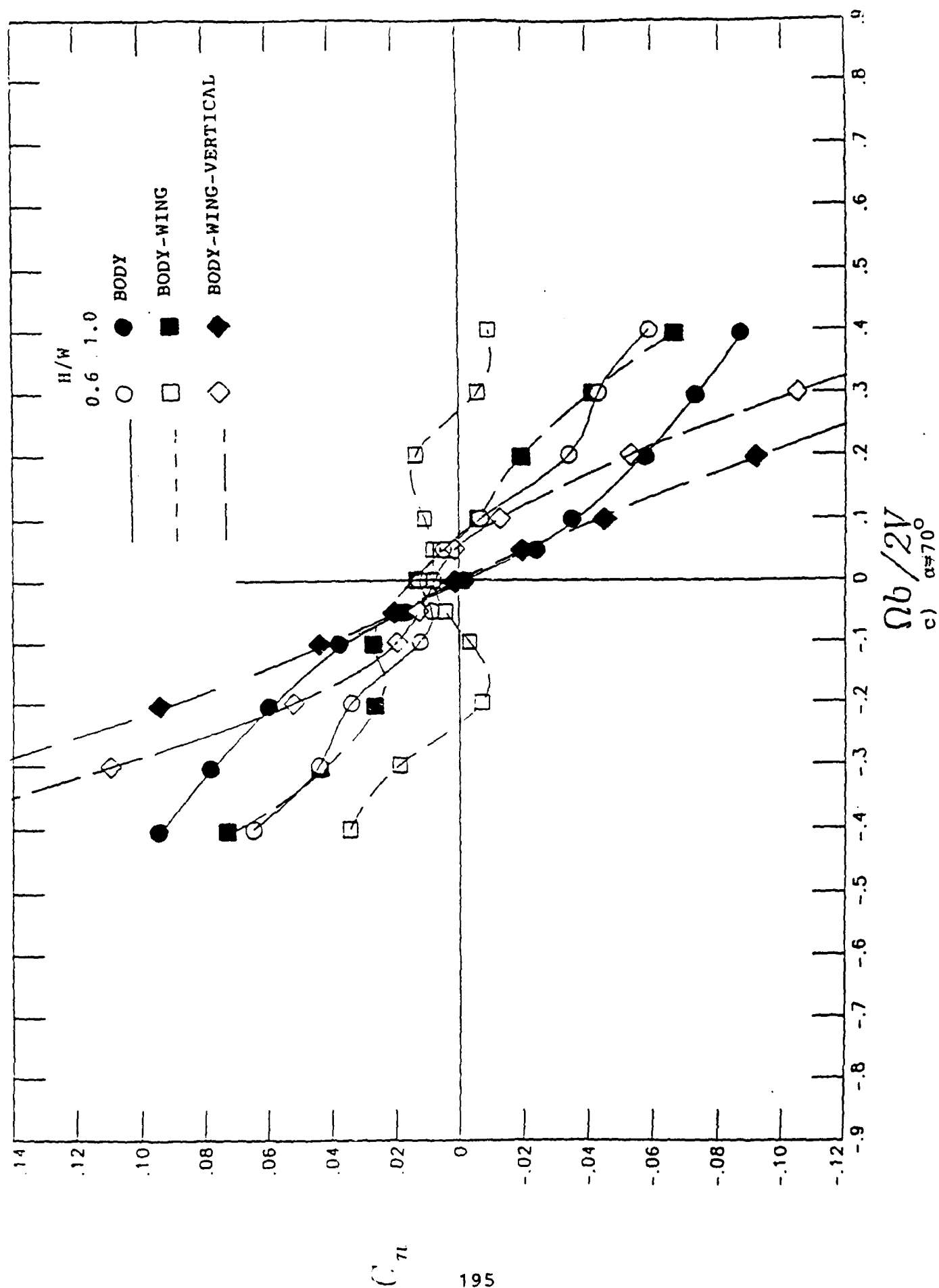
Figure 37.- Concluded

c) $\alpha = 70°$

$\Omega b / 2V$

C_{7l}

195
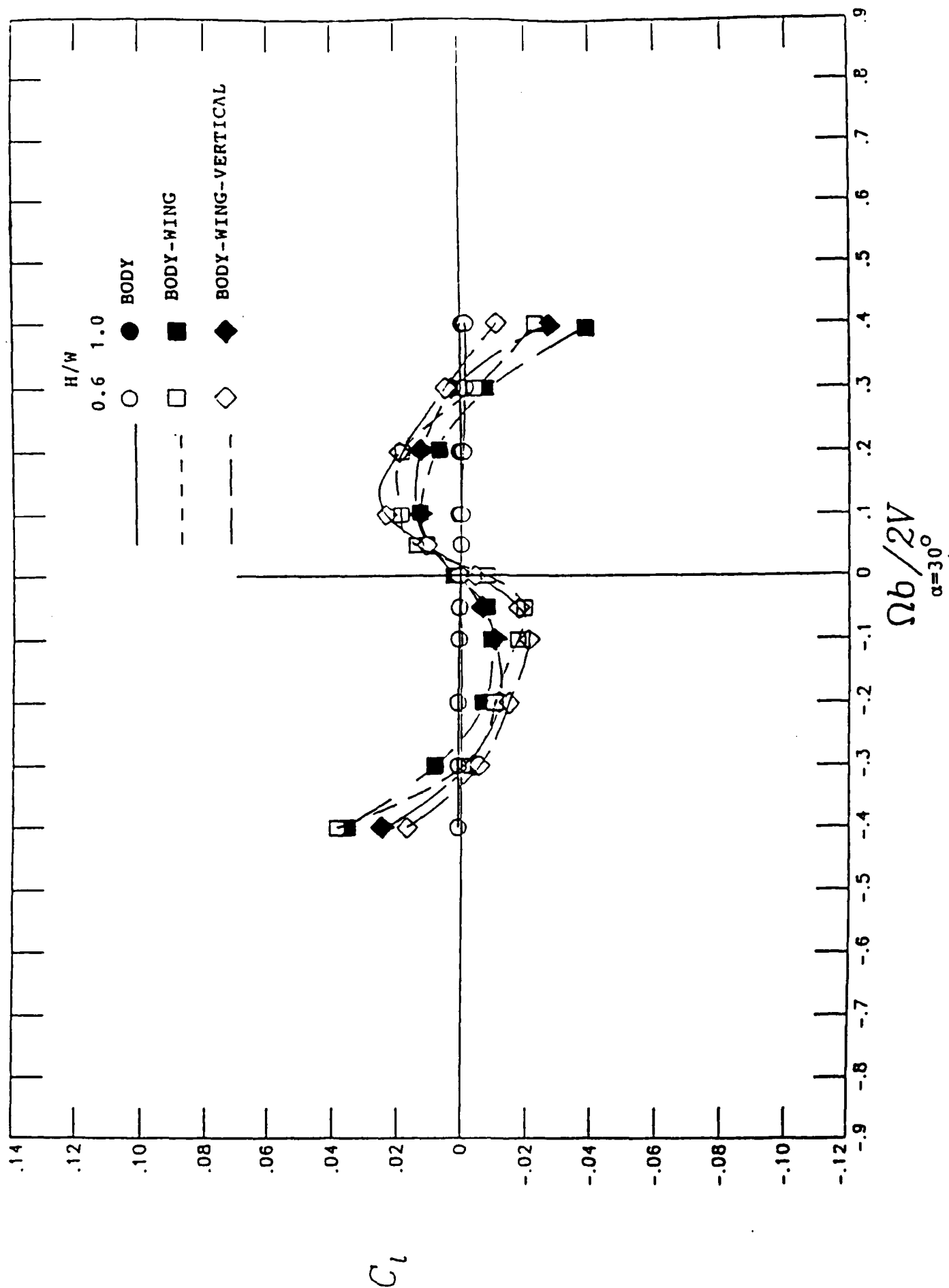
Figure 38.- Influence of forebody cross-sectional shape in the presence of other airplane components on the rotational rolling-moment coefficient characteristics for a FR=2 forebody
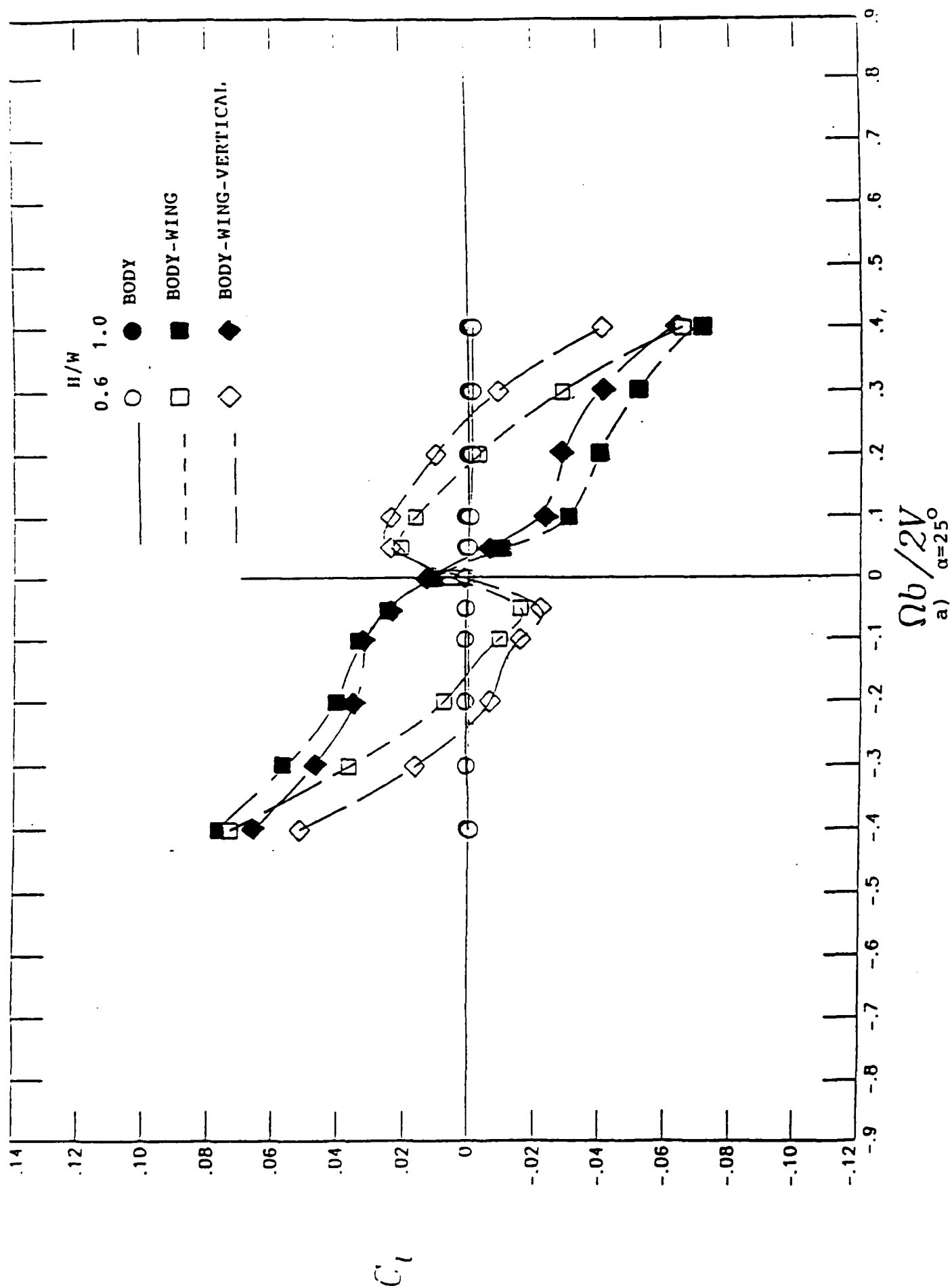
Figure 39.- Influence of forebody cross-sectional shape in the presence of other airplane components on the rotational rolling-moment coefficient characteristics for a FR=5 forebody

197

b) $\alpha = 30°$
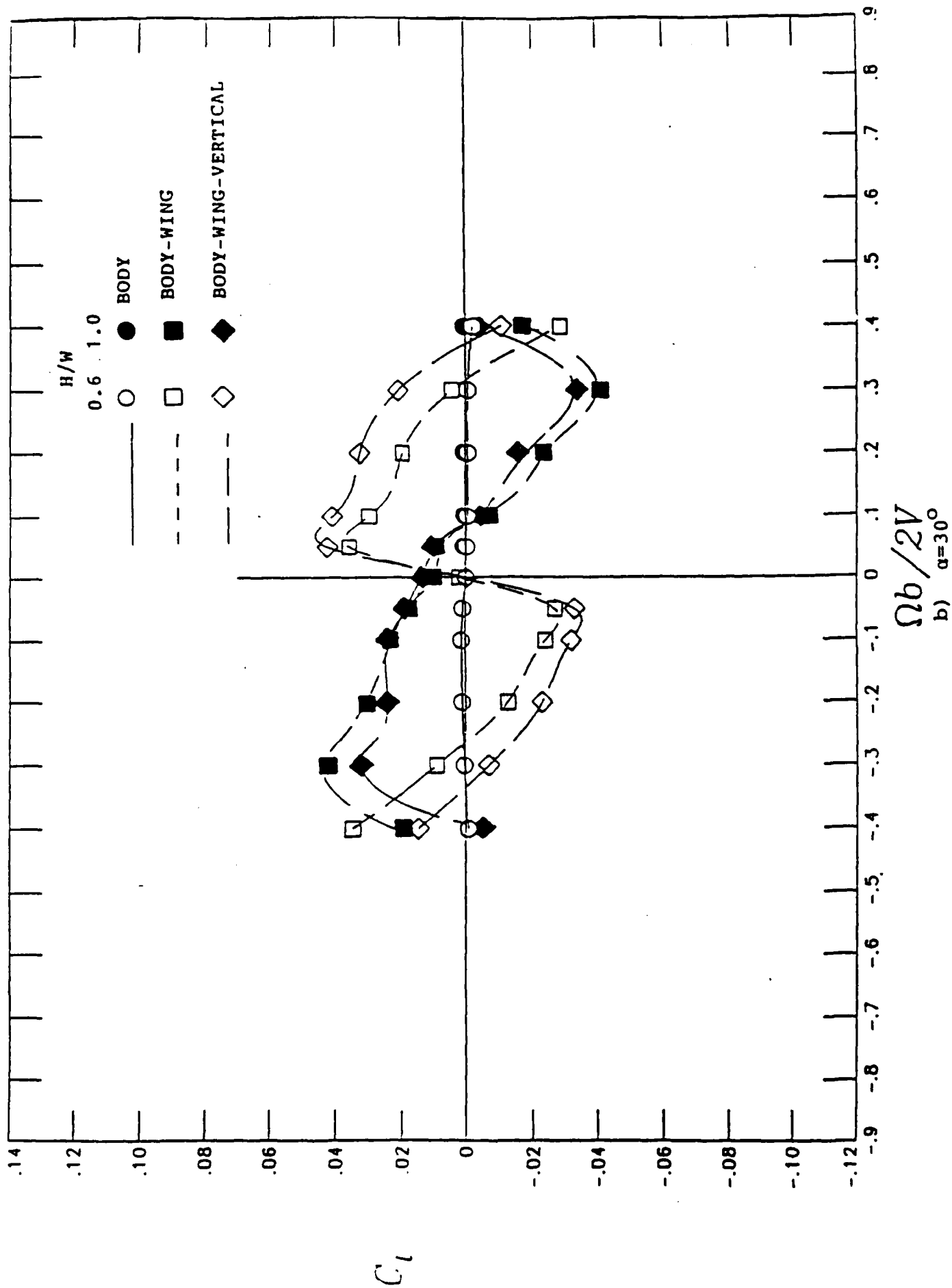
Figure 39.– Continued

198
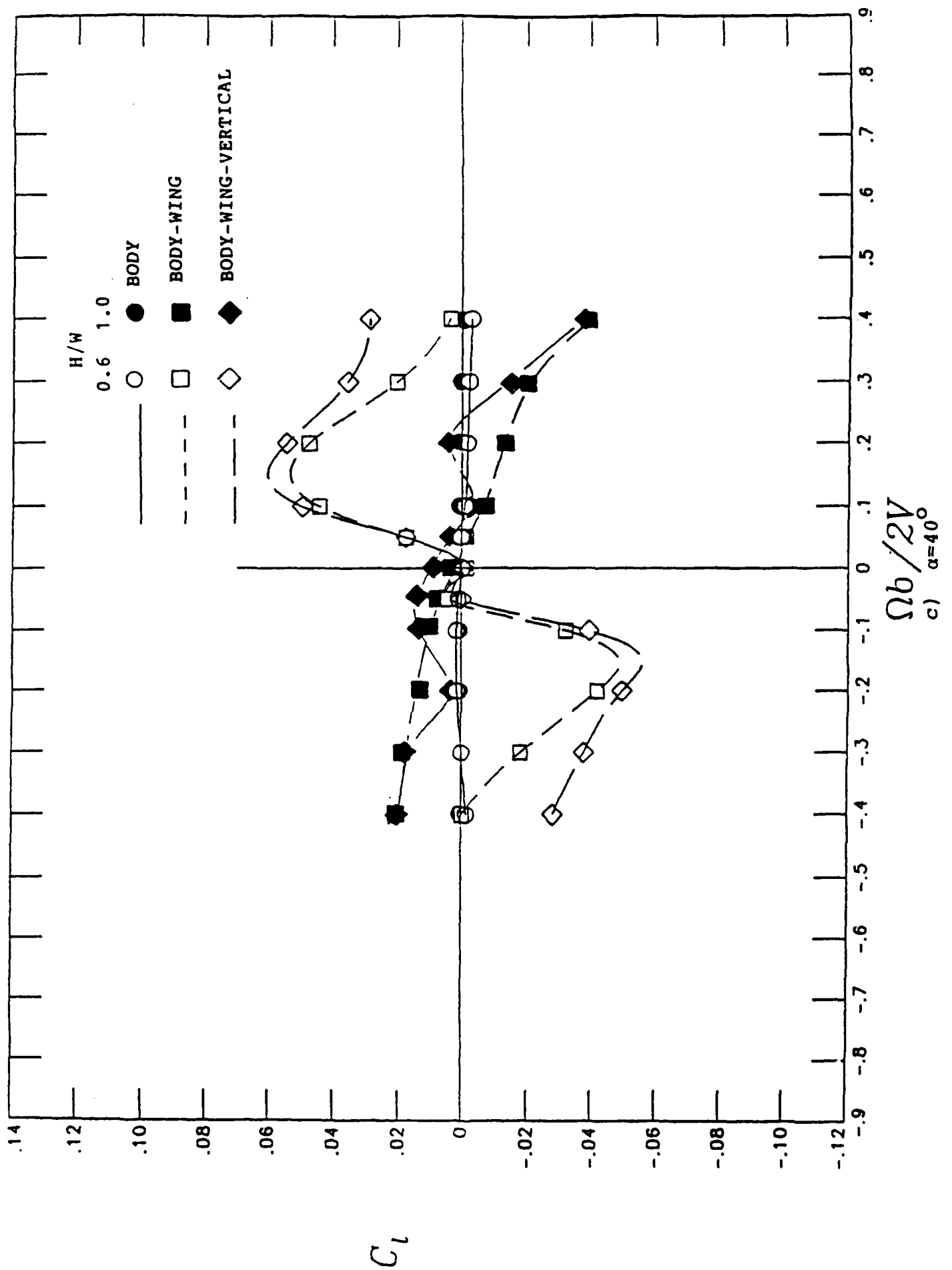
Figure 39.- Concluded

c) $\alpha = 40°$

$\Omega b / 2V$

C_l

199

Figure 40.- Effect of blunting H/W=0.6 cross-sectional forebodies on the lift and normal-force coefficient variation with angle of attack

a)   FR=5 blunted to 4.5

200
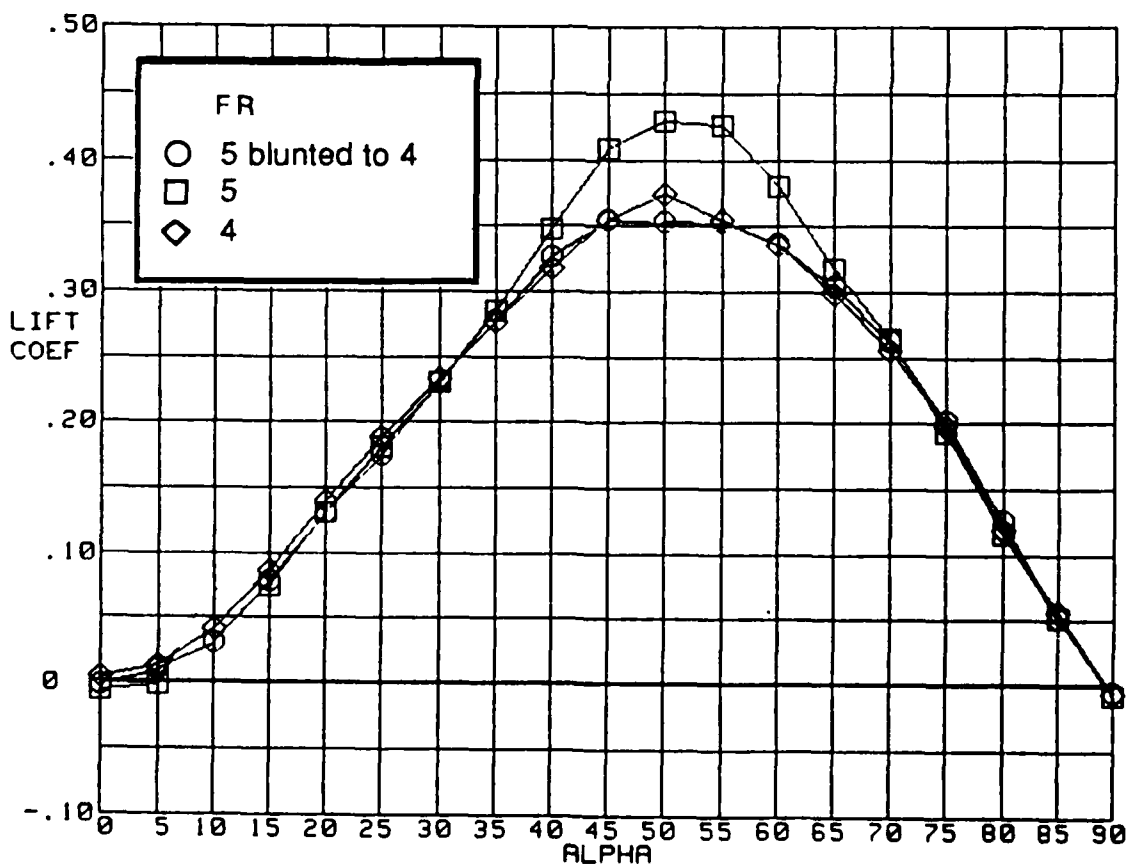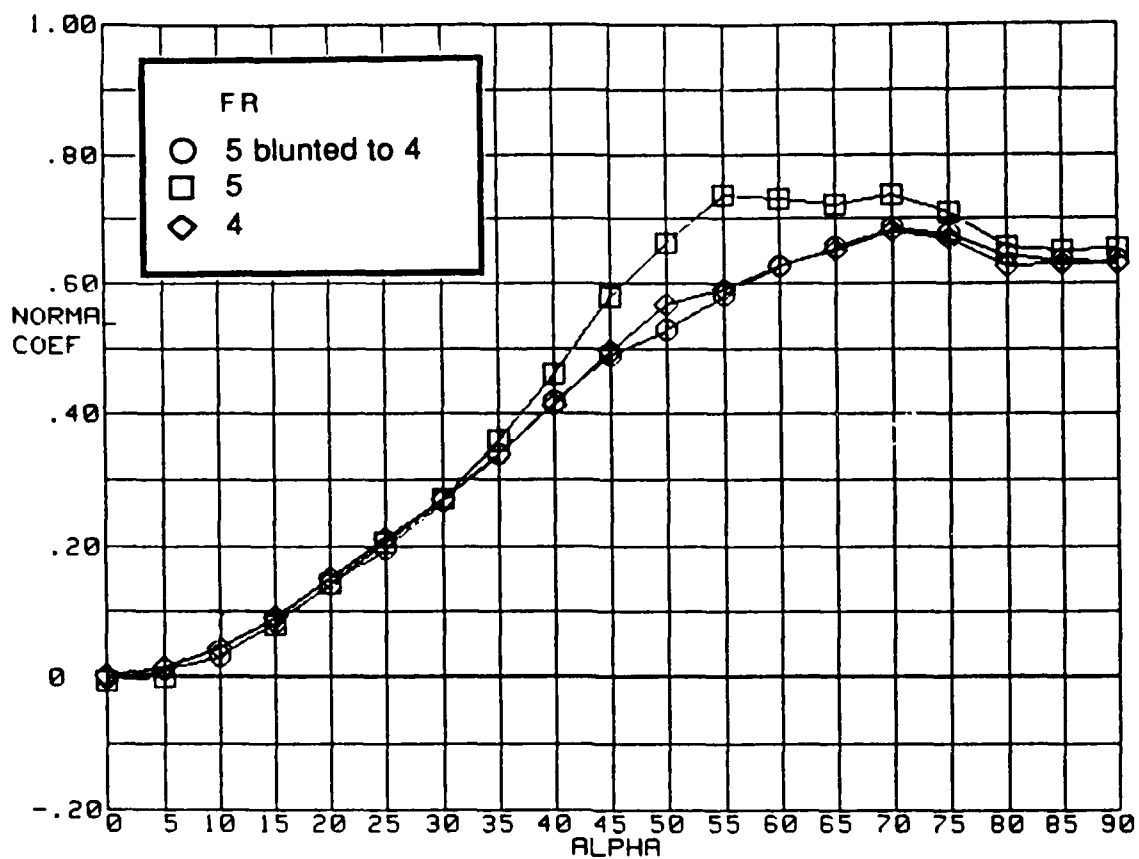
b) FR=5 blunted to 4

Figure 40.- Continued

201
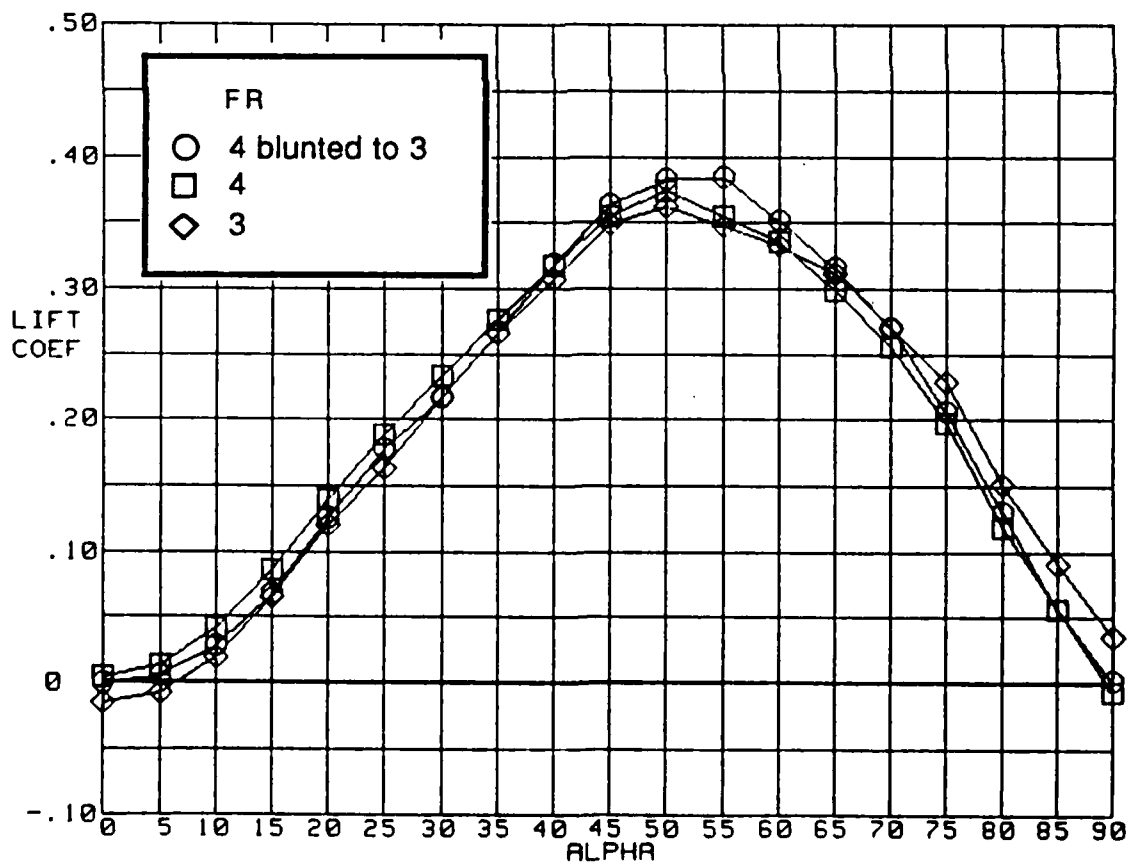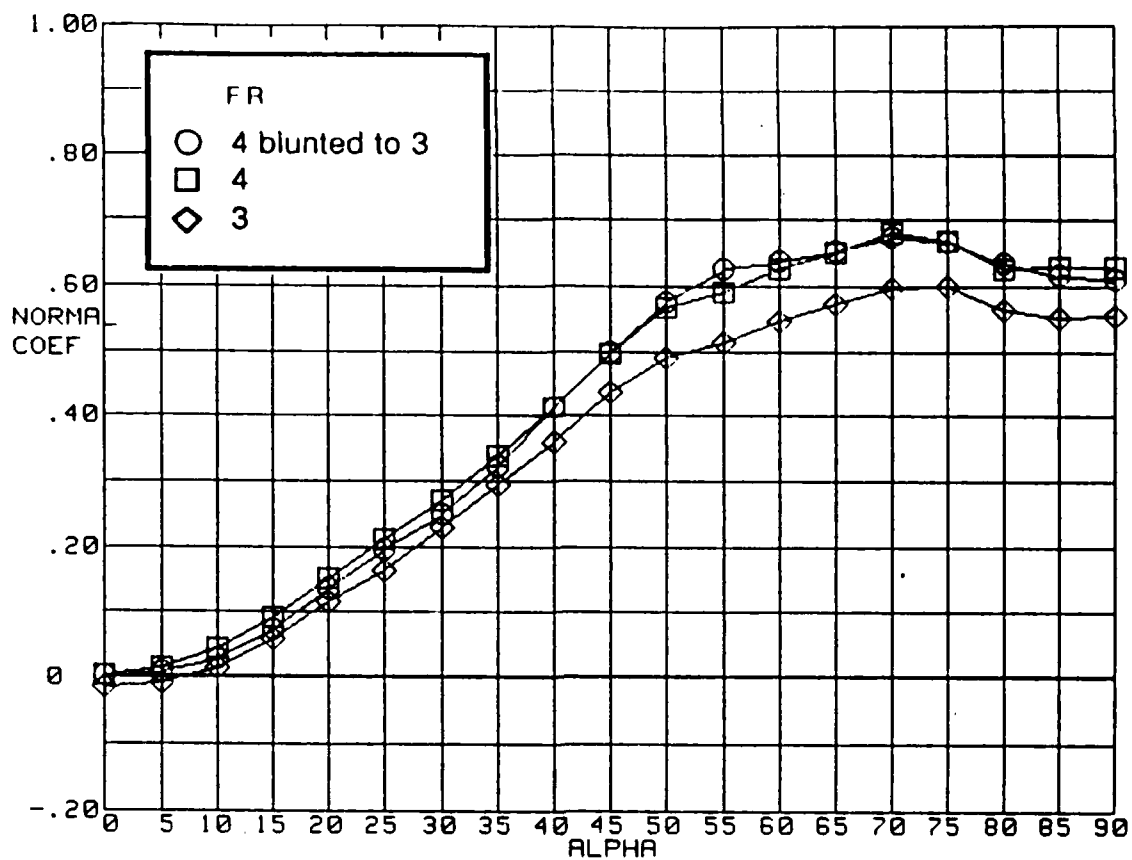
c) FR=4 blunted to 3

Figure 40.- Concluded

202
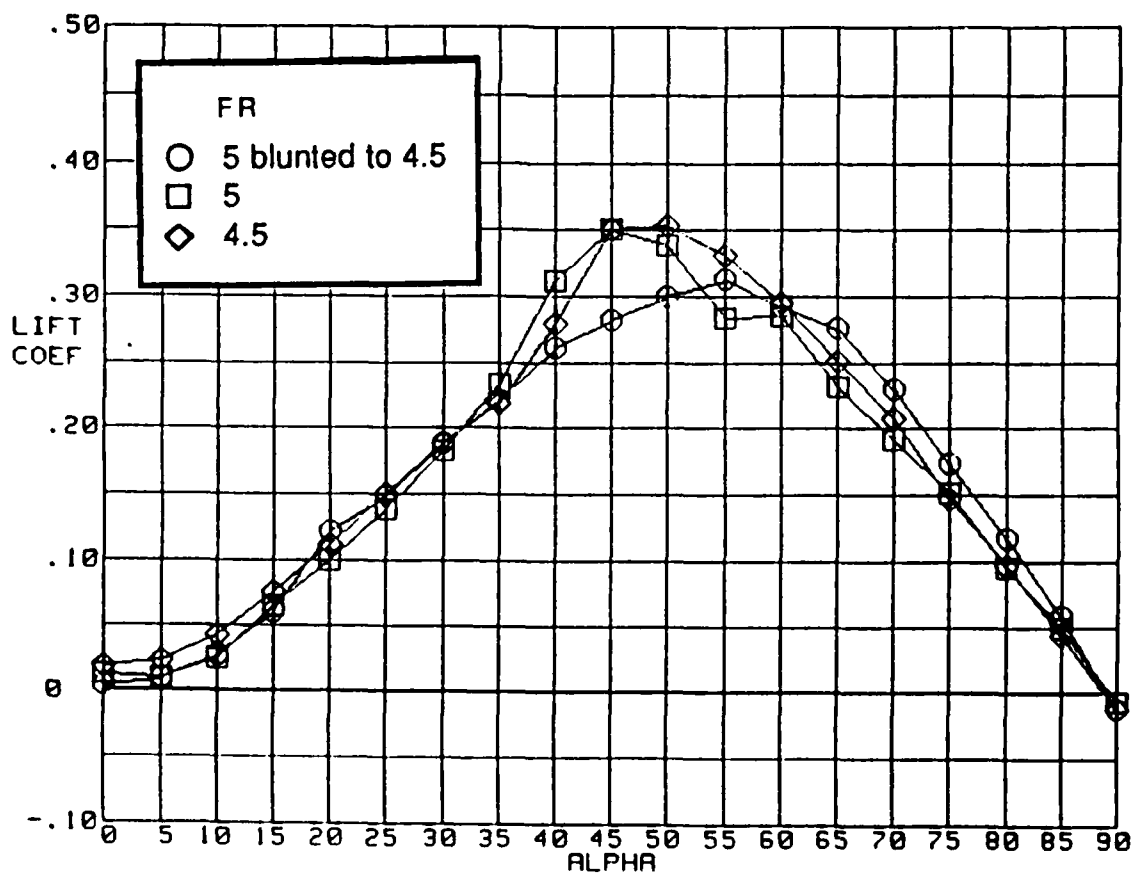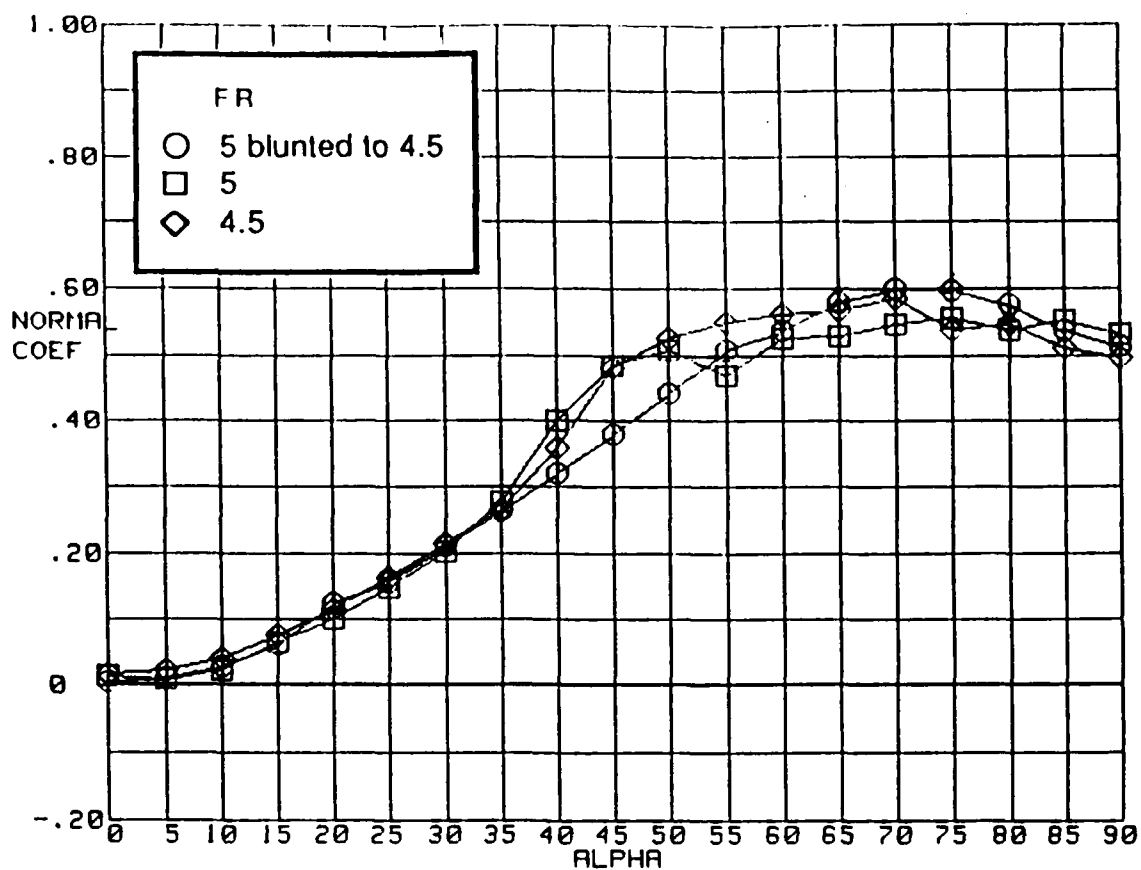
a)   FR=5 blunted to 4.5

Figure 41.- Effect of blunting H/W=0.8 cross-sectional forebodies on
the lift and normal-force coefficient variation with
angle of attack

203
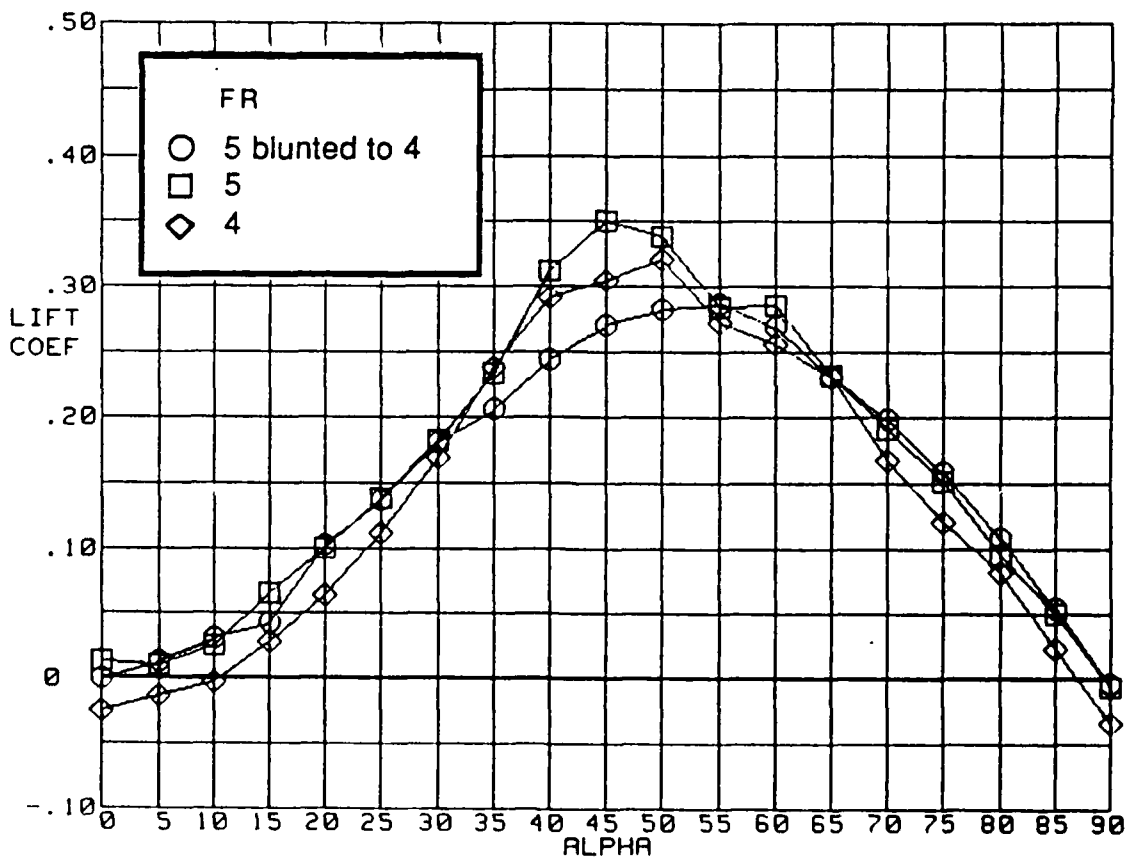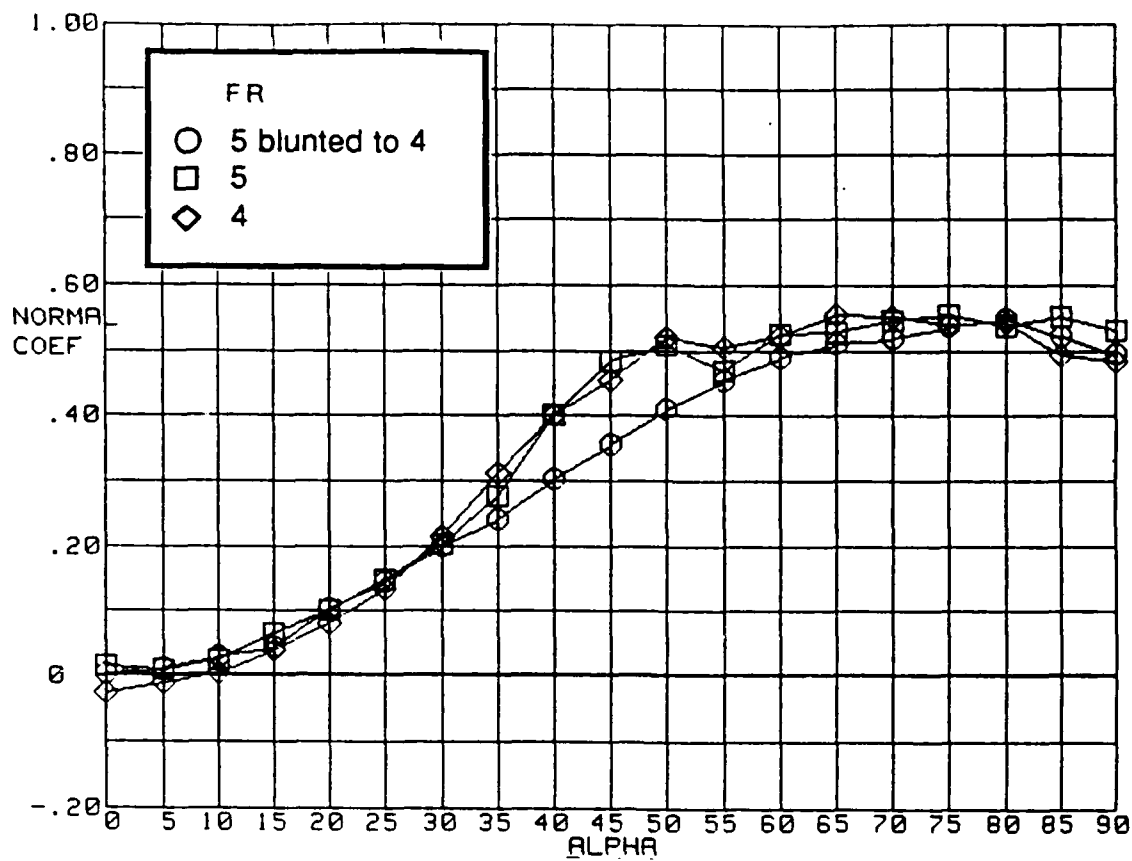
b) FR=5 blunted to 4

Figure 41.- Continued

204
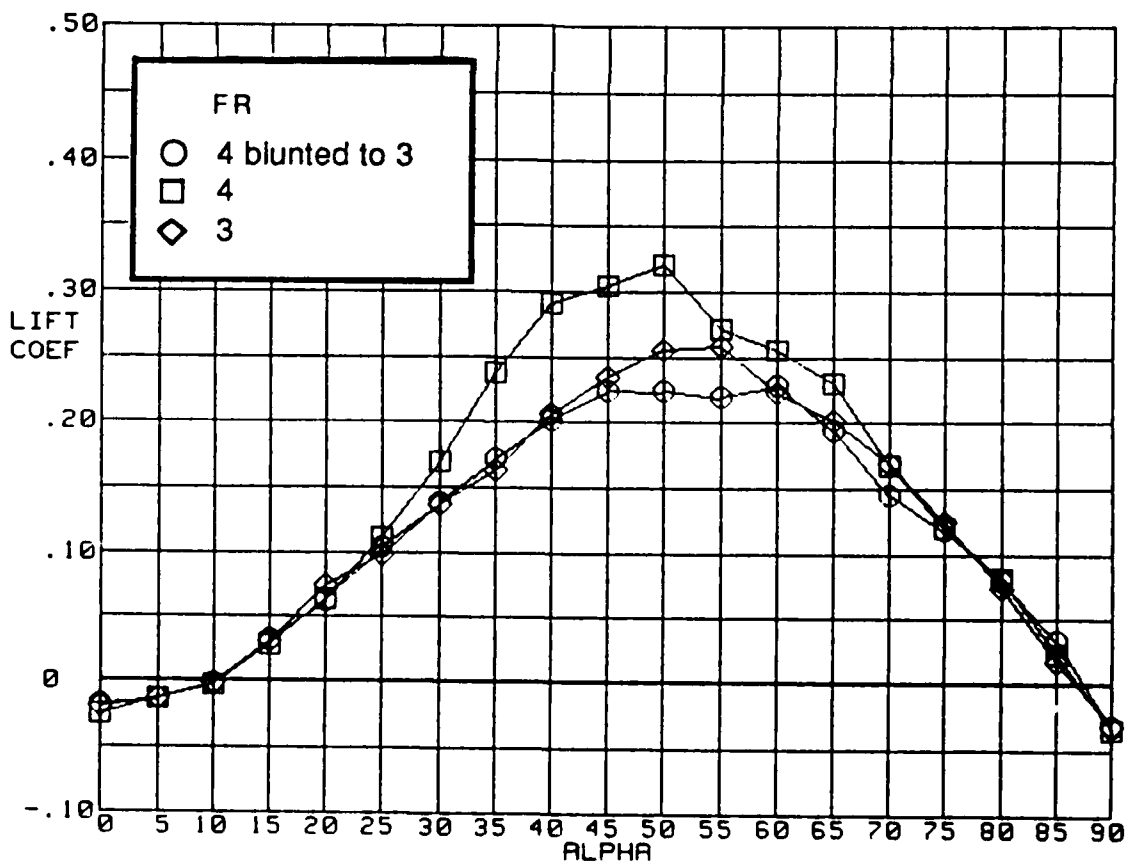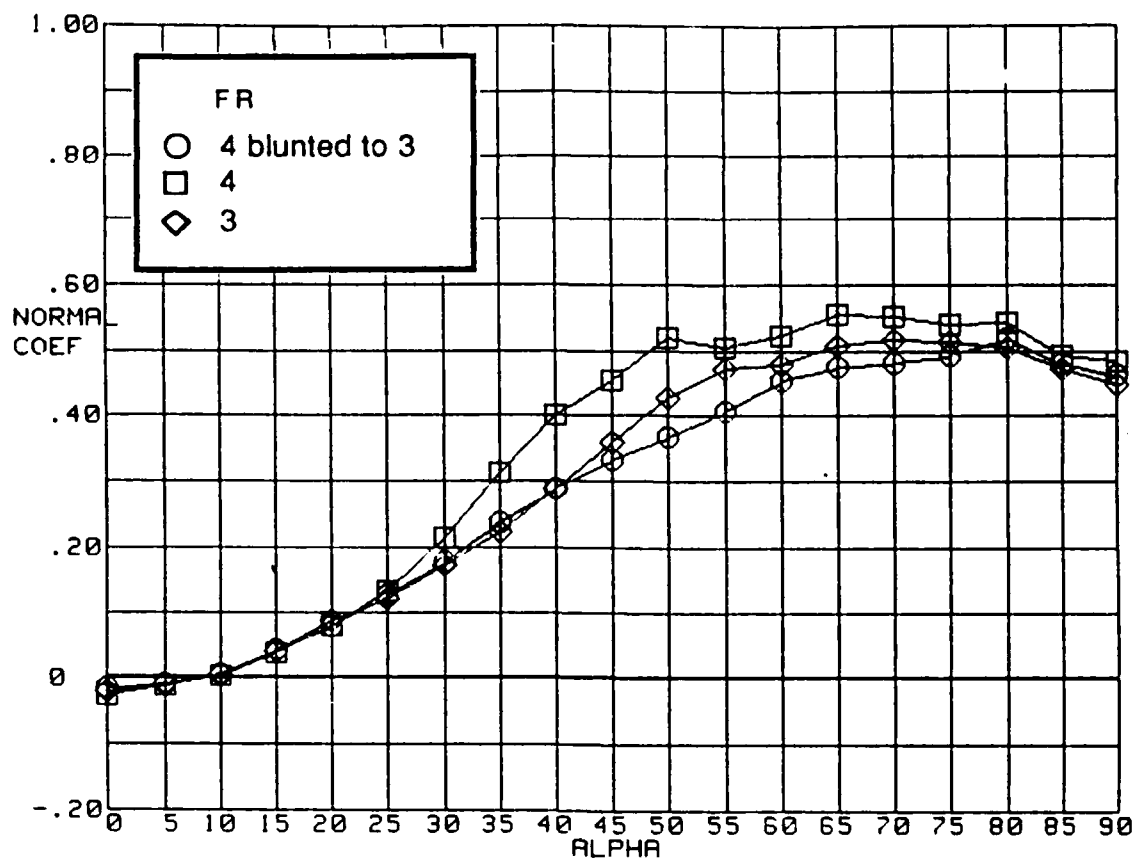
c) FR=4 blunted to 3

Figure 41.- Concluded

205
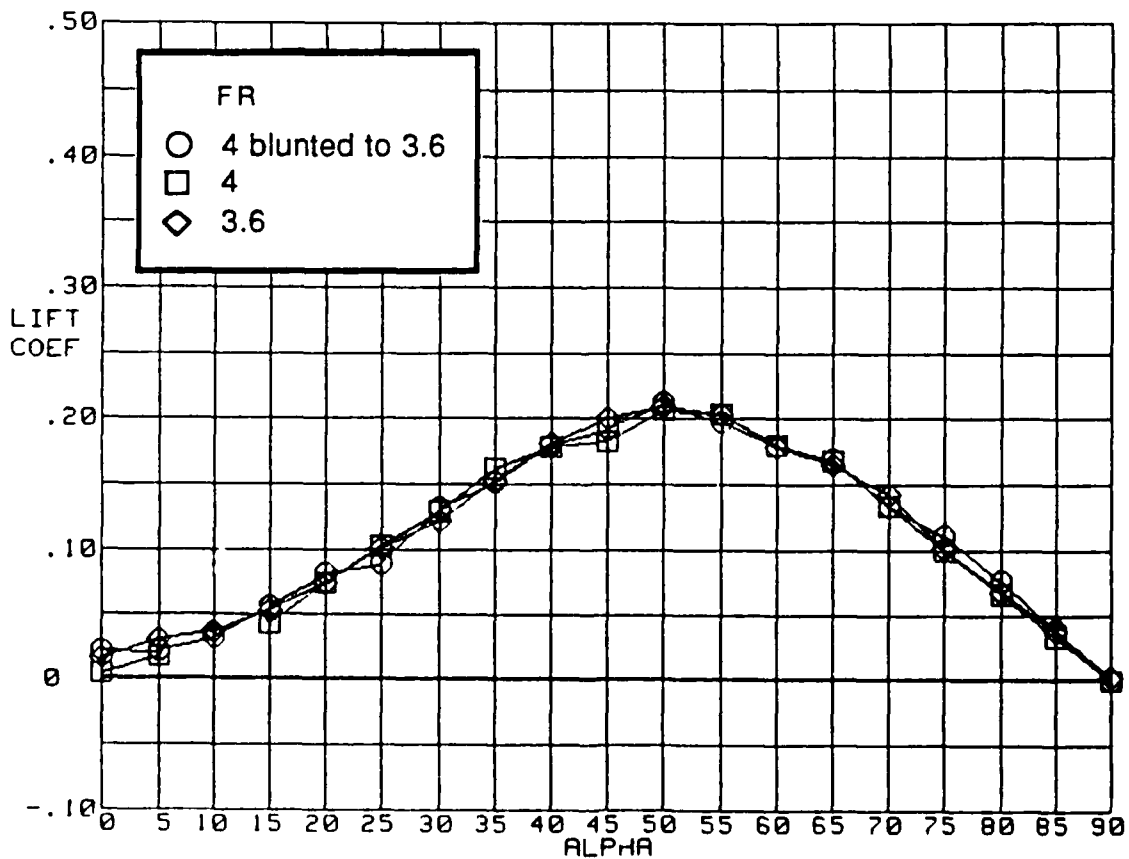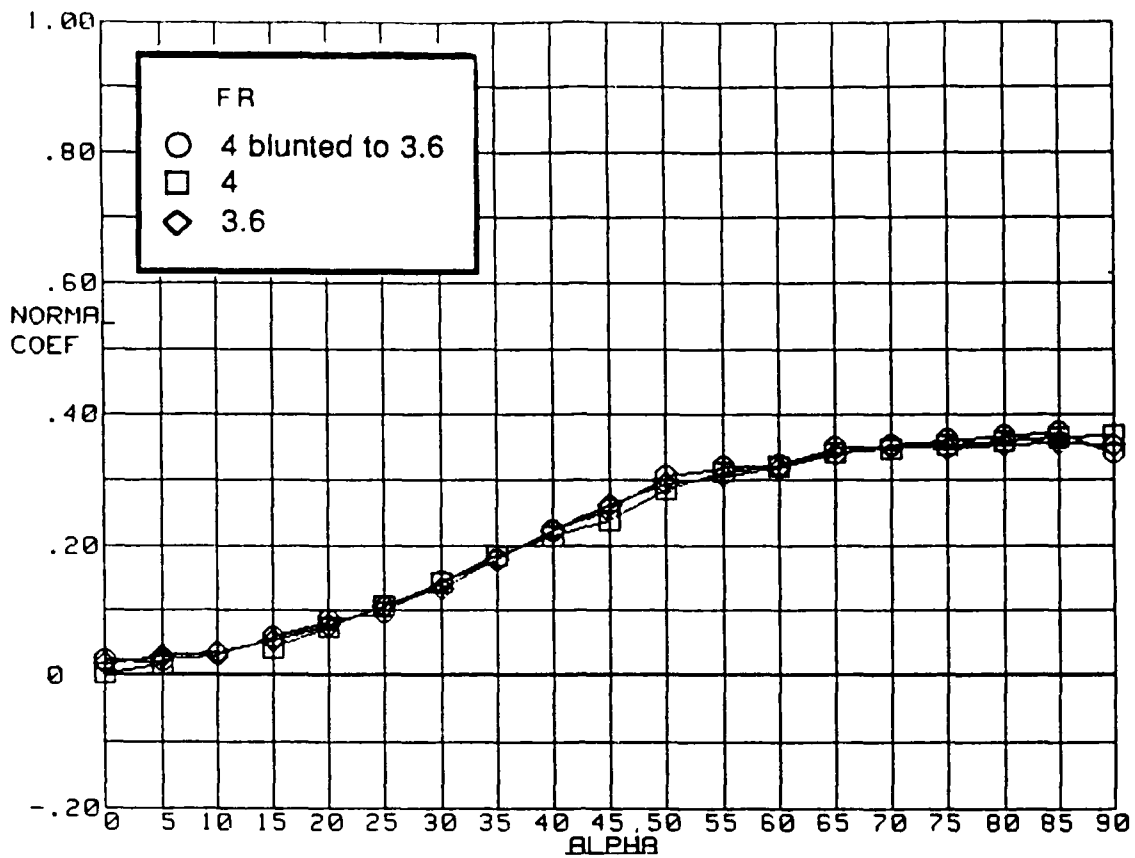
a)   FR=4 blunted to 3.6

Figure 42.- Effect of blunting H/W=1.25 cross-sectional forebodies
on the lift and normal-force coefficient variation with
angle of attack

206
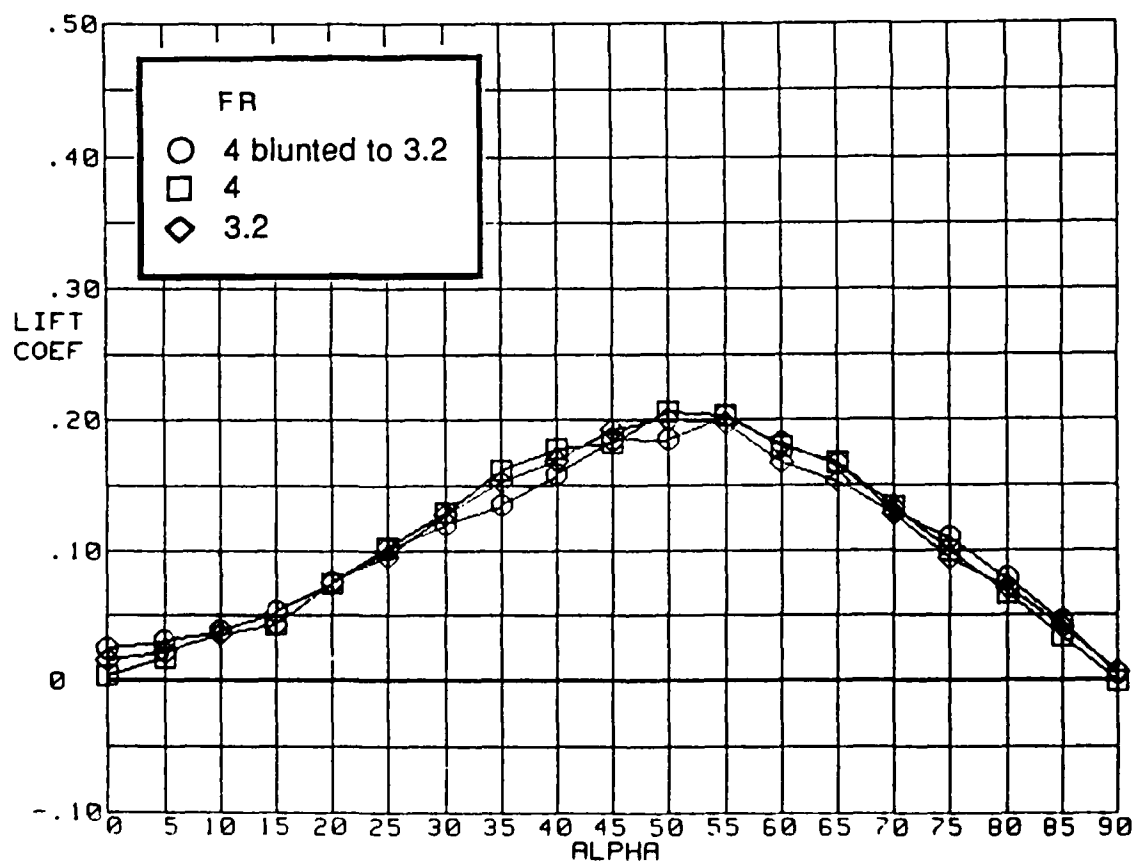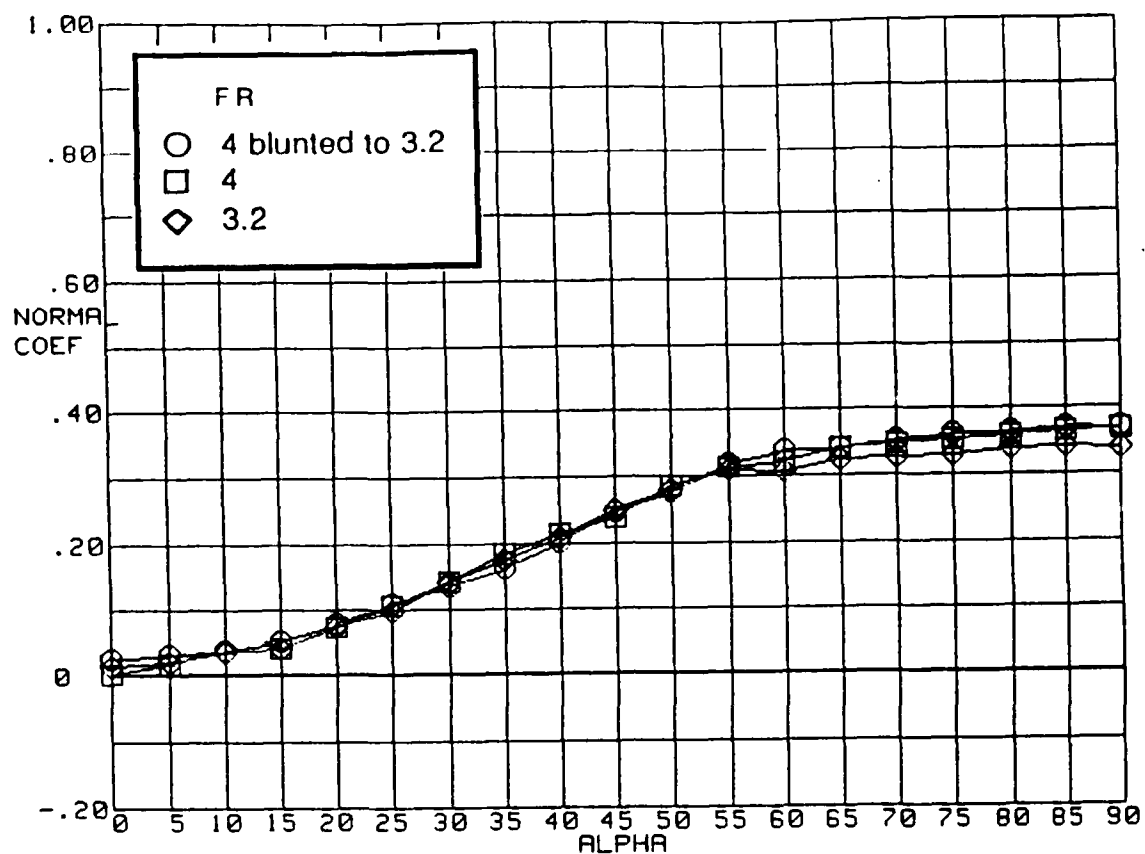
b)   FR=4 blunted to 3.2

Figure 42.- Continued
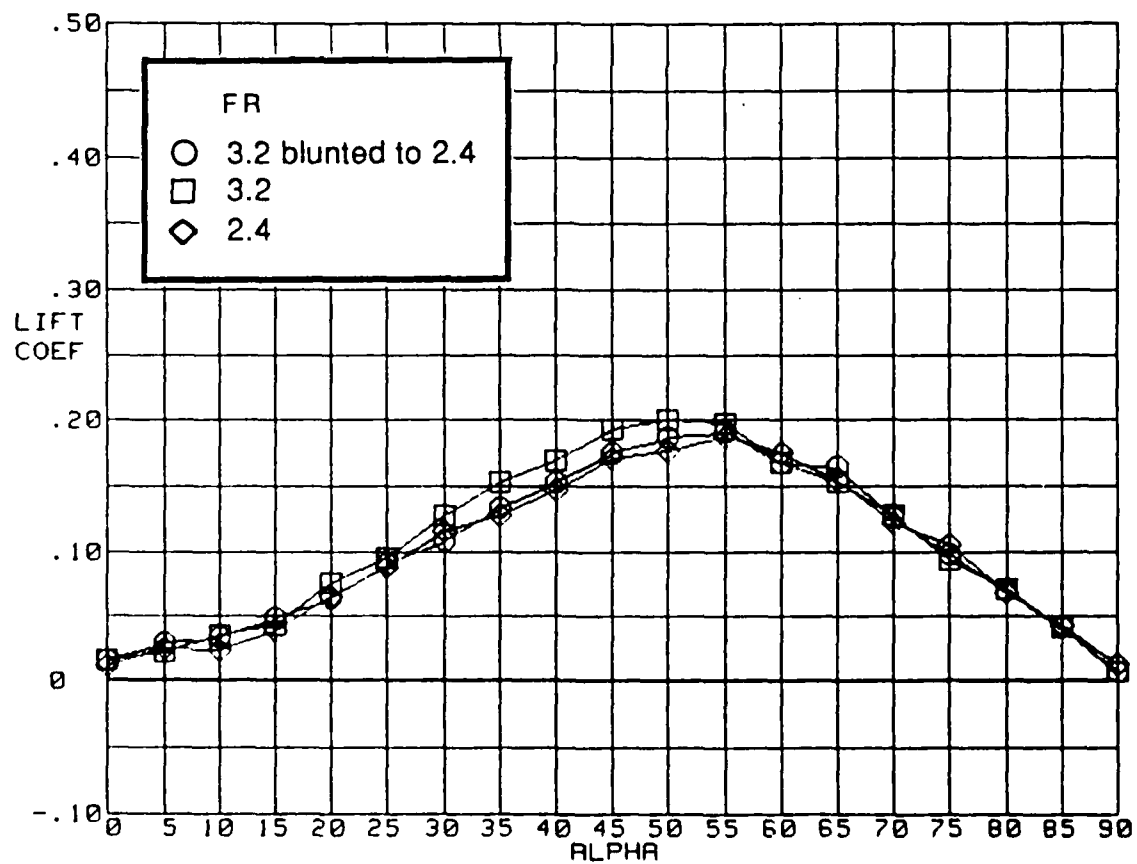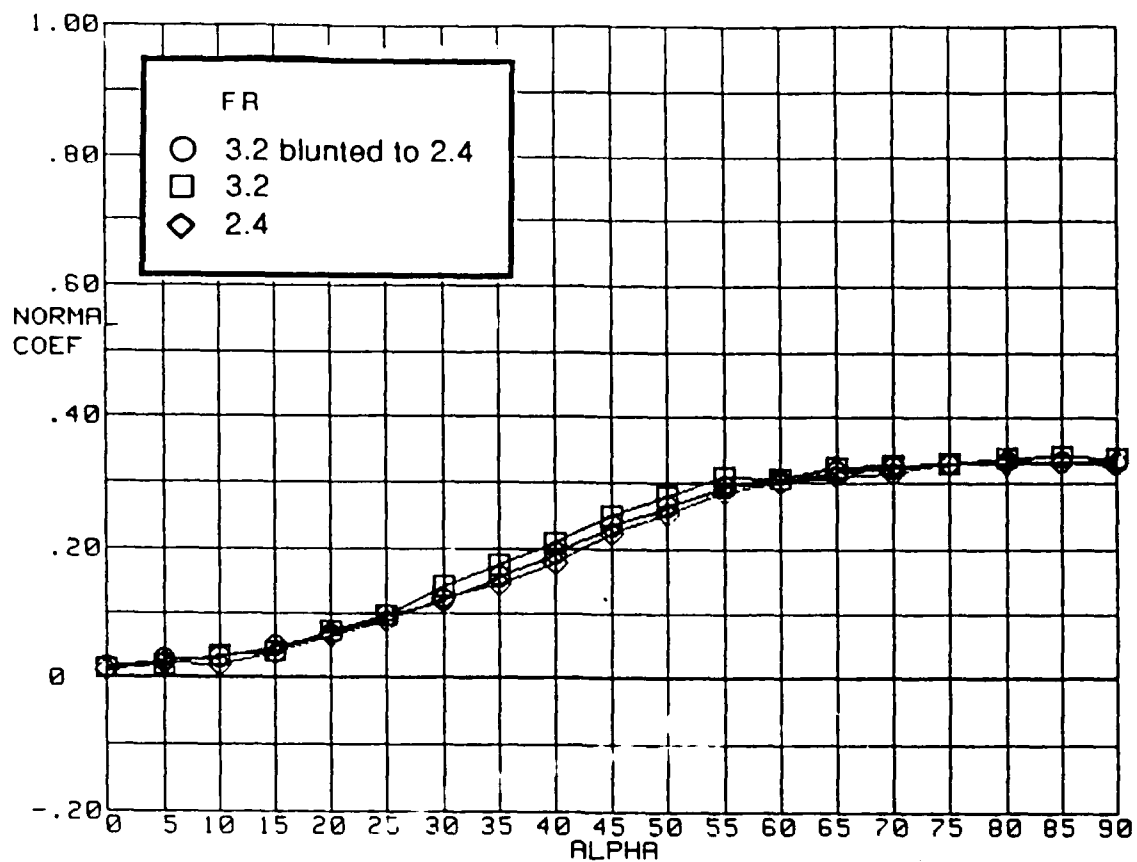
c) FR=3.2 blunted to 2.4

Figure 42.- Concluded
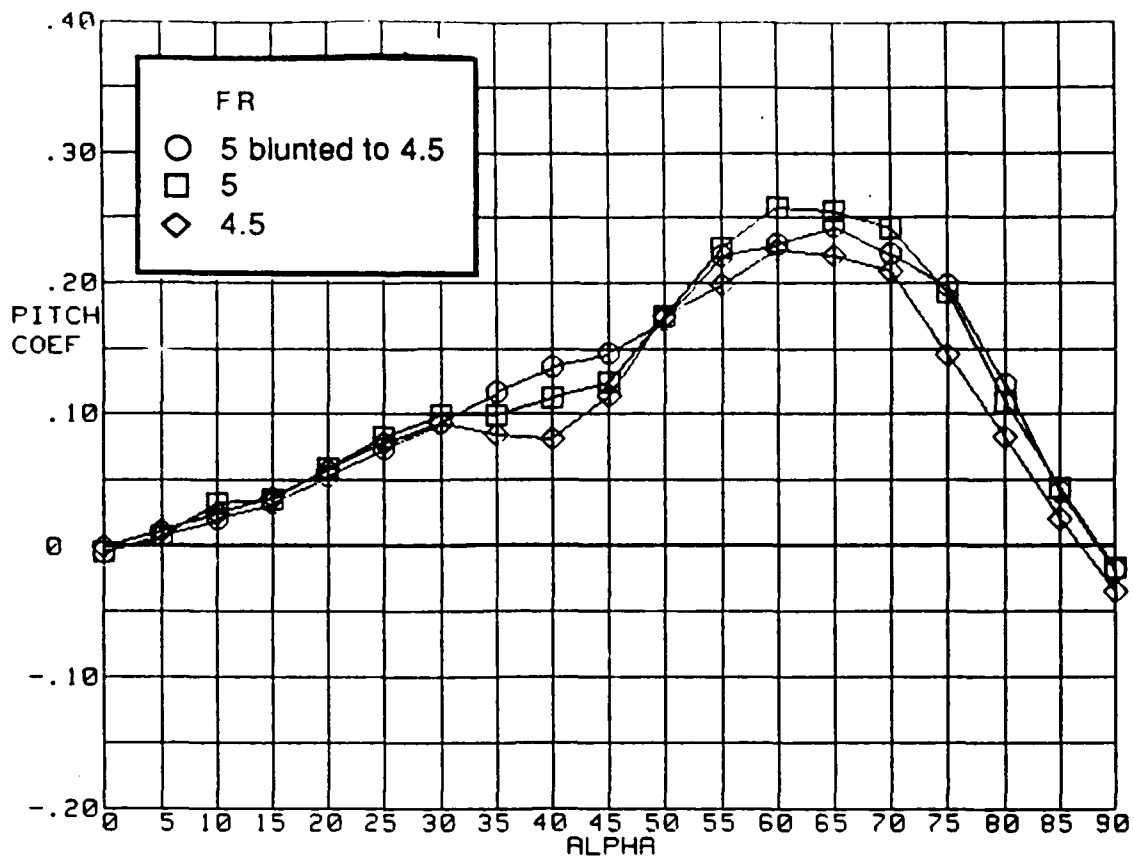
a) FR=5 blunted to 4.5
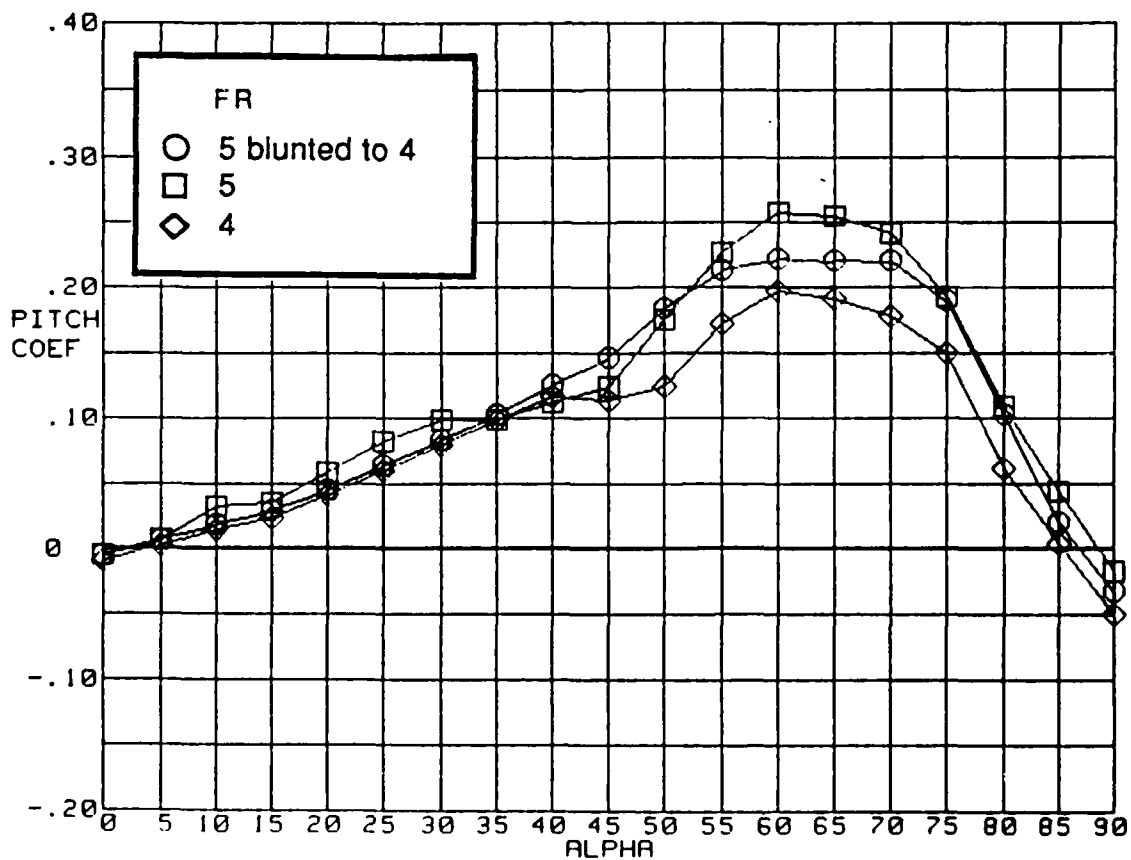
b) FR=5 blunted to 4

Figure 43.- Effect of blunting H/W=0.6 cross-sectional forebodies on pitching-moment coefficient variation with angle of attack

209
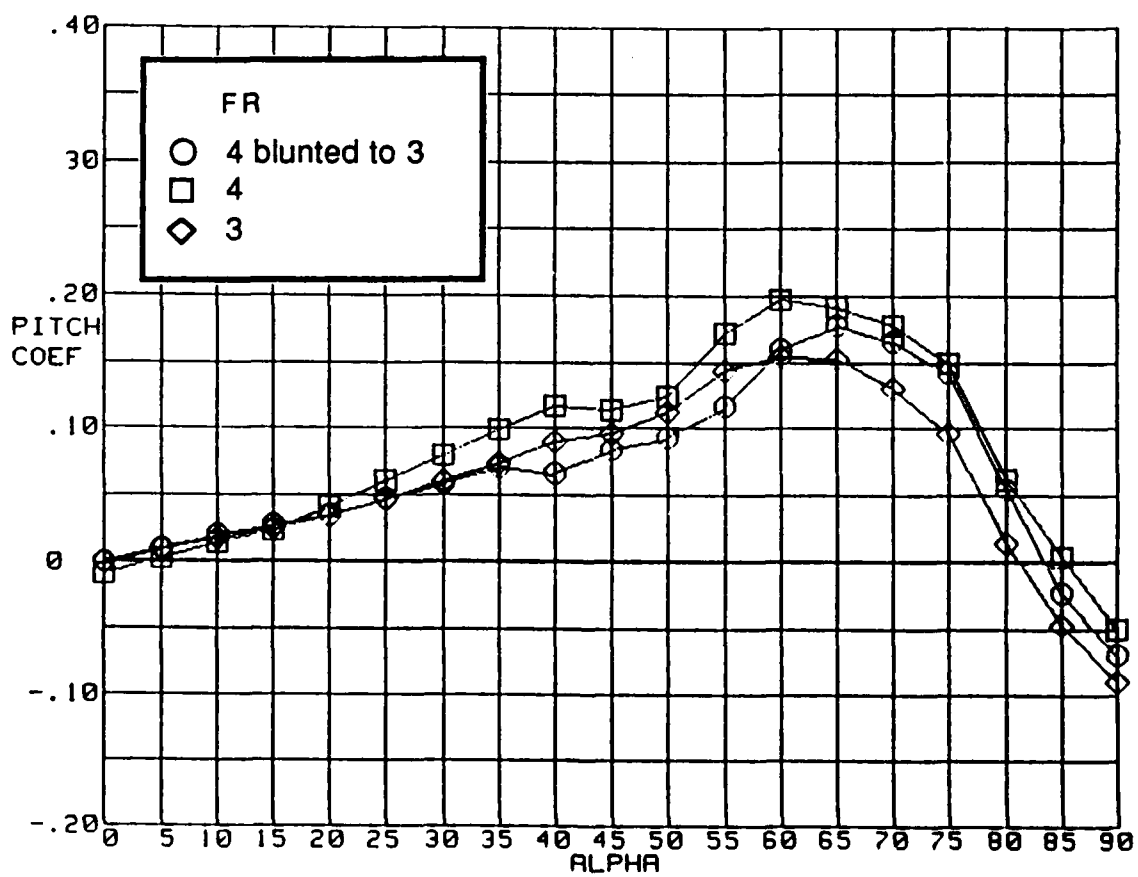
c)   FR=4 blunted to 3

Figure 43.- Concluded
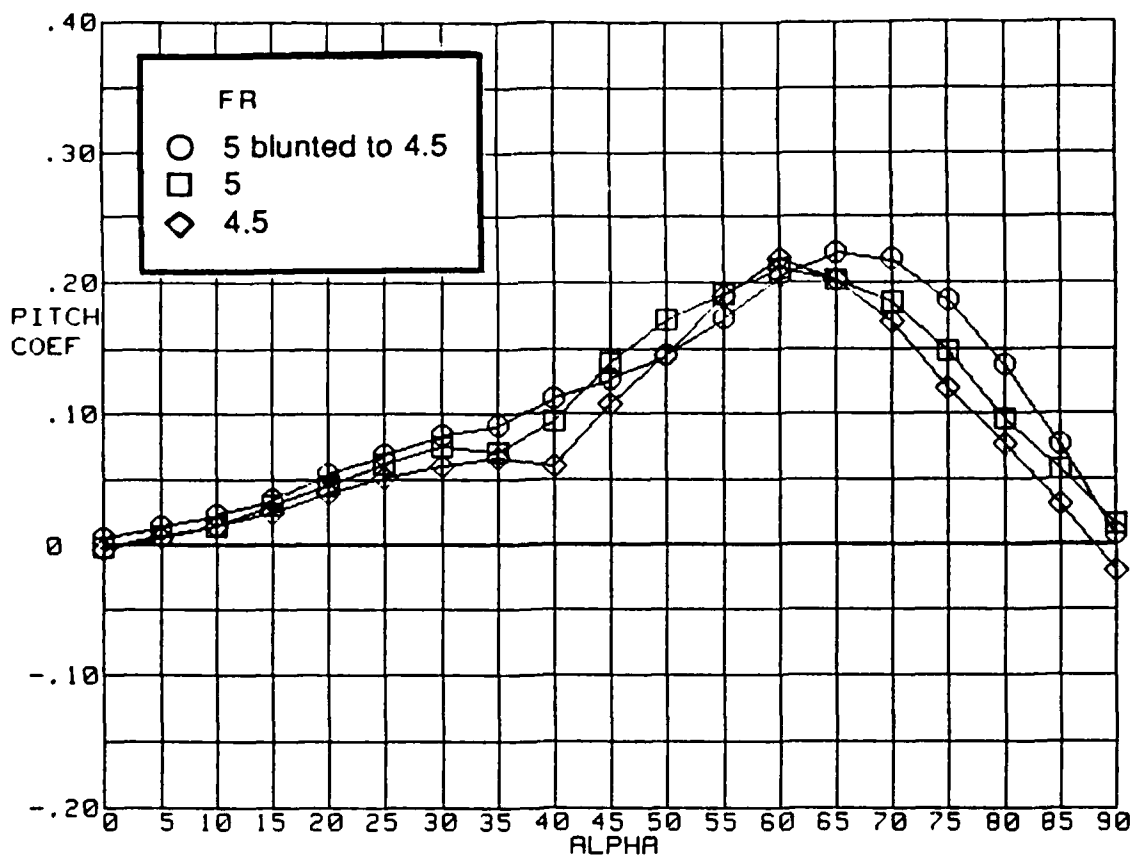
a)   FR=5 blunted to 4.5
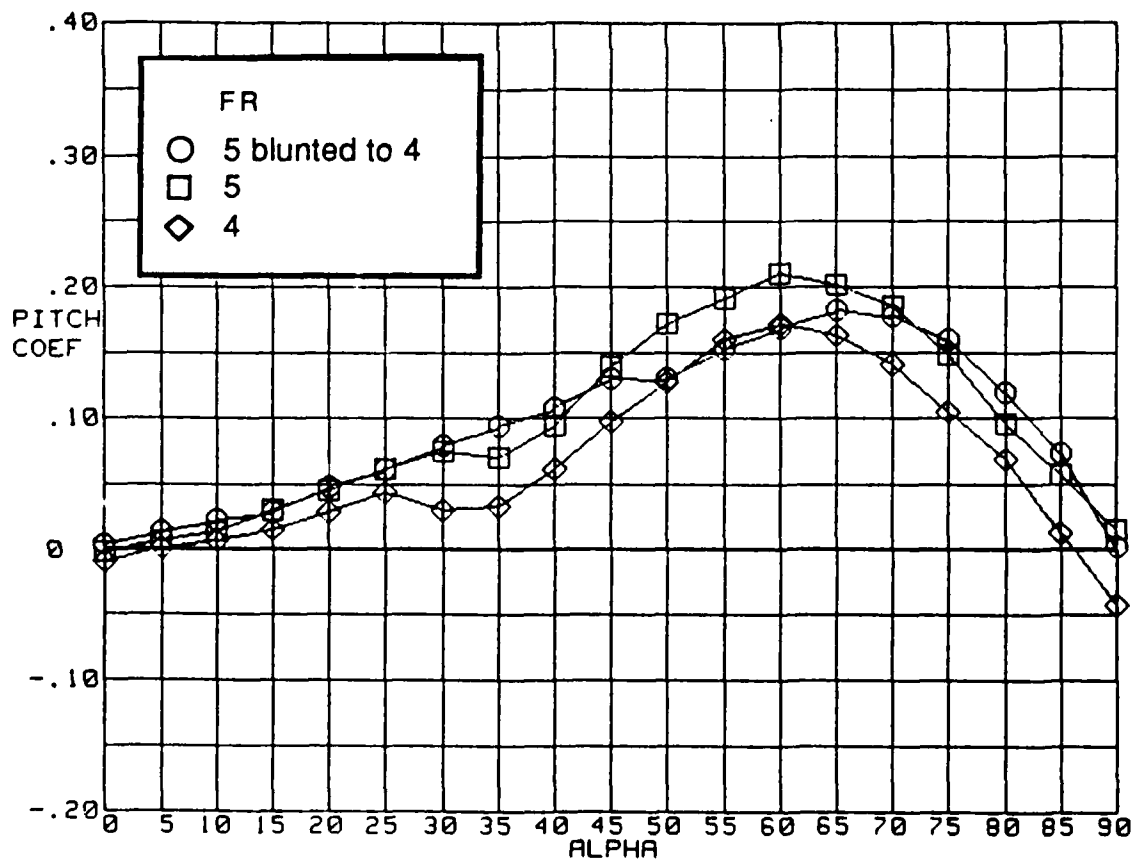
b)   FR=5 blunted to 4

Figure 44.- Effect of blunting H/W=0.8 cross-sectional forebodies on pitching-moment coefficient variation with angle of attack

211
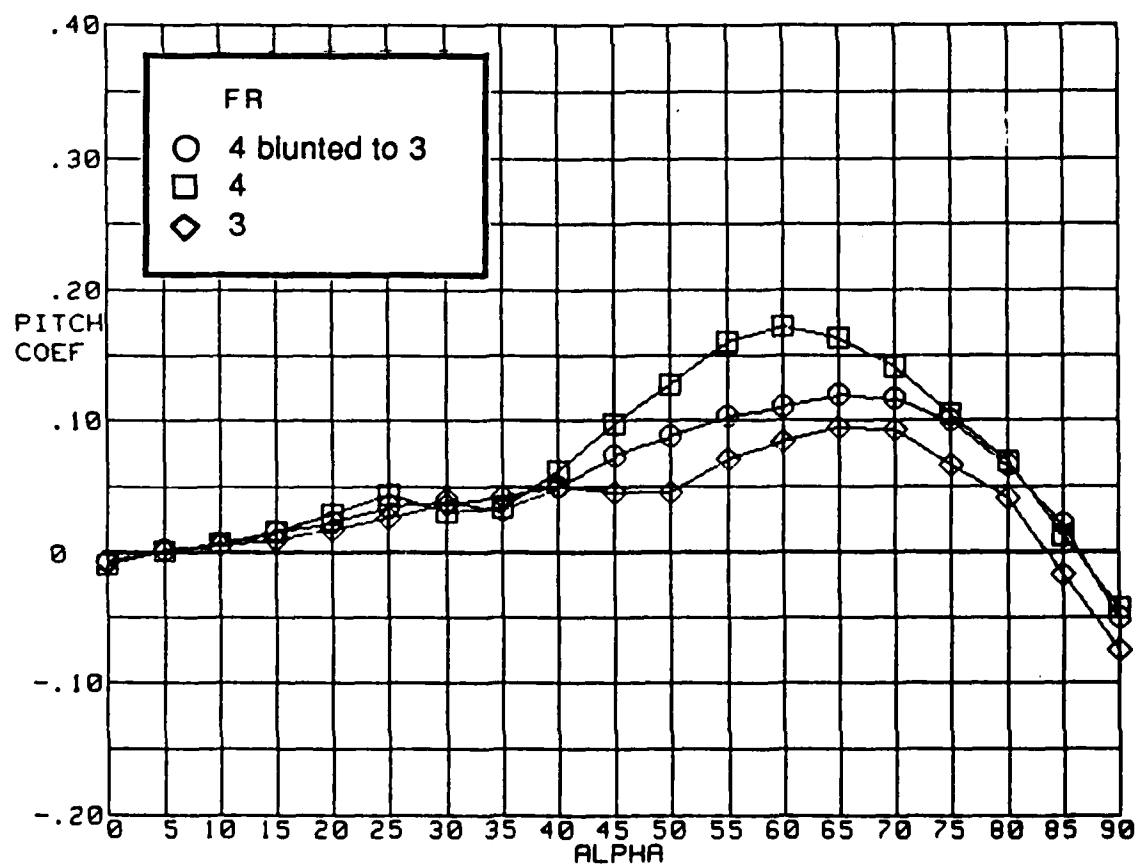
c) FR=4 blunted to 3

Figure 44.- Concluded

212
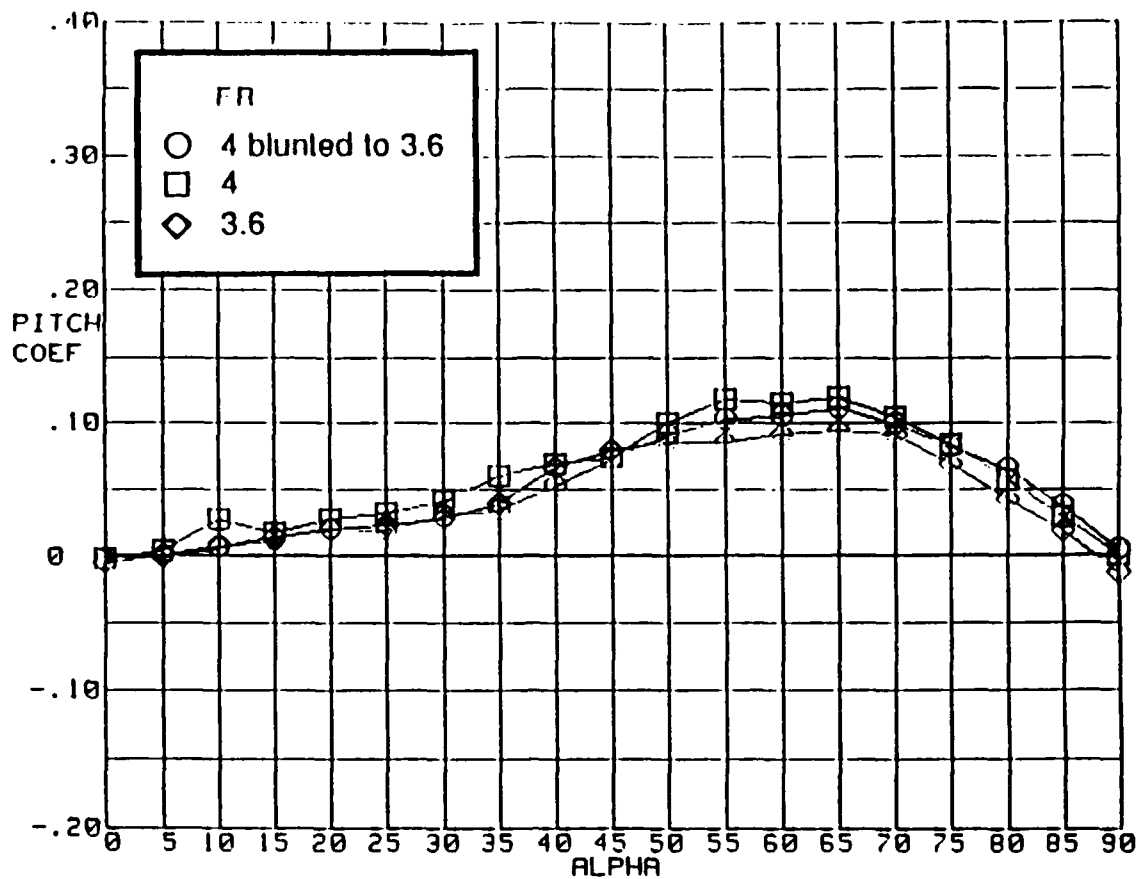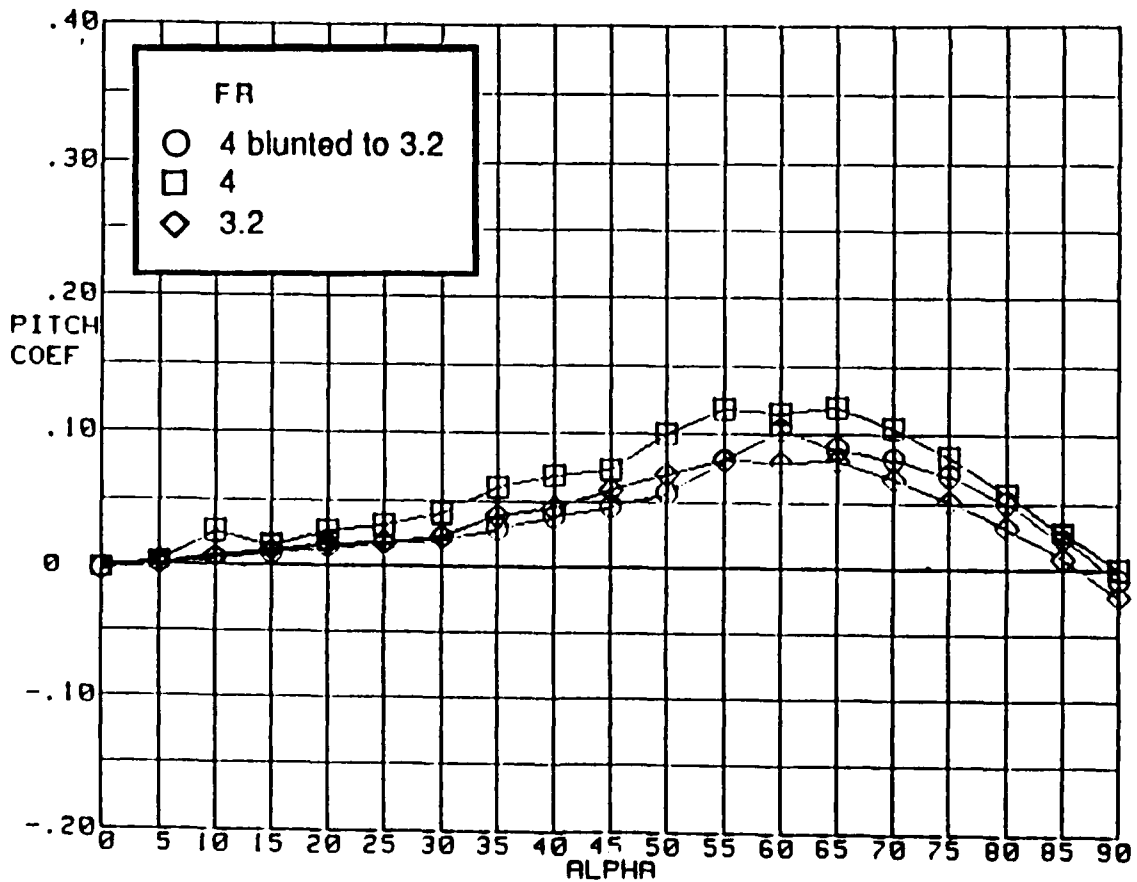
a) FR=4 blunted to 3.6

b) FR=4 blunted to 3.2

Figure 45.- Effect of blunting H/W=1.25 cross-sectional forebodies
on pitching-moment coefficient variation with angle of attack

213
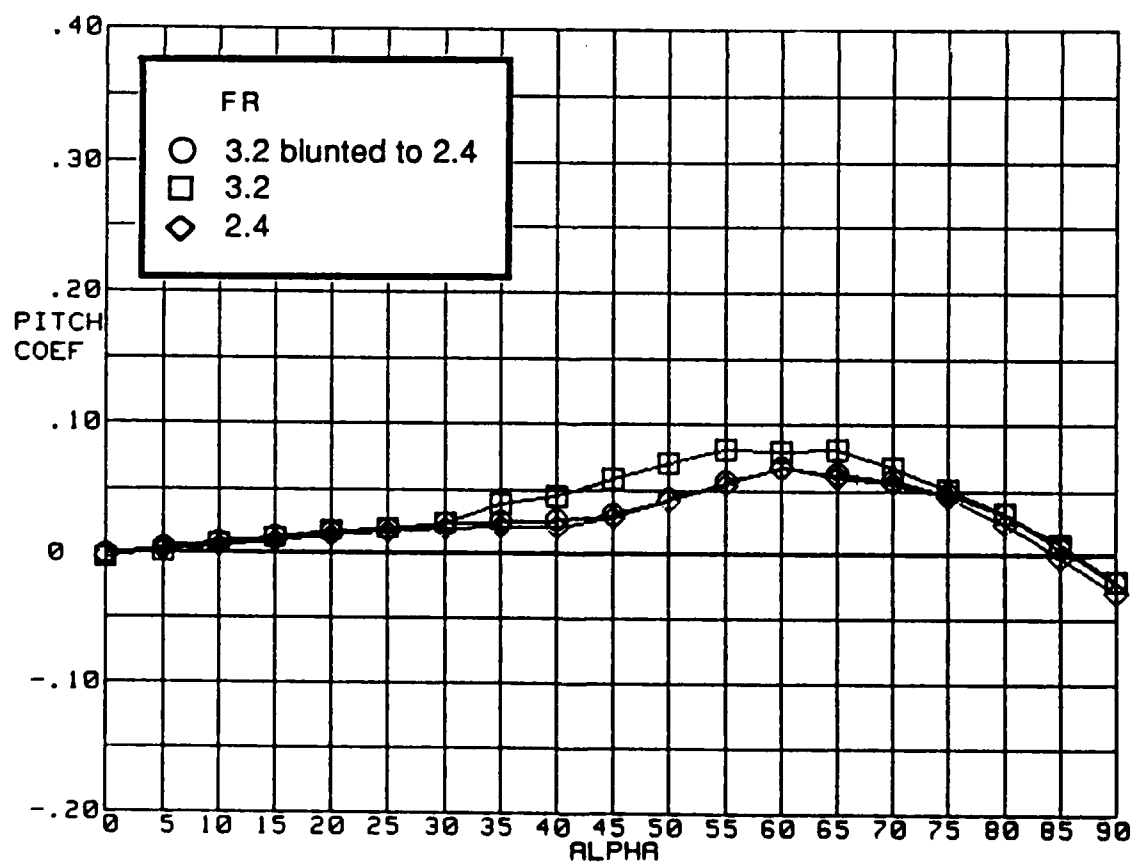
c)   FR=3.2 blunted to 2.4

Figure 45.- Concluded
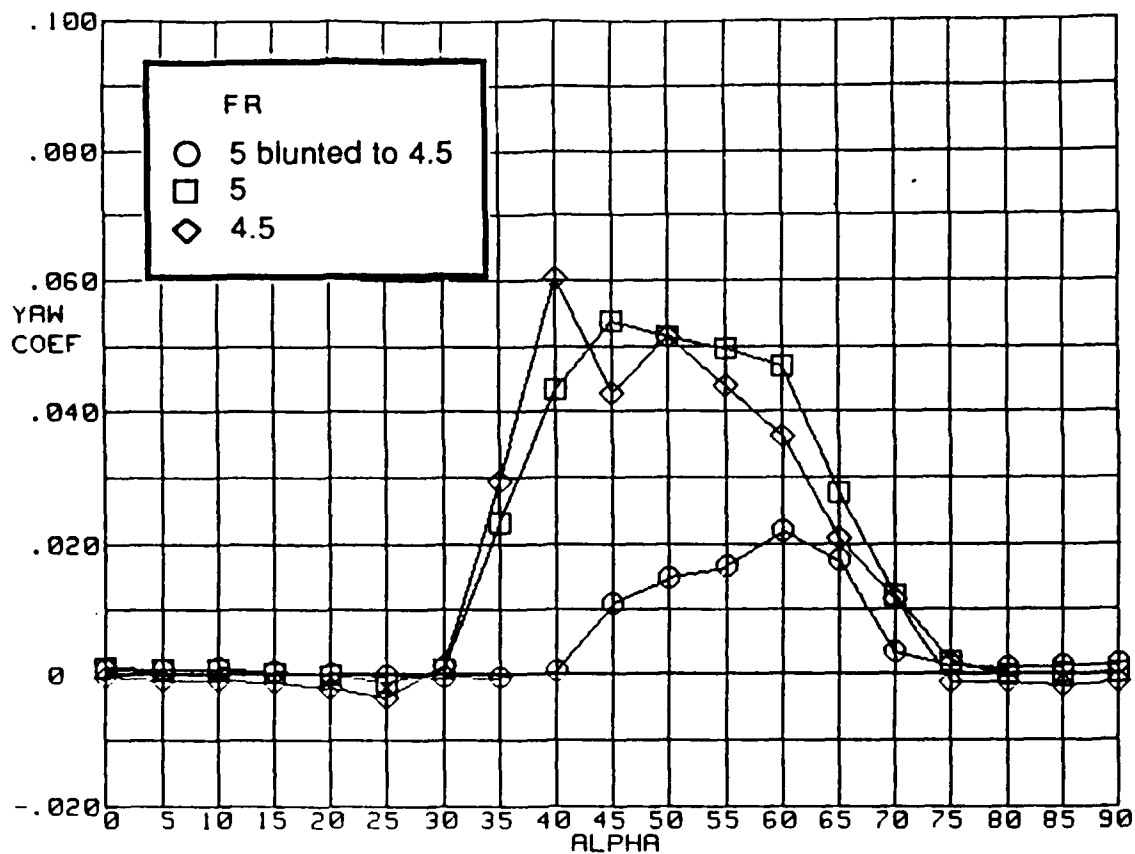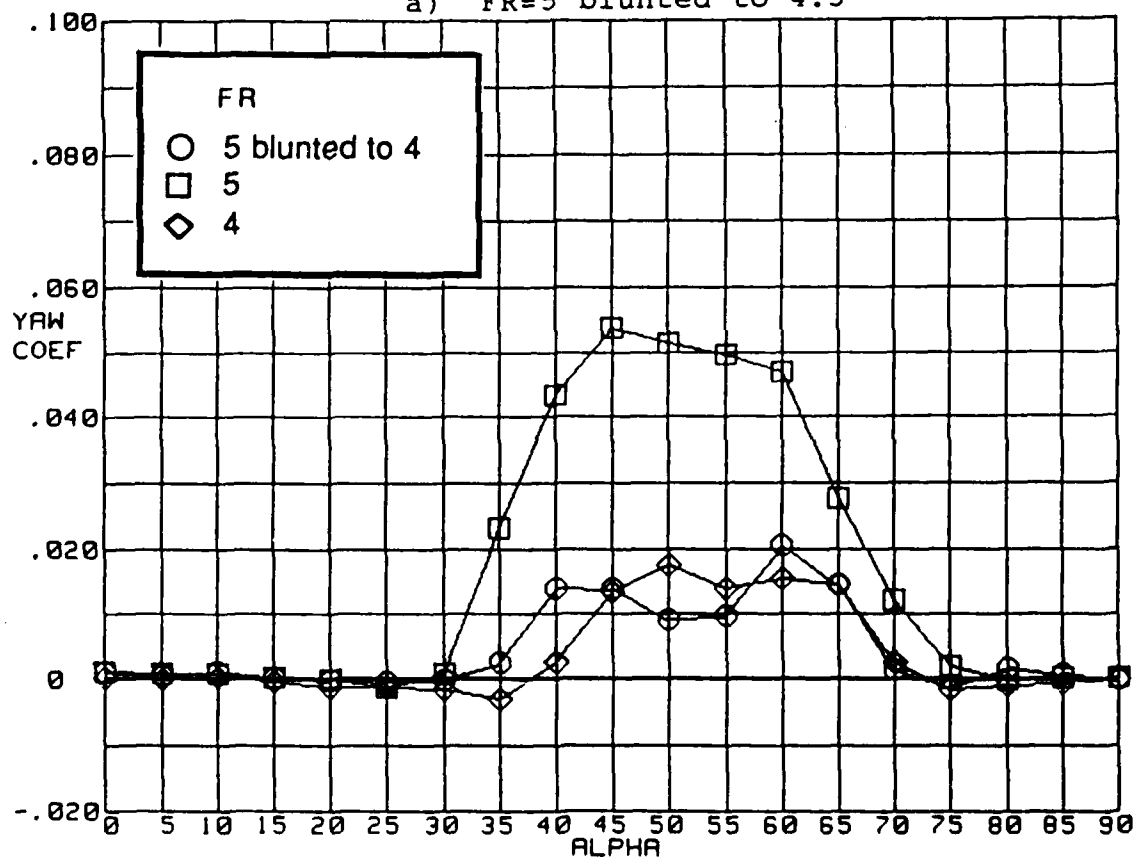
214

Figure 46.- Effect of blunting H/W=0.6 cross-sectional forebodies
on symmetrical flight yawing-moment coefficient variation
with angle of attack

215
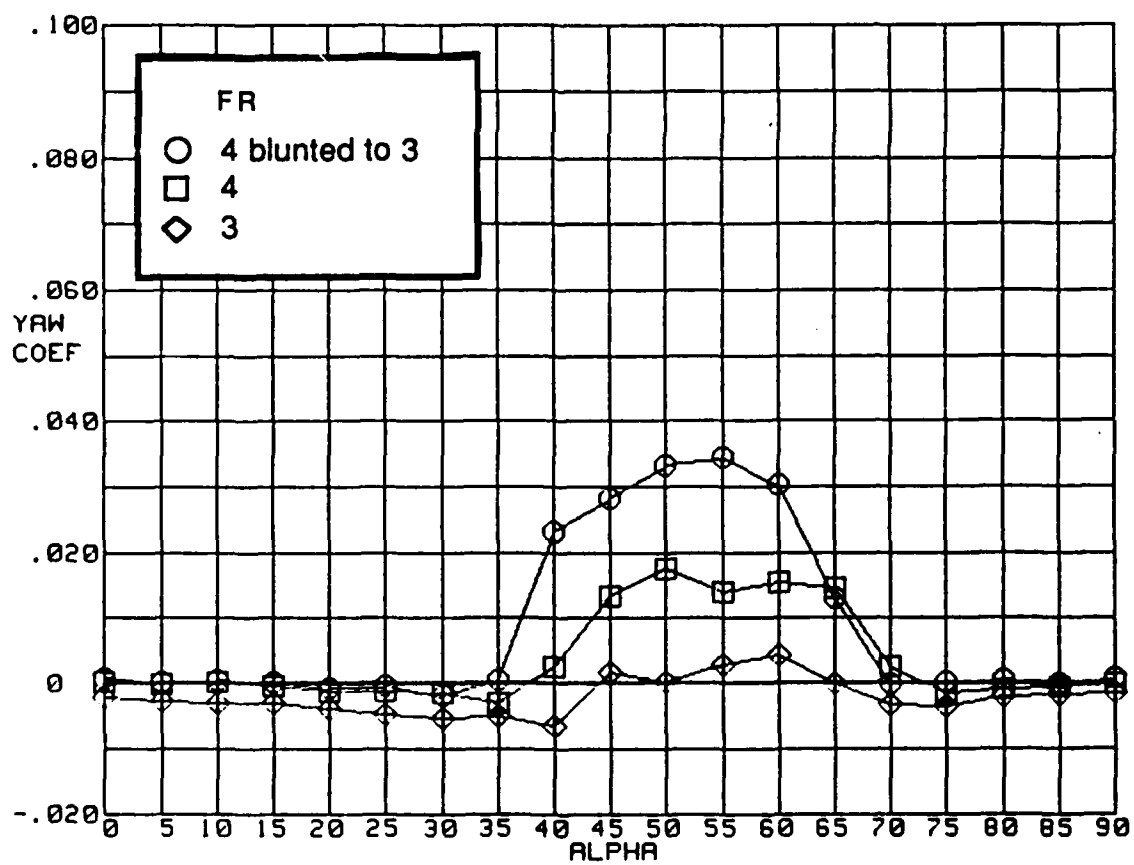
c) FR=4 blunted to 3

Figure 46.- Concluded

216
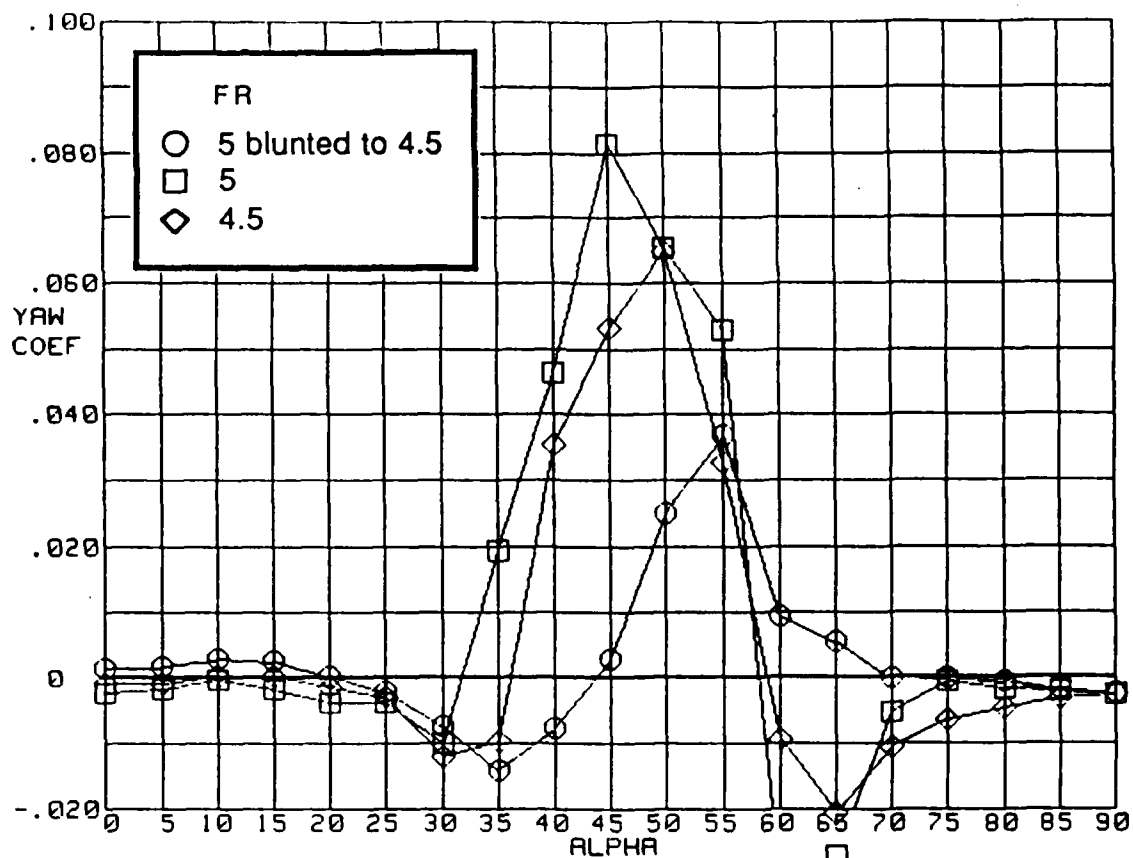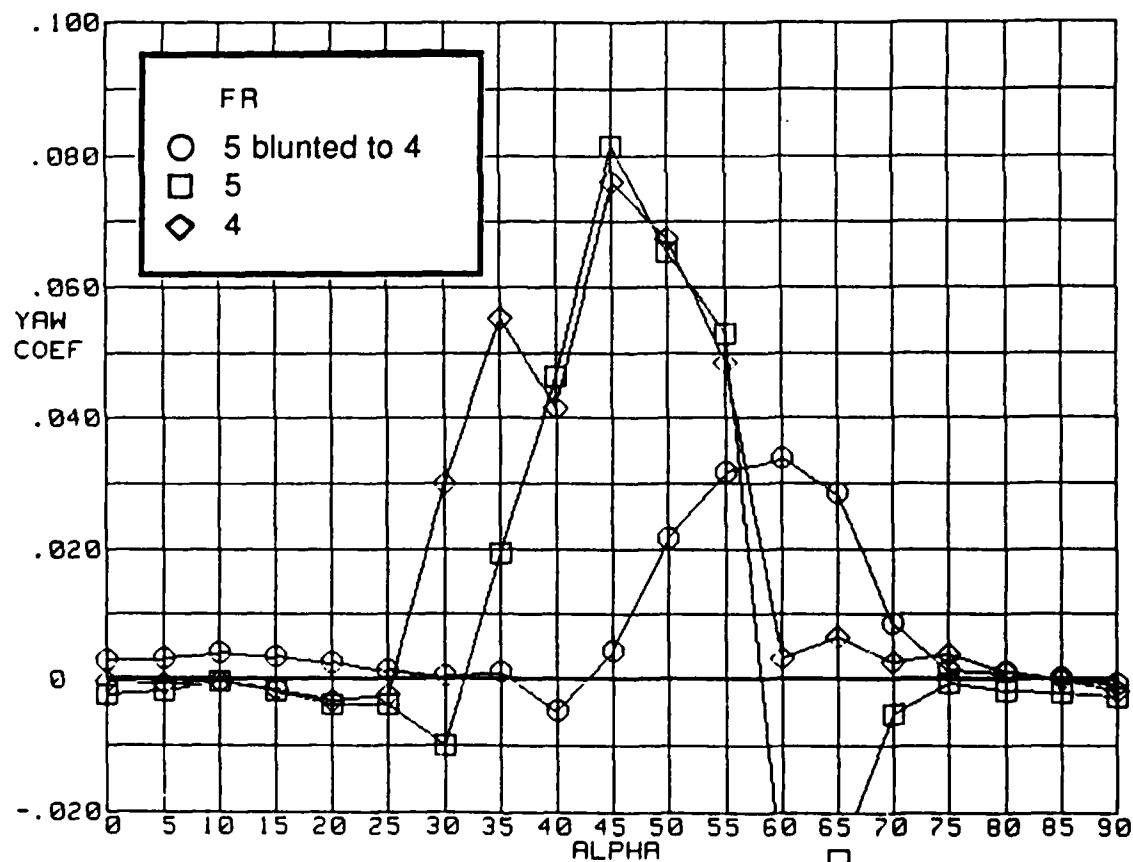
a) FR=5 blunted to 4.5

b) FR=5 blunted to 4

Figure 47.- Effect of blunting H/W=0.8 cross-sectional forebodies
on symmetrical flight yawing-moment coefficient variation with
angle of attack

c) FR=4 blunted to 3

Figure 47.- Concluded

218
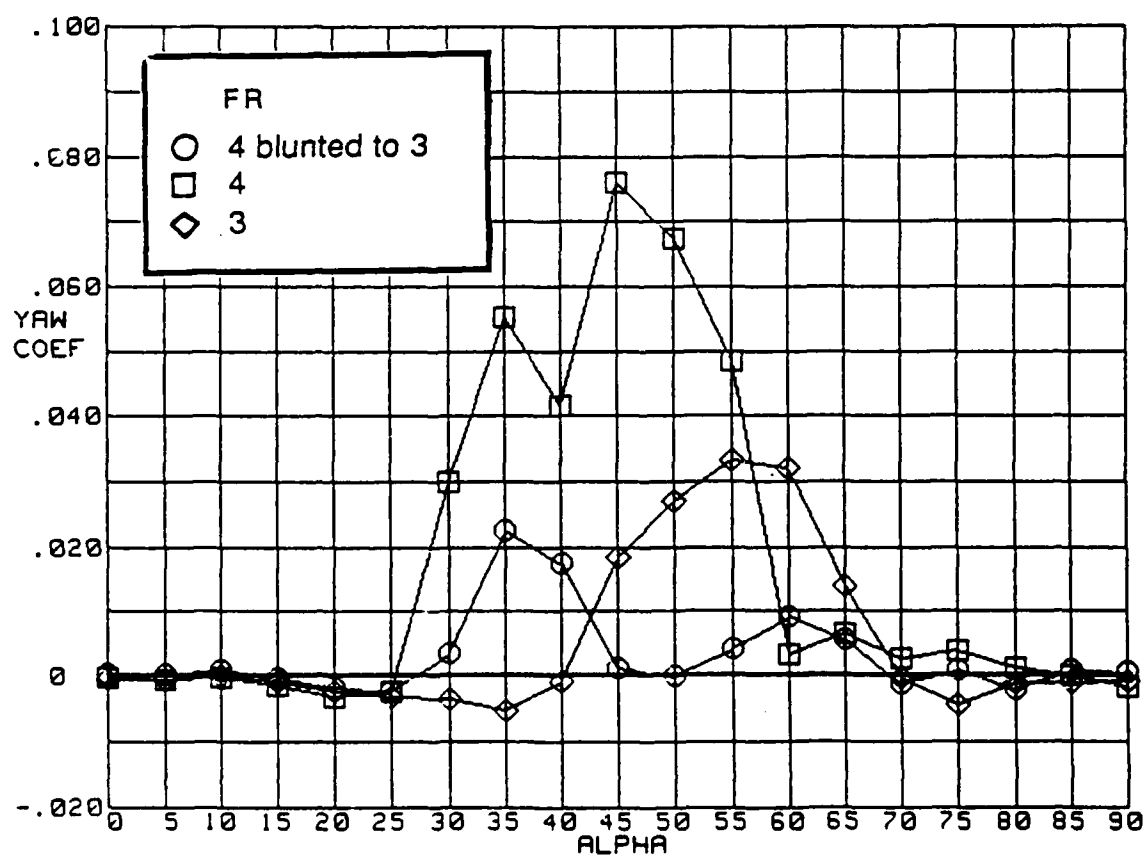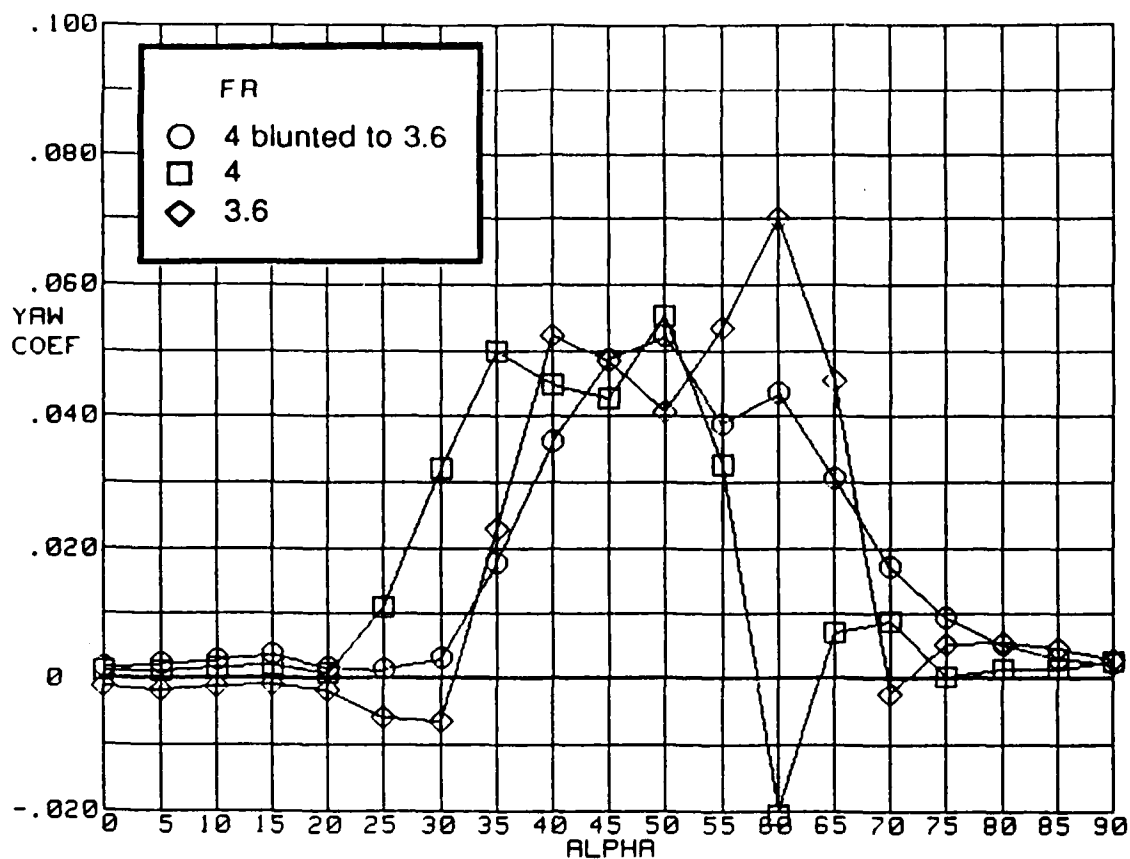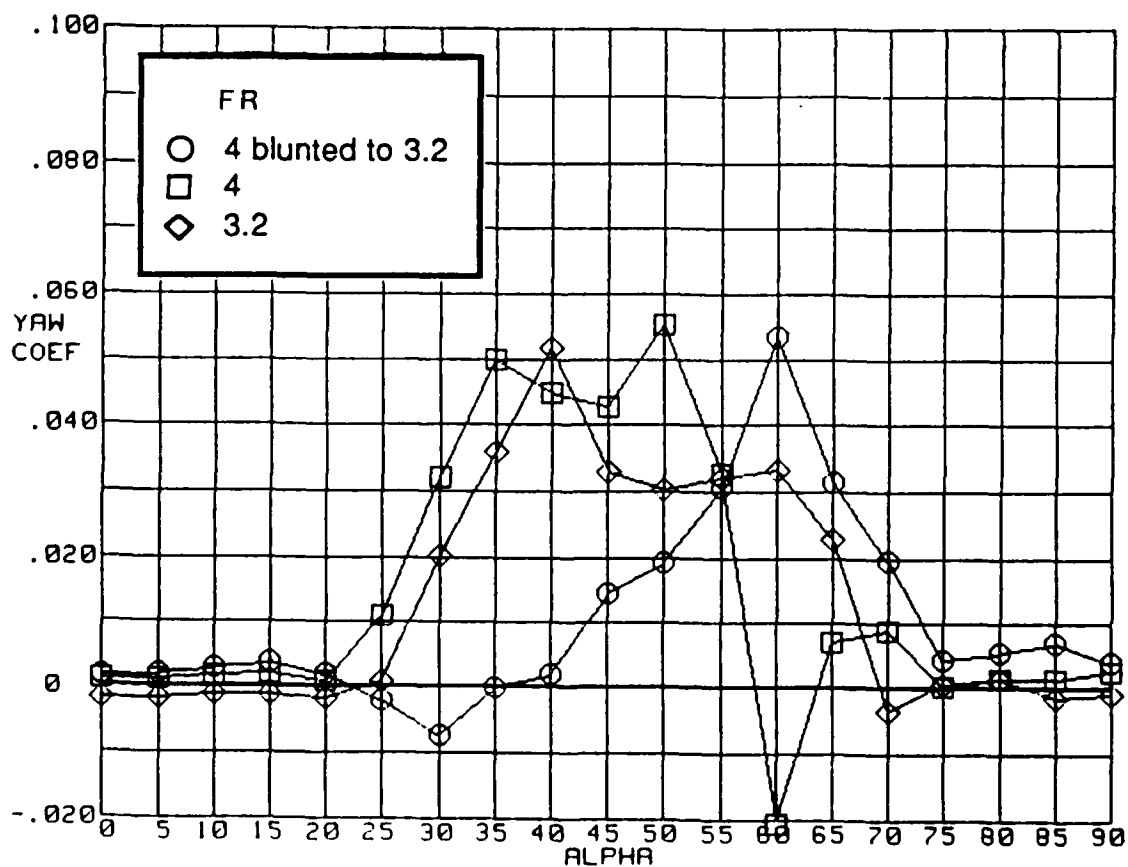
a) FR=4 blunted to 3.6

b) FR=4 blunted to 3.2

Figure 48.- Effect of blunting H/W=1.25 cross-sectional forebodies
on symmetrical flight yawing-moment coefficient variation with
angle of attack

219
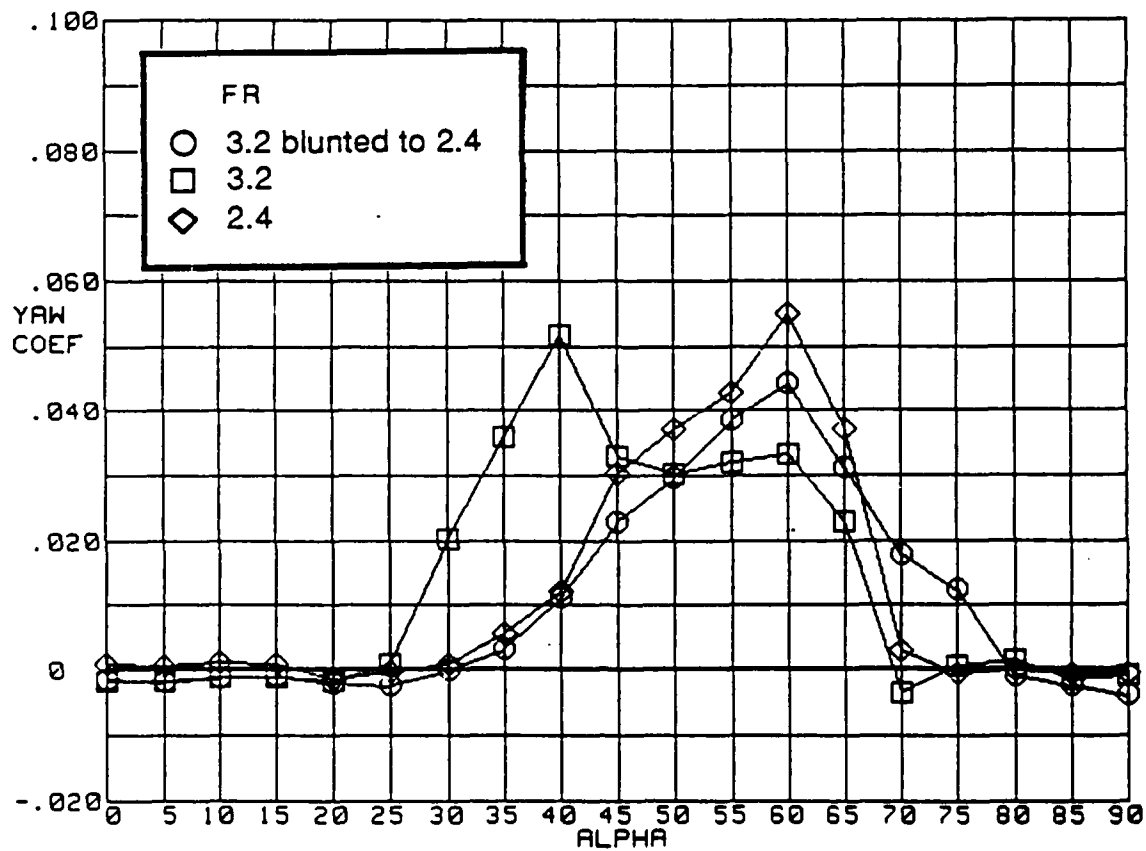
c) FR=3.2 blunted to 2.4

Figure 48.- Concluded
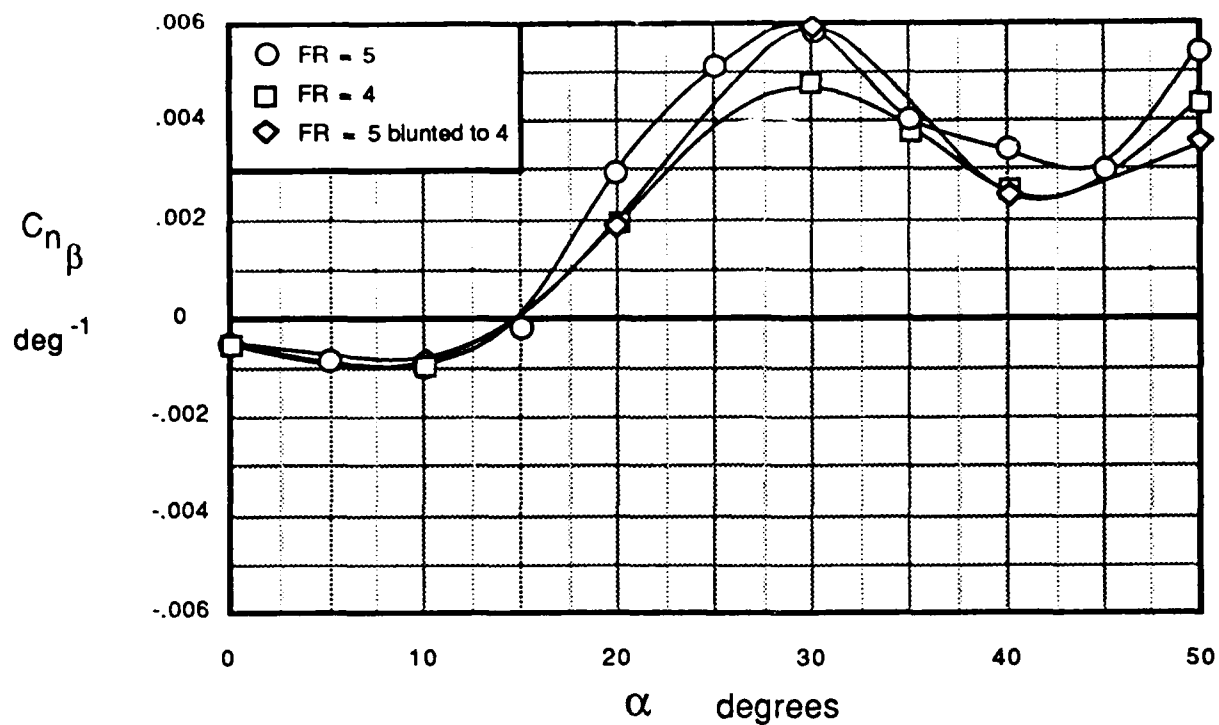
a) FR = 5 blunted to 4
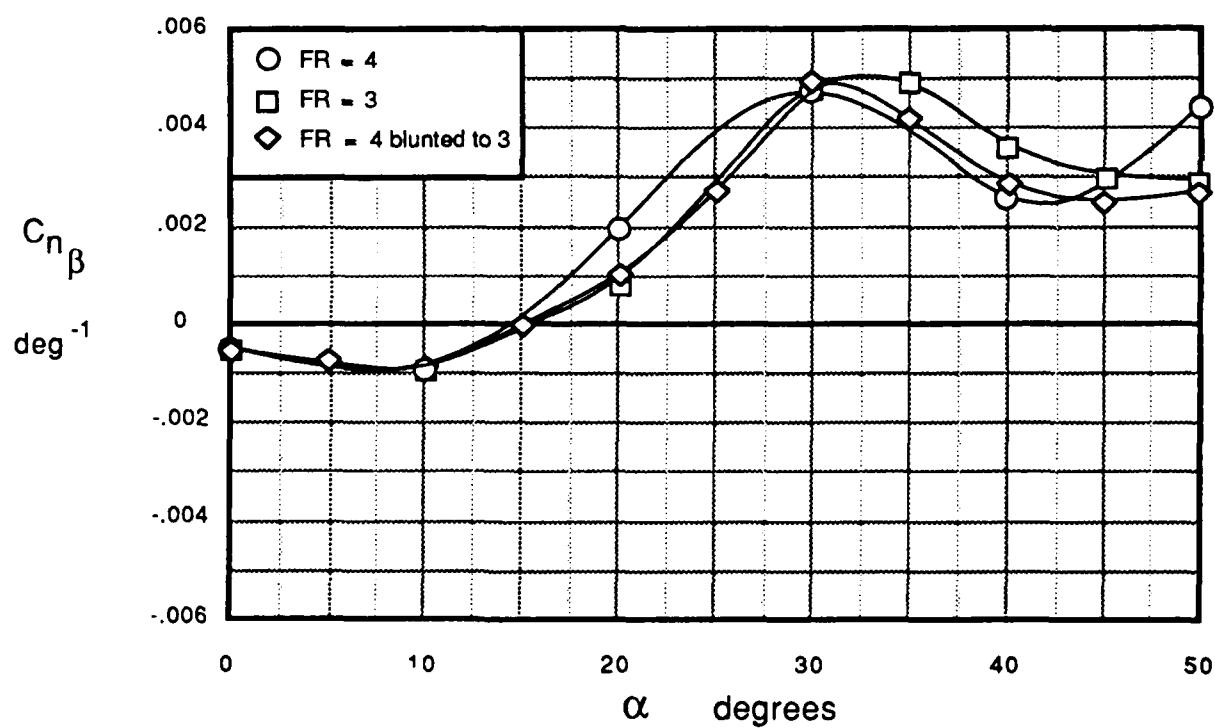
b) FR = 4 blunted to 3

Figure 49. - Effect of blunting H/W = 0.6 cross-sectional forebodies
on directional stability

221
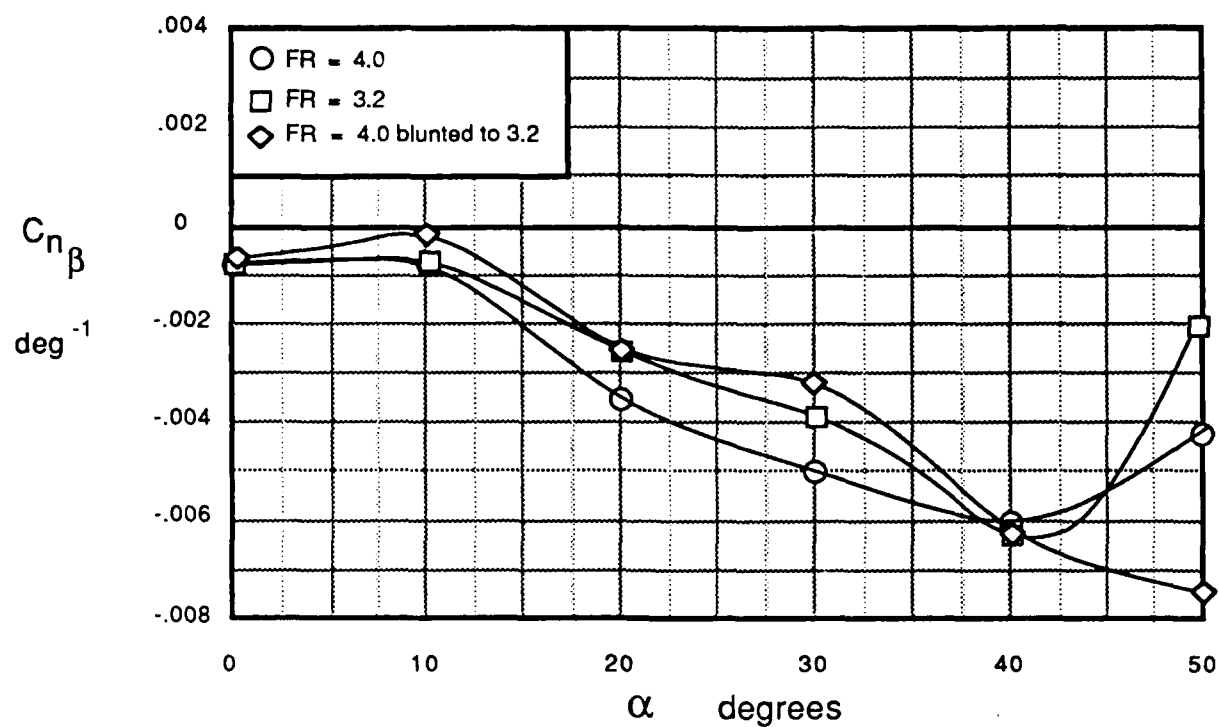
a) FR = 4.0 blunted to 3.2
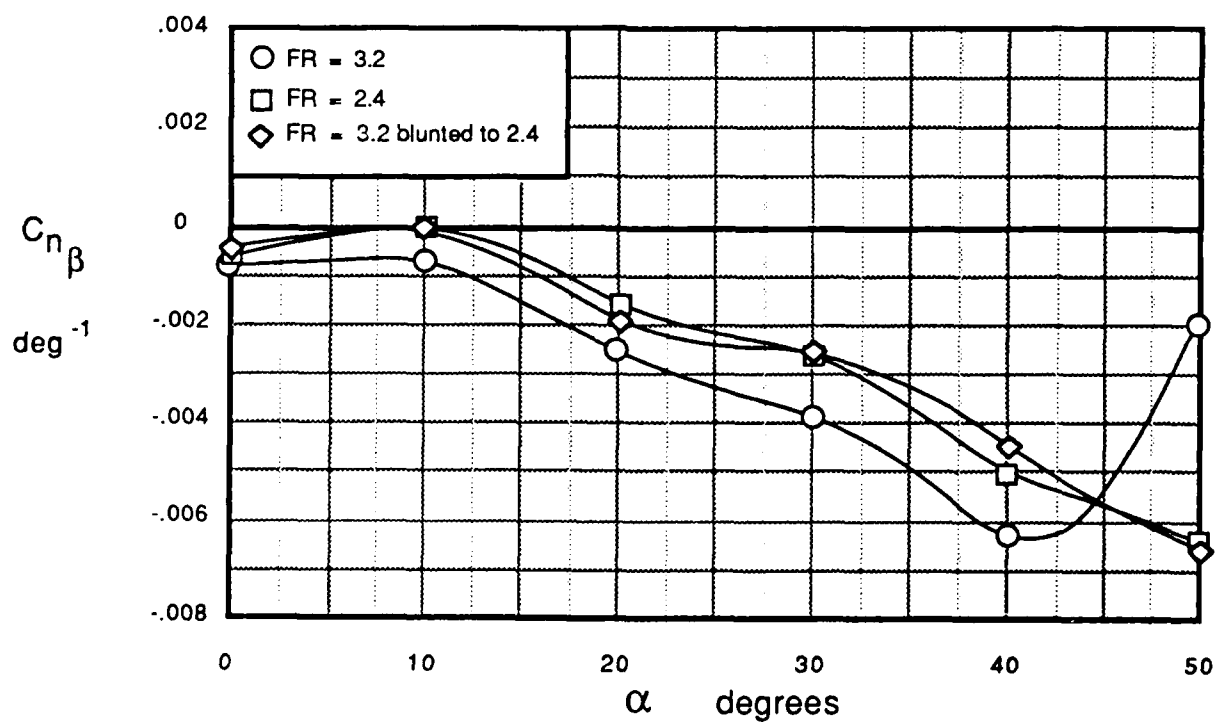
b) FR = 3.2 blunted to 2.4

Figure 50. - Effect of blunting H/W = 1.25 cross-sectional forebodies
on directional stability

222
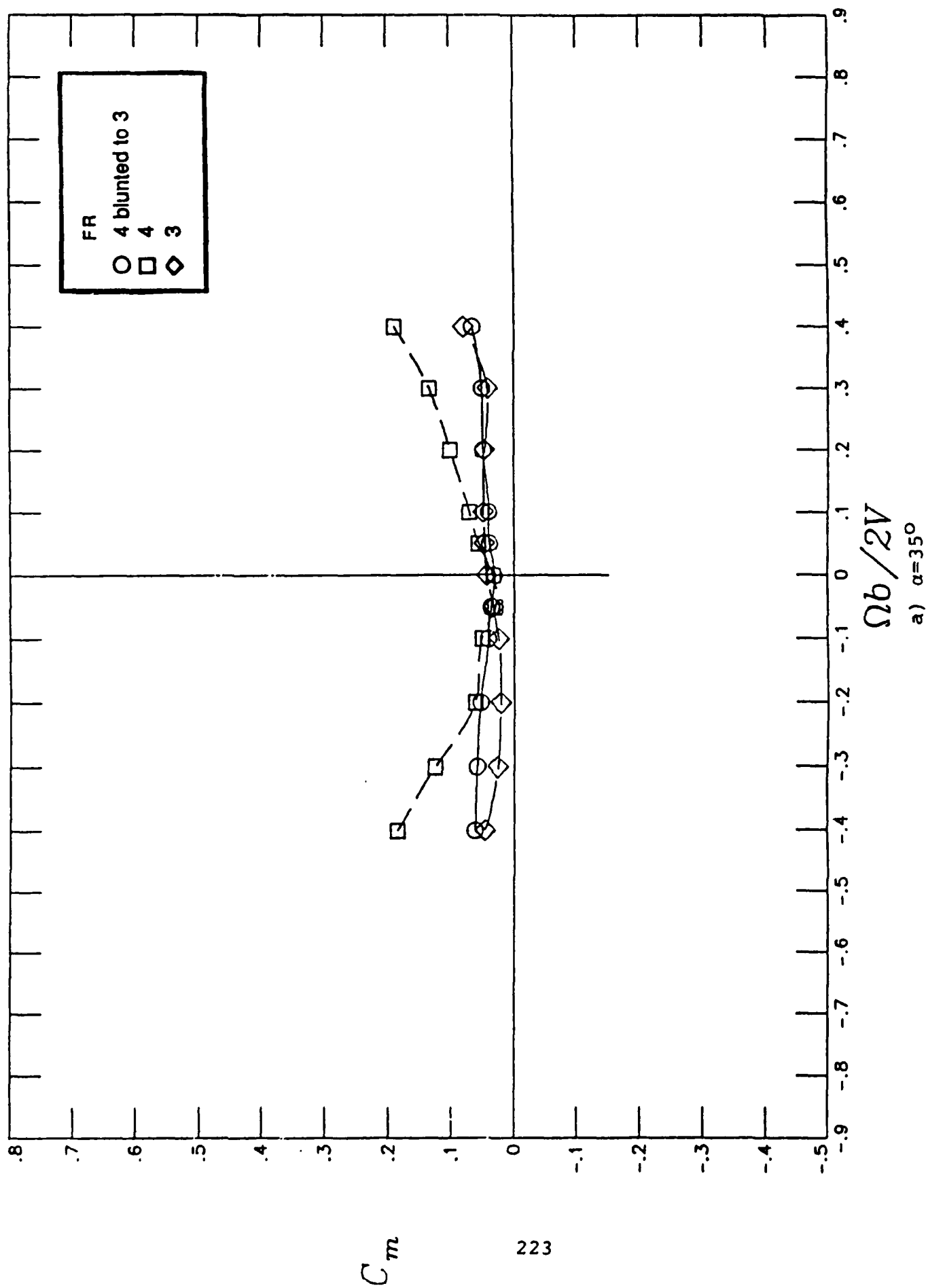
Figure 51.- Effect of blunting a H/W=0.8, FR=4 forebody on rotational pitching-moment coefficient characteristics

a) $\alpha=35^\circ$

223

Figure 51.- Continued

b) $\alpha = 50°$

$\Omega b / 2V$

C_m

224

C_m

$\Omega b/2V$

c) $\alpha = 60^\circ$
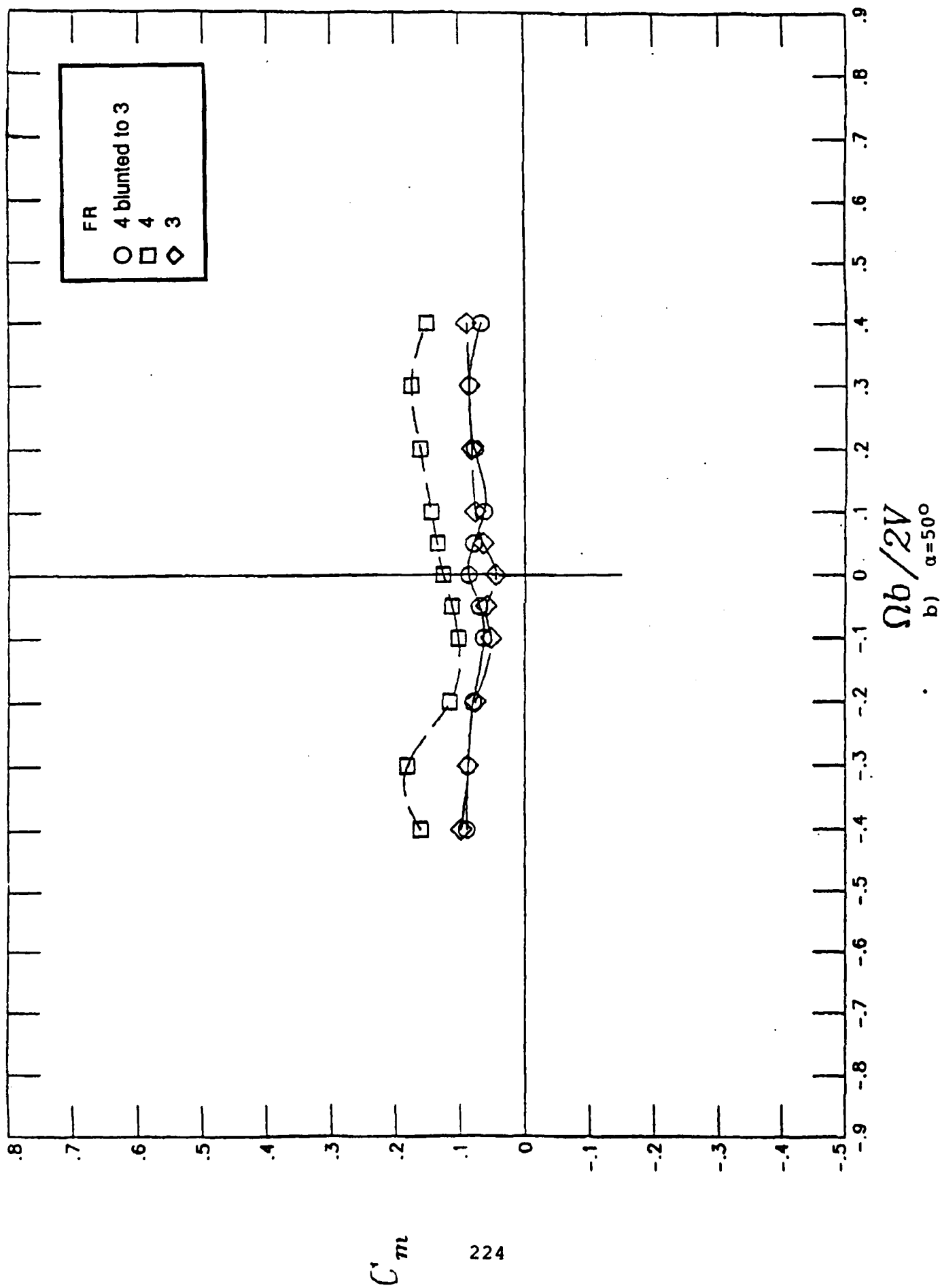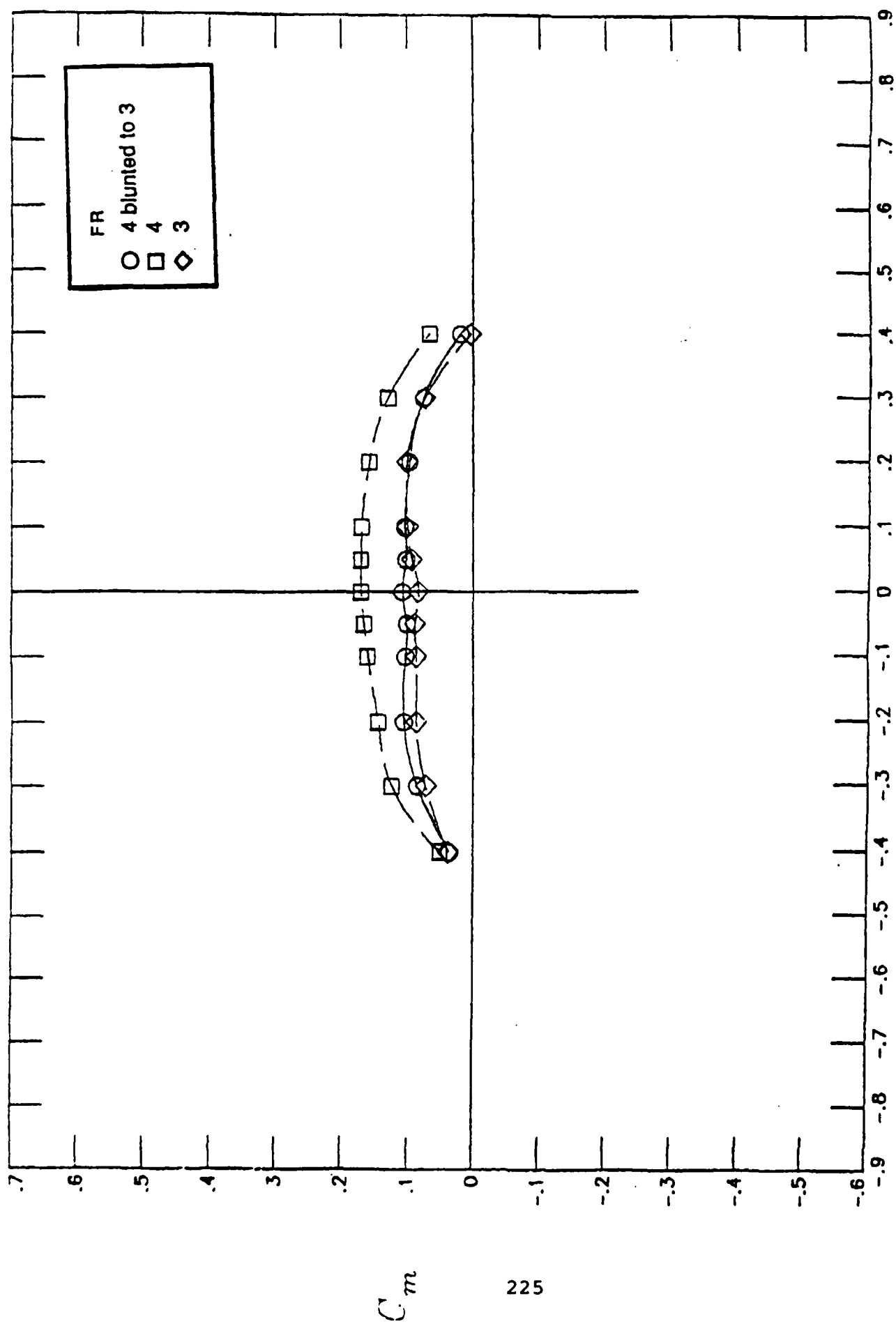
Figure 51.- Concluded

FR
O 4 blunted to 3
□ 4
◇ 3

225
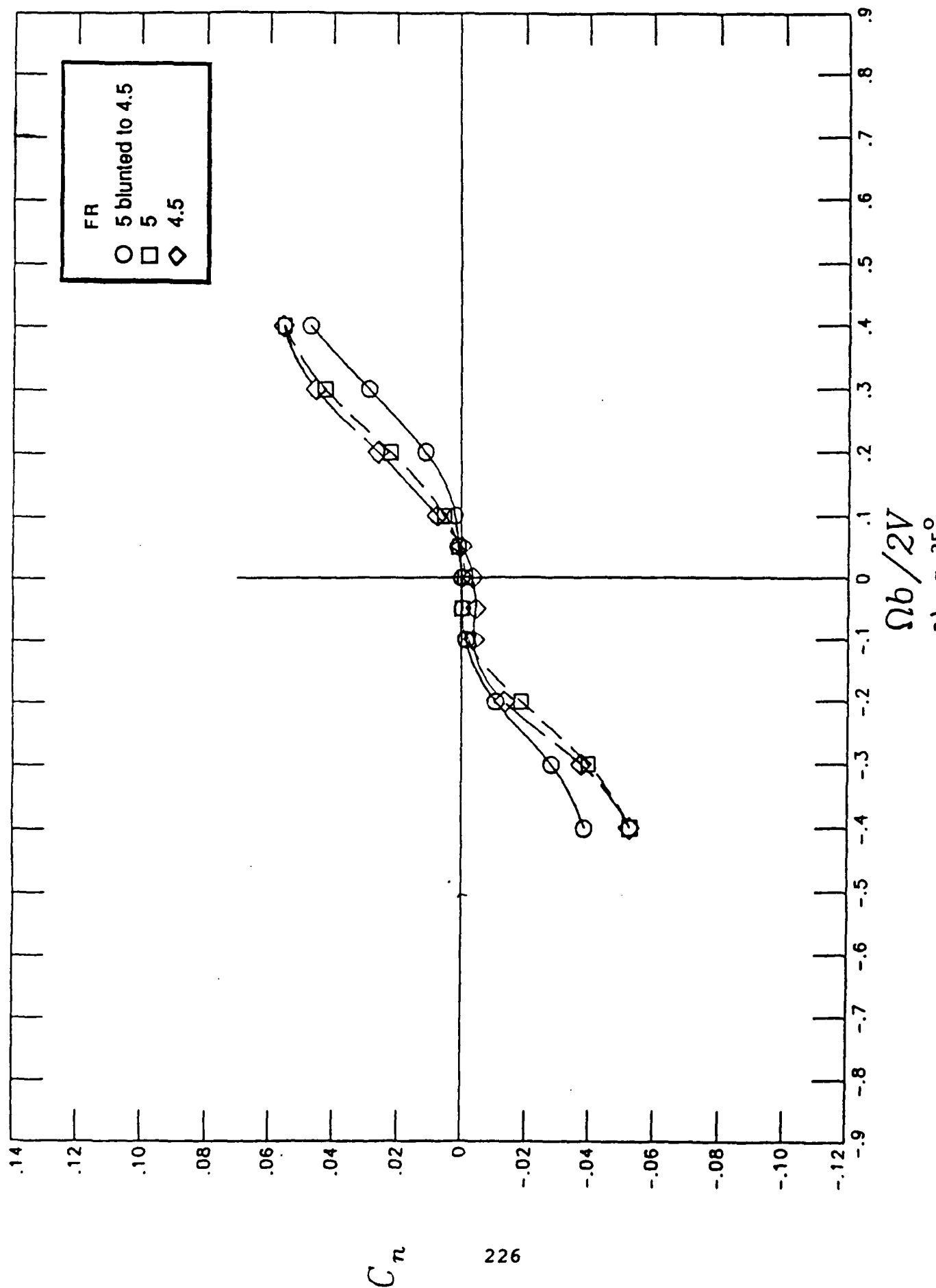
Figure 52.- Effect of blunting a H/W=0.6 cross-sectional forebody from FR 5 to 4.5 on rotational yawing-moment coefficient characteristics
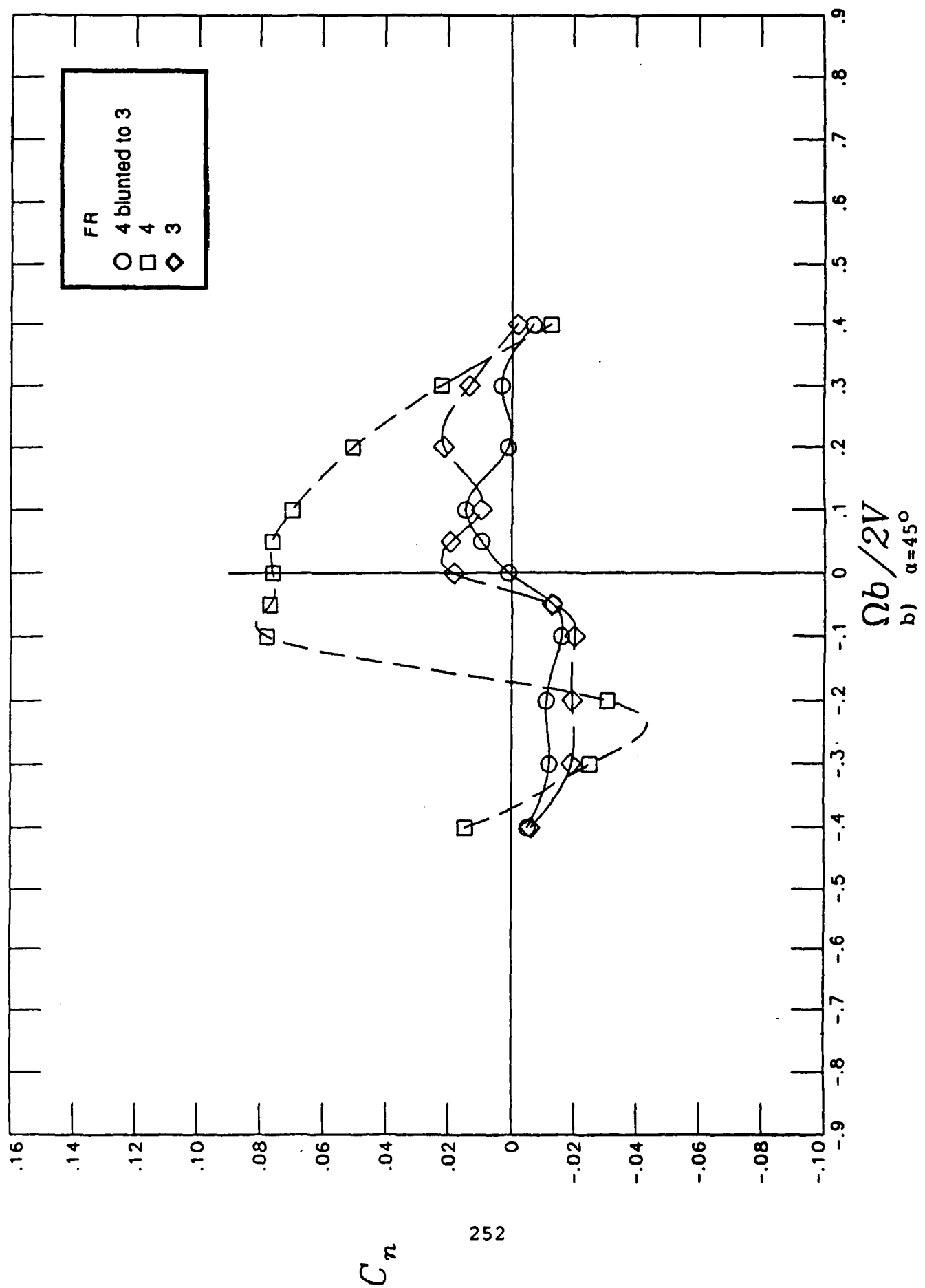
226

$\Omega b/2V$

b) $\alpha = 30^\circ$

Figure 52.- Continued

C_n

227

$$\frac{\Omega b}{2V}$$

c) $\alpha = 40°$

Figure 52.- Continued

228

Figure 52.- Continued

$\Omega b/2V$

d) $\alpha=50°$

C_n

229

e) $\alpha=60°$

Figure 52.- Continued

C_n

230
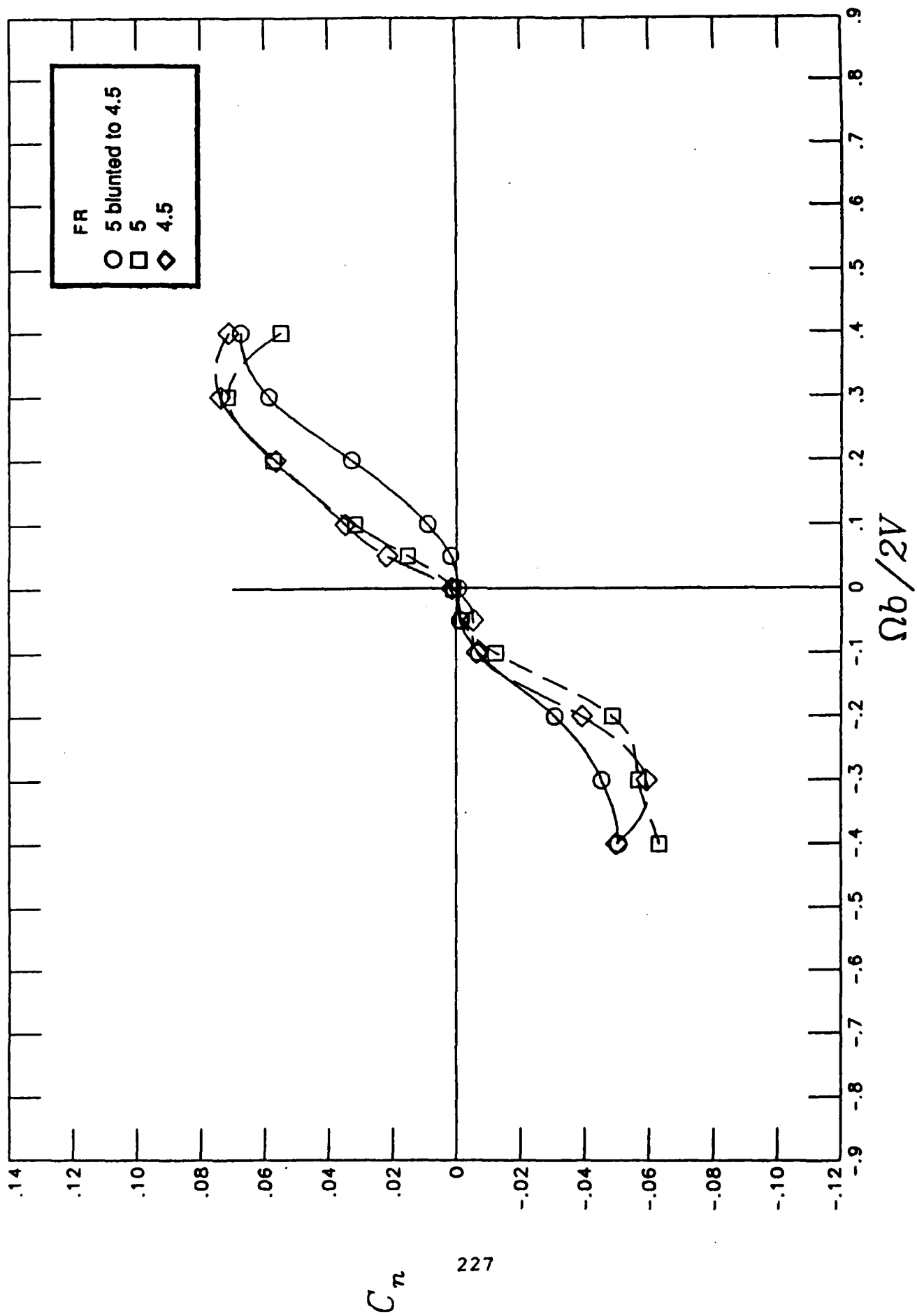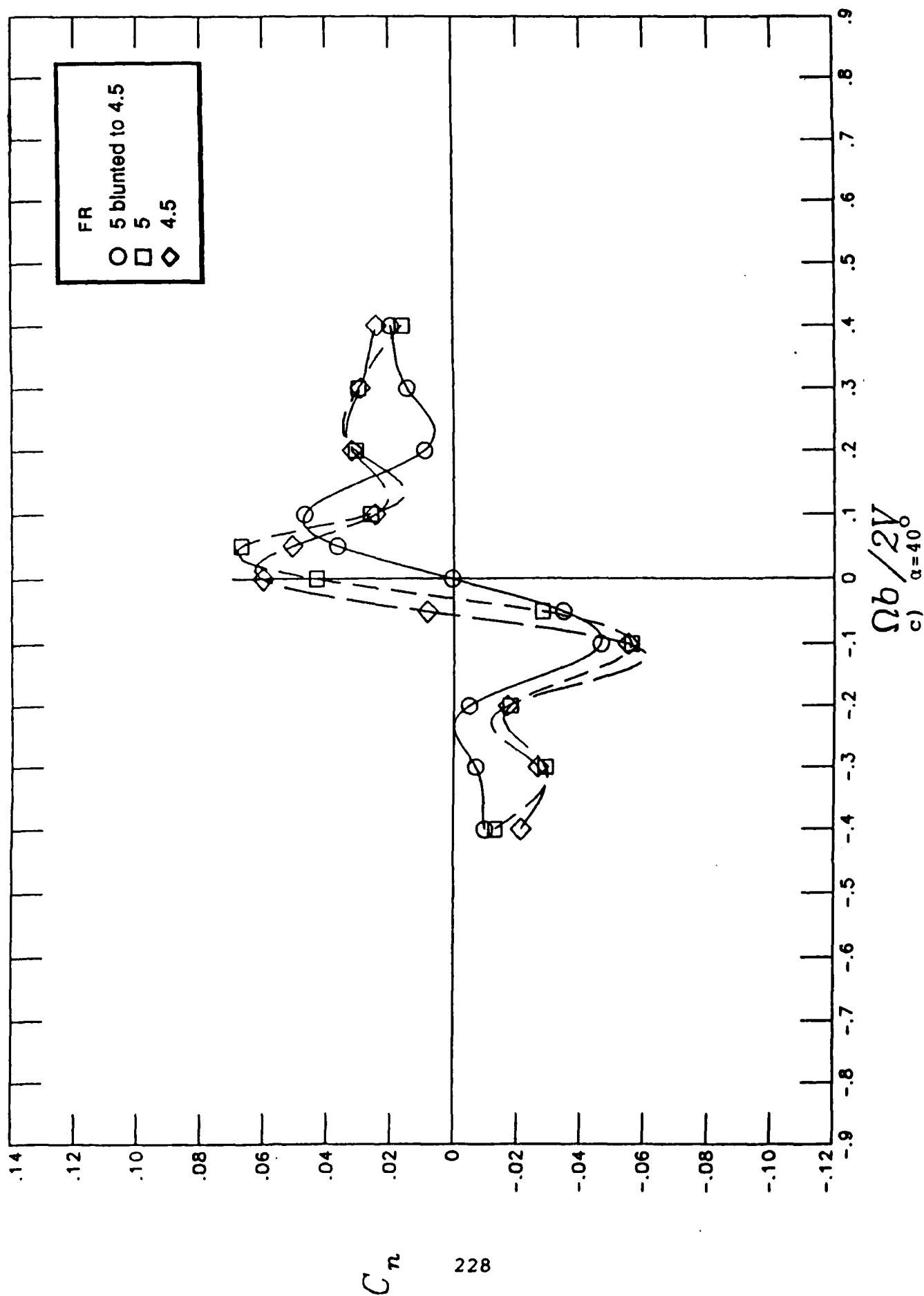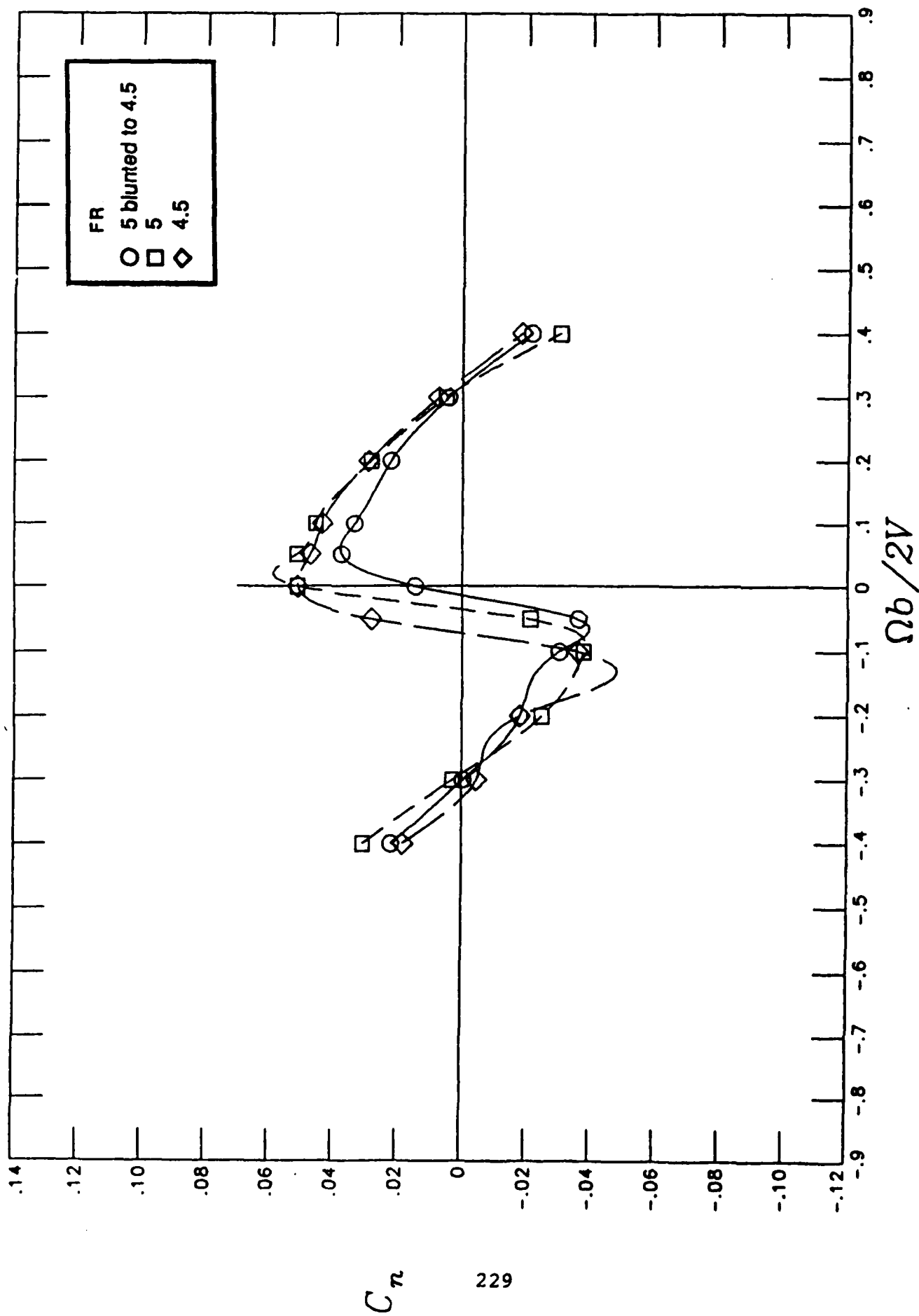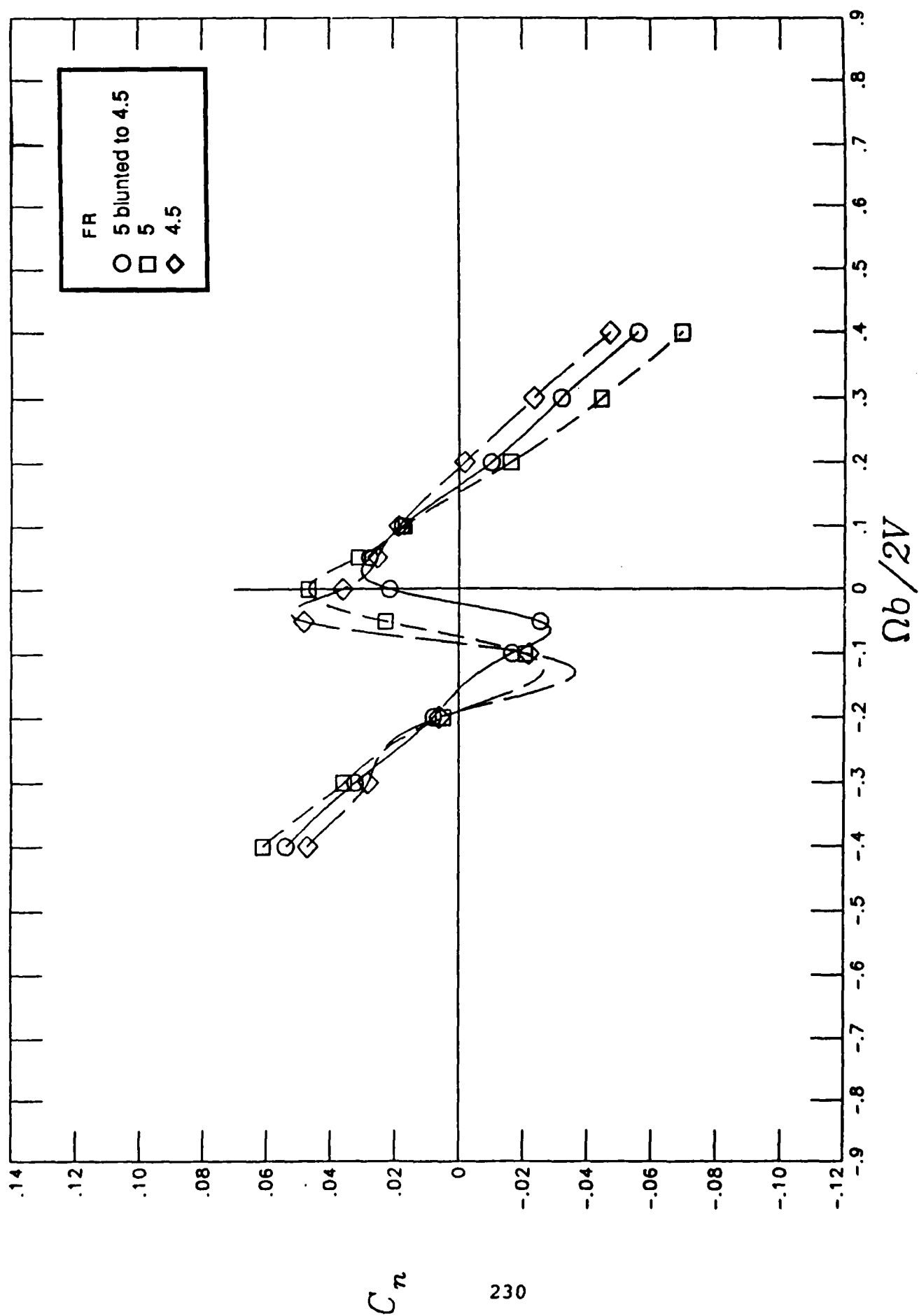
Figure 52.- Continued

f) $\alpha = 65^{\circ}$

$\Omega b / 2V$

C_n

231
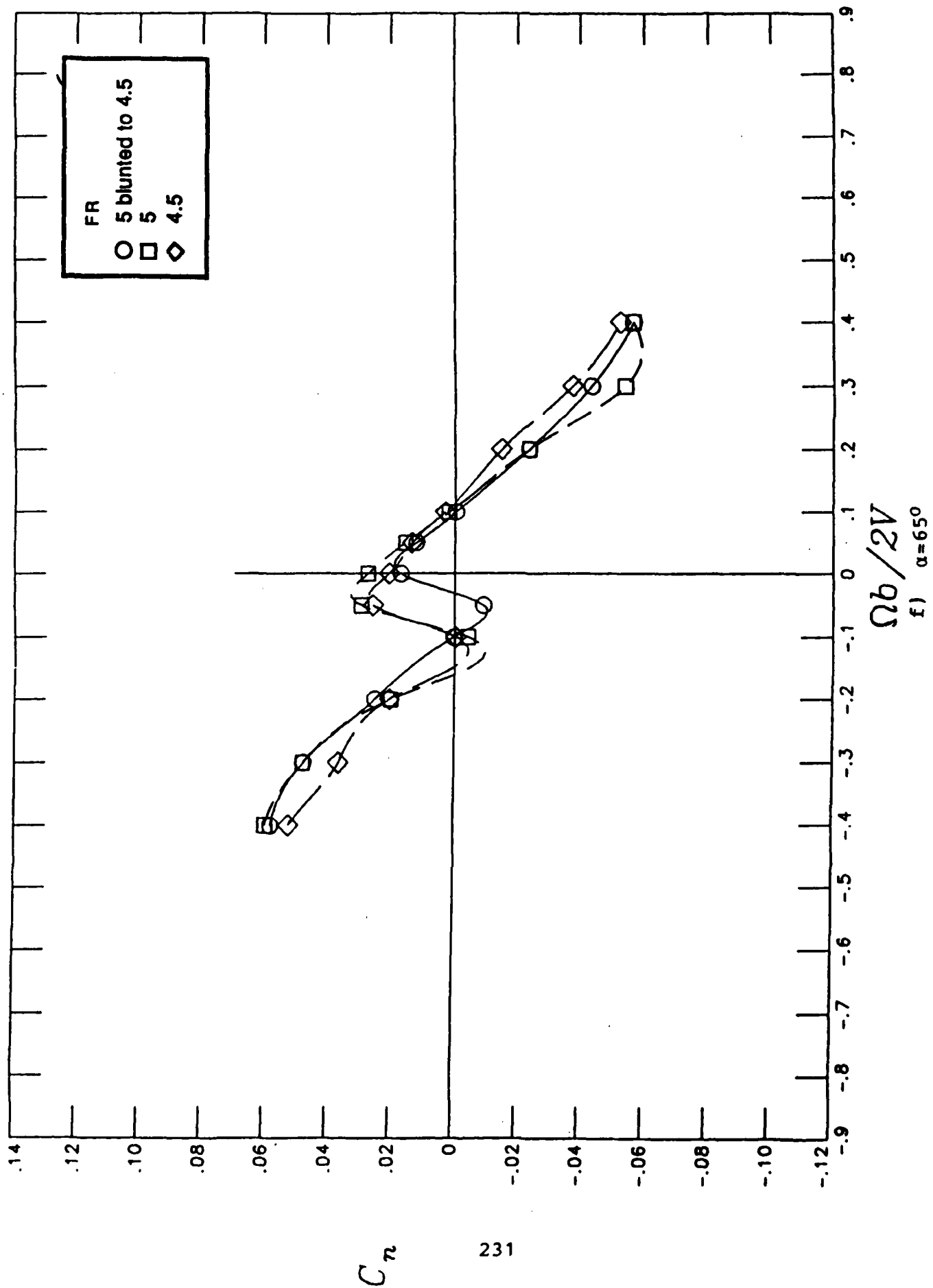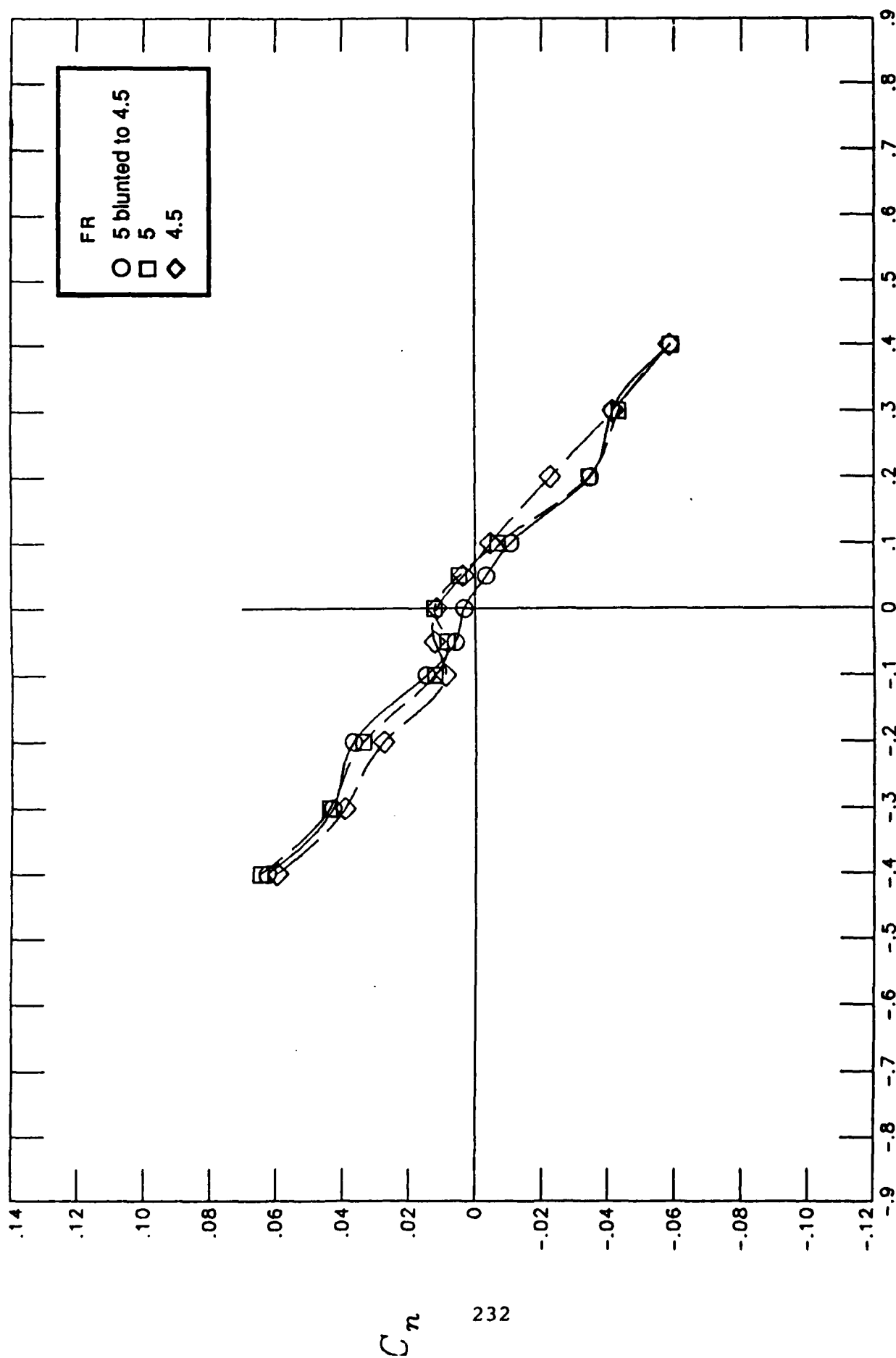
$$\Omega b/2V$$

g) $\alpha = 70°$

Figure 52.- Concluded

232
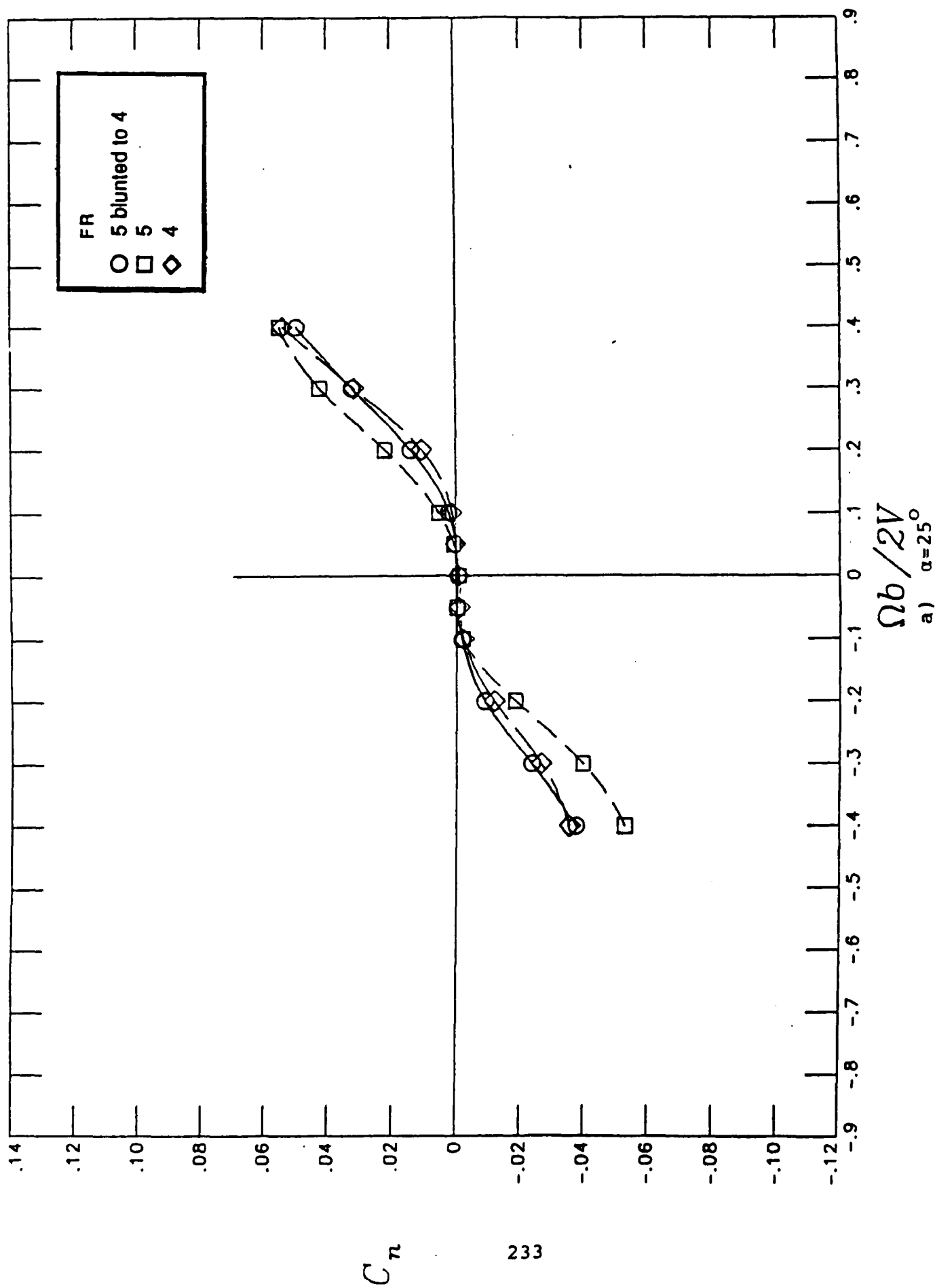
Figure 53.- Effect of blunting a H/W=0.6 cross-sectional forebody from FR 5 to 4 on rotational yawing-moment coefficient characteristics

233

$\frac{\Omega b}{2V}\Big|_{\alpha=30°}$

b) Figure 53.- Continued

C_n

234

$\Omega b/2V$

c) $\alpha=40°$

Figure 53.- Continued

235

Figure 53.- Continued

$\Omega b/2V$

d) $\alpha = 50°$

C_n

236

$\frac{\Omega b}{2V}_{\alpha=60°}$

e) $\alpha=60°$

Figure 53.- Continued

237

$\Omega b/2V$

f) $\alpha=65°$

Figure 53.- Continued

238
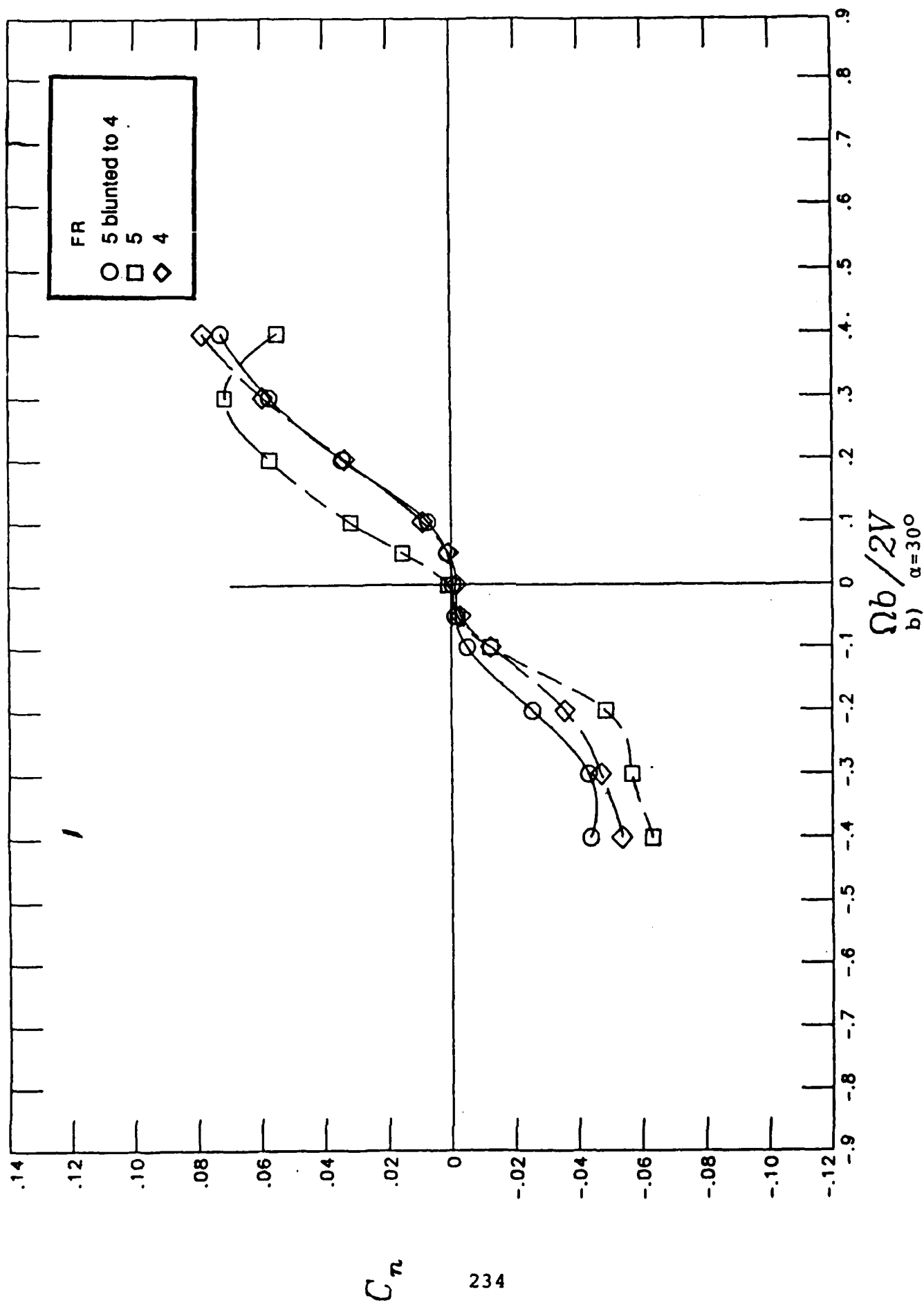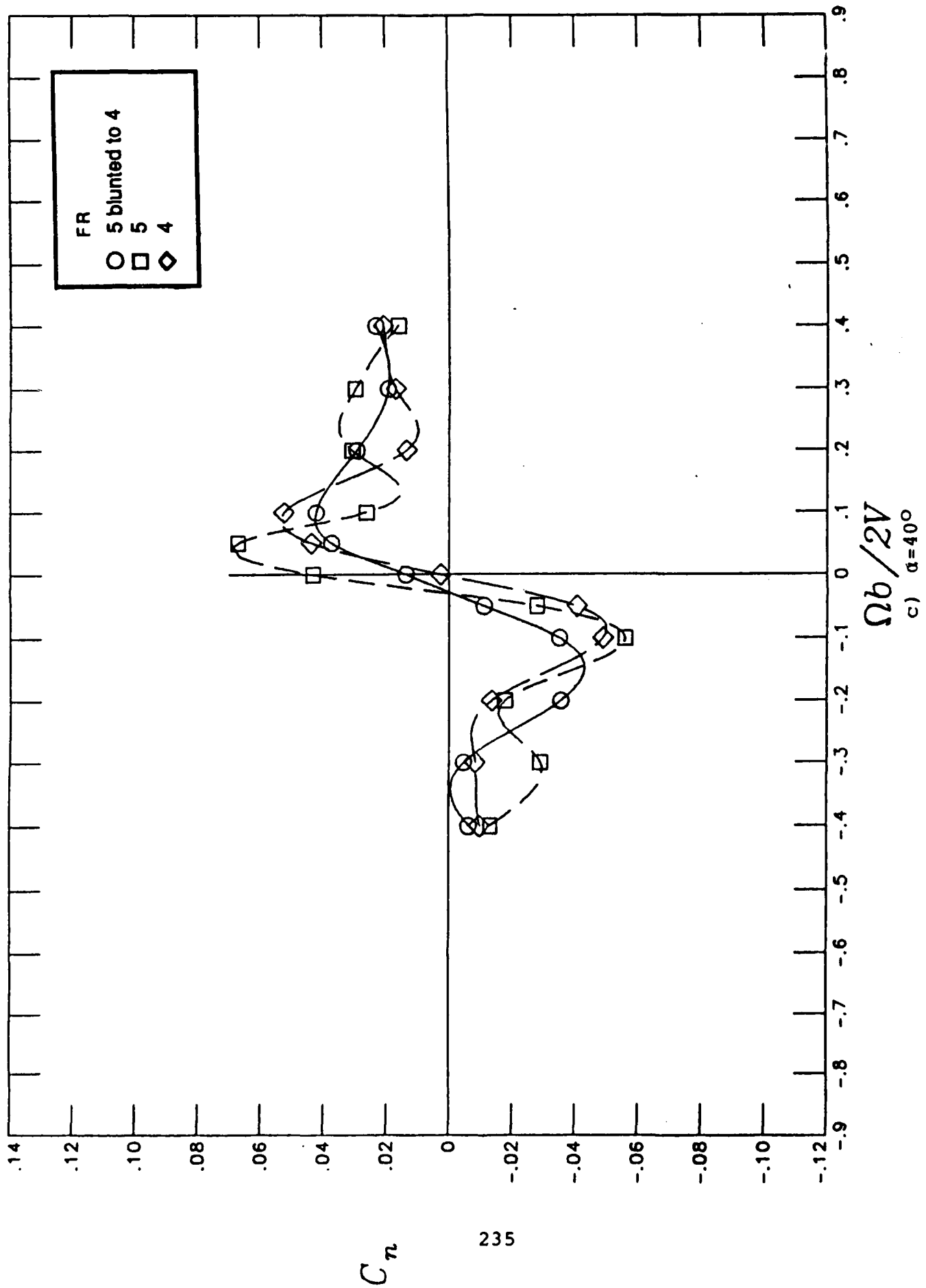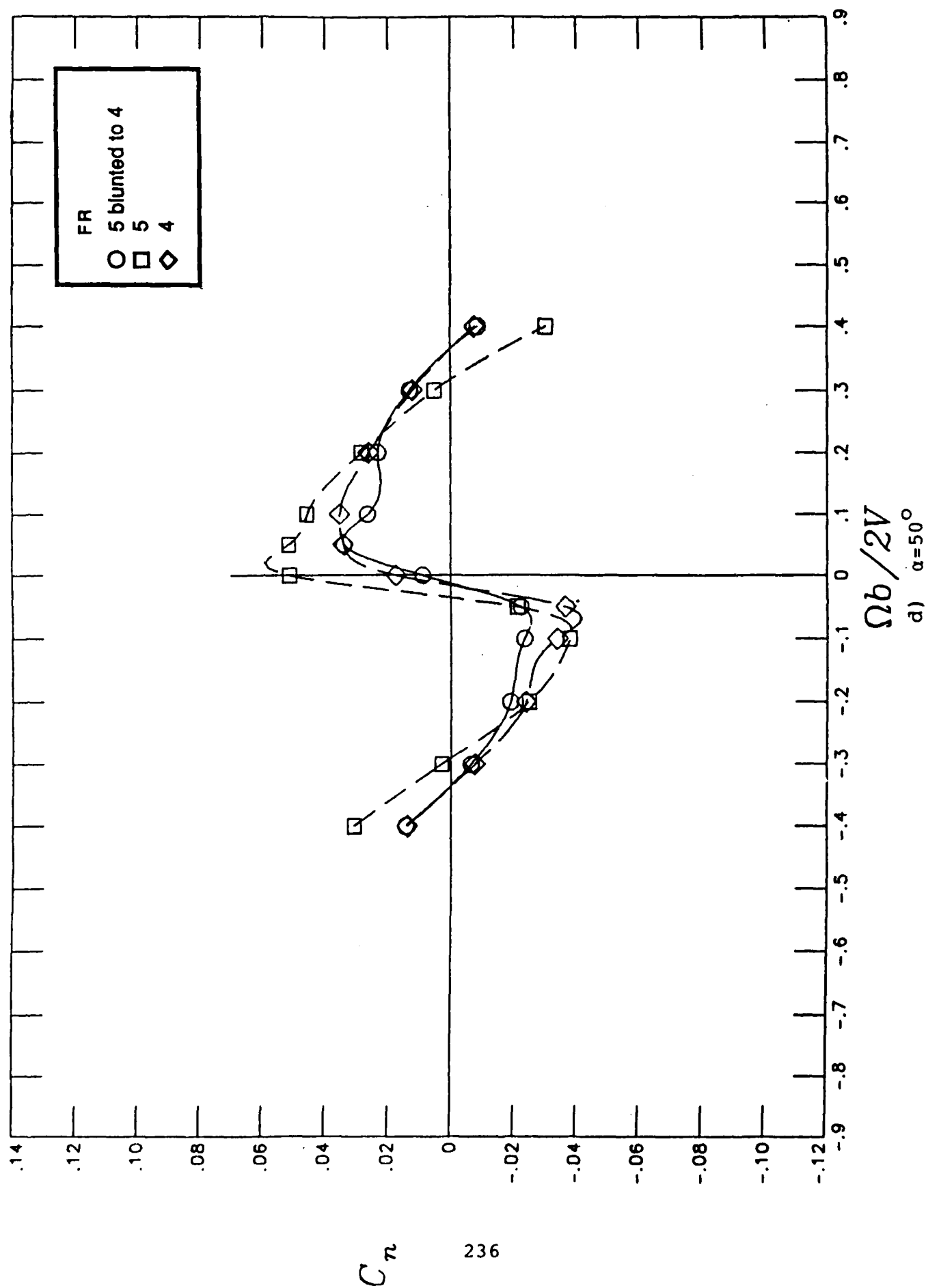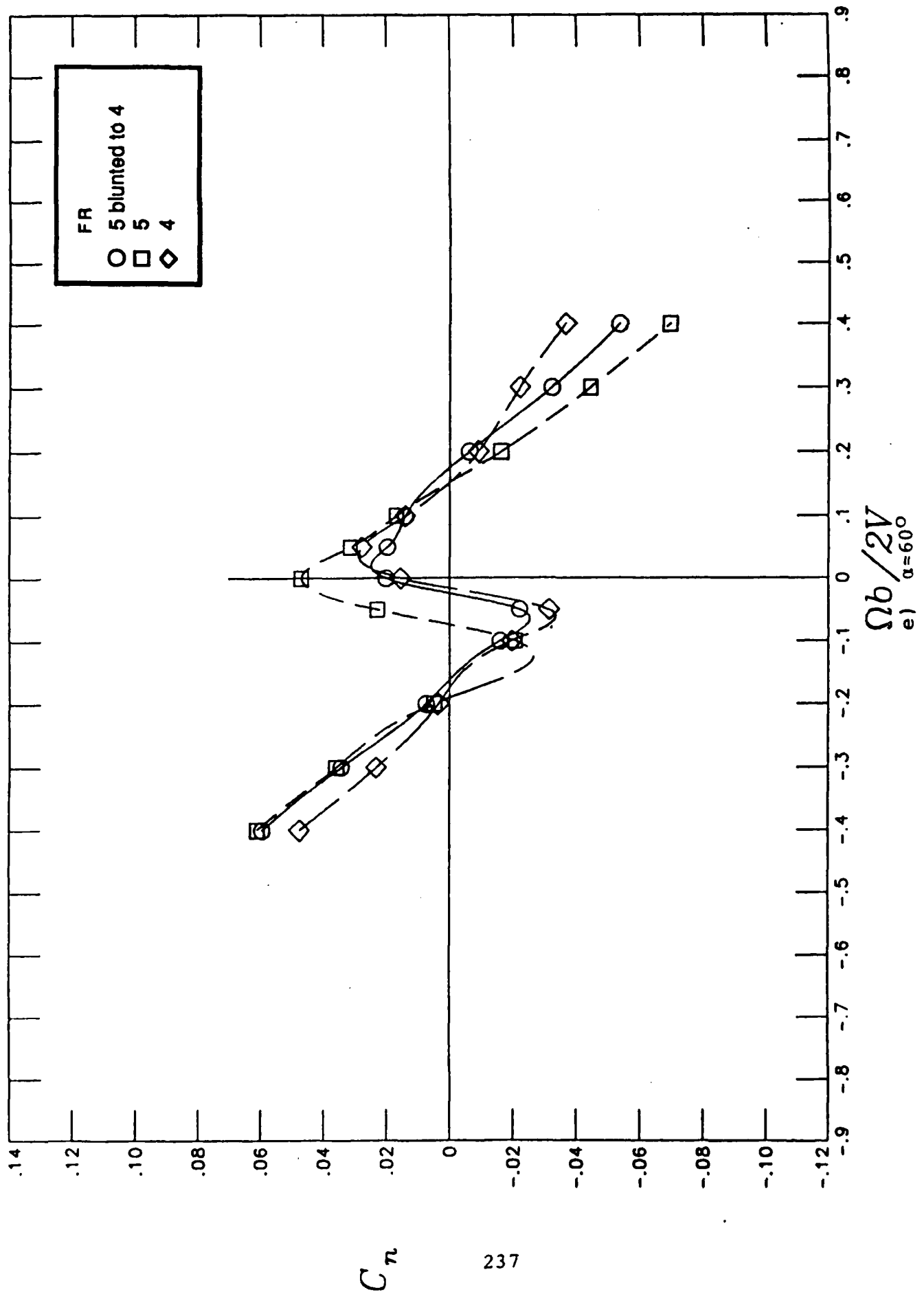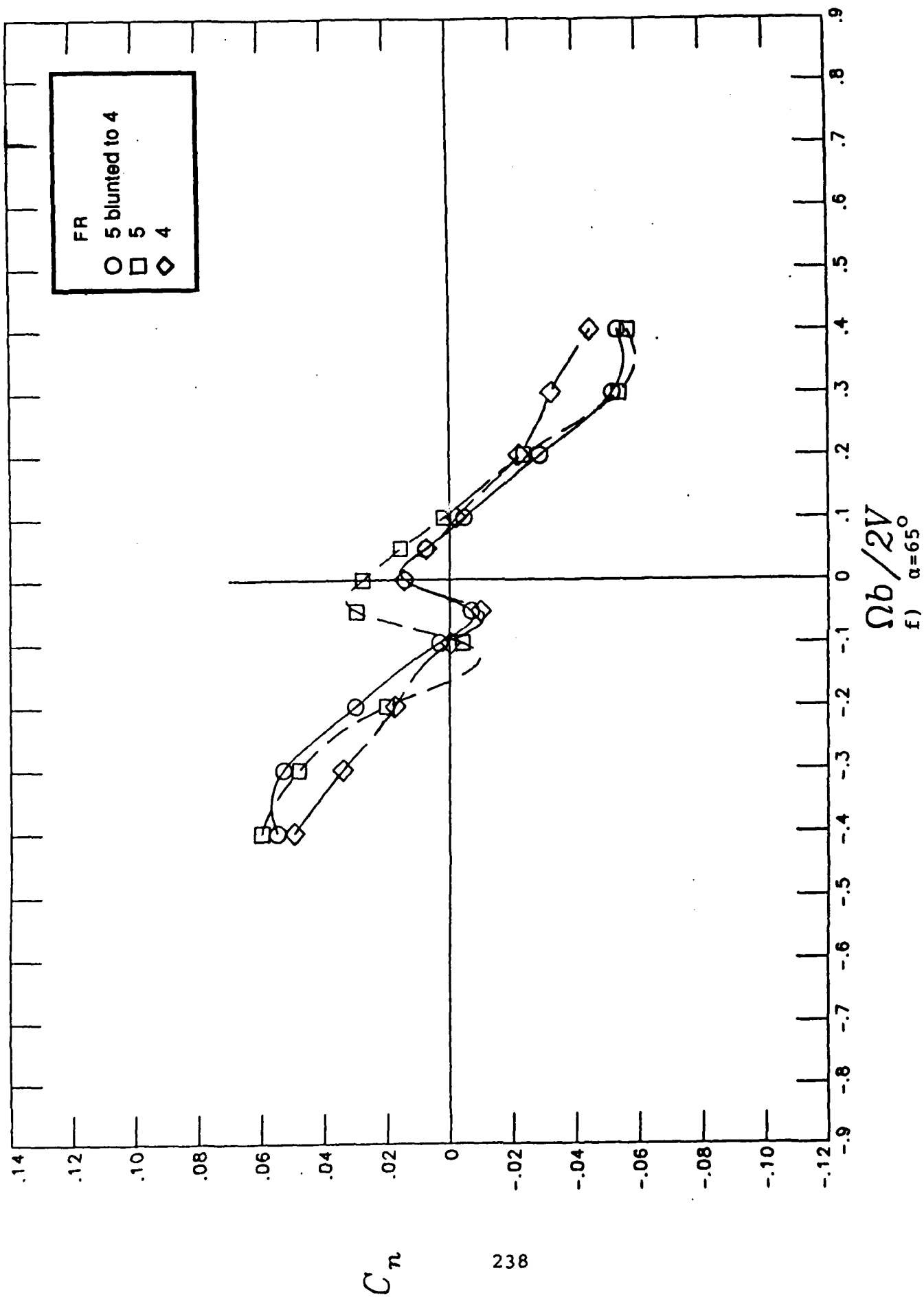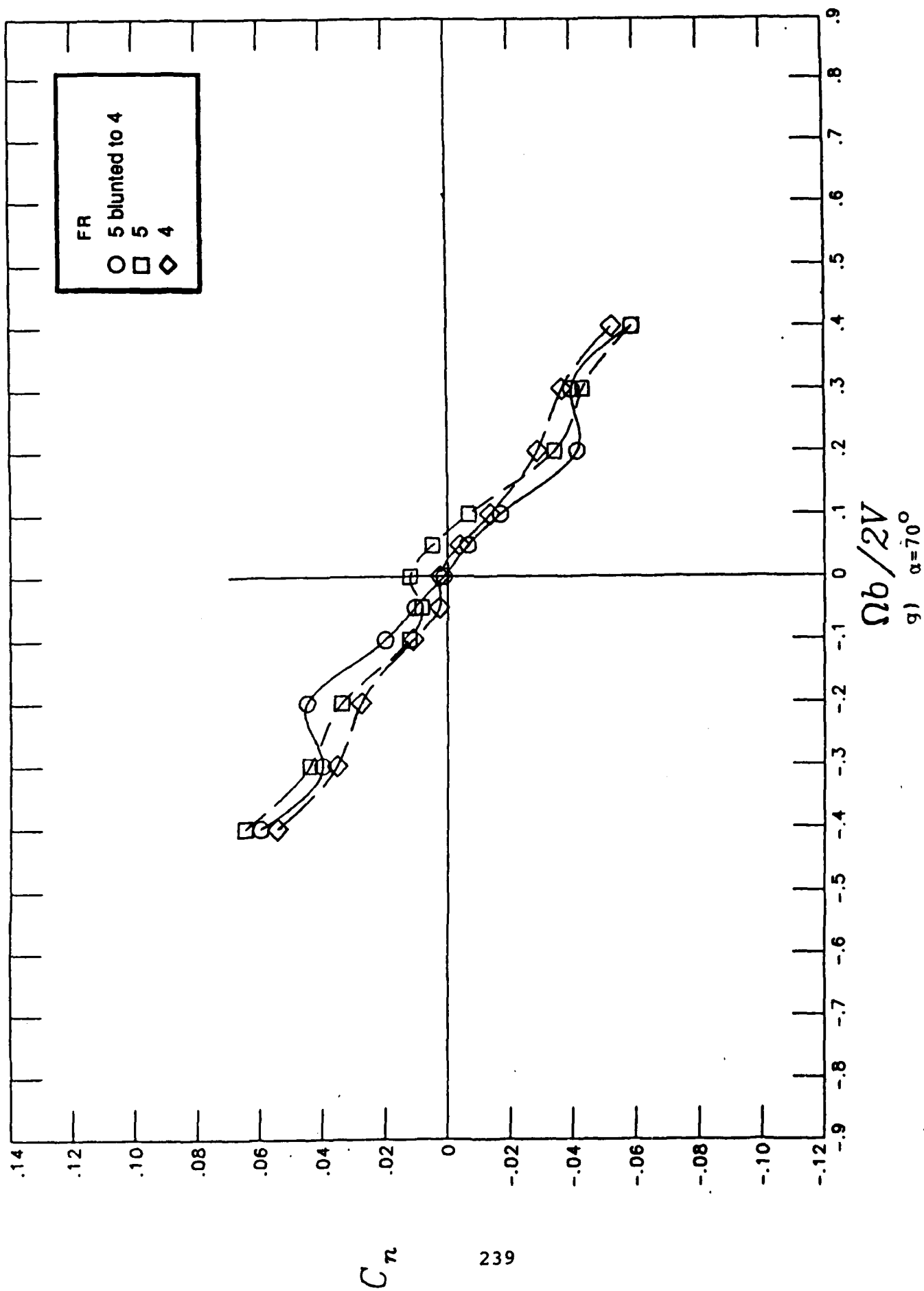
Figure 53.- Concluded

g) $\alpha = 70°$

239
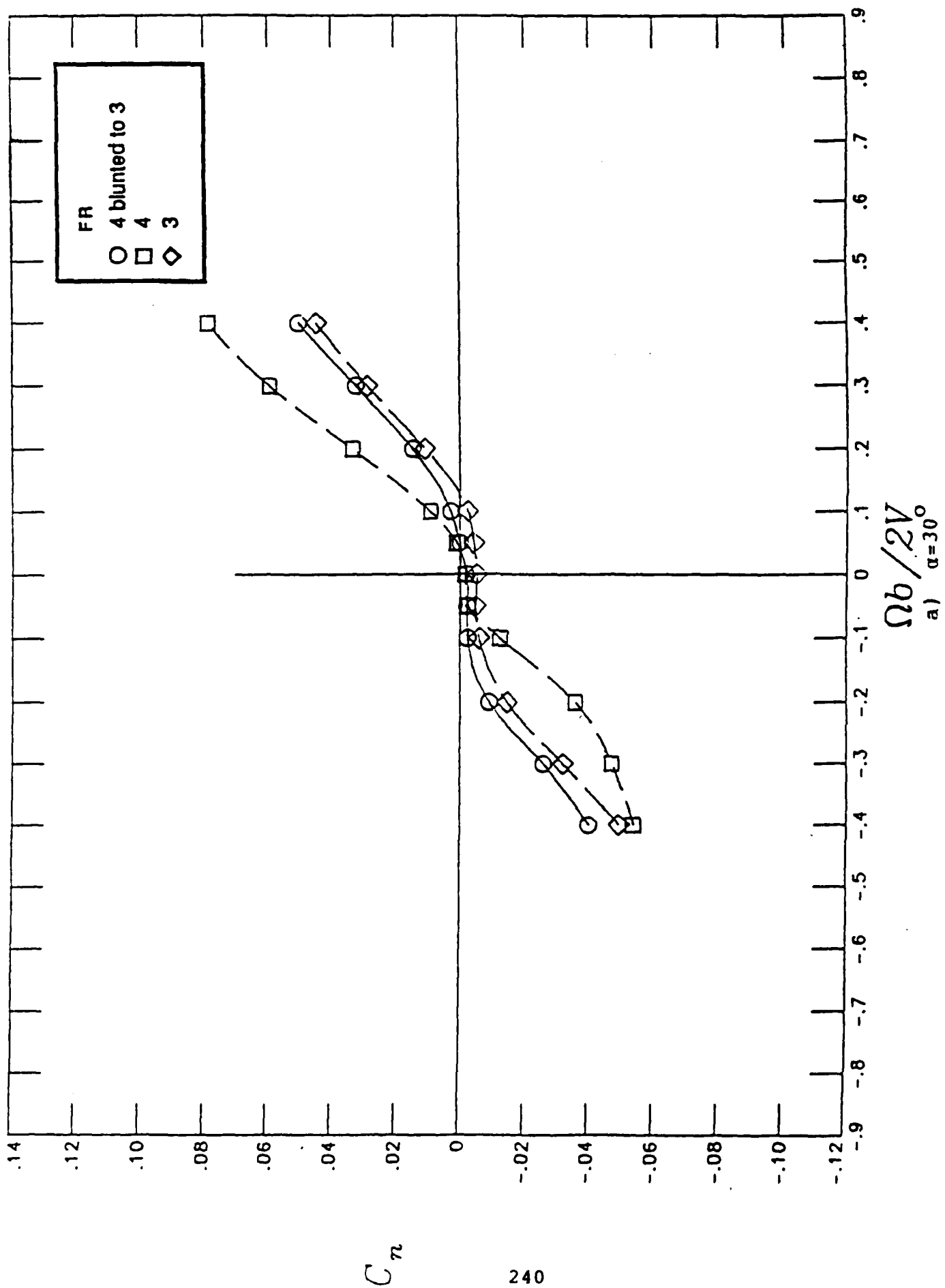
Figure 54.- Effect of blunting a H/W=0.6 cross-sectional forebody from FR 4 to 3 on rotational yawing-moment coefficient characteristics

240

C_n

$\Omega b/2V$

b) $\alpha = 40°$

Figure 54.- Continued

241

$\dfrac{\Omega b}{2V}$

c) $\alpha = 45^\circ$

Figure 54.- Continued

242

d) $\alpha = 50°$

Figure 54.- Continued

243

$\Omega b/2V$

e) $\alpha = 60°$
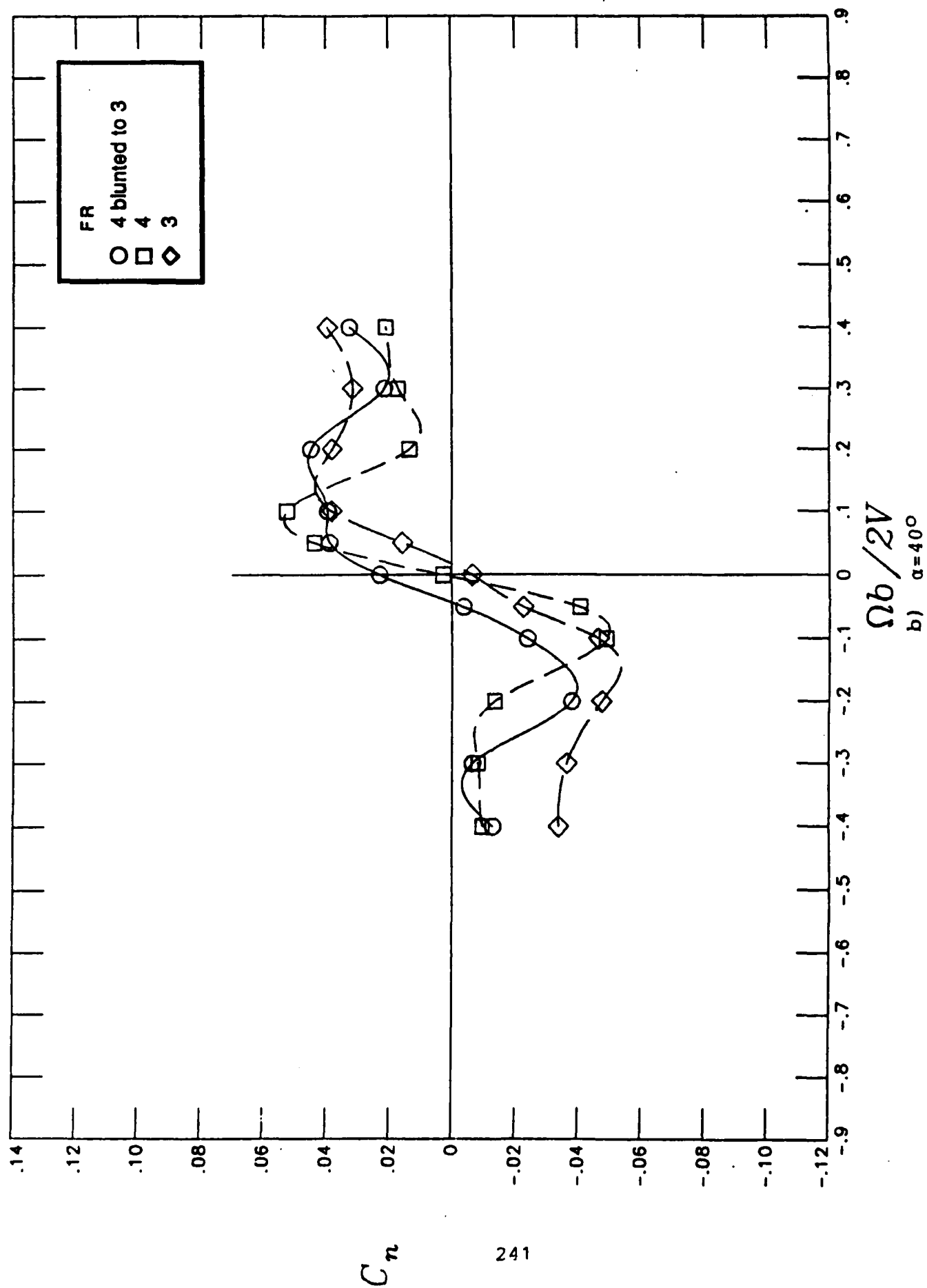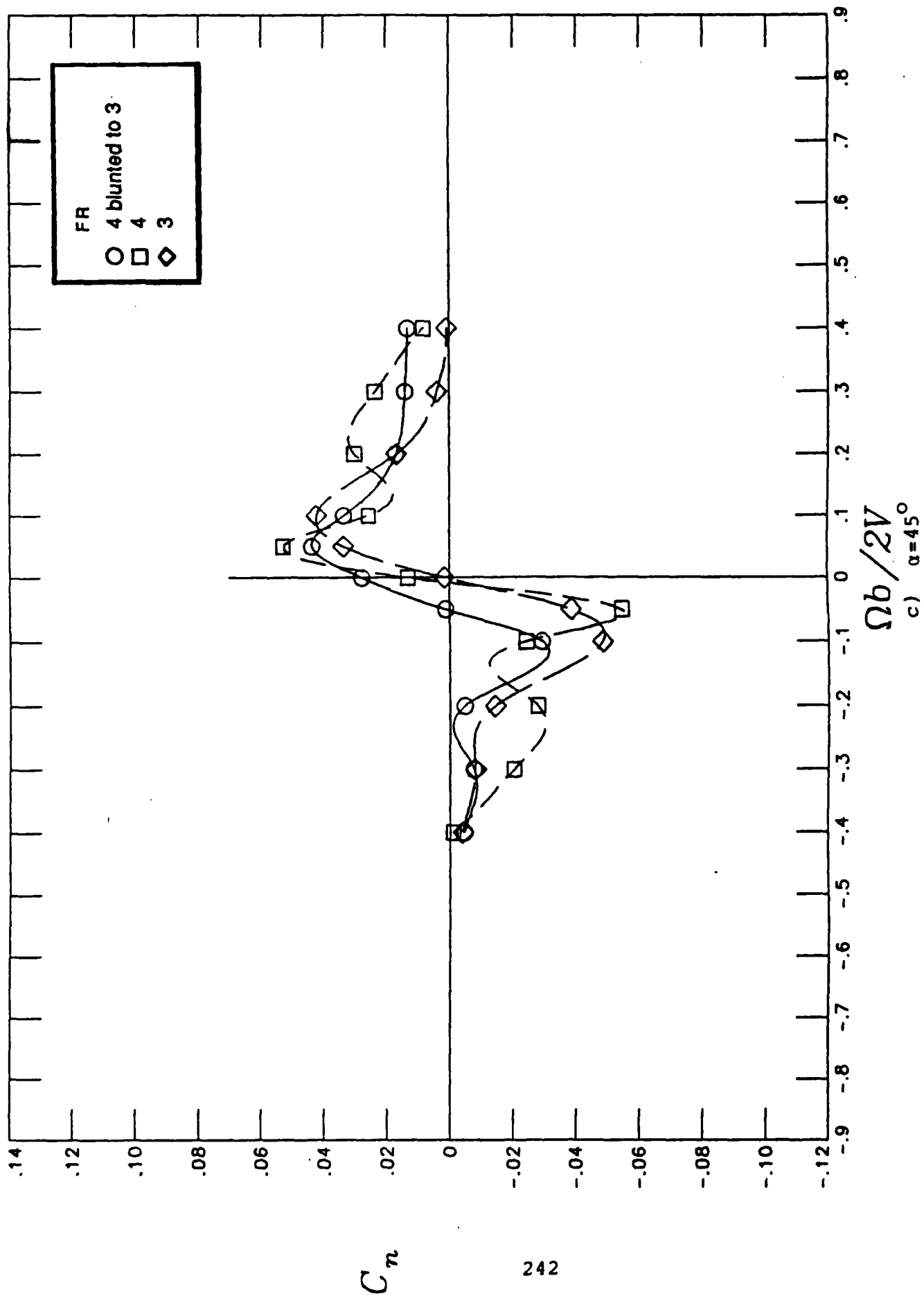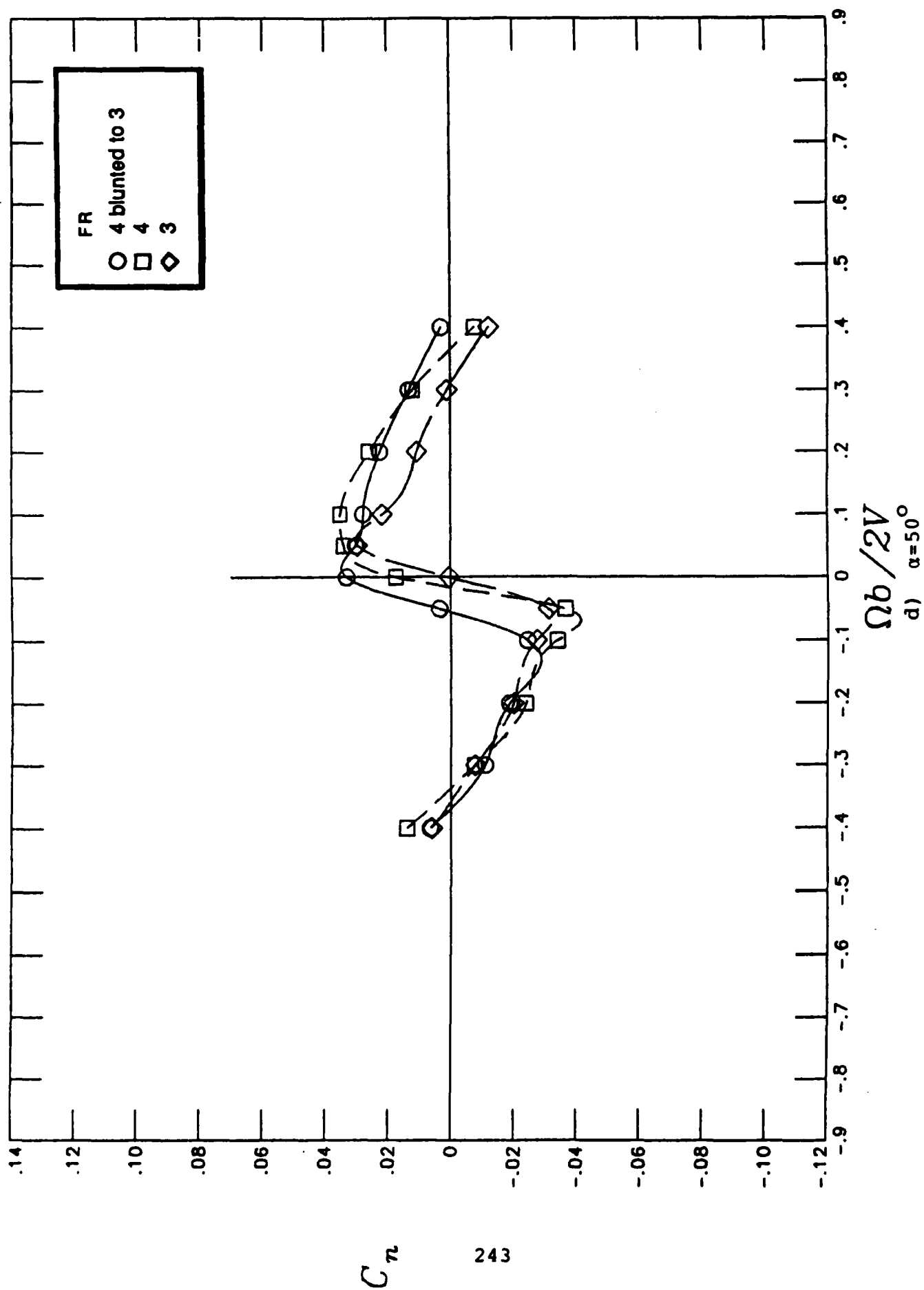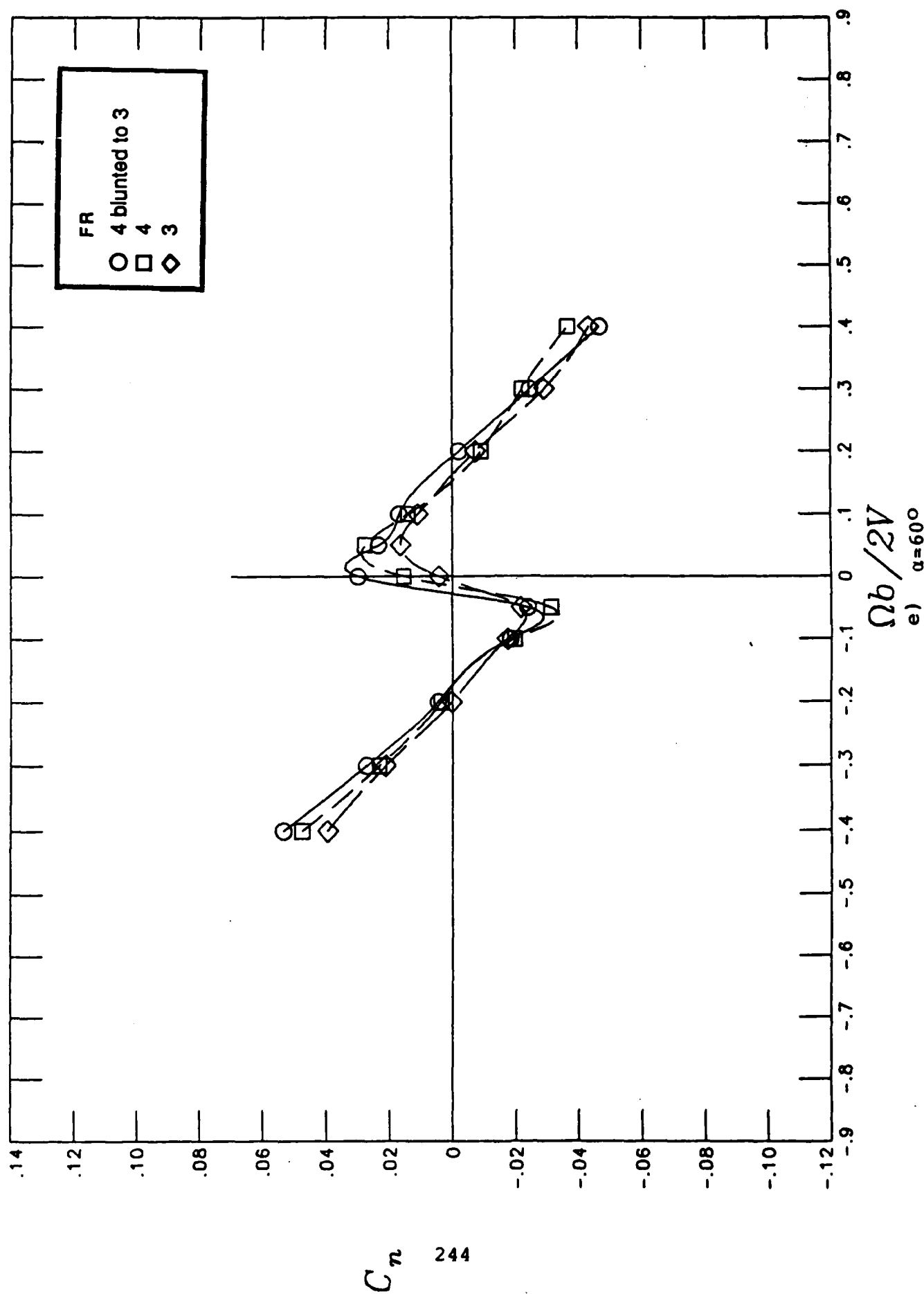
Figure 54.- Concluded

C_n

244
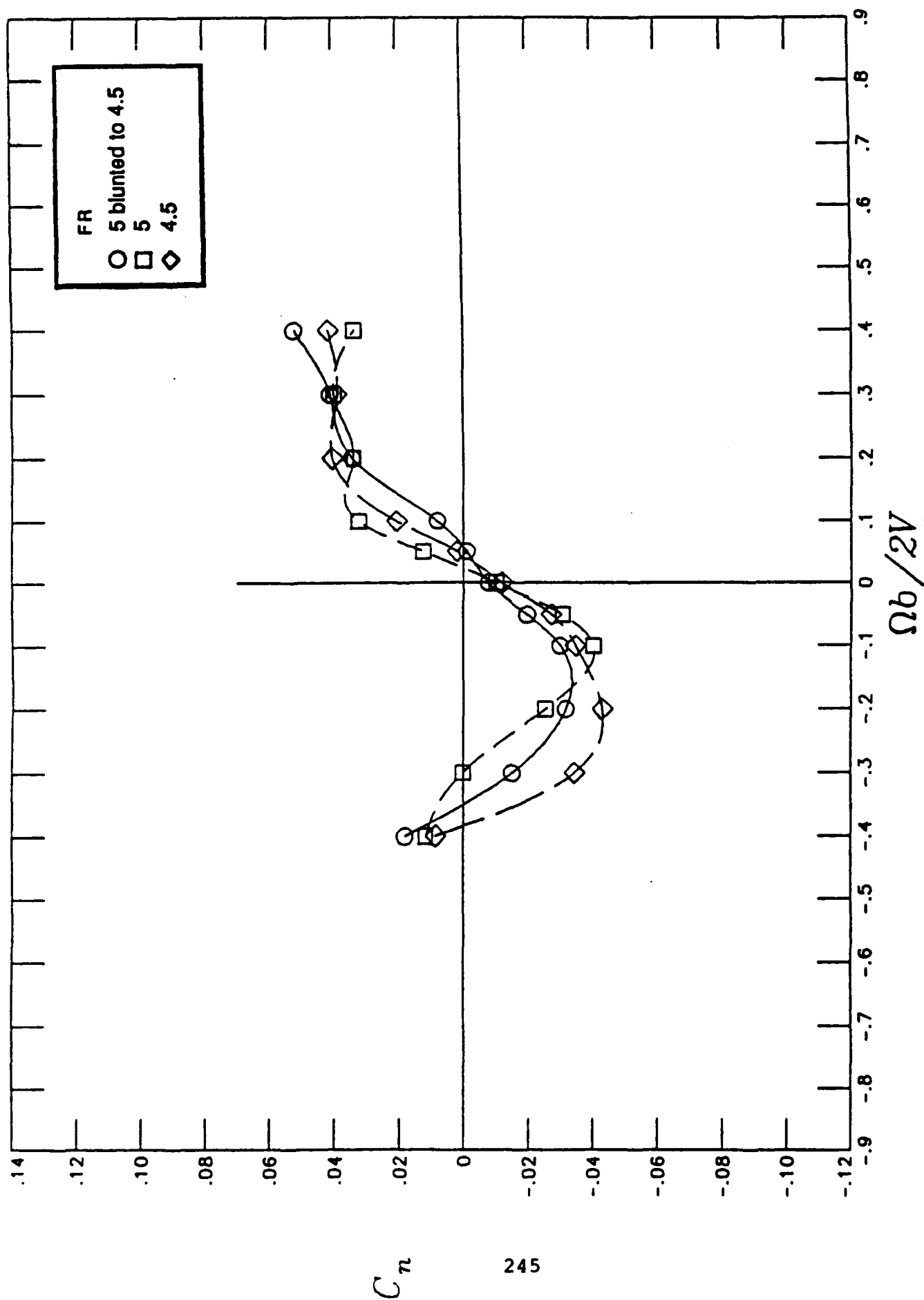
Figure 55.- Effect of blunting a H/W=0.8 cross-sectional forebody from FR 5 to 4.5 on rotational yawing-moment coefficient characteristics

245

C_n

$\Omega b/2V$

b) $\alpha=45°$

Figure 55.- Continued

FR
○ 5 blunted to 4.5
□ 5
◇ 4.5

246

Figure 55.- Continued

c) α=50°

C_n

247

d) α=60°
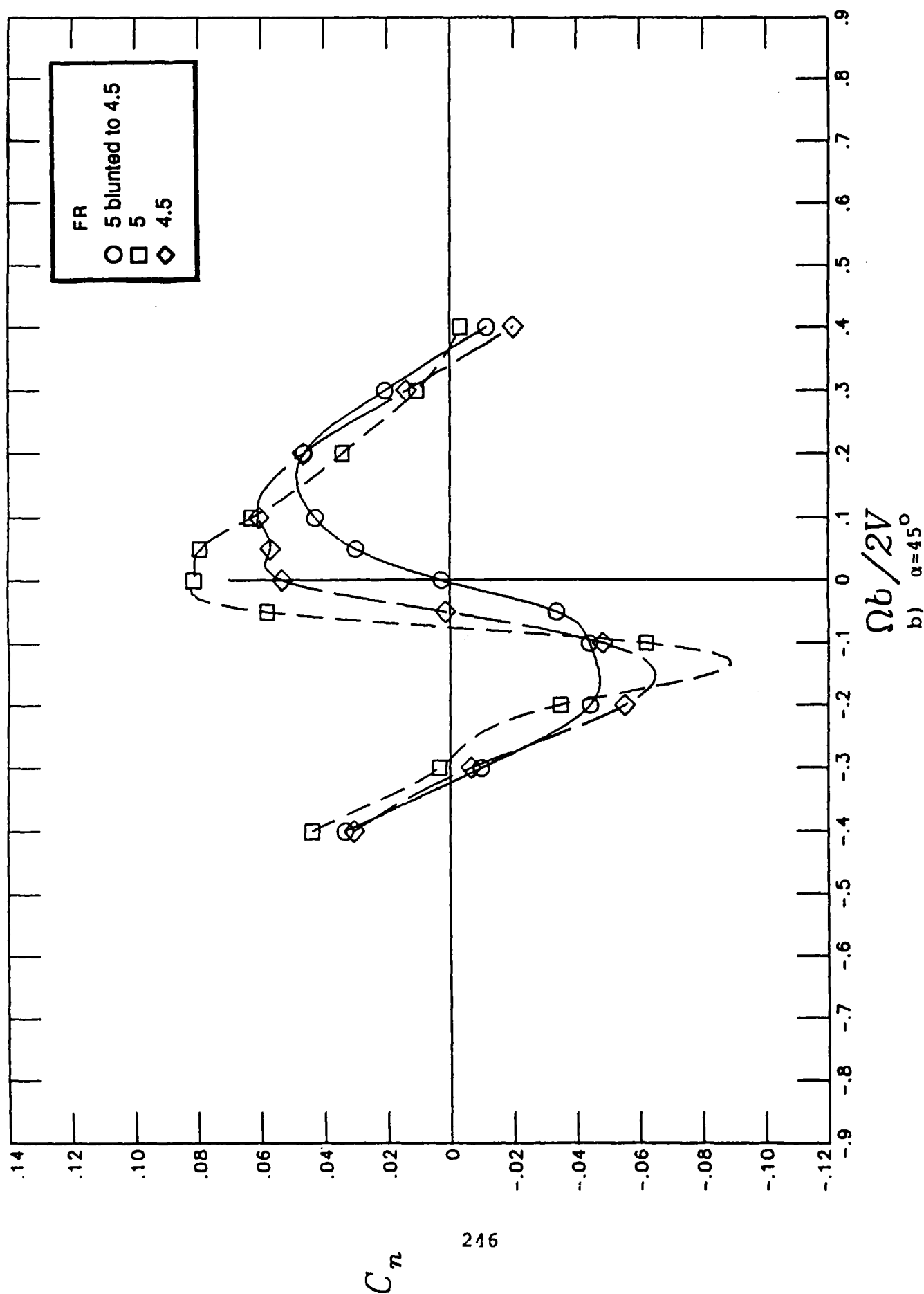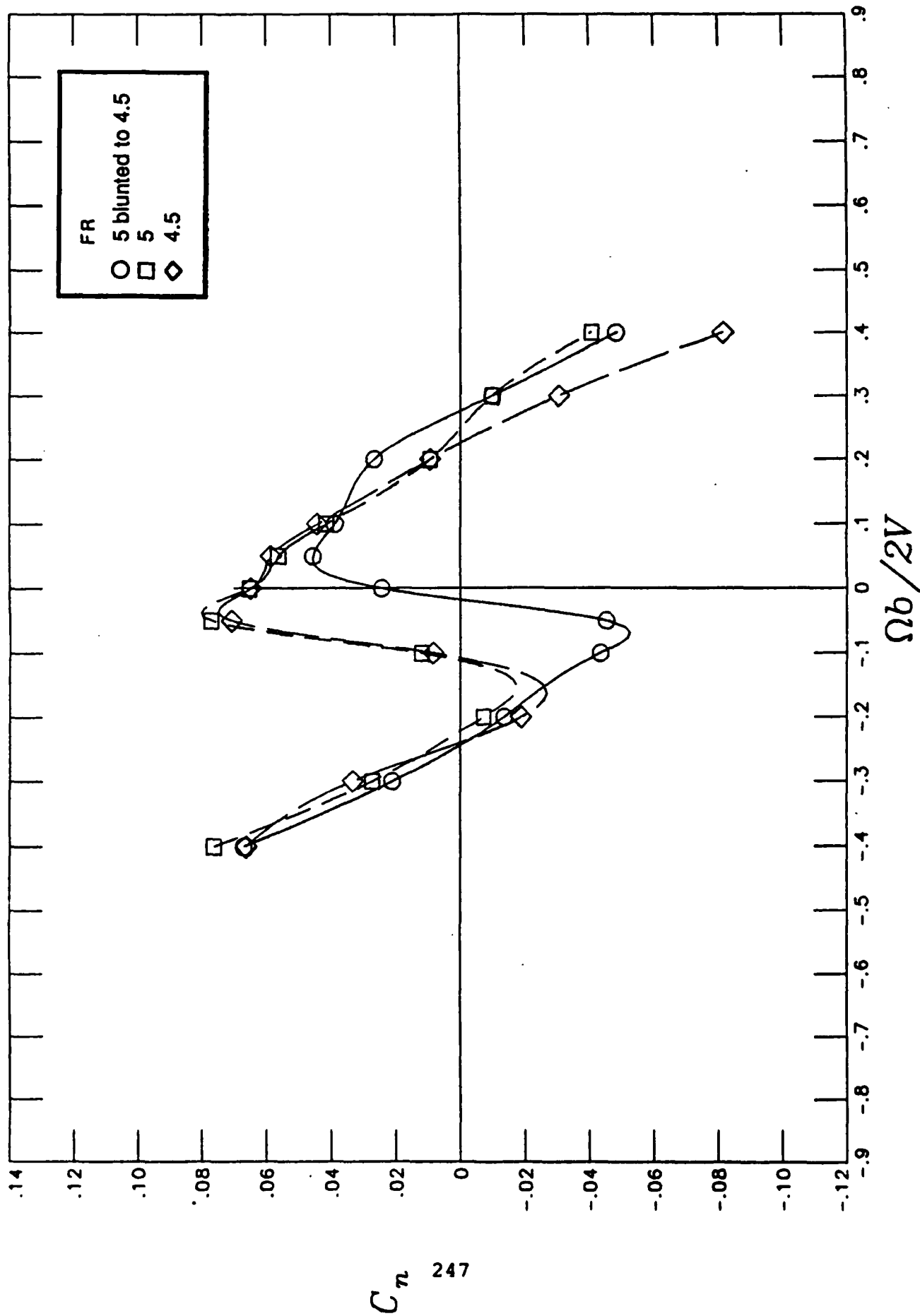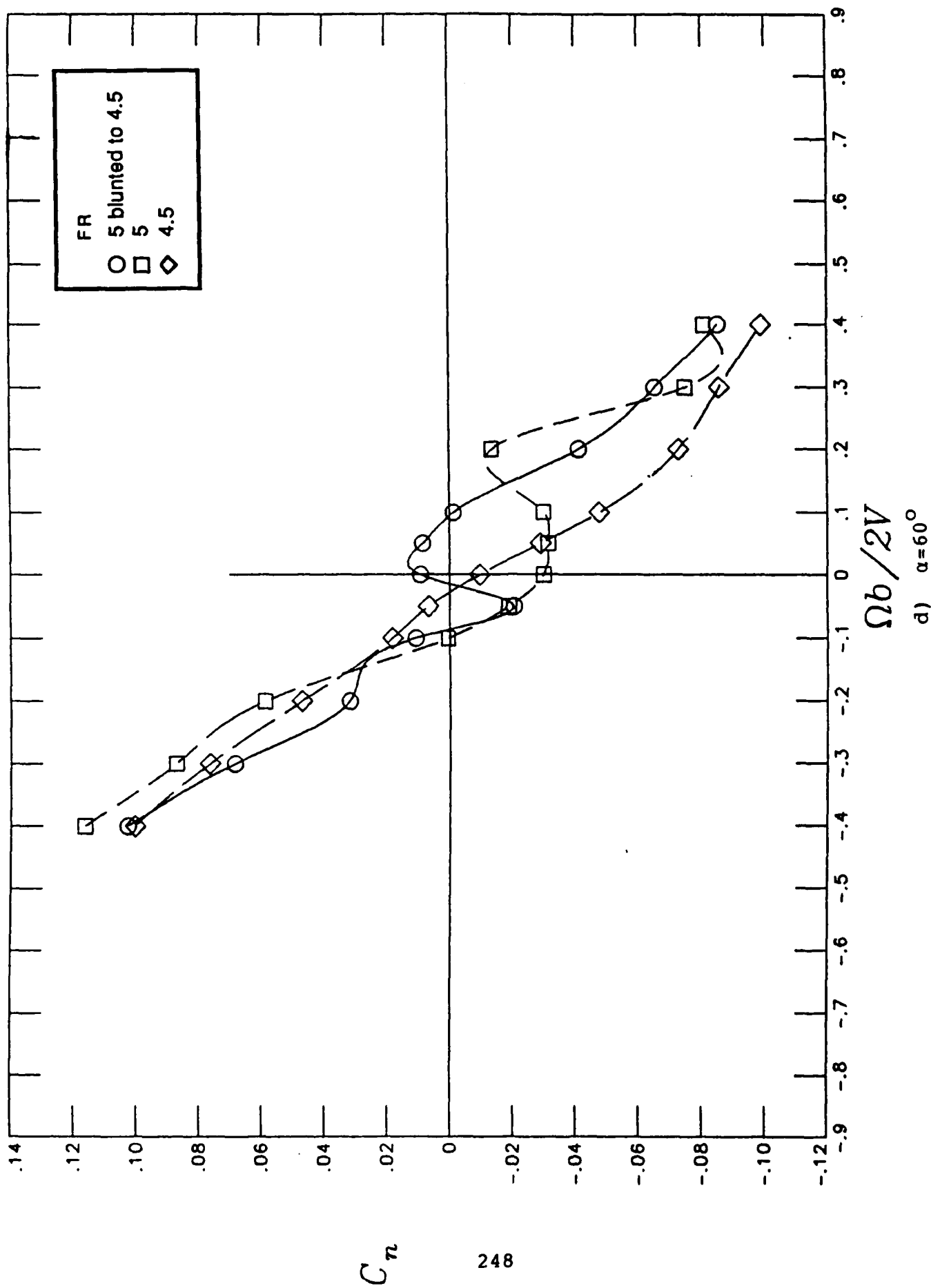
Figure 55.- Concluded
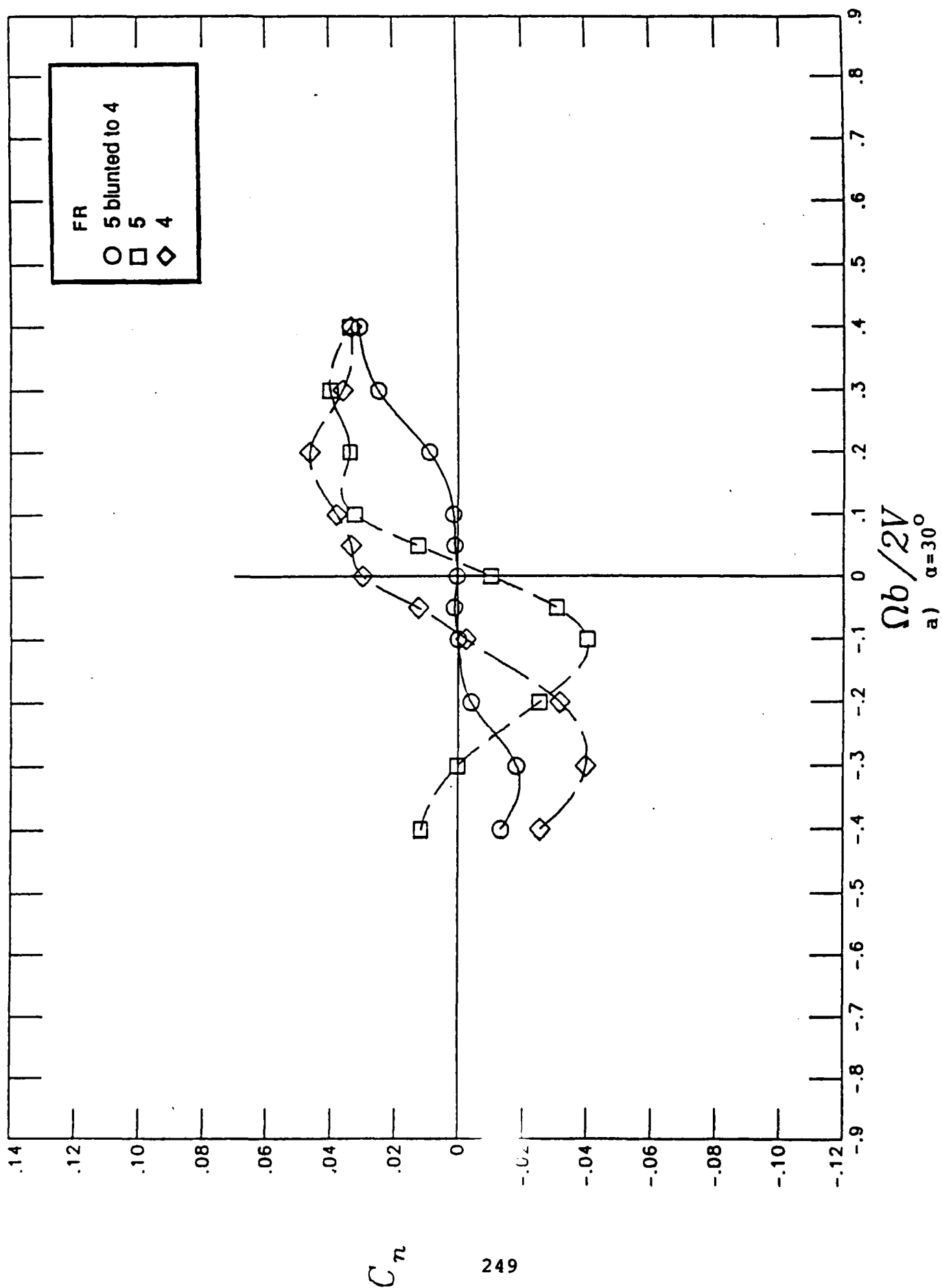
Figure 56.- Effect of blunting a H/W=0.8 cross-sectional forebody from FR 5 to 4 on rotational yawing-moment coefficient characteristics

249

(a) $\alpha = 45°$
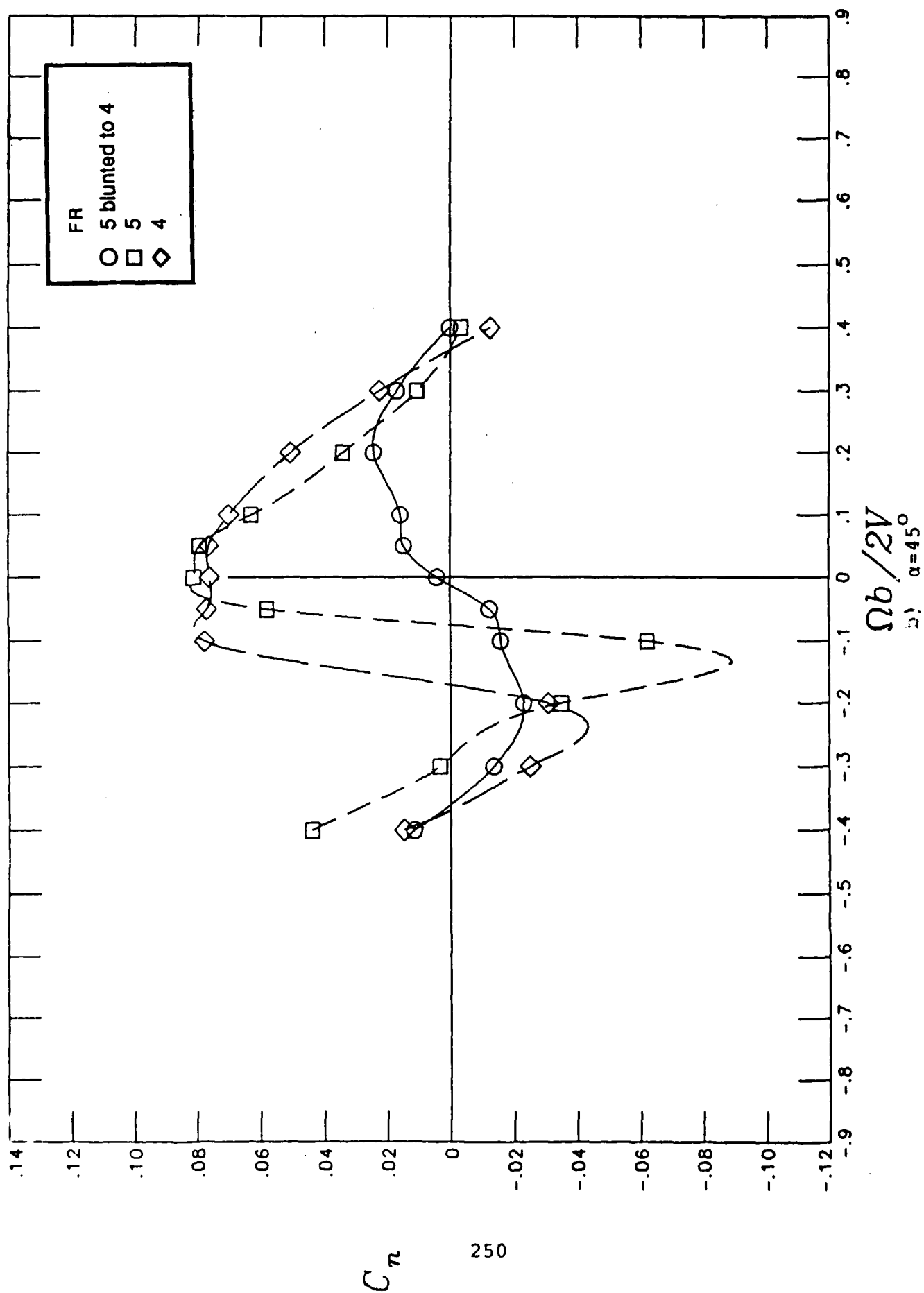
Figure 56.– Concluded

250
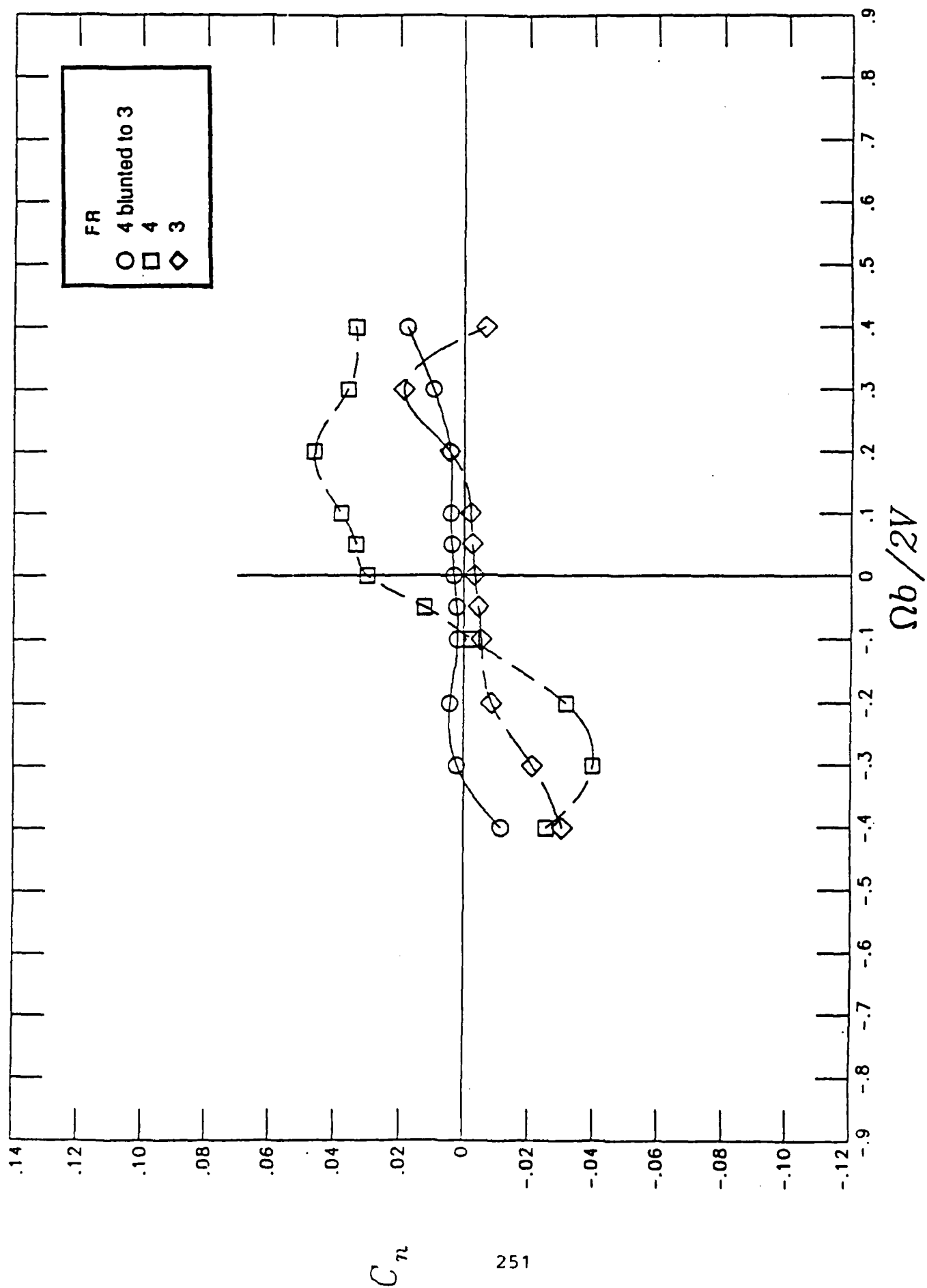
Figure 57.- Effect of blunting a H/W=0.8 cross-sectional forebody from FR 4 to 3 on rotational yawing-moment coefficient characteristics

a) α=30°

251

Figure 57.- Continued

b) $\alpha = 45°$

$\Omega b/2V$

C_n

252

$\Omega b/2V$

c) $\alpha = 50°$

Figure 57.- Continued

253
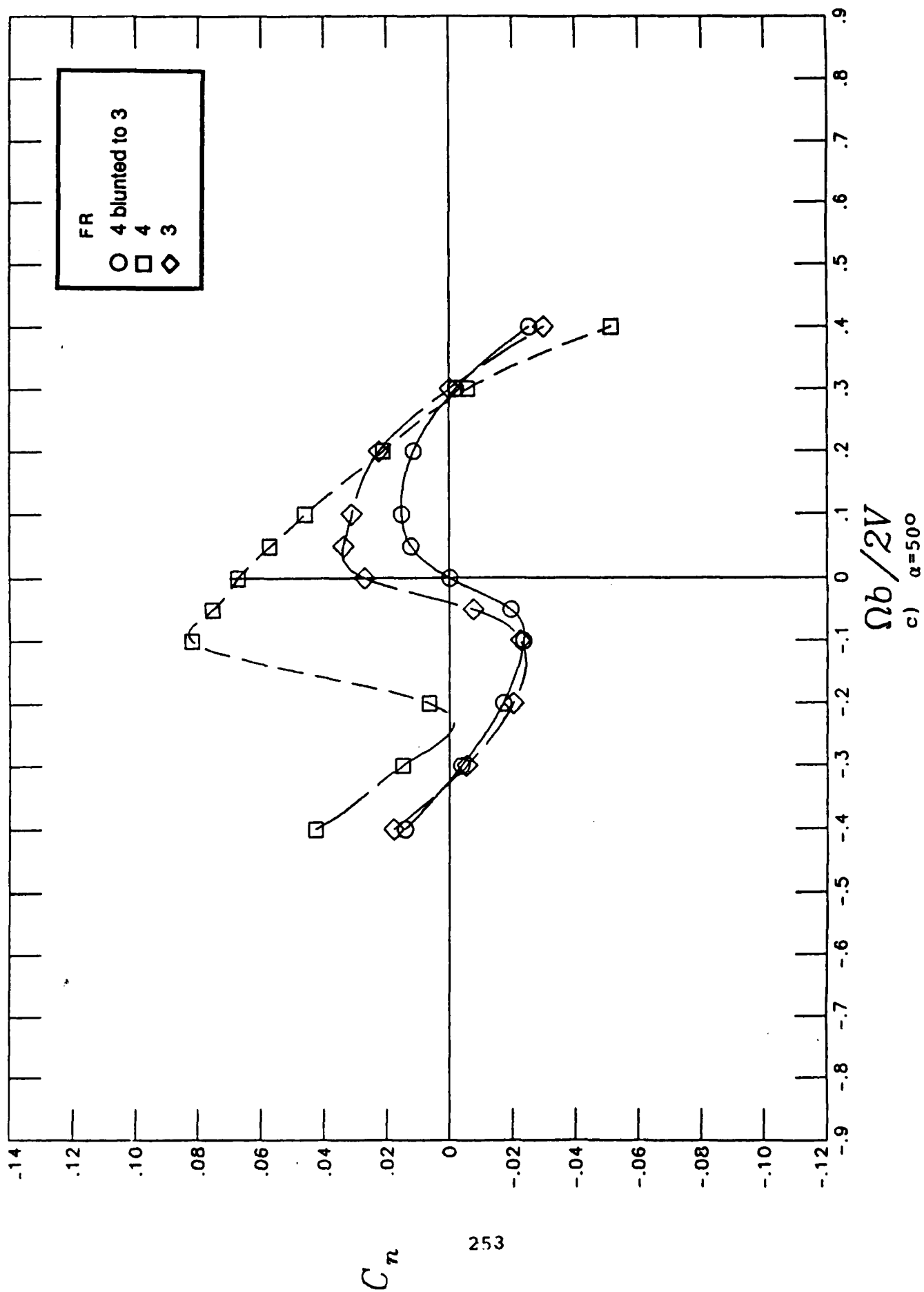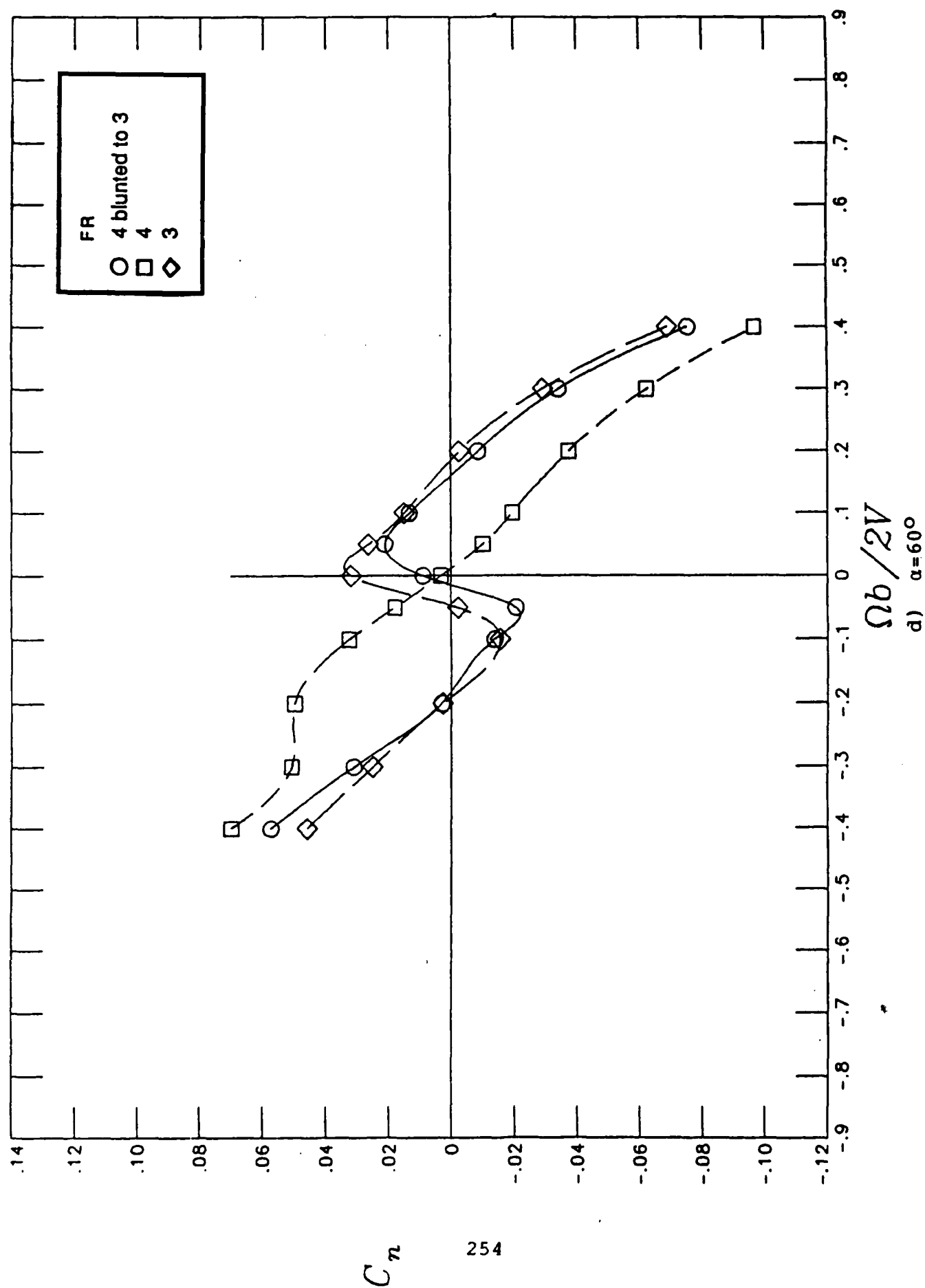
Figure 57.- Concluded

d) α=60°

$\Omega b/2V$

C_n
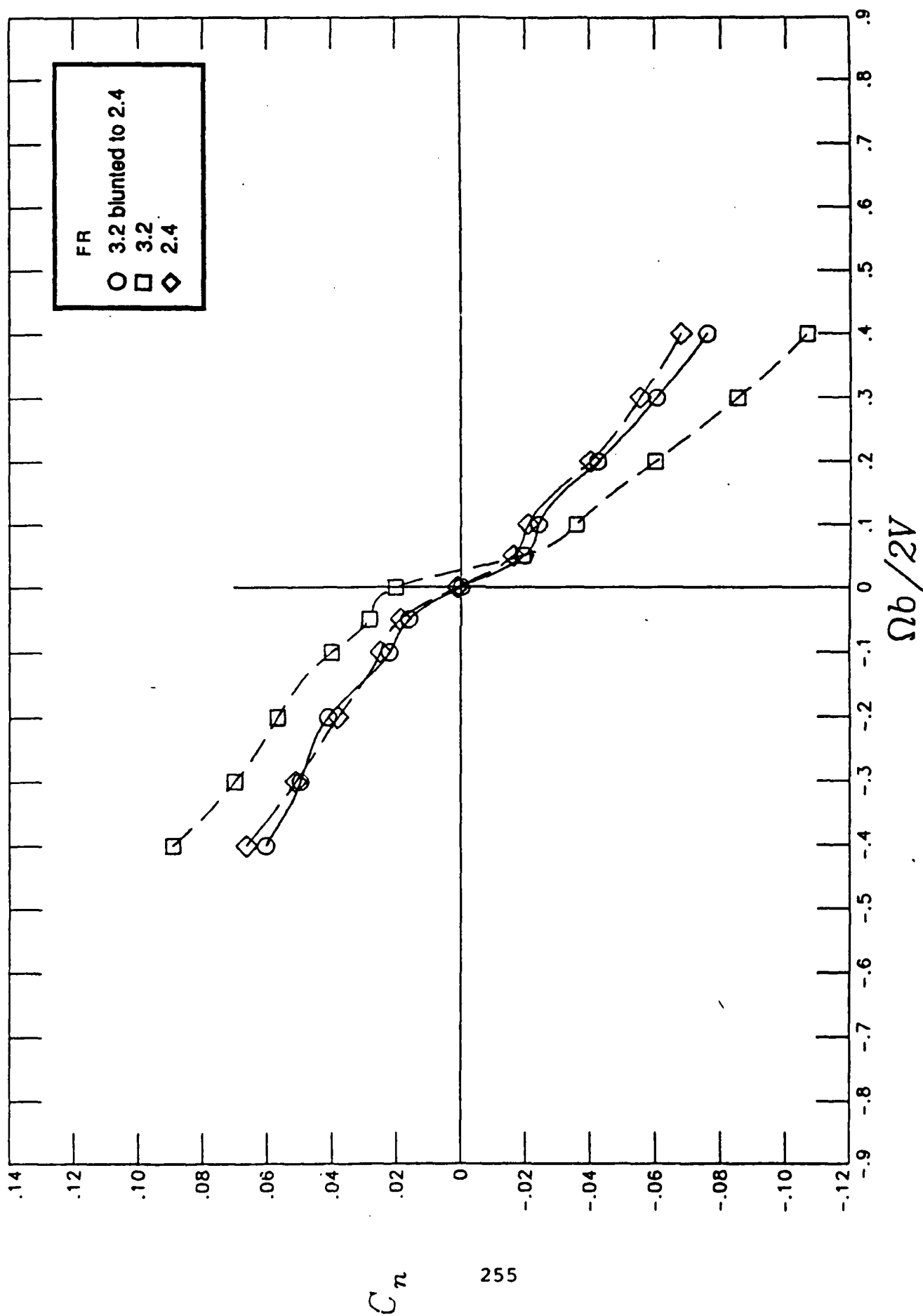
Figure 58.- Effect of blunting a H/W=1.25 cross-sectional forebody from 3.2 to 2.4 on rotational yawing-moment coefficient characteristics

Figure 58 .- Continued

b) $\alpha = 45°$

$\frac{\Omega b}{2V}$

C_n

256
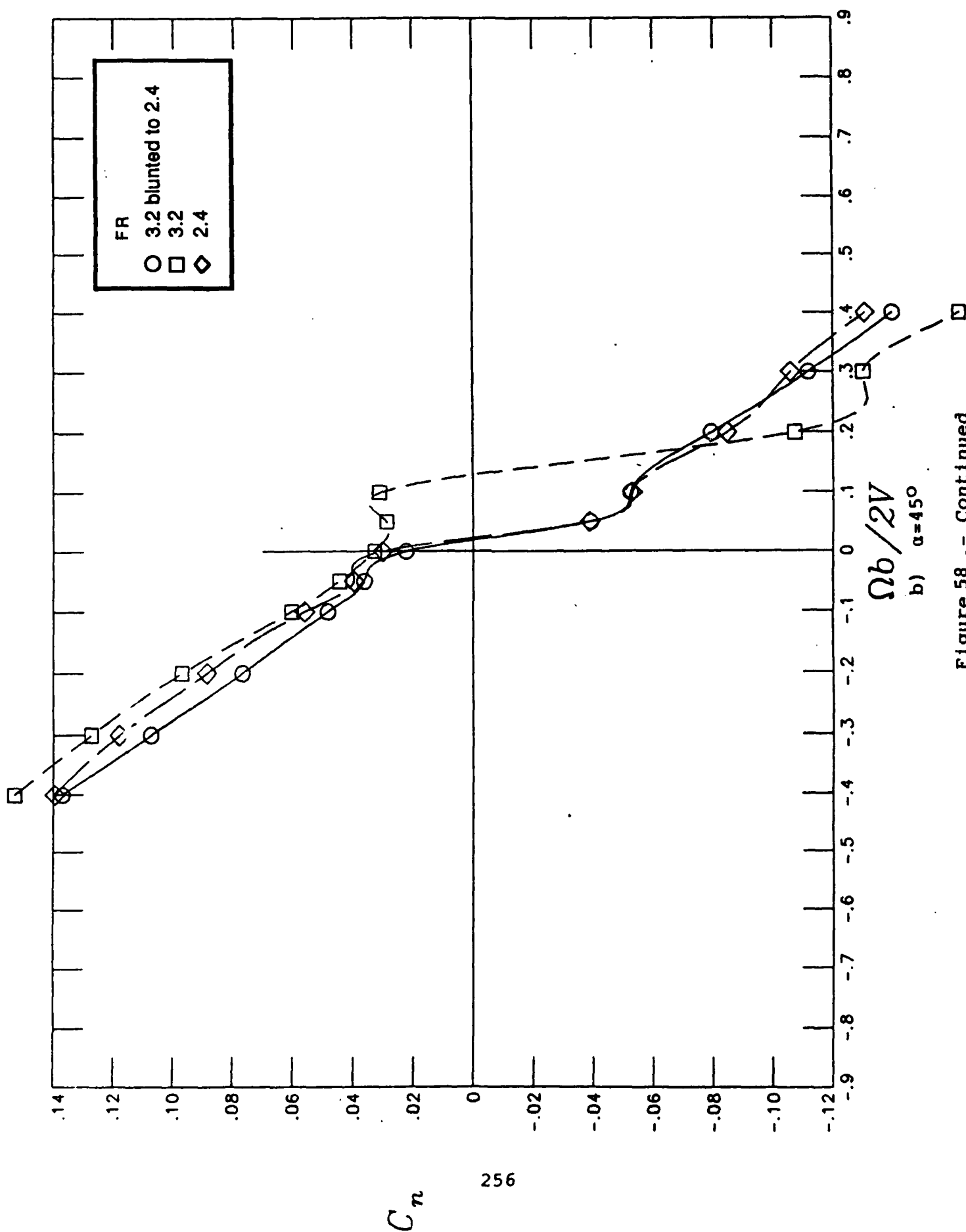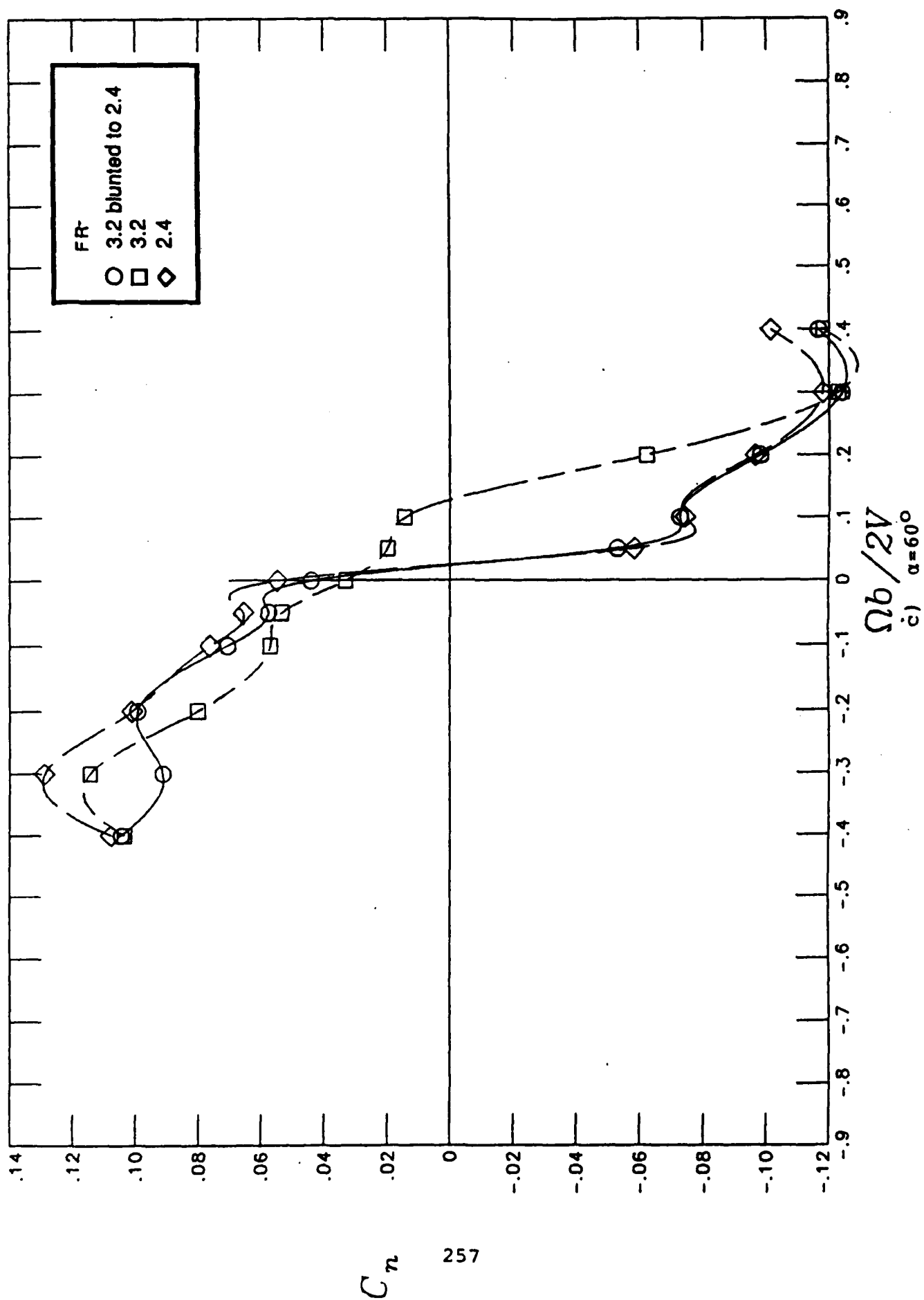
Figure 58 .- Concluded

c) $\alpha = 60^\circ$

$\Omega b/2V$

C_n

257
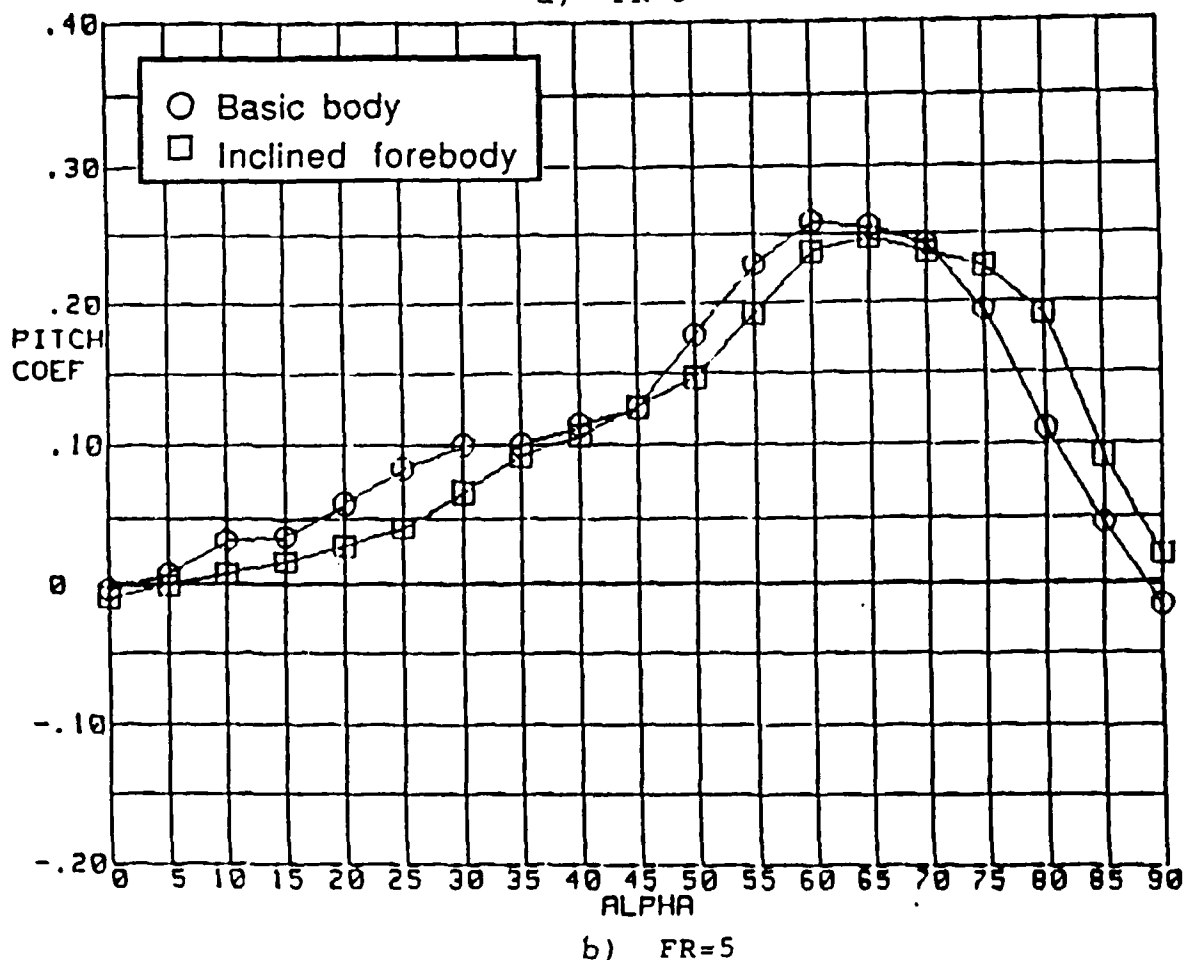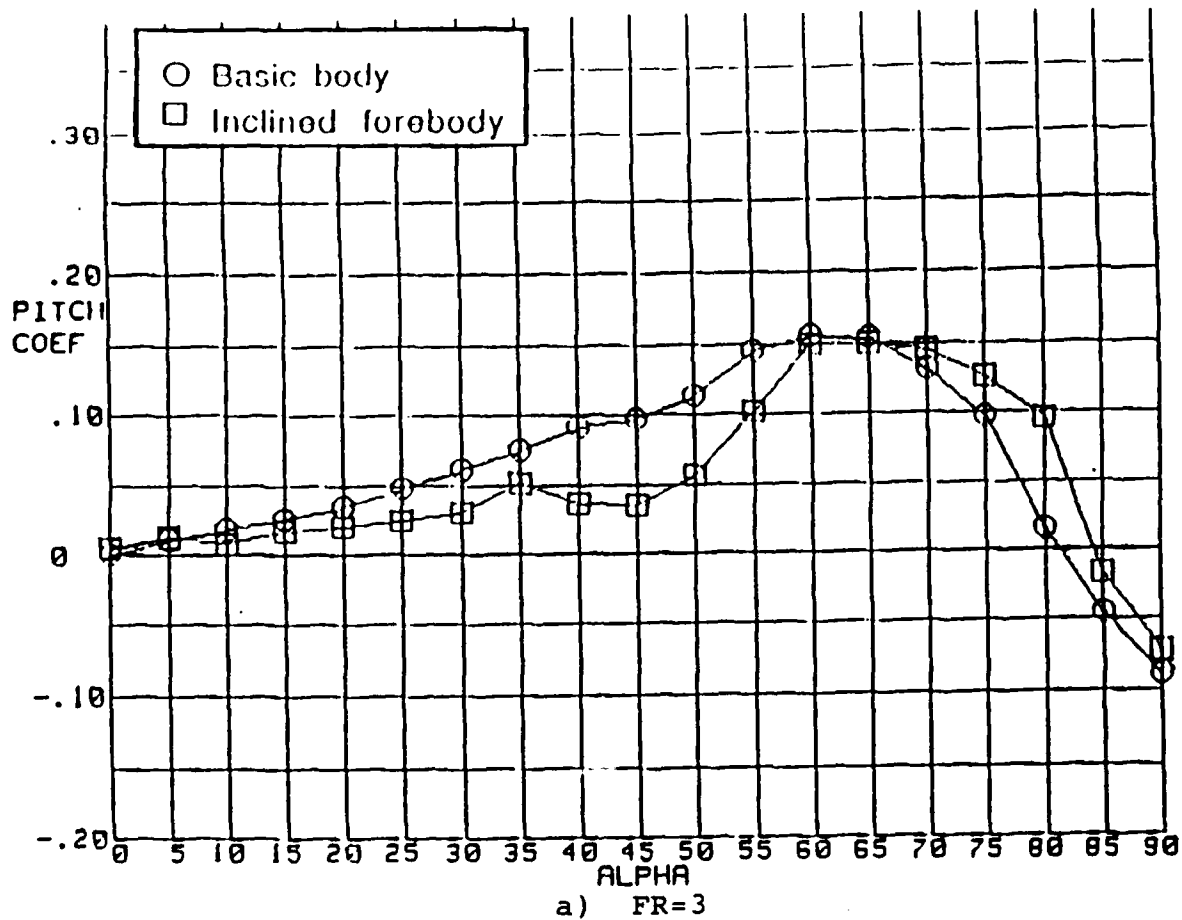
a)   FR=3

b)   FR=5

Figure 59.- Influence of inclining a H/W=0.6 cross-sectional
forebody on pitching-moment coefficient variation with angle
of attack for FR=3 and 5 forebodies

258
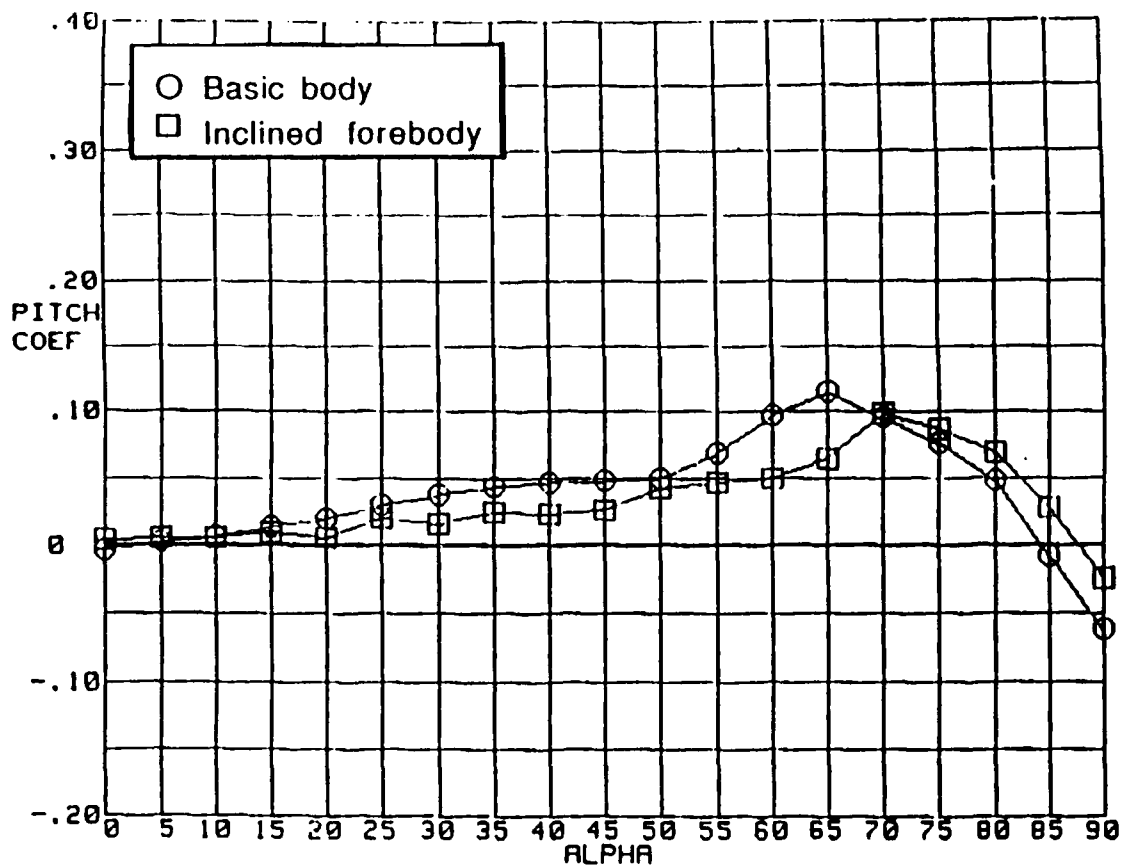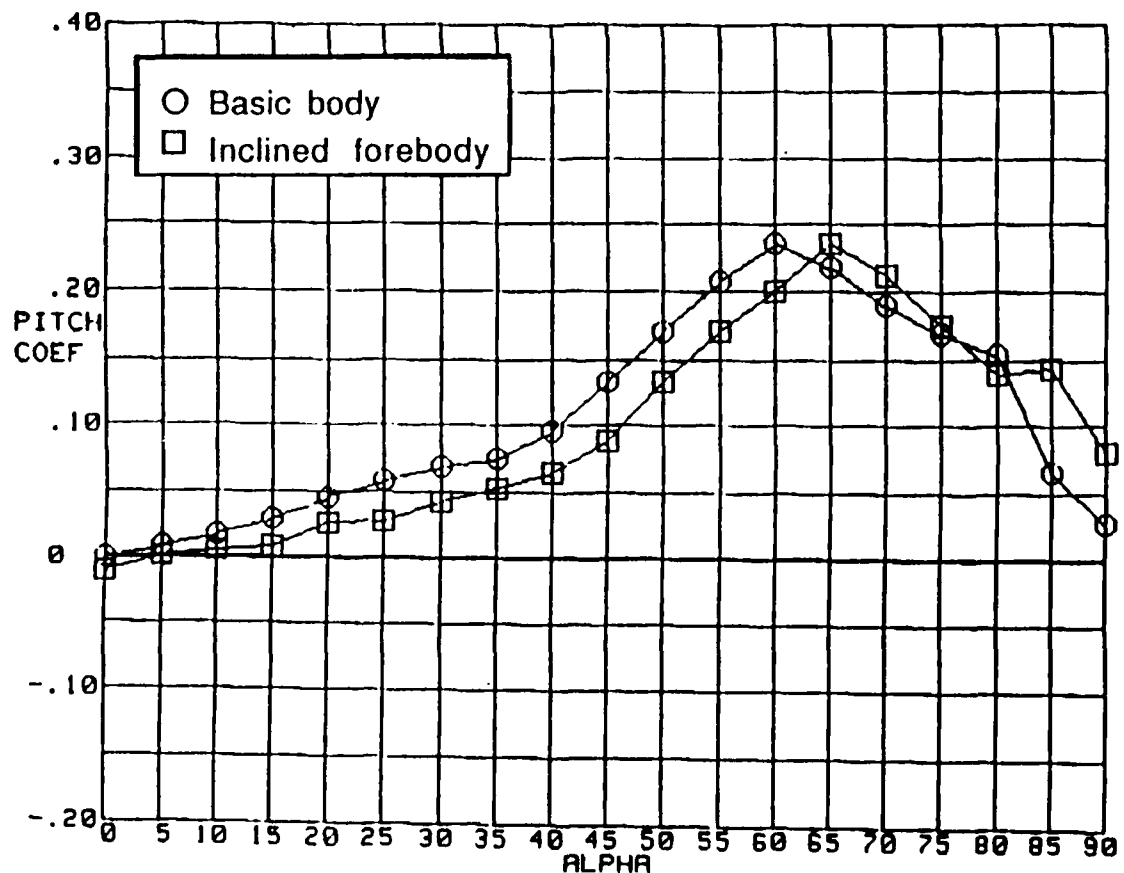
a)   FR=3

b)   FR=5

Figure 60.- Influence of inclining a H/W=1.0 cross-sectional fore-
body on pitching-moment coefficient variation with angle of attack
for FR=3 and 5 forebodies

259
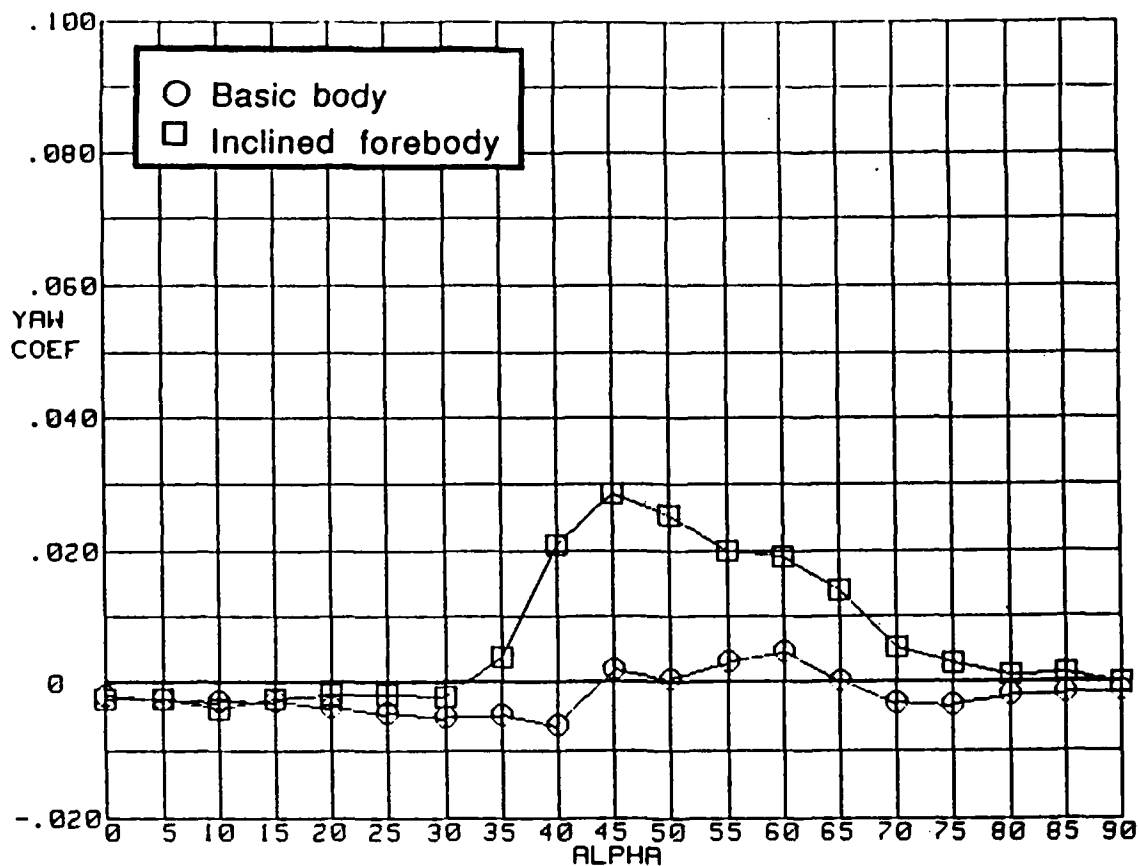
a)   FR=3
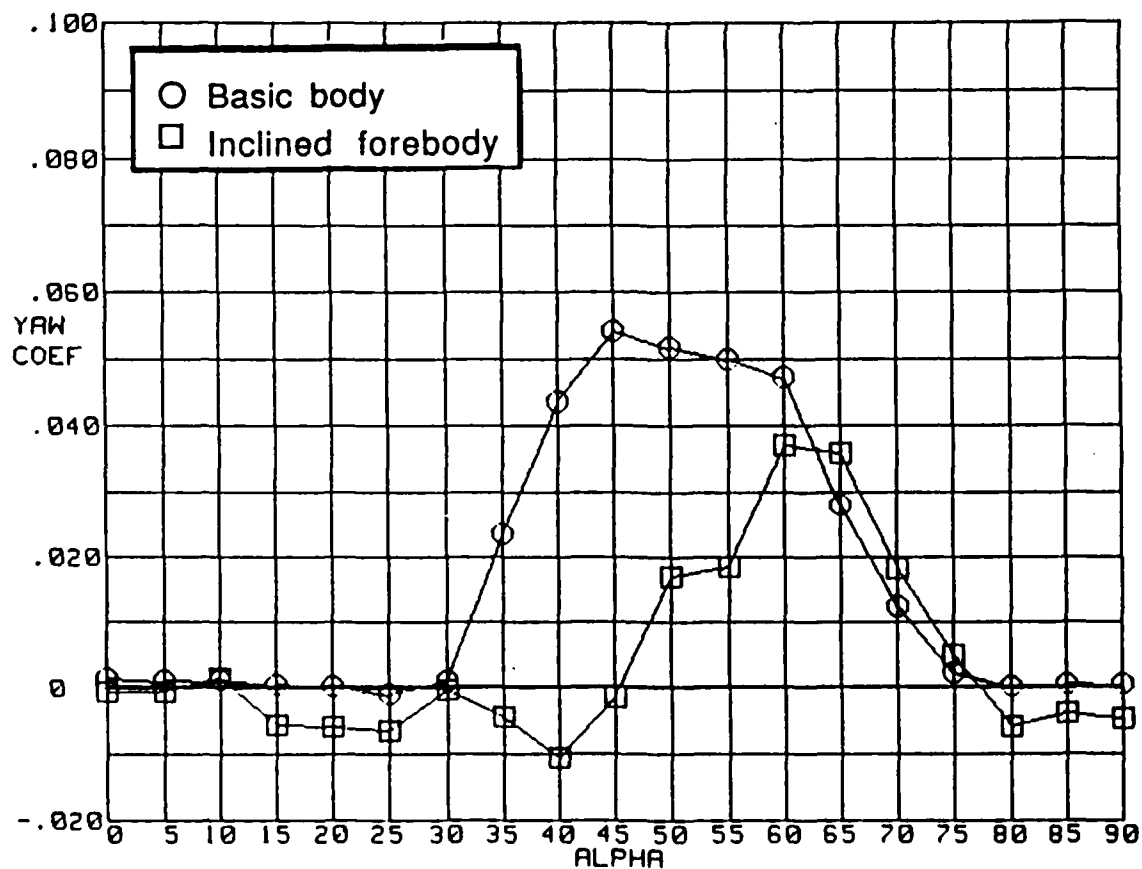
b)   FR=5

Figure 61.- Effect of inclining a H/W=0.6 cross-sectional forebody
on symmetrical flight yawing-moment coefficient variation with
angle of attack for FR=3 and 5 forebodies

260
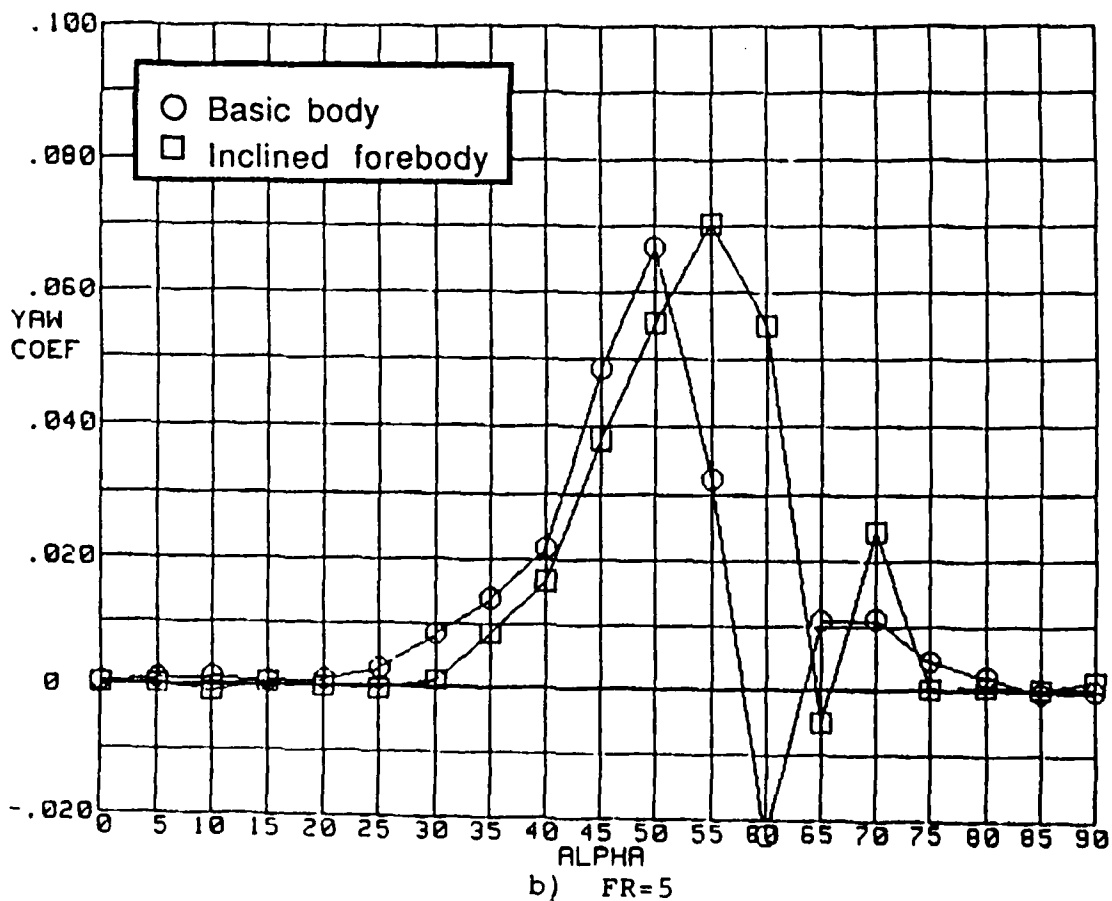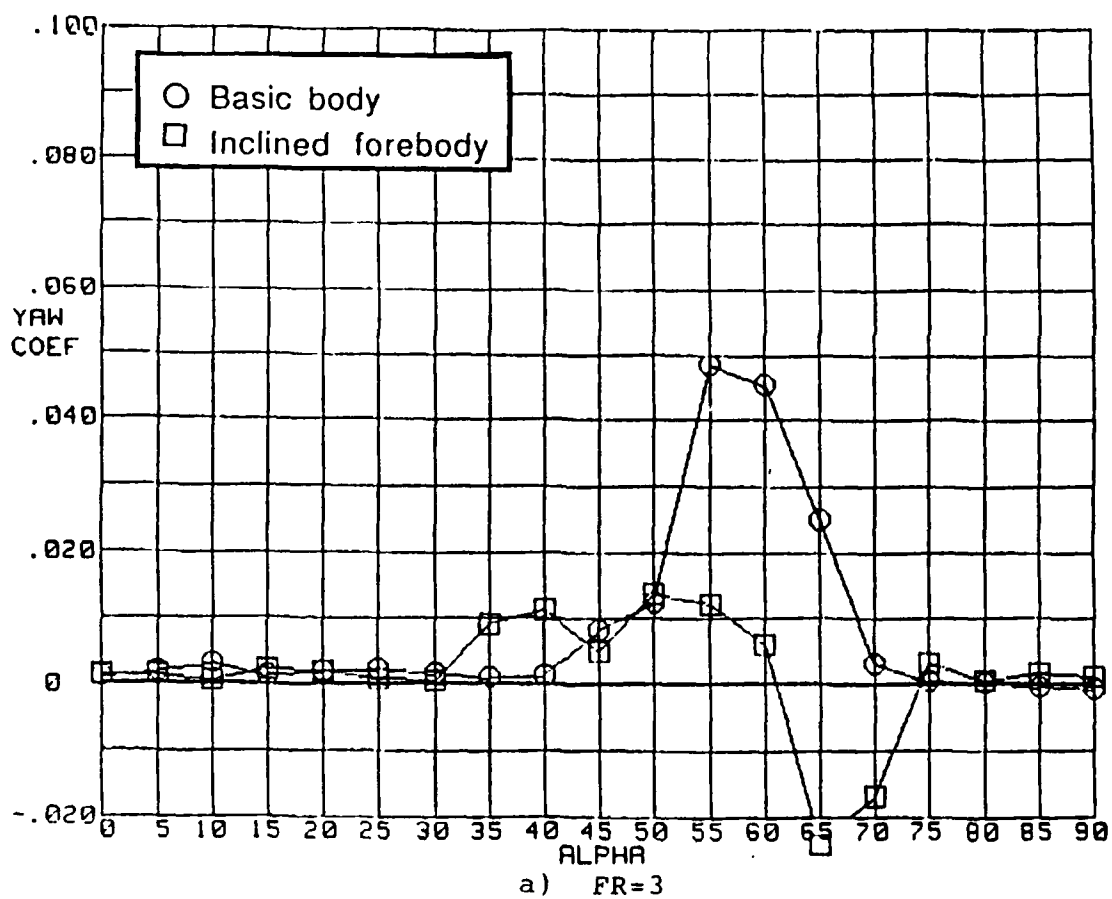
Figure 62.- Effect of inclining a H/W=1.0 cross-sectional forebody
on symmetrical flight yawing-moment coefficient variation with angle
of attack for FR=3 and 5 forebodies

261
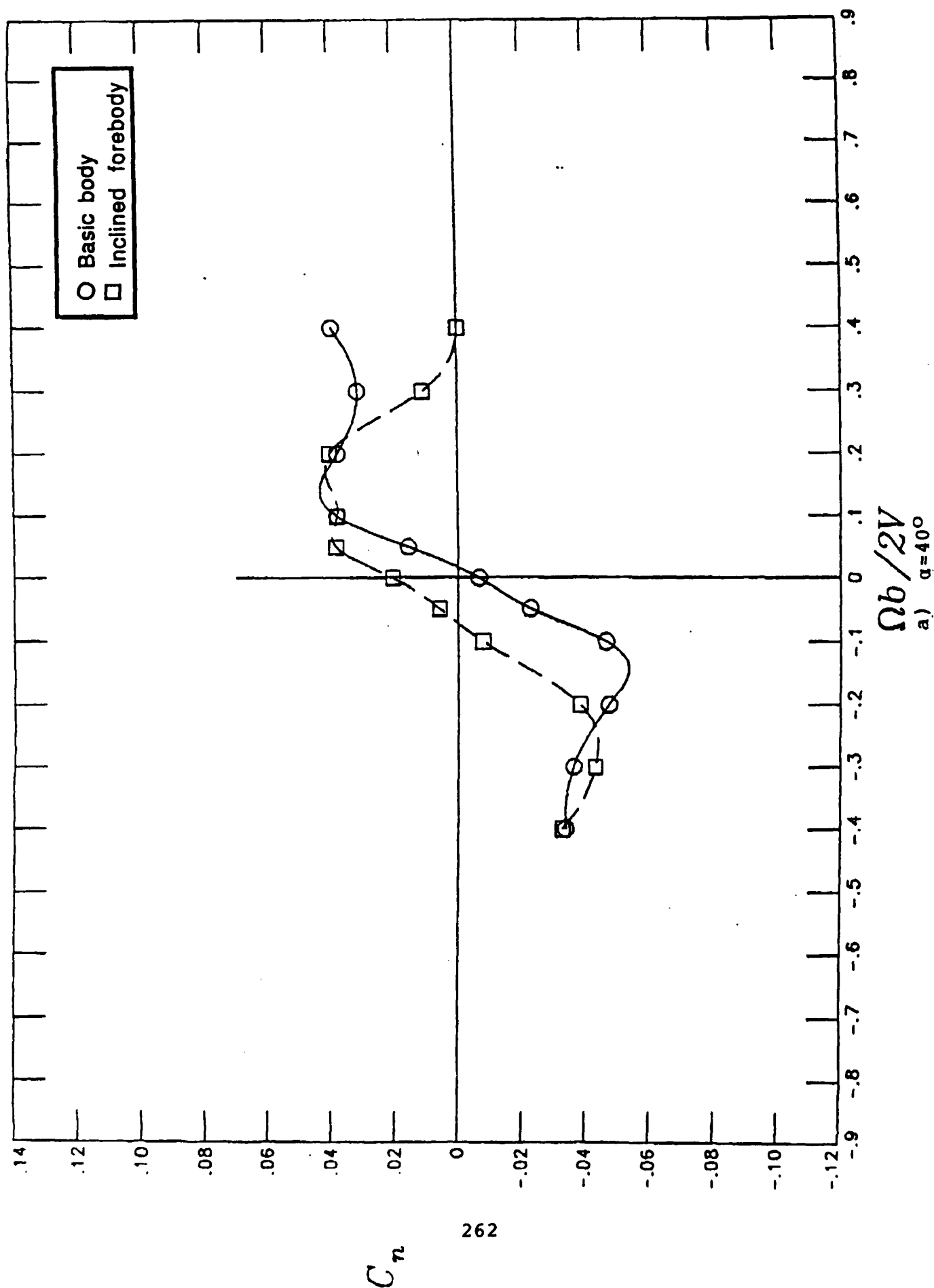
Figure 63.- Effect of inclining a H/W=0.6, FR=3 forebody on rotational yawing-moment coefficient characteristics

a) $\alpha = 40°$

262

$\Omega b/2V$

b) $\alpha = 50°$
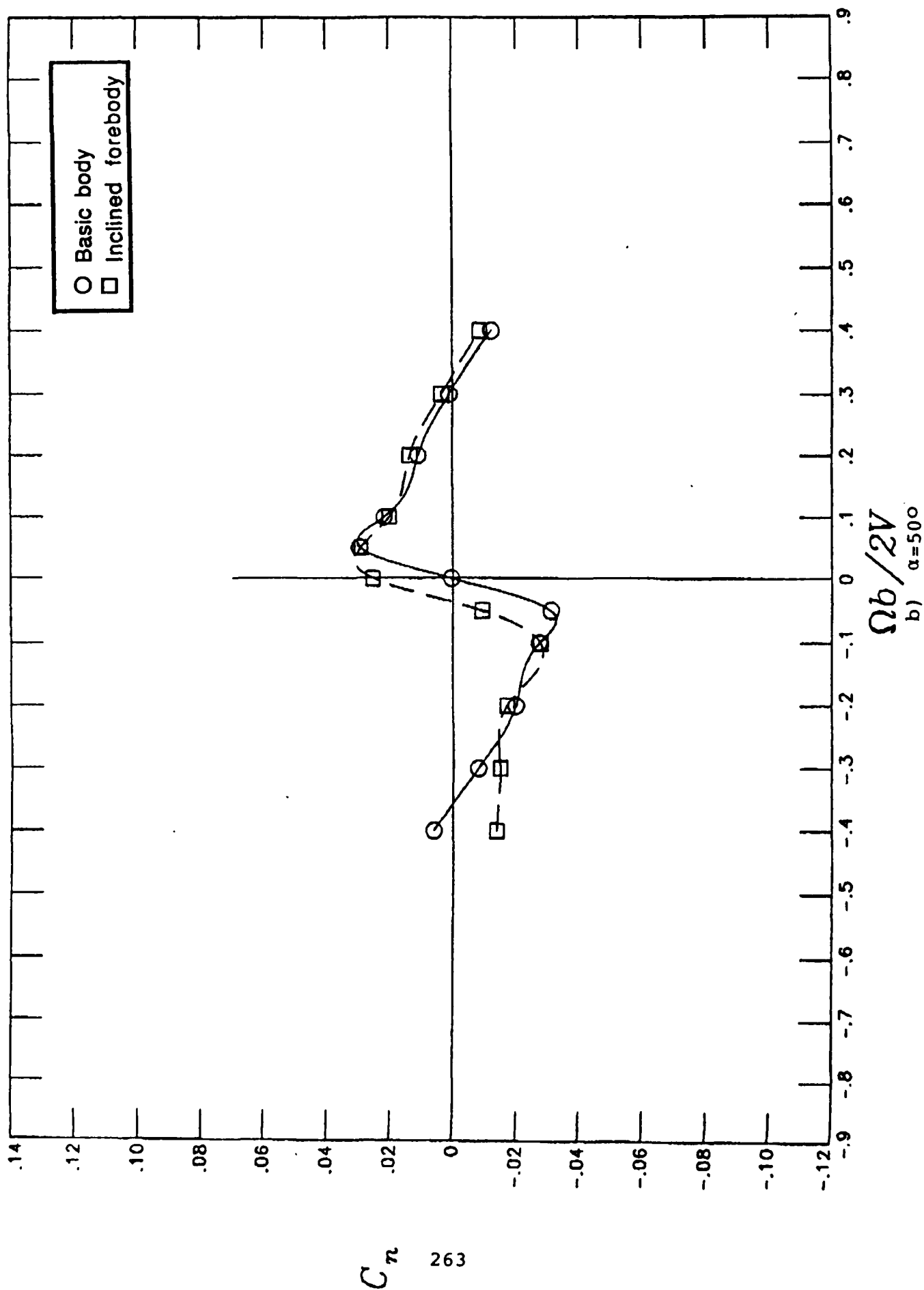
Figure 63.- Continued

263

c) $\alpha = 60°$
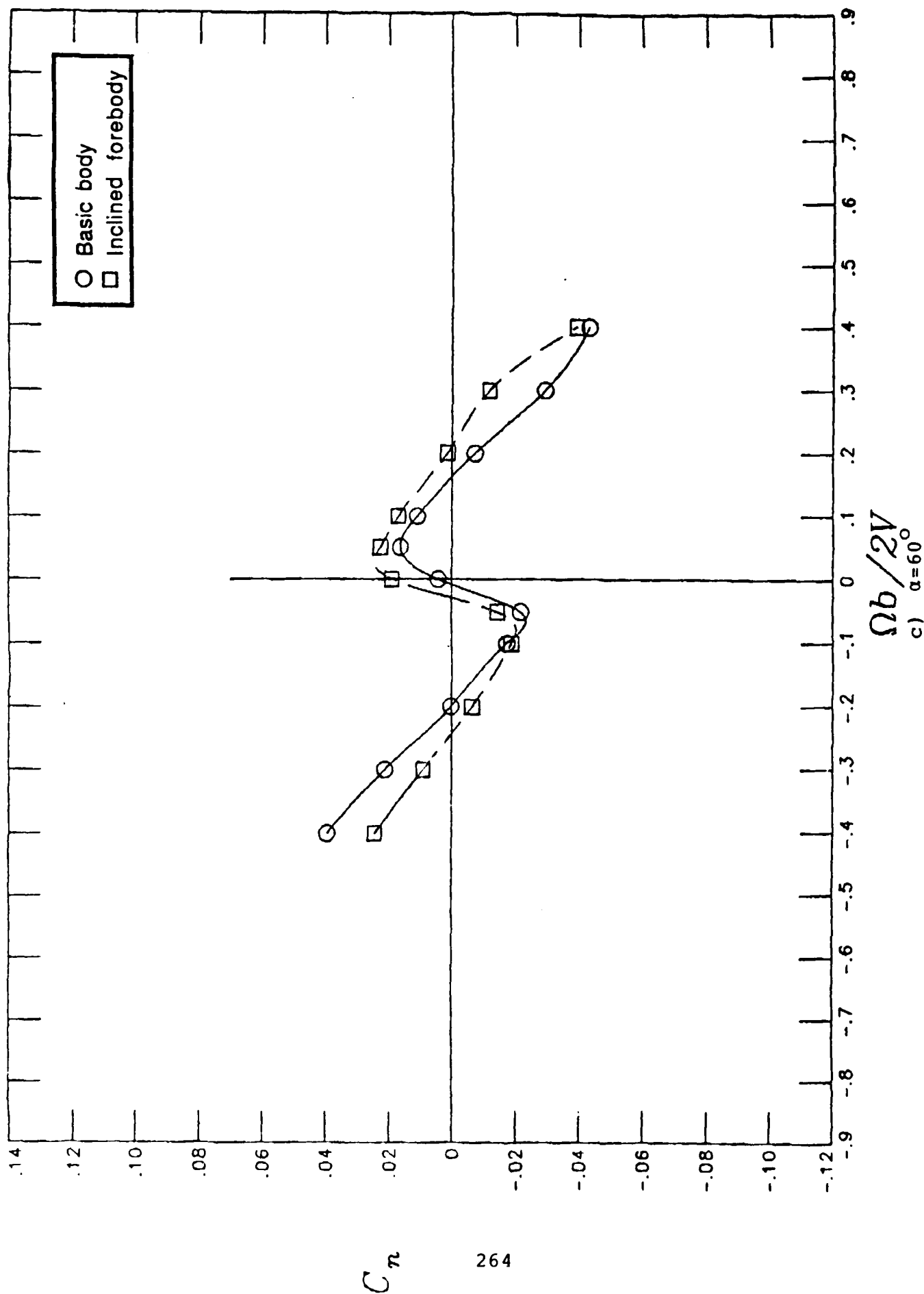
Figure 63.- Concluded

C_n

264
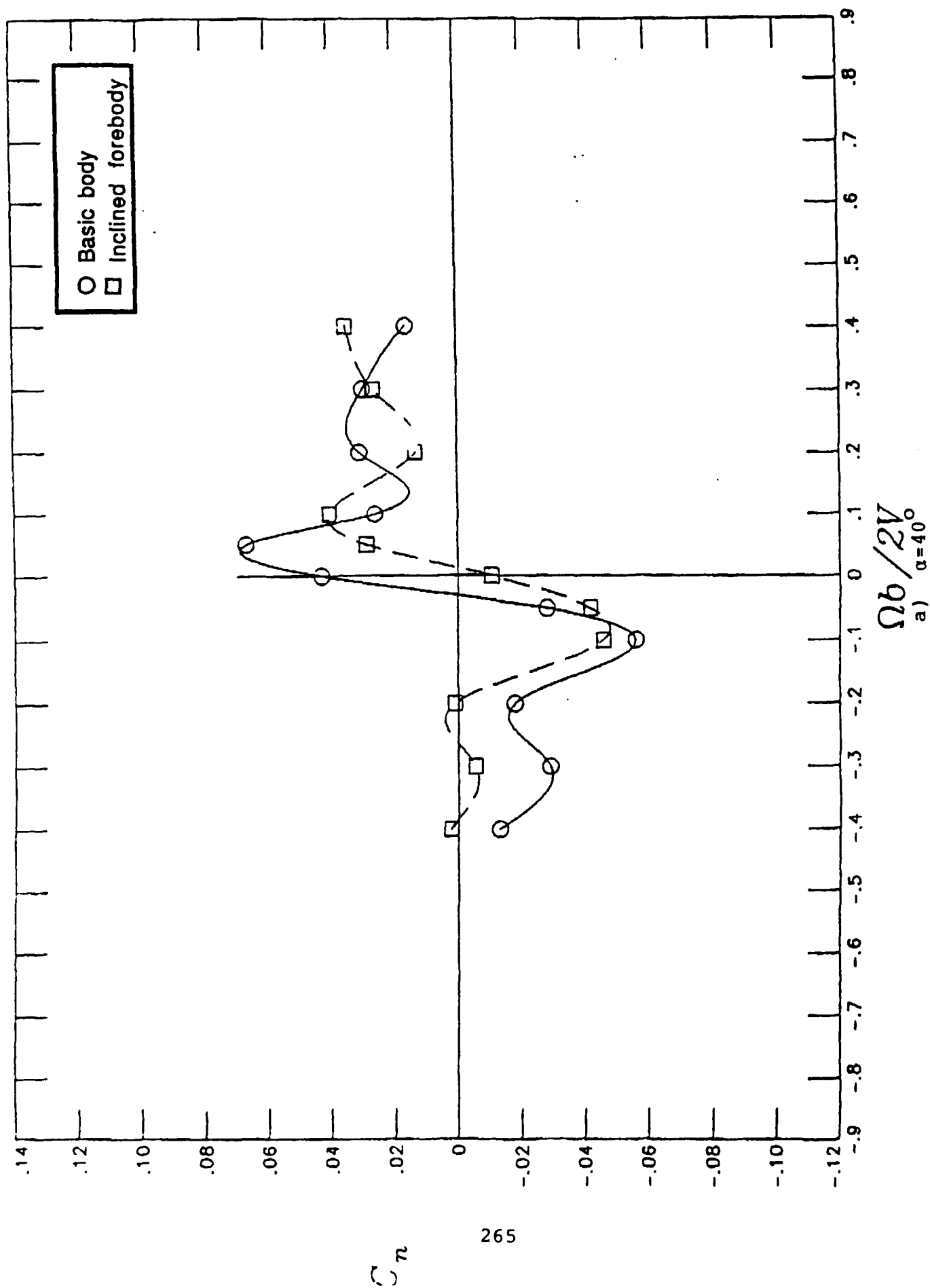
Figure 64.- Effect of inclining a H/W=0.6, FR=5 forebody on rotational yawing-moment coefficient characteristics

$$\Omega b/2V$$

b) $\alpha=50^\circ$
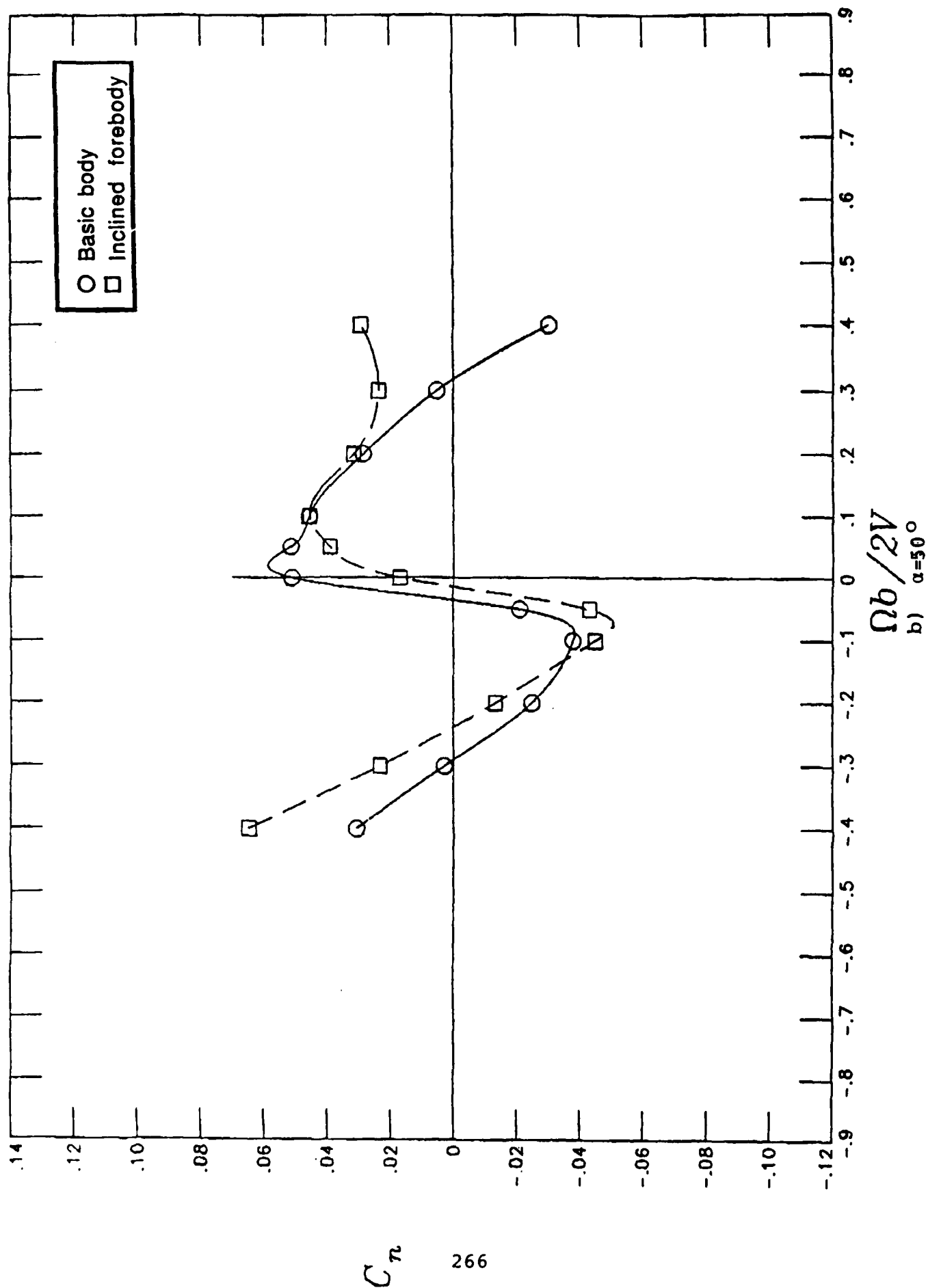
Figure 64.- Concluded

266
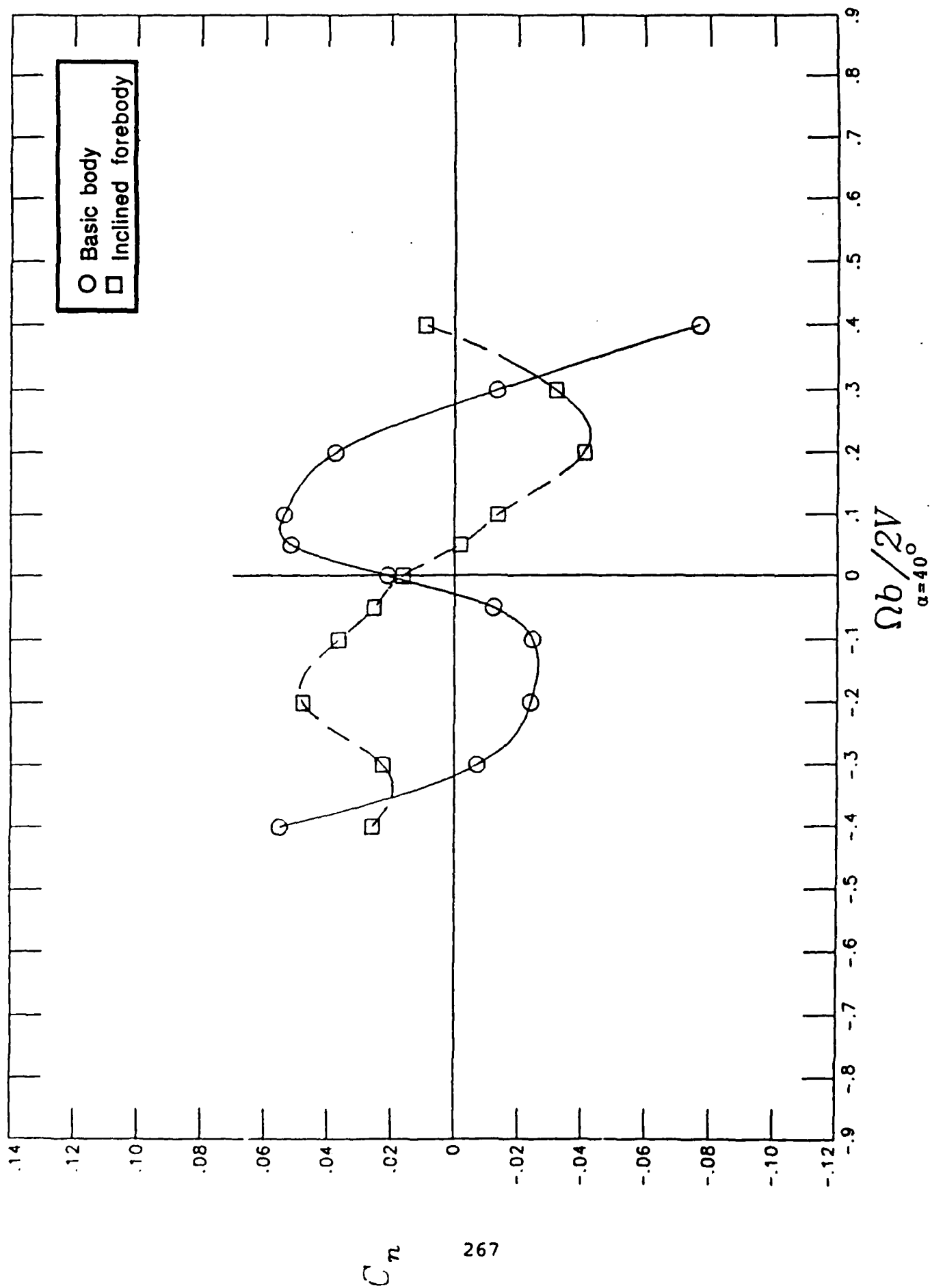
Figure 65.- Effect of inclining a H/W=1.0, FR=5 forebody on rotational yawing-moment coefficient characteristics

267
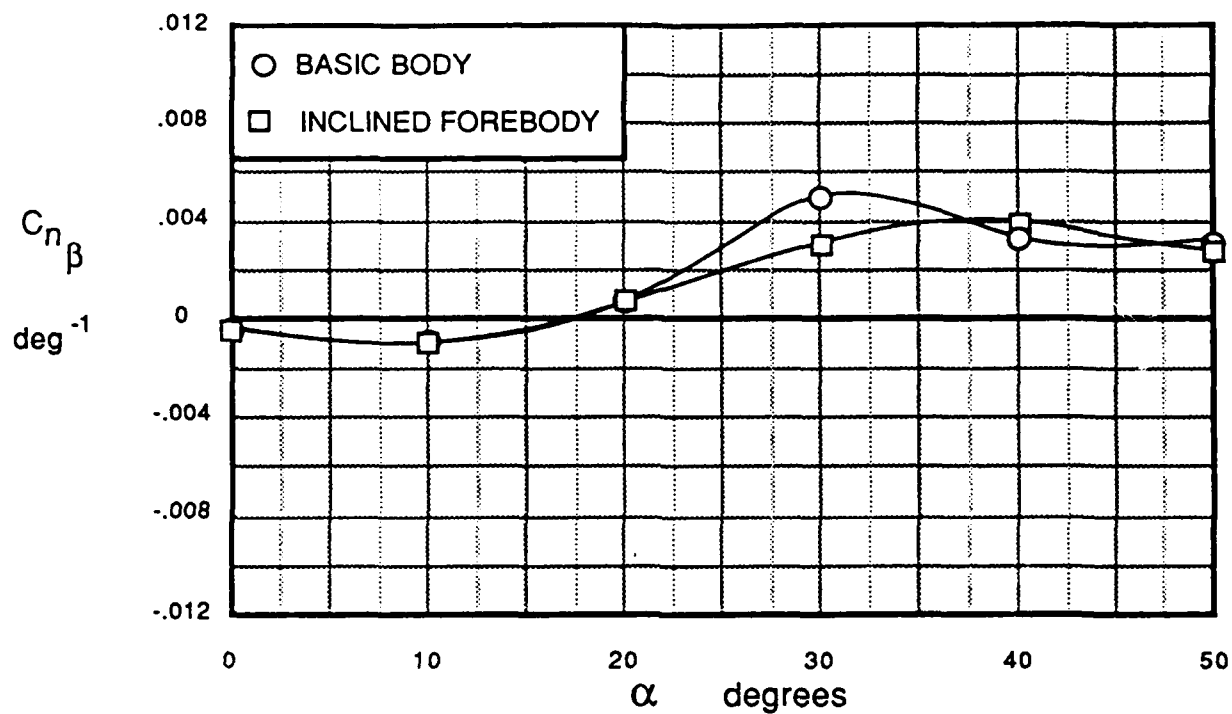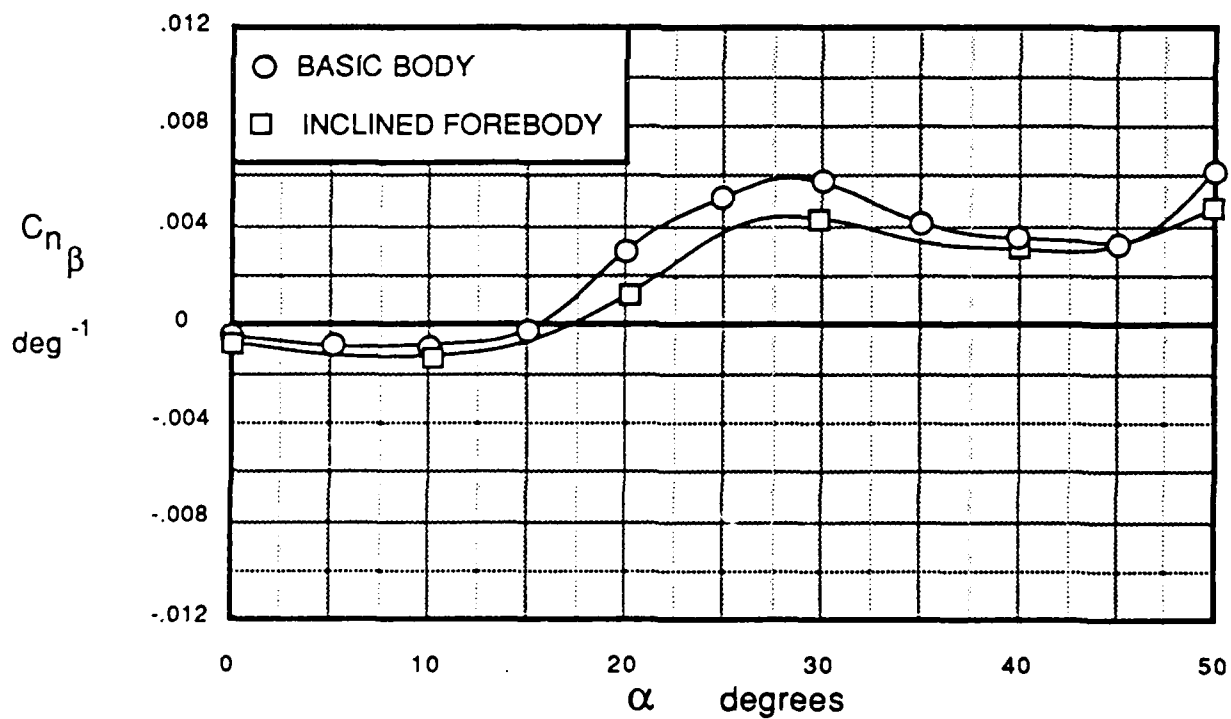
a) FR = 3

b) FR = 5

Figure 66. - Effect of inclining a H/W=0.6 cross-sectional forebody on body-alone
directional stability for FR=3 and 5 forebodies

268
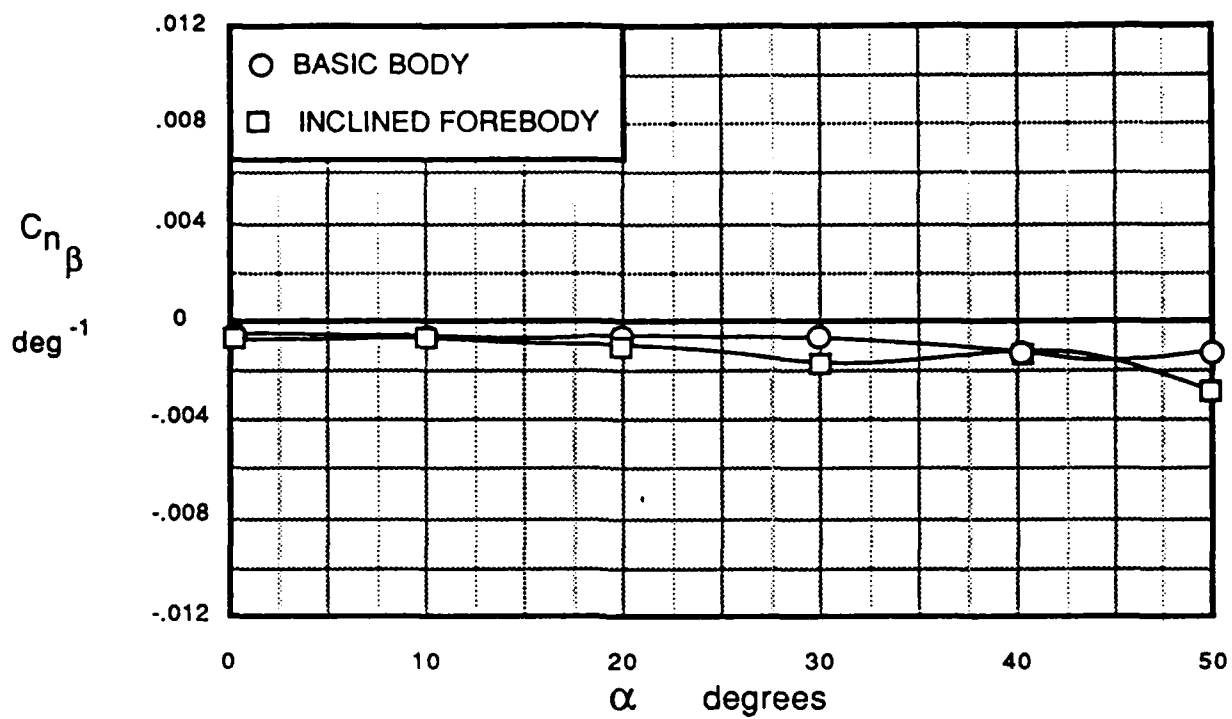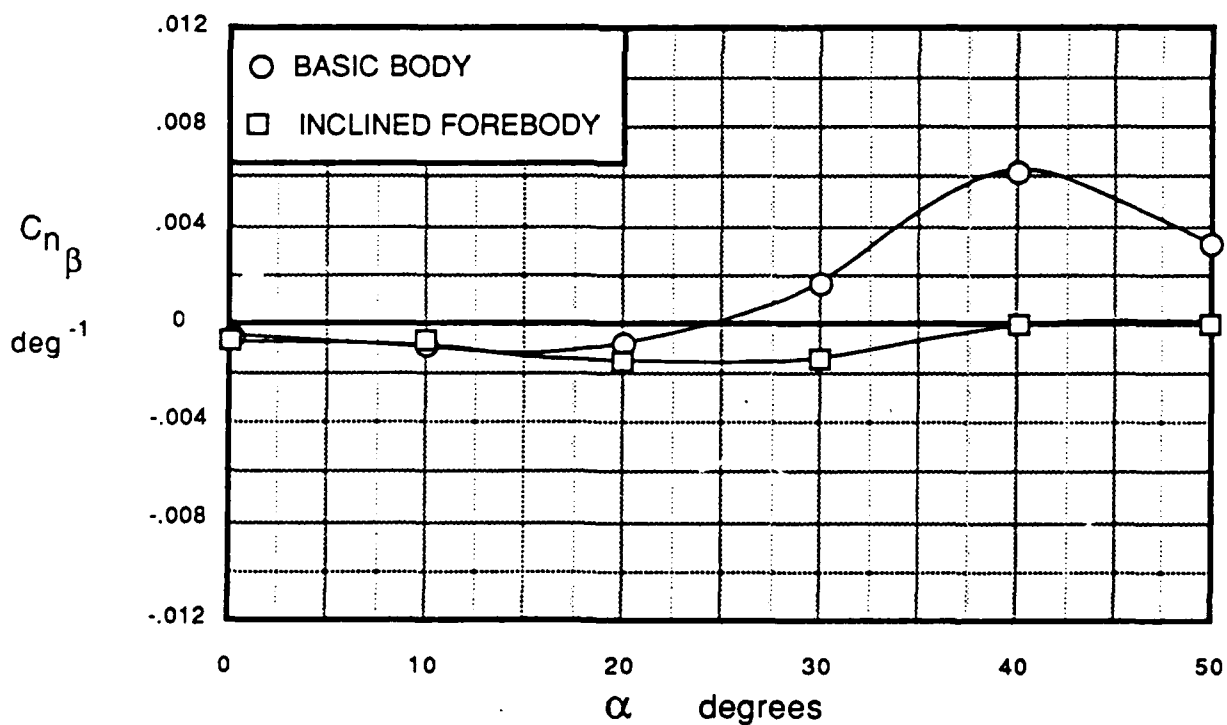
Figure 67. - Effect of inclining a H/W=1.0 cross-sectional forebody on body-alone directional stability for FR=3 and 5 forebodies
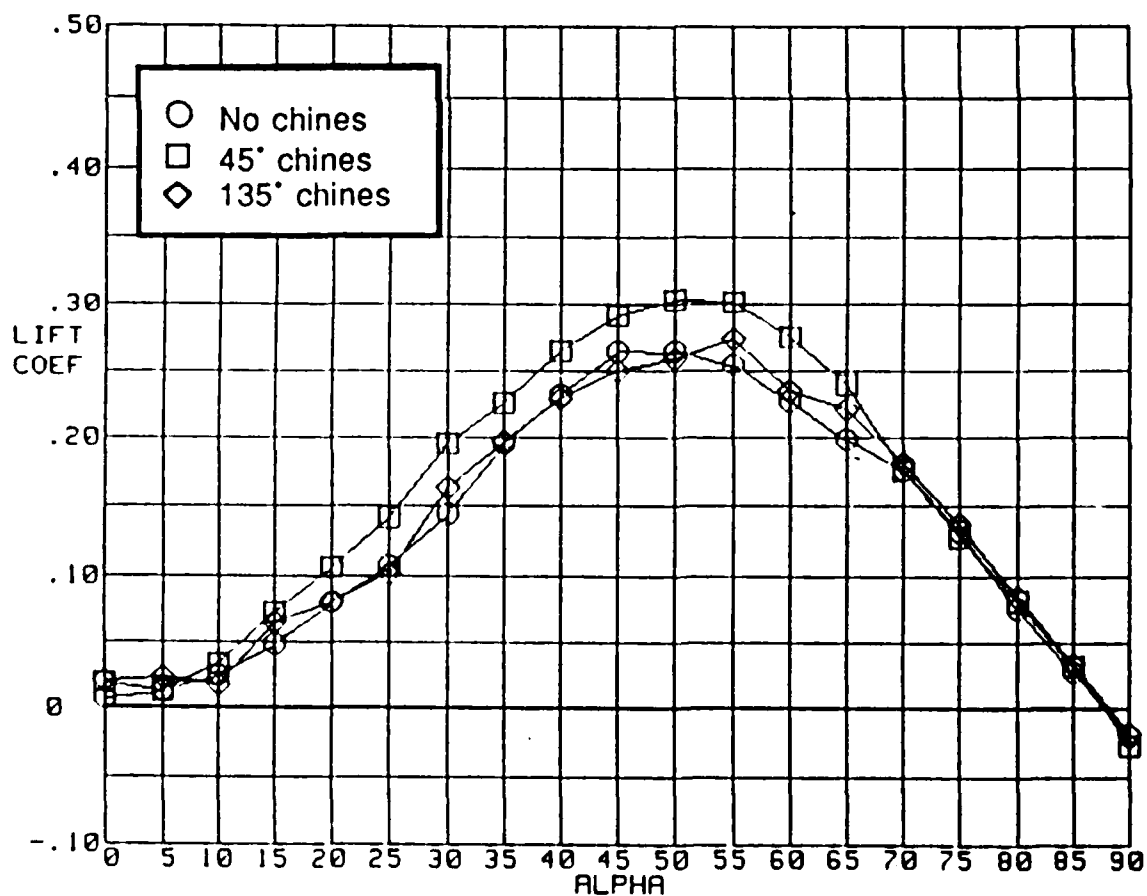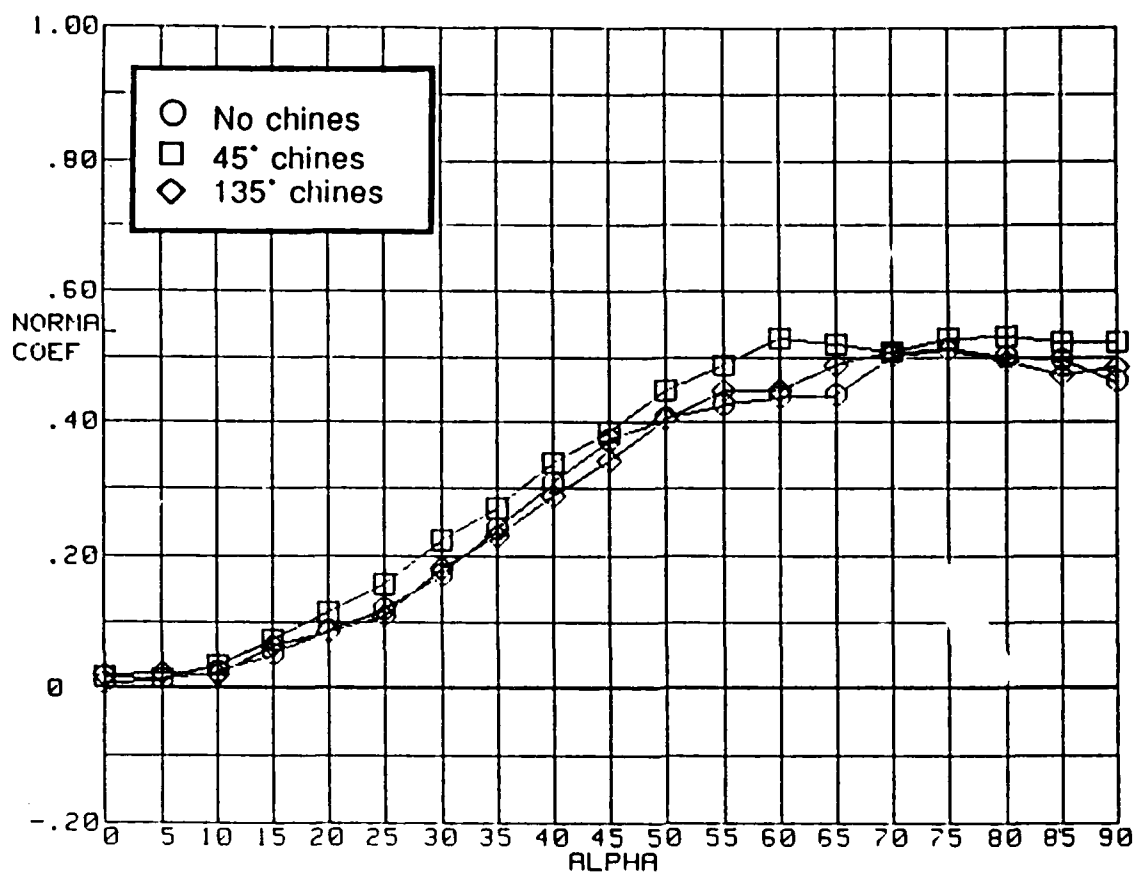
Figure 68.- Influence of forebody chines on lift and normal-force coefficient variation with angle of attack for a H/W=1.0, FR=4 forebody

270
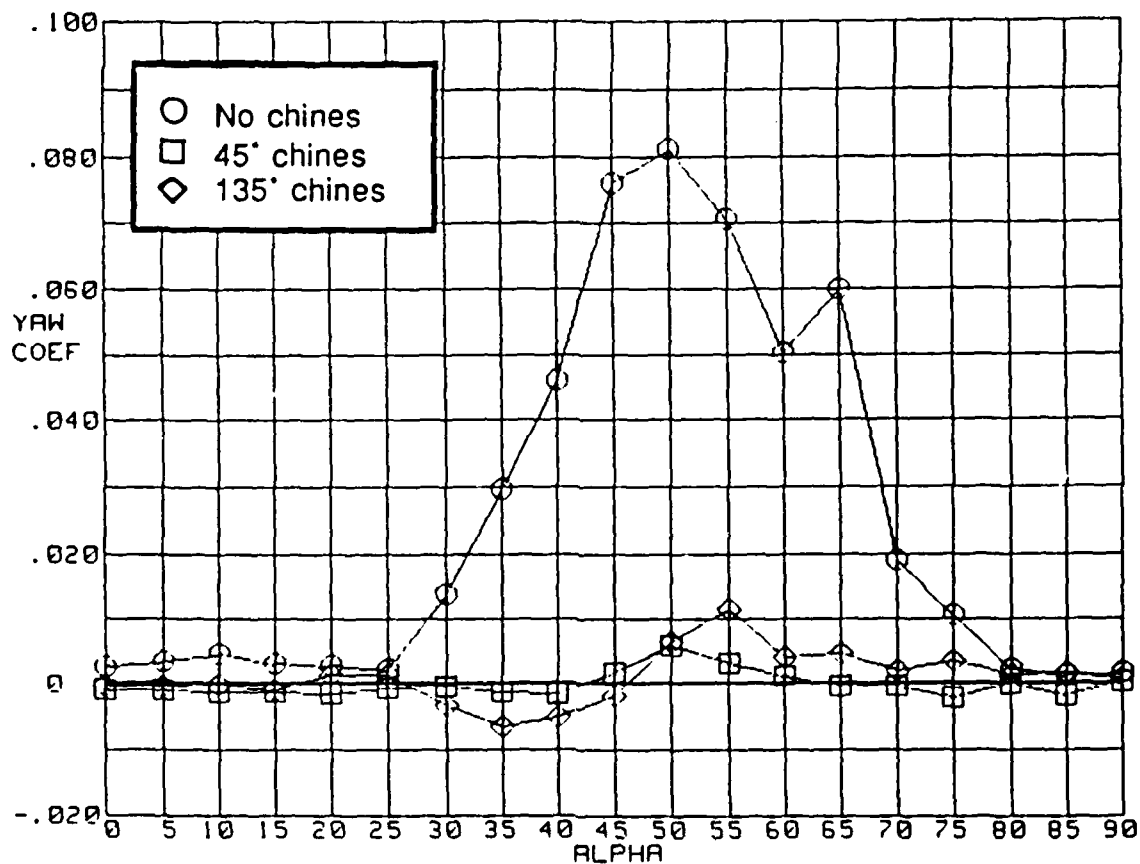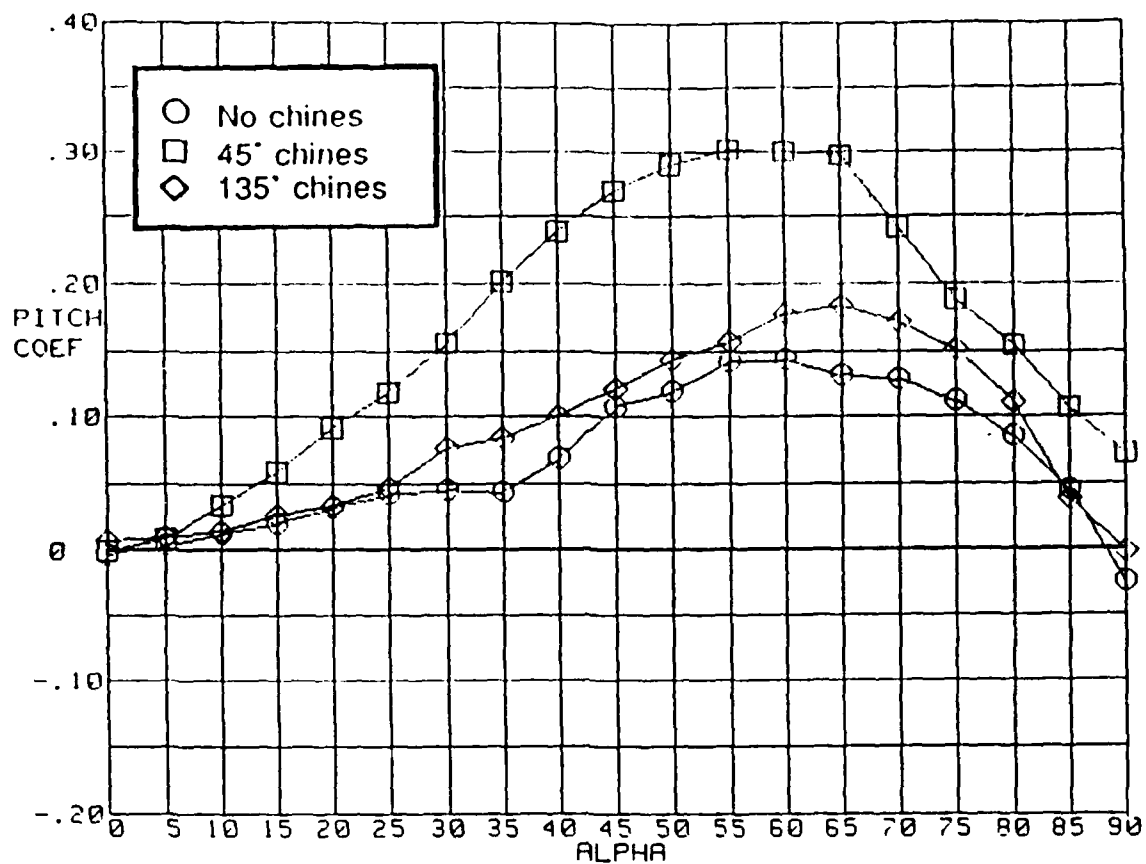
Figure 69.- Influence of forebody chines on pitching-moment
coefficient and symmetrical flight yawing-moment coefficient
variation with angle of attack for a H/W=1.0, FR=4 forebody

271
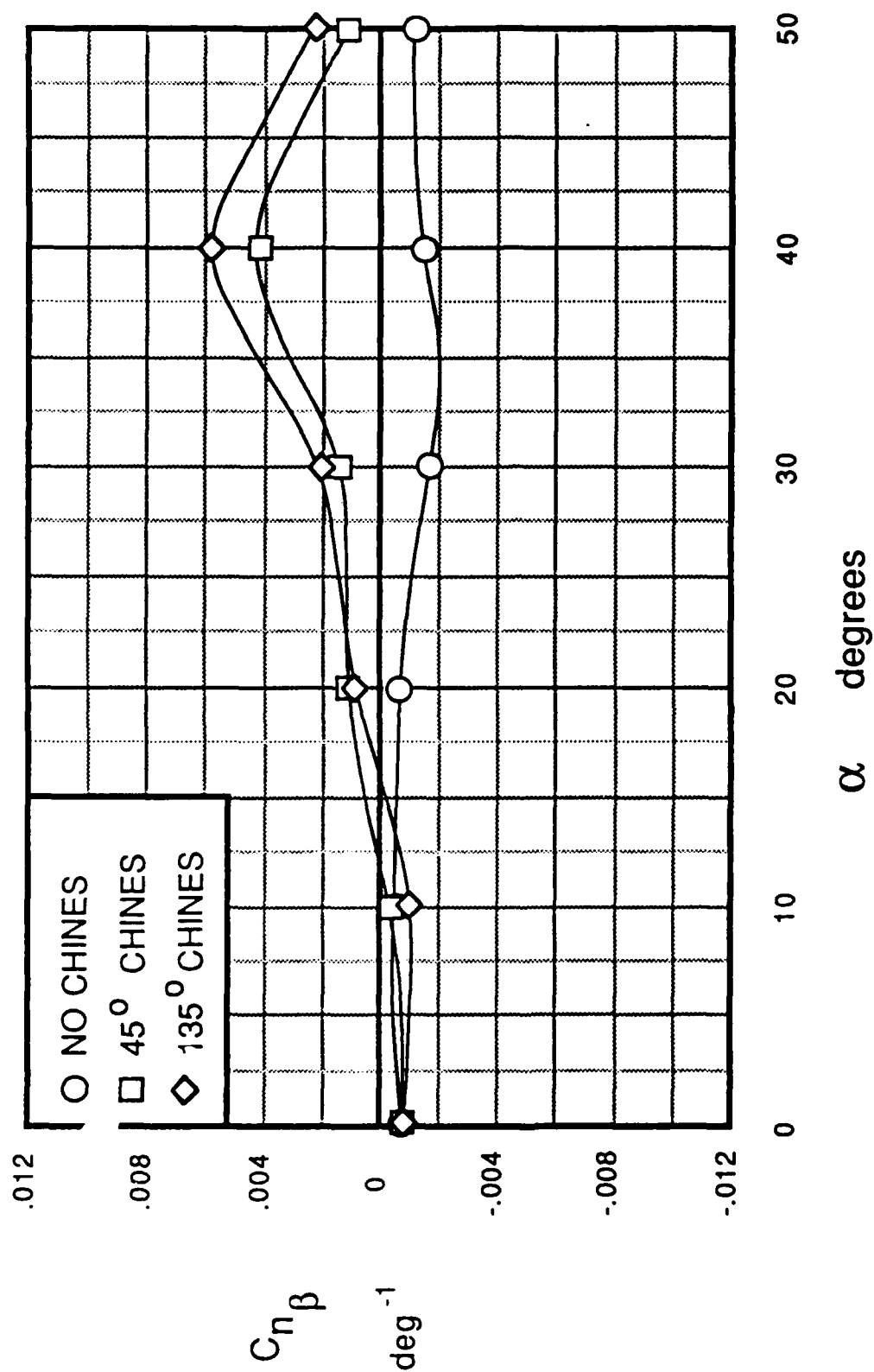
Figure 70. - Effect of chines on body-alone directional stability
for a H/W=1.0, FR=4 forebody
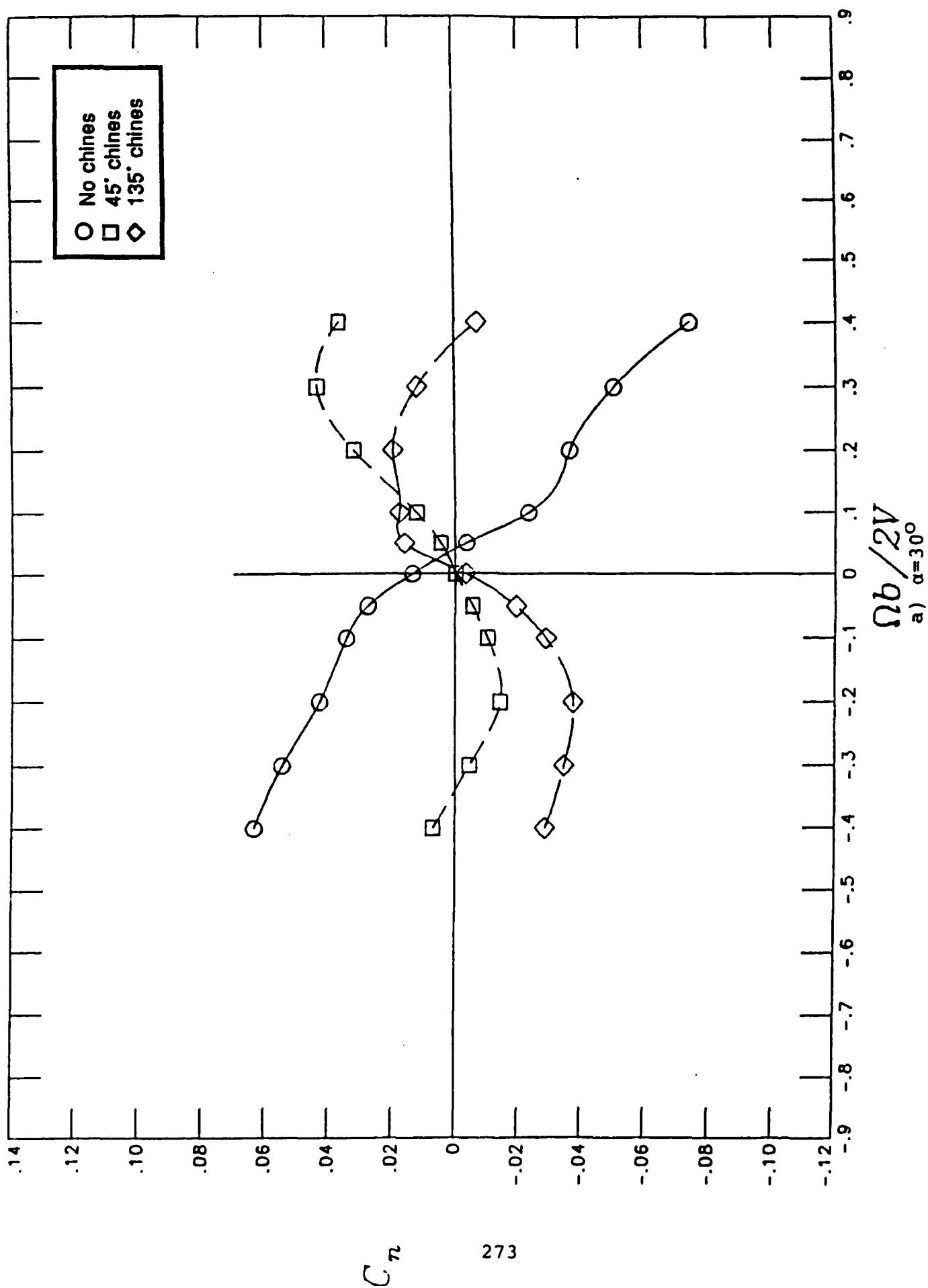
Figure 71.- Influence of forebody chines on rotational yawing-moment coefficient characteristics for a H/W=1.0, FR=4 forebody
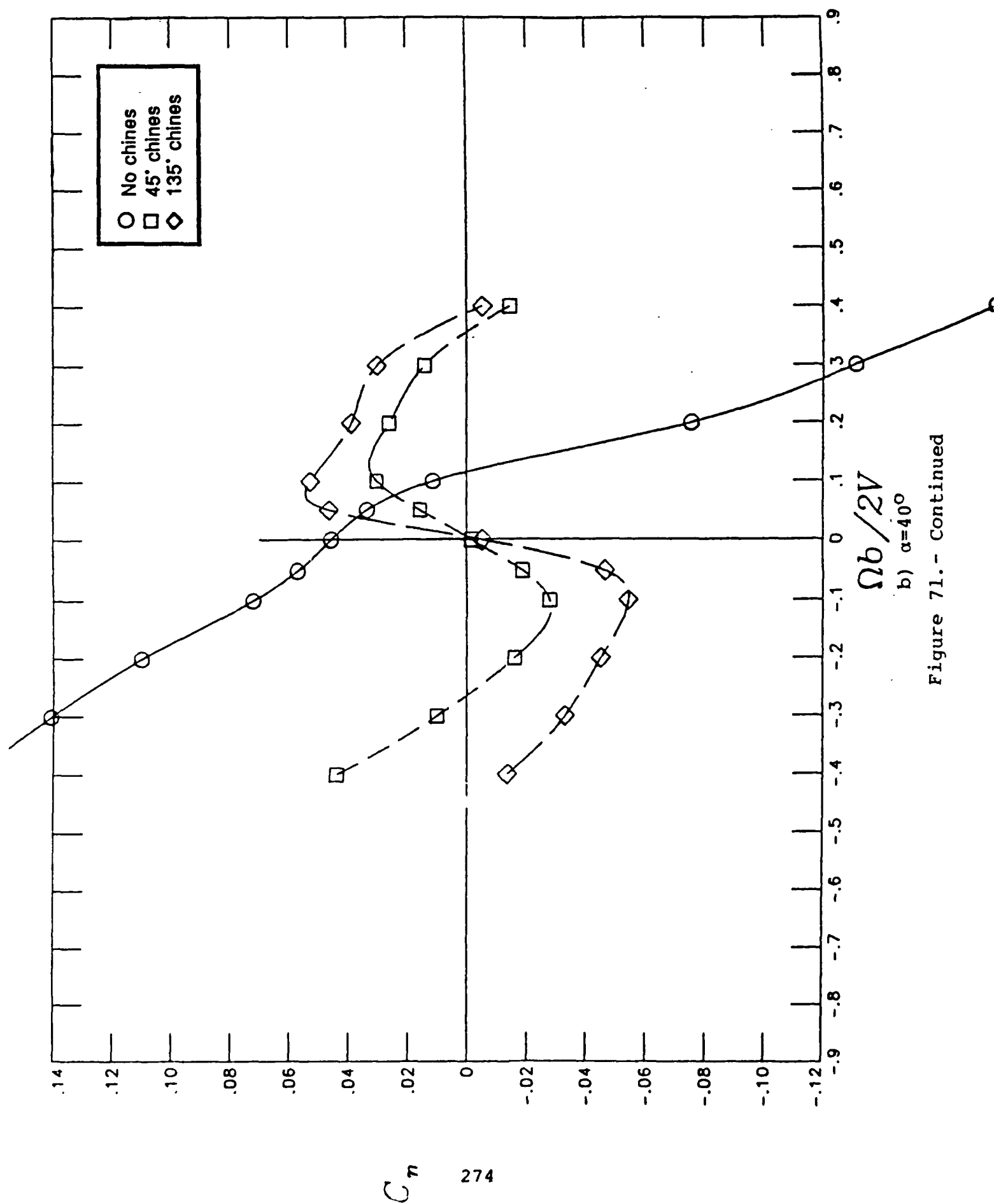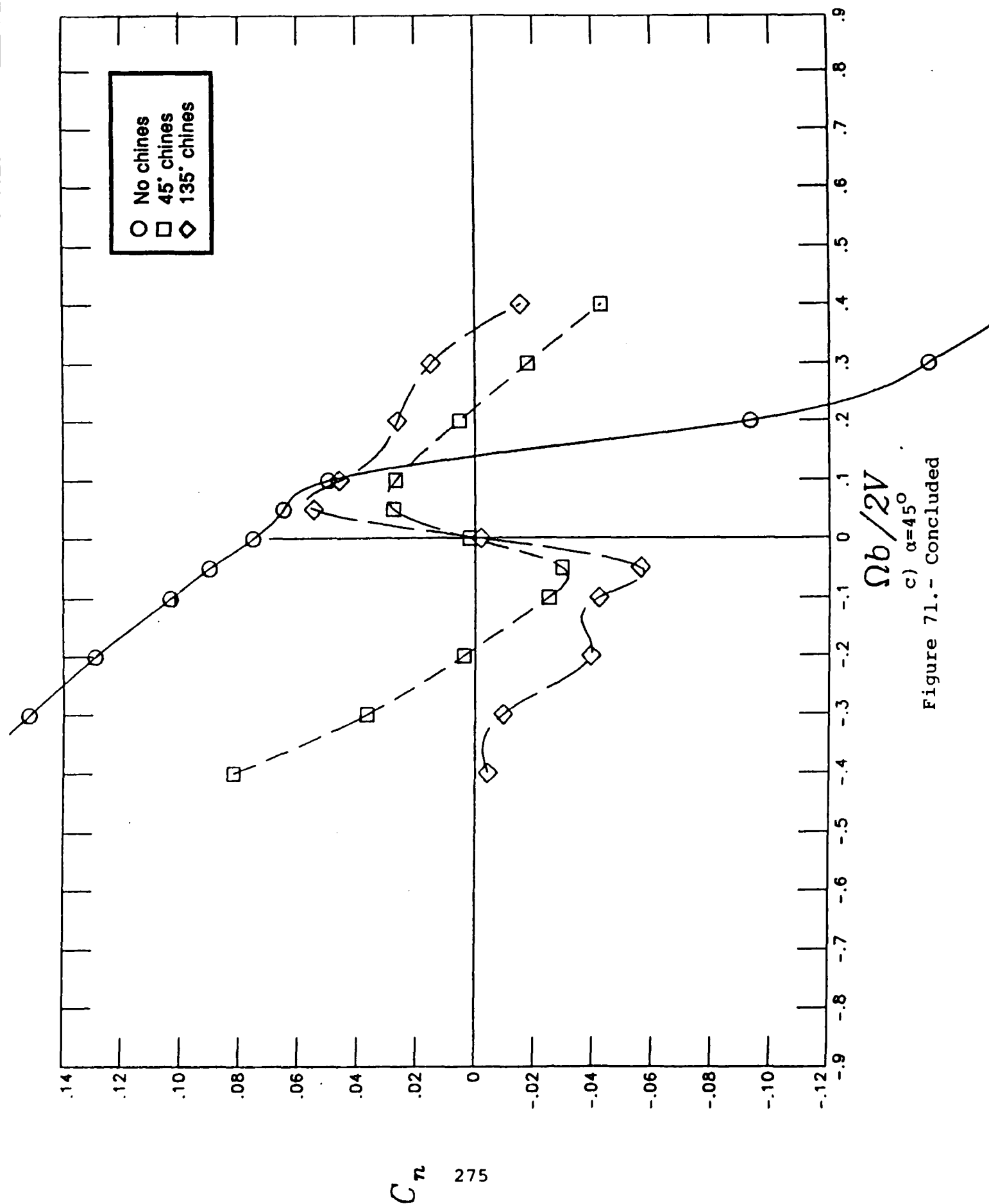
273

$\frac{\Omega b}{2V}$

b) $\alpha = 40°$

Figure 71.- Continued

C_n

274

Legend:
- ○ No chines
- □ 45° chines
- ◇ 135° chines

$\Omega b/2V$

c) $\alpha = 45°$

Figure 71.- Concluded

C_n

275
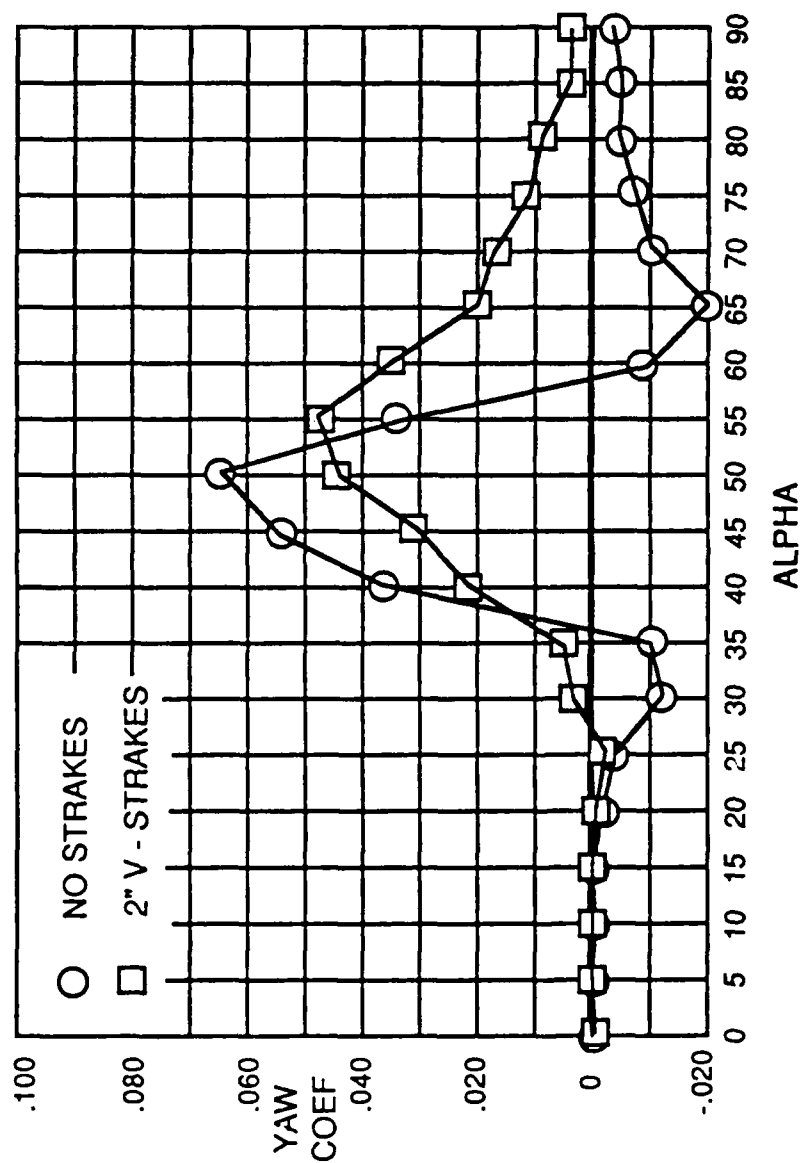
Figure 72. - Effect of V-strakes on body-alone symmetrical flight yawing-moment coefficient variation with angle of attack for a H/W=0.8,FR=4.5 forebody
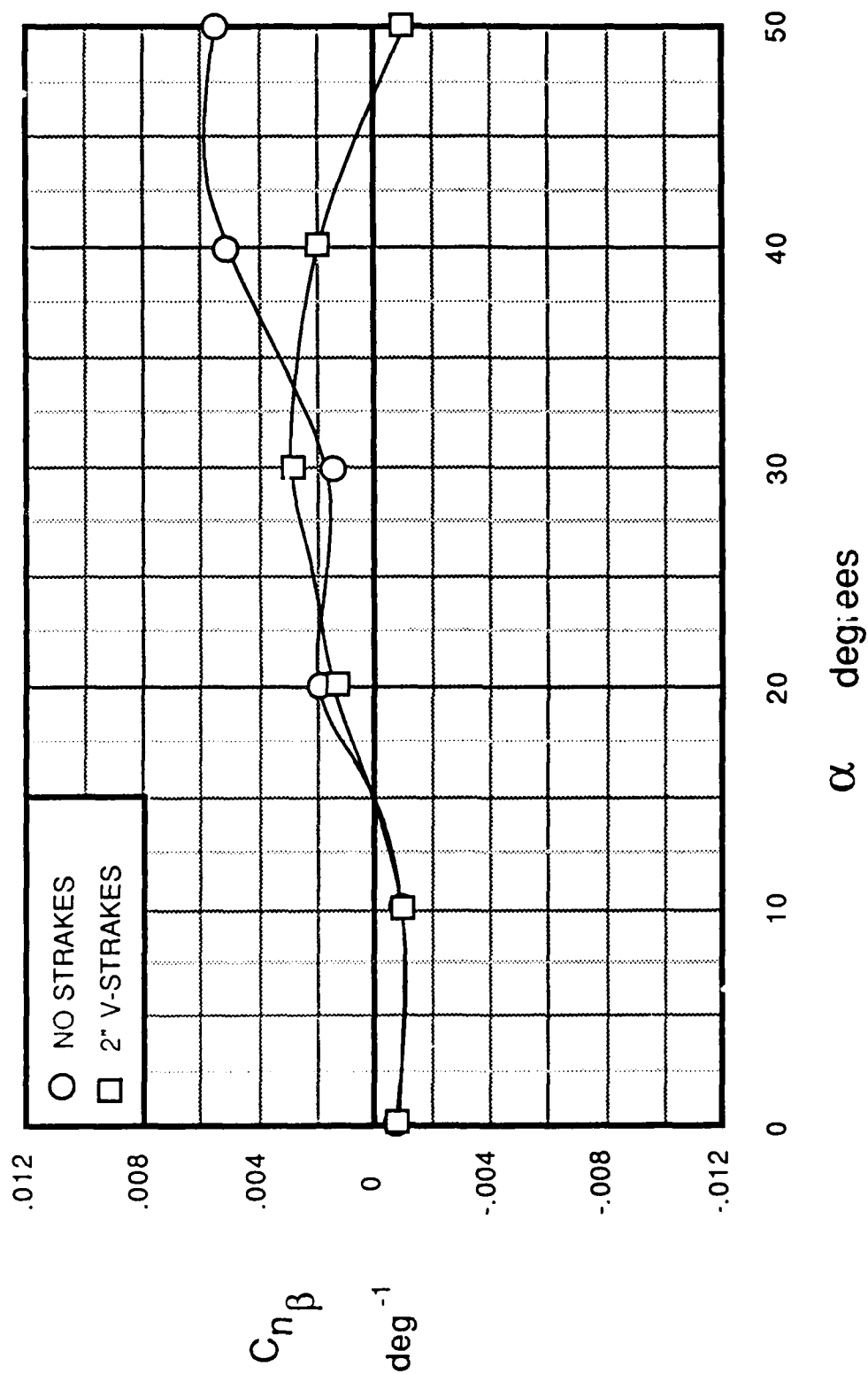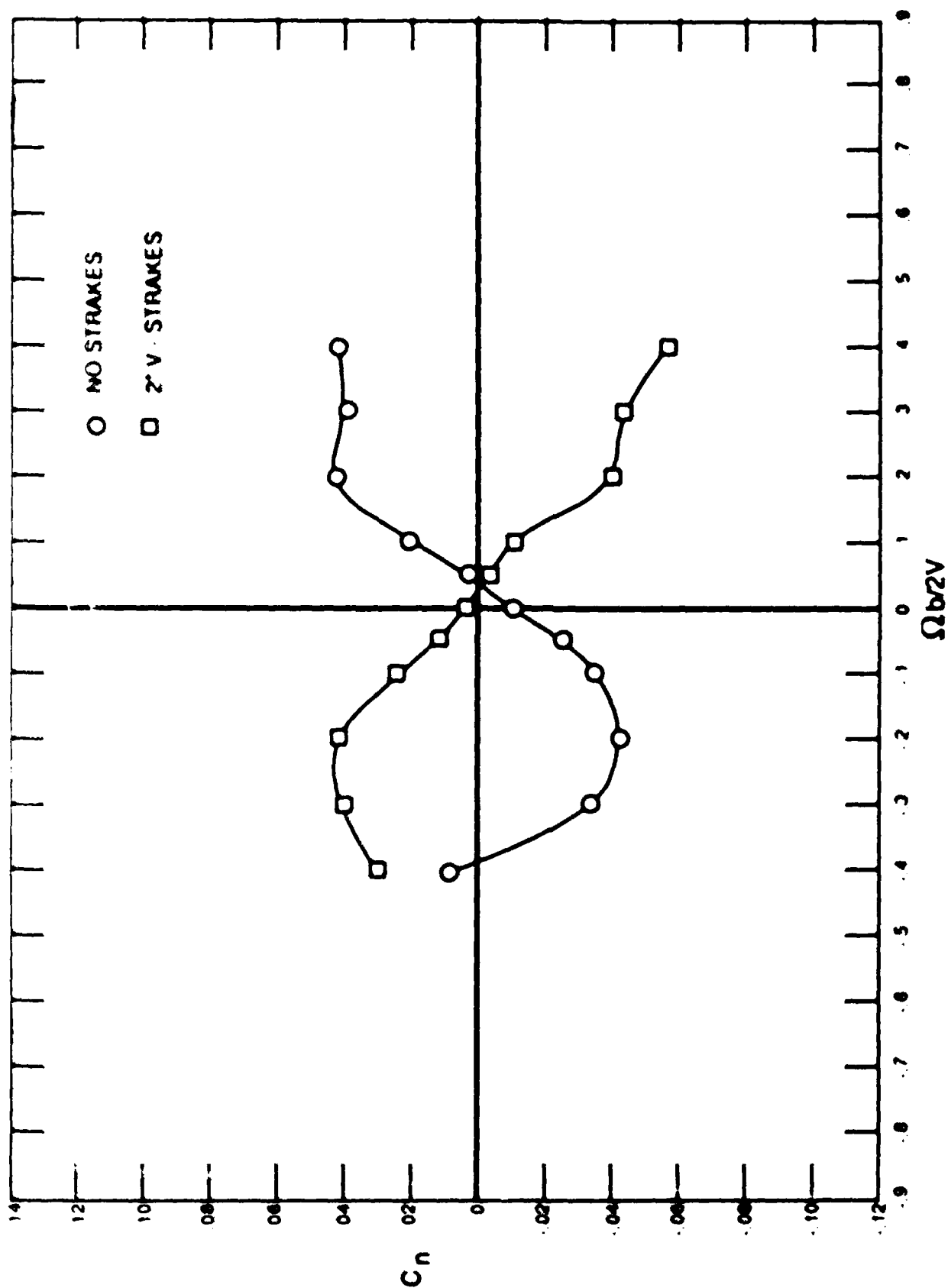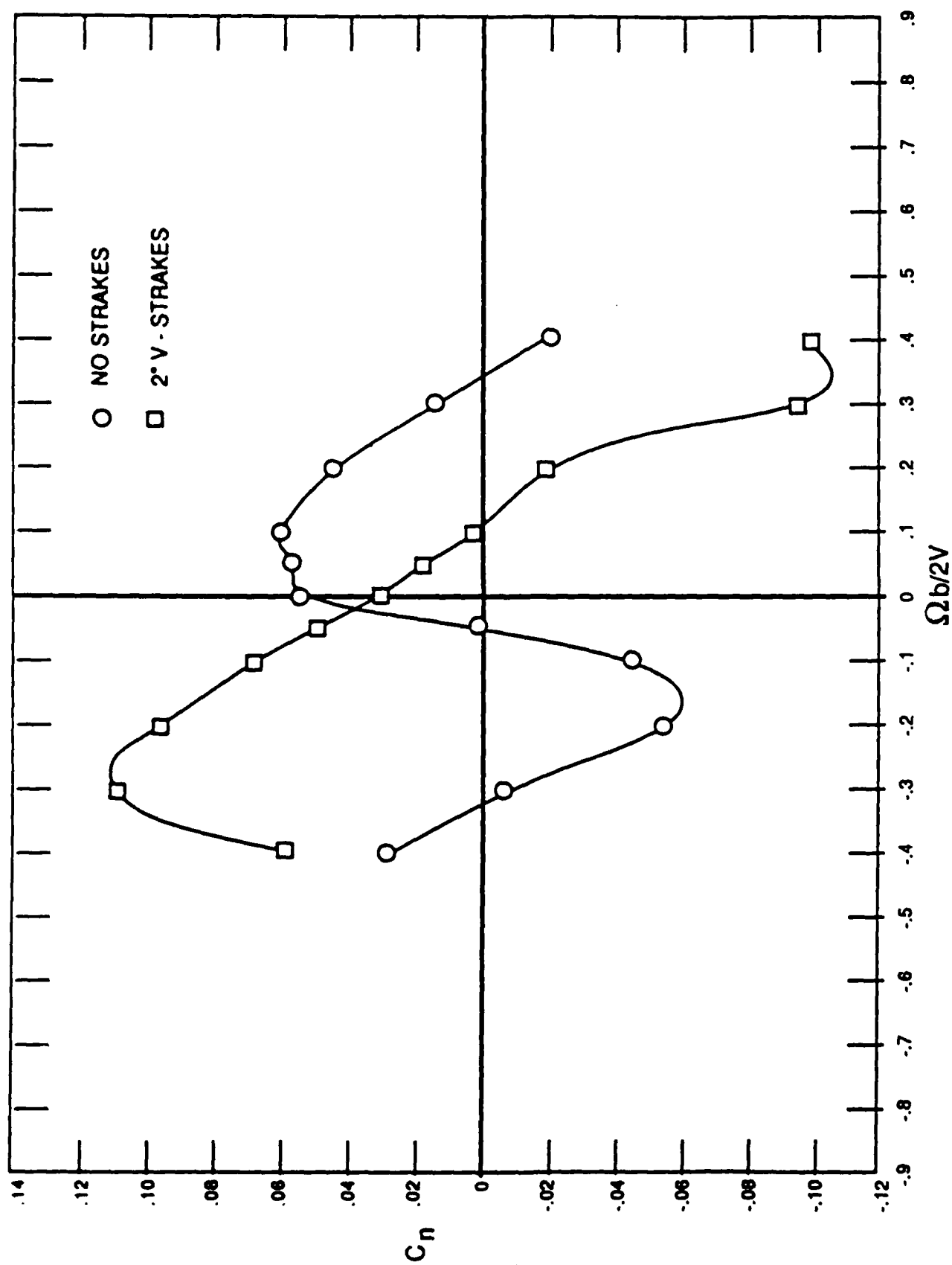
Figure 73. - Effect of V-strakes on body-alone directional stability
for a H/W = 0.8, FR = 4.5 forebody

Figure 74. - Effect of V-strakes on body-alone rotational yawing-moment coefficient characteristics for a H/W = 0.8. FR = 4.5 forebody

(a) α = 30°

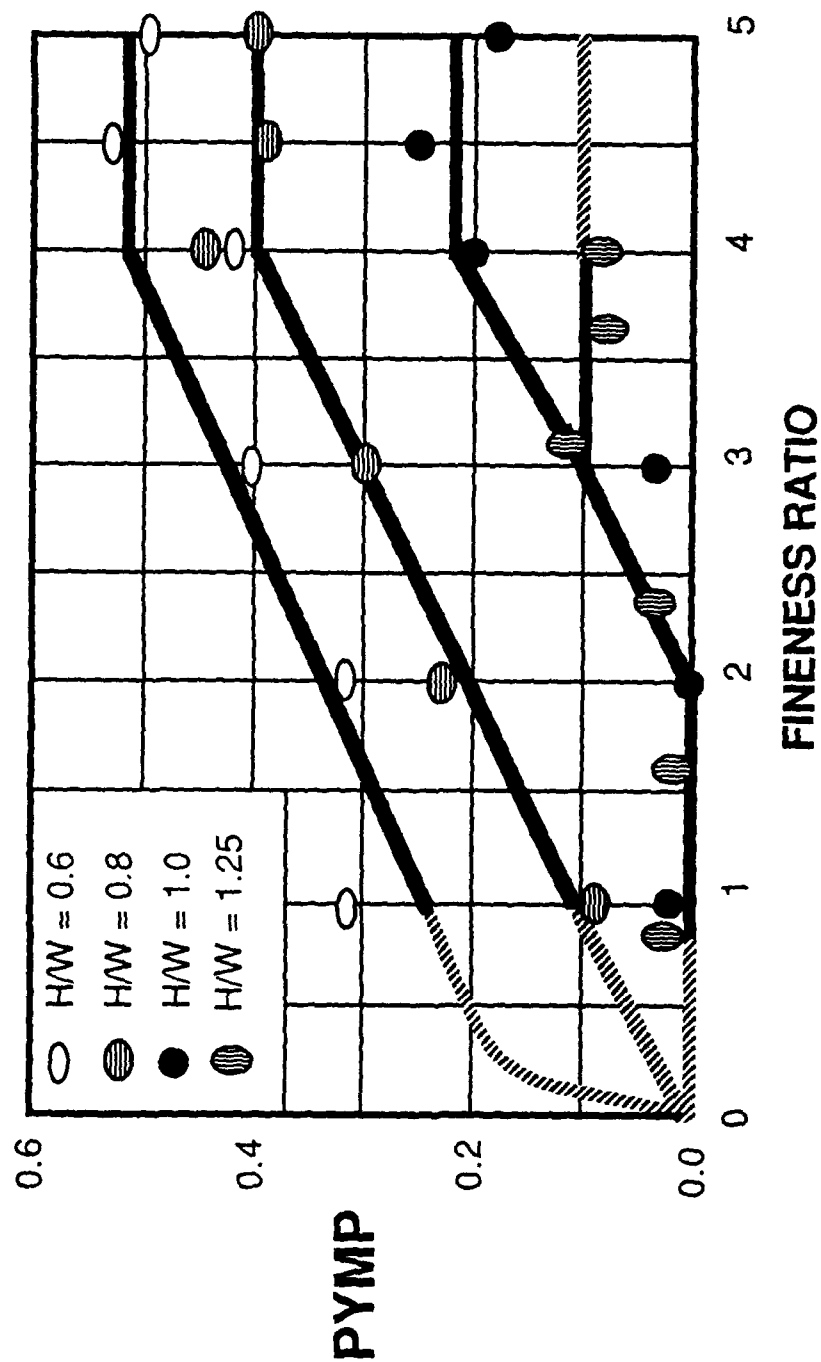Figure 74. - Concluded

b) $\alpha = 45°$

Figure 75.- Basic forebody propelling yawing-moment parameter values plotted as a function of fineness ratio for specified cross-sectional shapes
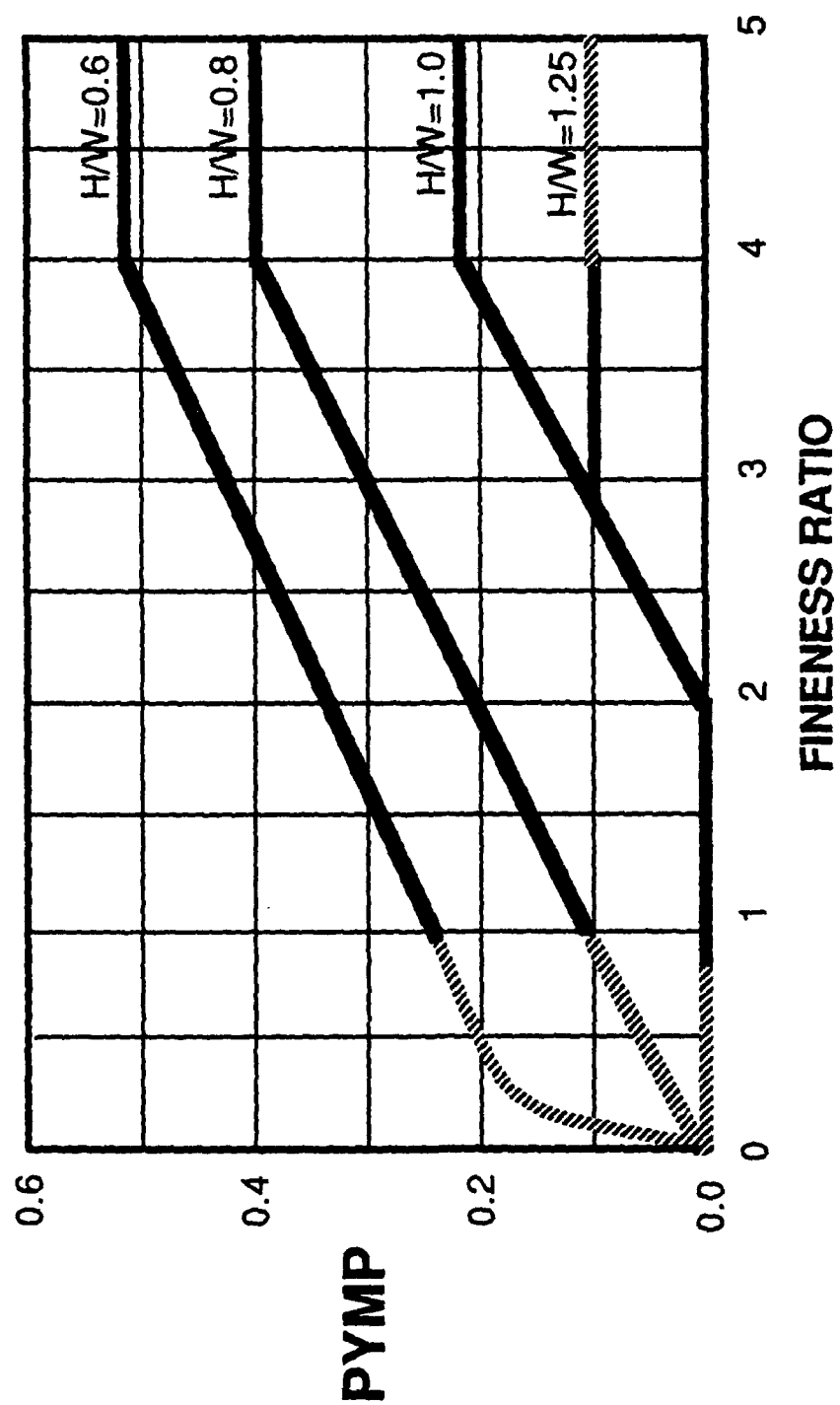
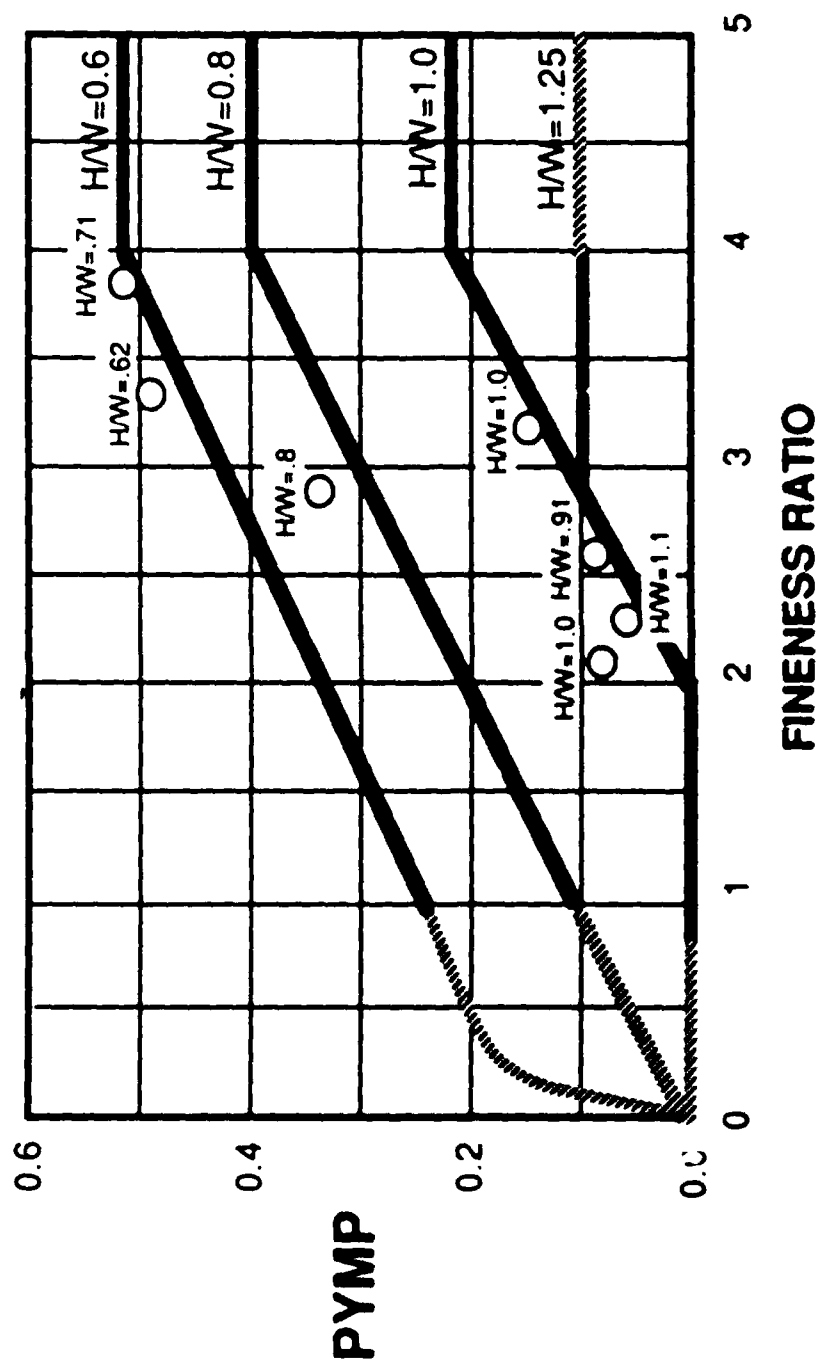Figure 76. - Propelling yawing moment parameter criterion chart

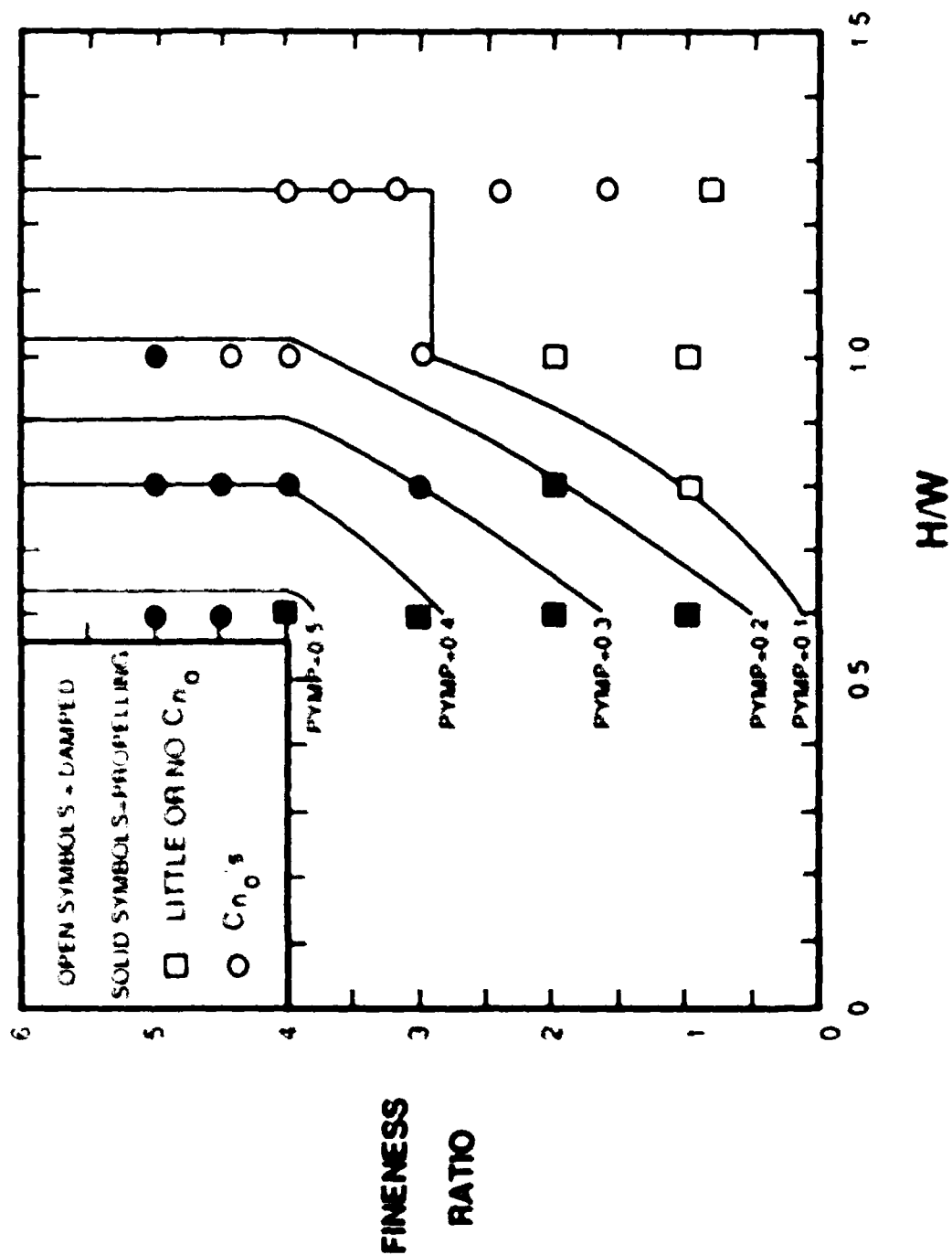Figure 77.- Propelling yawing-moment parameter values of actual airplane bodies compared with PYMP Criterion

Figure 78. - Constant PYMP boundaries as a function of forebody geometry compared with yaw characteristics of the tested forebodies
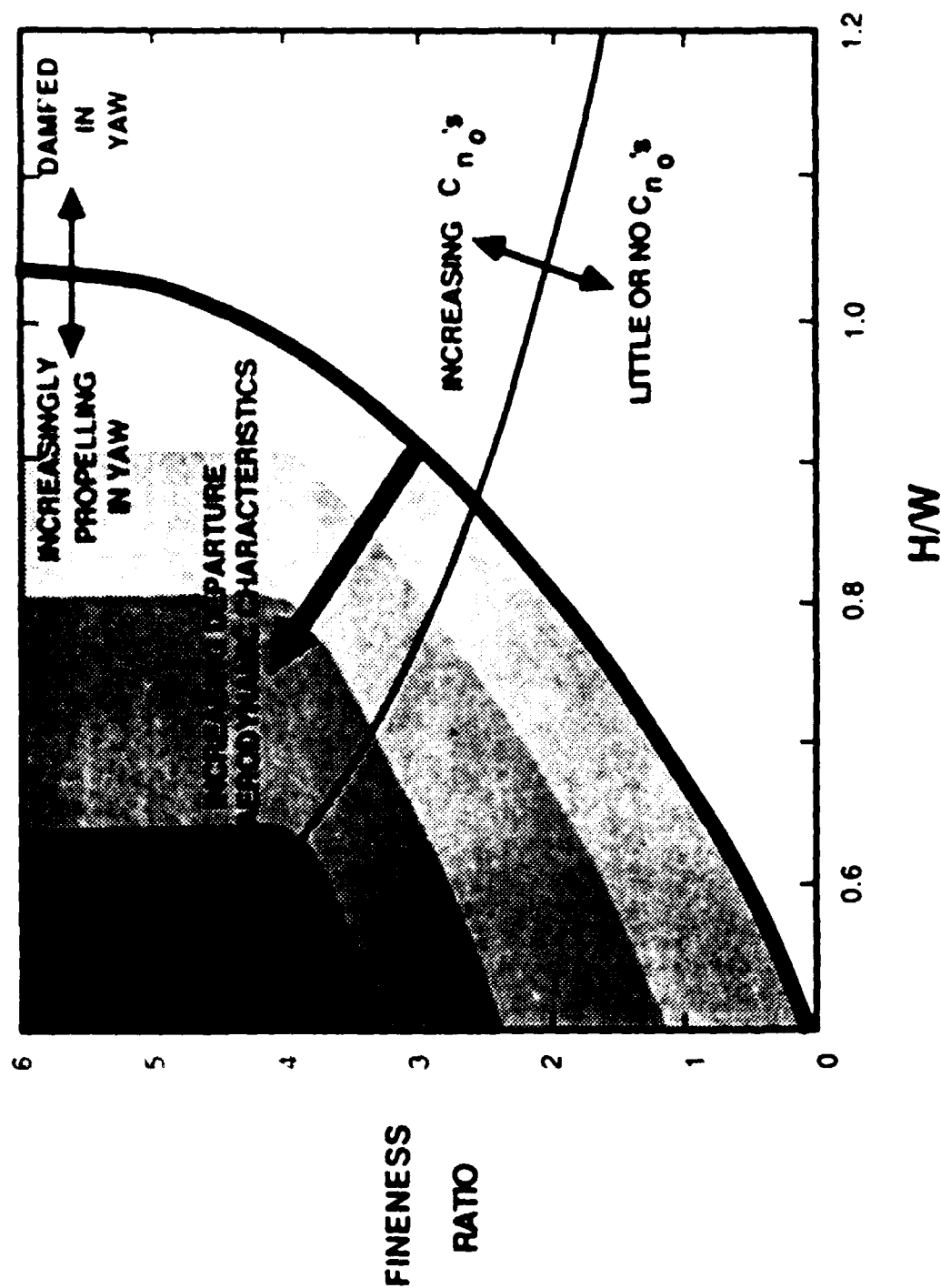
283

Figure 79. - Forebody design guide for minimizing adverse forebody aerodynamic characteristics at post-stall angles of attack